Transactions of the ASME

Journal of Fluids Engineering

Drag Reducing Polymer in Helicoidal Flow

J. T. Kuo[1]

L. S. G. Kovasznay[2]

The Johns Hopkins University,
Department of Mechanics & Materials
Science,
Baltimore, Md.

A novel flow configuration was explored for the study of the behavior of drag reducing polymers. A screw pump consisting of a smooth cylinder and a concentrically placed screw was used to create a strongly three-dimensional but essentially laminar flow. In the first phase of the study, the static pressure head developed by the screw pump was measured as a function of polymer concentration (polyox 10 to 100 ppm in water). A large increase of the developed head was observed that behaved in an analogous manner to drag reduction as far as concentration and straining of the polymer solution was concerned. In the second phase of the study, a new apparatus was constructed and the additional parameter of a superimposed through flow was included and the degree of failure of the superposition principle was established. Sensitivity of the phenomenon to chemicals like HCl, HNO₃, and NaOH in the polymer solution was also studied. When the effect of these chemicals on the polymer solution flow behavior was presented in terms of the pH value of the polymer solution, it showed a similar trend to those observed in drag reduction.

Introduction

It is a well-known phenomenon that the presence of a small amount of high polymer additives can reduce the drag remarkably in turbulent pipe flows and turbulent boundary layers. The unique and surprising feature of this phenomenon is that it takes only a very low concentration (a few parts per million) of certain polymers to show remarkable drag reducing effects. These very dilute polymer solutions (~ 10 ppm) show no measurable non-Newtonian behavior when using standard rheometric measurements. The unique feature of drag reduction by dilute polymer solutions becomes a challenging problem to those interested in the fundamental nature of turbulence. Many publications have appeared both from the fluid dynamicist and the molecular chemist point of view attempting to explain this interesting phenomenon. So far, the mechanisms of drag reduction are still not very well understood. The basic difficulty in dealing with turbulent flows is that the phenomenon can be assessed only by statistical means. On the other hand, if the large effect of polymer additives can be found in a deterministic flow pattern, it will be of great help to the study of drag reduction phenomenon.

The original idea for the work presented in this paper came from the intuitive suggestion that the large effects due to polymer additives may be connected to the intrinsically three-dimensional nature of turbulent flows. If this intuitive conjecture is correct, the effect of polymer additives would also be significant in "truly" three-dimensional laminar flows. A truly three-dimensional flow is defined as a flow where the velocity components in different directions are comparable in magnitude. The first naive picture of such a flow pattern was a Couette type flow with one wall being a flat plate and moving relative to another wavy wall. The flat plate may move at an angle with respect to the wavy wall and there may be an overall pressure gradient present. However, due to the difficulty in realistically creating such a flow system in the laboratory, a conceptually equivalent helicoidal configuration was chosen. This flow pattern was created by a screw pump system (see Fig. 1) which consists of a smooth hollow cylinder and inside it a concentrically placed smooth screw with a gap comparable to the dimensions of the screw threads. The center cylinder was free to rotate. The flow in the gap between the two cylinders resembles a "wrapped around" Couette flow.

With this novel flow configuration, there were two important questions to be asked: (1) Does the dilute polymer solution behave quite differently from the solvent in the suggested flow pattern? (2) Is the flow indeed laminar or is it just another way of manifesting the drag reduction by polymer addition in turbulent flows? The purpose of this research was to explore these questions. This paper presents the experimental study of the flow characteristics of water and dilute polymer solutions in the "screw-cylinder" configuration.

Experimental

Two sets of screw pumps were fabricated during the course of the investigation. The first screw pump system is shown in Fig. 1. The screw-cylinder system was placed vertically in an open rectangular Plexiglas tank. The screw was made of brass and was connected to a small d-c motor with speed control. The outer cylinder was made of Plexiglas. The tank was filled with liquid to the level above the threaded portion of the inner cylinder. With the center cylinder rotating, a certain head difference ΔH could be generated. A series of measurements
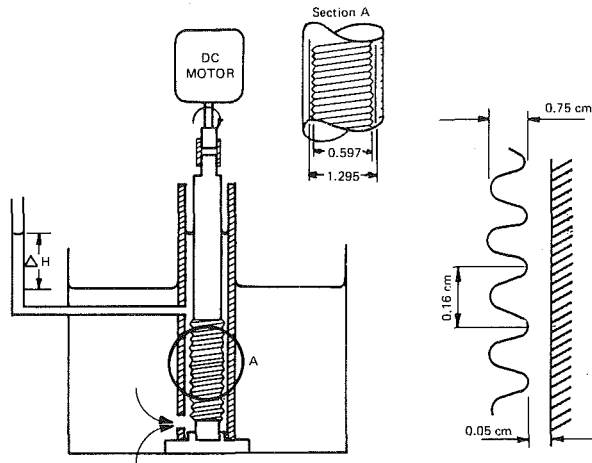
Fig. 1 Screw pump system (not to scale, dimensions in cm with uncertainty ± 0.0025 cm)

Fig. 2 Head difference versus rotational speeds at $Q = 0$ for different polymer concentrations (uncertainty in $\Delta H \pm 0.5$ cm, $n \pm 10$ rpm)

of ΔH at different rotating speeds was made using both water and polymer solutions of different concentrations. The polymer solution used in the tests was made with Polyox-FRA-1368-A-01. The characteristics of the polymer are:[3]

Chemical name – polyethylene oxide
Chemical structure – $-CH_2-O-CH_2-$
Molecular weight – 7.71×10^6
Intrinsic viscosity – 24.3 dl/gm.

At this stage, the tests were conducted with no net flow through the pump system. The results of the measurements were plotted as ΔH versus n (in rpm) and are shown in Fig. 2. When the polymer solutions were used, the ΔH would rise to a maximum value (in about 1 or 2 min), then slowly settle down to a lower value. This was due to the shear degradation of the polymer solutions in the gap. The ΔH shown in Fig. 2 represents the maximum observed values.

The results of this earlier study indicated that the screw pump could produce significantly larger head differences with dilute polymer solutions than with water. The results were encouraging and a second experimental configuration was designed.

In the modified flow configuration, a new parameter was introduced, namely, a net flow through the system. Before the screw was turned, the ΔH versus Q (flow rate) curve of the system would go through the origin. When the screw was turned, a head difference was produced and the ΔH versus Q curves were shifted. If there is a transition from laminar to turbulent flow in the system, we would expect some conspicuous shifting of the ΔH versus Q curves.

The second experimental facility is shown in Fig. 3 with details of the screw-cylinder assembly. The screw had 8 leads and a pitch of 2 threads/in. (25.4 mm) corresponding to a pitch angle of 9.5°. The screw was driven by a d-c motor (GE 5BN56HC2). The rotational speed was measured by a

[3] These were provided by the supplier of the polymer, the Naval Research Laboratory at Washington, D. C.
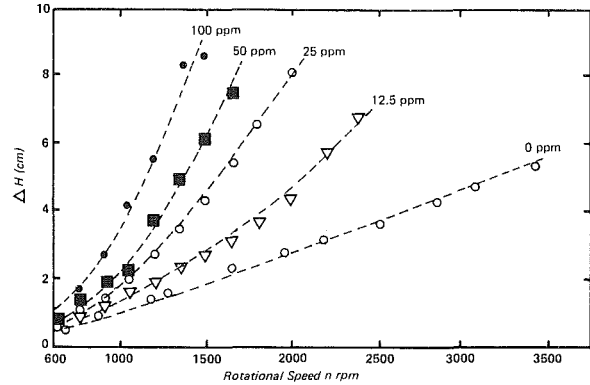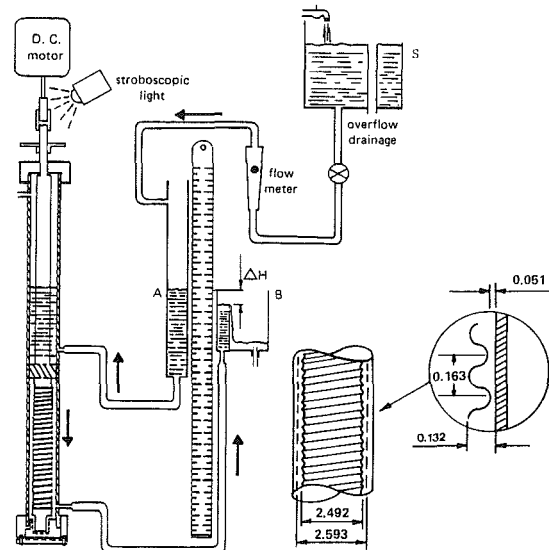
Fig. 3 Experimental apparatus and flow circuit (not to scale, dimensions shown in cm with ± 0.0025 cm uncertainty)

stroboscopic light (General Radio 631-B). The liquid was supplied from tank S which has an overflow tube to keep the liquid supplying level constant. The fluid went into the test cell through tank A and drained from tank B that has an overflow weir in order to maintain a constant liquid level. The vertical position of tank B was adjustable so that the liquid in tank A could be maintained at any reasonable level. The head difference ΔH between tanks A and B was measured by the steel scale placed between the two tanks.

The flow rates through the test section were measured by a rotameter with a maximum flow capacity of 290 ml/min for water at room temperature and atmospheric pressure. The rotameter was calibrated by metering the amount of liquid collected in a graduated cylinder within a certain time period.

———— Nomenclature ————

A = constant in equation (1)
B = constant in equation (1)
$H(n,Q)$ = difference in ΔH
ΔH = head difference developed by the screw pump (cm)
n = rotational speed in rpm
Q = flow rate (ml/min)
R = screw cylinder radius

T = Taylor number $\dfrac{\rho \omega R \delta}{\mu} \sqrt{\dfrac{\delta}{R}}$
α = power of Q defined in equation (1)
δ = gap width between cylinder and screw
σ = standard deviation
ρ = liquid density
μ = dynamic viscosity
ω = rotational speed (rad/s)
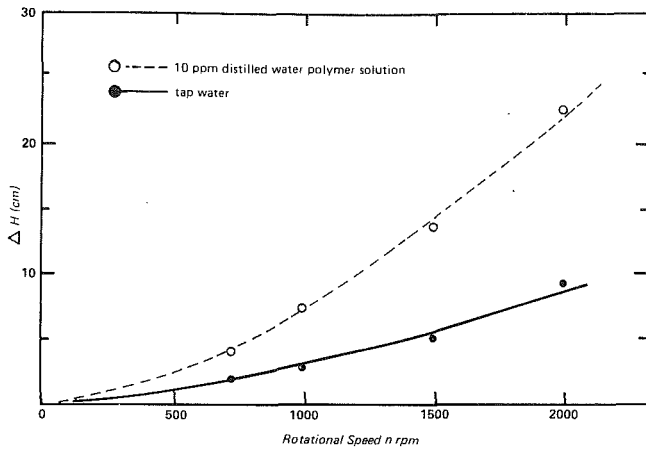
Fig. 4 Head difference versus rotational speeds at $Q=0$ for 10 ppm polymer solution and tap water (uncertainty in $\Delta H \pm 0.5$ cm, $n \pm 10$ rpm)
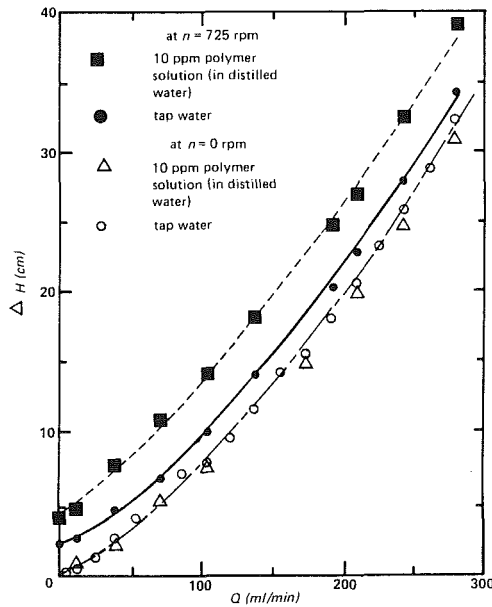
Fig. 5 Flow characteristics for 10 ppm polymer solution and tap water at $n=725$ rpm (uncertainty in $\Delta H \pm 0.5$ cm, $Q \pm 5$ ml/min and $n \pm 10$ rpm)

Fig. 6 Flow characteristics for 10 ppm polymer solution and tap water at $n=1000$ rpm (uncertainty in $\Delta H \pm 0.5$ cm, $Q \pm 5$ ml/min and $n \pm 10$ rpm)
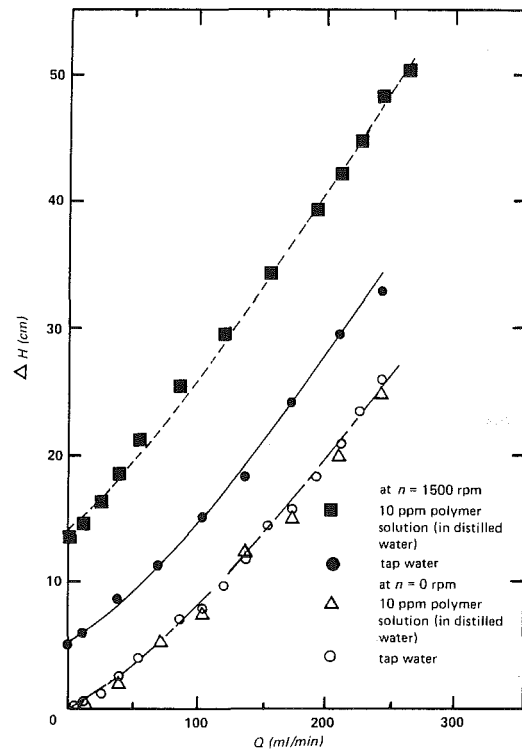
Fig. 7 Flow characteristics for 10 ppm polymer solution and tap water at $n=1500$ rpm (uncertainty in $\Delta H \pm 0.5$ cm, $Q \pm 5$ ml/min, and $n \pm 10$ rpm)

The calibration curves for water and 10 ppm Polyox solution were essentially identical. The agreement between the two calibration curves were within the measurement uncertainty (± 5ml/min max).

In the second phase of the investigation, the liquids used were water and a 10 ppm Polyox-FRA-1368-A-01 distilled water solution. The Polymer solutions were prepared and stored in a dark room under subdued light conditions to avoid possible photodegradation. The solution was first prepared at a higher concentration, then diluted to the desired concentration before testing. The solution stored in the dark room showed no appreciable aging degradation (in terms of ΔH measurements in the test facility) between a fresh solution (within 24 hr of preparation) and a ten-day old solution. In all the tests, the solutions were discarded after they went through the test facility.

Results

Since the head difference ($\Delta H = \Delta H(n,Q)$) is a function of both rotation, n, and through flow, Q, three types of operation were performed:
  (1) Measurement of "static" head difference ΔH as a

function of the screw rotational speeds $\Delta H = \Delta H(n,0)$ with no flow through the system ($Q=0$).
  (2) Measurement of the flow characteristics of the screw-cylinder system to obtain the ΔH versus Q relation with the screw at rest ($n=0$).
  (3) Measurement of the combined effect with both through flow and screw rotation.
  The results are shown in Figs. 4 to 9. Figure 4 gives the ΔH at different rotational speeds in the no-through flow
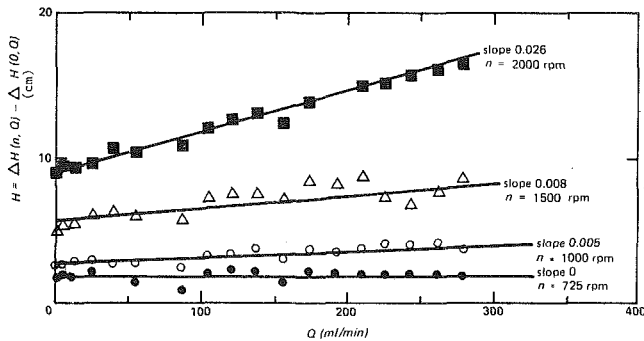
Fig. 8 Shifting of ΔH as a function of Q at different rotational speeds for tap water (certainty in $\Delta H \pm 0.5$ cm, $Q \pm 5$ ml/min and $n \pm 10$ rpm)

Fig. 9 Shifting of ΔH as a function of Q at different rotational speeds for 10 ppm distilled water polymer solution (uncertainty in $\Delta H \pm 0.5$ cm, $Q \pm 5$ ml/min and $n \pm 10$ rpm)

situation. The results are similar to the earlier measurements indicating a large effect due to the polymer additive. Figures 5 to 7 show the shifting of ΔH versus Q curves at different rotational speeds. When the center screw was at rest, the ΔH versus Q curves for water and the polymer solution were essentially the same. In order to investigate the shifting of the curves more closely, the data were plotted in the amount of shifting $(H(n,Q) = \Delta H(n,Q) - \Delta H(0,Q))$ as a function of the flow rates (see Figs. 8 and 9). The slopes of the straight lines determined by the least square fit indicate the degree of unparallel shifting. For water, at $n = 725$ rpm, the shifting was essentially parallel. At higher rotational speeds, the shifting became gradually unparallel shift was obvious even at $n = 725$ rpm. The amount of unparallel shifting was larger for the polymer solution than for water at the same rotational speed.

ΔH can be related to Q by an expression

$$\Delta H = AQ^\alpha + B \qquad (1)$$

where A, B, and α constants. B is directly proportional to the rotational speed of the screw. Table 1 gives the values of A, B, and α for water and the 10 ppm polymer solution at different rotational speeds. α was found between 1 and 1.4. The numerical values of A, B, and α were deduced from the log-log plot of the test data using the least squares fitting method. The unparallel shifting of the flow characteristic curves is also manifested in the decreasing of α higher rpm.

Discussion

(a) Flow Characteristics. It is difficult to show conclusively that the flow was laminar in the screw-cylinder test cell. Injection of dye into the gap region showed that at least at very slow rotation the flow was clearly laminar. When the rotational speed reached the test range of 600 to 2000 rpm, the dye spread around the circumference and appeared to be mixed uniformly. No definite conclusion could be made on whether or not the smearing of the dye around the circumference was due to turbulence or merely the overlapping of the streak lines. On the other hand, trying to reason from the data itself, we may state that from the experiments with water taken at $n = 725$ rpm and 1000 rpm, the characteristic curves were almost parallel. For the polymer solution, the curve fit results in Table 1 show that the shifting was not parallel, although the change in α was fairly small. This change did not appear to be of the same order of magnitude as one would expect when the flow changed from laminar to turbulent.

In the study of hydrodynamic instability of Newtonian fluids between two rotating cylinders [1], the flow instability was characterized by the Taylor number, defined as $T = \rho \omega R \delta / \mu \sqrt{\delta/R}$. The flow is laminar when $T < 41.3$ and turbulent when $T > 400$, and in between the flow is laminar with Taylor vortices. The Taylor number in the second ex-
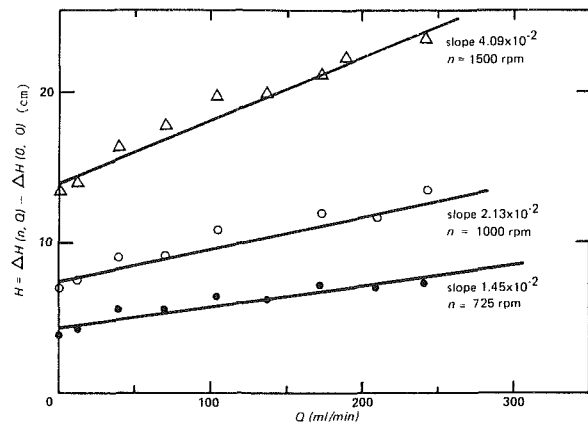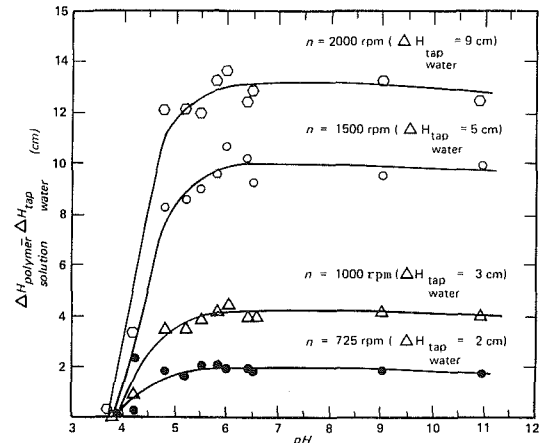
Fig. 10 Effect of chemicals (HCl or NaOH) on the polymer solution at $Q = 0$ (uncertainty in $\Delta H \pm 0.5$ cm, pH ± 0.1)

Table 1 Curve fit of the test data $\Delta H = AQ^\alpha + B (Q \le 242$ ml/min)

Rotational speed(rpm)	α	A	B(cm)	σ(cm)
Water				
0	1.26	0.0247	0	0.479
725	1.3	0.0204	2 ± 0.5	0.319
1000	1.28	0.0234	2.9	0.426
1500	1.11	0.061	5.0	0.788
2000	1.11	0.0686	9.1	0.849
10 ppm Polyox-FRA				
0	1.39	0.0122	0	0.519
725	1.13	0.0562	3.8 ± 0.5	0.494
1000	1.12	0.064	6.8	0.475
1500	1.15	0.0644	13.5	0.962

σ: Estimated standard deviation of the differences between the ΔH predicted by equation (1) and the measurements.

periment was in the range of 250 to 690. Based on this, the guess was that the flow in the test cell could be laminar with secondary flows at $n = 725$ rpm and 1000 rpm.

As mentioned earlier, the original idea of this study was to expect a large polymer solution effect in a three-dimensional flow situation where all the three velocity components were comparable in magnitude. The circumferential velocity at the screw surface was about 90 cm/s at $n = 725$ rpm, which was much higher than the average down flow velocity of 8 cm/s at $Q = 200$ ml/min. A circumferential velocity of 8 cm/s at the screw surface corresponded to $n \approx 63$ rpm, although at this low rpm, no polymer effect could be discerned. Apparently, the onset of the large polymer effect was due to the shearing and stretching of the polymer solution in the circumferential direction rather than merely the result of a three-dimensional flow situation.

Large effects of dilute polymer solutions in nonturbulent flows such as flow around the stagnation point of a Pitot tube probe [2], flow past a circular cylinder [3], or flow through a porous media [4] have been reported in the literature. The onset of the polymer solution effects in these flow situations was found related to a time scale which is proportional to the inverse of the onset strain rate [2, 5]. In this study, no special efforts were made to study the onset of the polymer effect. Judging from the data trend in Figs. 2 and 4, it did not appear that there would be a clear onset rpm. However, we believe that when n is below a certain rpm, it will become difficult to measure the dilute polymer solution effects. The trend of the data seemed to indicate that this would be the case when n was below 300 rpm. This was based on extrapolating the polymer solution data in Fig. 4 to find the rpm where ΔH becomes less than 1 cm which is the uncertainty range in ΔH measurement. The strain rate at $n = 300$ rpm was about 400 s^{-1}. This was estimated by dividing the circumferential velocity at the surface of the screw with the average gap width. The onset strain rate for Pitot tube error in a polymer solution varies with polymer concentration and molecular weight [2, 5]. Fruman and Tulin [2] indicated that for Polyox-FRA, the onset strain rate for Pitot tube error is on the order of 10^2 s^{-1}. The Pitot tube pressure defect in a polymer solution was found increasing with strain rate at the stagnation point and the rate of increase of pressure defect was higher for higher concentration polymer solutions [2]. This is similar to what we have observed in the no-net flow tests (Figs. 2 and 4) where the head developed by the screw pump was increasing with polymer solution concentration and screw rotational speed which is proportional to the strain rate.

(b) **Effect of Chemicals.** During the course of this investigation, it was accidentally observed that when the polymer solution was prepared with tap water, it behaved essentially like water in the screw pump. Only with higher concentration was it possible to observe a polymer effect with the tap water polymer solution. This observation initiated a series of studies on the effect of pH value on the polymer solution, although we later learned that the anomalous effect of the tap water was probably caused by some chemicals like chlorine in the tap water instead of a pH effect. Distilled water polymer solutions with different pH values were prepared by adding NaOH or HCl. Effect of pH values on ΔH at different screw rotational speeds is shown in Fig. 10. The results showed that a pH value between 6 and 7 gave the highest ΔH. The pH effect leveled off with further increase in pH. The pH effect on the drag reduction in turbulent pipe flow was reported by Little, et al. [6], using Polyacrylic Acid (PAA) homopolymer which is a highly flexible chain molecule, the expansion and hydration of which is sensitive to pH change in solution. The pH effect shown in reference [6] in percent of drag reduction versus pH was strikingly similar to that observed in Fig. 10.

The pH value of the tap water in the laboratory was about 7.3. Obviously, pH value variation was not the cause for the nullification of the polymer effect in the 10 ppm tap water polymer solution. Several runs were made using HNO_3 to make the polymer solution acidic and the results were similar to those with HCl. The reason for the polymer solution to lose its effectiveness in the presence of HCl or HNO_3 may be associated with some molecular structure changes due to these chemicals. For example, the chlorine ion (Cl^-) might cause the long polymer molecular chain to break at the carbon-oxygen bond and form a product like

$$
\begin{array}{ccc}
H & H \\
| & | \\
R - C - C - Cl \\
| & | \\
H & H
\end{array}
$$
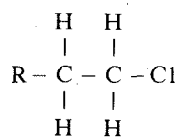
Or, it may be associated with conformation changes in the polyethylene oxide chains caused by the low pH (acidic) environment. On the other hand, adding NaOH did not affect the polymer solution effect significantly as indicated by those data points at high pH values (>7) in Fig. 10, indicating that NaOH did not disturb the Polyox-FRA molecular structure or conformation.

Conclusions

(1) A large effect of dilute polymer solution was observed in a novel flow configuration which is a flow in the annulus between a smooth outer cylinder and an inner rotating smooth screw.

(2) The polymer effect observed in this novel flow configuration was in many aspects analogous to the drag reduction phenomenon in turbulent flows and other anomalous effects in laminar flows as far as concentration and strain rate were concerned.

(3) It did not appear that there would be a clear onset point for the polymer solution effect in the screw pump system; rather, the polymer effect was developed continuously from laminar flow to turbulent flow.

(4) Chemicals such as HCl and HNO_3 which create an acid environment reduce the dilute polymer solution effect on the flow behavior.

The significance of this work is that this unique flow configuration, which is amenable to theoretical analysis, was proved to be an effective and well-defined flow system for studying the effect of dilute polymer solutions on fluid flow. For further studies, emphasis should be on pursuing flow visualization experiments to identify the flow patterns in the annulus and develop a theoretical model to incorporate the non-Newtonian effect of polymer solutions for predicting the observed polymer effect on the flow behavior.

Acknowledgments

References

1 Schlichting, H., *Boundary-Layer Theory*, 6th Edition, McGraw-Hill, 1968, pp. 500-504.

2 Fruman, D. H., and Tulin, M. P., "Dilute Polymer Flows at High Strain Rates: A Correlation of Data," *Phys. Fluids*, Vol. 21, No. 11, Nov. 1978.

3 James, D. F., and Acosta, A. J., "The Laminar Flow of Dilute Polymer Solutions Around Circular Cylinders," *Journal Fluid Mech.*, Vol. 42, Part 2, 1970, pp. 269-288.

4 James, D. F., and McLaren, D. R., "The Laminar Flow of Dilute Polymer Solutions Through Porous Media," *Journal Fluid Mech.*, Vol. 70, Part 4, 1975, pp. 733-752.

5 Berman, N. S., "Flow Time Scales and Drag Reduction," *Phys. Fluids*, Vol. 20, No. 10, Part II, Oct. 1977.

6 Little, R. C., et al., "The Drag Reduction Phenomenon. Observed Characteristics, Improved Agents, and Proposed Mechanisms," *Ind. Eng. Chem. Fundam.*, Vol. 14, No. 4, 1975, pp. 283-296.

APPENDIX

Uncertainty Analysis

The measured ΔH is a function of the flow rate Q, the screw rotational speed n and the polymer concentration. ΔH was measured by a scale with the smallest division in 0.1 cm. Considering only the uncertainty in visual observation, ΔH can be read accurately within $\pm$ 0.2 cm. However, the major contributing factors to the uncertainty of ΔH are the uncertainties in Q, n, and the polymer concentration. The un-

certainties of Q, n, and polymer concentration were estimated as follows:

Q: ± 5 ml/min
n: ± 10 rpm
polymer concentration: ± 1 ppm

The combined effect of these factors on ΔH was about ± 0.5 cm estimated based on a few samples of repeated measurements.

The uncertainty in pH value measurement is within ± 0.1 with 20 to 1 odds.

L. S. G. Kovasznay[2]

I. Tani
Presently Professor Emeritus,
University of Tokyo,
c/o National Aerospace Laboratory,
1880 Jindaiji, Chofu, Tokyo, Japan

M. Kawamura
Presently Professor,
Faculty of Engineering,
Hiroshima University,
Hiroshima, Japan

H. Fujita
Presently Senior Researcher,
Mechanical Engineering Research Laboratory,
Hitachi, Ltd.,
Tsuchiura, Ibaraki, Japan

Instantaneous Pressure Distribution Around a Sphere in Unsteady Flow[1]

Pressure fluctuations on a small sphere in a periodically pulsating jet are measured in relation to the study of measurements of instantaneous static pressure in unsteady flows, where the wavelength of unsteadiness is much longer than the probe dimensions and the amplitude of the velocity fluctuation is small. Both the instantaneous pressure on the sphere and the instantaneous velocity of the flow field in the absence of the sphere are measured by means of periodic sampling and averaging techniques. The measured surface pressure is expressed in terms of the measured velocity and acceleration of the flow. A simple inviscid theory is developed and compared with the experimental results. An application of the present results to the correct determination of instantaneous static pressure in unsteady flows is discussed.

Introduction

Measurement of the instantaneous values of static pressure within a turbulent flow is still an unresolved problem because the pressure probe placed in the unsteady flow field represents a solid boundary and the surface pressure at a point always contains important contributions from the inertial effects in the flow around the body. For steady flows, it is relatively easy to design "static" probes that indicate the static pressure by using potential theory to calculate the pressure distribution around the body of the probe, but the same approach does not give the correct instantaneous static pressure in unsteady flow. Although there are several works which try to measure pressure fields in unsteady flow, inertial effects on the probe body are either neglected [1, 2] or the compensation process is not straightforward [3].

In order to better understand the behavior of small probes placed in unsteady flows, an experiment was performed in a relatively simple configuration. A small sphere was placed in a periodically pulsating jet and the instantaneous surface pressure fluctuations were measured. Since there is a strong random component of fluctuations due to the turbulence in such a flow, and the objective is not to measure the high frequency fluctuations associated with the turbulence, a special signal processing technique, namely, periodic sampling and averaging, was performed on all signals in order to enhance the periodic (or deterministic) component and to suppress the random component. Furthermore, a simple inviscid theory was developed in order to provide a guide for

the assessment of the results and the experimental results were compared with it.

Experimental Facility and Procedure

The time-dependent pulsating flow used for the measurements is produced by the scheme indicated in Fig. 1. The steady air flow provided by the centrifugal blower was divided into two streams, one flowing through duct D_1 and the other through duct D_2. The component discharged through duct D_1 was periodically intercepted by a rotating disk with 16 holes. As a result, periodic pressure fluctuations were also induced in the other branch, D_2, and the discharge from this branch formed the pulsating air jet. The frequency and amplitude of the velocity fluctuations in the jet could be varied up to 500 Hz and to 6 m/s peak to peak, respectively, by varying the speed of the rotating disk and the standoff between the disk and the nozzle attached to D_1.

The pulsating velocity of the jet was measured by a constant temperature hot-wire anemometer [4] connected to a linearizer [5]. Since the linearized hot-wire signal contained random fluctuations due to turbulence in the jet, the technique of periodic sampling and averaging was performed over a large number (typically 1000–2000) of sweeps and the random component was correspondingly reduced by a factor of $\sqrt{1000} - \sqrt{2000}$, or 30–40. As a result, most of the random component was suppressed and only the periodic or deterministic component was recovered. The required synchronizing pulses were obtained from the rotating disk using a photocell pick up. Figure 2 shows an example of the processed periodic velocity fluctuations measured at a distance $x = 6$ cm from the nozzle at a pulsating frequency of $f = 450$ Hz. This averaging technique was also used to obtain the periodic pressure fluctuations on the sphere as described in the following.
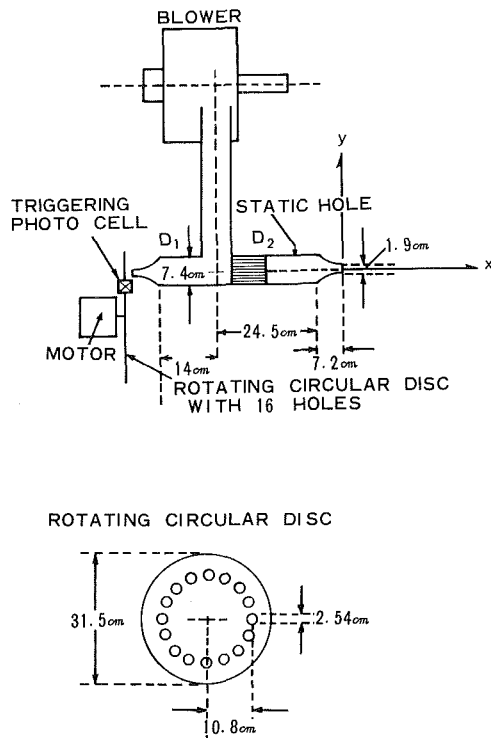
Fig. 1 Pulsating flow generator

Fig. 2 Pulsating velocity of the jet at x = 6 cm, f = 450 Hz
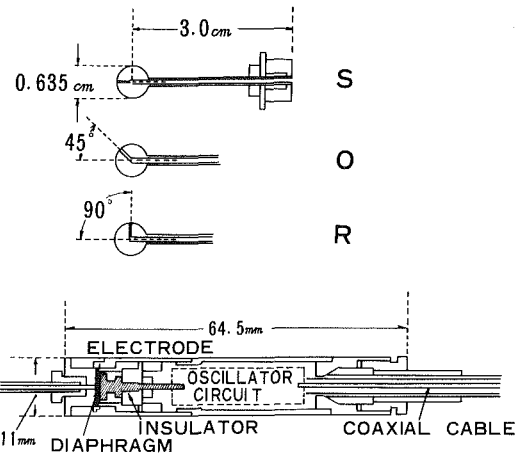
Fig. 3 Three sphere models and condenser microphone

Three spheres of the same diameter (6.35 mm), but with different pressure tap locations, were used as models. They are designated as S, O, and R as shown in Fig. 3. The diameter of the pressure tap was 0.5 mm, and it was located on the meridian at the angles $\theta = 0$ deg (opposite stem), 45 and 90 deg for S, O, and R, respectively. The sphere could be rotated around its center up to a maximum angle of ± 20 deg and by using all three models, it was possible to orient the pressure taps on the spheres at angles between -20 and 110 deg in increments of 5 deg.

The pressure tap was connected to a frequency modulated condenser microphone through the stem as shown in Fig. 3. In the case of pulsating frequency of 350 Hz and the sphere located at $x = 6$ cm, a transistorized version of the circuit used by Einstein and Li [6] was employed as the FM oscillator and the detector. In all other cases, an improved circuit with a carrier frequency in the commercial FM broadcast band was built into the probe as shown in Fig. 3 and an FM receiver was used as the detector.

The overall static sensitivity was found to be 570 and 24 μV-Pa, respectively. The dynamic sensitivity and the frequency response of the probe would have been best obtained by the "coupler method," which is based on a comparison with a standard microphone. Unfortunately, however, a standard microphone was not available and an alternative procedure was used by utilizing theoretical relations.

The overall frequency characteristics of the pressure probe

are generally limited by the resonance in the pipe leading to the microphone, as well as by the Helmholtz resonance of the cavity in front of the microphone diaphragm. The relative frequency response of the probe may be calculated theoretically by considering these effects as described by Kono [7]. Frequency responses calculated in this way are shown in Fig. 4 for the combination of a pipe diameter 1.0 mm and length 20.5 mm and for two values of the cavity volume 1.65 and 89.1 mm³, respectively. Resonances occur around 2500 and 800 Hz, respectively. The absolute value of the dynamic sensitivity was then determined as follows. According to the theoretical calculation given in a later section, the pressure fluctuation on a sphere is made up of two terms, one being proportional to the fluctuating velocity itself and the other being proportional to the time derivative of the fluctuating velocity. At the forward stagnation point, the non-dimensional coefficients of the two terms are calculated to be 1.0 and 1.5, respectively. By assuming an arbitrary phase lag between the pressure fluctuation on the sphere and at the microphone diaphragm due to the connecting pipe and the cavity volume, the ratio of the two coefficients for the stagnation point was calculated from the fluctuating velocity

_____ Nomenclature _____

A, B, C_n = coefficients
a = radius of a sphere
k = wave number
p = pressure
r, θ, λ = spherical polar coordinates

T = period of fluctuation
t = time
U_0 = mean streamwise velocity
u = fluctuating streamwise velocity

V = velocity
x, y, z = Cartesian coordinates
ϵ = constant
ρ = density of air
Φ_0, Φ_1, Φ_2 = velocity potentials
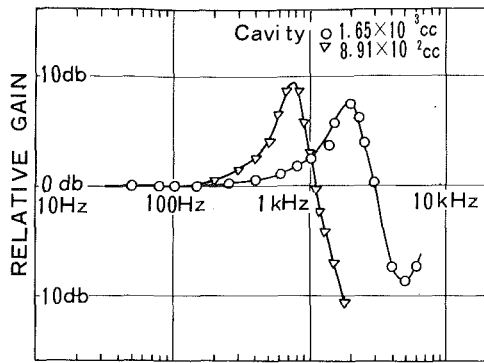
Fig. 4 Calculated frequency response of microphone with cavities
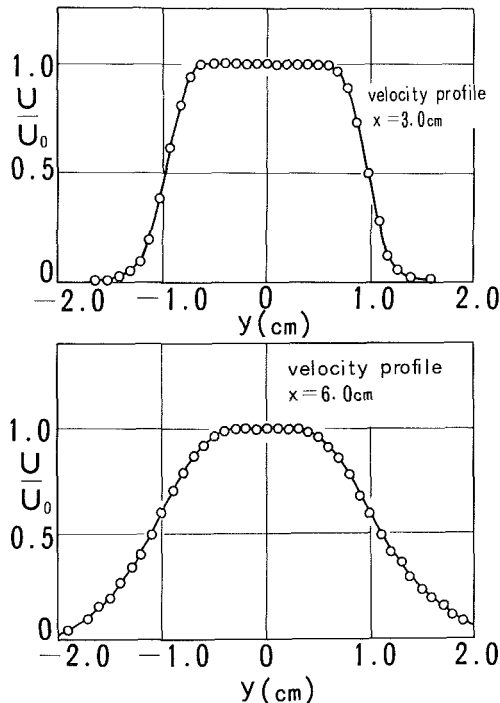
Fig. 5 Mean velocity distribution of steady jet at x = 3 and 6 cm

Fig. 6 Instantaneous velocity profiles for pulsating jet at x = 5 cm, f = 450 Hz, for various phase angles (n) in the period of oscillation (T)
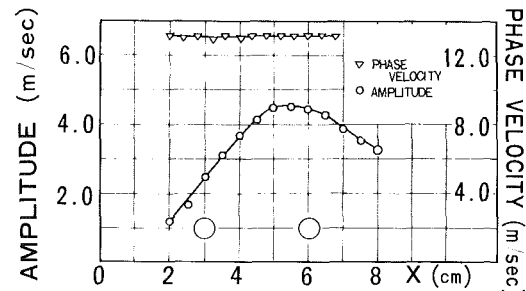
Fig. 7 Peak-to-peak amplitude and phase velocity of pulsating jet along the center line at f = 450 Hz

and its time derivative obtained by a hot-wire placed at the location of the sphere center in the absence of the sphere by equation (2) as described in the Experimental Results Section. The phase lag was varied until the ratio of the coefficients obtained coincided with the theoretical value of 1.5. The dynamic sensitivity was then determined in such a way that the coefficient of the first term had a value of 1 at the stagnation point.

The values of the phase lag and the dynamic sensitivity so determined were as follows:

Frequency(f)	Location(x)	Phase lag	Dynamic sensitivity
300 Hz	3 cm	5 deg	35 μV/Pa
350 Hz	6 cm	1 deg	611 μV/Pa
450 Hz	3 cm	5 deg	32 μV/Pa
450 Hz	6 cm	30 deg	33 μV/Pa

No systematic trend is seen from these values. The small value of phase lag for the case $f = 350$ Hz and $x = 6$ cm seems to be attributed to a relatively large cavity volume. The process of the pressure change is adiabatic for the frequency range above 100 Hz, but is isothermal at the static calibration. This difference could result in the higher dynamic sensitivity of the probe as compared to the static calibration.

Experimental Results

The entire set of measurements was obtained for a mean velocity of about 20 m/s on the jet axis. Figure 5 shows the velocity distribution across the steady, nonpulsating jet at two stations, $x = 3$ and 6 cm downstream from the nozzle. The core of the jet, defined as the region in which the velocity is greater than 90 percent of the mean velocity U_0 on the axis, has a diameter of 1.55 cm at $x = 3$ cm and a diameter of 1.28 cm at 6 cm. Figure 6 shows several instantaneous velocity profiles across the fluctuating jet at a station $x = 5$ cm for a pulsation frequency of 450 Hz. The core diameter as defined herein is about 1.20 cm, which is less than that of the steady jet. Figure 7 shows the streamwise variation of both the peak-to-peak amplitude and the phase velocity of the velocity fluctuation along the jet axis. Circles indicate the location and size of the sphere. For a sphere placed at $x = 3$ cm, the ratio of the core diameter of the steady jet to the sphere diameter is 2.4, but the amplitude of velocity fluctuation varies by as much as 30 percent in the region occupied by the sphere. For a sphere placed at $x = 6$ cm, the variation in fluctuation amplitude becomes negligible, but the ratio of the diameters is reduced to 2.0. The phase velocity as determined by two hot-wires separated by a fixed streamwise distance is approximately constant over the region covered by the experiment. The observed phase velocity was 13.2 m/s, or about two-thirds of the mean velocity at the jet axis. The phase velocity is regarded as the convection velocity of a traveling vortex ring produced at the nozzle exit.
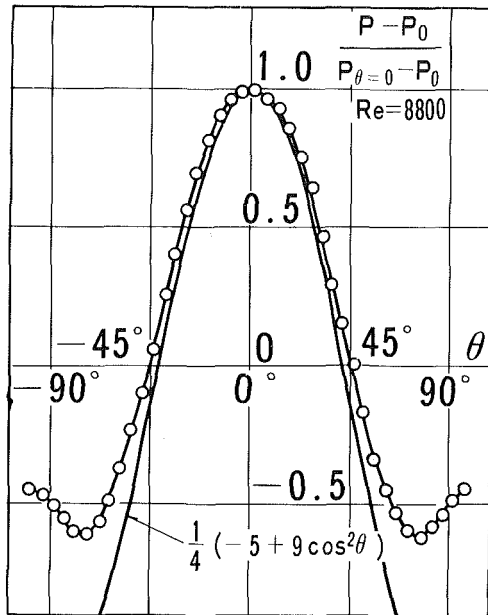
Fig. 8 Pressure distribution around the sphere in steady flow (solid line indicates inviscid theory)
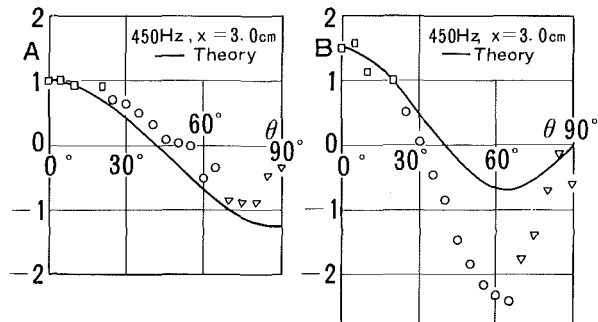
Fig. 9 Coefficients A and B at x = 3 cm, f = 450 Hz, residual error of pressure by least squares fitting is 6.0 percent

Fig. 10 Coefficients A and B at x = 3 cm, f = 300 Hz, residual error of pressure by least squares fitting is 10.2 percent
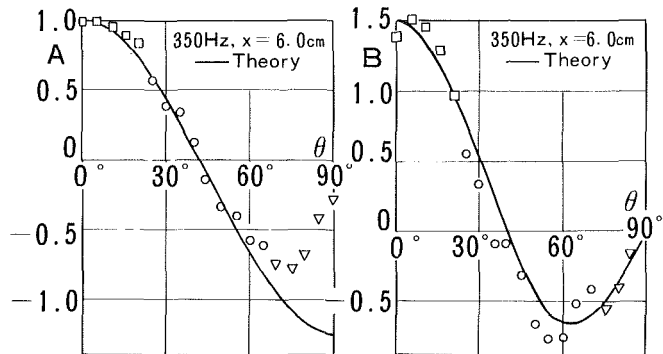
Fig. 11 Coefficients A and B at x = 6 cm, f = 350 Hz, residual error of pressure by least squares fitting is 9.7 percent
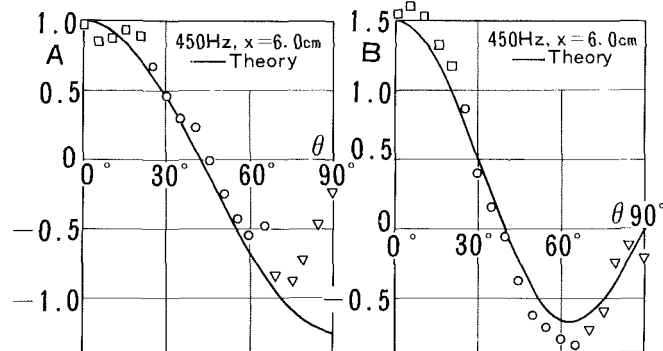
Fig. 12 Coefficients A and B at x = 6 cm, f = 450 Hz, residual error of pressure by least squares fitting is 6.0 percent

Figure 8 shows the measured mean pressure distribution on the sphere placed at $x = 3$ cm in the steady jet. The calculated potential flow distribution given by $(-5 + 9 \cos^2 \theta)/4$ is also shown for comparison. The Reynolds number based on the sphere diameter and on the mean velocity is $2U_0 a/\nu = 8.8 \times 10^3$. As shown later in the theory, the instantaneous pressure at a point on the surface can be expressed as

$$p = p_0 + A \frac{\rho}{2} U^2 + B\rho a \frac{dU}{dt} \qquad (1)$$

where U is the instantaneous streamwise velocity component at the center of the sphere, a is the radius of the sphere, and A and B are coefficients denoting the contribution from the instantaneous velocity and the instantaneous acceleration, respectively. The coefficients A and B are strong functions of the azimuthal coordinate and may also depend weakly on the Reynolds number. For the pulsating flow, the foregoing equation may be rewritten as

$$p'(\tau) = A \frac{U^2(\tau)}{2} + Ba\dot{U}(\tau) \qquad (2)$$

where $p' = (p - p_0)\rho$, $\tau = t/T$, T = period and $\dot{U} = dU/dt$ for a particular location on the sphere. After periodic sampling and averaging, measured values of $p'(\tau)$, $U^2(\tau)$, and $\dot{U}(\tau)$ were obtained for ten equal subintervals of the period. The coefficients A and B were then determined by the method of least squares so that the mean square error δ^2, where

$$\delta^2 = \sum_{i=1}^{10} \left[p'(\tau_i) - \left(\frac{A}{2} U^2(\tau_i) + Ba\dot{U}(\tau_i) \right) \right]^2 \qquad (3)$$

became minimum.

Figures 9–12 show the experimental values of A and B computed in this way. The values determined on the three models S, O, and R are indicated in these figures by square, circular, and triangular symbols, respectively. The solid curves in the figures give a theoretical prediction in each case based on the assumption of inviscid irrotational flow as described in the following section.

Theory

With a view toward gaining an insight into the problem, a theory is developed to predict the pressure acting on a sphere placed in a time-dependent flow of an inviscid fluid. A solution of the problem relevant to the present study is given by Lamb [8]. The pressure p on a sphere moving with time-dependent velocity V in an infinite mass of fluid at rest at infinity is given as

$$\frac{p-p_0}{\rho} = \frac{1}{4}(-5+9\cos^2\theta)\frac{V^2}{2} + \frac{1}{2}\cos\theta . a \frac{dV}{dt} \qquad (4)$$

where p_0 is the pressure at infinity, t the time, ρ the density of fluid, a the radius of the sphere, and θ the meridional angle measured from the forward stagnation point. Unfortunately, however, the problem treated there does not exactly correspond to the present experiment, since the time-dependent flow that can be readily produced in the laboratory is a steady uniform flow with superimposed traveling disturbances with no associated pressure fluctuations in the free stream.

It is not difficult to illustrate the possibility of such a time-dependent flow. With the Cartesian coordinates (x, y, z), for example, the momentum equations are satisfied by taking a flow field

$$v_x = U_0, \ v_y = (x - U_0 t), \ v_z = 0, \ p = \text{constant} \qquad (5)$$

which represent a steady flow of velocity U on which a two-dimensional traveling disturbance is superimposed. No change in pressure is produced by the disturbance. Since, however, the disturbance is rotational having a component of vorticity in the z-direction, the vortex filaments are stretched by the presence of a three-dimensional body such as a sphere. This means that the "compensating flow" introduced to satisfy the boundary conditions on the sphere must also be rotational. Moreover, the phase velocity of the traveling disturbance in the experiment was found to be different from the undisturbed velocity U_0. These circumstances should be incorporated in the analysis if an elaborate theory is required. In view of the limited range of application of the present theoretical calculations, however, it is doubtful whether the solution warrants the extra complication involved.

In order to simplify the calculations, it is assumed that the disturbance is relatively small, irrotational, and traveling with a velocity equal to that of the steady uniform flow. Using spherical polar coordinates (r, θ, λ) such that

$$x = -r\cos\theta, \ y = r\sin\theta\cos\lambda, \ z = r\sin\theta\sin\lambda \qquad (6)$$

the velocity potential is assumed to have the form

$$\Phi = \Phi_0 + \Phi_1 + \Phi_2 \qquad (7)$$

where

$$\Phi_0 = -U_0 r\left(1 + \frac{1}{2}\frac{a^3}{r^3}\right)\cos\theta \qquad (8)$$

is the velocity potential for the steady flow of velocity U_0 past a sphere of radius a with its center at origin. The second term

$$\Phi_1 = -\epsilon a U_0 \sin k(r\cos\theta + U_0 t) I_0(kr\sin\theta) \qquad (9)$$

is the velocity potential for the superimposed disturbance traveling with the phase velocity U_0 and wave number k. The final term

$$\Phi_2 = -\epsilon a U_0 \sum_{n=1}^{\infty} C_n \frac{a^{n+1}}{r^{n+1}} P_n(\cos\theta) \qquad (10)$$

is the velocity potential for the compensating flow, where ϵ is a nondimensional constant, I_0 is the modified Bessel function of the first kind, P_n is the Legendre polynomial of order n, and C_n are the nondimensional constants ($n = 1, 2, 3, \ldots$) to be determined by applying the boundary conditions on the sphere. If ϵ is assumed to be small as compared to unity, the disturbance represented by Φ_1 gives a velocity fluctuation of order $\epsilon k a U_0$ for finite values of $kr\sin\theta$, and, when superimposed on the steady uniform flow, produces a change in static pressure of order $\epsilon^2 k^2 a^2 \rho U_0^2$ which is second order and is considered negligible. Although the velocity fluctuation increases indefinitely as $kr\sin\theta$ tends to infinity, this does not seem to seriously affect the results provided that consideration is limited to the region close to the sphere and the
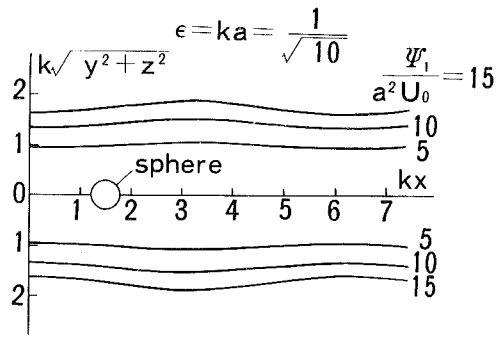
Fig. 13 Streamlines of theoretical model

radius of the sphere is small compared to the wavelength of the disturbance, i.e., $ka < < 1$. Figure 13 shows the instantaneous streamlines (with equidistant values of the Stokes stream function Ψ_1) for the velocity potential Φ_1 using the value $\epsilon = ka = 1/\sqrt{10}$.

Under the assumption that ka is small, the normal velocity induced by the traveling disturbance on the sphere is given by expanding equation (9) and keeping the first two terms

$$\left(\frac{\partial\Phi_1}{\partial r}\right)_{r=a} = -\epsilon k a U_0 \Big\{\cos\theta\cos k U_0 t$$

$$-\frac{1}{2}ka(3\cos^2\theta - 1)\sin k U_0 t\Big\}$$

which must be canceled by the normal velocity calculated from $(\partial\Phi_2/\partial r)_{r=a}$ in order to satisfy the boundary condition on the sphere. The constants in the expression for Φ_2 are then determined as

$$C_1 = \frac{1}{2}ka\cos k U_0 t, C_2 = -\frac{1}{3}k^2 a^2 \sin k U_0 t,$$

$$C_3 = C_4 = \cdots \cdots \cdots = 0$$

The pressure on the sphere is obtained from the equation

$$\frac{p}{\rho} + \frac{1}{2}q^2 + \frac{\partial\Phi}{\partial t} = F(t) \qquad (11)$$

where

$$q^2 = \left\{\frac{1}{r^2}\left(\frac{\partial\Phi_0}{\partial\theta} + \frac{\partial\Phi_1}{\partial\theta} + \frac{\partial\Phi_2}{\partial\theta}\right)^2\right\}_{r=a}$$

$$= \frac{9}{4}U_0^2\sin^2\theta\Big\{1 + 2\epsilon ka(\cos k U_0 t$$

$$-\frac{5}{3}ka\cos\theta\sin k U_0 t)\Big\},$$

$$\frac{\partial\Phi}{\partial t} = \left(\frac{\partial\Phi_1}{\partial t}\right)_{r=a} + \left(\frac{\partial\Phi_2}{\partial t}\right)_{r=a}$$

$$= -\epsilon k a U_0^2\Big\{\cos k U_0 t - \frac{3}{2}ka\cos\theta\sin k U_0 t\Big\},$$

$$F(t) = \frac{p_0}{\rho} + \frac{1}{2}U_0^2$$

and p_0 is again the static pressure at infinity. The pressure on the sphere is thus given by

$$\frac{p-p_0}{\rho} = \frac{1}{2}A U_0^2(1 + 2\epsilon ka\cos k U_0 t) - B\epsilon k^2 a^2 U_0^2 \sin k U_0 t \qquad (12)$$

where

$$A = \frac{1}{4}(-5 + 9\cos^2\theta), \quad B = \frac{3}{4}\cos\theta(-3 + 5\cos^2\theta) \qquad (13)$$

If the velocity V and the acceleration dV/dt at the location of the sphere center ($r = 0$) are introduced as

$$V = U_0 + \left(\frac{\theta\Phi_1}{\partial x}\right)_{r=0} = U_0(1 + \epsilon ka\cos kU_0 t), \qquad (14)$$

$$\frac{dV}{dt} = -\epsilon k^2 a U_0^2 \sin kU_0 t$$

the pressure on the sphere is expressed in the form

$$\frac{p - p_0}{\rho} = A\frac{V^2}{2} + Ba\frac{dV}{dt} \qquad (15)$$

Equation (15) indicates that the pressure on the sphere consists of two terms, the one being proportional to the instantaneous dynamic pressure $(1/2)\rho V^2$, and the other proportional to the time derivative of velocity $\rho a(dV/dt)$. The coefficient A of the first term is the same as for the classical solution (4), but the coefficient B of the second term is considerably different.

On writing $V = U_0 + u\cos kU_0 t$, the ratio of the two terms in equation (15) becomes

$$a\left|\frac{dV}{dt}\right| \Big/ \left|\frac{V^2}{2}\right| = \frac{4\pi a u}{L U_0} \qquad (16)$$

where $L = 2\pi/k$ is the wavelength of the traveling disturbance. This indicates that the flow can be considered as quasi-steady when the condition

$$4\pi\frac{a}{L}\frac{u}{U_0} \ll 1 \qquad (17)$$

is satisfied. The left-hand side of equation (17) in the present experiment ranged between 0.1 and 0.2, thus the contribution from the inertial term was 10 to 20 percent of the steady term.

Discussion

In the theoretical calculation, it is assumed that ϵ and ka are small compared to unity which requires that the amplitude of velocity fluctuation is small compared to the mean velocity on the jet axis, and that the radius of sphere is small compared to the wavelength of velocity fluctuation. These conditions were not obviously satisfied in the experiment, where the maximum values of ϵ and ka were 0.40 and 0.68, respectively. Moreover, the observed phase velocity of the disturbance was only two-thirds of the mean velocity, whereas the theory assumes a phase velocity equal to the mean velocity. In spite of these circumstances, however, the experimental values of the coefficients A and B agree fairly well with theoretical results for the sphere location at $x = 6$ cm (Figs. 11 and 12). The agreement is not as good for the sphere at $x = 3$ cm (Figs. 9 and 10), and this may be due to the relatively large axial variation of the velocity fluctuation amplitude for that region of the jet.

As seen from Fig. 2, the observed velocity fluctuation is not a simple sinusoid due to a slight distortion in the wave form which will result in higher harmonics. This distortion increased as the fundamental frequency decreased. This seems to account for the fact that the root-mean-square residual error from the least squares matching increased as the fundamental frequency decreased. The values of the residual error were 10.2, 9.7, and 6.0 percent of the fluctuation amplitude for the fundamental frequencies $f = 300$ Hz ($x = 3$ cm), 350 Hz ($x = 6$ cm), and 450 Hz ($x = 3$ and 6 cm), respectively.

No measurement of pressure was made on the rear portion of the sphere where the separation of flow modifies the pressure distribution. The effect of separation can be seen in the pressure distribution for meridional angle greater than $\theta = 70$ deg, where the experimental values of A begin to deviate from the theoretical curve (Figs. 11 and 12). On the other hand, the experimental values of B agree fairly well with the theoretical result up to as far as $\theta = 90$ deg (Figs. 11 and 12). It is uncertain to what extent the agreement is fortuitous.

Conclusions

Measurements of the instantaneous values of the surface pressure were carried out on a small sphere in a periodic pulsating jet in order to study the effects of unsteady flow on the surface pressure. Experimental values agreed moderately well with a concurrently developed inviscid theory. It is apparent from the present theoretical and experimental work that similar calculations can be performed on bodies other than spheres or even on a combination of bodies. By judicious choice of geometry, it may be possible to determine the location on the surface where the coefficients A and B vanish so that the measured pressure has no inertial contribution from the fluid velocity and acceleration. Pressure measurements at such points would indicate the static pressure fluctuations in the flow in the absence of the body in the same way as static probes are used in steady flow.

References

1 Senoo, Y., Kita, Y., and Ookuma, K., "Measurement of Two-Dimensional Periodic Flow with a Cobra Probe," ASME JOURNAL OF FLUIDS ENGINEERING, Vol. 95, No. 2, 1973, pp. 295–300.

2 Kerrebrock, J. L., Epstein, A. H., and Thompkins, W. T., "A Miniature High Frequency Sphere Probe," Measurement Methods in Rotating Components of Turbo-machinery, ASME, 1980, pp. 91–98.

3 Matsunaga, S., Ishibashi, H., and Nishi, M., "Accurate Measurement of Nonsteady Three-Dimensional Incompressible Flow by Means of a Combined Five-Hole Probe," Nonsteady Fluid Dynamics, ASME, 1978, pp. 65–72.

4 Kovasznay, L. S. G., Miller, L. T., and Vasudeva, B. R., "A Simple Hot-Wire Anemometer," Project Squid Tech. Rep., JHU-22-P, Dept. of Aerospace Engr., University of Virginia, 1963.

5 Kovasznay, L. S. G., and Chevray, R., "Temperature Compensated Linearizers for Hot-Wire Anemometer," Review of Scientific Instruments, Vol. 40, 1969, pp. 91–94.

6 Einstein, H. A., and Li, H., "Viscous Sublayer Along a Smooth Boundary," Proceedings of American Society of Civil Engineers, Paper 945, 1956.

7 Kono, N., "Frequency Response of Probe Microphone and Its Equalizer," Journal of Science, Hiroshima University, Vol. 26, No. 1, 1962, pp. 25–64.

8 Lamb, H., Hydrodynamics, 6th Edition, Dover, 1945, p. 124.

Search for Large-Scale Coherent Structures in the Nearly Self-Preserving Region of a Turbulent Axisymmetric Jet

J. Tso

L. S. G. Kovasznay

A. K. M. F. Hussain

Department of Mechanical
Engineering,
University of Houston,
Houston, Texas   77004

In an attempt to explore the existence of large-scale coherent structures in the nearly self-preserving region of an axisymmetric free air jet, a 2.54 cm air jet at a Reynolds number $Re_D = 6.8 \times 10^4$ has been investigated for $x/D \geq 40$ via both long and short time-averaged space-time correlation measurements. Conventional space-time correlation data with probe separations in the streamwise direction by as much as 25 diameters suggest the passage of large-scale organized structures. The radial extent of these structures is about one local jet diameter, and the azimuthal extent is about a quadrant of the cross-section. Recurring quasi-periodic patterns are observed in the time series of short time-averaged correlations between longitudinal velocity fluctuations obtained with two arrays of hot-wires separated in the streamwise direction. These orderly patterns provide direct evidence for the existence of these structures. Quantitative details of these structures are now being investigated.

I Introduction

Research advances in recent years continue to suggest that large-scale coherent vortical motions are characteristic features of turbulent shear flows. While the existence, though not necessarily the precise role, of large-scale coherent structures had been suspected or even known for quite some time and occasionally investigated [1–8], the recent upsurge of activity in this topic has been fostered by the discovery of quasi-deterministic vortex-like structures in flows which otherwise would be regarded as fully (random) turbulent [9–12]. As a result of this activity, there has evolved a persistent suggestion that these large-scale coherent structures play important roles in turbulent shear flows and perform most of the transport of heat, mass and momentum and production of turbulence energy and noise. Clearly, it is tempting to assume that an appropriate combination of these structures might capture the essential physics of shear flow turbulence and thus, form the basis of a viable theory [13–14].

While the presence of these structures in transitional flows and near fields of free turbulent shear flows has been established [11, 12, 15–21], some questions have been raised about the dependence of there nature and role on the Reynolds number, and initial or boundary conditions [22–25]. There appear to be sufficient evidences that these structures are also present in equilibrium turbulent boundary layer and wake flows [1–3, 7, 8, 26–29]. However, the role of the large-scale coherent structures in turbulent shear flows, when present, is still elusive.

As yet, there has been no conclusive evidence of the presence of large-scale coherent structures in the self-

preserving regions of turbulent jets. The broad structural similarities—as revealed by conventional time-average measurements—among wakes, jets, mixing layers, and constant pressure boundary layers [30, 31], however, would naturally lead to the speculation that the spatial coherence of large eddies should exist in jet flows as well. Measurements of wavenumber-celerity spectrum in the nearly self-preserving regions ($x/D \geq 30$) of plane and circular jets in our laboratory [32] also provided an indirect indication of their existence and average linear growth with x. Furthermore, other observations like modes recognized up to $x/D = 10$ [33, 34] and the periodic radial ejections observed at $x/D = 15$ [35] are suggestive of the existence of large-scale coherent structures farther downstream.

It is the purpose of the present investigation to conclusively document the existence as well as some details of large-scale coherent structures in the nearly self-preserving region of the axisymmetric free air jet. By a large-scale coherent structure we mean a turbulent fluid mass of a size comparable to the width of the flow, but having an underlying vorticity instantaneously correlated over the spatial extent of the structure. (For further details of their characteristics and analytical and experimental considerations involved in their investigations, see [36]). In the present study, the approach involved both conventional space-time correlation measurements as well as simultaneous sampling by two linear arrays of hot-wires separated in the streamwise direction and eduction of the structures through short-time averaged cross correlation techniques [25, 27].

II Apparatus and Procedure

The experiments have been carried out in a 2.54 cm

30 | 94 | 36 | 13 | 168 | 60 | 22

5 | 5

DIFFUSER 1 | DIFFUSER 2

SILENCER BOX

61
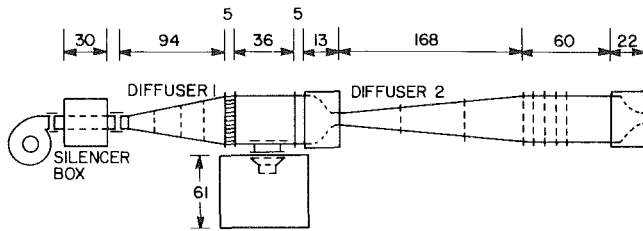
Fig. 1 2.54 cm axisymmetric air jet. The dimensions are in cm.

axisymmetric air jet at a Reynolds number (based on the exit nozzle diameter) of 6.8×10^4. The jet facility consists of two settling chambers in tandem designed for controlled excitation study [37]. The mean velocity and fluctuation intensity profiles at and near the exit of the jet were checked to be axisymmetric. The jet discharges through the center of a 30 cm diameter disc into a large laboratory (15m $\times$ 30m $\times$3.5m) with controlled temperature, humidity, and traffic, so that the flow is essentially free from significant ambient recirculation and disturbance [38]. The flow facility is schematically shown in Fig. 1, where the dimensions are in cm. The exit centerline fluctuation intensity is 0.25 percent and is free from any spectral spikes. Further details of the facility and the aerodynamic characteristics of the flow are available in reference [37].

Longitudinal velocity signals were obtained with tungsten hot-wires of 4μm diameter operated at a resistance ratio of 1.5 by commercial constant-temperature anemometers (both DISA and TSI). For long-time correlation measurements, the anemometer voltage was linearized by DISA linearizers (Model 55D10) before analysis by a PAR 101 Correlator. For the longitudinal velocity fluctuations $u_A(t)$ and $u_B(t)$ at spatial locations A and B, the long-time space-time correlation is defined as:

$$R_{AB}(\Delta x, \tau) \equiv \lim_{T \to \infty} \frac{1}{T} \int_0^T u_A(t' - \tau) u_B(t') dt' \qquad (1)$$

where Δx is the spatial separation between points A and B, and τ is the time shift between the signals at the two locations. In the data sampling of hot-wire arrays, however, the bridge voltages were directly recorded by an eight-channel FM analog tape recorder (HP model 3968A) at a recording speed of 15ips with a frequency response of 5kHz. This frequency response was considered to be adequate for our objective since the frequencies associated with the large-scale structures are considerably lower. The recorded voltages were subsequently digitized through a 12-bit a-d converter, then linearized using the hot-wire response equation and written onto a digital magnetic tape (HP 7970E) for numercial analysis by the

laboratory minicomputer (HP 2100S). Due to the limitation on the memory capacity available in the minicomputer, each record on the digital magnetic tape was 2.11s long.

In order to infer the presence of the coherent structures from the time traces of hot-wire rakes, the short time-averaged correlation coefficient $\hat{R}_{ij}$ between longitudinal velocity fluctuations $u_i(t)$ and $u_j(t)$ at the i-th and j-th hot-wire positions was determined through short-time integration defined as follows:

$$\hat{R}_{ij}(t; \Delta x, \tau, T) = \frac{1}{T} \int_0^T \frac{u_i(t + t' - \tau) u_j(t + t') dt'}{\hat{u}_i' \hat{u}_j'} \qquad (2)$$

where $\hat{u}_i'$ and $\hat{u}_j'$ are the short time-averaged rms of u_i and u_j over averaging interval T, i.e.,

$$\hat{u}_i' = \left[\frac{1}{T} \int_0^T u_i^2(t + t' - \tau) dt' \right]^{1/2} \qquad (3a)$$

$$\hat{u}_j' = \left[\frac{1}{T} \int_0^T u_j^2(t + t') dt' \right]^{1/2} \qquad (3b)$$

with

$$u_i = \bar{u}_i - <\bar{u}_i>.$$

$\bar{u}_i$ is the instantaneous longitudinal velocity and $<\bar{u}_i>$ is its long time-average. Note that the summation convention is not implied for the subscripts i, j in equation (2). For each short time-averaged correlation coefficient $\hat{R}_{ij}$, signals were obtained from either the two upstream probes or one upstream and one downstream probe, with i and j denoting the hot-wire locations in the arrays. Since the values of $\Delta x, \tau$, T in this study were selected to be fixed, the short-time correlations are simply functions of t alone and thus denoted as $\hat{R}_{ij}(t)$.

The measurement scheme involved data taken from seven hot-wires, arranged in two configurations. That is, the upstream location at $x/D = 40$ contained two hot-wires separated azimuthally, while the downstream location at $x/D = 50$ contained a linear array of hot-wires aligned radially or azimuthally. The arrangements are schematically shown in Fig. 2.

Relative to the conventional long-time average, the short-time averaging process defines a sense of locality in time. To the extent that Taylor's hypothesis of "frozen flows" is valid [39], the corresponding locality in space can be inferred. If the averaging interval T is chosen to be comparable with the time scale of large eddies, the temporal variations of short time-averaged quantities should be essentially contributed by large eddies. For neighboring spatial positions in an Eulerian frame, if the velocity patterns of those large eddies passing by the sensors happen to be nearly deterministic, one should expect to observe some patterns in neighboring time traces of

Nomenclature

$\hat{C}_{ij}$ = normalized short time-averaged correlation of $\hat{R}_{ij}$ with a sine wave

D = nozzle exit diameter

i, j = subscripts identifying probe locations

e = reference sine wave function

e' = rms value of e

Re_D = Reynolds number based on nozzle diameter and exit velocity

R_{AB} = conventional space-time correlation coefficient of streamwise velocity fluctuations at locations A and B

$\hat{R}_{ij}$ = short time-averaged correlation coefficient of streamwise velocity fluctuations at probe locations i and j

u_A, u_B = streamwise velocity fluctuations at locations A and B

u_i, u_j = streamwise velocity fluctuations at array probe locations i and j

$\hat{u}_i', \hat{u}_j'$ = short time-averaged rms values of u_i and u_j

$\bar{u}$ = instantaneous total longitudinal velocity

$<\bar{u}>$ = long time-average of $\bar{u}$

U_c = center-line velocity

x, y = longitudinal and transverse coordinates

$y_{0.5}$ = value of y where $U = 0.5 U_c$

τ = time-delay

τ_{op} = optimal time delay

$<( )>$ time-average $\equiv \lim_{T \to \infty} \frac{1}{T} \int_0^T ( ) dt$

$(\hat{\ })$ = short time-average $\equiv \frac{1}{T} \int_0^T ( ) dt$
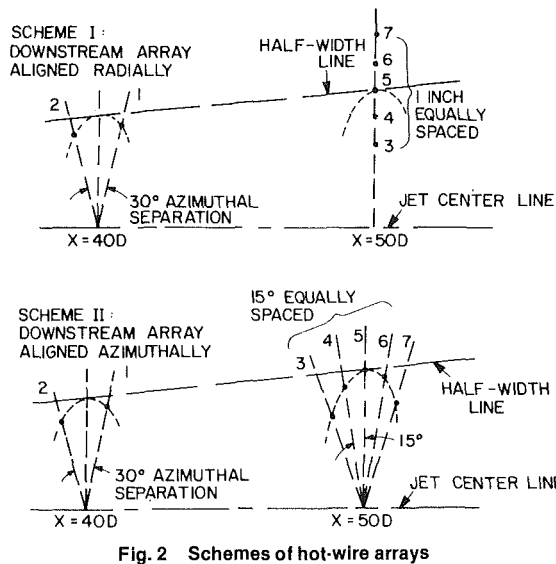
Fig. 2 Schemes of hot-wire arrays

Fig. 3 Scheme for conventional correlation measurements

$\hat{R}_{ij}(t)$, for example, reflecting corresponding events. If T is considerably larger than the time scale of large eddies, the identities of individual large eddies will be smeared out.

III Results and Discussions

III. 1 Conventional Space-Time Correlation Data. Before exploring time traces from arrays of hot-wires, it was considered worthwhile to first infer possible existence of coherent structures through conventional (long-time) space-time correlation data. These data were obtained with two hot-wires separated in the streamwise direction, as schematically shown in Fig. 3. The upstream reference wire was held fixed at the transverse location $y = y_{0.5}$ where the mean velocity is half of the centerline velocity at the same streamwise station. Data were obtained with the second wire traversed either along the same half-width line or over a downstream plane normal to the jet axis. Correlation of the two linearized hot-wire signals was obtained with the correlator.

For each position of the second wire, which is sufficiently far away from the reference wire, space-time correlation produces a curve of the typical form shown in the insert in Fig. 4. The peak value of this curve defines the optimum time delay τ_{op}. Figure 4 shows these long-time average correlations for several data sets obtained with the second wire traversed along the same half-width line. These data have been plotted as a function of time delay τ nondimensionalized by τ_{op}; the correlation functions are normalized by their peak values. In these nondimensional coordinates, the correlation functions are essentially the same, independent both of the location of the reference probe and of the spatial separation between the two probes. The contours of constant values of $(R_{AB})_{max}$ with the upstream probe A located at $y = y_{0.5}$ at $x/D = 40$ and probe B traversed in the axial plane at $x/D = 50$ are shown in Fig. 5. These values have been normalized by the rms values at $y = y_{0.5}$ at the two streamwise stations. The correlation is signficant within one quadrant and extends radially for about one local jet diameter.

Due to the spatial filtering effect of large separation, the space-time correlations measured should be dominated by the contributions of large eddies. The observed similarity of correlation curves could be interpreted by passages of similar large-scale structures. The sizes of these structures scale with local half-width $y_{0.5}$. They are convected downstream with a velocity nearly equal to $0.6U_c$. Their radial extent at any x (as estimated from Fig. 5) is about one local jet diameter. An estimate of the longitudinal size of the structure can be obtained from Fig. 4. By extending the R_{AB} data to smaller
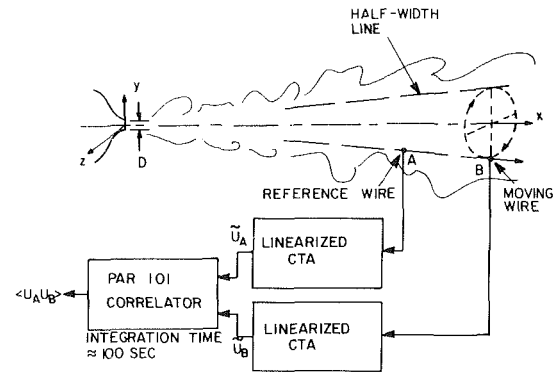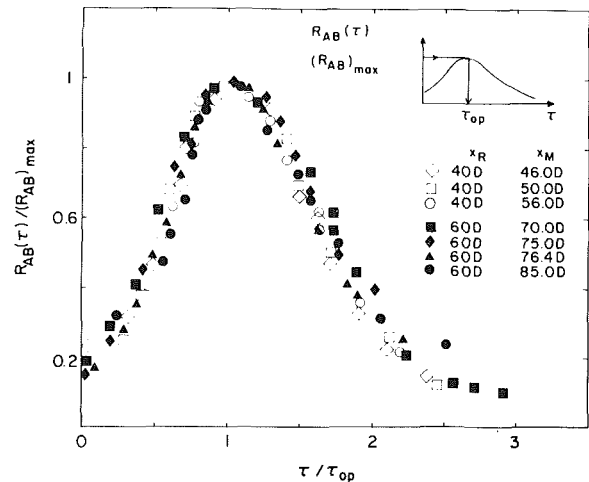
Fig. 4 Conventional space-time correlations. x_R and x_M, streamwise stations of reference and moving probes (uncertainties for $R_{AB}(\tau)/(R_{AB})_{max}$ and τ/τ_{op} are $\pm$ 10 percent and $\pm$ 1 percent, respectively).
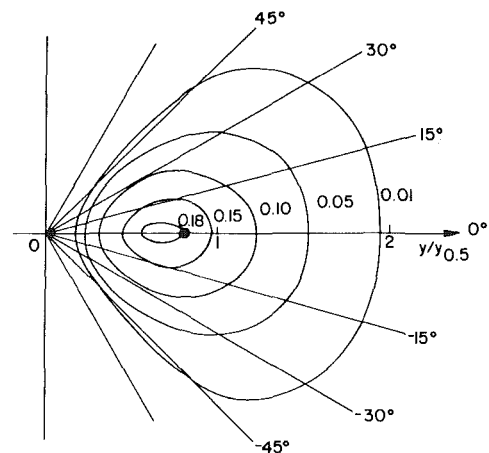
Fig. 5 Distribution of maximum space-time correlation over the transverse plane at $x = 50D$. The upstream reference probe is at $x = 40D$, $y = y_{0.5}$ denoted by • (uncertainty is $\pm$ 10 percent for correlation, $\pm$ 1 deg for angle, and $\pm$ 0.02 for $y/y_{0.5}$).

values at both ends, it is clear that the length of the structure in time is about $3\tau_{op}$. This corresponds to about $6y_{0.5}$ or 3 local jet diameters, which is consistent with the wavenumber-celerity spectrum data in the self-preserving region of a 2.54 cm circular jet [32]. Since the long time-average statistical data in this study as well as in reference [32] cannot reveal specific details of the individual structures, exploration through instantaneous signals from hot-wire arrays, discussed next, were undertaken in order to uncover these details.
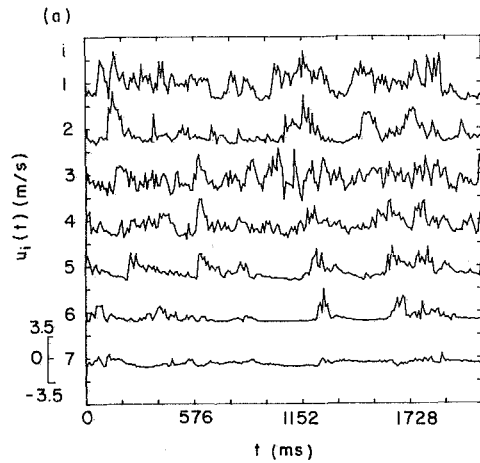
Fig. 6(a)
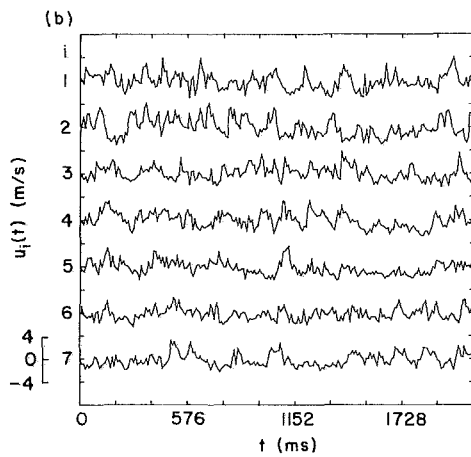
Fig. 6(b)

Fig. 6   Time traces of u_i (t) for Scheme I in (a) and Scheme II in (b) (uncertainty is ± 3 percent for u_i (t) and ± 0.5 ms for t)
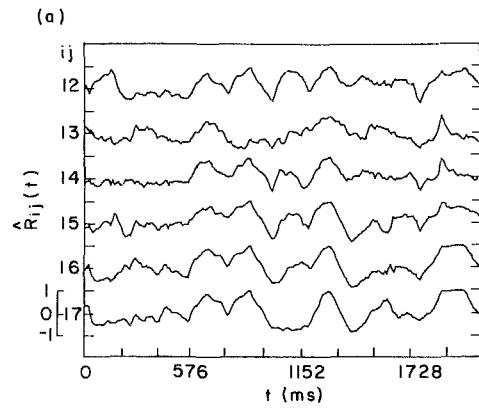
Fig. 7(a)
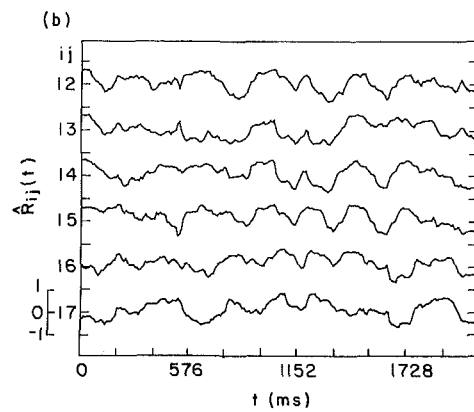
Fig. 7(b)

Fig. 7   Time traces of $\hat{R}_{ij}$ (t): (a) corresponding to Fig. 6(a); (b) corresponding to Fig. 6(b). The top trace is time shifted to the right by τ_{op} (≈ 80 ms) (uncertainity is ± 10 percent for $\hat{R}_{ij}$ and ± 0.5 ms for t).
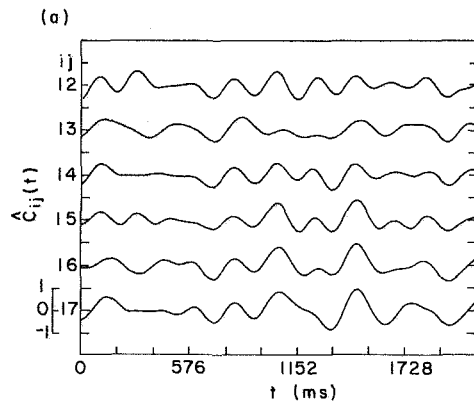
Fig. 8(a)
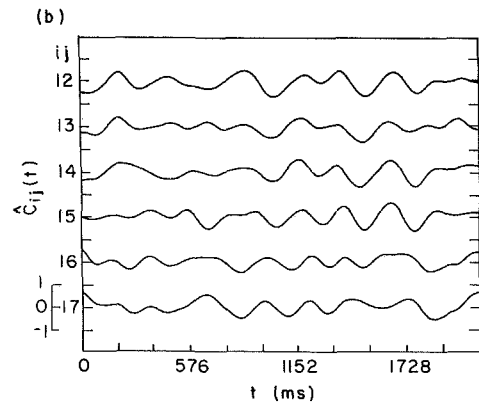
Fig. 8(b)

Fig. 8   Time traces of $\hat{C}_{ij}$(t): (a) corresponding to Fig. 7 (a); (b) corresponding to Fig. 7(b) (uncertainty is ± 10 percent for $\hat{C}_{ij}$, and ± 0.5 ms for t).
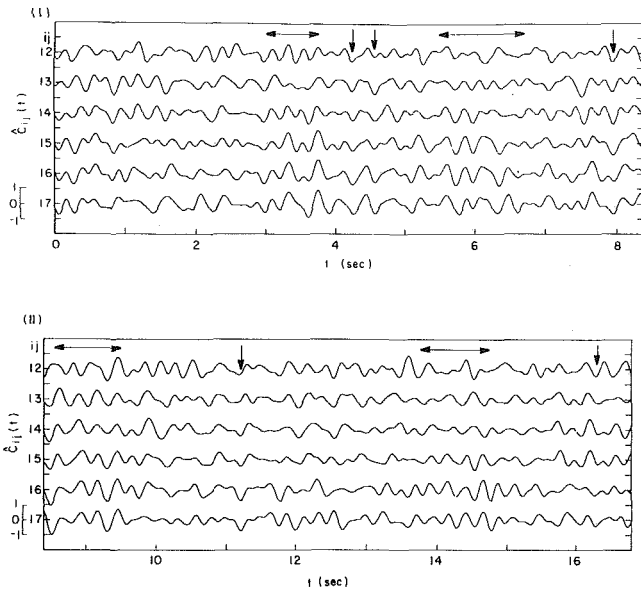
Fig. 9(a) Time traces of $\hat{C}_{ij}(t)$ for Scheme I (uncertainty is $\pm$ 10 percent for $\hat{C}_{ij}$, and $\pm$ 0.5 ms for t)
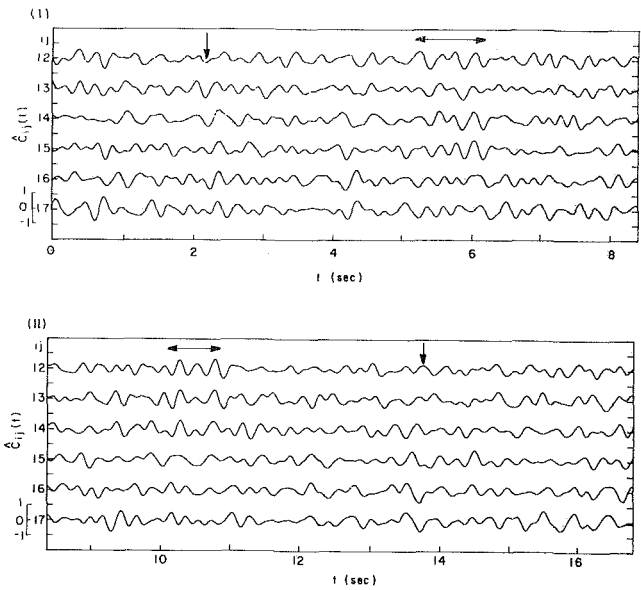
Fig. 9(b) Time traces of $\hat{C}_{ij}(t)$ for Scheme II (uncertainty is $\pm$ 10 percent for $\hat{C}_{ij}$, and $\pm$ 0.5 ms for t).

III.2 Time-Domain Study of Signals From Hot-Wire Arrays. Figure 6(a) shows a sample of time traces of longitudinal velocity fluctuations from the hot-wires in the radial configuration (see Fig. 2(a)). Figure 6(b) shows the corresponding time traces for the azimuthal configuration schematically drawn in Fig. 2(b). Some coincidences of velocity undulations are apparent among these turbulent traces. However, in order to uncover the possible existence of inherent structures, short time-averaged correlations of these traces are presented in Figs. 7(a), (b) corresponding to the radial and azimuthal data in Figs. 6(a), (b). The top trace is the cross correlation of signals from the two upstream probes. The remainder are short time-averaged correlations of signals from one upstream probe and one downstream probe. The top trace has been time-shifted by τ_{op} in order to provide a common time reference. It is now clear that there are intervals when the $\hat{R}_{ij}$ traces, especially from adjacent probes, show patterns which are quite similar, indicating passage over the hot-wire array of orderly velocity patterns. Note that groups of quasi-periodic peaks or valleys do intermittently occur in neighboring traces with identifiable phase relationship to one another.

The wake effects of the upstream probes seem to be insignificant. The mean velocities and the rms of longitudinal velocity fluctuations at the downstream probe positions were checked to be within the measurement uncertainty, with or without the upstream probes in place. The averaging interval T for the short time-averages was selected to be two and a half times the local time scale $[y_{0.5}/(\tfrac{1}{2}U_c)](\approx 47$ ms) of the mean flow at $x=50D$. The time delays for the short time-averaged space-time correlations $\hat{R}_{1j}(t)$, $j=3,\ldots,7$, were set to be equal to $\tau_{op}(\approx 80$ ms), the optimum time delay between $x=40D$ and $x=50D$ shown in Fig. 4. The calculated results, like those shown in Fig. 7, indicate that, at least for the purpose of detecting the existence of spatial coherence of large eddies, the choices are reasonable.

The observed orderly patterns and phase coincidences in neighboring traces apparently support the existence of spatial coherence of large eddies passing by the hot-wire arrays. The deterioration of regularities found in the outer traces $\hat{R}_{13}(t)$ and $\hat{R}_{17}(t)$ in Fig. 7(a) is consistent with the spatial extent of the structures, as also suggested by conventional correlation. The close resemblance among the trace patterns of the short

time-averaged cross correlation coefficient function $\hat{R}_{12}(t)$ of two upstream reference probes and those of space-time correlation coefficient functions $\hat{R}_{1j}(t)$, for $j=3,\ldots,7$, in addition, provides some measure of evolutions of large-scale coherent structures convected from upstream.

The $\hat{R}_{ij}(t)$ traces in Figs. 7(a), (b) were further correlated with a sine wave, and the resulting correlation curve $\hat{C}_{ij}(t)$ are shown in Figs. 8(a), (b). The quantities $\hat{C}_{ij}(t)$ are defined as,

$$\hat{C}_{ij}(t) = \frac{1}{T}\int_0^T \frac{\hat{R}_{ij}(t+t')e(t')dt'}{e'^2} \tag{4}$$

where $e(t)=\sin 2\pi t/T$, and e' is rms value of $e(t)$. The averaging interval T is equal to the period of the sine wave, chosen to be the average period of the nearly periodic peaks and valleys apparent in the traces in Figs. 7(a), (b). By this short-time cross correlation with the sine wave, the intermittent "periodicity" of trace patterns with "periods" in the neighborhood of that of the reference sine wave has been emphasized and, at the same time, the general phase coincidences and similarities between neighboring $\hat{R}_{ij}(t)$ traces have been preserved. Furthermore, this has resulted in smoothing of the signals. Careful examination will reveal close resemblance among traces in Figs. 7 and 8 even though the latter are smoother.

In order to depict more clearly the recurring organized patterns, longer traces $C_{ij}(t)$ have been presented in Figs. 9(a), (b) for the radial and azimuthal arrangements of the hot-wires. Each of these two cases contains sufficiently long traces so that each is divided into two parts: (I) and (II); the traces in (II) directly follow those in (I). It is clear from these traces that presence of large-scale coherent structures of differing sizes and strengths is identifiable. The intervals, when large-scale structures extending over sufficiently long streamwise length are present, have been identified by the dimension lines. In addition, there are intervals when, even though the duration of phase coincidence does not appear to be long, a characteristic "front" is apparent in most traces. These are marked by arrows.

IV   Concluding Remarks

The purpose of this study was to search for the existence of large-scale coherent structures in the self-preserving region of

Journal of Fluids Engineering

an axisymmetric free air jet. Conventional long time-averaged space-time correlations between hot-wires separated in the streamwise direction suggest passages of similar large-scale structures. These structures are as large as the local jet diameter. The azimuthal extent of these structures is about 90°. The streamwise extent of these structures is about 3 times the local jet diameter.

Direct evidence for the occurrences of these structures has been obtained from short time-averaged space-time cor- ·relation traces. These traces have been further smoothed by correlating them with a sine wave of a period typical of the intermittently occurring, nearly periodic peaks and valleys in the traces. The approach, in effect, emphasizes regularities of the trace patterns which are almost periodic with about the same period as that of the reference sine wave, while retaining the general phase coincidences and pattern similarities. The recurring quasi-periodic patterns are evident from these traces.

Even though the evidence for the existence of large-scale coherent structures is convincing, it is to be recognized that a number of questions regarding the nature of the structures remain unanswered. Since high-speed flow visualization movies of turbulent shear flows reveal rapid evolutionary characteristics and interactions of large-scale coherent structures, it is proably not realistic that the same structures survive longer than a few diameters. In a high Reynolds number mixing layer, we found that the survival distance of a structure is about one structure length [25]. If a structure survives for a comparable length or longer in the self-preserving region of the axisymmetric jet, there are proably mechanisms for structure renewal. That is, the structure might undergo a cyclical process of growth, breakdown and regeneration [26]. We have not yet obtained details of the evolutionary characteristics, the physical description of an average or the dominant structure, and the significance of these structures in Reynolds stress, turbulence production, and transport phenomena [36]. This study will be extended to address these questions.

References

1 Townsend, A. A., *The Structure of Turbulent Shear Flow*, Cambridge University Press, 1956, 1976.

2 Grant, H. L., "The Large Eddies of Turbulent Motion," *Journal of Fluid Mech.*, Vol. 4, 1958, pp. 149–190.

3 Keffer, J. F., "The Uniform Distortion of a Turbulent Wake," *Journal of Fluid Mech.*, Vol. 22, 1965, pp. 135–159.

4 Mollo-Christensen, E., "Jet Noise and Shear Flow Instability Seen From an Experimenter's Viewpoint," *Journal of Applied Mechanics*, Vol. 89, 1967, pp. 1–7.

5 Lumley, J. L., "The Structure of Inhomogeneous Turbulent Flows," *Atmospheric Turbulence and Radio Wave Propagation, Proc. Int. Colloq.*, Publishing House NAUK, Moscow, 1965, pp. 166–178.

6 Landahl, M. T., "A Wave-Guide Model for Turbulent Shear Flow," *Journal of Fluid Mech.*, Vol. 29, 1967, pp. 441–459.

7 Kline, S. J., Reynolds, W. C., Schraub, F. A., and Runstadler, P. W., "The Structure of Turbulent Boundary Layers," *Journal of Fluid Mech.*, Vol. 30, 1967, pp. 741–773.

8 Kovasznay, L. S. G., Kibens, V., and Blackwelder, R. F., "Large-Scale Motion in the Intermittent Region of a Turbulent Boundary Layer," *Journal of Fluid Mech.*, Vol. 41, 1970, pp. 283–325.

9 Crow, S. C., and Champagne, F. H., "Orderly Structure in Jet Turbulence," *Journal of Fluid Mech.*, Vol. 48, 1971, pp. 547–591.

10 Hussain, A. K. M. F. and Zaman, K. B. M. Q., "Effect of Acoustic Excitation on the Turbulent Structure of a Circular Jet," *Proc. Third Interagency Symp. Univ. Research Transp. Noise*, Univ. of Utah, 1975, pp. 314–325.

11 Brown, G. L., and Roshko, A., "On Density Effects and Large Structures in Turbulent Mixing Layers," *Journal of Fluid Mech.*, Vol. 64, 1974, pp. 775–816.

12 Winant, C. D. and Browand, F. K., "Vortex Pairing: The Mechanism of Turbulent Mixing-Layer Growth at Moderate Reynolds Number," *Journal of Fluid Mech.*, Vol. 63, 1974, pp. 237–255.

13 Kovasznay, L. S. G., "The Role of Large-Scale Coherent Structures in Turbulent Shear Flows," *5th Biennial Symposium on Turbulence*, Univ. of Missouri-Rolla, Mo., 1979, pp. 379–391.

14 Hussian, A. K. M. F., "Investigations of Coherent Structures in Free Turbulent Shear Flows," *6th Biennial Symposium on Turbulence*, Univ. of Missouri-Rolla, Mo. 1979, pp. 207–228.

15 Browand, F. K., and Laufer, L., "The Roles of Large-Scale Structures in the Initial Development of Circular Jets," *Turb. in Liquids*, Vol. 5, Univ. of Missouri-Rolla, Mo, 1975, pp. 333–334.

16 Davies, P. O. A. L., and Baxter, D. R. J., "Transition in Free Shear Layers," *Structure and Mechanisms of Turbulence I*, (ed., H. Fiedler), Springer-Verlag, New York, 1977, pp. 125–135.

17 Hussain, A. K. M. F., and Zaman, K. B. M. Q., "Vortex Pairing in a Circular Jet Under Controlled Extiation: Part 2. Coherent Structure Dynamics," *Journal of Fluid Mech.*, Vol. 101, 1980, pp. 493–544.

18 Brunn, H. H., "A Time-Domain Analysis of the Large-Scale Flow Structure in a Circular Jet, Part I: Moderate Reynolds Number," *Journal of Fluid Mech.*, Vol. 83, 1977, pp. 641–671.

19 Yule, A. J., "Large-Scale Structure in the Mixing Layer of Round Jet," *Journal of Fluid Mech.* Vol. 89, 1978, pp. 413–432.

20 Emmons, H. W., and Bryson, A. E., "The Laminar-turbulent Transition in a Boundary Layer," *Journal Aeronaut. Sciences*, Vol. 18, 1951, pp. 490–498.

21 Zilberman, M., Wygnanski, I., and Kaplan, R. E., "Transitional Boundary Layer Spot in a Fully Turbulent Environment," *Physics Fluids*, Vol. 20, 1977, pp. S258–S271.

22 Chandrsuda, C., Mehta, R. D., Weir, A. D., and Bradshaw, P., "Effect of Free-stream Turbulence on Large Structure in Turbulent Mixing Layers," *Journal of Fluid Mech.*, Vol. 85, 1978, pp. 693–704.

23 Batt, C. C., "Some Measurements on the Effect of Tripping the Two Dimensional Shear Layer," *AIAA Journal*, Vol. 13, 1975, pp. 245–247.

24 Pui, N. K. and Gartshore, I. S., "Measurements of the Growth Rate and Structure in Plane Turbulent Mixing Layers," *Journal of Fluid Mech.*, Vol. 91, 1978, pp. 111–130.

25 Hussain, A. K. M. F. and Clark, A. R., "On the Coherent Structure of the Axisymmetric Mixing Layer: A Flow-visualization Study," *Journal of Fluid Mech.*, Vol. 104, 1981, pp. 263–294.

26 Townsend, A. A., "Flow Patterns of Large Eddies in a Wake and in a Boundary Layer," *Journal of Fluid Mech.*, Vol. 95, 1979, pp. 515–537.

27 Gupta, A. K., Laufer, J., and Kaplan, R. E., "Spatial Structure in the Viscous Sublayer," *Journal of Fluid Mech.*, Vol. 50, 1971, pp. 493–512.

28 Bandyopadhyay, P. and Head, M. R., "A Unified View of Turbulent Boundary Layer Structure," *6th Biennial Symposium on Turbulence*, Univ. of Missouri-Rolla, Mo., 1979, pp. 16–25.

29 Falco, R., "Structural Aspects of Turbulence in Boundary Layer Flows," *6th Biennial Symposium on Turbulence,* Univ. of Missouri-Rolla, Mo., 1979, pp. 1–15.

30 Townsend, A. A., "Entrainment and the Structure of Turbulent Flow," *Journal of Fluid Mech.*, Vol. 41, 1970, pp. 13–46.

31 Bradshaw, P., Ferris, D. H., and Atwell, N. P., "Calculation of Boundary Layer Development Using Turbulent Energy Equation," *Journal of Fluid Mech.*, Vol. 28, 1967, pp. 593–616.

32 Hussain, A. K. M. F. and Clark, A. R., "Measurements of Wavenumber-celerity Spectrum in Plane and Axisymmetric Jets," *AIAA Journal*, Vol. 1, 1981, pp. 51–55.

33 Michalke, A. and Fuchs, H. V., "On Turbulence and Noise of an Axisymmetric Shear Flow," *Journal of Fluid Mech.*, Vol. 70, 1975, pp. 179–205.

34 Petersen, R. A., "Influence of Wave Dispersion on Vortex Pairing in a Jet," *Journal of Fluid Mech.*, Vol. 89, 1978, pp. 469–495.

35 Chevray, R., and Tutu, N. K., "Intermittency and Preferential Transport of Heat in a Round Jet," *Journal of Fluid Mech.*, Vol. 88, 1978, pp. 133–160.

36 Hussain, A. K. M. F., "Coherent Structures and Studies of Perturbed and Unperturbed Jets," presented at the *International Conference on the Role of Coherent Structures in Modelling Turbulence and Mixing*, Madrid, Spain, May 25–27, 1980, *Lecture Notes in Physics*, Vol. 136, 1980, pp. 252–291.

37 Zaman, K. B. M. Q., and Hussain, A. K. M. F., "Vortex Pairing in a Circular Jet Under Controlled Excitation. Part 1. General Jet Response," *Journal of Fluid Mech.*, Vol. 101, 1980, pp. 449–491.

38 Bradshaw, P., "Effect of External Disturbances on the Spreading Rate of a Plane Turbulent Jet," *Journal of Fluid Mech.*, Vol. 80, 1977, pp. 795–797.

39 Zaman, K. B. M. Q. and Hussain, A. K. M. F., "Taylor Hypothesis and Large-scale Coherent Structures," *Journal of Fluid Mech.*, Vol. 112, 1981, pp. 379–396.

O. C. Jones, Jr.

Professor of Nuclear Engineering,
Rensselaer Polytechnic Institute,
Troy, N.Y.   12181
Mem. ASME

F. Kreith

Chief,
Thermal Conversion Branch,
Solar Energy Research Institute,
Golden, Colo.   80401
Fellow ASME

F. M. White

Professor,
Mechanical Engineering Department,
University of Rhode Island,
Kingston, R.I.   02881,
Mem. ASME

Review—Basic Research Needs in Fluid Mechanics

A small segment of the engineering community was surveyed to obtain their judgment regarding the long-range needs for basic research in fluid mechanics. This segment consisted of approximately 600 persons active in heat transfer and fluid mechanics committees within The American Society of Mechanical Engineers. Close to 200 persons responded giving useful information relating to needed research. Of the many topics identified, six generic areas stood out: turbulence; multiphase flows; fluid structure interactions; boundary layer effects; biological, geological, and environmental fluid flow; and the need for new facilities and improved instrumentation. These six areas were summarized and an initial estimate of the research priorities presented to the DOE-ESCOE workshop on Fluid Dynamics and Thermal Processes held at the University of Kentucky on February 1–2, 1979. The priorities were modified and the final results of the workshop included herein.

Introduction

The U.S. Department of Energy (DOE), recognizing that the need for short-term, mission-oriented development work must be tempered with a longer range viewpoint, has sought to strengthen its support for fundamental studies upon which future technological advances may be based. To do this, it invited the support of the engineering community to aid in providing direction for this work. As a first step in accomplishing this, the DOE and the Engineering Societies Commission on Energy Inc. (ESCOE), a nonprofit corporation supported jointly by several engineering societies, sponsored a "Workshop on Fluid Dynamic and Thermal Processes" at the University of Kentucky on February 1–2, 1979. The result of the workshop serves as a guide for future program support of fundamental research upon which the next generation of technological advance is being based. The workshop addressed four subject areas: fluid flow, separation phenomena, energy processing, and reactions. The full report of the workshop is reported by Eichhorn et al., in reference [12]. It is the purpose of this paper to provide a summary of the report contained in reference [11] which identifies basic research needed in fluid mechanics. This summary was prepared especially for the *Journal of Fluids Engineering* to serve as a guide for initiation or support of energy-related programs.

Background

We have passed the age where energy is cheap and abundant. Over the next few decades, conservation and improved efficiency of energy utilization will be second in importance only to the finding of new sources and development of new systems. The direct savings resulting from improved efficiency of energy conversion devices is obvious. Not so

widely recognized are the "up front" energy investment savings which also result. A more efficient turbine or heat exchanger, for instance, can be smaller, utilizing less materials, reduced fabrication time, less production space, reduced packaging materials and transportation requirements, less insulation, and less installation space, all of which result in a net reduction in energy costs. Likewise, improved equipment lifetimes due to improved designs which experience lower wear, less vibration fatigue, or show more resistance to erosion or improved resistance to corrosion or environmental degradation, or which can reduce or be immune to biological attack or fouling, also will reduce our global energy needs.

In all these cases mentioned, long-range fundamental research is going to be required in order to improve current methods or develop new techniques to extend our energy reserves. This research must begin now in order to begin to have a significant effect by the mid-to-latter 1980s, and on to the end of the century.

It appears reasonable to expect that numerous developmental technology areas within DOE might benefit from fundamental research and the results obtained. For instance, analytical and experimental modeling in the area of flow-induced vibrations could result in optimization of component designs with respect to size, cost and performance, as well as to reduced downtime. Modeling of doubly-diffusive convection systems could lead to significant savings in the area of industrial process heat. Flooding is one of the fundamental limiting processes in multiphase flows having applications as diverse as packed beds and wetted wall columns in the chemical process industry and in emergency cooling of nuclear reactors. The area is so fundamental and widespread, it is impossible to assess the savings which could result from significant gains in this area. Knowledge gained through study of three-dimensional turbulence in rectangular ducts could be of substantial importance in estimating and improving MHD

generator performance. These and many other examples indicate the large potential payoff of basic fluid mechanics research, to say nothing of the spin-off technology as well.

Unfortunately, fundamental research cannot be guaranteed to yield successful results since discovery of underlying principles is implied. Neither the fact nor the nature of discovery can be scheduled or directed. It was risk and the willingness to accept the possibility of missing targeted objectives in order to achieve knowledge and success that once allowed this country to lead the world in achievement, real economic growth, and standard of living. By contrast, the support for fundamental research in terms of percent of the gross national product is the lowest it has been in modern times. Since the mid-1960s, the relative support for basic research has been diminishing in proportion to the applications research and development. The country's real economic growth has nearly vanished. The standard of living has dropped. The ability of this country to compete in world markets has declined. The continued flow of new products based on ever-advancing technology fed by fundamental research has been all but eliminated.

The coupling between the support of basic research and continued technical advance is obvious. The need for a return to increased support of fundamental research has been identified in numerous recent newspaper and magazine articles with the need to regain an economic leadership role in the world. This can only be done with an acceptance of risk — that missing the target in one direction may lead the way to success in another. Because of its long-term nature, fundamental research requires sustained support for extended periods of time to assure any reasonable probability of success. An interruption in support before a project can be brought to fruition frequently results in a total waste of the effort. In times of economic belt tightening or shifting of national priorities, consideration must be given to maintenance of the basic programs having long term objectives.

It was the concern for the need for new emphasis on energy-related fundamental research that prompted the authors to prepare this document. The results indicate their best judgment of the priorities for this work and represent what they believe to be a consensus of those participants of the ESCOE-DOE workshop. A detailed report of the needs in fluid mechanics is given in reference [11], and for the four categories of the workshop in reference [12].

Methodology

It is clearly impossible for two or three people to be cognizant or knowledgeable about the broad range of topics included within the realm of fluid mechanics. For this reason, the authors sought the assistance of a subset of the engineering community in a way which seemed both expeditious and practical to accomplish within the time constraints allowed. A letter was sent to each active committee participant within the Fluids Engineering and Heat Transfer Divisions of The American Society of Mechanical Engineers. The letter invited each recipient to respond by identifying basic research deemed necessary for future development. Several research categories, including those originally identified by the ESCOE organizing committee, were suggested. Each individual was given a simple form which requested their "fill-in" response to the following questions:

1. Needed Research Category (Primary)
2. Needed Research Category (Secondary)
3. Application for Future Need
4. Description of Needed Research
5. Reason This Research is Important

In addition, the recipient was to give his name, position, degrees held, company affiliation and address, major and secondary fields of interest, and, on a scale of 1 (least, or zero) to 5 (most, or 100 percent), the degree of expertise in the field, as well as the degree of long-range planning or research undertaken in his job.

Approximately 600 letters were mailed out and nearly 200 usable responses were obtained. Almost without exception, the respondents indicated both a high degree of expertise in their field of interest, as well as having 60–100 percent of their activities involved in long-range planning or research. In addition to the completed forms, many responded with additional comments by letter for which the authors were especially appreciative. Particularly useful were papers summarizing research needs as identified in references [2–9], while additional source material was found in reference [10].

From the responses to the survey, a list of research categories was developed, as shown in Table 1. Obviously, many of these categories are more design-related than fundamental. However, as the responses were reviewed, patterns appeared indicating several overriding generic areas where individuals from many different disciplines within the broad definition of fluid mechanics expressed the same need or lack of fundamental understanding. It is these areas toward which the balance of this paper is directed. The topics included are:

1 Turbulence
    1.1 fundamental understanding
    1.2 computational techniques (especially multidimensional internal and external flows)
    1.3 questions of scale of turbulence, including atmospheric
    1.4 body force effects (anisotropy)

2 Multiphase and Multicomponent Flows
    2.1 fundamental understanding
    2.2 interface transfers and nonequilibrium
    2.3 multidimensional and orientational effects and computational methods
    2.4 body force and miscellaneous effects

3 Fluid-Structure Interactions
    3.1 flow over bluff bodies
    3.2 flow-induced vibrations

4 Boundary Layer Effects
    4.1 turbomachinery
    4.2 forced and free convection
    4.3 instrumentation and measurement
    4.4 unsteady flow
    4.5 computational techniques
    4.6 atmospheric flows
    4.7 vehicle drag

5 Biological, Geological, and Environmental Fluid Flow Effects

6 Facilities and Instrumentation
    6.1 instrumentation
    6.2 facilities

Each topic shall be summarized in the next section according to the foregoing order. In addition, the workshop participants felt there were certain overriding criteria or modes of activity toward which basic research projects should be directed, or within which framework should be undertaken. These are identified in a later section, "Research Activity Modes." It is believed that the consensus of the respondents is faithfully reported herein. The consensus was compiled with the additional input of the workshop participants (see the acknowledgments) and included the reflections of the authors themselves.

Table 1 Fluid flow research categories (primary and secondary) as consolidated from mailing responses

1. Analysis and Modeling of Multiple Phase Flow

    a. Single component systems
    b. Multiple component systems
    c. Slurries
    d. Steady and unsteady flow
    e. Laminar and turbulent flow
    f. Mixing and separation
    g. Magnetohydrodynamic
    h. Pressure drop
    i. Flow pattern
    j. Internal flows
    k. Granular or particulate flows
    l. Nonequilibrium phase change
    m. Facility development
    n. Cavitation, corrosion or erosion
    o. Water hammer
    p. Turbomachinery
    q. Pump behavior
    r. Fundamental behavior
    s. Multidimensional flows
    t. Erosion
    u. Boundary layers and secondary flows
    v. Instrumentation development
    w. Bubble dynamics
    x. Surface tension effects

2. Analysis and Modeling of Fluid Structure Interactions

    a. Analytical methods
    b. Turbulent effects
    c. Heat exchangers
    d. Acoustic-pipe vibration
    e. Experimental verification
    f. Fluid/structure interactions in turbomachines
    g. Fluid forcing function
    h. Fluid energy systems
    i. Rapid transients
    j. Turbomachinery
    k. Fundamentals
    l. Vibration and noise
    m. Unsteady flows
    n. Turbulence structural interactions

3. Rheology

    a. Suspensions of fines
    b. Other non-Newtonian fluids
    c. Polymers and emulsions
    d. Blood flow
    e. Low turb trans.
    f. Particulate flows
    g. Slurries

4. Particulate Behavior

    a. Particles > 10
    b. Particles > 3 but ≤ 10μ
    c. Particles ≤ 3μ (respirable fines)
    d. Submicron part. behavior
    e. Particle separation
    f. Heat transfer
    g. Hot facility
    h. Filtration
    i. Particle trajectories and erosions
    j. Improved instrumentation
    k. Field (body force) effects

5. Flow Through Porous Media

    a. Capillary flow and surface tension effects
    b. Two-phase flow and phase change
    c. Combustion
    d. Heat and mass transfer
    e. Compressible flow
    f. Fluidized beds

    g. Basic formulations
    h. Non-Newtonian behavior
    i. Physical properties
    j. Compressible porous media
    k. Surface tension effects

6. Combustion

    a. Basic understanding and mechanisms
    b. Turbulence
    c. Fires and fire research
    d. Liquid sprays and droplet behavior
    e. Internal combustors
    f. Heat and mass transfer effects
    g. Fouling
    h. Flame propagation
    i. Particulate and gaseous fuels
    j. Surface tension effects
    k. Catalytic effects
    l. Microemulsions

7. Heat Transfer

    a. Heat transfer through and between various fluids
    b. Ultra high energy density heat transfer
    c. Radiation
    d. Turbulent convection (forced and free)
    e. Combustion
    f. Film boiling
    g. Unsteady turbulent flow
    h. Turbomachinery
    i. Enhancement or augmentation
    j. Composites
    k. Multiphase extreme environments
    l. Measurements in extreme environments
    m. Gas-particle systems
    n. Coupled modes
    o. Thin films
    p. Separation or stagnation effects
    q. Oxides
    r. Between fluids and fibers

8. Fluid Flow/Kinetic Interactions

    a. Fouling and degradation
    b. Slagging, corrosion, erosion

9. Surface Tension Driven Effects

    a. Marongoni flows
    b. Porous media

10. Electro-Fluid Dynamics

    a. Transport processes

11. Atmospherics

    a. Turbulence
    b. Marine
    c. Thermal energy sources
    d. Nucleation theory
    e. Weather prediction
    f. Power generation/pollution control
    g. Wind energy
    h. Solar-wind energy coupling
    i. Natural and forced convection
    j. Global energetics

12. New and Improved Instrumentation and Measurement Techniques

    a. Particle sizing
    b. Fluid flow
    c. Extreme environments
    d. Laser anemometries
    e. Unsteady flows

Identification of Needed Research

Turbulence. Throughout this century, the problem of turbulence has remained a frontier for research. There have been some remarkable strides in the last decade, but, except for the simplest shear layers, routine engineering analysis of turbulent flow is not yet a reality.

Attention was directed to practical turbulent flow problems, namely, boundary layers. There were relatively fewer cited problems of a fundamental nature, and these are summarized in Table 2. A related list of practical boundary layer problems is given later in Table 8.

Basic research in turbulence can be extremely fruitful in spawning applications to many applied problems, whereas boundary layer studies often lead to excessively problem-centered empiricisms. Support of basic turbulence research should therefore be maintained as a priority.

Journal of Fluids Engineering

Table 1 (cont.)

f. Multiphase flows
h. Rotating machinery

13. Development of a Flexible Flow Facility

   a. Cold facility. Modeling by ambient simulation.
   b. Hot facility. High temperature and pressure operation.
   c. Standards facility

14. Fundamentals

   a. Laminar turbulent transition
   b. Turbulence and turbulent closure
   c. Turbulent heat transfer
   d. Turbulent mixing vessel
   e. Large-scale turbulence
   f. Separation and reattachment (steady and unsteady)
   g. Vortex motion
   h. Wave motion
   i. Boundary layers – general
   j. Boundary layer – structural inter.
   k. Boundary layer – separation
   l. Turbulence modeling
   m. Roughness effects
   n. Multiphase interactions
   o. General transient behavior
   p. Body force effects
   q. Electro-optical interactions
   r. Capillarity
   s. Lubrication

15. Geometric Effects

   a. Piping components
   b. Transient flow
   c. General 3D flows
   d. Internal flows
   e. Blades and passages
   f. Bluff-body aerodynamics

16. Compressible Flow

   a. Transonic flows
   b. Shock interactions
   c. Gas kinetics
   d. Turbulent rotating fields
   e. Nonequilibrium gas dynamics
   f. Acoustics
   g. Acoustic vibrations
   h. Turbomachinery
   i. Real gas effects

17. Hydrology

   a. Land rehabilitation

18. Energy Storage

   a. Natural convection

19. Computational Methods

   a. Finite element analysis
   b. Turbulence-free flows, enclosed flows, and boundary layers
   c. Turbomachines-hydrodynamics, aerodynamics, unsteady flows
   d. Blades and passages

20. Food Processing

   a. Energy retention

21. Groundwater use of deep saline waters

   a. Oil recovery and injection

22. Thermal/Physical Properties

Fundamental Understanding. Although computational modeling received the most attention from respondents in Table 2, such models depend explicitly upon data sets having a high degree of reliability to give generality to the analysis. Thus, it is essential that basic research be supported for experiments in the structure of turbulence. Recently, the newer instruments, such as the laser anemometer and the conditioned-sampler hot wires, have revealed important new structures on both a large and small scale for turbulent and transitional flow. These data have resulted not only in much better understanding, but lead to improved models as attested by the many sophisticated new analyses presented at the 1977 Penn State Symposium on Turbulent Shear Flows. The future of turbulence research probably lies in further detailed measurements, especially for complex flows, with the hope of yielding a more general theoretical approach with less empiricism.

Computational Modeling. The global modeling of turbulent motions is a fundamental research area of great importance, but most applications are to free shear layers and to wall layers which are of a boundary layer character. Thus, most discussion of this area is included in the section on boundary layer computational techniques. There has been considerable progress in free turbulence modeling. The Penn State 1977 Symposium presented several different second-order closure models capable of making reasonable estimates of turbulent details such as intensity, fluctuation energy, Reynolds stresses, turbulent heat flux, production, and dissipation. These are still research tools not yet useful for engineering design applications, but the potential is there and support should be continued for turbulence modeling. User-oriented models should be especially encouraged.

Atmospheric Turbulence. Turbulent flow in the ocean and atmosphere becomes increasingly important as the environment in which most of our badly needed alternate energy systems operate. More knowledge is needed of the fundamental nonstationary statistical structure of the atmospheric boundary layer, so that more efficient and reliable energy systems can be designed. Further study is needed of the effect of atmospheric flows on these systems. Of particular interest are the flow-induced vibrations which often limit the usefulness of windmills, OTEC designs, and large-scale solar power systems.

The large-scale intermittent motions of the atmosphere are strongly affected by geometry and stratification. Although considerable success in numerical modeling of atmospheric turbulence was reported at the Penn State Symposium, this is still a fruitful area for research.

Multiphase and Multicomponent Flows. Probably the most significant characteristic of multiphase/multicomponent flow technology is that, in spite of the huge amount of research undertaken and publications available, there remains a vast separation between our qualitative understanding and our ability to predict general multiphase behavior accurately. Design techniques today for almost any energy-system-related hardware must still either rely on exhaustive prototypical performance testing or suffer severe design conservatism and/or operational restrictions. Large penalties continue to be paid in terms of construction materials and processes, and reduced efficiency of operation. The excess energy requirements both in the manufacturing and in the operating stages are an area where large gains remain to be realized.

A recent panel discussing . . . "Further Research and Urgent Problems on Two-Phase Flows . . . " [5] listed the coupling between gas-liquid pressure drop and flow patterns at the top of the list. Three of the first eight topics involved two-phase pressure loss in gas-liquid systems – probably the oldest topic of research in the field. Other needs include distribution of flows in manifolds and tees, flows with nonequilibrium phase change, transient bubble growth, and mass transfer in concurrent gas liquid flows. Even the correct form for the multiphase energy equation remains in doubt and people are still asking, " . . . which equation implies the least drastic hypothesis?" It is an instructive commentary on both the difficulty of the subject and on the emphasis of previous research that we have practically no idea today of the forces that drive void migration or cause phase distribution

Table 2 Research needs in fundamental turbulence summary of questionnaire responses

Topic	Number of suggestions
1. Computational modeling	14
2. Structure of turbulence	7
3. Atmospheric turbulence.	6
4. Stability and transition.	5
5. Diffusion and mixing	4
Total suggestions	36

Table 3 Basic research needs for fundamental understanding of multiphase flows

1. Field equations
2. General extension of single-phase theories to multiphase flows (Poiseuille, Couette, rotation, stability, etc.)
3. Flow patterns, extension of range
4. Flow pattern stability with heat transfer
5. Flow pattern transition and stability
6. Laminar and turbulent transport
7. Modeling of turbulent transport
8. Regions of laminar separation
9. Turbulent dispersion
10. Turbulent transport of droplets and particles
11. Unsteady flow effects on pressure drop and heat transfer in multidimensional systems
12. Unsteady flow effects
13. Unsteady flow effects in multidimensional boundary layers
14. Unsteady flow effects
15. Pressure drop in packed beds
16. Improved understanding of pressure losses
17. Packed bed behavior
18. Motion of granular materials
19. Fluid profile effects, voids, velocities, temperatures in both steady and transient flows
20. Multidimensional experimental data
21. Boundary layer and secondary flows
22. Heat transfer
23. Bubble dynamics
24. Interactions with solid structure from erosion or damage standpoint

and separation, and virtually no work has been undertaken in this area.

Experimentally, it is still almost impossible to measure two-phase mass flows or individual phase velocities under any but the most simple conditions. Yet current tests being undertaken costing hundreds of millions of dollars require these measurements.

As the size of equipment of all kinds continues to increase, so does the need for accurate computational techniques. It becomes more and more difficult to experimentally determine safety margins or operational characteristics in sufficient detail for optimization purposes. Full scale prototypical or operational *in situ* tests become more difficult or unsafe as sizes increase. The alternative is development of sophisticated computational systems using accurate physical modeling principles, to be tested against a wide variety of smaller scale experiments. Baseline data for qualification of these codes for a broad range of advanced energy system configurations, technologies, and component hardware is required.

Even with the development of qualified advanced computational techniques, application to full scale systems requires knowledge of geometric scaling which is currently lacking. The computer codes themselves provide a scaling link, generally "opaque" from a fundamental viewpoint, between models and prototypes as long as the physical behavior of the phenomena are adequately described within the computational framework. But only the phenomena and interactive combinations which were originally recognized and therefore included in the modeling are subsequently incorporated into "scaling by computation."

Fundamental Understanding. A summary of the research needed is shown in Table 3. Details of the applications and reasons for the need are included in reference [11]. Curiously lacking from the literature are simple extensions to well-known single-phase analyses, for instance, for flows in ducts or tubes or between rotating cylinders. No extensions of analyses of laminar flow stability in boundary layers appears to have been undertaken. It would seem that a significant body of intuitive knowledge could be gained and then extrapolated to more complex situations. Indeed, universal agreement is yet to be obtained regarding even the exact form for the multiphase field equations.

The relationship between single-phase flow regime and transport phenomena has been well known for many years. Recent works have pointed out similar dependence for the more complex case of multiphase flows, where not only the turbulent structure, but also the phase interface structure is important in governing transport of mass, momentum, and energy. Except in very simple cases, no objective means have yet been tested even to identify and classify flow regimes, much less to define their extent or stability. Extensions to transient situations are practically nonexistent.

Questions of turbulence, turbulent mixing and dispersion, and turbulent transport of droplets and particles along with laminar-turbulent transition need to be addressed. The question of laminar separation remains an open issue having both economic and safety implications.

A broad area of concern with which some degree of success is beginning to be achieved in limited areas includes methods to predict unsteady or transient behavior in multiphase-related equipment. Simple accelerating flows, unsteady boundary layer effects, and especially unsteady flow-structure interactions, present a generally unknown area affecting questions of fatigue failure, excess pressure losses, and system efficiency. Most methodology and correlations developed to date are valid only for steady state, well-controlled situations.

Numerous other questions need attention, including multiphase flows in packed beds and flows of granular materials. Perhaps the area requiring the most intensified efforts deals with experimental data of a fundamental nature. Both steady state and transient profiles of component and phase volume fractions, velocities, and temperatures are needed for exactly the same reason as they were needed in single-phase flows – to allow a comparison with fundamental theories of behavior to be made.

Interface Transfers and Nonequilibrium. While one-dimensional modeling of multiphase phenomena has predominated to date, it is clear that future models will be more complex. Multidimensional methods will have to be developed. While models which rely on descriptions of the local mixture (barycentric) velocity coupled with a description of the phase velocity relative to the mixture may prove useful in future multidimensional applications, multifluid models describing each phase or component separately have gained early success and acceptance. It appears that utilization and expansion of such models over the next decade will predominate, even though the models require quantification of interfacial transfers which are virtually impossible to measure today. While of a very fundamental nature, this class of problems will achieve such central importance that it must be considered by itself.

While there are many areas requiring definition, some delineated in Table 4 with applications and justification given in reference [11], one must really examine the basis of mass, momentum, and energy transfers in both steady and transient situations. Transfer laws by themselves, however, are only half the story since the transfer areas must also be specified. This latter problem is, of course, closely allied to specification of flow regimes and regime stability and transition. Some

Table 4 Basic research needs for interphase transfers and nonequilibrium

1. Improved understanding of interfacial transfer of mass, momentum, and energy
2. Improved understanding of transient and steady state transfer mechanisms
3. Improved understanding of interface formation, deformation, and renewal mechanisms
4. Molecular scale modeling
5. Improved understanding of cavitation phenomena
6. Improved understanding of cavitation phenomena in entering passages
7. Direct contact condensation – limit of condensing rates
8. Vapor release in suddenly expanded systems
9. Transient phase geometry determination
10. Particulate or droplet continuum coupling
11. Establishment, maintenance, and boiling in thin films

Table 5 Basic research needs for multidimensional and orientational effects in multiphase flows

1. Fundamental analysis and data in general internal flow systems such as diffusers, bends, around obstructions, etc.
2. General multidimensional behavior in laminar and turbulent flows
3. Flow mixing due to strong and weak cross flows
4. General multidimensional modeling in turbulent flows including general stability criteria
5. Inside blades and passages, multidimensional flow fields, branches
6. Relative velocity and phase distribution in horizontal and inclined ducts
7. Fundamental analysis and data in general internal flow systems as diffusers, bends, around obstructions, etc.
8. Flow mixing due to strong and weak cross flows
9. General multidimensional modeling in turbulent flows including general stability criteria
10. Relative velocity and phase distribution in horizontal and inclined ducts
11. Develop theory and data in rotating flows
12. Steady and unsteady flow behavior in blades and passages
13. Steady and unsteady flows in orifices, entrances, exits, branches
14. Theories for flashing flows through valves and orifices
15. Movement of droplet fields through nozzles
16. Multidimensional particulate and granular flows
17. Flows around tubes and baffles
18. Three-dimensional flows with shocks
19. Develop two-phase "Reynolds" flow methods

behavior may be adequately described through transfer coefficients or combined specification of transfer coefficients and areas. It appears, however, that nonequilibrium and transient interfacial transfers require separate descriptions of both the exchange mechanisms and the interfacial areas. These must then be coupled with ideas concerning surface or boundary layer renewal. There is an implication of molecular scale modeling which might be necessary in some instances.

It appears that a further understanding of nonequilibrium phenomena may yield an improved understanding of cavitation and flashing phenomena. These phenomena play important roles in turbomachinery, pumps, propellers, impellors, flow control devices, and the like. Cavitation and flashing are basically the same phenomena studied by different workers for generally different reasons, but having safety and efficiency implications in most areas. Similarly, concerns regarding direct contact condensation, especially when leading to rapid local decompression, are important as the resultant water hammer effects may lead to equipment failure.

Multidimensional and Orientational Effects and Computational Methods. The development of qualified computational methods was stressed in the introduction to the section on Multiphase and Multicomponent Flows as being fundamental to future design and optimization of energy conversion equipment. Before such methods will be of wide utility, however, an increased understanding of multidimensional flow field behavior must be achieved. As identified in Table 5, areas dealing with general internal flows, flow mixing and turbulence, and nonsymmetric flow fields, such as with flows not directed colinearly with the major body force, must be understood. An understanding of steady and time-dependent flows in blades and passages will be especially important in development of turbomachinery, while flows around tubes, baffles, and the like must be studied to improve heat exchanger designs. There is a possibility that increased coal utilization for power plants will have to depend on slurry transport, requiring studies in this area. (It appears that continued postponement of the nuclear option coupled with decreasing oil supplies make coal utilization inevitable, regardless of its lack of attractiveness from cost, pollution, and health standpoints.)

Closely coupled with increased knowledge of multidimensional behavior will be the development of computational methods based on the understanding gained. Three major immediate needs appear to be:

1 general multidimensional behavior in laminar and turbulent flows;
2 inside blades and passages, multidimensional flow fields, branches;
3 around tubes, plates, and baffles.

Body Force and Miscellaneous Effects. Increasing emphasis on nongravitational field, body force effects is occurring in all areas of fluid mechanics. Multiphase flows appear to be no exception. Research is needed relative to steady and pulsed magnetic field effects to pursue developments in MHD systems and in fusion system blankets and inertial confinement systems. Centrifugal separation flows and electrostatic flows must be studied to improve efficiency of rotating turbomachinery as well as particulate separation systems.

Other concerns which do not seem to fit any particular category (Table 6) concern slurry behavior and interactions between droplets or particulates and solids, and between cavitation and corrosion. The former are of interest in many different applications such as spray systems, combustors, MHD generators, fuel transport systems, and rotating machinery, especially coal-fired turbines.

Fluid-Structure Interactions. In the area of fluid-structure interactions, there appear to be two principal research areas that recur, as summarized in Table 7. One deals with flow over bluff bodies, and this area can be divided into 1) mean effects, 2) instantaneous local effects, and 3) integrated effects. The second area of research that appears to be paramount in fluid-structure interaction is the field of flow-induced vibrations.

Flow Over Bluff Bodies. Research in this field is needed dealing with vortex shedding, flow separation and reattachment, similarity requirements to interpret model tests in terms of the full-scale measurements, time scale of turbulence for full scale and models, and unsteady forces and moments. Applications of research in this field would lead to better design of buildings, large structures, bridges, solar collectors, power towers, wind turbine support, and OTEC pipes, as well as support structures.

Flow-Induced Vibrations. Flow-induced vibrations are often the primary design constraint on large power machinery such as turbines, reactors, and off-shore platforms. While considerable progress is being made on mechanisms such as galloping, flutter, or heat exchanger tube instabilities where quasi-steady analysis yields good agreement with data in single-phase flow, there are vast uncertainties in two-phase flow and for inherently unsteady mechanisms such as vortex shedding and interaction of fluid jets. Considerable effort

needs to be made in both acoustic flow-induced vibration such as noise generated by separated flow, vortex-induced edge tones, and heat exchanger acoustic resonance, as well as in the prediction of the associated pressure fields and their influence on adjacent structures. Vortex-induced structural vibration in an oscillating flow, such as for off-shore platforms, remains largely unexplored. Very little data are available on the influence of two-phase flow heat exchangers, even on some of the better-defined vibration mechanisms.

Boundary Layer Effects. Almost all practical flow processes involve shear layers. Further, nearly all flow processes associated with energy production and transfer involve macroscopic scales and either gases or liquids of low viscosity, so that Reynolds numbers are relatively high. Thus, most energy-related flows are turbulent and often of a boundary layer type. Possible exceptions are the flows associated with delicate instrumentation, porous media, thick oils, and certain separation techniques. In many cases, the behavior of the turbulent boundary layers surrounding an energy device is the controlling factor in the performance of the device. Yet, even after 75 years of boundary layer research, both our fundamental and practical knowledge of boundary layers remains inadequate for efficient design and utilization of such devices. One can conclude that boundary layer research continues to be a vital part of the national energy program. New ideas and viewpoints are especially needed. The problem is not whether boundary layers are important, but rather which areas are most important and can yield the best return in a national basic energy research program.

Of the nearly 300 research needs detailed on the questionnaires, 150 were directly related to boundary layer effects. A breakdown is given in Table 8. Excluded topics were primarily concerned with areas specifically treated in other sections, fundamental turbulence concepts, multiphase flows, fluid-structural interactions, biofluid interactions, and flow facilities. Let us summarize the important needs in the most significant areas from Table 8.

Turbomachinery. Some of these boundary layer problems are strongly coupled to other effects. Probably the most serious problem in turbomachine design is the ability to

withstand destructive fluid-structural oscillations. Improved design procedures in this area are vital. The next most serious problem is designing turbomachines to handle two-phase fluids involving mixtures of gases, liquids, and solids. Strongly coupled to these problems is the inadequacy of present methods for analyzing unsteady boundary layer flow in complex turbomachine geometries. Almost all existing unsteady boundary layer analyses are for laminar flow; the problem of unsteady three-dimensional turbulent boundary layer separation is only just being addressed. More work needs to be done on compressor stall and surge problems.

Although turbomachine design is well developed in an empirical sense, more effort needs to be devoted to improving machine efficiency, especially for smaller devices with unusually low or high heads. Low head applications abound in the form of thousands of small flood-control dams in this country. It is estimated that more than 10,000 MW of power could be recovered from such dams if suitable low cost, efficient, reliable turbines were available. Similarly, reliable, low cost high-head devices are needed for pump-turbine waste energy utilization, such as the use of deep aquifers to store waste warm or cold water for later use.

A few percent improvement in turbomachine efficiency will have a large effect on national energy savings. Too much effort has been expended on blade design, leaving unsolved problems with the turbomachine's poor stepchild: nonmoving passages such as inlets, guide vanes, and diffusers. Clearly, such improvements will involve both theory and experiment. Manufacturers lack the resources to make such detailed studies, so the research efforts fall to large-scale national support.

Forced and Free Convection. Certain problems are associated with laminar flow with combustion in fluidized beds, but most convection problems are directly related to turbulent boundary layers. High energy density in liquids is still limited by the burnout problem, where further research is needed.

Blade cooling in very high temperature applications continues to be a limiting factor to the efficiency of turbomachines. Support in this area, especially for new ideas, could be quite productive. A similar situation exists in heat exchangers, where boundary layer separation limits the burnout flux. Some new ideas are needed in the rod-bundle field, perhaps involving noncircular shapes. Much heat exchange equipment is also limited by sooting and fouling, which is dealt with in more detail in the section on biofluid interactions.

Many new heat transfer applications involve complex or unusual fluids, where theory and experiment are less developed. The resurgence of coal, wood chips, and other solid fuel devices clearly calls for new research into efficient extraction of energy from complex substances. Probably the

Table 6 Miscellaneous basic research needs for multiphase flows

1. Particulate or droplet behavior in liquid slurries and gas/vapor carriers
2. Pressure drop, concentration, wear, abrasion relationships in slurries
3. Optimize mixture and particle size in coal slurries
4. Study effects of liquid or particulate impacts on materials
5. Cavitation-corrosion interactions

Table 7 Basic research needs in fluid-structure interactions

Research needed	Application	Reason for need
1. Flow Over bluff bodies • mean effects • instantaneous local effects • integrated effects	Design of buildings, large structures. Bridges, solar collectors, power towers, wind turbine supports, OTEC pipes, and support structures	Proper designs, earthquake protection energy conservation, prevention of failures and damages to collector fields and wind turbines. Placement and design of cold water pipe in OTEC.
2. Flow-induced vibrations • flow separation • reattachment • vortex shedding • fluid structure interactions • flow over tube bundles and in nuclear reactor cores	Design of heat exchangers, nuclear reactors, turbines, rotating machinery	Higher efficiencies and lower cost in heat exchange equipment, better rotating machinery, safer nuclear reactors

Journal of Fluids Engineering

Table 8 Research needs in boundary layer effects summary of questionnaire responses

Topic	Number of suggestions
1. Turbomachinery	28
2. Forced and free convection	23
3. Instrumentation and measurements	15
4. Unsteady flow	13
5. Computational techniques	13
6. Atmospheric flows	12
7. Flow in porous media	10
8. Separation and reattachment	9
9. Drag of vehicles	5
10. Rheology	4
11. Cavitation	3
12. Acoustics and noise	3
13. Magnetohydrodynamics	3
14. Film flows	2
15. Secondary flows	1
16. Diffuser flows	1
17. Fire flows	1
18. Blood flow	1
19. Water waves	1
20. Body force effects	1
21. Surface tension effects	1
Total suggestions	150

most economically promising area in heat transfer is the development of sources formerly unused or wasted, such as ocean temperature differences, exhaust heat from process devices, solar ponds, aquifer storage, or geothermal energy. New designs are needed to utilize heat transferred across very low temperature differences or low potentials. In general, the entire field of heat transfer offers a fruitful place to search for improvements in efficiency and utilization of energy.

Instrumentation and Measurements. Concurrent with the need for a nationally supported flow facility, to be discussed in the following, is the need for comprehensive flow data and instruments. The entire field of turbulence modeling depends explicitly upon careful three-dimensional measurements of complex flows. Of special interest are measurements of unsteady or pulsating flows. New instruments are needed for applications to high temperature, high heat flux, particle sizing, and reacting flows.

The laser anemometer is an extremely attractive new instrument which has already broken ground in measurement of velocity profiles in turbomachine passages. Such detailed data, however laborious and expensive, are vital to the quest for a realistic prediction model for complex turbulent flows. In the future, progress will be rapid if laser instruments can be made cheaper and simpler, so that small businesses and colleges can enjoy the fruits of this new tool.

Development is needed for reliable unsteady flow instruments. If possible, all new instruments should be capable of being incorporated into automatic measurement and control systems.

Unsteady Flow. Research is needed, especially for high Reynolds numbers, in many topics: pulsating flow, vortex shedding, water hammer, bubble collapse, and random phenomena. Most such unsteady flows react strongly with structural aspects of the design. Prediction schemes for steady flow are hampered by inadequate knowledge of the mechanics of transient, three-dimensional turbulent boundary layer separation. Research in this area could be very fruitful. Most of the destructive instabilities which occur in turbomachines are large-scale effects which need further study. As mentioned earlier, better instrumentation is the key to assessing these problems. Better documented, and therefore of less pressing research need, are nonlinear transients which occur in ducting systems.

Computational Techniques. Over and over, flow research-

ers express a need for a prediction tool to supplement experimentation. Earlier hopes that the digital computer could soon serve as a "numerical wind tunnel" have been dashed by unattainable needs for very large core storage and computation time. Computer modeling in the foreseeable future is limited either to low Reynolds numbers (about 10^5 at best) or to large-scale turbulence. Many needed modeling studies are, of course, fundamental problems in turbulence. The problems are of two types: free turbulence, such as in the atmosphere, jets, or wakes; wall-related turbulence. Many problems such as bluff-body vortex shedding or jet discharge into confined regions involve both types of models.

The great enthusiasm of researchers for turbulence models has not been matched by the quality of the results obtained. The only generally reliable turbulence computer codes in existence are for two-dimensional thin boundary layers and for vertically-averaged tidal flow in estuaries. The boundary layer codes were established by the Stanford Competition of 1968, at which many of the traditional accepted codes were found to be hopelessly at variance with experiment and hence discarded. A similar international competition in 1975 for three-dimensional turbulent boundary layer codes revealed no winners; that is, not a single submitted code was able to predict the correct shape of the separation zone in front of the root section of a cylindrical fin. Even the best of these boundary layer codes is presently unable to compute any significant distance into a separation zone, and hence to interact with the outer stream in separating flows. Future research in boundary layer computation should stress this area of separation and reattachment interactions. More pedigreed three-dimensional boundary layer data should be obtained, new broadly-based competitions should be held, and the losing codes should be firmly discarded. Support in this area should be guided by inspired agencies especially sympathetic to new ideas. Some researchers feel it is much more likely that the modeling keys will lie in new concepts such as, for instance, the surface renewal concept, rather than in further refinement of the traditional eddy-viscosity concepts.

The preceding discussion of boundary layer codes applies in equal manner to the need for reliable turbulent-mixing codes, especially when coupled to complex effects such as stratification, combustion, multiple phases, and unsteadiness. Improved mixing models are especially needed for atmospheric and oceanographic flows. For example, plans to utilize Ocean Thermal Energy Conversion (OTEC) are primarily dependent upon our ability to assess accurately the redistribution and mixing of ocean thermal structure caused by such large floating heat engines.

There is more to be gained than basic knowledge from these turbulence computer codes. If reliable codes can be documented and utilized, they will greatly reduce the cost of design, development, and testing. Eventually, true design optimization of energy-related systems could become a reality.

Vehicle Drag. Of great potential importance, but cited rather seldom by questionnaire respondents, is the problem of vehicle drag reduction. The average fuel cost for a cargo ship is three to five million dollars per year. Automobiles and trucks and buses in this country consume some fifty billion gallons of gasoline per year. Even a small reduction in drag of these vehicles represents a vast saving in this nation's fuel consumption. Perhaps the ripest area for aerodynamic research is in domestic autos, where styling and other social considerations presently outweigh aerodynamic drag penalties. The average drag coefficient, based on frontal area, of an American auto is approximately 0.4. The minimum achievable drag coefficient is about 0.1 – a 75 percent reduction – but no one is presently conditioned to drive

downtown in a four-wheeled tear drop. There is clearly a lot of room to negotiate a compromise between styling and drag to obtain, after suitable research, a 30 percent reduction in auto drag. At highway speeds, such an auto would use one-half gallon less fuel per hour. Similar research would benefit trucks and buses and other vehicles. In many cases, the solution will merely involve window placement, rear hatch angle, grill shape, or underbody protuberances. This is potentially a very fruitful field for energy research.

Biological, Geological, and Environmental Fluid Flow. Research in this category is of significance to a number of energy-related problems. The sample from which data were obtained consisted mostly of professors in mechanical and chemical engineering departments or engineers working in industries such as the automotive or the aircraft industry. There appears to be no large input from the community of bioengineers, physicists, and people concerned with atmospheric phenomena. Nevertheless, there appears to be a very strong feeling that the following secondary research categories are of importance:

1 Basic understanding of flow phenomena in porous media, including pressure drop and heat transfer needed for oil recovery (secondary), filtration, cleanup of oil spills, geothermal heat recovery, and thermal insulation.

2 Fouling of heat exchangers, especially in marine environments required for improved heat exchanger performance needed for closed cycle OTEC applications.

3 Basic studies of flow and stability of stratified fluids with body forces. Experimental verification on a large scale is needed for solar ponds, atmospheric phenomena, inversion layers, and geophysical fluid mechanics.

4 Non-Newtonian flow in capillaries to yield a basic understanding of blood flow required in the biomedical area.

In all cases, there appears to be a lack of basic understanding of flow phenomena and fundamentals of processes and sufficient experience in application to real systems to permit good design. Research along experimental-analytical lines with concurrent investigation of applications should be undertaken.

Atmospheric Flows. Atmospheric and oceanographic flows are the controlling factor in many alternate energy sources. Modeling of such flows, which are large-scale, turbulent, and nonstationary, is an area of fundamental turbulence research. Problems in application are of a very practical engineering nature. Cooling towers, windmills, solar collectors, tidal generators, and OTEC systems are all exposed to these flows and have severe reliability problems especially due to structural interactions. Efficiency is impaired by their intermittent performance. Terrain and persistency effects must be studied, and methods developed for selection of favorable sites. Air/sea interactions should receive study to assist in setting maximum design conditions. Weather predictions, though less useful, can contribute to overall policy on siting decisions.

Facilities and Instrumentation. Improved understanding of fundamental behavior, application of fundamentals to complex situations, and development of advanced computational techniques must all rely on experimental verification for acceptance. Efforts involved in such verification are generally much more extensive in their range and cost than those required in the initial development of the concept. Specialized measurement techniques and test facilities are required, some of which currently do not exist. Many people responding to the survey identified needs in this area which are summarized below.

Instrumentation. Improvements in both steady and

transient velocity measurement capability for remote fields, extreme environments, and for various multiphase situations were high on the list of instrument needs (Table 9). Specialized devices to evaluate interfacial transfers in multiphase flows are also needed. Specialized devices to measure parameters within fluid machinery and especially turbomachines are needed. Finally, improved commercial and industrial instrumentation is needed to improve operational efficiencies of energy conversion and utilization devices and systems.

Facilities. Numerous fluid flow and thermal hydraulic test facilities exist in the United States. Many universities, research laboratories in industry, and national laboratories have facilities of various capabilities. These are generally developed for particular applications and are in continuing use for long projected times. The availability for other purposes is usually limited. Numerous respondents identified the need for various classes of experimental facilities which would be available for generic developmental studies in a broad class of research fields. Individual workers or small research groups would thus have a vehicle for testing devices or theories in a manner otherwise impossible due to lack of equipment.

There were a large number of stated suggestions, their categories being summarized in reference [11]. All seemed to fall into the following three categories:

(*a*) Calibration facility for single-phase or multiphase gas-liquid or particulate flows. This facility would provide very close control of flow parameters and make available the most accurate calibration standards available.

(*b*) A facility for achieving ultra high Reynolds numbers is required. This facility would be utilized for studying atmospheric-structural interactions, ocean-structure effects, and other effects on large equipment and structures.

(*c*) A high temperature, high pressure facility for single-phase and multiphase studies of a fundamental nature using both steady and unsteady flows. A facility having multicomponent capability would suffice for both adiabatic flows without mass transfer between phases, as well as for nonadiabatic situations with phase change.

Research Activity Modes. We see that there are certain modes of research activity that will often characterize effective work toward achieving the objectives we have stated.

Experimental Investigation of Component Phenomena. Greater attention ought to be given to formulating experiments which isolate aspects of complex phenomena. Such

Table 9 Research needs in instrumentation development

1. Develop remote field velocity sensors and flow visualization techniques
2. Develop remote particle or droplet sensing and sizing techniques
3. Develop remote bubble velocity and sizing methods
4. Develop local phase volume fraction and velocity measuring systems for intermediate and high speed flow
5. Develop inexpensive sensors for consumer use
6. Develop dam flow monitor
7. Development of various instruments for extreme environments (pressure, temperature, dynamics)
8. Develop inexpensive, portable, reliable Laser anemometer
9. Process and reaction monitors – improvement
10. Transient and unsteady flow and pressure measurement
11. Develop interphase transport measuring devices
12. Develop improved velocity measuring devices for difficult environments
13. Devices for measuring flow phenomena in rotating passages at transonic conditions
14. Devices for measuring components and phase flow rates in multiphase flows
15. Particulate or droplet velocity and size classification methods

experiments can greatly improve the understanding of prototype behavior, and even help to predict it.

The Formulation of Physical Theory. The most profitable kind of scientific or technological progress is the formulation of correct underlying physical theory or basic physical mechanism – Prandtl's boundary layer concept, von Karman's turbulence theory, the Kutateladze burnout mechanism, for example. Every attempt should be made to support the successful formulation of valid scientific theory.

The Development of Reliable Scaling Laws. Scaled experiments hold the promise of greatly reducing the cost of experimental investigation, and for generalizing limited data. They also give means for visualizing or otherwise improving understanding of phenomena which may be very hard to "get at." In some cases, scaling laws are very solidly established – the drag coefficient/Reynolds number relation for a given body, for example. In other cases, we have scaling laws which are not fully articulated or cannot be fully trusted. If the scaling laws for a particular important process can be solidly established, two other benefits immediately accrue: component phenomena will be better understood, and computer code validation can be facilitated.

The Formulation of Computational Models. Such descriptions might be numerical solutions of differential equations; they might be large correlations; they might be other interpolations of experience. However, a major attempt should be made to provide the best physical understanding possible in any computer code simulation of an engineering system.

Instrument Development. Many of the high priority research areas that we have advocated depend on the development of better instrumentation than is presently available. Examples would include: rapid response temperature instrumentation, void fraction instrumentation of many kinds, and measurement of composition. Such development might appear as a part of a particular research effort, or as a subject to be undertaken independently of any stated mission. In either case, it should be fostered.

Physical Property Evaluations. The evaluation of physical properties often becomes an *integral* part of the solution of certain fluid flow problems, and should not be left as a separate activity. Notable examples include: the evaluation of properties of certain liquid metals or exotic liquids that find use as power plant coolants, the evaluation of properties of liquids and gases in the metastable thermodynamic states, the specification of homogeneous nucleation limits and the properties required to calculate them, the rheological properties of non-Newtonian process fluids; the development of analytical representations of fluid data, and the specification of diffusion coefficients.

Integral System Stability. There are some rather fundamental questions concerning the interconnection of separate components to form an integral system. These have to do with interaction effects of modified or new phenomena which arise due solely to the coupling, and questions of efficiency, effectiveness, economics, and stability. Modeling of complex systems such as multiple pumps, feedwater systems, steam generators, and other energy system components for analysis of these and similar concerns is in need of work.

Summary Recommendations and Priorities

The time available for preparation or pursuance of this survey has been much too short to allow exhaustive use of available resource material. For instance, there exists another significant resource which was not used, but which also

should be tapped. The ASME periodically sponsors the Freeman lecture which provides a grant of $3000 for the outstanding authority in a specific subfield of fluid mechanics to present a status report of his field, as well as to make recommendations for needed research. There have so far been six Freeman lectures identified as follows:

1971   J. W. Hoyt
       The Effect of Additives on Fluid Friction

1971   R. F. Probstein
       Fluid Mechanical Problems in Desalination

1974   J. E. Cermak
       Application of Fluid Mechanics to Wind
       Engineering

1976   W. J. McCroskey
       Some Current Research in Unsteady Fluid Dynamics

1978   B. Gebhart
       Buoyancy Induced Fluid Motions Characteristic of
       Applications in Technology
1980   E. M. Greitzer
       The Stability of Pumping Stations

The success of the Freeman program rests upon careful selection of an internationally recognized scholar who is given sufficient time and remuneration to prepare a truly thoughtful and comprehensive assessment of the research potential of a specific field in engineering. The resulting lecture-reviews listed above have been outstanding. It was the consensus of the workshop participants that similar scholars could provide careful reviews of energy-related research potential. Therefore, it is recommended that serious consideration be given to the establishment of a scholar program to initiate a series of annual or periodic reviews of specific research areas appropriate to the basic engineering goals of the workshop and the Department. A stipend of $10,000–$15,000 each year per individual for this purpose seems appropriate, perhaps channeled through the appropriate technical society. This could significantly further aims of providing ". . . technical and economic evaluations of key energy technologies . . . and analyses of significant RD&D programmatic issues."

Of all the topics which were identified as requiring further research of a fundamental nature (Table 1), five areas of research appeared to represent generic gaps in our understanding of fluid mechanics. These five broad areas which must be pursued include: turbulence; multiphase flows; fluid-structure interactions; boundary layer effects, and biological, geological and environmental flow effects. It appears that major advances are required in each of these areas before a significant new generation of energy conversion devices will emerge having broad impact on reduced constructional and operational utilization of energy resources.

The priorities in each of the five areas appear to be ordered as follows:

1 Multiphase and Multicomponent Flows
   (*a*) Application to and experimental verification of extensions of single-phase flow theory to multiphase, multicomponent turbulent flows.
   (*b*) Detailed studies of nucleation phenomena and of interfacial structure and transfers. This should be done in simple and multidimensional geometries and free field flows. *Objective* determination of flow regimes and of phase and/or component space-time distributions should be undertaken in laminar and turbulent flows.
   (*c*) Fundamental studies regarding effects of scaling

laws, building on knowledge gained in the previously defined studies.

2 Fluid Structure Interactions

(*a*) Research should be undertaken in energy-related problems of flow-induced vibrations due to both periodic or stochastic loadings. Such loadings may be due to such effects as vortex shedding or turbulent interactions in both free fields and boundary layers. Attention should be given to both coupled and uncoupled interactions. Areas of concern include, but are not limited to, tubes in heat exchangers and blades in turbines and compressors.

(*b*) Fluid-structural coupling in cases of both impulsive and aperiodic loadings should also be investigated. Such situations include condensation-induced water hammer and transient decompressive reactions.

3 Shear, Mixing, and Reactive Flow Effects

(*a*) In spite of continuous emphasis in boundary layer research, the difficult problems dealing with real systems still exist. The area of separation and reattachment remains unresolved and appears to be of central importance affecting performance, lifetime, and safety of turbomachinery, among others.

(*b*) Fundamental studies into the flow patterns around road vehicles are needed and can be of great benefit. These flows involve three-dimensional bluff bodies, in extremely close proximity to a ground plane, with strong vortical wakes. Both wind-tunnel and analytical modeling studies are recommended.

(*c*) Research is needed in internal flow with chemical reactions, leading to a detailed understanding of the coupled processes which enable the development of more efficient, cleaner combustion systems. In this category, particular emphasis should be placed on advanced analysis techniques and instrumentation to study internal combustion automotive engines and others.

Considering the overall picture, it seems that one expectation is clear. It is likely that, in spite of all the empirical methodology developed for highly specialized situations, major advances in our fundamental understanding will probably be achieved through development of simple theories for simple and understandable situations followed by application to more complex cases. These will then be coupled with development of computational systems generalizing upon the simple cases. In all cases, acceptance and advance will arise only through mutual development of theory and experiment.

Improvements in developing a low cost, accurate, remote velocity measuring device or extension of an existing device such as the Laser Doppler method, could lead to a resurgence in extended basic research at institutions such as small research laboratories or universities currently unable to afford the more exotic methods currently available.

In addition to the fundamental work previously summarized, there appears to be a general consensus that *small*, general purpose research facilities are needed which can be dedicated to the support of nationally sponsored, fundamental, fluid flow (or thermal hydraulic) research including: a specialized calibration and standards facility for testing new fluid flow instrumentation; a high Reynolds number facility; and a high pressure, high temperature facility which can also serve as a two-phase flow facility. It seems appropriate that there be a National Thermal Hydraulics Laboratory established over a period of years devoted to energy-related research. This laboratory, having these capabilities, should be supportive of fundamental, energy-related work sponsored by governmental agencies undertaken in industry and universities, as well as at national laboratories. It should be established at a location predominantly keyed to basic rather than applied research so that administrative support of both the sponsoring agency and the contractor administration will be forthcoming. Advantage should be taken of existing facilities and expertise in the thermal hydraulic field commensurate with the preceding recommendations. For instance, excellent facilities currently exist at several national laboratories.

References

1 Anderson, J., "Fundamental Research Needs: A Status Report of the Task Force on Fundamental Research," ASME Paper 76WA/RGPC-5, presented at the 1976 Winter ASME Meeting, New York.

2 Uram, M., "Current and Future Trends and Problems in Combustion," ASME JOURNAL OF FLUIDS ENGINEERING, Vol. 71, 1975, pp. 285-286.

3 Shah, R. K., and London, A. L., "Areas of Future Research," in *Laminar Flow Forced Convection in Ducts*, Academic Press, New York, 1978, pp. 419-420.

4 Schlunder, E. U., and Shah, R. K., "Panel Workshop on Heat Exchanger Design and System Optimization," *Proc. 6th Int. Heat Trans. Conf.*, Vol. 7, 1978.

5 Bergles, A. E., et al., "Suggestions for Further Research and Urgent Problems on Two-Phase Flow and Heat Transfer," in *Two-Phase Flows and Heat Transfer*, III S. Kakac and T. N. Veziroglu, eds., 1976.

6 Tuzson, J., "Stability of a Curved Free Streamline," ASME JOURNAL OF FLUIDS ENGINEERING, Vol. 99, No. 1, 1977, pp. 603-605.

7 Welliver, A. D., "Propulsion Research Requirements for Powered Lift Aircraft," Proc. Proj. SQUID Workshop on Engine-Airframe Integration, pp. 199-244, with discussion, 1977.

8 Welliver, A. D., "Flow Separation," private communication.

9 Birch, S. F., "Turbulence Models for the Point of View of an Industrial User," *Future Computer Requirements for Computational Aerodynamics*, NASA Conf. *Proc. 2032, Proc. of Workshop*, NASA American Research Center, Oct. 4-6, 1977.

10 Gratch, S., *Research Needs Report: Energy Conversion Research*, prepared by the Task Force on Energy Conversion Research, ASME Policy Board, Research, 1976.

11 Jones, O. C., Jr., Kreith, F., and White, F. M., "Basic Research Needs in Fluid Mechanics," BNL-50995, Mar. 1979, available from the National Technical Information Service, U. S. Department of Commerce, Springfield, Va., 22161.

12 Eichhorn, R., Conta, L. D., and Hill, R. F., "Basic Research in Engineering—Fluid Dynamics and Thermal Processes," ESCOE Report FE-2468-54, Aug., 1979, Available from The National Technical Information Service, U.S. Department of Commerce, Springfield, Va., 22161.

REVIEW—A Review of Some Phenomena in Turbulent Flow Separation

R. L. Simpson

Professor of Mechanical Engineering,
Southern Methodist University,
Dallas, Texas   75275
Mem. ASME

Although turbulent flow separation is an old topic, little credible information is available on the flow details that must be understood to predict flows of this type. Until the last decade, there was little serious effort to develop and use experimental techniques that give unambiguous results. Consequently, flow models that are based on valid data are not well developed. Furthermore, the terminology used in discussing separation has been loosely defined, adding further confusion to the subject. This brief review presents a cross-sectional view of recent experimental techniques and results, development of models for flow prediction, efforts to define a meaningful common terminology to describe the flow, unsteady effects, and efforts to control separation.

1 Introduction

Turbulent flow separation continues to be a nuisance to fluid dynamicists because it may be present in many practical machines or devices, thus reducing their performance, and because there is no adequate method to calculate such flows. In general, the maximum performance of such machines occurs at conditions close to the onset of separation. In order of increasing difficulty, designers need to know

(a) whether or not a boundary layer separates for a prescribed pressure distribution,

(b) how the pressure distribution is affected by boundary layer development with small regions of separated flow, and

(c) how the overall performance is affected when large regions of separation are present.

Some of the situations of interest occur in diffusers, engine inlets, fans and compressors, and on aircraft. The mean separated flow is nominally two-dimensional in many cases, but is three-dimensional in many more configurations, e.g., on a wing, on propulsive components, on an intake, on local protuberances, and on swept edges emanating from an apex. Separation from bluff bodies is just as important as for streamlined shapes, e.g., boat-tailed bodies, flame stabilizers in gas turbines, and large buildings subjected to wind loadings. From a structural viewpoint, the aeroelastic response of the surface to strong pressure fluctuations produced by separation is an important consideration.

The Colloquium on Turbulent Flow Separation [1] was held by Project SQUID at SMU to discuss fruitful areas for future research. A number of active researchers participated in discussions on five topics: terminology, measurements, flow modeling, unsteady effects, and control of separated flow. These topics are fundamental to future advances since a common nomenclature should be used to describe phenomena that are measured and modeled.

The present review paper was prepared after the Colloquium took place. It includes, where appropriate, the author's interpretation of some of the discussions at the Colloquium.

2 Terminology

The term *"separation"* must mean the entire process of *"departure"* or *"breakaway"* [2–4] or the breakdown of boundary-layer flow. An abrupt thickening of the rotational flow region next to a wall and significant values of the normal-to-wall velocity component must accompany breakaway, else this region will not have any significant interaction with the freestream flow. This unwanted interaction causes a reduction in the performance of the flow device of interest, e.g., loss of lift on an airfoil or loss of pressure rise in a diffuser.

It is too narrow a view to use vanishing surface shearing stress or flow reversal as the criterion for separation. Only in steady freestream two-dimensional flow do these conditions usually accompany separation. In unsteady two-dimensional flow, the surface shear stress can change sign with flow reversal, but without breakaway. Conversely the breakdown of the boundary layer concept can occur before any flow reversal is encountered [2, 3].

In three-dimensional flow, the rotational layer can depart without the surface shear stress necessarily falling to zero; the wall shear is zero only at the singular points where the surface vorticity is also zero [5, 6]. At a nodal singular point of detachment, all of the skin-friction lines are directed inward toward the node. At a focal singular point of detachment, all of the skin-friction lines spiral around the point and into it. Only two particular lines pass through a saddle singular point. The direction on either side of the point is inward on one skin-friction line and outward on the other. All other skin-friction lines miss the saddle singular point and take directions consistent with the directions of the adjacent particular lines.

Contributed by the Fluids Engineering Division for publication in the JOURNAL OF FLUIDS ENGINEERING. Manuscript received by the Fluids Engineering Division August 4, 1980.
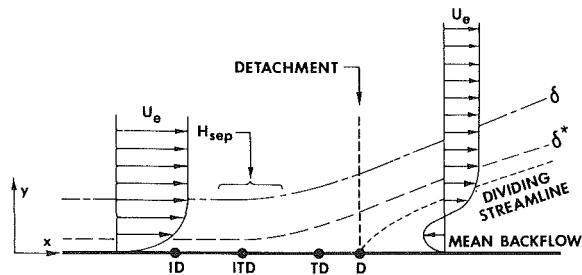
Fig. 1 Definitions of two-dimensional turbulent detachment states. Distances not to scale. "Percent Instantaneous Backflow" means along a spanwise line at a given time, or percent of time at a point.

OLD TERM	SYMBOL	NEW TERM	CONDITION
none	ID	Incipient Detachment	1% Instantaneous Backflow
Intermittent Separation [11]	ITD	Intermittent Transitory Detachment	20% Instantaneous Backflow
none	TD	Transitory Detachment	50% Instantaneous Backflow
Steady or Fully-Developed Separtion [11]	D	Detachment	$\tau_w = 0$

These singular points are readily observed by a thin oil-visualization indicator that marks surface skin-friction lines [6, 7]. These skin friction lines are defined everywhere on the surface, even in the vicinity of lines of flow departure from the surface (separation lines according to Peake and Tobak [5]) which are themselves ordinary skin-friction lines. Without going into the fine detail given by Peake and Tobak on page 5 of their review, they state that there is a dividing surface in the flow that intersects the body along the line of detachment and prevents the converging shear layer on each side of the detachment line from coalescing.

There is no basis for inferring the behavior of limiting streamlines from skin-friction lines in the vicinity of lines of flow departure. Since skin-friction lines are unique everywhere on the surface, they form a continuous vector field. Lighthill [6] showed that the number and types of singularities on the surface obey a topological rule: The number of nodal and/or foci singular points exceed the number of saddle point singular points by two. Hunt, et al. [8], have shown recently that this rule can be extended to the flow above the surface on planes of symmetry, on projections of conical flow, and on cross-flow planes [5].

Until recently, little new information about mean two-dimensional steady free-stream turbulent separation has been available. With measurements made with different types of instrumentation in different apparati, it is important to adopt a terminology that will allow quantitative comparisons and make the most of data that are difficult to obtain. S. J. Kline, J. P. Johnston, and other participants at the Colloquium

proposed the following general terms for two-dimensional steady freestream separation [1]:

A. *Detachment*--the location where the boundary layer flow leaves the wall; the locus of points where the limiting streamline of the flow leaves the surface.

B. *Reattachment*--locus of points where the limiting streamline of the time-averaged flow rejoins the surface.

C. *Separation*--the total process consisting of detachment, recirculation, flow free-shear layer, and, in cases not involving a free wake, reattachment.

D. *Stall*--zone of recirculating fluid created by pressure forces.

E. *Stalled Fluid*--fluid with reverse or low velocity within a recirculating zone.

Newman [1] pointed out that normal usage in the past held "detachment" to be the same as "separation"; that definition C usually was used for the "separation region and wake"; that "stall" was defined as the condition of maximum lift; and that definition D would be used for "backflow."

Figure 1 shows other proposed definitions of flow characteristics nearest the surface on which the separation process occurs. Except in singular cases such as a backward facing step, turbulent detachment is a zone. Sandborn and Liu [9] and Simpson, et al. [10], have noted that the fraction of time that the flow moves downstream, γ_p, varies gradually from unity toward zero along this detachment zone. "Incipient detachment" has been observed in old experiments when flow markers such as a dye filament injected into liquids at the wall or a tuft mounted on the surface would move upstream occasionally. In the past, this location has been loosely called incipient separation. (Here we will not use this latter term since it appears to have been used loosely to mean a flow near conditions required for the separation process to occur. In some cases such as in supersonic flow, the separation process occurred, but was not documented; it was often called incipient separation.)

"Intermittent transitory detachment" was observed in old experiments when tufts or dye filaments move upstream a noticeably greater fraction of time than "occasionally." Sandborn and Kline indicate that this location corresponds to the location previously called "turbulent separation" or "intermittent separation" [11]. Currently Sandborn [12] labels the velocity profile at this position as "unrelaxed." "Transitory detachment" and "detachment" may correspond to the same location if the streamwise velocity probability distribution at that location is nearly Gaussian. Detachment was called the location of "steady" separation by Sandborn and Kline while Sandborn [12] notes that the

---

Nomenclature

AR = diffuser area ratio
C_p = diffuser static pressure recovery factor
c = airfoil chord length
H = displacement to momentum thickness ratio
L = length of diffuser
N = distance from wall to maximum negative value
n = wall bursting frequency
P = pressure
S = pulsed wire spacing
U = mean velocity component in x-direction
u = rms velocity fluctuation in x-direction
U_τ = $(\tau_W/\rho)^{1/2}$, shear velocity
U^+ = $U/U_\tau = f(y^+)$
$-\overline{uv}$ = cross-correlation of fluctuations, Reynolds' shear stress
V = mean velocity component in y-direction
v = rms velocity fluctuation in y-direction
W = inlet width of a diffuser

x,y = Cartesian coordinates along and perpendicular to the wall, respectively
y^+ = yU_τ/ν
γ_P = fraction of time flow moves downstream
δ = boundary layer thickness
δ^* = displacement thickness
θ = half angle of diffuser divergence
λ_Z = viscous sublayer spanwise spacing
ν = kinematic viscosity
ρ = density
τ = shearing stress

Subscripts

e = denotes value outside boundary layer
max = maximum value
N = denotes maximum negative magnitude
w = wall value
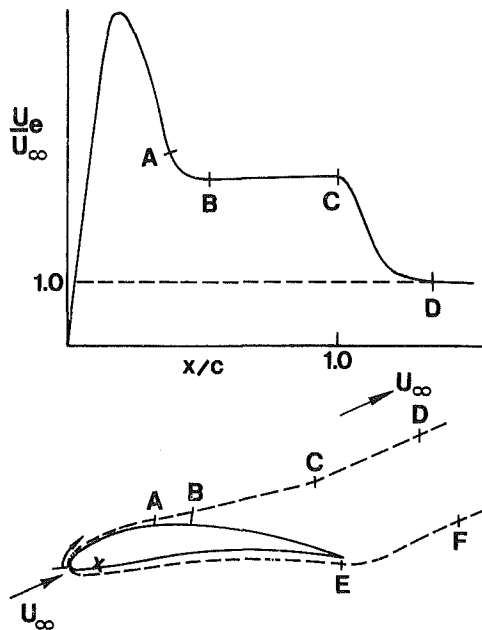∞ = far freestream condition

Fig. 2 Conceptual schematic of free-streamline separation: top figure – characteristic velocity distribution just outside the shear layer on the suction side: pressure gradient relief region between A and B, free-streamline region between B and C, wake relaxation region between C and D; lower figure – body (solid line) and the effective body (dashed line) that consists of the real body plus the displacement thickness, with comparable A, B, C, and D suction side locations and pressure side wake relaxation region between E and F. Suction side wake velocity and length scales are much larger than those for the pressure side wake.

velocity profile at this location is "relaxed." Until recently, most predictors were concerned only with predicting D, ignoring the fact that the turbulent separation process starts upstream of this location in all but singular cases where ID and D are at the same location.

The length of the region between the ID, ITD, TD, and D points will depend on the geometry and the flow, but the definitions of these points are the same. γ_p is not a sufficient variable to describe the flow behavior since it represents only the fraction of a streamwise velocity probability distribution that is positive. However, it is important that such a feature be documented in all future work. As mentioned in section 5 accurate quantitative techniques are available for measuring these features.

3 Flow Physics

A. Observations of the Inviscid Flow Behavior in Steady Two-Dimensional External Flow. Figure 2 shows the chordwise distribution of U_e, the suction side velocity just outside the boundary layer, for an airfoil at the angle of attack. Experimental observations indicate that when detachment occurs well upstream of the trailing edge, complete pressure gradient relief occurs until the trailing edge of the airfoil is reached as shown between B and C. In general, this same behavior is observed for a variety of bodies, including a circular cylinder and many different airfoil designs, several examples of which are presented by Cebeci, et al. [13]. For these cases, one must conclude that in the separated flow zone downstream of detachment, the velocity and pressure just outside the shear layer approach the free-streamline condition of constant pressure and velocity. It appears that free-streamline separation occurs when the velocity and length scales of the suction side shear layer are much larger than those found on the pressure side.
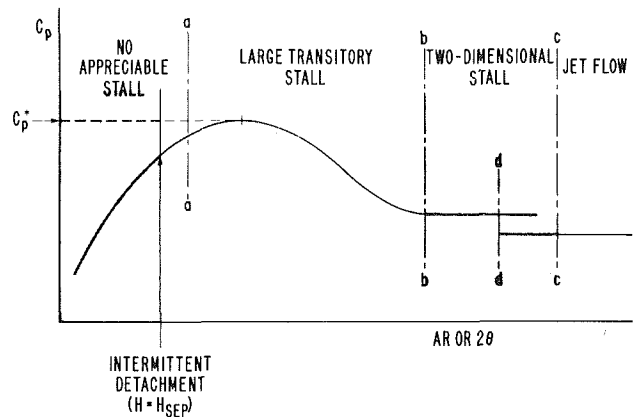
Fig. 3 Behavior of C_p with increasing area ratio AR or 2θ for constant L/W two-dimensional diffusers [16,17]. Good predictions possible in shaded regions.

Downstream of the trailing edge, U_e must eventually return to U_∞ in both magnitude and direction, since the irrotational flow outside the shear layer obeys Bernoulli's equation. In cases where separation occurs close to the trailing edge, no constant pressure region is observed and the freestream velocity continues to decrease, sometimes to below the value U_∞. In these cases, the velocity downstream of the trailing edge must increase to U_∞. In this case of trailing edge separation, there apparently is strong interaction between the wakes of the suction and pressure sides, since the thickness and velocity scales are not very different. Thus, the freestream velocity distribution in the region between detachment and the near wake is controlled by both shear layers.

The near wake region (CD in Fig. 2) is a critical part of separation since it is characterized by strong interaction of both separated shear layers with the inviscid flow and controls the downstream distance to the location where the pressure is uniform. It is clear from the work of Jacob [14] that an accurate description of this region is very important to the overall drag prediction. With the exception of the recent measurements of Coles and Wadcock [15], there is no reliable detailed flow structure data for the near wake shear flow of a lifting airfoil with turbulent separation.

B. Observations of the Flow Behavior in Two-Dimensional Diffusers. The flow behavior is primarily dependent on the diffuser geometry in two-dimensional diffusers [16, 17]. A typical curve of static pressure recovery, C_p, for four flow regimes is shown as a function of the divergence angle 2θ in Fig. 3. Line a–a represents the approximate dividing line between the unstalled and transitory stall regimes. The separation process does not occur in the unstalled regime. Line b–b divides the transitory stall regime from the fully-stalled regime. Complete pressure gradient relief occurs in the latter regime, similar to free-streamline separation for external flow.

Transitory stalls are large, pulsating separations which occur primarily in relatively narrow passages of very symmetric shape. A positive pressure gradient exists all along the surfaces in all known data. The peak pressure recovery is achieved in this regime. The flow first detaches near the end of the diffuser, forming a stall. The stalled region grows toward the diffuser throat, pulling in fluid from the diffuser exit. After sufficient growth, the stall becomes unstable, is entrained by the mainstream flow and is washed out of the diffuser. The sequence repeats itself. These large scale, low frequency washouts are believed to represent an interaction between the diffuser flow and the flow in the system to which the diffuser is coupled. Kline and Johnston [1] suggest that the positive dP/dx is essential in sustaining the transitory stall

fluctuating flow pattern, since Smith and Kline [18] have shown that the maximum unsteadiness occurs just before some fixed stall zone is observed. Large transitory stalls appear to occur only in internal flow. Of the four flow regimes, it is the most complex and the least predictable.

C. Some Features of the Turbulent Boundary Layer. The present author and colleagues [10, 19–21] have made detailed laser anemometer measurements of the structure of a steady freestream, two-dimensional turbulent boundary layer. Although there was no transitory stall in these experiments, there was not complete pressure gradient relief downstream of detachment, but rather a minimal pressure gradient. Figure 4 shows the airfoil type inviscid freestream velocity distribution for the earlier flow [10] that was produced in a two-dimensional converging-diverging wind tunnel. Boundary layer measurements were made on the flat straight floor. A similar, but different, streamwise velocity distribution was used in later experiments.

Upstream of Separation. Upstream of the vicinity of separation, a mean two-dimensional turbulent boundary layer in an adverse pressure gradient has well accepted characteristics. The "law of the wall" and "law of the wake" describe the mean velocity profile while the qualitative turbulence structure is not markedly different from the zero-pressure-gradient case; the turbulence energy, dissipation, production, and spectral distributions behave in a known fashion. The maximum turbulent shearing stress $-\overline{uv}_{max}$ is less than $1.5 \, (\tau/\rho)_w$. The wall "bursting" frequency n behavior and the spanwise structure spacing λ_z in the viscous sublayer behave similarly to that for the zero-pressure-gradient case, i.e., $U_e/n\delta$ = constant and $\lambda_z(-\overline{uv})_{max}^{1/2}/\nu \approx 100$. The bursting frequency correlation constant is 10, not 5 as in the zero-pressure-gradient case, because of lag produced by the pressure gradient.

Perry and Schofield [22] proposed a correlation for the mean velocity profiles in unseparated flow in the presence of strong adverse pressure gradients, based upon 145 mean velocity profiles taken from Coles and Hirst [23], including equilibrium and nonequilibrium profiles. This correlation applies only when the maximum shearing stress $-\overline{uv}_{max}$ exceeds $1.5 \, (\tau/\rho)_w$. Nearest the wall, the traditional law-of-the-wall velocity profile holds. Further away, a half-power profile exists, while in the outer region a velocity-defect correlation exists. The data of Simpson, et al. [10, 19], and Samuel and Joubert [24] support this correlation.

The normal stresses terms $\partial(\overline{u^2}-\overline{v^2})/\partial x$ and $(\overline{u^2}-\overline{v^2})\partial U/\partial x$ in the momentum and turbulence energy equations, respectively, are significant near separation in the region where the Perry and Schofield correlation holds. Up to one-third of the turbulence energy production in the outer region is due to normal stress effects [10, 20] as separation is approached. The relations between dissipation rate, turbulence energy, and turbulent shearing stress are modified slightly since some turbulence production is not related to the shearing stress. The convective terms of the momentum equation make the shearing stress gradient less than the streamwise pressure gradient so that the traditional law of the wall is valid.

The turbulence structure is slightly different also. While $U_e/n\delta$ = constant continues to describe the bursting frequency, n decreases as separation is approached since the boundary layer thickness δ grows and U_e decreases. The parameter $\lambda_z(-\overline{uv})_{max}^{1/2}/\nu=100$, indicating that since $(-\overline{uv})_{max} > (\tau_w/\rho)$ this is a more universal correlation for separating flows. The wave speed of the eddies near the wall was about 14 U_τ all along the flow, similar to the wave speed for zero pressure gradient flows. Beginning upstream of separation and continuing downstream, the spanwise integral length scale of the turbulence near the wall increases with δ^2. Since δ
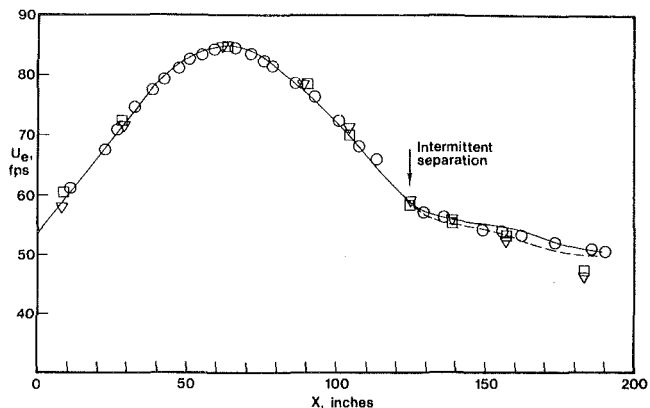
Fig. 4 Freestream velocity distribution at boundary layer outer edge: ○ from bottom wall static taps; □ from the bottom boundary layer pitot probe; ▽ from top boundary layer pitot probe. Solid and dashed lines denote results from minimum pressure gradient model of Collins and Simpson [46].

also grows rapidly along the flow, this means that the near wall separating flow is increasingly dominated by the large-scale outer flow.

Downstream of Separation. As the turbulent boundary layer approaches separation, there is flow reversal near the wall intermittently or only a fraction of time (incipient detachment). The time-averaged mean pressure gradient drops rapidly downstream of the beginning of intermittent backflow. Since the velocity probability distribution at a given x and y location is almost Gaussian when the shearing stress is small, intermittent backflow is present where $u/U > 1/3$. The pressure gradient appears to have reached a minimal level at the detachment location. A consensus view is that any length between ID and D in Fig. 1 is possible and is probably related to the ratio of scales of motion in the outer and reversed flow regions. In terms of the flow geometry, the length of the detachment zone should decrease for increasing divergence of the surface from the mainstream flow direction. Continual backflow near the wall will occur when the divergence of the surface exceeds the rate at which streamwise momentum and energy can be transported toward the wall.

The two-parameter correlation of Sandborn [11, 12] (Fig. 5) for intermittent transitory detachment (intermittent separation) and detachment (fully developed separation) seems to represent the known data accurately. Scatter in this correlation appear to be due to the different experimental techniques used. No known one-parameter correlation seems to work as well.

Downstream of detachment, λ_z is an order of magnitude greater than upstream of intermittent transitory detachment. $U_e/n\delta$ = constant still appears to be valid, indicating that large eddies govern the wall flow. The spanwise integral scale grows from about one-sixth the boundary layer thickness upstream to about one-third the shear layer thickness downstream.

The region with intermittent backflow, which grows in the streamwise direction, never extends outward past the location of the maximum shearing stress. The region of the turbulent-nonturbulent interface next to the freestream also grows in the streamwise direction, but does not extend closer to the wall than the location of the maximum shearing stress. Thus, these two regions do not overlap. The separated flow field shows some profile similarity for U, u, γ_p, and other fluctuation quantities, with the maximum fluctuation u_{max} or $(-\overline{uv}_{max})^{1/2}$ serving as a velocity scale and the distance from the wall to the maximum fluctuations being the length scale. The separated flow field behaves progressively more like a free shear mixing layer in the streamwise direction.
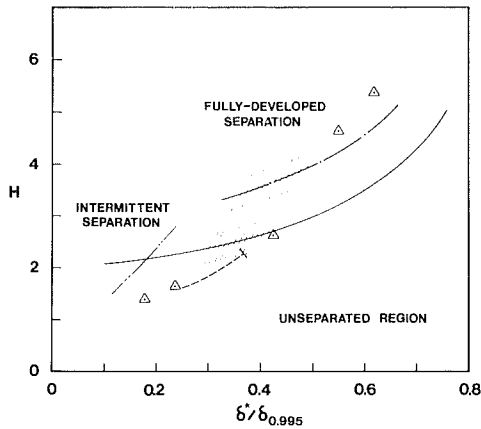
Fig. 5 Sandborn's correlation, H versus $\delta^*/\delta_{0.995}$. $\triangle$ are data from Simpson, et al. [10]. Shaded area − data for intermittent and fully developed separation [11]. Dashed line − path predicted by Perry and Schofield correlation [22]; solid line − intermittent separation; single dot line − fully developed separation; double-dot line − data [9] for a diverging curved surface.

Figure 6 shows our most recent LDV measurements in the vicinity of separation [25]. $\gamma_p < 1$ downstream of the 127 in. location. A one-half power velocity profile region and a logarithmic velocity profile region are distinct further on downstream until the detachment location (fully developed separation) at 135.5 in. Further downstream, the mean backflow velocity profiles have similar shapes and appear to scale on boundary layer thickness δ. The backflow region is strongly dominated by turbulent fluctuations that are greater than, or at least comparable to, the mean velocities as shown in Fig. 7. Since the freestream flow is observed to be rather steady, this means that the near wall fluctuations are not due mainly to a flapping of the entire shear layer, but due to turbulence within the separated shear layer. The mean backflow in this flow and the earlier flow [10] appear to be just large enough to satisfy continuity requirements after the shear flow separates to minimize streamwise pressure gradients. γ_p never reaches zero in either flow, indicating that there is no location with backflow all of the time.

It appears clear to this writer that since the mean backflow is governed by the turbulence and by continuity requirements, it is unrealistic to try to force the mean shearing stress $-\overline{uv}$ to be a function of the local mean velocity gradient. Eddy viscosity and mixing length models infer that the fluctuations in velocity are small compared to the mean flow and that mean velocity gradients are not much different from instantaneous velocity gradients. Unfortunately, separated turbulent flows like the type studied at SMU do not satisfy these assumptions.

It does not appear that the "law-of-the-wall" type of velocity profile ($U^+ = f(y^+)$) based on a wall shearing stress can be valid for the backflow unless significant turbulence energy production occurs near the wall. Turbulence energy balances deduced from the current SMU series of experiments indicate that an almost negligible amount of turbulence energy production occurs in the mean backflow region as compared to normal and shear stress production in the outer region. Large-scaled turbulence diffusion appears to be the main mechanism bringing turbulence energy into the wall region. Since the mean advection of turbulence energy appears to be small in the backflow region, dissipation must balance this influx by diffusion. Classical turbulence energy arguments [27] indicate that production must equal dissipation in a logarithmic region governed by the law of the wall. This rule is not satisfied by the mean backflow region.

Of course, this large-scale structure mechanism for sup-
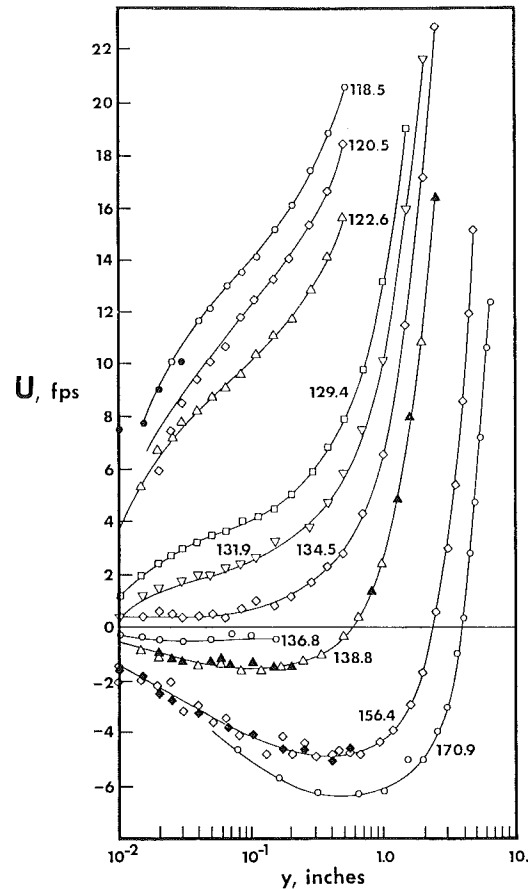
Fig. 6 Mean velocity profiles at several stream wise locations, given in inches, for steady freestream separating flow [25, 26]. Solid lines for visual aid only.
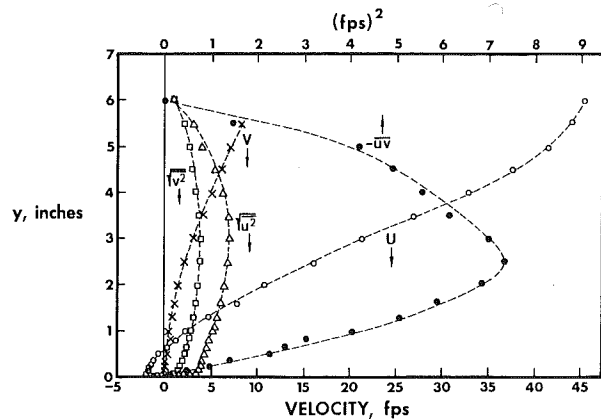
Fig. 7 Mean and fluctuation velocity profiles for the 138.8 in. location.

plying the backflow may be dominant only when the thickness of the backflow region is small as compared with the turbulent shear layer thickness, as in the SMU experiments. Experiments on separation in wide-angle diffusers [16] indicate that the mean backflow can come from far downstream when the thickness of the backflow region is comparable to the thickness of the forward flow. However, the measurements of Ashjaee and Johnston [28] indicate that for large transitory stall, γ_p is never zero! Thus, some forward flow is supplied to the near wall region by the large eddies.

Figure 8 shows a good correlation of the mean velocity profiles in the backflow region of the current SMU flow when
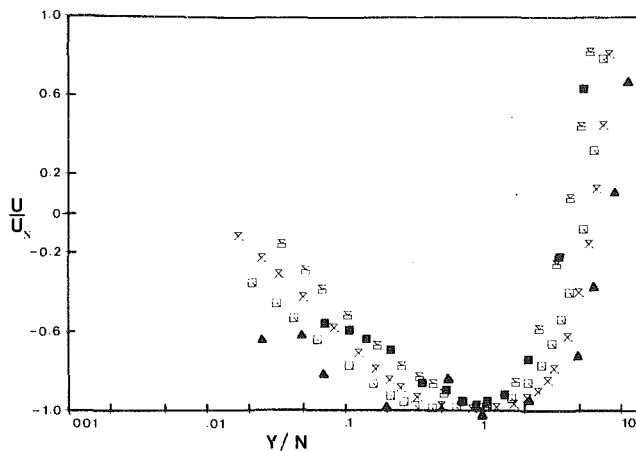
Fig. 8 Backflow mean velocity profiles [19]. ■ 138.8 in.; ▽ 144.9; ▯ 156.4; ✕ 170.9. Simpson, et al. [10]: ▲, 165.8.

Fig. 9 Backward-facing step flow field

normalized on the maximum negative mean velocity U_N and its distance from the wall N. A slightly poorer correlation results when δ is used instead of N. The law of the wall is not consistent with this correlation since both U_N and N increase with streamwise distance while the law-of-the-wall length scale ν/U_τ varies inversely with its velocity scale U_τ. Thus, it appears that representation of the backflow with the law of the wall does not have much merit.

D. Separation From Sharp-Edged Bluff Bodies. The main obstacle to understanding this class of flows comes from the fact that major separation occurs near the sharp edges of the body, with accompanying large variations in velocity and pressure around the detachment location. Here, intermittent detachment is located very near detachment. Some type of Kutta condition must be used to describe the flow in the vicinity of detachment. This condition is very difficult to define with the current lack of experimental data in this vicinity. Downstream of detachment, the length scale of the energetic outer region flow is comparable in size to that of the backflow region. The zone of recirculating fluid is a substantial portion of the entire detached shear layer.

Gosman [1] has pointed out that insufficient reliable data exist to define the structure of the backflow region. Future experiments should be on large-scale models using laser anemometry or other quantitative directionally-sensitive techniques. Moss, et al. [29] and Eaton and Johnston [30] have recently presented turbulence structure measurements for a backward facing step obtained with pulsed-wire anemometry. Unfortunately, no near wall measurements were obtained because of the large size of the probe. Tropea and Durst at the University of Karlsruhe are using an LDV to study this type flow.

Although the backward-facing step is the simplest reattaching flow, the flow field is still very complex. Figure 9 illustrates some of the complexities. The upstream boundary layer separates at the sharp corner forming a free-shear layer. If the boundary layer is laminar, transition begins soon after separation, unless the Reynolds number is very low.

The separated shear layer appears to be much like an ordinary plane-mixing layer through the first half of the separated flow region. The dividing streamline is only slightly curved, and the shear layer is thin enough that it is not affected by the presence of the wall. However, the reattaching shear layer differs from the plane-mixing layer in one important aspect; the flow on the low-speed side of the shear layer is highly turbulent, as opposed to the low turbulence-level stream in a typical plane-mixing layer. Some authors, including Chandrsuda, et al. [31], have suggested that the
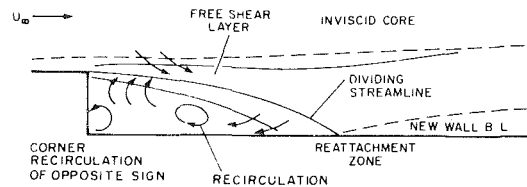
turbulent recirculating flow causes the reattaching shear layer to be substantially different from a plane-mixing layer.

The separated shear layer curves sharply downwards in the reattachment zone and impinges on the wall. Part of the shear-layer fluid is deflected upstream into the recirculating flow by a stong adverse pressure gradient. The shear layer is subjected to the effects of stabilizing curvature, adverse pressure gradient, and strong interaction with the wall in the reattachment zone. One or more of these mechanisms cause(s) a rapid decay of Reynolds normal and shear stresses within the reattachment zone. The flow in this zone is very unsteady. Very large turbulence structures with length scales at least as large as the step height pass through the reattachment region. In addition, flow visualization by Abbott and Kline [23] showed that the length of the separation region fluctuated so that the impingement point of the shear layer moved up and downstremam. Quantitative measurements by Eaton and Johnston [30] confirmed this conclusion. The turbulence intensity level is 5-10 percent higher than for plane-mixing layers, which is believed to be due to a very low frequency vertical or flapping motion of the reattaching shear layer.

The recirculating flow region below the shear layer cannot be characterized as a dead air zone. The maximum measured backflow velocity is usually over 20 percent of the freestream velocity, and negative skin-friction coefficients as large as $C_f = -.0012$ (based on the freestream velocity) have been measured [30].

Downstream of reattachment, the Reynolds stresses continue to decay rapidly for a distance of several step heights. Simultaneously, a new subboundary layer begins to grow up through the reattached shear layer. The measurements of Bradshaw and Wong [33] and more recent measurements by Smyth [34] have shown that the outer part of the reattached shear layer still has most of the characteristics of a free-shear layer as much as 50 step heights downstream of reattachment. This observation demonstrates the persistence of the large-scale eddies which are developed in the separated free-shear layer.

Figure 10 shows some recent laser anemometer results for flow over an airfoil at a large angle of attack [35]. While detachment from this surface does not occur at a sharp edge, this flow contains many of the features of such a flow, such as comparable length scales in the outer shear flow and backflow regions. Mean velocity profiles obey a similarity distribution downstream of the quarter-chord point. The shape of the profile in the outer part of the backflow region is similar to that obtained in the backflow region of the current SMU experiments [10, 19].

At a higher Reynolds number of 1.4×10^6, discrete vortices are shed from near the crest of the airfoil at regular time intervals. They initially move up and then move in the streamwise direction near the 15 percent chord location. The vortex speed accelerates from about one-half of the freestream value near the crest to nearly the freestream speed at the trailing edge. The vortex paths are less regular near the trailing edge, but the repeatability of the period of the vortex passage remains high from leading edge to trailing edge. While this vortex-shedding behavior is not completely explained yet, it emphasizes again the important influence that
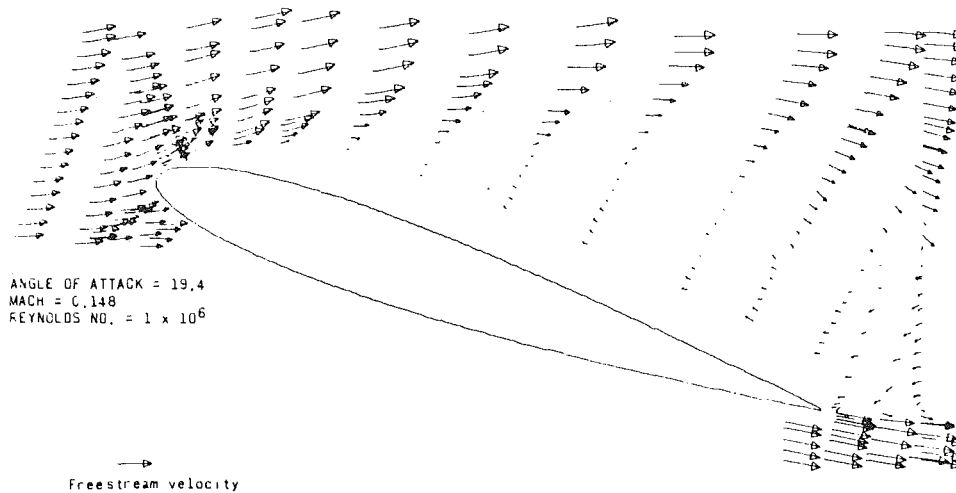
Fig. 10 Low-Mach-number resultant mean velocity vectors for an airfoil with large separation [35]

ANGLE OF ATTACK = 19.4
MACH = 0.148
REYNOLDS NO. = 1 x 10^6

Freestream velocity

DETACHMENT LINE

DIRECTION OF FREE STREAM
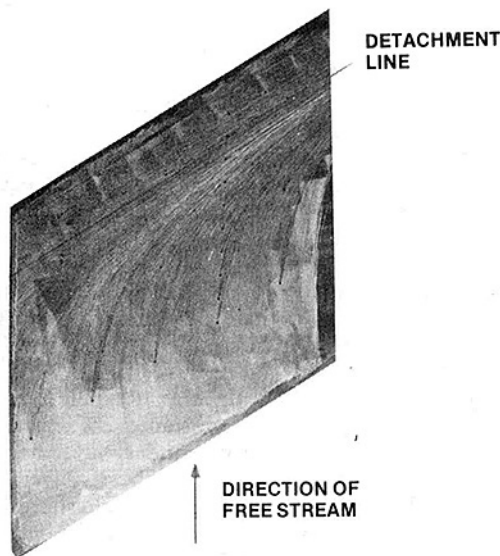
Fig. 11 Surface oil-flow pattern on a swept wing. Courtesy of A. Elsenaar, NLR Netherlands.

the flow behavior near detachment has on the downstream flow and the entire flowfield.

E. Three-Dimensional Separation. All of the flows mentioned previously are nominally two-dimensional in nature. An adverse pressure gradient or an abrupt sharp edge can cause separation in the two-dimensional case. Backflow occurs and is supplied locally by the large eddies when the backflow region is thin compared to the shear layer thickness. Massive backflow can occur when the backflow region is a large fraction of a separated shear layer. The spanwise extent of the separated zone is large compared to the spanwise extent of individual large eddies. The backflow is not supplied by a mean crossflow.

Three-dimensional turbulent boundary layers near separation have an extra degree of freedom to move in a lateral direction that is not present in nominally two-dimensional cases. Three-dimensional pressure gradients produced by the flow geometry, body forces, and shock waves can induce three-dimensional flow. All known flows appear to be either of the swept or the shed vortex or focus types; no turbulent three-dimensional separation bubbles are observed

[1, 5]. Peake and Tobak [5] present a good review of three-dimensional separation.

The wall shear stress is zero only at singular points, as discussed in Section 2. From this viewpoint, three-dimensional cases are less complex than two-dimensional ones. Mean flow measurements are easier to make since pitot-static and hot-wire anemometer techniques can be used satisfactorily, but without great angular sensitivity. Hot-wire turbulence measurements are more difficult to obtain because the sensor must be properly aligned with the flow. Only recently are measurements being made using the laser anemometer [36].

In the swept type of three dimensional separation, the near wall flow moves laterally, as shown in Fig. 11. The mean crossflow near the trailing edge and beyond the separation line of a surface is supplied by a secondary flow. A horseshoe vortex may be shed as the boundary layer of the side wall flows around a turbomachine blade. In the shed vortex or focus types, the region of the separation is small and surrounds a singularity. (See Section 2 for the types of singularities. Peake and Tobak [5] describe many examples.)

A swept shock generated by an adjacent surface can produce three-dimensional motion. This type of shock tends to form a fold in the mean flow, in contrast to a vortex which rotates more than one complete revolution [37].

The turbulence structure in such three-dimensional flows is more like that of an attached turbulent boundary layer than that of a separated two-dimensional turbulent shear flow. The absolute value of the wall shear stress remains large although the direction is at a large angle to the flow outside the boundary layer. The large eddies are diverted from the streamwise direction by the spanwise pressure gradients. The wall bursting behavior occurs, in which high speed flow displaces the low speed sublayer flow. Significant turbulence energy production occurs near the wall. Thus, the eddy viscosity and mixing length models are able to describe many features of this type of separation [37].

4 Flow Modeling

The weaknesses and limitations of modeling turbulent separation largely reflect the same weaknesses and limitations of any other turbulent flow case. All methods are "post-dictive," to use Saffman's word, rather than predictive because so much experimental information has been used to develop them. Few, if any, of these methods apply to a wide class of flows [38]. Nondimensional correlations, zonal

models, and numerical solutions for the Reynolds-averaged equations appear to be the most useful engineering approaches for the next 10 years [38]. Large eddy simulation with subgrid closure and complete solution of the Navier-Strokes equations will remain as research methods until significant advances in computation speed and cost reduction occur.

The objective of zonal modeling is to divide the flow field into several regions, each dominated by a particular type of flow, and to analyze each region by the computationally optimum numerical technique for that region. No single turbulence closure model is the best for all regions, so one needs to use the best available for that region. In order to make the best use of available computer capability for large flow fields of interest. It is important that the following approaches be followed:

1 locally asymptotic solutions should be used in regions where the flow detail is known, e.g., the law of the wall should be used when applicable;

2 locally-fine computing meshes should be used in regions where large changes of terms in the governing equations occur;

3 curvilinear flow-oriented coordinates should be used so that relatively large grids can be used without sacrificing flow detail;

4 the simplest form of the governing equations that contain all important terms should be used; the simplest turbulence models that will work should be used.

Two general types of models for separated flows have been used: rotational and/or irrotational inviscid "simulations" for the entire flow field, or inviscid/turbulent shear flow interaction models for the freestream and the turbulent shear flow. Most of this work has been done for steady two-dimensional cases, as described next, but some attention has been devoted to three-dimensional cases.

A. Inviscid Separated Flow Field Simulation. Several models of this type have been developed, each with some kind of ad hoc assumption about the separated flow pressure distribution or vorticity. The separated flow field (BCDFE) in Fig. 2) is represented as a dead flow region in most applications to airfoils. Bhateley and Bradley [39] used an equivalent airfoil system consisting of a linearly varying vorticity distribution over the surface of each airfoil element to simulate the separated wake. The computed boundary layer displacement thickness was superimposed on the airfoil contour to form an equivalent airfoil surface for each element. This procedure was iterated until convergence occurred. The flow downstream of a separation point was allowed to develop as a free-streamline flow on only that part of the equivalent airfoil having attached flow. The pressure distribution downstream of the separation was assumed constant and equal to that value of pressure obtained by linear extrapolation of the equivalent body boundary point pressures to the separation point. They used the experimentally obtained separation point.

Very good predictions of lift and pressure coefficient were made with this method as long as the free-streamline model satisfied the data. For low angles of attack, trailing edge separation was present for their test cases and pressure coefficient predictions in this regime were not good. When there was a long relaxation zone (AB on Fig. 2) their estimate of the free-streamline pressure was also in error. They pointed out the deficiency of not having a wake model. In summary, their method did not include any pressure gradient relief model (for AB in Fig. 2), no wake model, and used experimental data to locate separation. It still did a good job in many cases of predicting the pressure coefficient, and basically supported the free-streamline idea. Maskew and Dvorak [40] developed a similar model that was used to predict the gross features of the flow shown in Fig. 10.

Jacob presented a similar method for single airfoils [41] and for multiple-element airfoils with the capability of inclusion of ground effects [42]. Vortex and source distributions on the contour were used and a boundary layer calculation was made for the attached flow. The location of transition was found to be as important as the location of detachment in these predictions. The detachment point was predicted to be where $H = 4$, which (as observed from Fig. 5) is in good agreement with Sandborn's criterion for detachment (fully developed separation) for low curvature bodies such as in the flow of Simpson, et al. [10]. The displacement thickness effect was described as an outflow from the airflow. The "dead air" or detached zone was simulated with a separation streamline that was required to be tangent to the surface beneath B in Fig. 2, rather than tangential to the superimposed displacement thickness distribution at B, as it should be. The pressure was required to be equal at three special points of the separating streamlines: at the separation locations on the suction and pressure sides, and at point C above the trailing edge. In addition, the pressure was allowed to vary "very little" between points B and C. Thus, the separation streamline was not exactly a free-streamline, but in practice was close to being one. A source distribution along the body in the dead air region provided the outflow in this region. The circulation-contributing part of the potential flow and the outflow were adjusted to obtain the equal pressures at the three points. Geller's [43] method for cascade flow is basically very similar to Jacob's [41] earliest procedure. The boundary layer displacement effect was assumed small and the simulated wake was assumed to have an infinite length.

The model of Jacob gives good predictions for the lift coefficient with free-streamline separation. Like Bhateley and Bradley, this method did not include any pressure gradient relief model at separation nor any wake model. These authors pointed out that the pressure drag calculation is very sensitive to the dead air pressure value, much more so than the lift. They concluded that their dead air pressure prediction needed improvement for pressure drag calculations.

Jacob [14] modified his method to simulate the effect of the wake on the drag and lift. The position of a sink, whose magnitude equaled the source strength in the dead air region, was located in the wake with a simple algebraic model equation that produced good drag results for a wide variety of cases. A very important conclusion from this work is that the wake flow behavior strongly influences the drag.

Perry and Fairlie [44] simulated a separating and reattaching two-dimensional turbulent bubble as an inviscid region with constant vorticity. This model is partially justified since the vorticity in the outer region of the Perry and Schofield velocity profile correlation is nearly independent of distance from the wall for the upstream attached flow. The elliptic nature of the flow is reflected by the streamfunction equation. The inner part of the boundary layer and the effects of viscosity are neglected. Generally good agreement was achieved between experimental and predicted streamline patterns. Perry and Fairlie felt that the weaknesses of this simultation were due to the neglect of entrainment and the diffusion of vorticity.

B. Inviscid/Turbulent Shear Flow Interaction Models. The approach in all of the models of this type is to simultaneously or iteratively calculate the inviscid potential flow and the separated turbulent shear flow. Various numerical methods have been used for the inviscid flow, and for the shear flow, various turbulence models in integral or finite-difference formulations have been used. Rather than review all procedures that are known at this writing, a representative sample of the physical models will be discussed.

Two methods use an ad hoc assumption about the inviscid flow pressure. Woolley and Kline [45] calculated fully-stalled diffuser flows with the *valid* assumption that the pressure is constant downstream of detachment. An acceptable attached boundary layer calculation method is used upstream of detachment. The Sandborn criterion is used to predict intermittent transitory detachment. The displacement thickness in the detached flow zone is treated as a free boundary with the same static pressure as that at the latest calculated detachment location. A Plemelj integral technique is used to evaluate the potential flow. Good results were obtained for fully-stalled flows.

Collins and Simpson [46] used the somewhat more generalized assumption that a *minimum freestream pressure gradient* is achieved downstream of detachment. This degenerates to the constant pressure assumption in the case of fully-stalled diffuser flows, but also handles cases such as the SMU flows where a small residual positive pressure gradient remains after detachment. In this method, an attached turbulent boundary layer procedure is used until intermittent transitory detachment (intermittent separation). The displacement thickness and displacement thickness gradient calculated at this location are used as initial conditions for the detached flow displacement thickness. A far downstream condition on δ^* is used that is physically realistic, e.g., that the direction of the displacement thickness locus approaches the direction of the far downstream potential flow. With these conditions, the potential flow is solved iteratively with permissible displacement thickness distributions until one is found that satisfies the minimum pressure gradient condition.

Notice that neither of these methods require any turbulence model to predict the potential flow. Collins and Simpson used the resulting U and V velocity distributions at the boundary layer edge and calculated inward toward the wall. Only a continuity requirement was used in the backflow, but good estimates of the mean backflow resulted.

All of the other methods use a turbulence model for the entire detached shear layer that is tied to the local mean velocity gradient. This approach appears reasonable for the outer region, but not the mean backflow, considering the discussion in Section 3.C. Ghose and Kline [17] used the Plemelj integral approach for the inviscid freestream flow and an integral method with the law-of-the-wall and law-of-the-wake velocity profiles for the shear layer. An entrainment model and a shear lag equation with different constants upstream and downstream of detachment were used. Sandborn's detachment criterion also was used. Predictions of pressure rise in transitory diffuser stall were reasonably good, but the backflow velocity profiles were not very good. Moses, et al. [47], used integral momentum and kinetic energy equations and the law of the wall and the law of the wake for the shear layer. These equations were solved simultaneously with those for the inviscid freestream in finite difference form by successive line relaxation [48]. Predictions of pressure rise were good, but backflow velocity profiles need improvement.

Others [45, 50, 51] use a mixing length and/or eddy viscosity model in the backflow. Even with adjustment of turbulence model parameters to fit one feature or another, these models do not predict simultaneously the backflow velocity profile, the streamwise pressure distribution, and the fact that length scales increase along the flow.

The NASA-Ames group solves the time-dependent, Reynolds-averaged Navier-Stokes equations with an explicit finite-difference method that uses an eddy-viscosity model [52, 53]. The elliptic nature of the separated flow fields and the coupling between the viscous and inviscid regions are handled automatically. In contrast to iterative schemes, the solution is marched in time to a steady state if one exists. As discussed in Section 7, this approach can predict some unsteady flow cases. Results for a circular arc airfoil in steady transonic flow are in good agreement with experimental pressure and skin-friction data when small regions of mean backflow are present. However, for flows with larger regions of separated flow, it was stated [52] that improvements in turbulence modeling are required before good agreement with experiment can be expected.

The situation for prediction of separation from sharp-edged bluff bodies is in no better condition. The inviscid and shear flows need to be calculated simultaneously since the direction of the separating streamline at detachment cannot be specified a priori. Gosman [1] also notes that the most obvious turbulence model weakness in current methods is the use of the law-of-the-wall velocity profile, especially near detachment and reattachment locations. He further notes that research on more general methods of modeling the wall layer will beneficial.

It appears reasonable, in view of the experimental observations in Section 3.C., to search for a backflow model not grounded on mixing length theory and a wall shear velocity U_τ scale, but instead on turbulence energy diffusion and dissipation processes and $(-\overline{uv})_{max}^{1/2}$ as a velocity scale. Clearly, more experimental data are needed to define the structure of the backflow if any fundamental improvement in prediction methods is to be made. The next generation of turbulence models also should try to predict γ_p to test further their validity, since data for this parameter are available and provide further flow information. In essence, we are in an impasse situation until further data are obtained that will reveal proper backflow model(s).

C. Three-Dimensional Predictions. Three-dimensional turbulent boundary layers near separation are more complicated than two-dimensional flows in almost every way, except for the general lack of backflow beneath a given part of the outer region flow. The additional spatial variable makes the permitted flow pattern more difficult to determine than in the two-dimensional case. The kinematic topological rules must be used to aid the selection of allowable flow patterns. Since "separation" means "breakaway" of the shear flow as discussed in Section 2, significant interaction occurs between the three-dimensional turbulent and inviscid flows.

Unfortunately most known boundary layer prediction methods appear to have been validated only well upstream of separation, where only a small interaction occurs. At the now famous "Tronheim trials" [54], quasi-three-dimensional flows were calculated, in which only two spatial coordinates were required locally for fully three-dimensional cases. Rotta [55] has extended a two-dimensional k-ϵ model to the three-dimensional case. In developing new methods, several groups are using advanced numerical techniques to deal with complicated body shapes and the large number of unknowns.

Varying degrees of success have been reported with different turbulence models near separation. The mixing length model appears to be inadequate for flow near separation on a swept wing. The eddy viscosity model does not appear to work well for flows with vortex separation. When only the shear flow inertia and vorticity are important, fairly good predictions can be made with a poor turbulence model.

The time-dependent computational approach by the NASA-Ames group that was mentioned in Section 4B has been applied to some three-dimensional steady-flow cases with encouraging results. For example, the three-dimensional interaction of a swept shock wave with a turbulent boundary layer was computed with better agreement with measurements than two-dimensional separated flow field computations with a similar turbulence model [37]. This is probably because there appears to be no flow phenomenon present that resembles the reversed flow that is present for two-dimensional separated flows.

Table 1 Brief comparison of some measurement techniques for separated flow

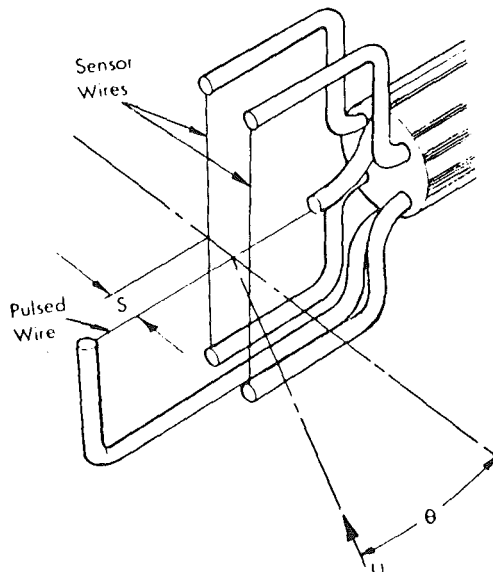|	Quantity	Method and references	Comments
1.	Surface shear	Preston tube [58]	a,b,d,f
		Floating element [59]	c,f
		Surface heat transfer [60, 61]	$b,g,$
2.	Velocity	Pitot-static	a,b,e,f,d,m
		Hot wire array or hot films on substrate (s)	a,b,d,m,n,s,t
		Laser anemometer [26, 66]	h,l,n,o,r
		Pulsed-wire anemometer [62, 63]	d,l,m,n,q
		Flying hot wire [15, 64]	d,h,j,k,n,o,s,t
		Reverse flow sensing hot wire [65]	i,j,p,q,s,t
3.	γ_p	Thermal tuft [69]	d
4.	Static pressure	Surface fluctuations [70]	
		Fluctuations in flow field [71]	a,d,i,j,k,l,m,n

Fig. 12 Schematic of the pulsed-wire anemometer [62]

For large three-dimensional separated flow regions the situation is even more complicated. When the separated flow has a well-defined structure, as in the case of leading edge vortices, theories predominantly based on an inviscid approach can be developed with some success [56]. However, when the location and formation of the three-dimensional separated region is critically dependent on the interaction of the turbulent and inviscid flow fields, no method seems to be applicable today.

Even more than in the two-dimensional case, there is insufficient data available to describe the structure of swept and shed vortex types of flow with large regions of separation. Peake [1] suggested that the external or internal flow over an axisymmetric duct at an angle of attack would make a good case from which to learn much about the turbulence structure. Turbulence measurements also are needed for separation from a cone at an angle of attack. None are currently available.

5 Measurements and Techniques

The general philosophy toward measurements should be that only techniques that are sensitive to the magnitude and direction of the flow and have sufficient spatial resolution should be used. No comparisons of predictions should be made with experimental data obtained by techniques that lack these requirements for a given flow zone of interest. Flow visualization always should accompany quantitative measurements. Redundant measurements using different techniques should be made when possible. Measurements of as much flow detail as possible should be made in experiments used for developing turbulence models. Other measurements,

List of Comments

a Not directionally sensitive in presence of flow reversal; can be used in most types of three-dimensional flow with proper alignment.
b Difficult to interpret in zones of high local turbulence intensity.
c Measurements need correction for pressure gradients.
d Can cause interference with flow and/or itself, especially near a wall.
e Cannot measure turbulence.
f More reliable at high velocities.
g Requires careful calibration.
h Very expensive to implement.
i Confidence in method low because of limited reported experience.
j Not on the market, must be custom-built.
k Mechanically very complex in some applications, perhaps impossible in internal flows.
l In air flow turbulence, data obtained by sampling individual particle speeds rather than as continuous time series.
m Large probe volume.
n Problems with measurement very close to solid surfaces.
o Measuring system and flow field must be closely integrated and require expensive, custom design of traversing equipment.
p Appears to preclude measurement of cross-correlation $\overline{uv}$.
q Basic limit on maximum velocity measurable with presently known configurations.
r Requires seeding with particles.
s Requires clean fluid for stable, long-time calibration.
t Requires careful management of fluid temperature.

in perhaps more practical flow conditions, should be made in enough detail to permit validation of these models.

Table 1 represents a brief comparison of some measurement techniques for separated flow [57]. Several additional comments are needed. Rubesin, et al. [60], used a fine hot wire on the surface of a polystyrene substrate for a surface heat transfer gage. Since the thermal conductivity of the polystyrene is about one-seventh the value of that for commonly used quartz, a significantly lower heat loss to the substrate results and the effective size of the sensor is greatly reduced. This important development permits the calibration of this type gage in laminar flow for direct use in turbulent flow. Higuchi and Peake [61] have developed and used similar surface gages to determine the magnitude and direction of the surface shearing stress in three-dimensional flows.

The pulsed-wire anemometer probe, shown schematically in Fig. 12, has three fine wires. The central wire is pulsed with a short duration voltage pulse that in turn heats the fluid that is passing over that wire at that time. This heated fluid is convected away with the local instantaneous velocity of the flow. The other two wires on the probe are operated as resistance thermometers. They are used to measure the time for the heated fluid tracer to travel from the pulsed wire to

one of the other wires. The component of velocity that is perpendicular to all three wires is measured, being the distance S between each wire divided by the pulse travel time. The flow direction is determined by which wire detects the thermal pulse. Recently Westphal et al. [63], used a three-parallel-wire probe to measure velocities 0.2 mm from a wall.

The "flying hot wire anemometer" [15, 64] is swung through the flow at a known velocity and position as a function of time. Basically this introduces a sufficiently high bias velocity to the hot wire so that the flow with respect to the wire is in an approximately known direction. Subtracting the bias velocity from the signal velocity determines the unknown fluid velocity contribution. Many passes through the flow are required to obtain enough samples and sophisticated computer data reduction is required.

Laser anemometry [66] holds the best future for providing accurate, continuous, and simultaneous measurement of all three velocity components. The most practical optical arrangement is a dual beam, real fringe, system where one beam has been frequency-shifted by a Bragg cell. The frequency-shifting causes the real fringes to move through the focal volume and distinguish the flow direction. A dual beam system permits a large received signal aperture, produces higher signal-to-noise ratio (SNR) signals for sparse seeding, does not require critical beam alignment to obtain good signals, does not require a laser etalon as long as incident beam paths are equal, and does not require a high quality optical table. Beams with different colors or frequency shifts can be used to measure multiple velocity components.

When small seeding particles that are about half the fringe spacing are used sparcely, near optimum signals will be obtained. High SNR intermittent signals (45dB) can be processed with commercially available digital signal burst counters. Photon-correlation signal processing can be used with poor back-scattered signals from a lightly seeded flow with a low power laser [67, 68]. While the photon-correlation electronics are several times more expensive than other signal processing methods, the future for this technique is bright.

Eaton, et al. [69], have developed simple inexpensive detector electronics to measure γ_p from a pulse-wire probe. The heater wire of this "thermal tuft" is continuously heated and the sensor wire that detects the hot wake determines the flow direction. While any directionally-sensitive velocity measurement technique can be used to measure γ_p, the thermal tuft is the simplest to construct and operate.

6 Unsteady Effects

While all turbulent flows are inherently unsteady, the term "unsteady" will mean here a highly repeatable organized time dependent motion in contrast to the relatively aperiodic motion of turbulence. Periodic flow is by far the most common organized time-dependent motion. Two types are possible: One where a periodic flow condition is imposed on a turbulent boundary layer; and the other where the turbulent flow interacts with adjacent flow regions to set up a quasi-periodic motion.

Dynamic stall on helicopter and compressor blades is an example of the first type [72, 73]. The transitory stall in a diffuser which was previously discussed is an example of the second type. Recently [53, 74, 75], an induced quasi-periodic motion was observed under some conditions (Fig. 13) in shock-induced separation from an airfoil for steady transonic flow upstream. Shock-induced and trailing edge separation alternated between the two sides of the airfoil.

Calculations using the time-dependent Reynolds-averaged Navier-Stokes equations with a quasi-steady mixing length turbulence model gave fairly good predictions of the oscillation period, which was long compared to turbulence time scales. In this case, the standard deviation of the period

was about 2 percent, while that for transitory diffuser stall is about 40 percent [18]. This indicates that an induced organized unsteadiness can still have varying degrees of periodicity. An important practical implication of the airfoil result is that it may be possible to predict when airfoil buffet will occur.

In cases where the period of the unsteadiness is relatively long as compared to turbulence time scales, it should be acceptable to use the quasi-steady approximation that the turbulence structure is unaffected by the unsteadiness. When the frequency of the organized unsteadiness is comparable to energy-containing turbulence frequencies, this approximation cannot be used. For example, Acharya and Reynolds [76] have shown that available turbulence models fail for the latter conditions in an unseparated channel flow.

As hereinbefore mentioned, the bursting frequency of the energy-containing motions in a turbulent boundary layer decreases as separation is approached. Thus, while a quasi-steady turbulence model may be adequate far upstream of separation, more interaction between the organized and turbulent unsteady motions occurs downstream [77, 78]. Until recently, little experimental data were available for unsteady turbulent boundary layers. Data [78, 79] now indicate that the quasi-steady assumption is adequate away from the wall when the energy-containing turbulence frequencies are well away from the periodic frequency. In the near wall region significant non-quasi-steady flow behavior occurs [78].

While the quasi-steady turbulence models can be used with caution in near term prediction efforts, a deeper understanding of organized unsteady effects is needed from experiments. As mentioned in the following section some imposed periodic motions appear to have benefit for separation control.

7 Control of Separated Flow

The minimum requirement for a separation control device is that it improve the performance of the flow device enough to warrant its installation. Design constraints decide which control can be used. In essence, boundary layer control devices either inject tangential momentum laden flow, remove momentum deficient fluid, or cause greater entrainment of energetic freestream fluid into the boundary layer for the desired result [80].

Tangential injection is effective in preventing separation [82], but is avoided by manufacturers because of flow ducting and energy requirements. Vortex generators and slightly loaded sharp-edged vanes that control separation by mixing are preferred by these manufacturers because they are relatively simple to add and to change and require no additional energy source. Injection of air normal to the flow surface at discrete locations has the same effect as a sharp-edged vane [83].

Nevertheless, there are still some cases where tangential injection can be useful. For example, vanes, flaps, and vortex generators probably cannot effectively control dynamic stall on a helicopter blade for two reasons. Considerably increased drag would be realized during the part of the cycle that stall does not occur, unless a mechanism to retract these protuberances into the blade is used during that time. More importantly, due to the thick unsteady separated flow that accompanies stall, these protuberances would be mixing low momentum fluid and not energizing the stalled flow.

The merits of several injection arrangements have not been fully investigated. Recent work [84] indicates that about 30 percent lower tangential injection momentum and mass flow rate are required for a given boundary layer control benefit when an asymmetric velocity profile jet is used. In essence, the portion of the jet flow near the wall has a significantly lower

velocity than the outer part, so less momentum is wasted on unnecessarily large surface shearing stresses. Turbulent flow prediction methods for uniform and asymmetric velocity profile jets are fairly well developed [84, 85].

Little information is published on pulsating tangential wall jets. Only two previous studies are known. In these cases, the flow abruptly increases to a constant maximum value and then abruptly decreases to zero flow a short time later. A discrete vortex is formed and moves downstream along the surface [86]. A 50 percent reduction in the mass flow rate required for a given control benefit was achieved by Oyler and Palmer [87] as compared to steady blowing. The effectiveness was attributed to its improved ability to entrain and mix with the surrounding fluid, which was primarily due to the greater jet velocity produced for a given average mass flow rate. The boundary layer quickly attached to the surface when the pulsating jet turned on, but detached slowly when the jet was turned off [88]. As long as the discrete vortex that was formed by the pulsation remained above the surface, there was attached flow on the surface.

The foregoing flows are two-dimensional in the mean. There exists the possibility that spatially-intermittent blowing, from, say, a series of round jets or from a continuous slot blocked at regular intervals with spacers, would be more effective than blowing with the same momentum from a continuous two-dimensional slot. The basis for suggesting this comes from observations of the delay of separation behind vortex generators. With counterrotating generators, the kinetic energy of the mean flow near the surface is enhanced downsteam of each diverging pair of vanes and reduced in the passages on either side. These effects are due to the counterrotating vortices near the surface. The net effect of such mixing is beneficial in delaying global separation. It is likely that local separation has to be prevented only at periodic spanwise positions to avoid complete breakdown of the flow.

A "whistler nozzle" [89] for the wall jet lip may also improve the performance of these cases. This device consists of a convergent nozzle section, a constant area section, and a step change to an exit section with a larger constant area. The exit section excites a standing acoustic wave which greatly increases mixing near the jet. Work is needed to verify this possible improvement.

Concluding Remarks

The preceding sections have given an indication of the types of approaches that have been and are being pursued to understand and predict separated turbulent flow. A key question, that was a central theme for the Project SQUID Coloqium, was "Is there any way or any thing that can be used to make a significant breakthrough in the prediction of turbulent separated flow?" Unfortunately, no quick and inexpensive approach appears to be likely. However, much better experimental measurement techniques and computational capability are available than in the past. The key to furture developments lies in detailed benchmark experiments that will unlock the structure of separated flows in two and three dimensions. Without these data to validate models, predictors will be unable to make any real progress.

Clearly, the unsteady nature of the large eddy structure plays a key role in determining the backflow behavior of both steady and unsteady freestream separated turbulent flows. Nearly periodic oscillations of the freestream can also result in strongly interacting flows. A pulsating flow boundary layer control appears to be effective. These observations should be pursued in future research.

Acknowledgments

The author would like to thank the U.S. Army Research
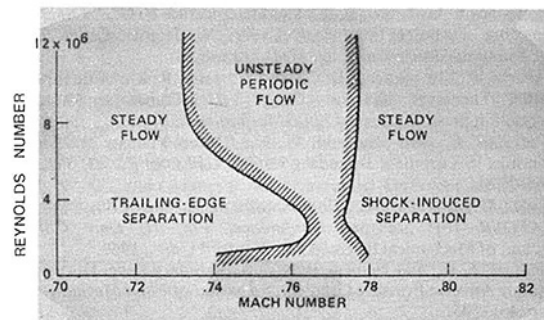
Fig. 13 Experimental flow domains [74]

References

1 Simpson, R. L., "Summary Report on the Colloquium on Flow Separation," Project SQUID Report SMU-3-PU, 1979.

2 Sears, W. R., and Telionis, D. P., "Boundary-Layer Separation in Unsteady Flow," *SIAM J. Applied Math.*, Vol. 28, No. 1, 1975.

3 Shen, S. F., "Unsteady Separation According to the Boundary Layer Equation," *Advances in Applied Mechanics*, Vol. 18, 1978.

4 Bradshaw, P., "Prediction of Separation Using Boundary Layer Theory," Paper 11, AGARD-LS-94, 1978.

5 Peake, D. J., and Tobak, M., "Three-Dimensional Interactions and Vortical Flows with Emphasis on High Speeds," AGARDograph 252, 1980.

6 Lighthill, M. J., "Attachment and Separation in Three-Dimensional Flow," *Laminar Boundary Layers*, L. Rosenhead, ed., Oxford Univ. Press, pp. 72–82, 1963.

7 Maltby, R. L., "Flow Visualization in Wind Tunnels Using Indicators," AGARDograph 70, 1962.

8 Hunt, J. C. R., Abell, C. J., Peterka, J. A., and Woo, H., "Kinematical Studies of the Flows Around Free or Surface-Mounted Obstacles; Applying Topology to Flow Visualization," *J. Fluid Mech.*, Vol. 86, 1978, pp. 179–200.

9 Sandborn, V. A., and Liu, C. Y., "On Turbulent Boundary-Layer Separation," *J. Fluid Mech.*, Vol. 32, 1968, pp. 293–304.

10 Simpson, R. L., Strickland, J. H., and Barr, P. W., "Features of a Separating Turbulent Boundary Layer in the Vicinity of Separation," *Journal of Fluid Mechanics*, Vol. 79, 1977, pp. 553–594.

11 Sandborn, V. A., and Kline, S. J., "Flow Models in Boundary-Layer Stall Inception," ASME *Journal of Basic Engineering*, Vol. 83, 1961, pp. 317–327.

12 Sandborn, V. A., "Boundary Layer Separation and Reattachment," NASA-SP-304, 1970, pp. 279–299.

13 Cebeci, T., Mosinskis, G. J., and Smith, A. M. O., "Calculation of Separation Points in Incompressible Turbulent Flows," *Journal of Aircraft*, Vol. 9, 1972, pp. 618–624.

14 Jacob, K., "Weiterentwicklung eines Verfahrens zur Berechnung abgelösten Profilstromung mit besonderer Berücksichtigung des Profilwiderstandes," DFVLR-AVA-Internal Report 251–75A16, June 1975.

15 Coles, D., and Wadcock, A. J., "A Flying Hotwire Study of Two-Dimensional Mean Flow Past an NACA 4412 Airfoil at Maximum Lift," *AIAA J.*, 17, 1979, pp. 321–329; also Ph. D thesis, A. J. Wadcock, Cal. Inst. Tech., 1978.

16 Fox, R. W., and Kline, S. J., "Flows Regimes for Curved Subsonic Diffusers," ASME *Journal Basic Engineering*, Vol. 84, 1962, pp. 303–312.

17 Ghose, S., and Kline, S. J., "Prediction of Transitory Stall in Two-Dimensional Diffusers," Report MD-36, Thermosciences Div., Department of Mechanical Engineering, Stanford Univ., 1976.

18 Smith, C. R., and Kline, S. J., "An Experimental Investigation of the Transitory Stall Regime in Two-Dimensional Diffusers," ASME JOURNAL FLUIDS ENGINEERING, Vol. 96, 1974, pp. 11–15.

19 Simpson, R. L., Chew, Y.-T., and Shivaprasad, B. G., "The Structure of a Separating Turbulent Boundary Layer: I, Mean Flow and Reynolds Stresses," in press, *Journal of Fluid Mechanics*, 1981.

20 Simpson, R. L., Chew, Y.-T., and Shivaprasad, B. G., "The Structure of a Separating Turbulent Boundary Layer: II, Higher Order Turbulence Results," in press, *Journal of Fluid Mechanics*, 1981.

21 Shiloh, K., Shivaprasad, B. G., and Simpson, R. L., "The Structure of a Separating Turbulent Boundary Layer: III, Transverse Velocity Measurements," in press, *Journal of Fluid Mechanics*, 1981.

22 Perry, A. E., and Schofield, W. H., "Mean Velocity and Shear Stress Distributions in Turbulent Boundary Layers," *Physics Fluids*, Vol. 16, 1973, pp. 2068–2074.

23 Coles, D., and Hirst, E., *Computation of Turbulent Boundary Layers— 1968 AFOSR—IFP Stanford Conference, Vol. II, Data Compilation*, Department of Mechanical Engineering, Stanford Univ., 1969.

24 Samuel, A. E., and Joubert, P. N., "A Boundary Layer Developing in an Increasingly Adverse Pressure Gradient," *Journal of Fluid Mechanics*, Vol. 66, 1974, pp. 481–505.

25 Simpson, R. L., Chew, Y.-T., and Shivaprasad, B. G., "Measurements of a Separating Turbulent Boundary Layer," Project SQUID Report SMU-4-PU, 1980; to appear as DTIC or NTIS report.

26 Simpson, R. L., and Chew, Y.-T., "Measurements in Highly Turbulent Flows: Steady and Unsteady Separated Turbulent Boundary Layers," *Proceedings of Third International Workshop on Laser Velocimetry*, 1979, Hemisphere, pp. 179–196.

27 Rotta, J. C., "Turbulent Boundary Layers in Incompressible Flow," *Progress in Aeronautical Sciences*, Vol. 2, Pergamon Press, 1962.

28 Ashjaee, J., and Johnston, J. P., "Straight-Walled Two-Dimensional Diffusers—Transitory Stall and Peak Pressure Recovery," ASME JOURNAL FLUIDS ENGINEERING, Vol. 102, 1980, pp. 275–282.

29 Moss, W. D., Baker, S., and Bradbury, L. J. S., "Measurements of Mean Velocity and Reynolds Stresses in Some Regions of Recirculating Flow," *Symposium on Turbulent Shear Flows*, Vol. 1, 1977, pp. 1301–1308.

30 Eaton, J. K., and Johnston, J. P., "Turbulent Flow Reattachment: An Experimental Study of the Flow and Structure Behind a Backward-Facing Step," Report MD-39, Department of Mechanical Engineering, Stanford Univ., 1980.

31 Chandrsuda, C., Mehta, R. D., Weir, A. D., and Bradshaw, P., "Effect of Free-Stream Turbulence on Large Structure in Turbulent Mixing Layers," *J. Fluid Mech.*, Vol. 85, Part 4, 1978, pp. 693–704.

32 Abbott, D. E., and Kline, S. J., "Experimental Investigation of Subsonic Turbulent Flow over Single and Double Backward-Facing Steps," ASME *Journal Basic Engineering*, Vol. 84, 1962, pp. 317–325.

33 Bradshaw, P., and Wong, F. Y. F., "The Reattachment and Relaxation of a Turbulent Shear Layer," *Journal of Fluid Mechanics*, Vol. 52, Part 1, 1972, pp. 113–135.

34 Smyth, R., "Turbulent Flow over a Plane Symmetric Sudden Expansion," ASME JOURNAL OF FLUIDS ENGINEERING, Vol. 101, No. 3, 1979, pp. 348–353.

35 Young, W. H., Meyers, J. F., and Hoad, D. R., "A Laser Velocimeter Flow Survey above a Stalled Wing," NASA TP 1266, 1978.

36 Owen, K., and Peake, D. J., "Control of Forebody Three-Dimensional Flow Separation," AGARD-CP-262, May 1979.

37 Horstman, C. C., and Hung, C. M., "Computation of Three-Dimensional Turbulent Separated Flows at Supersonic Speeds," *AIAA Journal*, Vol. 17, 1979, pp. 1155–1156.

38 Kline, S. J., Ferziger, J. H., and Johnston, J. P., Opinion—"The Calculation of Turbulent Shear Flows: Status and Ten-Year Outlook," JOURNAL FLUIDS ENGINEERING, Vol. 100, 1978, pp. 3–5.

39 Bhateley, I. C., and Bradley, R. G., "A Simplified Mathematical Model for the Analysis of Multi-Element Airfoils near Stall," Paper 12, AGARD-CP-102, 1972.

40 Maskew, B., and Dvorak, F. A., "Investigation of Separation Models for the Prediction of C_{LMAX}," *Proceedings of the 33rd Annual National Forum*, Am. Hel. Soc., 1977.

41 Jacob, K., "Berechnung der abgelosten incompressiblen Strömung um Tragflügelprofile und Bestimung des maximalen Auftriebs," *Z. für Flugwiss*, 17, 1969, pp. 221–230.

42 Jacob, K., and Steinbach, D., "A Method for Prediction of Lift for Multi-Element Airfoil Systems with Separation," Paper 12, AGARD-CP-143, 1974.

43 Geller, W., "Calculation of the Turning Angle of Two-Dimensional Incompressible Cascade Flow," *AIAA J*, Vol. 14, 1976, pp. 297–298.

44 Perry, A. E., and Fairlie, B. D., "A Study of Turbulent Boundary-Layer Separation and Reattachment," *Journal of Fluids Mechanics*, Vol. 69, 1975, pp. 657–672.

45 Woolley, R. L., and Kline, S. J., "A Procedure for Computation of Fully-Stalled Flows in Two-Dimensional Passages," ASME JOURNAL OF FLUIDS ENGINEERING, Vol. 100, 1978, pp. 180–186.

46 Collins, M. A., and Simpson, R. L., "Flowfield Prediction for Separating Turbulent Shear Layers," *AIAA J.*, Vol. 16, 1978, pp. 291–292.

47 Moses, H. L., Jones, R. R., III, and Sparks, J. F., "An Integral Method for the Turbulent Boundary Layer with Separated Flow," *Turbulent Boundary Layers*, H. E., Weber, ed., ASME Fluids Engrg. Conference, Niagara Falls, June 18-20, 1979, pp. 69–73.

48 Moses, H. L., Jones, R. R., O'Brien, W. G., and Peterson, R. S., "Simultaneous Solution of the Boundary Layer and Freestream with Separated Flow," *AIAA Journal*, Vol. 16, 1978, pp. 61–66.

49 Pletcher, R. H., "Prediction of Incompressible Turbulent Separation Flow," ASME JOURNAL OF FLUIDS ENGINEERING, Vol. 100, 1978, pp. 427–433.

50 Cebeci, T., Khalid, E. E., and Whitelaw, J. H., "Calculation of Separated Boundary Layer Flows," *AIAA Journal*, Vol. 17, 1979, pp. 1291–1292.

51 Gerhart, P. M., "An Integral Method for Predicting Subsonic Turbulent Separating Boundary Layers with Specified Free-stream Input," *Turbulent Boundary Layers*, H. E. Weber, ed., ASME Fluids Engrg. Conference, Niagara Falls, June 18-20, 1979, pp. 59–68.

52 Levy, L. L., Jr., "Experimental and Computational Steady and Unsteady Transonic Flows about a Thick Airfoil," *AIAA Journal*, Vol. 16, No. 6, 1978, pp. 564–572.

53 Marvin, J. G., Levy, L. L., Jr., and Seegmiller, H. L., "On Turbulence Modeling for Unsteady Transonic Flows," *AIAA Journal*, Vol. 18, 1980, pp. 489–496.

54 Fannelop, T. K., and Krogstad, P. A., "Three-Dimensional Turbulent Boundary Layer in External Flows: A Report on Euromech 50," *Journal of Fluid Mechanics*, Vol. 71, 1975, pp. 815–826

55 Rotta, J., "A Family of Turbulence Models for Three-Dimensional Thin Shear Layers," *Symposium on Turbulent Shear Flows*, Vol. 1, 1977, pp. 10.27–10.34.

56 Hoeijmakers, H. W. M., "A Computational Model for the Calculations of the Flow About Wings with Leading-Edge Vortices," AGARD Symposium on High Angle of Attack Aerodynamics, Sandefjord, Norway, 1978.

57 Simpson, R. L., "Experimental Techniques for Separated Flow," *Reviews in Viscous Flow*, Proceedings of the Lockheed-Georgia Co. Viscous Flow Symposium, June 22-23, 1976, pp. 153–195.

58 Patel, V. C., "Calibration of the Preston Tube and Limitations on its Use in Pressure Gradients," *Journal of Fluid Mechanics*, Vol. 23, 1965, pp. 185–208.

59 Dhawan, S., "Direct Measurements of Skin Friction," NASA TN 2567, 1952.

60 Rubesin, M. W., Okuno, A. F., Mateer, G. G., and Brosh, A., "A Hot-wire Surface Gage for Skin Friction and Separation Detection Measurements," NASA TM X-62,465, 1975.

61 Higuchi, H., and Peake, D. J., "Bi-Directional, Buried-Wire Skin Friction Gage," NASA-TM 78531, 1978.

62 Bradbury, L. J. S., and Castro I. P., "A Pulsed-Wire Technique for Velocity Measurement in Highly Turbulent Flow," *Journal of Fluid Mechanics*, Vol. 49, 1971, pp. 657–691.

63 Westphal, R. V., Eaton, J. K., and Johnston, J. P., "A New Probe for Measurement of Velocity and Wall Shear Stress in Unsteady, Reversing Flow," HTD-Vol. 13, ASME Winter Annual Meeting, Nov. 16-21, 1980.

64 Uberoi, M. S., and Singh, P. I., "Turbulent Mixing in a Two-Dimensional Jet," *Physics Fluids*, Vol. 18, 1975, pp. 764–769.

65 Downing, P. M., "Reverse-Flow Sensing Hot-wire Anemometer," *J. Physics E: Sci. Inst.*, Vol. 5, 1972, pp. 849–851.

66 Durst, F., Melling, A., and Whitelaw, J. H., *Principles and Practice of Laser-Doppler Anemometry*, Academic Press, 1976.

67 Cummins, H. Z., and Pike, E. R., ed., *Photon Correlation Spectroscopy and Velocimetry*, Plenum Press, N.Y., 1977; NATO Advanced Study Institute, July 26-Aug. 6, 1976.

68 Mayo, W. T., and Smart, A. E., ed., *Photon Correlation Techniques in Fluid Mechanics*, Proceedings 4th Inter. Conf., Aug. 25-27, 1980, Stanford Univ. Dept. Aero. and Astro.

69 Eaton, J. K., Jeans, A. H., Ashjaee, J., and Johnston, J. P., "A Wall-Flow-Direction Probe for Use in Separating and Reattaching Flows," ASME *Journal of Fluids Engineering*, Vol. 101, 1979, pp. 364–366.

70 Willmarth, W. W., "Unsteady Force and Pressure Measurements," *Annual Review Fluid Mech.*, Vol. 3, 1971, pp. 147–170.

71 Siddon, T. E., "Investigation of Pressure Probe Response in Unsteady Flow," NASA SP-207, 1969, pp. 455–466.

72 Crimi, P., "Dynamic Stall," AGARD-AG-1972, 1973.

73 McCroskey, W. J., "Some Current Research in Unsteady Fluid Dynamics," ASME *Journal of Fluids Engineering*, Vol. 99, 1977, pp. 8–37.

74 Seegmiller, H. L., Marvin, J. G., and Levy, L. L., Jr., "Steady and Unsteady Transonic Flows," *AIAA Journal*, Vol. 16, No. 12, 1978.

75 McDevitt, J. B., "Supercritical Flow About a Thick Circular-Arc Airfoil," NASA TM 78549, Jan. 1979.

76 Acharya, M., and Reynolds, W. C., "Measurements and Predictions of a Fully-Developed Turbulent Channel Flow with Imposed Controlled Oscillations," Stanford University, Department of Mechanical Engineering Thermosciences Div. Report TF-8, May 1975.

77 Simpson, R. L., "Features of Unsteady Turbulent Boundary Layers as Revealed from Experiments," Paper 19, Symposium on Unsteady Aerodynamics, NATA-AGARD, Ottawa, Canada, Sept. 1977; AGARD-CP-227.

78 Simpson, R. L., Chew, Y.-T., and Shivaprasad, B. G., "Measurements of Unsteady Turbulent Boundary Layers with Pressure Gradients," Southern Methodist University, Department of Civil and Mechanical Engineering Report, in press, 1981 (to appear as NASA CR Report).

79 Cousteix, J., Desopper, A., and Houdeville, R., "Structure and Development of a Turbulent Boundary Layer in an Oscillatory External Stream," *Symposium on Turbulent Shear Flow*, Paper 8-B, Pa. State Univ., Apr. 18-20, 1977.

80 Chang, P. K., *Control of Flow Separation*, Hemisphere-McGraw-Hill, N.Y., 1976.

81 Peake, D. J., "The Use of Air Injection to Prevent Separation of the Turbulent Boundary Layer in Supersonic Flow," ARC-CP-980, 1966.

82 Peake, D. J., "Three-Dimensional Swept Shock/Turbulent Boundary-Layer Separation with Control by Air Injection," National Aeronautical Establishment Report LR-592, Ottawa, Canada, 1976.

83 Wallis, R. A., "A Preliminary Note on a Modified Type of Air Jet for Boundary Layer Control," ARC-CP 513, 1956.

84 Saripalli, K. R., and Simpson, R. L., "An Improved Wall Jet for Boundary Layer Control," NASA CR 3340, 1980.

85 Irwin, H. P. A. H., Measurements in Blown Boundary Layers and Their Prediction by Reynolds Stress Modeling," Ph.D. thesis, McGill Univ., 1974.

86 Verhoff, A., "Steady and Pulsating Two-Dimensional Turbulent Wall Jets in a Uniform Stream," Report AMS-723, Department of Aeronautical and Mechanical Science, Princeton Univ., 1970, AD 705 235.

87 Oyler, T. E., and Palmer, W. E., "Exploratory Investigation of Pulse Blowing for Boundary Layer Control," North American-Rockwell Corp., Columbus, Ohio, Report NR 72H–12, 1972, AD 742–085.

88 Williams, J. R., Ambrosiani, J. P., and Palmer, W. E., "Analysis of a Pulsating Wall Jet," North American-Rockwell Corp., Columbus, Ohio Report NR 72H–325, 1972, AD 758–390.

89 Hill, W. G., and Greene, P. R., "Increased Turbulent Jet Mixing Rates Obtained by Self-Excited Acoustic Oscillations," ASME Paper 77-FE-18, 1977.

M. L. Billet
Research Associate.

J. W. Holl
Professor of Aerospace Engineering.

D. S. Weir
Former Graduate Student.
Applied Research Laboratory,
The Pennsylvania State University,
State College Pa.   16801

Correlations of Thermodynamic Effects for Developed Cavitation

The net positive suction head (NPSH) requirements for a pump are determined by the combined effects of cavitation, fluid properties, pump geometry, and pump operating point. An important part of this determination is the temperature depression (ΔT) defined as the difference between ambient liquid temperature and cavity temperature. Correlations are presented of the temperature depression for various degrees of developed cavitation on venturis and ogives. These correlations, based on a semiempirical entrainment theory, express ΔT in terms of the dimensionless numbers of Nusselt, Reynolds, Froude, Weber, and Péclét, and dimensionless cavity length (L/D). The ΔT data were obtained in Freon 114, hydrogen, and nitrogen for the venturis and in Freon 113 and water for the ogives.

Introduction

Cavitation is an important consideration in the design, analysis, and application of liquid handling pumps. Limited cavitation occurs whenever the local pressure is reduced to some critical value. A further reduction in pressure results in developed cavitation. In this flow regime, it is difficult to predict the net positive suction head (NPSH) required for the satisfactory performance of a pump. The NPSH requirements are determined by the combined effects of cavitation, fluid properties, pump geometry, and pump operating point.

The determination of the cavity pressure is of primary importance in understanding the influence of developed cavitation on pump performance. In most cases, the designer assumes that the cavity pressure is equal to the vapor pressure at the bulk temperature of the liquid. This estimate is quite good in the absence of noncondensable gases and at states significantly below the critical temperature where P_v and dP_v/dT are both small. For example, this is a reasonable approximation for water at room temperature with a low gas content, but for many fluids, such as cryogens, the operating temperature can be such that P_v and dP_v/dT are both large. In these cases, the assumption that the cavity pressure is equal to the vapor pressure corresponding to the bulk temperature of the liquid can lead to very large errors.

A continuous vaporization process which is dependent upon heat transfer at the liquid-vapor interface is required to sustain a developed cavity in a pump. As a result of vaporization, the cavity temperature is less than the inlet bulk liquid temperature so that the cavity vapor pressure is less than the vapor pressure corresponding to the inlet bulk liquid temperature. This phenomenon is called the thermodynamic effect and is dependent on fluid properties, velocity, size, and geometry. The thermodynamic effect is important because the NPSH required to produce a given cavity volume will decrease as the temperature depression at the cavity increases. The

relationship between the thermodynamic effect and the NPSH requirements for a pump can be obtained from the definition of cavitation number.

In principle, one can define a cavitation number for pump applications (σ_c) which is based on the cavity pressure (P_c). Thus

$$\sigma_c = \frac{P_\infty - P_c}{1/2\rho V_\infty^2} = \frac{h_\infty - h_c}{\dfrac{V_\infty^2}{2g}} \qquad (1)$$

This can also be expressed in the form

$$\sigma_c = \sigma_v + \frac{\Delta P_T}{1/2\rho V_\infty^2} = \sigma_v + \frac{\Delta h_T}{\dfrac{V_\infty^2}{2g}} \qquad (2)$$

where σ_v is the conventional cavitation number based on vapor pressure (P_v) corresponding to the bulk temperature (T_∞) and is defined by the relation

$$\sigma_v = \frac{P_\infty - P_v}{1/2\rho V_\infty^2} = \frac{h_\infty - h_v}{\dfrac{V_\infty^2}{2g}} \qquad (3)$$

In the foregoing relations, it is apparent that h_∞, h_c, h_v, and Δh_T are the various types of head corresponding to the pressures P_∞, P_c, P_v, and ΔP_T respectively.

In the absence of noncondensable gas in the cavity, the cavity pressure (P_c) would be equal to the vapor pressure corresponding to the cavity temperature. Thus the head difference (Δh_T) given by

$$\Delta h_T = \frac{P_v - P_c}{\rho g} \qquad (4)$$

may be taken as a measure of the thermodynamic effect.

The net-positive-suction-head is defined as

$$\text{NPSH} = h_\infty + \frac{V_\infty^2}{2g} - h_v \qquad (5)$$

Employing equation (2) in equation (5) for the term $h_\infty - h_v$ yields

$$\text{NPSH} = (1 + \sigma_c) \frac{V_\infty^2}{2g} - \Delta h_T \qquad (6)$$

which relates NPSH, cavitation number (σ_c), and thermodynamic effect (Δh_T). The velocity in equation (6) can be written in terms of the pump flow coefficient (ϕ) given by

$$\phi = \frac{V_\infty}{nD_T} \qquad (7)$$

In general, the cavitation number (σ_c) varies with pump flow coefficient (ϕ). However, if a value of σ_c and ϕ is specified, then only a relationship for the thermodynamic effect is needed in order to estimate the NPSH requirements.

Stahl and Stepanoff [1] [1] were the first to analyze the thermodynamic effect for cavitation with particular emphasis on pump applications. They formulated the B factor method which is quasi-static in nature. Fisher [2], Jacobs [3], and Acosta and Hollander [4] also considered the B factor method and its application.

The equation for predicting the thermodynamic effect in terms of a temperature depression (ΔT) from the B factor theory is

$$\Delta T = B \frac{\rho_v}{\rho_L} \cdot \frac{\lambda}{C_P} \qquad (8)$$

where the factor B is defined as the ratio of vapor volume to liquid volume involved in the vaporization process. However, the primary practical problem which a designer encounters in attempting to use equation (8) is the calculation of B.

In order to make the B factor method more useful as a data correlation method, Gelder, et al. [5], and Moore and Ruggeri [6] extended it in a semiempirical manner. They expressed the B factor in terms of dimensionless ratios as

$$B = B_R \left\{ \frac{V_\infty}{V_{\infty R}} \right\}^{N_1} \left\{ \frac{D}{D_R} \right\}^{N_2} \left\{ \frac{L/D}{(L/D)_R} \right\}^{N_3} \left\{ \frac{\alpha}{\alpha_R} \right\}^{N_4} \qquad (9)$$

[1] Numbers in brackets refer to documents in list of references.

and then determined the exponents empirically. The subscript R employed in equation (9) indicates a reference value. Hord, et al. [7-9], have further extended this approach by including other factors in the correlation equation for the B factor. A new parameter was used which is a liquid phase velocity ratio derived from two-phase flow parameters. The parameter is defined as

$$\text{MTWO} = \frac{V_\infty}{a_L} \left\{ \frac{1 + B(\rho_L/\rho_v)(a_L/a_v)^2}{1 + B(\rho_v/\rho_L)} \right\}^{\frac{1}{2}} \qquad (10)$$

Data were then correlated by employing the relation

$$B = B_R \left\{ \frac{\alpha_R}{\alpha} \right\}^{E1} \left\{ \frac{\text{MTWO}}{\text{MTWO}_R} \right\}^{E2} \left\{ \frac{L}{L_R} \right\}^{E3}$$

$$\times \left\{ \frac{\nu_R}{\nu} \right\}^{E4} \left\{ \frac{\sigma_{c_R}}{\sigma_c} \right\}^{E5} \left\{ \frac{D}{D_R} \right\}^{E6} \qquad (11)$$

It is significant that this new correlation, i.e., equation (11), satisfactorily correlated the combined venturi, hydrofoil, and ogive data. In addition, Hord [10] has applied equation (11) to pumps.

The entrainment theory was developed as an alternate to the B factor method for predicting the thermodynamic effect for developed cavitation. It is a dynamical approach based on an energy balance for the cavity. Although it is semiempirical, it has the advantage of dividing the vaporization process into basic physical quantities. The principal theoretical and experimental aspects of this theory are presented in Holl, et al. [11], and Weir [12]. The foundations of the entrainment theory originated from Holl and Wislicenus [13] and in a discussion by Acosta and Parkin [14] of that paper.

From the entrainment theory [2], the temperature depression (ΔT) is given by

$$\Delta T = \frac{C_{\dot{Q}}}{C_A} \cdot \frac{\text{Pe}}{\text{Nu}} \cdot \frac{\rho_v}{\rho_L} \cdot \frac{\lambda}{C_P} \qquad (12)$$

[2] This theory is derived in the Appendix.

Nomenclature

A_v = cross sectional area of cavity
A_w = cavity surface area
a = speed of sound
B = ratio of vapor volume to liquid volume involved in sustaining a natural cavity
C_A = area coefficient $\equiv A_w/D^2$
C_p = specific heat of the liquid
$C_{\dot{Q}}$ = flow rate coefficient $\equiv \dot{Q}/V_\infty D^2$
D = model diameter
D_T = tip diameter
Fr = Froude number $\equiv V_\infty \sqrt{gD}$
g = acceleration of gravity
h = film coefficient $\equiv \dot{q}/A_w \Delta T$
h_∞, h_c, h_v, and Δh_T = various values of head – see equations (1)-(6)
k = thermal conductivity of liquid
L = cavity length
$\dot{m}_v$ = mass flowrate of vapor in the cavity
n = rotational speed
Nu = Nusselt number $\equiv hD/k$
P_c = cavity pressure
Pe = Péclét number $\equiv V_\infty D/\alpha$
Pr = Prandtl number $\equiv \nu/\alpha$
P_v = vapor pressure based on bulk temperature
P_∞ = free stream pressure

$\dot{q}$ = heat transfer rate
$\dot{Q}$ = volume flowrate of the vapor in the cavity
Re = Reynolds number $\equiv V_\infty D/\nu$
s = surface tension
T_c = cavity temperature
T_∞ = free stream temperature
ΔT = temperature depression $\equiv T_\infty - T_c$
ΔT_{max} = maximum temperature depression $= T_\infty - T_{c\text{-min}}$
V_v = velocity of the vapor in the cavity
V_∞ = free stream velocity
We = Weber number $\equiv V_\infty \sqrt{D}/\sqrt{s/\rho}$
α = thermal diffusivity of liquid
λ = latent heat of vaporization
ν = kinematic viscosity of the liquid
ρ_L = mass density of the liquid
ρ_v = mass density of the vapor
σ_c = cavitation number based on cavity pressure
σ_v = cavitation number based on vapor pressure
ϕ = pump flow coefficient

Subscripts

L = denotes liquid
v = denotes vapor

The Peclet number and fluid property terms are known from the free stream conditions (T_∞ and V_∞) and the characteristic model dimension (D). However, $C_A C_Q$ and Nu are characteristic of the cavity flow and are to be determined empirically.

An attempt is made in this investigation to establish a relationship for the thermodynamic effect which can be applied to scaling problems. The resulting relationship is based on the correlation of temperature depression data for developed cavitation using the entrainment theory. It includes the application of the entrainment theory to the venturi temperature depression data of Moore and Ruggeri [6] and Hord, et al. [7], along with re-evaluation of previous ΔT correlations for two-axisymmetric bodies, namely, zero and quarter-caliber ogives. The investigation of the ogives is presented in references [11], [12], and [25]. The ΔT data for the venturis were obtained in Freon 114, hydrogen, and nitrogen whereas the ogive ΔT data were obtained in Freon 113 and water.

The axial variation of the temperature depression along the cavity was found to be roughly linear with the maximum temperature depression (ΔT_{max}) occurring near the leading edge of the cavity. Examples of the axial variation of ΔT are given in references [5], [7], and [25].

In addition to the aforementioned correlations of ΔT, cavitation number data for both limited and developed cavitation in venturis are also presented in this paper.

Empirical Equations for C_A, C_Q, Nu, and ΔT

In order to determine an equation which correlates ΔT data by means of the entrainment theory i.e., equation (12), it is necessary to determine empirical equations for C_A, C_Q, and Nu in terms of pertinent physical parameters. An examination of the problem led to the following general forms for C_A, C_Q, and Nu

$$C_A = C_1 \{L/D\}^a \tag{13}$$

$$C_Q = C_2 \mathrm{Re}^b \mathrm{Fr}^c \mathrm{We}^d \{L/D\}^e \tag{14}$$

$$\mathrm{Nu} = C_3 Re^f \mathrm{Fr}^g \mathrm{We}^h \mathrm{Pr}^i \{L/D\}^j \tag{15}$$

As will be seen in subsequent sections, two combinations of terms were tried for C_Q and Nu. The *first correlation* refers to that correlation in which Weber number was not considered, i.e., $d = h = 0$. Whereas, the *second correlation* refers to that correlation in which Froude number was eliminated, i.e., $c = g = 0$.

Employing equation (13)–(15) in equation (12) yields the general empirical form for ΔT

$$\Delta T = C_4 (L/D)^k \mathrm{Re}^l \mathrm{Fr}^m \mathrm{We}^n \mathrm{Pr}^p \mathrm{Pe} \frac{\rho_v}{\rho_L} \frac{\lambda}{C_P} \tag{16}$$

The unknown constants for all the correlations were determined by a modified least-squares approximations technique. Taking the logarithm reduces the equation to the linear form. Then, as outlined by Becket and Hunt [15], minimizing the sum of the squares of the difference between the logarithm of the measured data and the correlative expression yields a set of simultaneous equations which can be solved for unknown constants.

Experimental Results for the Venturis

Extensive temperature depression data correlated by means of the entrainment theory have been reported for ogive nosed bodies [11]. In addition, temperature depression data correlated by means of the B factor theory have been reported for venturis [6], [7]. It was decided that it would be desirable to compare the venturi and ogive data when correlated by the entrainment theory. In order to accomplish this goal, it was

necessary to experimentally determine the area coefficient (C_A) and flow rate coefficient (C_Q) for the venturis. These were then employed in equation (12) to determine the Nusselt number by using the temperature depression data of Moore and Ruggeri [6] and Hord, et al. [7].

The coefficients C_A and C_Q were determined for two venturi models having the same shape. In addition, the cavitation numbers for both limited and developed cavitation were determined as a function of the flow parameters for the two models. The tests were conducted in the 38.1 mm ultra-high-speed cavitation tunnel located in the Garfield Thomas Water Tunnel Building of the Applied Research Laboratory. A detailed description of the facility and supporting equipment is given in references [16], [17].

The internal contours of the two venturi test sections are the same as those developed by NASA [6], [7]. The full scale venturi has a minimum internal diameter of 35.0 mm and the 7/10th scale venturi has a minimum diameter of 24.8 mm. A schematic of the full scale venturi is shown in Fig. 1 together with a sketch of the ogive models.

The geometric characteristics of developed cavities were determined for both full scale and 7/10th scale venturis. Cavity profiles were established for various operating conditions. The position of the cavity wall was determined by inserting a thin probe through the cavity wall until it pierced

Fig. 1 Schematic of models
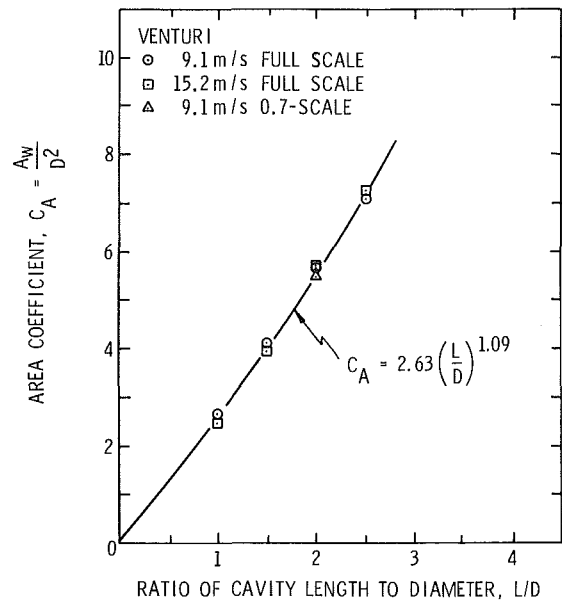
Fig. 2 Area coefficient for the venturis

the cavity interface. This was done at two positions along the cavity length.

Once the profile of the cavity wall was determined by the aforementioned method, the cavity surface area (A_w) was obtained by an integration as described in reference [16]. The resulting area coefficient (C_A) is shown as a function of dimensionless cavity length (L/D) in Fig. 2 for the two venturis at various velocities. It is seen that as in the case of the ogives, C_A is solely a function of L/D. The data for C_A were approximated by equation (13) and the empirically determined constants are shown in Table 1 together with the data for the ogives from reference [11]. It is seen that the exponent for L/D varies over the narrow range 1.09-1.19 for the three configurations.

In order to determine $C_{\dot{Q}}$, it was assumed that the value of $C_{\dot{Q}}$ for a ventilated cavity with minimal diffusion effects approximates the actual $C_{\dot{Q}}$ for a natural cavity having the same value of L/D. This basic assumption is discussed in reference [11]. Measurements of the volume flowrate of gas required to sustain ventilated cavities were made for a velocity range of 5.2 to 12.2 m/s and dimensionless cavity length (L/D) of 1.0 to 3.0 for the two models in room temperature water. Nitrogen was used as the ventilation gas and attempts were made to reduce the effect of gas diffusion on the measured flowrate. This was done by adjusting the flow conditions such that the cavity pressure was close to the partial pressure of gas in the liquid (see reference [18] for more details). Typical results from these tests are shown in Fig. 3 where the volume flowrate of gas expressed as a dimensionless flowrate coefficient $(C_{\dot{Q}})$ is shown as a function of dimensionless cavity length (L/D). The data for $C_{\dot{Q}}$ were approximated by equation (14) and the empirically determined constants are shown in Tables 2 and 3 for the first and second correlations together with the data for the ogives from references [11] and [25]. These correlations will be discussed in subsequent sections.

The experimental values of the desinent cavitation number for the venturis are presented in Fig. 4. It is seen that the desinent cavitation number for water compares favorably with the minimum pressure coefficient. However, the water results are consistently higher than the experimental results for Freon 114 [19] and liquid hydrogen [20]. Gas effects in water and surface tension effects in liquid hydrogen [20] may cause trends of this type.

The cavitation number based on cavity pressure is approximately constant for both venturis over the range of cavity lengths and velocities tested. As shown in Fig. 5 for the full scale venturi, a single cavitation number of 2.32 can be ulilized to represent the ventilated and natural cavity data. This compares to a constant cavitation number of 2.47 from earlier tests by Moore and Ruggeri [6] and Hord, et al. [7].

Many investigators, see for example references [18] and [21], have shown that the cavitation number is a single valued function of dimensionless cavity length (L/D). However, the venturi data in Fig. 5 do not display this characteristic. As shown by Weir [22], blockage effects on ogive nosed bodies are such that as the blockage increases the cavitation number tends to become independent of L/D. Perhaps the constant cavitation number characteristic of the venturis is due to similar effects.

Application of the Entrainment Theory

The initial correlation made by the entrainment theory referred to as the *first correlation* did not include Weber number. These results are shown in Table 2 in which the data for the ogives were obtained from reference [11]. The comparisons between the experimental ogive data and the first correlation are given in reference [11] for ΔT and references [18] and [23] for $C_{\dot{Q}}$. The results for the *second correlation*, namely, the correlation which did not include Froude number, are given in Table 3. Comparisons between the experimental ΔT data and ΔT calculated by both correlations for the venturis are given in Table 4. Comparisons between measured values of $C_{\dot{Q}}$ and ΔT with values calculated from both correlations are given in reference [25] for the ogives.

Referring to the ogive data for $C_{\dot{Q}}$ and Nu in Table 2, it is seen that the correlations are consistent, i.e., the exponents of like terms have the same sign. The correlations for the ΔT ogive data are nearly independent of Froude number. This is

Table 1 Constants for C_A correlations (equation (13))

Model	Constant C_1	L/D Exponent
Venturi	2.63	1.09
Zero-Caliber Ogive*	4.59	1.19
Quarter-Caliber Ogive*	2.06	1.18

*Data from Reference [11]
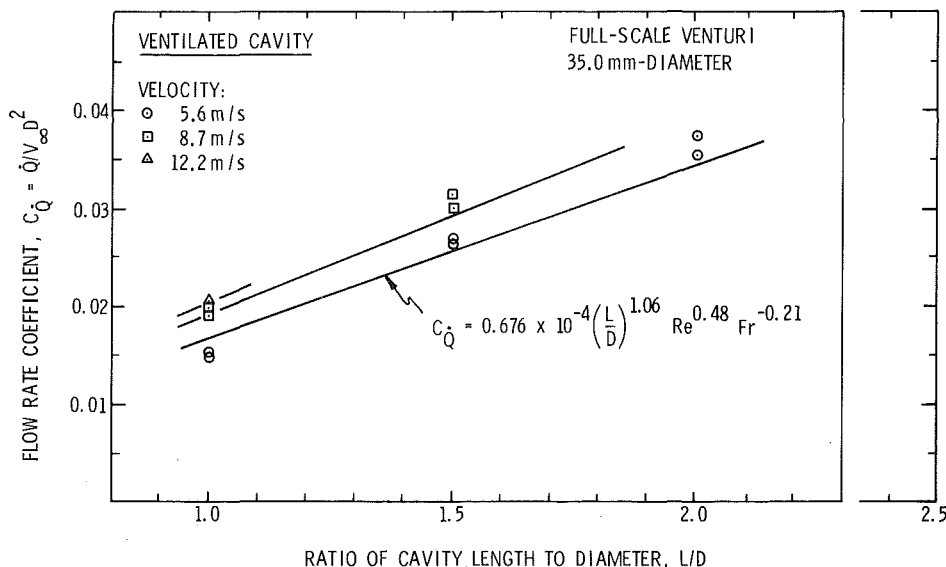
Fig. 3   Flow rate coefficient data for the 35.0 mm dia venturi
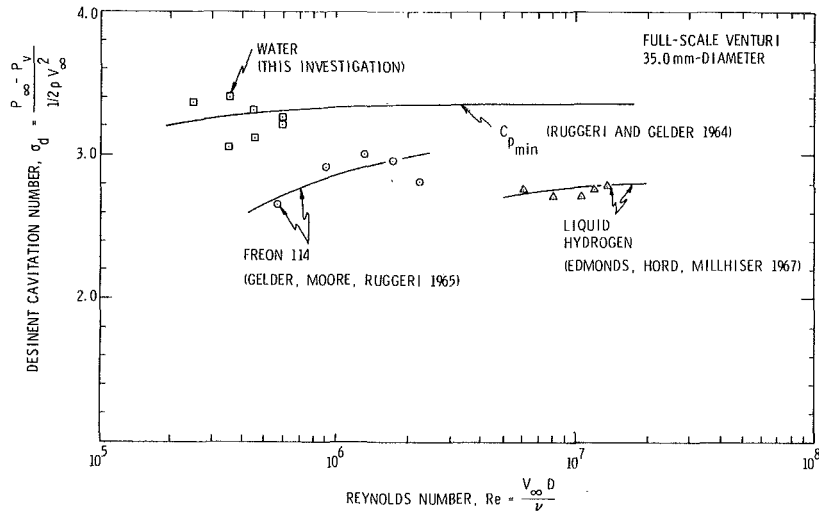
Fig. 4 Desinent cavitation number versus Reynolds number for the venturis
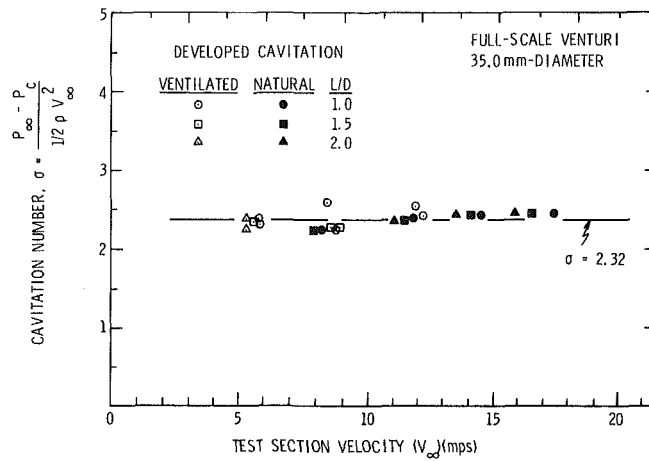
Fig. 5 Cavitation number for developed cavitation in the 35.0 mm venturi

Table 2 Constants and exponents for entrainment theory — first correlation

Model	Quantity	Eq. No.	Constant C_2, C_3 or C_r	L/D Exp.	Re Exp.	Fr Exp.	We Exp.	Pr Exp.	Pe Exp.
Venturi	C_Q	14	0.676×10^{-4}	1.06	0.48	-0.21	0	----	----
	Nu	15	0.611×10^{-3}	-0.39	1.36	-0.59	0	0.04	----
	ΔT_{max}	16	0.421×10^{-1}	0.36	-0.88	0.38	0	-0.04	1.0
Zero-Caliber* Ogive	C_Q	14	0.424×10^{-2}	0.69	0.16	0.13	0	----	----
	Nu	15	0.148×10^{-3}	-1.33	1.39	0.15	0	0.85	----
	ΔT_{max}	16	6.221	0.83	-1.23	-0.02	0	-0.85	1.0
Quarter-Caliber* Ogive	C_Q	14	0.320×10^{-4}	0.74	0.46	0.26	0	----	----
	Nu	15	0.464×10^{-2}	-0.70	1.03	0.30	0	0.41	----
	ΔT_{max}	16	0.335×10^{-2}	0.26	-0.57	-0.04	0	-0.41	1.0

*These correlations are the same as those given in Reference [11] except for small adjustments in the constants due to the use of new fluid property data.

Table 3 Constants and exponents for entrainment theory — second correlation

Model	Quantity	Eq. No.	Constant C_2, C_3 or C_4	L/D Exp.	Re Exp.	Fr Exp.	We Exp.	Pr Exp.	Pe Exp.
Venturi	C_Q	14	0.618×10^{-5}	1.09	0.88	0	-0.62	----	----
	Nu	15	0.275×10^{-5}	-0.32	2.33	0	-1.67	0.46	----
	ΔT_{max}	16	0.854	0.32	-1.45	0	1.05	-0.46	1.0
Zero-Caliber Ogive	C_Q	14	0.225×10^{-1}	0.69	-0.10	0	0.40	----	----
	Nu	15	0.415×10^{-2}	-1.37	0.90	0	0.68	0.64	----
	ΔT_{max}	16	1.183	0.87	-1.00	0	-0.28	-0.64	1.0
Quarter-Caliber Ogive	C_Q	14	0.836×10^{-3}	0.74	-0.06	0	0.79	----	----
	Nu	15	0.271	-0.70	0.41	0	0.93	0.31	----
	ΔT_{max}	16	1.498×10^{-3}	0.26	-0.47	0	-0.14	-0.31	1.0

perhaps not surprising since the Froude number was rather high in these tests. This suggested the possibility that Froude number could be eliminated in the expressions for C_Q, Nu, and ΔT and other parameters considered. Since the entrainment mechanism may possibly depend upon surface tension effects, it seemed reasonable to consider Weber number as a scaling parameter. Thus Froude number was replaced by Weber number and new correlations for C_Q Nu, and ΔT were obtained as shown in Table 3.

Referring to the ogive data for C_Q, Nu, and ΔT in Table 3, it is seen that the exponents of like terms have the same sign and thus the results are consistent. Furthermore, the exponents on the Weber number terms in Table 3 are consistently higher than the corresponding exponents on the Froude number terms in Table 2. Perhaps this indicates that in this instance the Weber number is better than Froude number as a scaling parameter.

Although the ogive data appear to be consistent for both correlations, it is seen that the venturi data do not have the same trends. For example, referring to Table 2, the Froude number exponent for the venturi is negative in the expressions for C_Q and Nu, whereas the same set of exponents for the ogives is positive. Referring to the second correlation in Table 3, it is seen that the signs of both the Weber number and Reynolds number exponents in the C_Q expression for the venturi are opposite to the corresponding exponents for the ogives.

It is interesting to compare the exponents on the Prandtl number for the various correlations given in Tables 2 and 3. Referring to the venturi correlations, it is seen that Prandtl number exponent for the ΔT equation is -0.04 and -0.46 for the first and second correlations, respectively. Thus the exponent has increased by an order of magnitude from the first to the second correlation. In contrast to this result, the Prandtl number exponent for the ogive ΔT correlation changes from -0.85 to -0.64 for the zero caliber ogive and from -0.41 to -0.31 for the quarter caliber ogive in going from the first to the second correlation. The much larger change in the Prandtl number exponent for the venturi is due to the introduction of surface tension into the ΔT correlation which has a large variation for the fluids used in the correlation, namely, Freon 114, nitrogen, and hydrogen. The magnitude of the Prandtl number exponent for the second correlation, namely, 0.46 is more typical of heat transfer

data. Perhaps this suggests that the second correlation is better than the first correlation for the venturis.

The various entrainment theory correlations for ΔT are compared in Table 5 for the case of constant fluid properties where ΔT has the form

$$\Delta T_{max} = C\left(\frac{L}{D}\right)^{M_1} V_\infty{}^{M_2} D^{M_3} \qquad (17)$$

in which the constants are different for each configuration. In addition, two of the B factor correlations are shown in Table 5. (Apparently, these are the only B factor correlations available for the venturis and ogives which include size, i.e., D, directly as a parameter. Weir [12] has summarized the various B factor correlations.) Comparing the first and second entrainment method correlations for a given configuration with each other indicates that the two correlations give nearly the same exponents for like terms. Both of the correlations for the venturis show that the size effect is very small. The B factor correlation for the venturis shows a larger size effect with ΔT varying as the 0.2 power of D. However, it is important to note that the venturi models had only a 1.0 to 0.7 variation in diameter. The exponent on L/D varies between 0.26 and 0.36 for the venturis and quarter caliber ogives, whereas the zero caliber ogives display a much larger effect for the average L/D exponent is 0.85. All of the configurations and correlations indicate that ΔT increases with velocity with the exception of the zero caliber ogive. In addition, all of the configurations and correlations indicate that ΔT increases with, or is not affected by, size with the exception of the zero caliber ogive which shows a decrease of ΔT with size. Thus the zero caliber ogive tends to be the exception when examined for the case of constant fluid properties. This may be due in part to the observed cavity instability associated with the separated flow about the zero caliber ogive. Subsequent to this study, high-speed photographic investigations by Stinebring [26] indicated that the cavity broke away from the leading edge of the body during part of the cavity oscillation cycle due to the reentrant jet striking the cavity wall. This phenomenon may have caused significant departures from the assumptions of the steady state entrainment theory.

Conclusions

Correlations for the temperature depression (ΔT) defined as

Fluid	Venturi Diameter mm	Cavity Length L/D	Velocity m/s	Fluid Temp °K	Measured ΔT(°C)	Predicted ΔT$_2$(°C)	Predicted ΔT$_1$(°C)
Hydrogen	24.8	2.05	31.3	19.9	1.77	1.41	1.53
..		2.56	30.1	19.8	1.45	1.48	1.63
..		3.33	30.4	19.8	1.88	1.62	1.80
..		3.33	43.7	20.7	2.37	2.38	2.52
..		1.79	46.0	20.4	1.99	1.91	1.97
etc.		2.82	45.6	20.3	2.74	2.17	2.28
		2.56	49.7	22.4	2.71	3.31	3.33
		3.33	50.8	22.3	3.01	3.61	3.67
		3.59	51.3	22.4	3.04	3.77	3.83
		1.79	52.6	20.6	2.58	2.17	2.19
		2.70	53.3	20.6	3.02	2.47	2.54
		3.33	52.7	20.1	3.36	2.58	2.68
		3.33	52.7	20.6	3.19	2.62	2.72
		1.28	57.2	22.4	2.25	2.91	2.81
		2.05	58.0	20.7	2.91	2.41	2.43
		2.05	58.7	20.7	2.96	2.44	2.45
		3.33	58.1	20.7	3.43	2.84	2.92
		3.59	59.1	20.6	3.16	2.91	2.99
		2.05	58.6	22.6	2.81	3.54	3.46
		3.33	57.9	22.4	3.43	4.01	4.01
		3.33	58.6	22.5	3.53	4.08	4.08

*Measured values from Moore and Ruggeri (1962) and Hord, Anderson and Hall (1972)

Fluid	Venturi Diameter mm	Cavity Length L/D	Velocity m/s	Fluid Temp °K	Measured ΔT(°C)	Predicted ΔT$_2$(°C)	Predicted ΔT$_1$(°C)
Freon 114	24.8	1.64	9.5	289.1	3.78	3.84	4.03
..		1.64	9.9	299.8	4.94	5.17	5.36
..		1.64	6.7	277.1	2.22	2.27	2.49
..		1.64	6.9	288.7	3.00	3.14	3.41
..		1.64	7.0	299.7	4.33	4.17	4.48
etc.		1.64	13.5	288.9	4.89	4.73	4.79
		1.64	13.6	299.9	5.83	6.27	6.28
		0.72	16.5	289.1	2.89	3.10	3.12
		3.08	8.2	289.1	4.00	4.32	4.73
Hydrogen	24.8	1.28	46.1	20.5	1.43	1.74	1.77
..		2.05	46.6	20.6	1.97	2.08	2.15
..		3.33	46.6	20.6	2.32	2.45	2.58
..		1.28	39.2	21.4	1.91	1.91	1.95
..		2.05	38.7	21.5	2.06	2.23	2.32
etc.		3.33	39.8	21.6	2.33	2.69	2.84
		1.28	42.6	22.5	2.38	2.47	2.45
		2.05	43.9	22.6	2.81	2.94	2.97
		3.33	44.1	22.8	3.19	3.61	3.69
		1.28	60.0	20.8	1.96	2.19	2.15
		2.05	60.8	20.9	2.50	2.61	2.61
		3.33	62.2	20.8	3.47	3.06	3.11
		1.28	59.6	21.4	2.48	2.46	2.39
		2.05	60.2	21.4	3.06	2.89	2.87

Fluid	Venturi Diameter mm	Cavity Length L/D	Velocity m/s	Fluid Temp °K	Measured ΔT(°C)	Predicted ΔT$_2$(°C)	Predicted ΔT$_1$(°C)
Hydrogen	24.8	3.33	59.7	21.3	3.58	3.29	3.34
..		1.28	58.0	22.6	2.91	3.03	2.91
..		2.05	57.7	22.6	3.16	3.49	3.43
..		3.33	57.8	22.6	3.72	4.09	4.09
..		1.28	59.8	20.9	2.77	2.21	2.17
etc.		1.28	61.8	22.7	3.47	3.18	3.03
		2.05	61.8	22.6	3.62	3.64	3.54
		3.33	62.4	22.7	4.27	4.42	4.37
		1.28	60.2	21.4	2.83	2.45	2.39
		2.05	60.5	21.4	2.99	2.87	2.84
		3.33	61.3	21.6	3.48	3.53	3.56
		1.28	42.4	21.6	2.21	2.04	2.07
		2.05	43.0	21.5	2.65	2.39	2.46
		3.33	43.8	22.1	2.98	3.14	3.26
		1.28	47.4	20.6	1.96	1.81	1.82
		2.05	47.2	20.4	2.42	2.03	2.09
		3.33	46.9	20.7	3.03	2.61	2.76
		2.05	46.2	22.7	2.47	3.11	3.12
		3.33	46.7	22.7	2.91	3.71	3.78
		1.28	33.8	20.3	1.55	1.38	1.44
		2.05	34.5	20.3	1.64	1.62	1.73

Fluid	Venturi Diameter mm	Cavity Length L/D	Velocity m/s	Fluid Temp °K	Measured ΔT(°C)	Predicted ΔT$_2$(°C)	Predicted ΔT$_1$(°C)
Nitrogen	24.8	3.33	10.7	77.8	1.67	1.45	1.40
..		3.33	15.4	77.7	1.72	1.77	1.64
..		3.33	14.0	83.7	2.39	2.86	2.63
..		3.33	19.9	89.1	4.83	5.62	4.82
..		3.33	22.6	89.3	4.78	6.14	5.19
etc.		3.33	22.3	83.6	3.61	3.76	3.29
		3.33	22.3	78.3	2.33	2.35	2.10
		3.33	22.2	78.2	2.39	2.32	2.07
		3.33	15.1	78.1	1.83	1.82	1.69
		3.33	14.7	78.1	2.00	1.79	1.67
Freon 114	35.0	2.00	9.6	272.8	3.00	2.59	2.60
..		2.00	9.7	273.0	4.06	4.16	4.17
..		2.00	9.7	272.9	5.11	5.49	5.44
..		2.00	5.8	265.9	1.50	1.38	1.46
..		2.00	5.7	265.8	1.83	1.89	2.00
etc.		2.00	5.8	265.8	2.78	3.11	3.28
		2.00	13.2	279.4	4.06	3.26	3.16
		2.00	13.4	279.8	5.06	5.31	5.13
		0.36	10.1	273.8	2.17	2.44	2.27
		0.91	10.0	273.7	3.50	3.27	3.16
		2.90	9.2	272.2	4.44	4.56	4.66

Fluid	Venturi Diameter mm	Cavity Length L/D	Velocity m/s	Fluid Temp °K	Measured ΔT(°C)	Predicted ΔT$_2$(°C)	Predicted ΔT$_1$(°C)
Nitrogen	35.0	0.73	6.2	77.8	0.61	0.64	0.59
..		1.45	6.1	77.8	0.72	0.80	0.75
..		2.90	5.9	77.8	1.00	0.98	0.95
..		2.90	7.6	78.0	1.28	1.18	1.11
..		2.90	9.6	78.3	1.50	1.39	1.28
etc.		2.90	12.8	79.2	1.67	1.79	1.59

$\Delta T_1 = \Delta T_{max}$ predicted by first correlation

$\Delta T_2 = \Delta T_{max}$ predicted by second correlation

Table 5 ΔT correlations for constant fluid properties

BOUNDARY	SOURCE	FLUIDS	CORRELATION METHOD	EQUATIONS FOR ΔT
Venturi	This study, Moore and Ruggeri 1968 and Hord et al. 1972	Hydrogen Nitrogen Freon 114	Entrainment Method First Correlation	$\Delta T = C(L/D)^{0.36}\,V_\infty^{0.5}\,D^{-0.07}$
Venturi		Hydrogen Nitrogen Freon 114	Entrainment Method Second Correlation	$\Delta T = C(L/D)^{0.32}\,V_\infty^{0.6}\,D^{0.07}$
Venturi	Moore and Ruggeri 1968	Hydrogen Freon 114	B Factor Method	$\Delta T = C(L/D)^{0.3}\,V_\infty^{0.8}\,D^{0.2}$
Zero Caliber Ogive	This study, and Holl, Billet and Weir 1975	Water Freon 113	Entrainment Method First Correlation	$\Delta T = C(L/D)^{0.83}\,V^{-0.25}\,D^{-0.22}$
Zero Caliber Ogive		Water Freon 113	Entrainment Method Second Correlation	$\Delta T = C(L/D)^{0.87}\,V^{-0.28}\,D^{-0.14}$
Quarter Caliber Ogive		Water Freon 113	Entrainment Method First Correlation	$\Delta T = C(L/D)^{0.26}\,V^{0.39}\,D^{0.45}$
Quarter Caliber Ogive		Water Freon 113	Entrainment Method Second Correlation	$\Delta T = C(L/D)^{0.26}\,V^{0.39}\,D^{0.46}$
Quarter Caliber Ogive	Hord 1973	Hydrogen Nitrogen	B Factor Method	$\Delta T = C(L/D)^{0.34}\,V^{0.21}\,D^{0.94}$

Table 6 Experimental uncertainty

Experimental Uncertainty

Figure No.	Item	Uncertainty Estimates
2	Cavity length (L)	±5%
	Cavity surface area (A_w)	±10%
3	Cavity length (L).	±5%
	Volume flowrate (Q)	±1% (based on flow meter accuracy)
4	Velocity (V_∞)	±1%
	Cavitation number (σ_d)	±10%
5	Velocity (V_∞)	±1%
	Cavitation number (σ)	±3%

the difference between ambient liquid temperature and cavity temperature for a developed cavity are presented for various degrees of developed cavitation on venturis and ogives. These correlations were done with a semiempirical entrainment theory. Results show that the entrainment theory appears to be a reasonable alternative to the B factor method.

Two correlations were made for the temperature depression using the entrainment theory. The first correlation uses a Froude number term which was found to be very small and can be neglected. This result was the basis for obtaining the second correlation in which Froude number was replaced by Weber number.

Conclusions about the correlations and the experimental data are as follows:

1 The temperature depression for the quarter caliber ogives increases with T_∞, L/D, V_∞, and D. This result is in general agreement with other investigations of quarter caliber ogives, hydrofoils, and venturis.

2 The temperature depression for the zero caliber ogives increases with T_∞ and L/D, but tends to decrease with V_∞ and D.

3 Both the first and second correlations show consistent results for the ogives within the context of the entrainment theory in that the exponents of like terms have the same sign in the expressions for C_Q', Nu, and ΔT.

4 In general, within the context of the entrainment theory, the venturi expressions for ΔT, C_Q', and Nu for both the first and second correlations do not show the same trends as those for the ogives.

5 The cavitation number is independent of L/D for the venturis, whereas it is a single valued function of L/D in the case of the ogives.

6 For the venturis, the magnitude of the Prandtl number exponent for the second correlation appears to be more consistent with other heat transfer data than does the Prandtl number exponent for the first correlation. Perhaps this suggests that the second correlation is better than the first for the venturi data.

Acknowledgment

References

1 Stahl, H. A., and Stephanoff, A. J., "Thermodynamic Aspects of Cavitation in Centrifugal Pumps," ASME *Journal of Basic Engineering*, Vol. 78, 1956, pp. 1691–1693.

2 Fisher, R. C., Discussion of "A Survey of Modern Centrifugal Pump Practice for Oilfield and Oil Refining Services," by N. Tetlou, *Proc. Inst. Mech. Engrs.*, Vol. 152, 1945, pp. 305–306.

3 Jacobs, R. B., "Prediction of Symptoms of Cavitation," *J. Res. NBS*, Vol. 65C, No. 3, 1961.

4 Acosta, A. J., and Hollander, A., "Remarks on Cavitation in Turbomachines," Hydromechanics Laboratory, California Institute of Technology, Report 79.3, Oct. 1959.

5 Gelder, T. F., Ruggeri, R. S., and Moore, R. D., "Cavitation Similarity Considerations Based on Measured Pressure and Temperature Depressions in Cavitated Regions of Freon 114, NASA TN D-3509, 1966.

6 Moore, R. D., and Ruggeri, R. S., "Prediction of Thermodynamic Effects of Developed Cavitation Based on Liquid-Nitrogen and Freon 114 Data in Scaled Venturis," NASA TN D-4899, 1962.

7 Hord, J., Anderson, L. M., and Hall, W. J., "Cavitation in Liquid Cryogens, Volume I—Venturi," NASA CR-2054, 1972.

8 Hord, J., "Cavitation in Liquid Cryogens, Volume II—Hydrofoil," NASA CR-2156, Jan. 1973.

9 Hord, J., "Cavitation in Liquid Cryogens, Volume III—Ogives," NASA CR-2242, May 1973.

10 Hord, J., "Cavitation in Liquid Cryogens, Volume IV—Combined Correlations for Venturi, Hydrofoil, Ogives, and Pumps," NASA CR-2448, 1974.

11 Holl, J. W., Billet, M. L., and Weir, D. S., "Thermodynamic Effects on Developed Cavitation," ASME JOURNAL OF FLUIDS ENGINEERING, Vol. 97, No. 4, Dec. 1975, pp. 507–514.

12 Weir, D. S., "An Experimental and Theoretical Investigation of Thermodynamic Effects on Developed Cavitation," M.S. thesis, The Pennsylvania State University, May 1975 (also ARL Technical Memorandum 75-34).

13 Holl, J. W., and Wislicenus, G. F., "Scale Effects on Cavitation," ASME *Journal of Basic Engineering*, Vol. 83, 1961, pp. 385–398.

14 Acosta, A. J., and Parkin, B. R., Discussion of "Scale Effects on

Cavitation," by J. W. Holl and G. F. Wislicenus, ASME *Journal of Basic Engineering*, Vol. 83, 1961, pp. 395–396.

15 Becket, R., and Hunt, J., *Numerical Calculations and Algorithms*, McGraw-Hill, New York, 1967.

16 Billet, M. L., "Thermodynamic Effects on Developed Cavitation in Water and Freon 113," M.S. thesis, The Pennsylvania State University, Mar. 1970.

17 Weir, D. S., Billet, M. L., and Holl, J. W., "The 1.5 Inch Ultra High-Speed Cavitation Tunnel at the Applied Research Laboratory of The Pennsylvania State University," ARL Technical Memorandum 75–188, July 10, 1975.

18 Billet, M. L., and Weir, D. S., "The Effect of Gas Diffusion on the Flow Coefficient for a Ventilated Cavity," ASME JOURNAL OF FLUIDS ENGINEERING, Vol. 97, No. 4, Dec. 1975, pp. 501–506.

19 Gelder, R. F., Moore, R. D., and Ruggeri, R. S., "Incipient Cavitation of Freon 114 in a Tunnel Venturi," NASA TN D-2662, Feb. 1965.

20 Edmonds, D. K., Hord, J., and Millhiser, D. R., "Cavitation Inception in Liquid Nitrogen and Liquid Hydrogen Flowing in a Venturi," NASA Cr-72285, Aug. 1967.

21 Reichardt, H., "The Laws of Cavitation Bubbles at Axially Symmetrical Bodies in a Flow," Reports and Translations No. 766, Office of Naval Research, Oct. 1947.

22 Weir, D. S., "The Effect of Velocity, Temperature, and Blockage on the Cavitation Number for a Developed Cavity," *Proceedings of the 1975 Cavitation and Polyphase Flow Forum*, ASME Fluids Engineering Conference, Minneapolis, Minn., May 1975, pp. 7–10.

23 Billet, M. L., and Weir, D. S., "The Effect of Gas Diffusion and Vaporization on the Entrainment Coefficient for a Ventilated Cavity," ARL Technical Memorandum 75–15, Jan. 24, 1974.

24 Ruggeri, R. S., and Gelder, T. F., "Cavitation and Effective Liquid Tension of Nitrogen in a Tunnel Venturi," NASA TN D-2088, Feb. 1964.

25 Holl, J. W., Billet, M. L., and Weir, D. S., "Tabulation and Summary of Thermodynamic Effects Data for Developed Cavitation on Ogive-Nosed Bodies," ARL Technical Memorandum 78–18, Jan. 30, 1978.

26 Stinebring, D. R., "Scaling of Cavitation Damage", M.S thesis, The Pennsylvania State University, Aug. 1976.

APPENDIX

Derivation of Temperature Depression Equation

The heat required to convert the liquid to vapor is given by

$$\dot{q} = \lambda \dot{m}_v = \rho_v \lambda C_{\dot{Q}} D^2 V_\infty \tag{18}$$

The heat transfer through the cavity wall is given by

$$\dot{q} = h A_w (T_\infty - T_c) = h A_w \Delta T \tag{19}$$

The mass flowrate of the vapor in the cavity $(\dot{m}_v)$ is given by

$$\dot{m}_v = \rho_v V_v A_v = \rho_v \dot{Q} = \rho_v D^2 V_\infty C_{\dot{Q}} \tag{20}$$

where $C_{\dot{Q}}$ is the flowrate coefficient defined as

$$C_{\dot{Q}} = \frac{\dot{Q}}{D^2 V_\infty} \tag{21}$$

Equating equations (18) and (19) and solving for the temperature depression (ΔT) gives

$$\Delta T = \frac{C_{\dot{Q}}}{h} \frac{D^2}{A_W} V_\infty \lambda \rho_v \tag{22}$$

This equation can then be expressed in terms of dimensionless parameters, namely

$$\Delta T = \frac{C_{\dot{Q}}}{C_A} \frac{\text{Pe}}{\text{Nu}} \frac{\rho_v}{\rho_L} \frac{\lambda}{C_P} \tag{23}$$

Equation (23) is the basic relation employed in this investigation to correlate the temperature depression data.

The Initiation Of Gaseous Microbubble Growth In Laminar Separation Bubbles

B. R. Parkin

Professor of Aerospace Engineering,
Applied Research Laboratory,
The Pennsylvania State University,
State College, Pa.　16801
Mem. ASME

Flow conditions surrounding bubble-ring cavitation inception on hemispherical headforms are analyzed with respect to the initiation of air diffusion into microbubbles as is observed to occur at fixed positions in the boundary layer. Fairly recent observations have shown this phenomenon to occur in the laminar separation bubble on the body.

The analysis shows, in agreement with the body of experimental evidence now available, that gaseous growth must be preceded by a period of vaporous growth starting in regions of low pressure upstream of the laminar separation bubble. It also appears that the most favorable condition for the initiation of gaseous growth should occur when a typical vapor bubble reaches its maximum radius as it enters the laminar separation bubble. The conditions for the initiation of subsequent gaseous growth, once the cavitation bubble is stabilized in the laminar separation zone, are more demanding. Nevertheless, it is found that the liquid in the water surrounding the bubble in the separation zone is definitely supersaturated for most flows of experimental or practical interest. Therefore, gaseous growth, as well as vaporous growth, is definitely to be associated with the onset of bubble-ring cavitation on both theoretical and experimental grounds.

Introduction

For some time, it has been known when the onset of cavitation is observed on hemispherical headforms under some conditions, that very small bubbles are found to grow at fixed places on the body, references [1, 2]. It was noted that the observed growth is probably caused by air diffusion from the water into the bubbles, which we shall call gaseous growth. It was also thought that in all likelihood, this gaseous growth could be preceded by a period of vaporous growth, by which dynamic growth of cavitation bubbles is known to occur, because it was found during gaseous growth that the minimum static pressure on the body upstream of the region of gaseous growth was less than the vapor pressure. However, the conditions responsible for the fact that this gaseous growth takes place at fixed points on the body were not understood.

Our understanding of the conditions responsible for the ability of these bubbles to remain at a fixed point in the boundary layer on the headforms has been significantly enhanced by the discovery that a laminar separation bubble is calculated to be present on hemispherical headforms at Reynolds numbers, based on headform diameter, as high as 5 $\times$ 10^6 [3–6]. A schematic diagram of this flow is shown in Fig. 1. Comparison of the reported location of the laminar bubble with the position on the headform where gaseous growth was observed [1, 2], suggests that gaseous growth occurs inside the laminar separation bubble. This new knowledge makes it apparent that small gas bubbles can
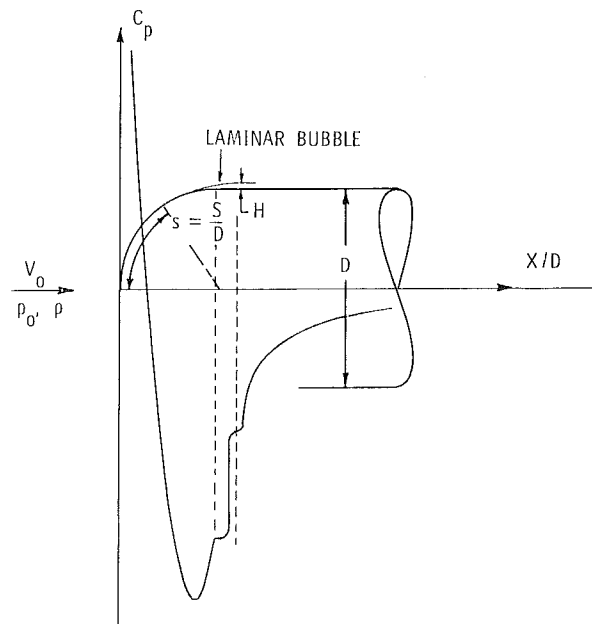
Fig. 1   Schematic diagram of flow about a hemispherical headform when laminar separation is present

become fixed at a point on the body in the laminar separation bubble and then there certainly will be more than enough time for gaseous growth to occur [1, 2], because such growth will continue until the bubble becomes large enough to interact

with the laminar free shear layer which divides the laminar bubble and the external flow upstream of the turbulent reattachment zone. Thus whether or not the diffusion rate is large or small is of secondary interest in this study.[1] Even so, it is of interest to explore in somewhat more detail the nature of conditions which can lead to gaseous growth in the boundary layer and to improve our understanding of the reasons why it is necessary that the observed gaseous growth is preceded by a period of vaporous growth. Aside from the fact that our observations appear to show that this must be true, no explanation of the experimental evidence appears to have been offered to date.

The investigation hinges upon a comparison between two distinct physical possibilities. The first is the possibility that gaseous growth occurs in the laminar separation zone after a cavitation nucleus has experienced a short period of isothermal vaporous growth. The second is the possibility that no vaporous growth occurs. Instead, a free stream nucleus enters the boundary layer and is transported into the laminar bubble by the flow. During this motion, there is no time for appreciable gaseous growth. Changes in bubble size will occur

as though the bubble were an isothermal flaccid balloon. Then once the bubble has come to rest in the laminar separation zone, subsequent gaseous growth could occur, or if the flaccid bubble is large enough, vaporous cavitation would take place.

The Cavitation Nucleus

It is generally accepted that spherical air bubbles, if left to themselves in a quiescent body of water, will either dissolve under the influence of surface tension or they will grow by air diffusion and rise to the surface and thus be lost [7]. In either case, spherical air bubbles are ruled out as persistent cavitation nuclei and it is concluded that some mechanism must be present which can counteract the effects of surface tension in order to explain the observed persistence of cavitation nuclei. There is an extensive literature on cavitation nuclei which we cannot discuss here. Instead, we shall content ourselves by employing a nucleus which initially has zero surface energy. As the bubble grows from an initial effective radius R_0 to a larger size, say $R = n R_0$, with $n \geq 1$, we shall suppose that the surface tension will attain its full value which we shall designate by σ. The surface tension remains constant for values of $r = R/R_0 \geq n$. The simplest assumption that one can make for the range $1 \leq r < n$ is that the variation be linear. Thus we shall take the pressure increment due to surface tension to be given by $2S(R, \sigma)/R$ where the surface tension law is given by

$$S(R, \sigma) = \begin{cases} \dfrac{R - R_0}{(n - 1)R_0}\sigma & , \quad R_0 \leq R < nR_0 \quad , \\ \\ \sigma & , \quad nR_0 \leq R \end{cases} \tag{1}$$

Typical streamlines and velocity profiles associated with laminar separation and separation bubbles are illustrated in *Incompressible Aerodynamics*, B. Thwaites, ed., Oxford, 1960. These flow patterns for *slowly moving* fluid in the laminar bubble are shown on pages 47 and 50 of this reference. These flow patterns help one visualize how the fixed positions of microbubbles in the laminar separation bubble might be possible.

Another point about laminar bubbles is that in the zone of turbulent reattachment significant wall pressure fluctuations have been observed [5]. Since this flow region is not considered favorable for gaseous growth of the fixed microbubbles under study here, no further mention of this matter seems necessary. Similarly, rectified diffusion into oscillating bubbles is excluded from this analysis although such events are possible. The important point is that rectified diffusion affects the overall diffusion rate. However, our interest centers on *threshold* conditions under which gaseous growth is possible in the first place. Subsequent diffusion rates are not considered.

———— Nomenclature ————

a = magnitude of the dimensionless acceleration of the bubble wall

C = concentration of air dissolved in the water, moles of air per million moles of water (ppm) at any point in the flow

C_i = initial concentration of dissolved air measured in a sample of tunnel water

C_p = pressure coefficient: $C_p = (p - p_0)/\frac{1}{2}\rho V_0^2$

C_{p_s} = static pressure coefficient in laminar separation bubble

C_σ = ratio of characteristic surface tension pressure to dynamic pressure: $C_\sigma = \dfrac{4\sigma}{R_0 \rho V_0^2} = 4/\text{We}^2$

D = diameter of the water tunnel model

H = maximum height of the laminar separation bubble

K = cavitation number: $K = (p_0 - p_v)/\frac{1}{2}\rho V_0^2$

n = surface tension parameter which governs the slope of the linearly increasing part of the surface tension law $S(r, \sigma)$

p = static pressure at any point in the flow

p_a = partial pressure of air in the free stream nuclei at the measured dissolved air concentration

p_g = partial pressure of air in the bubble

p_0 = static pressure at upstream infinity

p_v = pressure of the vapor inside the cavitation bubble

p_s = static pressure of the liquid in the separation bubble

r = dimensionless radius: $r = R/R_0$

r_c = critical dimensionless radius for air diffusion according to equations (14) and (15) of text

r_e = equilibrium dimensionless radius: $r_e = R_e/R_0$

r_m = maximum dimensionless radius: $r_m = R_m/R_0$

R_e = equilibrium bubble radius

Re = Reynolds number based on body diameter

R_m = maximum bubble radius

R_0 = "radius" of typical nucleus

$S(r, \sigma)$ = surface tension law

t = laboratory or "real" time

v = dimensionless bubble-wall velocity

V_0 = free stream velocity

We = Weber number: $\text{We} = V_0/\sqrt{\sigma/\rho R_0}$

β = dimensionless parameter characterizing static pressure in laminar separation zone: $\beta = \dfrac{K + C_{p_s}}{C_\sigma}$

β_e = value of β when $r = r_e$

β_c = value of β when $r = r_c$

γ = dimensionless air content parameter: $\gamma = p_a/(2\sigma/R_0)$

Γ = $\gamma - \beta$

ρ = liquid density

σ = coefficient of surface tension

τ = dimensionless time: $\tau = t\sqrt{2\sigma/\rho R_0^3}$

λ = constant of proportionality in Henry's law

ξ = normalized radius: $\xi = r/\sqrt{\gamma}$

ξ_e = value of ξ when $r = r_e$

ξ_m = value of ξ when $r = r_m$

544 / Vol. 103, DECEMBER 1981

Transactions of the ASME

Downloaded 02 Jun 2010 to 171.66.16.86. Redistribution subject to ASME license or copyright; see http://www.asme.org/terms/Terms_Use.cfm

and we shall call this simple model and idealized Harvey nucleus. In terms of the dimensionless radius $r = R/R_0$, one can write equation (1) as

$$S(r, \sigma) = \begin{cases} \dfrac{r-1}{n-1}\,\sigma & , \quad 1 \le r < n \\[3mm] \sigma & , \quad n \le r \end{cases} \qquad (2)$$

Evidently equations (1) and (2) reduce to $S(r, \sigma) = \sigma$ as $n \to 1$ so that the nucleus is a spherical bubble in this case. It is important that the spherical bubble be included in the present nucleus model because in water tunnel experiments and in other situations involving flowing water, spherical microbubbles will be present and they can act as cavitation nuclei.

Threshold Criterion for Gaseous Growth

Since the following analysis is concerned only with the conditions under which gaseous growth is possible, it would seem to be a reasonable approximation to neglect the convective effects of any water flow around a fixed or moving bubble because the growing vapor bubble moves with the boundary layer and rectilinear convective velocities about the bubble will tend to be small and the time will be a few milliseconds or less. We shall treat the process as though there is no relative motion of the water with respect to the bubble. Moreover, at the risk of introducing further error, we will also suppose that all convective effects due to radial bubble growth can be neglected even when very rapid changes, such as those occuring in vaporous growth, take place. Our interest centers on the simplest possible threshold conditions which are favorable to gaseous growth and we shall follow Epstein and Plesset [7] by taking the threshold to be determined by

$$C_i - C = 0 \qquad (3)$$

where C_i is the measured concentration of dissolved air in the water and C is the saturation concentration of air in the water at the bubble wall. The saturation concentration is given by

$$\lambda C = p(R) \qquad (4)$$

where $p(R)$ is the partial pressure of air inside the bubble as influenced by surface tension and other effects of bubble radius, and λ is the constant of proportionality in Henry's law [8]. If $C > C_i$, the bubble will dissolve and if $C < C_i$, the bubble will grow.

Conditions Favorable For Gaseous Growth Initiation

In the following, it is assumed that as the nucleus moves in the boundary layer, a period of vaporous growth precedes the gaseous growth. Vaporous growth occurs from the time that the bubble first encounters a static pressure less that vapor pressure and continues until the laminar separation bubble is reached [1, 2]. It is also supposed that this vapor bubble reaches a maximum radius R_m at the time it arrives in the laminar separation bubble. We shall study the effect of these bubble motions on the conditions for air diffusion under the assumptions noted in the preceding paragraph, and one purpose of the analysis is to see whether or not this assumption is reasonable because the period of vaporous growth has never been observed directly. We can only infer its existence indirectly [1, 2]. Indeed, since this process has not been observed, we can only speculate upon the details by which the vapor bubble penetrates the laminar separation bubble. The fact is that only those nuclei which are in the laminar boundary layer, where the pressures are necessarily the lowest

pressures in the flow, participate in the process. Therefore, it seems plausible to suppose that the laminar free-shear layer, which separates the laminar bubble from other regions in the flow, will pose no barrier to the penetration of the vapor bubble into the laminar bubble. Another possibility for penetration of vapor bubbles might originate in the turbulent reattachment region. Some cavitation bubbles from this mixing zone could be pushed into a region of reversed flow inside the laminar separation zone and then move forward by convection to become fixed at a point inside the laminar bubble where gaseous growth is observed. No experimental evidence supports this speculation about this process. If left to itself, a typical vapor bubble will collapse once it reaches the laminar separation bubble because the pressures there will exceed the vapor pressure. Therefore, the maximum vapor bubble radius will often occur when the cavitation bubble is in the laminar separation zone, where the bubbles are observed to be at rest with respect to the body and growth by air diffusion appears to take place [1, 2].

Thus we can write the equation of motion [9] for isothermal bubble growth in the laminar boundary layer at the point of laminar separation as

$$R\ddot{R} + \frac{3}{2}\dot{R}^2 = \frac{1}{\rho}\left(p_v + p_a(R_0/R)^3\right.$$
$$\left. - 2S(R,\sigma)/R - p_0 - C_{p_s}\frac{1}{2}\rho V_0{}^2\right) \qquad (5)$$

where

p_v = vapor pressure,
p_a = air pressure in the free stream nucleus of radius R_0,
p_0 = free stream static pressure,
C_{p_s} = pressure coefficient in the laminar separation bubble,
ρ = density of water, and
V_0 = free stream velocity.

In a sense, equation (5) is a hybrid equation. It is designed to bridge the gap between the period of vaporous growth when no appreciable air diffusion is assumed to occur and the subsequent phase of gaseous growth which takes place when the cavitation bubble assumes a fixed position in the laminar separation zone. It is possible for the cavitation bubble to enter the laminar bubble before it has reached its maximum radius so that some short period would be necessary to allow the bubble to attain its maximum radius by vaporous growth before gaseous diffusion can become well established. Our task is to use equation (5) in order to ascertain which part of the vaporous growth phase puts the bubble in the most favorable condition to accept gaseous growth and after that, to determine what condition is most demanding if subsequent air diffusion is to continue.

Next we can introduce the cavitation number

$$K = (p_0 - p_v)/\frac{1}{2}\rho V_0{}^2 \qquad (6)$$

which makes it convenient to group the term in (5) involving C_{p_s} with p_0 and p_v in order to express the combination in the form

$$-(K + C_{p_s})\frac{1}{2}\rho V_0{}^2$$

Then if we let $R = rR_0$ and introduce the dimensionless time, τ, by defining

$$\tau^2 = t^2(2\sigma/\rho R_0{}^3) \qquad (7)$$

where $\sqrt{\rho R_0{}^3/2\delta}$ is a characteristic time scale for motions of a bubble of radius R_0. Therefore, we can write equation (5) in dimensionless form as

$$r \frac{d^2 r}{d\tau^2} + \frac{3}{2}\left(\frac{dr}{d\tau}\right)^2 = \gamma/r^3 - \frac{1}{r}\begin{bmatrix} \dfrac{r-1}{n-1} \\[2mm] 1 \end{bmatrix} - \beta \quad (8)$$

In equation (8), the air content parameter is $\gamma = p_a R_0/2\sigma$, and $\beta = (K + C_{p_s})/C_\sigma$ with $C_\sigma = 4\sigma/R_0\rho V_0{}^2$.[2] The quantity β characterizes the static pressure experienced by the vapor bubble which tends to cause its collapse after it has passed through the region of lower pressures which promote vaporous growth in the first place. Experiments reported by Holl and Carroll [10] have shown that if we take this static pressure to be the pressure at the laminar separation point, we can put $C_{p_s} = -0.63$.

Suppose that we designate the partial pressure of air in the isothermal bubble at any instant by p_g. Then we can rewrite equation (5) as

$$\rho[R\ddot{R} + 3\dot{R}^2/2] = p_g - 2S(R,\sigma)/R$$
$$- (K + C_{p_s})\rho V_0{}^2/2 \quad (5a)$$

But the saturation concentration of dissolved air in the water at the isothermal bubble surface will be

$$p_g = \lambda C$$

in accordance with equation (4) and where $p(R) = p_g$ if saturation were to exist. The actual concentration of dissolved air *initially* present at this point is given by

$$p_a = \lambda C_i$$

Therefore we can form the concentration difference defined in equation (3), which with the help of equation (5a), becomes

$$\lambda(C_i - C) = p_a - 2S(R,\sigma)/R - (K + C_{p_s})\rho V_0{}^2/2$$
$$- (R\ddot{R} + 3\dot{R}^2/2) \geq 0 \quad (9)$$

for gaseous growth to be possible. In accordance with equation (3), the threshold condition is given by the equality on the far right-hand side of equation (9).

It is convenient to introduce the dimensionless quantities exhibited previously in equations (6–8). In addition, we can write the dimensionless radial velocity of the bubble wall as

$$v = dr/d\tau \quad (10)$$

and the dimensionless radial acceleration of the bubble wall as

$$a = -d^2 r/d\tau^2 \quad (11)$$

In equation (11), the minus sign is introduced in order to account for the fact that in the neighborhood of the maximum radius r_m when $v(r_m) = 0$, the acceleration is necessarily negative so that a is the magnitude of the radial acceleration in this case.[3] Moreover, we will see later that our interest centers on those cases in which $r \geq n$ in equation (9). Therefore we can express the critical threshold condition in equation (9) in dimensionless form as

$$\gamma - \frac{1}{r} - \beta + ra - 3v^2/2 = 0$$

which can be rearranged as the quadratic

$$r^2 + [(\gamma - \beta - 3v^2/2)a]r - \frac{1}{a} = 0 \quad (12)$$

---

[2] Note that $C_\sigma = 4/\text{We}^2$ where We is the Weber number based on nucleus radius as defined in the Nomenclature.

[3] Referring to the well-known derivation of equation (5a), we recall that the instantaneous pressure in the liquid at the bubble wall is related to $\rho[R\ddot{R} + 3\dot{R}^2/2]$, where the quantity in brackets is the instantaneous fluid acceleration at the wall. In terms of the dimensionless bubble wall quantities a and v, the dimensionless fluid acceleration at the bubble wall is $-ra + 3v^2/2$. Thus an increase in a decreases the pressure in the fluid, while an increase in v increases the pressure.

The critical radius obtained from equation (12) is

$$r = \frac{\gamma - \beta - 3v^2/2}{2a}\left(-1 + \sqrt{1 + \frac{4a}{(\gamma - \beta - 3v^2/2)^2}}\right) \quad (13)$$

where we take the positive square root and assume that

$$\gamma - \beta - 3v^2/2 > 0$$

in order that $r > 0$. Moreover, if $4a/(\gamma - \beta - 3v^2/2)^2 << 1$ we can expand the radical in equation (13) and get

$$r = \frac{1}{\gamma - \beta - 3v^2/2} - \frac{a}{(\gamma - \beta - 3v^2/2)^3}$$
$$+ \frac{2a^2}{(\gamma - \beta - 3v^2/2)^5} - \cdots \quad (13a)$$

If r exceeds the critical radius given by equations (13) or (13a), gaseous bubble growth will start. The examination of equation (13a) leads us to make two comparisons involving three values of the critical radius assuming $a << 1$. In the first, we compare the critical radius when $r = r_m$ and $v = 0$ with the value of r at neighboring points at which $v \neq 0$. Evidently the radius r will be larger when $v \neq 0$ than it will be if $v = 0$. Therefore we may conclude that air diffusion is more likely to start when $r = r_m$ than will be the case at neighboring points. The physical reason for this rests with the distinction between the bubble wall acceleration and the bubble wall velocity, and the acceleration of the fluid at the bubble wall as explained previously. As we have seen, the inertia of the water around the bubble causes the bubble wall velocity to increase the instantaneous pressure in the fluid at the bubble wall. But if the pressure increases, the saturation concentration of dissolved air is increased at the bubble wall and, as a result, air diffusion from the liquid into the bubble wall becomes more difficult than it would be if $v = 0$. In the second, once the vapor bubble has assumed a fixed position in the laminar separation bubble, the radial acceleration and velocity of the bubble wall can be neglected altogether compared to their values when equation (8) applies. Accordingly, the critical radius for subsequent gaseous growth is given by

$$r_c = \frac{1}{\gamma - \beta}, \quad r_c \geq n \quad (14)$$

and this radius will be larger than the critical radius at $r = r_m$, and with radial accelerations in the water. Therefore, if equation (14) is taken as the critical condition, the condition when $r = r_m$, namely:

$$r_m = \frac{1}{\gamma - \beta}\left(1 - \frac{a}{(\gamma - \beta)^2}\right)$$

will certainly be satisfied. For this reason, we shall regard equation (14) as the defining condition for subsequent gaseous growth after vaporous growth ceases when $r = r_m$. For the moment, if we rule out the possibility of explosive growth, we note from equations (13) and (14) with $\beta < 0$, corresponding to $K < -C_{p_s}$, that $r > 0$ even if the air content parameter vanishes. This can certainly not be said if $\beta > 0$. Therefore we might expect to observe subsequent gaseous growth at cavitation numbers corresponding to $\beta > 0$, although if the air content is low enough, it would be possible for a vapor bubble to start gaseous growth at $r = r_m$ and then because $r_m < r_c$ this bubble might subsequently dissolve.

We recall that equation (14) gives the critical radius of subsequent gaseous growth after vaporous growth and that r_c is not necessarily the same as the equilibrium radius of an isothermal bubble. Since equation (14) applies only to those cases for which $r_c \geq n$, we consider the other case in which $1 \leq r_c < n$. The corresponding relationship for the critical radius is
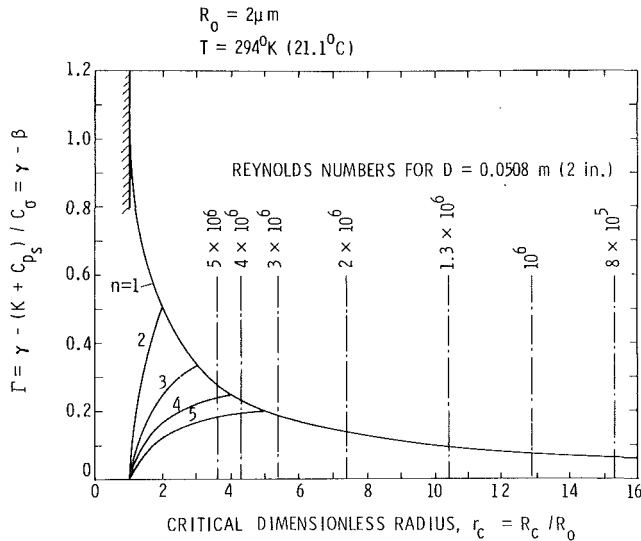
$R_0 = 2 \mu m$
$T = 294^0 K \ (21.1^0 C)$

REYNOLDS NUMBERS FOR D = 0.0508 m (2 in.)

CRITICAL DIMENSIONLESS RADIUS, $r_c = R_c / R_0$

Fig. 2 Critical parameters for initiation of subsequent gaseous growth in the laminar separation bubble

$$r_c = \frac{1}{1 - (n-1)(\gamma - \beta)} \ , \ 1 \leq r_c < n \tag{15}$$

At a prescribed value of n, the critical curve in a Γ versus r_c plane is a composite from equations (14) and (15) and the peak value at $r_c = n$ will be at a sharp corner. Figure 2 shows plots of $\Gamma = \gamma - \beta$ versus r_c for this composite critical curve with several values of n. Except for $n = 1$, this figure shows for values of $\gamma - \beta$ less than $1/n$, that two values of r_c are possible. In references [11] and [12], it is argued that the larger value provides for the initiation of gaseous growth, and not the smaller value to the left of $r_c = n$. Therefore, if gaseous growth is to take place at values of $\Gamma < 1/n$, one should select that value of $r_m \geq r_c$ to the right of $r_m = n$ but within the limit established by the height of the laminar separation bubble.

Measurements of the maximum height of the laminar separation bubble have been reported by Arakeri [3] and Van der Meulen [6]. Data from these sources are shown in Fig. 3. An analytical approximation to the observed trend is given by

$$H/D = 111/Re^{0.79} \tag{16}$$

where

H = Maximum height of the laminar separation bubble,
D = headform diameter, and
Re = Reynolds number based on headform diameter.

The Reynolds numbers marked in Fig. 2 show values of r_m obtained from (16) by assuming that $2R_m = H/2$ for a 2 in. (0.0508 m) dia headform with the added assumptions that the nucleus size R_0 is 2 microns and the temperature of the water is 21.1°C.

The Flaccid Bubble

There can be changes of nucleus size which may take place without any vaporous growth. At sufficiently high cavitation numbers, the nucleus can still travel in the boundary layer until it becomes stabilized in the separation zone on the body without experiencing vaporous growth. As in the example of a flaccid balloon, the size of the bubble would change by progressing through a succession of equilibrium thermodynamic states as it passes through regions of changing external pressure. It is assumed that these equilibrium size changes occur without appreciable air diffusion because there is insufficient time for such a comparatively slow process to take place. Under the isothermal assumption, the equilibrium
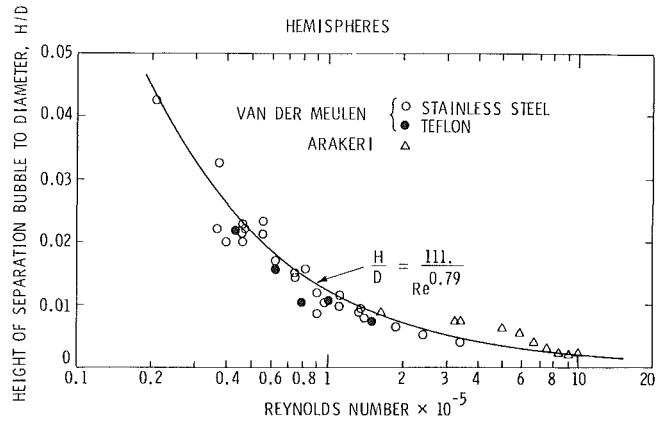

Fig. 3 The ratio of maximum height of laminar separation bubble to headform diameter, H/D, as a function of Reynolds number. Plotted points are taken from references [3] and [6].

size of interest here is that size which would be obtained in the separation bubble.

The essential relationship which governs the equilibrium size change of an isothermal bubble is

$$p_a R_0^3 = p_g R^3 \tag{17}$$

where p_a is the partial pressure of air in the free stream nucleus and p_g is the partial pressure of air in the bubble when it is fixed at a point in the laminar separation zone. In the separation zone, the balance of pressures on the bubble wall is

$$p_g + p_v = 2 \frac{S(R, \sigma)}{R} + p_s \tag{18}$$

Equations (17) and (18) can be combined to give

$$p_a R_0^3 = \left(p_s - p_v + \frac{2S}{R} \right) R^3 \tag{19}$$

Upon introducing the dimensionless quantities, r, β, and γ as incorporated in equation (8), we find

$$\frac{\gamma}{r^3} = \beta + \frac{S(r, \sigma)}{r} \tag{20}$$

Thus, the new radius is given by

$$\left. \begin{array}{ll} r^3 - \dfrac{r^2}{1 + (n-1)\beta} - \dfrac{(n-1)\gamma}{1 + (n-1)\beta} = 0 & , \ r < n \ , \\[3mm] r^3 + \dfrac{1}{\beta} r^2 - \dfrac{\gamma}{\beta} = 0 & , \ r \geq n \end{array} \right\} \tag{21}$$

The equilibrium radius, r_e, is found from these cubics as the smaller real root for which $r_e \geq 1$. If this radius is less than r_c from equation (14) when $r_c \geq n$, the bubble will dissolve. Otherwise, subsequent diffusive growth is possible. In order to investigate the conditions leading to diffusive growth when $r_e \geq n$, let us rewrite the second of equations (21) as

$$\beta \sqrt{\gamma} = \frac{\sqrt{\gamma}}{r_e} \left(\left(\frac{\sqrt{\gamma}}{r_e} \right)^2 - 1 \right) , \ n \leq r_e < r_b \tag{22}$$

where r_b denotes the limiting value of r_m derived from the laminar separation bubble height of equation (16). In terms of normalized variables $\beta \sqrt{\gamma}$ and $(r_e / \sqrt{\gamma})$, equation (22) defines a single curve. When this equation is satisfied, since r_e and γ are positive and $\gamma < r_e^2$ in most instances, we see that this flaccid bubble result can give negative values of β although $\beta \geq 0$ if $r_e^2 \leq \gamma$.

Equation (22) contrasts with the form of equation (14) in which $r_c \geq n$; namely,

$$\beta = \gamma - \frac{1}{r_c} \tag{14}$$

As long as $\gamma - \beta > 0$ in equation (14), r_c will be positive and β can have positive or negative values. Moreover, β will be positive as long as $r_c > 1/\gamma$. But the flaccid bubble equation (22) can be rewritten as

$$\beta + \frac{1}{r_e} = \frac{\gamma}{r_e^3}$$

and from (14)

$$\beta + \frac{1}{r_c} = \gamma$$

In a particular flow, these equations will apply for identical values of R_0, V_0, γ, and so forth. But the values of β will be different in these two cases. Designate them by β_e and β_c, respectively. We have argued earlier that the cavitation number K_c, corresponding to r_c, will be associated with a previous history of vaporous bubble growth even though equation (14) defines r_c as the critical radius with respect to air diffusion. Of course, r_c may not be the same as the maximum radius r_m actually achieved after vaporous growth. The equilibrium radius r_e for the flaccid bubble is not associated with vaporous growth and the cavitation number K_e will be greater than K_c. Therefore, $\beta_e > \beta_c$ as can be seen from the definition of β following equation (8).

In order to illustrate the implications of this state of affairs, Fig. 4 presents a plot of $\beta\sqrt{\gamma}$ versus $\xi = r/\sqrt{\gamma}$ of equations (14) and (22). As noted previously the equilibrium condition for a spherical flaccid bubble, equation (22) with $n = 1$, is represented by a single curve in this plot. Equation (14), also for $n = 1$, appears as a one-parameter family of curves which depends upon $\gamma^{3/2}$. For negative values of β_e, we expect the root of interest for the flaccid bubble to be along the dashed part of the curve in Fig. 4 corresponding to $r_e > 1$. Nonetheless, we will consider radii on either side of $r = 1$. Figure 4 shows two members of the family of critical curves intersecting the equilibrium curve.

If we select an air content γ, we can draw a vertical line at a prescribed value of ξ to the right of the intersection of the equilibrium curve and the prescribed critical curve. In this case, the veritcal will cut the critical curve at $\beta\sqrt{\gamma}$ and it cuts the equilibrium curve at $\beta_e\sqrt{\gamma}$ with $\beta_c > \beta_e$ in contradiction with the inequality noted earlier. The physical implication of this finding is that since $K_e < K_c$ and we have associated K_c with vaporous growth, it is not possible for a flaccid bubble to survive a passage through the low pressure region on the headform upstream of the separation zone without vaporous growth. Thus, we see that if $r_c = r_e$ and corresponding to the class of larger radii, this value lies to the right of the intersection. Then a flaccid bubble cannot reach the laminar separation zone and experience subsequent gaseous growth.

On the other hand, suppose we imagine a horizontal line drawn through the point $(\xi_e, \beta_e\sqrt{\gamma})$ defined by the intersection of the vertical line with the equilibrium curve as previously noted. This horizontal line will cut the critical curve at a point at which $r_c < r_e$ and gaseous growth of a flaccid bubble would certainly be possible except for the fact that in this case when $\beta_e = \beta_c$, the cavitation number is less than the onset cavitation number and the flaccid bubble would experience vaporous growth. If we consider a horizontal line through the point $(\xi_c, \beta_c\sqrt{\gamma})$ defined by the intersection of the vertical line above with the critical curve, we find that this upper horizontal cuts the equilibrium curve at a value of ξ_e such that $r_e < r_c$. In this case, a flaccid bubble would dissolve even if it could reach the laminar bubble without first experiencing vaporous growth. Evidently, if the vertical reference line is to the right of the intersection, it is generally true that a flaccid bubble cannot settle in the separation bubble, experience subsequent gaseous growth, and thereby cause the onset of cavitation.
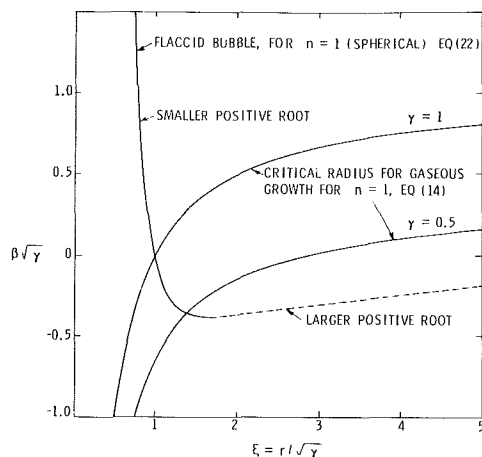

Fig. 4 Comparison of flaccid bubble and critical bubble radii in the laminar separation zone

Turning next to a reference line to the left of the intersection, we see that this line will cut the equilibrium and critical curves at points corresponding to $K_e > K_c$ and since K_c corresponds to cavitation onset, cavitation will not occur at K_e even though the flaccid bubble might experience gaseous growth in the laminar separation zone. A lower horizontal line through the intersection of this new reference vertical with the critical curve leads to two possible values for the flaccid bubble which have $r_e > r_c$ and gaseous growth is possible. But once again, such a flaccid bubble would be interrupted in its passage to the laminar separation zone by vaporous growth. Along the upper horizontal, we find $r_e < r_c$ and the flaccid bubble will dissolve.

We conclude therefore that flaccid bubbles which drift into the laminar bubble will not lead to incipient (or desinent) cavitation. Either they will dissolve or they will experience vaporous growth before reaching the laminar separation zone.

Conclusions

It appears that when there is a laminar separation bubble on a hemispherical headform, the separation zone can provide a favorable environment for the initiation of gaseous growth of cavitation bubbles. From a comparison of a flaccid bubble and other possibilities, we have also found that gaseous growth of a typical microbubble must be preceded by a period of vaporous growth which starts in the low pressure region upstream of the laminar separation zone. In this study, we have neglected all convective effects, including those of bubble-wall motion, on conditions favorable for the start of air diffusion. We have found that the most favorable condition for gaseous growth occurs at the time when a bubble undergoing vaporous growth just reaches its maximum radius when it reaches the laminar separation zone. Therefore, the probability of microbubble stabilization at a fixed point in the laminar separation zone would be highest at this instant. The conditions for the start of subsequent gaseous growth, once the vapor bubble has become fixed on the body, are somewhat more demanding. Nevertheless, it is found that the liquid in the water surrounding the bubble in the separation zone is definitely supersaturated for most flows of experimental or practical interest. Therefore, gaseous growth is most likely to occur once the vapor bubble is in the separation zone provided the dissolved air concentration of the water is sufficient to support air diffusion into the bubble.

Acknowledgment

Command under the cognizance of Code SEA 63R-31. The author also wishes to acknowledge many useful discussions with Drs. J. W. Holl and M. L. Billet during the course of the study.

References

1 Parkin, B. R., and Kermeen, R. W., "Incipient Cavitation and Boundary Layer Interaction on a Streamlined Body," California Institute of Technology, Hydrodynamics Laboratory Report No. E-35.2, Dec. 1953.

2 Parkin, B. R., and Kermeen, R. W., "The Roles of Convective Air Diffusion and Liquid Tensile Stresses During Cavitation Inception," in F. Numachi, ed., *Cavitation and Hydraulic Machinery*, Proc. IAHR-Symposium, Sendai, Japan, 1962, p. 17.

3 Arakeri, V. H., "Viscous Effects in Inception and Development of Cavitation on Axi-Symmetric Bodies," Ph.D. thesis, California Institute of Technology, 1973 (also released as Report No. 3183.1, Division of Engineering and Applied Science, California Institute of Technology, 1973).

4 Arakeri, V. H., and Acosta, A. J., "Viscous Effects in the Inception of Cavitation on Axisymmetric Bodies," ASME JOURNAL OF FLUIDS ENGINEERING, Vol. 95, No. 4, Dec. 1973.

5 Arakeri, V. H., "A Note on Transition Observations on an Axisymmetric Body and Some Related Fluctuating Wall Pressure Measurements," ASME JOURNAL OF FLUIDS ENGINEERING, Vol. 79, No. 1, Mar. 1975, pp. 82–86.

6 Van der Meulen, J. H. J., "A Holographic Study of the Influence of Boundary Layer and Surface Characteristics on Incipient and Developed Cavitation on Axisymmetric Bodies," *Proceedings of the 12th Symposium on Naval Hydrodynamics*, National Academy of Sciences, Washington, D.C., 1978.

7 Epstein, P. S., and Plesset, M. S., "On the Stability of Gas Bubbles in Liquid-Gas Solutions," *Journal of Chemical Physics*, Vol. 18, 1959, pp. 1505–1509.

8 Epstein, P. S., *Text Book of Thermodynamics*, J. Wiley, 1933, Chapter IX, p. 159.

9 Plesset, M. S., "Dynamics of Cavitation Bubbles," ASME *Journal of Applied Mechanics*, Vol. 16, 1949, p. 277.

10 Holl, J. W., and Carroll, J. A., "Observations of the Various Types of Limited Cavitation on Axisymmetric Bodies," *International Symposium on Cavitation Inception*, The American Society of Mechanical Engineers, New York, Dec. 1979, p. 87.

11 Parkin, B. R., "A Theory for Cavitation Inception in a Flow Having Laminar Separation," Applied Research Laboratory Technical Memorandum File No. TM 79-198, AD A082 851, The Pennsylvania State University, Nov. 1979.

12 Parkin, B. R., "Conditions Favorable for Gaseous Microbubble Growth in Laminar Separation Bubbles," *Cavitation and Polyphase Flow Forum*, 1980, The American Society of Mechanical Engineers, New York, pp. 1–6.

Command under the cognizance of Code SEA 63R-31. The author also wishes to acknowledge many useful discussions with Drs. J. W. Holl and M. L. Billet during the course of the study.

References

1 Parkin, B. R., and Kermeen, R. W., "Incipient Cavitation and Boundary Layer Interaction on a Streamlined Body," California Institute of Technology, Hydrodynamics Laboratory Report No. E-35.2, Dec. 1953.

2 Parkin, B. R., and Kermeen, R. W., "The Roles of Convective Air Diffusion and Liquid Tensile Stresses During Cavitation Inception," in F. Numachi, ed., *Cavitation and Hydraulic Machinery*, Proc. IAHR-Symposium, Sendai, Japan, 1962, p. 17.

3 Arakeri, V. H., "Viscous Effects in Inception and Development of Cavitation on Axi-Symmetric Bodies," Ph.D. thesis, California Institute of Technology, 1973 (also released as Report No. 3183.1, Division of Engineering and Applied Science, California Institute of Technology, 1973).

4 Arakeri, V. H., and Acosta, A. J., "Viscous Effects in the Inception of Cavitation on Axisymmetric Bodies," ASME JOURNAL OF FLUIDS ENGINEERING, Vol. 95, No. 4, Dec. 1973.

5 Arakeri, V. H., "A Note on Transition Observations on an Axisymmetric Body and Some Related Fluctuating Wall Pressure Measurements," ASME JOURNAL OF FLUIDS ENGINEERING, Vol. 79, No. 1, Mar. 1975, pp. 82–86.

6 Van der Meulen, J. H. J., "A Holographic Study of the Influence of Boundary Layer and Surface Characteristics on Incipient and Developed Cavitation on Axisymmetric Bodies," *Proceedings of the 12th Symposium on Naval Hydrodynamics*, National Academy of Sciences, Washington, D.C., 1978.

7 Epstein, P. S., and Plesset, M. S., "On the Stability of Gas Bubbles in Liquid-Gas Solutions," *Journal of Chemical Physics*, Vol. 18, 1959, pp. 1505–1509.

8 Epstein, P. S., *Text Book of Thermodynamics*, J. Wiley, 1933, Chapter IX, p. 159.

9 Plesset, M. S., "Dynamics of Cavitation Bubbles," ASME *Journal of Applied Mechanics*, Vol. 16, 1949, p. 277.

10 Holl, J. W., and Carroll, J. A., "Observations of the Various Types of Limited Cavitation on Axisymmetric Bodies," *International Symposium on Cavitation Inception*, The American Society of Mechanical Engineers, New York, Dec. 1979, p. 87.

11 Parkin, B. R., "A Theory for Cavitation Inception in a Flow Having Laminar Separation," Applied Research Laboratory Technical Memorandum File No. TM 79-198, AD A082 851, The Pennsylvania State University, Nov. 1979.

12 Parkin, B. R., "Conditions Favorable for Gaseous Microbubble Growth in Laminar Separation Bubbles," *Cavitation and Polyphase Flow Forum*, 1980, The American Society of Mechanical Engineers, New York, pp. 1–6.

DISCUSSION

V. H. Arakeri[1]

The paper is a very significant contribution to our understanding of the basic mechanism of cavitation inception in the presence of separated flows. The role of viscous effects in the process of nucleation leading to inception is clearly brought out.

It would be helpful to the readers if the author would clarify the following observations:

(i) The author has stated that the laminar free-shear layer will pose no barrier to the penetration of the vapour bubble into the separated region. However, it is not clear exactly what mechanism and in particular the source of lateral force which would drive the bubble once in the free-shear layer into the separated region. It would appear that the dominant mechanism for the penetration of vapour bubbles into the separated region would be through the reattachment region.

(ii) It is also stated by the author that the presence of unsteady pressures would not necessarily mean that rectified diffusion could be an important mechanism for bubble growth in particular with respect to threshold condition. However, Flynn [1] for example has pointed out that the

[1] Department of Mechanical Engineering, Indian Institute of Science, Bangalore 560012, India

threshold condition for cavitation inception is influenced by rectified diffusion. It would be helpful if the author elaborates on the explanation provided by him with respect to rectified diffusion.

(iii) It is well known that for a given tension in the liquid there is a critical radius Rcr such that nuclei with $R_0 > R_{cr}$ would grow vapourously whereas nuclei with $R_0 < Rcr$ will not grow. The author has presented possibility of vapour growth of a bubble of $R_0 = 2 \mu$m. Under normal surface tension law this bubble would have to be subjected to a tension of the order of 1 bar before any vapourous growth is possible. This tension certainly does not exist on the hemispherical nose at incipient conditions and the growth is made possible only by the introduction of modified surface tension law by Professor Parkin. However, once growth begins the modified surface tension law approaches the normal law and then the concept of critical radius still should be valid. Therefore, would the author like to comment on the concept of critical radius with the modified surface tension law.

Finally the author is to be congratulated on this excellent contribution.

Additional References

1 Flynn, H. G., "Physics of Acoustical Cavitation in Liquids," *Physical Acoustics*, ed. W. P. Mason, Vol IB, Academic, 1964, (see Fig. 23 on p. 122).

Author's Closure

The author thanks Professor Arakeri for his interest in the present paper and for his questions which certainly require further discussion. We will try to answer these questions in the order posed by Dr. Arakeri.

(i) We agree that the paper advances no postulate to explain how a nucleus might penetrate the free shear layer in order to become stabilized at a fixed point in the laminar separation bubble. We can make two observations concerning this point. The first is that the free shear layer is a slowly moving region of the fluid, having just left a stagnation point at the separation point on the body. The fluid on either side of the free streamline will have somewhat higher velocities and the fluid in the laminar bubble recirculates. The second is that this eddy inside the laminar bubble probably has its lowest pressure at its center with the pressure gradient being positive as one moves away from the center and through the shear layer beyond. Although this is a weak gradient we would guess that this slight suction force could cause some free-stream nuclei in the boundary layer to penetrate the laminar separation bubble. The verification of this speculation remains for future investigations, although the curvature of the streamlines in this flow region suggests that it could be true.

Since there is recirculation in the laminar bubble, it is possible for bits of foam (microbubbles, that is) to move upstream into the laminar bubble, but we have not actually observed this process to result from bubble ring cavitation. My own experience to data suggests that most nuclei, being free-stream nuclei, move downstream into the laminar bubble, although we have observed a few cases in which larger nuclei failed to enter the laminar bubbles and quickly moved on downstream [1]. Further experimental evidence on these points would be welcome.

(ii) The unsteady pressures considered by Dr. Arakeri are probably those to be found in the reattachment region where macroscopic bubble-ring cavitation is observed. Perhaps such unsteadiness is less pronounced upstream of the laminar separation bubble where we neglect rectified diffusion.

Once the nucleus comes to rest in the laminar bubble ahead of the reattachment region, rectified diffusion could be possible if the bubbles oscillate radially. However, such photographic records as I have analyzed [1] seem to show

smoothly growing microbubbles fixed at a point in the laminar bubble. If radial oscillations of these bubbles took place, we can only say that the resolution of the high-speed photographs did not permit the detection of such oscillations. Therefore, we do not know whether Flynn's discussion of rectified diffusion, as cited by Professor Arakeri, is applicable or not. Moreover, even if oscillations are neglected, we find that conditions favorable for air diffusion exist when bubble-ring cavitation is present. We agree that the possibility of rectified diffusion would enhance the favorable environment for air diffusion.

My own thoughts which are reflected in the last paragragh of Section III-B, page 123 of Flynn, lead me to believe that rectified diffusion is not important for transient microbubbles in the region of the boundary layer ahead of the laminar bubble.

(iii) Liquid tensions do not exist in the laminar bubble upstream of the reattachment region, as Professor Arakeri states. And for that reason, vaporous growth is not considered by microbubbles in the laminar separation bubble. However, during bubble-ring cavitation, static pressures less than vapor pressure have been observed on the body in the neighborhood of the minimum pressure point [2]. In this region of the boundary layer flow, we have calculated vaporous growth for stable nuclei and spherical bubbles and we find that the surface tension law is important chiefly because it permits growth from bubbles having smaller "initial radii" than would be the case for spherical microbubbles [11]. Unfortunately, these additional calculations could not be included in the present paper, but they are discussed in subsequent publications which are now in press.

S. Kamiyama
Professor,
Institute of High Speed Mechanics,
Tohoku University,
Sendai, Japan

T. Yamasaki
Assistant Professor,
Faculty of Agriculture,
Kochi University,
Kochi Prefecture, Japan

Prediction of Gaseous Cavitation Occurrence in Various Liquids Based on Two-Phase Flow Analogy

An analytical method for predicting the cavitation occurrence is developed applying an analogy with the choking condition of two-phase flow. The effects of the presence of inert gas and thermodynamic depression on the inception of cavitation are estimated in various liquids such as water, freon, hydrogen, and sodium. It is clearly shown that the thermodynamic effects are remarkable in the case of low flow velocity in fluids with small Spraker's B-factor ($<1.0m^{-1}$). Also, the predicted values show reasonable agreement with some experimental data.

Introduction

Recently, cavitation occurrence in high speed flow of various liquids is of considerable and increasing importance in many fields, especially the design and development of the sodium-cooled fast-breeder reactors in nuclear power engineering and the cryogenic liquid pumps in aerospace engineering.

In the present situation, it would be desirable to establish the theoretical methods for predicting the cavitation occurrence in various liquids because of difficulty of the cavitation tests in such liquids and scarcity of the experimental data. Since each liquid behaves differently in cavitation process owing to its particular thermodynamic properties, the predicting methods must be theoretically studied taking into account liquid properties and flow condition.

There are many reports about the thermodynamic effects on cavitation phenomena [1-11]. First, Stepanoff proposed the B-factor method to explain the thermodynamic effects on the cavitation characteristics in pumps handling various liquids other than water [1]. The B-factor theory has been developed by several researchers [2-4]. Also, an entrainment theory was proposed by Holl, et al. [5]. However, these methods are mainly applicable to the states of fully developed cavitation.

On the other hand, there are a few analyses of the thermodynamic effects on cavitation inception from the viewpoint of the bubble dynamics [6-8]. However, the calculated values of the incipient (or desinent) cavitation sigma based on the bubble dynamics have not explained well the experimental results in water at various temperatures [8].

Another way of cavitation prediction is an approach from

an analogy with two-phase bubble flow phenomena. There are several studies for the predictions of the cavitating states and the cavitation characteristics of pumps based on the analogy with the two-phase choked flow condition [2, 9-11].

However, in these analyses, the volume of gas phase is estimated as the vapor volume produced by cavitation and only the fully developed cavity flow is considered.

It is well known that the inert gas contained in the flowing liquid plays an important role in the inception of cavitation, especially in gaseous cavitation occurrence in which the expansion of noncondensible gas becomes more important than the vaporization of liquid in contrast to vaporous cavitation.

It is, therefore, very important to study the thermodynamic effects in the liquid state including a noncondensable gas for the prediction of cavitation inception in various liquids.

Authors have already proposed one method for predicting the incipient condition of the gaseous cavitation by analogy with the local choked flow condition of homogeneous bubble mixture without consideration of the thermodynamic effects [12, 13].

It is, therefore, the purpose of the present paper to develop the predicting method taking into account the effects of the thermodynamic depression on the cavitation sigma for various liquids.

Analysis of Criterion for Cavitation Occurrence

Sonic Velocity in Bubble Mixture. The flowing fluid must be regarded as a mixture composed of liquid, its vapor and foreign gas (or inert gas) nuclei when it passes through lower pressure region where gaseous cavitation occurs. As stated in the previous paper [12], the local critical condition in two-phase flow is adopted as a criterion of cavitation occurrence.

It is assumed that the two-phase flow considered here is adiabatic, steady, homogeneous (no slip), frictionless, and irrotational. The gas phase is also assumed to be thermal equilibrium with the liquid phase and consists of many tiny

bubbles of the same equivalent radius R which contain both the vapor and noncondensable gas.

Then, the basic equations (i.e., the continuity, momentum, and energy equations) for a control volume of fluid can be written as follows:

$$d(\rho_T V) = 0 \tag{1}$$

$$dp_l + d(\rho_T V^2) = 0 \tag{2}$$

$$dh_T + d\left(\frac{V^2}{2}\right) = 0 \tag{3}$$

where V = velocity, p = pressure, h = enthalpy, ρ_T = apparent density of bubble mixture. Denoting the void fraction by $\alpha = \alpha_g + \alpha_v$, the density ρ_T at pressure p are expressed as:

$$\rho_T(p) = \rho_v(p)\alpha_v(p) + \rho_g(p)\alpha_g(p) + \rho_l\{1 - \alpha(p)\} \tag{4}$$

also, the subscripts g, l, and v refer to the noncondensable gas, liquid and vapor, respectively, and also T expresses the state of two-phase mixture.

Neglecting the inertia force term in equation of a single bubble motion, the following pressure balance equation is obtained.

$$p_l + \frac{2\gamma}{R} = p_i \tag{5}$$

where p_i = internal pressure of bubble
γ = surface tension

It is, further, assumed that the gas and the vapor obey an ideal gas law, i.e.,

$$\rho_v(p_i) = \frac{p_i}{R_v T}, \rho_g(p_i) = \frac{p_i}{R_g T} \tag{6}$$

where R_v and R_g are gas constants of vapor and gas, respectively.

Applying the Dalton law to the mixed gas in the bubble,

$$p_i = p_g + p_v \tag{7}$$

and

$$\alpha(p_i) = \alpha_g(p_i) + \alpha_v(p_i) = \alpha_v(p_v) = \alpha_g(p_g) \tag{8}$$

where p_v and p_g are the partial pressure of vapor and noncondensable gas, respectively.

Now, considering the vaporization process of the liquid by pressure decrease from saturated state similar to Spraker's analysis [3], the following relation is obtained from equations (1)–(3).

$$c_{pT}\left(\frac{\partial T}{\partial p_l}\right)dp_l + \lambda dx_v = \rho_T^{-1} dp_l \tag{9}$$

where

$$c_{pT} = c_{pl}(1-x) + c_{pg}x_g + c_{pv}x_v$$
$$\text{:specific heat of two-phase mixture} \tag{10}$$

$$x = x_g + x_v = (\alpha_v \rho_v + \alpha_g \rho_g)/\{(1-\alpha)\rho_l + \alpha_v\rho_v + \alpha_g\rho_g\}$$
$$\text{:quality of gas phase} \tag{11}$$

and

$$\lambda = \text{latent heat of vaporization}$$

Also, in the case of adiabatic and equilibrium process of two-phase flow, the following equation of state of noncondensable gas is obtained with the assumption of no gas solubility $(dx_g/dp_l = 0)$ [14].

$$p_g \rho_g^{-3n} = \text{const or } p_g = p_{gref}(R_{ref}/R)^{3n} \tag{12}$$

where

$$n \cong \frac{xc_{pg} + (1-x)c_{pl}}{xc_{vg} + (1-x)c_{pl}} \text{ : polytropic index} \tag{13}$$

and c_p, c_v are specific heat at constant pressure and constant volume, respectively and also, ref means the reference state.

It is clear from equation (13) that the polytropic index n approaches 1.0 when x is very small.

Considering the liquid state near the condition of cavitation inception, the quality of gas phase x is very small and then the assumption of $n \approx 1.0$ is reasonably accepted.

Then, equation (5) can be written by

$$p_l = p_v + p_g - \left(\frac{2\gamma}{R_{ref}}\right)\left(\frac{p_g}{p_{gref}}\right)^{1/3} = f(p_v, p_g) \tag{14}$$

Using the relations of $\partial p_l/\partial p_v = 1$, $\partial x_v/\partial p_g = 0$ and $\partial T/\partial p_g \cong 0$ with $n = 1.0$, equation (9) reduces to

$$\lambda\frac{dx_v}{dp_l} = \lambda\frac{dx_v}{dp_v} = \rho_T^{-1} - c_{pT}\left\{\frac{\partial T}{\partial p_v}\frac{\partial p_v}{\partial p_l} + \frac{\partial T}{\partial p_g}\frac{\partial p_g}{\partial p_l}\right\}$$

$$\cong \rho_T^{-1} - c_{pT}\frac{\partial T}{\partial p_v} \tag{9'}$$

Equation (4) can be written as

$$\rho_T(p_l) = \rho_v(p_i)\alpha_v(p_v) + \{\rho_g(p_i) - \rho_v(p_i)\}\alpha_g(p_i)$$
$$+ \rho_l\{1 - \alpha_v(p_v)\} \tag{4'}$$

From equation (4)', sonic velocity C in a bubble mixture at liquid pressure p_l is obtained as follows:

$$C^{-2} = \left(\frac{d\rho_T}{dp_l}\right) = \{\rho_v(p_i) - \rho_l\}\frac{d\alpha_v(p_v)}{dp_l}$$

$$+ \{\rho_g(p_i) - \rho_v(p_i)\}\frac{d\alpha_g(p_i)}{dp_l}$$

$$+ \left(\frac{\alpha_v(p_i)}{R_v} + \frac{\alpha_g(p_i)}{R_g}\right)\frac{1}{T}\frac{dp_i}{dp_l} \tag{15}$$

Further, the term of $d\alpha_v(p_v)/dp_l$ in equation (15) is expressed as follows:

$$\frac{d\alpha_v(p_v)}{dp_l} = \left\{\frac{d\left(p_v + p_g - \frac{2\gamma}{R}\right)}{d\alpha_v(p_v)}\right\}^{-1} = \left\{\left(\frac{d\alpha(p_v)}{dp_v}\right)^{-1}\right.$$

$$\left. + \left(\frac{dp_g}{dr} + \frac{2\gamma}{r^2 R_{ref}}\right)\frac{dr}{d\alpha_g(p_g)}\right\}^{-1} \tag{16}$$

Nomenclature

B = Spraker's B-factor, m^{-1}
C = sonic velocity, m/s
c_p = specific heat, J/(kg·K)
g = acceleration of gravity, m/s^2
h = enthalpy, J/kg
K = $\beta_{ref}p_{gref}$
p = pressure, kPa
p_i = total pressure in Dalton's law, kPa
R = bubble radius, m, or gas constant, J/(kg·K)
r = R/R_{ref}

T = absolute temperature, K
v = specific volume, m^3/kg
V = velocity, m/s
x = quality
α = void fraction of gas phase
β = $\alpha/(1-\alpha)$
γ = surface tension, N/m
δ = specific volume ratio (v_v/v_l)
λ = latent heat of vaporization, J/kg
ρ = density, kg/m^3
ρ_T = apparent density of

homogeneous bubble mixture, kg/m^3
σ^* = critical cavitation number

Subscripts

g = gas
l = liquid
s = saturation condition
T = two-phase mixture
v = vapor
ref = reference condition (standard state)

The void fraction α is related to bubble radius R by

$$\alpha = \frac{\beta_{\text{ref}} r^3}{1 + \beta_{\text{ref}} r^3} \qquad (17)$$

where

$$\left.\begin{aligned} \beta &= \frac{\alpha}{1-\alpha} \\ r &= R/R_{\text{ref}} \end{aligned}\right\} \qquad (18)$$

Using equations (5), (8), (12), and (17) with $n = 1.0$, the following relations are obtained.

$$\frac{d\alpha}{dr} = \frac{3\beta_{\text{ref}} r^3}{(1 + \beta_{\text{ref}} r^3)^2} = \frac{3\alpha_v(p_v)\{1 - \alpha_v(p_v)\}}{r} \qquad (19)$$

$$\frac{dp_g}{dr} = -\frac{3p_g}{r} \qquad (20)$$

$$\frac{dp_i}{dp_l} = d\left(p_l + \frac{2\gamma}{R}\right)\Big/dp_l = 1 - \frac{2\gamma}{3R}\frac{(1 + \beta_{\text{ref}} r^3)^2}{\beta_{\text{ref}} r^3}$$
$$\times \left(\frac{d\alpha_v(p_v)}{dp_l}\right) \qquad (21)$$

$$\frac{d\alpha_g(p_i)}{dp_l} = \frac{d\alpha_g(p_i)}{dp_i}\frac{dp_i}{dp_l} = -\frac{\alpha_g(p_i)\{1 - \alpha_g(p_i)\}}{p_i}\frac{dp_i}{dp_l} \qquad (22)$$

Finally, equation (15) can be written in the following form.

$$C^{-2} = [\rho_v(p_i) - \rho_l - \left\{\frac{\alpha_v(p_i)\rho_v(p_i) + \alpha_g(p_i)\rho_g(p_i) - \alpha_g(p_i)(1 - \alpha_g(p_i))(\rho_g(p_i) - \rho_v(p_i))}{\alpha(p_i)(1 - \alpha(p_i))p_i}\right\}\frac{2\gamma}{3R}]$$

$$\times \left\{\frac{dp_v}{d\alpha_v(p_v)} - \frac{p_l - p_v + \dfrac{4\gamma}{3R}}{\alpha(p_i)(1 - \alpha(p_i))}\right\}^{-1} + \frac{\alpha_v(p_i)\rho_v(p_i) + \alpha_g(p_i)\rho_g(p_i)}{p_i} - \frac{\{\rho_g(p_i) - \rho_v(p_i)\}}{p_i}$$

$$\times \alpha_g(p_i)(1 - \alpha_g(p_i)) \qquad (23)$$

---

where

$$\frac{d\alpha_v(p_v)}{dp_v} = \frac{\partial \alpha_v}{\partial x_v}\frac{\partial x_v}{\partial p_v} + \frac{\partial \alpha_v}{\partial v_v}\frac{\partial v_v}{\partial p_v}$$

$$= \frac{1}{\rho_l}\left[\{\alpha_v + \delta(1 - \alpha_v)\}\left\{\frac{1}{\lambda} - \frac{\rho_T c_{pl}}{\lambda}\frac{\partial T}{\partial p_v}\right\} - \frac{\alpha_v(1 - \alpha_v)}{R_v T}\delta\right] \qquad (24)$$

and $\delta = v_v/v_l$: specific volume ratio $\qquad (25)$

Substituting equation (24) into equation (23), the values of sonic velocity in the two-phase mixture in an arbitrary pressure p_l can be determined.

Now, in the case of small α,

$$\rho_T \cong \rho_l\{1 - \alpha(p_i)\} = \rho_l\{1 - \alpha_v(p_v)\} \qquad (26)$$

and with the assumptions of $\delta \gg 1$, $c_{pT} \approx c_{pl}$, $\rho_l c_{pl}(\partial T/\partial p_v) - 1 \gg 1$ and $(\delta - 1)(p_s - p_v)/\lambda\rho_l < 1$, the void fraction $\alpha_v(p_v)$ is reduced to the approximate one derived by Spraker [3], i.e.,

$$\alpha_v(p_v) = B(p_s - p_v)/\{B(p_s - p_v) - \rho_l g\} \qquad (27)$$

where p_s is saturation pressure and

$$B = \frac{v_v}{v_l}\frac{c_{pl}}{\lambda}\frac{\partial T}{\partial(p_v/\rho_l g)} : \text{Spraker's } B\text{-factor} \qquad (28)$$

If equations (26) and (27) are used, equation (23) can be approximated by

$$C^2 = \left(\frac{dp_l}{dp_l}\right)^{-1} \cong \frac{g}{B(1 - \alpha_v)^2} + \frac{(p_g + K)^2}{\rho K}\left(1 - \frac{2\gamma}{3Rp_g}\right)$$
$$= C_g^2\left\{1 + \frac{g\beta^2}{KBv_l}\left(1 - \frac{2\gamma}{3Rp_g}\right)^{-1}\right\} \qquad (29)$$

where

$$K = \beta_{\text{ref}} p_{g\text{ref}} \qquad (30)$$

and

$$C_g^2 \cong \frac{(p_g + K)^2}{\rho_l K}\left(1 - \frac{2\gamma}{3Rp_g}\right) \qquad (31)$$

Here, C_g is sonic velocity in two-phase mixture without vaporization and also, the factor $g\beta^2/KBv_l(1 - 2\gamma/3Rp_g)$ expresses the thermodynamic effects on the sonic velocity.

It is clear from equation (29) that the smaller the B-factor is, the larger the thermodynamic effects become.

Calculating Method of Critical Cavitation Number. If we define the cavitation inception[1] in nozzle flow as the state at which the throat velocity in one dimensional flow reaches the sonic velocity ($V = C$) under pressure p_l and void fraction α, the critical cavitation number σ^* is written as follows:

$$\sigma^* = \frac{2(p_l - p_s)}{\rho_l C^2} \qquad (32)$$

Then, equations (23) and (32) give the relation of σ^* to C.

If equation (29) is used, the following simplified equation is derived.

$$\sigma^* = 2\alpha_v(1 - \alpha_v) - \frac{1}{C^2}\left\{\frac{2\alpha_v g}{B(1 - \alpha_v)} + \frac{2(p_s - p_v) + (8\gamma/3R)}{\rho_l}\right\} \qquad (33)$$

Numerical Calculation and Discussion. Figure 1 shows the values of B-factor in various liquids such as sodium, oxygen, hydrogen, nitrogen, Freon 12, Freon 113, NaCl and CaCl$_2$-solutions and water.

As stated before, if the B-factor is large, the thermodynamic effects on the critical sigma σ^* are negligible. Hence, it may be estimated that the thermodynamic effects have relation to the choked flow condition (i.e., the incipient condition of gaseous cavitation) only in the fluids with small B-factor such as liquid hydrogen (20K), Freon 12(323K), liquid oxygen, and liquid nitrogen at higher temperature ($T \sim 100$ K).

The Runge-Kutta-Gill method was employed in the numerical procedure for obtaining the $p_v \sim \alpha_v$ relation (24) and the sonic velocity C in an arbitrary liquid pressure p_l is calculated from equation (23) without consideration of surface tension because the effects of surface tension on σ^* are relatively small for $R_{\text{ref}} > 10^{-5}$ m (see Fig. 5).

Figure 2 shows the relation of void fraction α to gas partial pressure p_g and vapor pressure p_v in the case of liquid hydrogen at 20 K. It is clear from this figure that in the initial stage with a small void fraction, the partial gas presure p_g changes remarkably compared with the vapor pressure p_v.

Figure 3 shows the relation of critical cavitation sigma to flow velocity in liquid hydrogen, where the full line is

---

[1]Here, we do not consider about the difference between the incipient and the desinent cavitations.
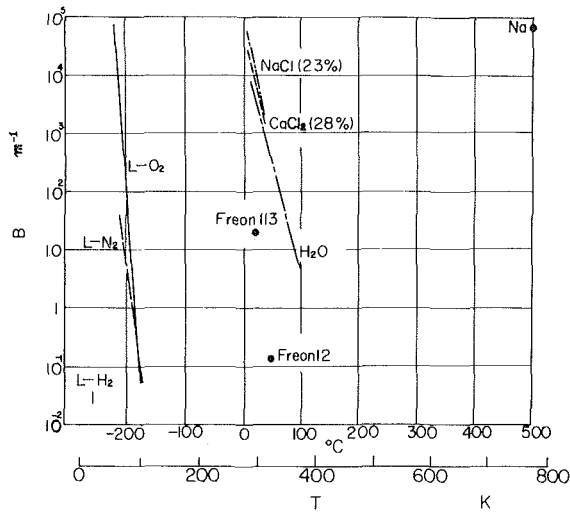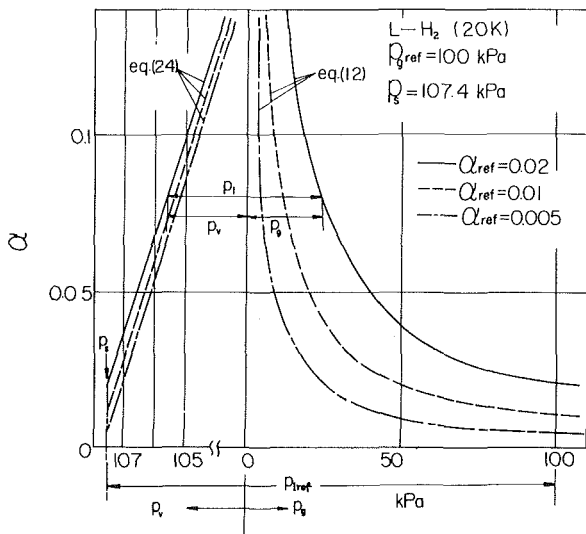
Fig. 1 B-factors in various liquids

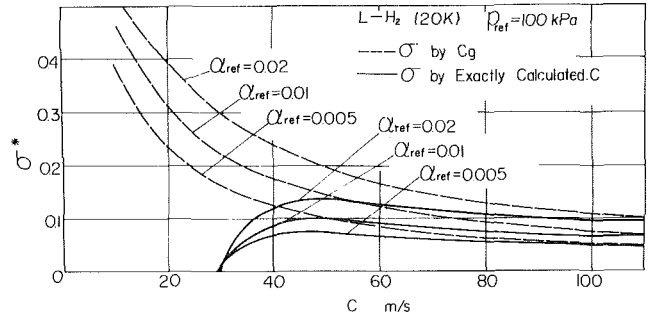Fig. 2 Relation of void fraction α to partial pressure p_g and p_v

Fig. 3 Relation of critical cavitation sigma σ^* to flow velocity $V(=C)$ in liquid hydrogen
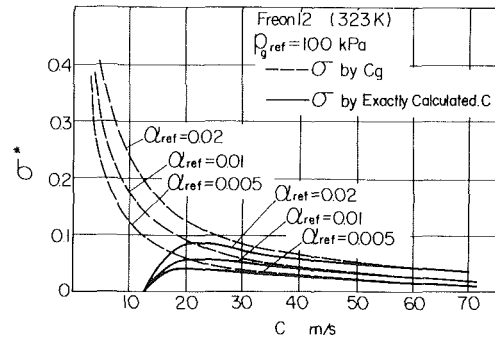

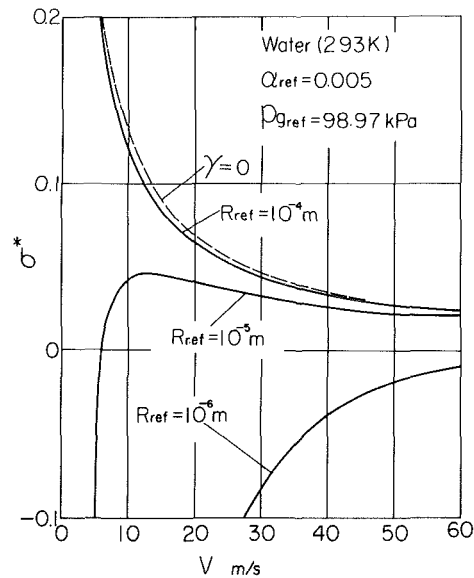Fig. 4 Relation of critical cavitation sigma σ^* to flow velocity $V(=C)$ in Freon 12

Fig. 5 Effect of surface tension on critical cavitation sigma in water

calculated from C-values of equation (23) and the broken line is from $C = C_g$. Hence, the differences between them mean the thermodynamic effects on cavitation occurrence.

It can be seen from Fig. 3 that the thermodynamic effects are larger in the low flow velocity range. The almost similar tendency are found in the case of Freon 12 as shown in Fig. 4.

On the other hand, it may be suggested that the effects of the thermal depression on σ^* are very small and the expansion of noncondensable gas plays an important role in the cavitation occurrence in the fluids with large B-factor such as cold water and liquid sodium (T < 773 K) and the flow in such liquids shows the two-phase flow characteristics with no evaporation [12].

Figure 5 shows the effect of initial bubble radius $R_{ref}(= 10^{-4} \sim 10^{-6} m)$ on σ^* in the case of cold water (293 K) calculated from equation (33).

It is clear from this figure that the relation of critical cavitation number σ^* to flow velocity V changes largely with the initial bubble radius R_{ref}, i.e., the condition of cavitation nuclei. It will further be suggested that when water includes relatively large nuclei such as $R_{ref} \cong 10^{-4} m \sim 10^{-5} m$ which have been measured by several investigators, the effects of surface tension on the critical sigma σ^* are relatively small and, on the other hand, if water includes only small nuclei such as $R_{ref} = 10^{-6} m$, the σ^*-values decrease with decreasing flow velocity.

Now, let us consider the validity of approximation employed here. For example, if the void fraction of $\alpha = 0.1$ is assumed in the case of Freon 113 (298 K), the values of $\delta = 430$ and $x \cong \alpha/\{(1-\alpha)\delta + \alpha\} = 2.6 \times 10^{-4}$ are found. Therefore, the approximation of $\delta >> 1$ and $c_{pT} \cong c_{pl}$ is reasonably accepted. However, some cautions are necessary for the use of approximate equation (27).

Figure 6 shows the comparison of the void fraction α_v between approximate expression (27) and more exact one (24).

It is clear from this figure that equation (27) is a reasonable approximation in the case of small α_{ref}, but the difference between equations (24) and (27) becomes larger in large values of α_{ref}, especially in the case of small α_v.

However, the effect of this discrepancy on the prediction of σ^* is not serious because it occurs in the case of small α_v.
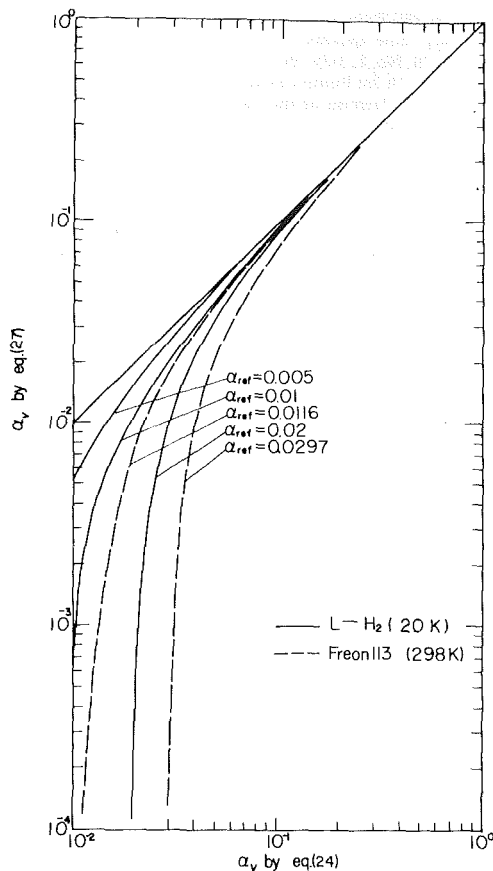
Fig. 6 Comparison of Spraker's approximation for α_v with exact equation

Fig. 7 Effect of temperature in liquid hydrogen on critical cavitation sigma

Comparison With Experimental Results. To confirm applicability of the predicting method, analytical results are compared with some experimental data.

Authors have already shown some experimental results with hot water in two-dimensional contraction nozzle [12].

Mean void fraction α at the throat was measured at various pressure with γ-ray attenuation technique [13].

It was clearly shown that the experimental data on the relation of critical pressure to flow velocity agree well with the predicted values of critical two-phase flow condition within the accuracy of the experimental uncertainty (i.e., a data scatter) of approximately ± 5 percent in measured pressure and also the throat pressure is considerably higher than the vapor pressure [12, 13]. In the case of water (T = 288-333K), the thermodynamic effects are almost negligible as estimated from the values of B-factor and then the predicted values correspond to the case of two-phase flow including only the noncondensable gas. Thus, in the case of large B-factor, equation (31) gives a reasonable explanation of the experimental results.

At present, there are no suitable experimental data in the case of small B-factor for comparison with the present theory.

Hord [15] obtained experimental data with liquid hydrogen flowing around a hydrofoil and showed the relation of critical cavitation sigma to flow velocity and liquid temperature. Although the direct comparison of σ^*-values with the predicted one is impossible because of some unknown factors in the experimental condition, the calculated results of the relation of σ^*-values to flow velocity in liquid hydrogen at various temperatures from equation (33) with $\gamma = 0$ is shown in Fig. 7 as an example of $\alpha_{ref} = 0.005$.

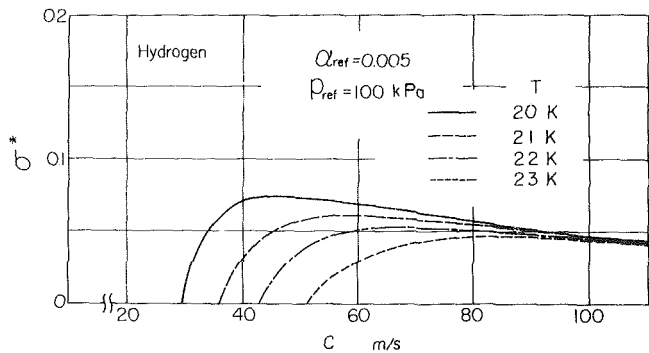The tendency of lower σ^*-values at higher temperatures and the sharp decrease in σ^*-values in low flow-velocity regime

explains qualitatively well the experimental data obtained by Hord [15].

It is well known that the inception of cavitation is generally a complex phenomena dependent on the concentration of nuclei within the flow and many other features of the real flows. It may, therefore, be noted that application of the present method to the practice is restricted to the case where the liquid contains gas bubbles and the free stream nuclei play an important role in gaseous cavitation occurrence.

Hence, it is important, first, to know the nuclei distribution in the real liquid flow.

Also, the extension of the present analysis will be necessary to include the effect of gas solubility $(dx_g/dp_l \neq 0)$ for application to the liquid with large gas solubility such as oil.

Further, in the case of flow having a large velocity distribution in the flow section, the present method should approximately be applied only to the streamline of the local flow regime near the body.

The other predicting method must be considered in the case of vaporous cavitation occurrence in the special liquid state such as a degassed water.

Conclusion

A predicting method of gaseous cavitation occurrence is proposed on the basis of analogy with the critical two-phase flow of homogeneous bubble mixture.

Sonic velocity of bubble mixture was obtained taking into account the liquid evaporation and the critical cavitation number was presented with the typical numerical examples in various liquids.

The main results obtained here are summarized as follows:

1 The thermodynamic effects on the predicted values of cavitation sigma become remarkable in the case of lower flow velocity in fluids with small B-factor.

2 Initial void fraction α_{ref} plays an important role on the prediction of critical sigma and the evaluation of thermodynamic effects.

3 The predicting method explains well the experimental results conducted by authors and Hord.

References

1 Stahl, H. A., and Stepanoff, A. J., "Thermodynamic Aspects of Cavitation in Centrifugal Pumps," *Journal of Basic Engineering*, Vol. 78, No. 4, Nov. 1956, pp. 1691–1693.

2 Jakobsen, J. K., "On the Mechanism of Head Breakdown in Cavitating Inducers," ASME *Journal of Basic Engineering*, Vol. 86, No. 2, June 1964, pp. 291–305.

3 Spraker, W. A., "The Effects of Fluid Properties on Cavitation in Centrifugal Pumps," ASME *Journal of Engineering for Power*, Vol. 87, No. 3, July 1965, pp. 309–318.

4 Ruggeri, R. S., and Moore, R. D., "Method for Prediction of Pump Cavitation Performance for Various Liquids, Liquid Temperatures, and

Rotative Speeds," TN D-5292, June 1969, National Aeronautics and Space Administration, Washington, D. C.

5 Holl, J. W., Billet, M. L., and Weir, D. S., "Thermodynamic Effects on Developed Cavitation," ASME JOURNAL OF FLUIDS ENGINEERING, Vol. 97, No. 4, Dec. 1975, pp. 507–514.

6 Florschuetz, L. W., and Chao, B. T., "On the Mechanics of Vapor Bubble Collapse," ASME *Journal of Heat Transfer*, Vol. 87, No. 2, May, 1965, pp. 209–220.

7 Bonnin, J., "Theoretical and Experimental Investigations of Incipient Cavitation in Different Liquids," Preprint of the Winter Annual Meeting of the ASME, Nov. 1972, No. 72WA/FE-31.

8 Holl, J. W., and Kornhauser, A. L., "Thermodynamic Effects on Desinent Cavitation on Hemispherical Nosed Bodies in Water at Temperatures from 80 Deg F to 260 Deg F," ASME *Journal of Basic Engineering*, Vol. 92, No. 1, Mar. 1970, pp. 44–58.

9 Spraker, W. A., "Two-Phase Compressibility Effects on Pump Cavitation," *Proceedings of the Symposium of Cavitation in Fluid Machinery*, ASME, Nov. 1965, pp. 162–171.

10 Hammitt, F. G., Robinson, M. J., and Lafferty, J. F., "Choked-Flow Analogy for Very Low Quality Two-Phase Flows," *Nuclear Science and Engineering*, Vol. 29, No. 1, July 1967, pp. 131–142.

11 Wilson, J. A., "A Jet Pump Cavitation Parameter Using Sonic Velocities in Two-Phase Flow," Preprint of the Cavitation and Polyphase Flow Forum, ASME, 1969, pp. 29–30.

12 Kamiyama, S., and Yamasaki, T., "Prediction of Gaseous Cavitation Occurrence in Sodium and Water Based on Two-Phase Critical Flow Analogy," Preprint of the Cavitation and Polyphase Flow Forum, ASME, 1976, pp. 46–48.

13 Kamiyama, S., and Yamasaki, T., "One Predicting Method of Gaseous Cavitation Occurrence in Water and Sodium," *Bulletin of the Japan Society of Mechanical Engineers*, Vol. 23, No. 183, Sept. 1980, pp. 1428–1434.

14 Akagawa, K., *Gas-Liquid Two-Phase Flow*, 1974, Corona Publishing, Co., LTD (in Japanese), pp. 171–172.

15 Hord, J., "Cavitation in Liquid Cryogens, II–Hydrofoil," CR-2156, Dec. 1972, National Aeronautics and Space Administration, Washington, D. C.

Y. Kodama

Ship Research Institute,
Tokyo, Japan

N. Take

Graduate Student,
University of Tokyo,
Tokyo, Japan; Presently, Software Works,
Hitachi, Ltd.

S. Tamiya

Professor,
University of Tsukuba,
Ibaragi, Japan

H. Kato

Professor,
University of Tokyo,
Tokyo, Japan

The Effect of Nuclei on the Inception of Bubble and Sheet Cavitation on Axisymmetric Bodies

Hydrogen bubbles were generated as cavitation nuclei and their distributions were measured. The number and size distribution of bubble cavities generated on axisymmetric bodies was calculated and compared with experimental results. The measured size distribution of bubble cavities agreed qualitatively with the calculated value, but the total number of cavities was about one half of the calculation. The role of stream nuclei on the inception of sheet cavity was investigated experimentally. Without added nuclei, the value of the incipient cavitation number σ_i showed a large scattering, whereas with added nuclei the scattering became fairly small and σ_i converged to the upper limit of that when no nuclei were added. σ_i with added nuclei also coincided with the desinent cavitation number σ_d, and σ_d remained unchanged by adding nuclei.

Introduction

The importance of cavitation nuclei on the inception of cavitation has been clarified by many investigators. Keller [1] reduced the number of nuclei in water by using filters and made cavitation inception tests with various axisymmetric test bodies. He found that the incipient cavitation number σ_i became lower when the test water contained less nuclei.

On the other hand, some experimenters report the fact that cavitation inception can be prompted by adding nuclei using nuclei generators [2–4].

In the present paper, the influence of stream nuclei on the inception of cavitation was investigated under the known nuclei distribution. A new cavitation tunnel was constructed which was specially designed for adding nuclei artificially. First, the relation between added nuclei and the bubble cavities formed on the test body surface was investigated experimentally, and was compared with calculated results. Second, inception tests of sheet cavity were made in the water with added nuclei, and the role of nuclei on inception was investigated.

Bubble Cavitation

Test Facility. TE-type Cavitation Tunnel, newly built at the University of Tokyo, was used in the present investigation. The test section arrangement is shown in Fig. 1.

The tunnel has a nuclei generator which is located at upstream of the contraction section (Fig. 2). It consists of tungsten wires 50 μm in dia placed at right angles to the flow,
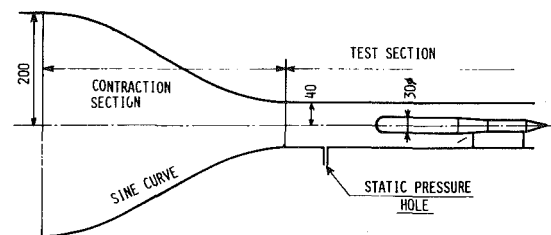

Fig. 1 Arrangement of contraction section and test section (unit: mm)

and small hydrogen bubbles are generated by electrolysis. The turbulence level in the test section is 0.2 ~ 0.4 percent by the hot film measurement, and the velocity distribution is uniform within 1 percent.

The Nuclei Generator and Its Nuclei Distribution. As no device at hand was fitted to measure directly the nuclei distribution in the tunnel, a small transparent flow channel was made for calibration.

Hydrogen bubbles were photographed through a microscope and their size distribution was measured by counting them on photographs. A typical microscopic photograph is shown in Fig. 3. The measured result is shown in Table 1. It was assumed that the same distribution of nuclei was obtained in the tunnel when following properties were the same, such as diameter and material of wire, flow speed, static pressure, and electric current.

The hydrogen volume generated per unit time was calculated by Coulomb's law, based on the measured electric current. This volume was distributed according to the fraction shown in Table 1. It was also assumed that in case tungsten wires were placed 3 cm apart from each other as shown in Fig.

Fig. 2 Installation of nuclei generator in cavitation tunnel (unit: mm)

TWENTY 30 MM
50 μM | DIAMETER
TUNGSTEN | WIRES (-)

BRASS PLATE (+)
BRASS PLATE (+)
BRASS PLATE (+)
BRASS PLATE (+)

Fig. 3 Hydrogen bubbles photographed with microscope. $U = 40$ cm/s, $i = 8$ mA/cm

Table 1 Hydrogen nuclei distributions (unit: percent in numbers).
$P = 1$ atm, $i = 9$ mA/cm (* denotes 8 mA/cm)

Rn (μm) \ U (cm/s)	20	40*	60*	94	Typical error
5 ~ 10	92.3	67.5	82.4	78.0	± 1.0
10 ~ 15	3.8	15.5	12.6	18.8	± 1.0
15 ~ 20	0.3	10.4	4.2	3.2	± 0.5
20 ~ 30	0.9	6.1	0.8	0.0	± 0.2
30 ~ 50	2.7	0.5	0.0	0.0	± 0.1

Calculation of Bubble Cavity

Formulation. The bubble growth and trajectory along axisymmetric bodies were calculated. Calculation was made for two test bodies, that is, Hemispherical and ITTC bodies, of 30 mm in dia. Axisymmetric Hess and Smith method was used to calculate the flow field near the body, where the wall effect was taken into account by placing a cylindrical wall whose sectional area was equal to the actual octagonal section.

Following Johnson and Hsieh [6], the equation of bubble motion is as follows.

$$\frac{1}{2} \times \frac{4}{3} \pi R^3 \rho \frac{d\mathbf{w}_b}{dt}$$

$$= \frac{1}{2} \rho(\mathbf{w} - \mathbf{w}_b) |\mathbf{w} - \mathbf{w}_b| C_d \pi R^2 - \frac{3}{2} \times \frac{4}{3} \pi R^3 \nabla P$$

$$+ (\mathbf{w} - \mathbf{w}_b) \times \frac{d}{dt}\left(\frac{1}{2} \times \frac{4}{3} \pi R^3 \rho\right) \qquad (1)$$

The left-side term in the equation (1) is the inertia term. It shows that a bubble has added mass which is one-half of the fluid mass it displaces. The first term of the right side is the drag in which C_d is given by the Haberman's empirical formula [6]. The second term is the pressure gradient term. The third term arises from the change of added mass. In case $dR/dt < 0$, it acts to increase the relative velocity between the bubble and the surrounding fluid (increase slip). And in case $dR/dt > 0$, it acts to decrease it.

The bubble was assumed to grow spherically, and the Rayleigh-Plesset equation was used to represent the growth.

$$\rho\left\{R \frac{d^2R}{dt^2} + \frac{3}{2}\left(\frac{dR}{dt}\right)^2\right\}$$

$$= P_v - P - \frac{2S}{R} + \frac{G}{R^3} - 4\mu \frac{dR/dt}{R} \qquad (2)$$

Calculated Results. Equations (1) and (2) were solved numerically along the bubble trajectory. Calculations were started at 20 mm upstream of the test body nose.

An example of the bubble trajectory is shown in Fig. 4. It is seen that the bubble trajectory does not deviate much from the streamline.

The relation between the initial bubble radius R_0 and the

2, hydrogen bubbles were evenly distributed into the water which flowed within 1.5 cm from the wire. Thus the number of nuclei per unit volume of water can be calculated.

The decrease of the nuclei radius owing to the diffusion of hydrogen into water was taken into account by the Epstein-Plesset equation [5]. When $U_\infty = 10$ m/s, it takes 1.05 sec for a nucleus to reach the test body after it is generated by the generator.

The effect of diffusion is more important with smaller nuclei. For example, in case $U_\infty = 10$ m/s and $\sigma = 0.80$, nuclei with radius less than 12 μm will vanish before they reach the test section. As seen in Table 1 (the case $U = 40$ cm/s), they are about 70 percent of the generated nuclei.

_____ Nomenclature _____

C_{p_s} = pressure coefficient at separation point
G = gas fraction constant of a bubble, which is determined by initial condition
i = electric current per unit length of cathode, mA/cm
R_{max} = maximum bubble radius
R_0 = initial bubble radius
R^* = critical bubble radius at static instability

r_n = ratio of added nuclei density to the standard density
U_∞ = uniform flow speed at test section
$\mathbf{w}$ = velocity vector of fluid particle
$\mathbf{w}_b$ = velocity vector of a bubble
y_0 = initial distance of a bubble from axis of symmetry
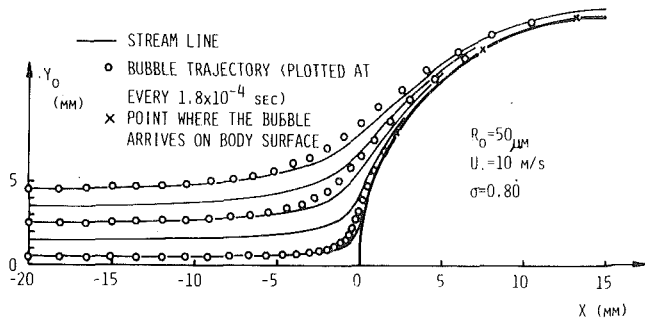σ_d = desinent cavitation number
σ_i = incipient cavitation number

Fig. 4 Calculated trajectory of bubbles and streamlines around Hemispherical body

Fig. 5 Relation between initial bubble radius R_0 and maximum bubble radius R_{max}. $U_\infty = 10$ m/s, $\sigma = 0.80$

Fig. 6 Calculated bubble radius in potential flow on Hemispherical body

Fig. 7 Bubble cavities on Hemispherical body. $U_\infty = 10$ m/s, $\sigma = 0.81$ with added nuclei $r_n = 1.0$

maximum radius R_{max} is shown in Fig. 5, where y_0 is the distance between initial point of the bubble and axis of symmetry of the test body. As y_0 increases from zero, R_{max} changes little at first (i.e., the cases $y_0 = 0.5$ and 2.5). But as it further increases, R_{max} decreases markedly as seen in the cases $y_0 = 4.5$ and 6.5.

It is interesting in Fig. 5 that R_{max} does not depend so much on R_0 when R_0 is well beyond the critical radius for static instability. From this, it may be said that bubble cavitation is not much influenced by the nuclei size distribution, and only the total number of nuclei whose radius is larger than the critical radius is important.

The growth of a bubble traveling along Hemispherical body is shown in Fig. 6. It grows rapidly in the region of static instability and still keeps growing for a while after it passes through that region. The collapsing process is rapid and in the final stage the bubble moves upstream a little as shown in Fig. 6. This upstream motion was caused by the third term in equation (2), that is, the effect of added mass change.

Next, making use of the bubble growth calculation, the number and size distribution of bubble cavities which would be present on the test body at a certain instant was calculated. It was assumed that the nuclei distribution at the test section was that given in Table 1, modified by the diffusion process as stated previously. The calculated results are given in Fig. 8 together with the experimental results.[1] Comments on these results will be made later.

Experiment of Bubble Cavitation. A nuclei generator shown in Fig. 2 was used in the present experiment. Its cathode consists of 20 tungsten wires (50 μm in dia) and they are fixed, with a space of 3 cm, on a perspex frame to form a lattice. During the experiment, another lattice with 10 tungsten wires (6 cm space) was also set in the nuclei generator. By switching on either or both of the two lattices, three different levels of nuclei number density can be readily realized. Those number densities will be termed $r_n = 0.5, 1.0$, and 1.5, respectively, where $r_n = 1.0$ is realized by the use of the single 20 tungsten wire lattice.

In order to keep the generated hydrogen volume constant, the electric current per unit length of cathode i was adjusted in proportion to the static pressure at the generator section P_m. The standard electric current is $i = 9$ mA/cm at $P_m = 1$ atm. For example, at $P_m = 0.5$ atm, the current is set at $i = 4.5$ mA/cm, and it is termed as $i^* = 9$ mA/cm.

Water was well deaerated before the experiment. The water temperature was 25°C and air content was 3.0 ppm, 15 percent to the saturated condition at 1 atm.

Photographs of bubble cavities on a test body were taken in a short period of time with various amounts of added nuclei at constant U_∞ and σ. It was found that the number of bubble

cavities increased in proportion to the amount of added nuclei. An example of the photographs is shown in Fig. 7. With no added nuclei, few cavities were formed. Consequently, almost all cavities in the photograph were generated by the added nuclei.

Comparison of Measured and Calculated Bubble Cavity Distribution. Actual bubble cavities are mostly hemispherical or elliptical in shape. And their longer radius was used to compare with the radius of the calculated spherical bubbles.

The number and size distribution of bubble cavities was counted in four cases from the photographs as shown in Fig. 7. These cases are,

---

[1] Typical uncertainties shown in all figures and tables are based on the uncertainty method of Kline and McClintock [7] used with 20:1 odds.
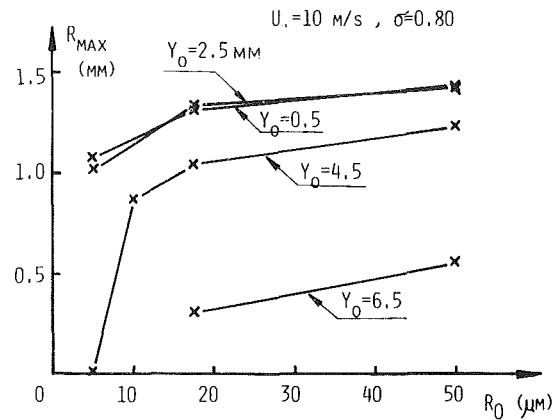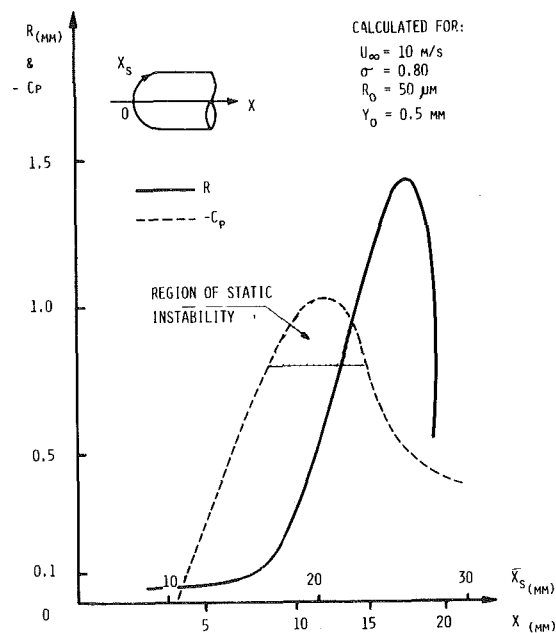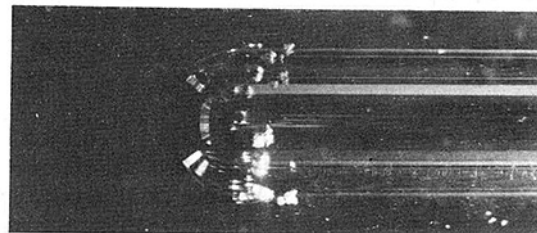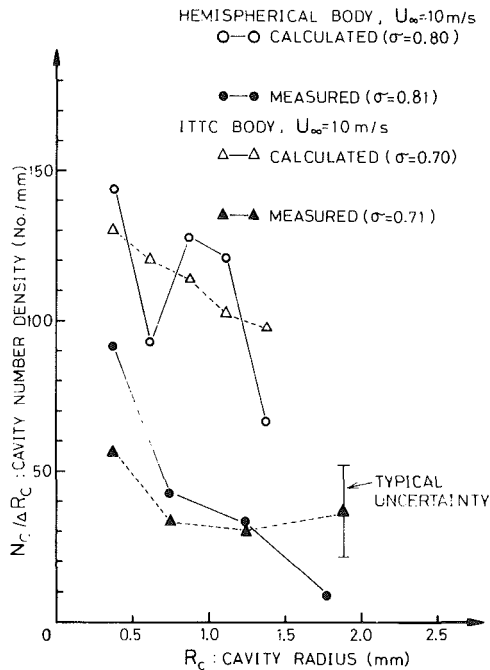
HEMISPHERICAL BODY, $U_\infty = 10$ m/s
O—O CALCULATED ($\sigma = 0.80$)

●—● MEASURED ($\sigma = 0.81$)
ITTC BODY, $U_\infty = 10$ m/s
△—△ CALCULATED ($\sigma = 0.70$)
▲—▲ MEASURED ($\sigma = 0.71$)

Fig. 8 Bubble cavity distribution on Hemispherical and ITTC bodies

------ HEMISPHERICAL BODY (CALCULATED)
—·—·— ITTC BODY (CALCULATED)
———— KOKESHI BODY (CALCULATED)
○ " (MEASURED BY LDV $U_\infty = 10.1$ m/s)
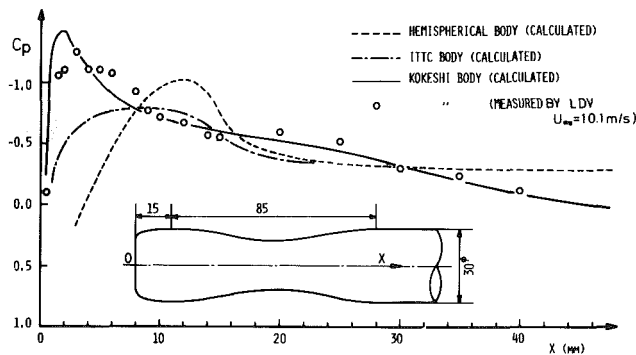
Fig. 9 Pressure distribution on three test bodies (with wall effect) and Kokeshi body profile

(1) Hemisphere. $U_\infty = 10$ m/s, $\sigma = 0.81$
(2) Hemisphere. $U_\infty = 10$ m/s, $\sigma = 0.96$
(3) Hemisphere. $U_\infty = 15$ m/s, $\sigma = 0.96$
(4) ITTC. $U_\infty = 10$ m/s, $\sigma = 0.71$

where the tungsten wires were placed only at the center of the flow section as shown in Fig. 2. However, further experiment was made for the case (1) where the tungsten wires were placed in every part of 30 cm × 30 cm lattice frame, and the total number of bubble cavities increased by about 1.7 times while the size distribution remained unchanged. Nuclei are widely scattered into the whole flow sectional area. So all the measured cavity numbers were modified (that is, increased by 1.7 times) in the other three cases. The modified results are shown in Fig. 8 and Table 2, together with the calculated results. Table 2 shows the total number of bubble cavities, and the measured value is about one-half of the calculated value in all four cases. From this, it may be said that this calculation model follows well the actual phenomenon in a qualitative sense. In the same table, it is also shown that the calculation without diffusion consideration gives the value nine times as much as the observation. This fact suggests that diffusion process is important at the present experiment. In Fig. 8, the calculated and measured size distribution profile

Table 2   Total number of bubble cavities (unit: numbers).
(* gas diffusion not considered)

Test body	U_∞(m/s)	σ	Calcu-lated	Measured	Cal./Meas.
Hemisphere	10	0.95 ±0.02	22.2	11.7 ±0.3	1.9
"	10	0.80 ±0.02	138.1 (556*)	64.9 ±3.0	2.1 (8.6*)
"	15	0.95 ±0.02	37.2	16.7 ±0.5	2.2
ITTC	10	0.70 ±0.02	140.8	73.7 ±3.0	1.9

seem to agree with each other except that the measured bubbles are slightly larger.

A few reasons may be pointed out for the difference between measurement and calculation. The first one is the nuclei distribution which was obtained by counting bubbles as shown in Fig. 3. If it occurs that the larger bubbles are more easily carried away from the wake region of the tungsten wire into the uniform flow, the actual distribution will be different from that given in Table 1, that is, there will be more large bubbles and the total number will be much smaller. The other reasons are: the existence of laminar separation bubble, the Haberman's empirical formula for Cd in which the unsteady bubble motion is not taken into account, and the rate of gas diffusion which is expected to be higher in the presence of slip.

On the other hand, one reason should be pointed out which increases the difference. It is the diffusion of oxygen and nitrogen into the bubble, which compensates the hydrogen diffusion into the water. Further progress will become possible only by the direct measurement of the nuclei distribution in the test section.

Sheet Cavitation

Test Bodies. Three axisymmetric test bodies, i.e., Hemispherical, ITTC, and Kokeshi bodies were used.[2] The pressure distributions calculated by the Hess and Smith method are shown in Fig. 9. Hemispherical body and ITTC body are the same as those used in the bubble cavitation experiment.

Kokeshi body was newly designed in the present investigation. Its profile is,

$$\left(\frac{x-15}{15}\right)^2 + \left(\frac{y}{15}\right)^{\frac{1}{0.1025}} = 1$$

$$(0 \leqq x \leqq 15 \text{ mm}) \qquad (3a)$$

$$y = 10 + 2.5(1 + \cos\{2\pi(x-15)/85\})$$

$$(15 \leqq x \leqq 100 \text{ mm}) \qquad (3b)$$

At $x = 15$ mm, both values of dy/dx and d^2y/dx^2 change continuously. This test body has a sharp negative pressure peak followed by a gradual pressure rise which continues much longer than the other two bodies. The calculated pressure distribution agrees well with the measured result by LDV (Laser Doppler Velocimeter).

Fully Wetted Flow Observation. The pressure distribution of ITTC body is shown in Fig. 10. It is clear that the wall effect is considerable. The actual profile of the test body was measured and its pressure distribution was calculated. It was somewhat different from that of the expected theoretical profile.

The velocity distribution on the body surface was also measured by LDV and the pressure distribution was estimated

---

[2] "Kokeshi" is a traditional Japanese doll made of wood and its shape looks like the present third test body.
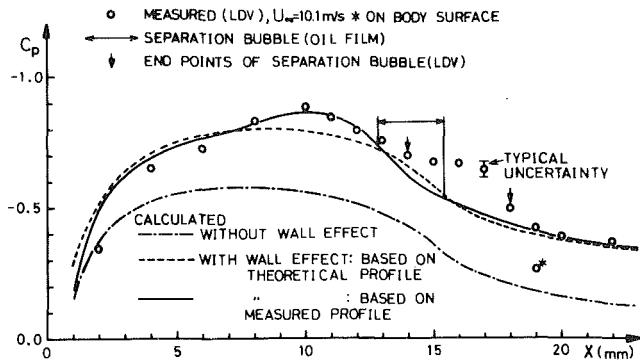
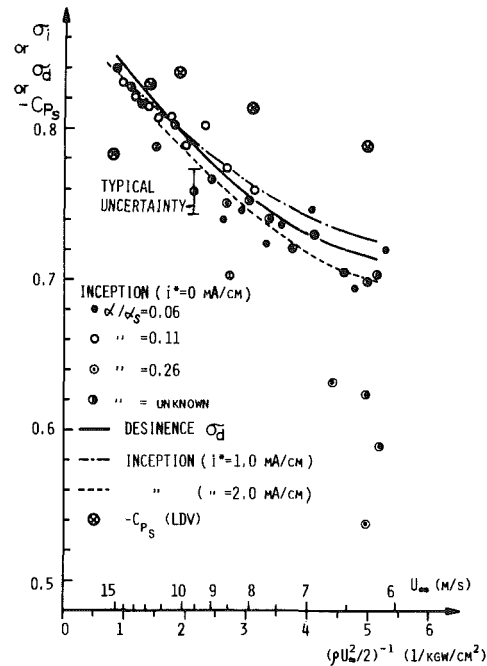**Fig. 10 Pressure distribution and location of separation bubble on ITTC body**

Fig. 11(a) Inception and desinence of sheet cavity on hemispherical body
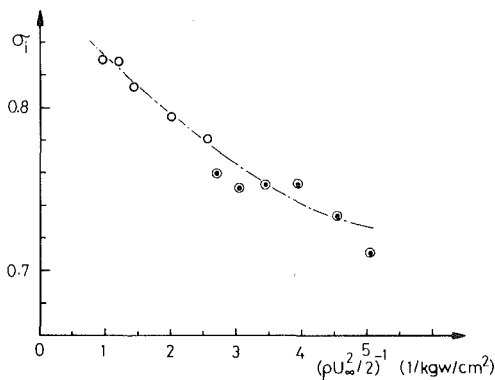

Fig. 11(b) Inception of sheet cavity on Hemispherical body ($i^* = 1.0$ mA/cm)

using the Bernoulli's equation. The measured result agrees well with the calculated result which is based on the measured profile. It is seen that a separation bubble exists at $x = 14 \sim 18$ mm. Its location was determined from the change of the slope of the measured C_p values.

In LDV measurement, as the measuring point was gradually made closer to the body surface, the flow velocity gradually increased, and in the unseparated region the
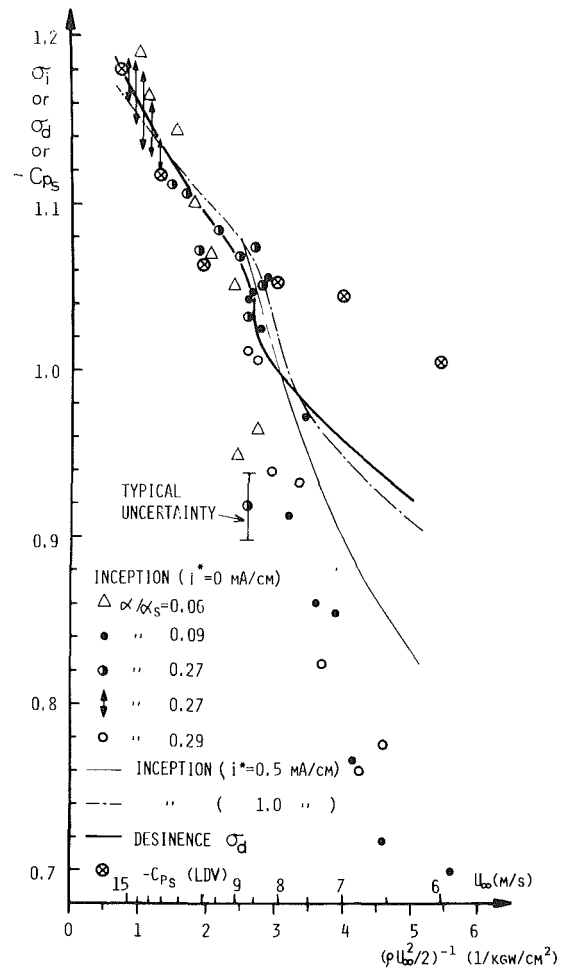
Fig. 12 Inception and desinence of sheet cavity on Kokeshi body

maximum velocity was obtained at a point very close to the body surface, not more than 0.2 mm apart. After that the velocity decreased by a few percent probably because the measuring point went inside the boundary layer, and suddendly the measurement failed as the Laser beams intersected the body surface. The maximum velocity thus obtained was used to estimate the pressure coefficient.

Inception of Sheet Cavity. The experiment of sheet cavity inception was made through naked-eye observation under the stroboscopic light. The definition of sheet cavity inception is as follows: a band-type cavity appears covering more than $1/3 \sim 1/2$ of the circumference of a test body and it lasts for more than a certain period of time (say, 0.5 s) and it repeats more than once every $5 \sim 10$ s or lasts without vanishing.

In order to decrease the nuclei naturally contained in water, the water was fully deaerated to the air content ratio of less than 30 percent to the saturated value at 1 atm (i.e., $\alpha/\alpha_s < 0.3$). Using the nuclei generator, inception tests were made with or without added nuclei. The electric current i^* for electrolysis was $0.5 \sim 2.0$ mA/cm, which was fairly low compared with the value of 9 mA/cm in the bubble cavity experiment.

The results are shown in Figs. 11 and 12. The abscissa is reciprocal of the dynamic pressure of uniform flow $(\rho U_\infty^2/2)^{-1}$.

In the case of Hemispherical body (Fig. 11), the incipient cavitation number σ_i with no added nuclei is scattered considerably and the scattering is wider at smaller U_∞. When the inception takes place at a very low cavitation number, a long cavity is suddenly formed. On the contrary, scattering of σ_i
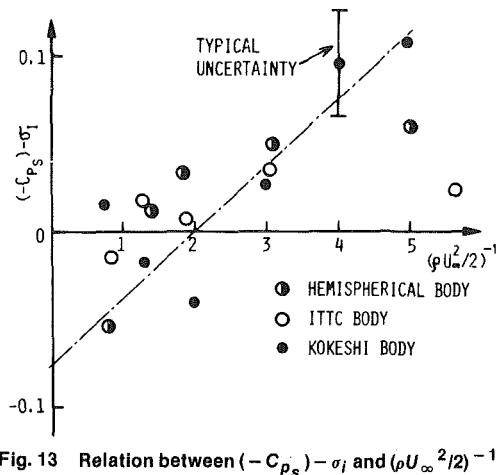
Fig. 13 Relation between $(-C_{p_s}) - \sigma_i$ and $(\rho U_\infty^2/2)^{-1}$

Fig. 14 Comparison of added nuclei distribution with measured nuclei distribution in other facilities (from reference [10])

becomes very small when nuclei are added artificially by electrolysis, and σ_i converges to the upper limit of that with no added nuclei. It also coincides with the desinent cavitation number σ_d. From these experiments it is clear that the cavitation hysteresis does not exist when abundant nuclei are in the water. The scattering of σ_d was as small as that of σ_i with added nuclei, and σ_d did not change by adding nuclei.

In Fig. 11(a), σ_i at $i^* = 2.0$ mA/cm is smaller than σ_i at $i^* = 1.0$ mA/cm. It is the reverse of the expected tendency that the more nuclei promote cavitation inception. It is because the formation of sheet cavity is affected by the presence of bubble cavities, which disturb the flow. This trend was more pronounced at smaller U_∞.

Similar results were obtained with ITTC and Kokeshi bodies. In Fig. 12, σ_i at $i^* = 0.5$ mA/cm deviates considerably from σ_i at $i^* = 1.0$ mA/cm in the range $U_\infty = 6 \sim 7$ m/s. To investigate the reason for this difference, the nuclei distribution at the test section under these conditions was estimated, following the same procedure as stated before. And it was found that the number of nuclei with radius $R_n \doteqdot 20$ μm differed most greatly (about 10 times) between the cases $i^* = 0.5$ and 1.0 mA/cm. It suggests that the nuclei of that size may be responsible for the sheet cavity inception on Kokeshi body under that condition.

It may be argued that larger nuclei are more likely to contribute to the sheet cavity inception. But it must be remembered that at upstream of a separation bubble, there always exists the minimum pressure point, where large nuclei will cavitate and become traveling-type cavities. If it is assumed that those traveling cavities do not contribute to the sheet cavity inception, which is likely because the macroscopic cavities may be too large to go inside the very thin separation bubble, then the smaller nuclei will result to contribute to the inception of sheet cavity.

Pressure coefficient at separation point C_{p_s} may be obtained from LDV measurement. When it is compared with σ_i, the relation $(-C_{p_s}) \geqq \sigma_i$ is roughly satisfied, which indicates that the sheet cavity inception occurs when the pressure inside the separation bubble is lower than the vapor pressure P_v.

Mechanism of Sheet Cavitation Inception. Arakeri [8] has pointed out that sheet cavitation inception occurs in the separated flow of a laminar boundary layer. Based on this, a hypothesis for the mechanism of sheet cavitation inception is introduced as follows. "A sheet cavity is generated when the highly turbulent fluctuation in the reattachment zone of a separated flow gives a nucleus a chance to expand in the separation region."
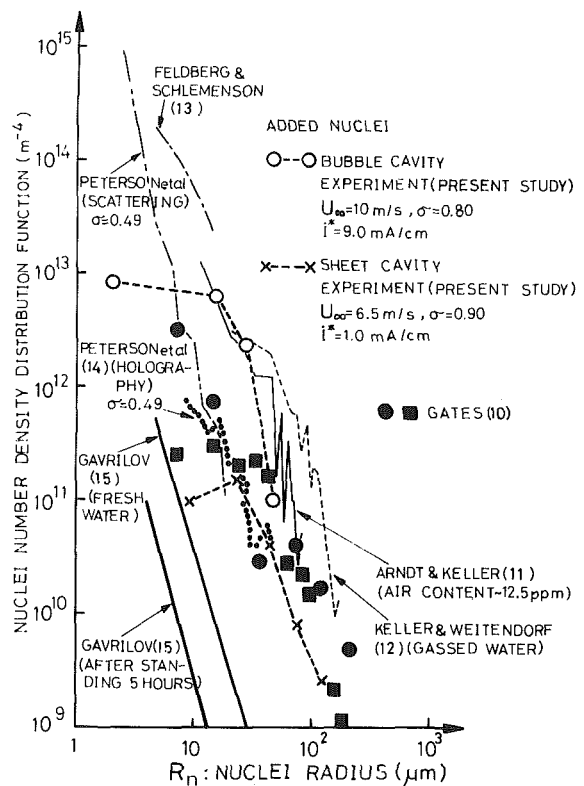
Let $\bar{P}_i$ be the time-averaged local pressure at inception, and by considering the pressure fluctuation ΔP_t due to turbulence and the contribution ΔP_r due to the surface tension,

$$\bar{P}_i - \Delta P_t = P_v - \Delta P_r \qquad (4)$$

where,

$$\Delta P_r = \frac{4S}{3R^*}$$

Let C_{pi} be the pressure coefficient at the point of inception. Then it is set to be equal to C_{p_s} which is the pressure coefficient at separation point. From equation (4),

$$\sigma_i = \frac{\bar{P}_i - P_v}{\rho U_\infty^2/2} - C_{pi} = \frac{\Delta P_t - \Delta P_r}{\rho U_\infty^2/2} - C_{p_s} \qquad (5)$$

Assuming ΔP_t is proportional to the dynamic pressure $\rho U_\infty^2/2$, and by using equation (5),

$$\Delta P_t \equiv k \times \rho U_\infty^2/2 \qquad (6)$$

$$(-C_{p_s}) - \sigma_i = \Delta P_r \times \frac{1}{\rho U_\infty^2/2} - k \qquad (7)$$

Consequently, if the size of the nuclei which contribute to the inception is independent of U_∞, equation (7) will be expressed as a straight line having a positive gradient when plotted as Fig. 13.

In the same figure, the measured results with added nuclei are also plotted. They seem to support the aforementioned hypothesis. The straight line in Fig. 13 is drawn for Kokeshi body. From this line, the radius of the nuclei which contribute to the inception may be estimated to be $R_0 = 10$ μm, which is in the same order of magnitude with the value of $R_0 = 20$ μm estimated previously from the added nuclei distribution data. The value k is also estimated to be about 0.08, which is in the same order with the value of 0.15 measured by Huang, et al. [9] with an axisymmetric body named "Forebody S."

According to equation (7), the scattering of σ_i may be explained to be due to the scattering of ΔP_r, that is, the nuclei size R^*. And if the range of the scattering of R^* is independent of U_∞, σ_i will be scattered more widely at smaller U_∞, which is in agreement with the experiment.

Finally, the distribution of the added nuclei is compared with the measured values in other facilities (Fig. 14). The added nuclei distribution for the bubble cavity experiment ($i^* = 9$ mA/cm) is approximately at the upper limit of other data. That for the sheet cavity experiment ($i^* = 1$ mA/cm) coincides with the data given by Peterson [14] and Gates [10]. Judging from the present experiments, the stability of the cavitation inception phenomena will become poor if the nuclei distribution line falls on the left side of the line $i^* = 1$ mA/cm.

Conclusions

1 The number and size of the bubble cavities formed on the axisymmetric test body were calculated using the equations of bubble growth and trajectory. The experiment for the bubble cavity was made. The calculated and measured size distributions of bubble cavities seemed to agree with each other. The measured total number was about one-half of the calculation.

2 The inception test of the sheet cavity was made using three axisymmetric bodies, Hemispherical, ITTC, and Kokeshi bodies. The scattering of σ_i became fairly small when nuclei were added. In that case, σ_i nearly coincided with σ_d, and σ_d was not affected by adding nuclei.

3 A hypothesis for the mechanism of sheet cavity inception was made, taking into account the surface tension of nuclei and the pressure fluctuation at the reattachment zone of a separated flow. It explained, at least qualitatively, the dependence of σ_i on U_∞ and the relation between σ_i and ($-C_{p_s}$).

Acknowledgment

References

1 Keller, A. P., "Investigations Concerning Scale Effects of the Inception of Cavitation," Conference on Cavitation, Edinburgh, 1974, pp. 109–117.

2 Albrecht, K., and Bjorheden, O., "Cavitation Testing of Propellers in a Free Surface Tunnel Utilizing Micro Air Bubble Control," ASME JOURNAL OF FLUIDS ENGINEERING, Vol. 97, Dec. 1975, pp. 523–532.

3 Noordzij, L., "Some Experiments on Cavitation Inception with Propellers in the NSMB Depressurized Towing Tank," International Shipbuilding Progress, Vol. 23, 1976, pp. 1–7.

4 Kuiper, G., "Scale Effects on Propeller Cavitation Inception," Twelfth Symposium on Naval Hydrodynamics, Washington, D. C., 1978, pp. 400–429.

5 Epstein, P. S., and Plesset, M. S., "On the Stability of Gas Bubbles in Liquid-Gas Solutions," Journal of Chemical Physics, Vol. 18, 1950, pp. 1505–1509.

6 Johnson, V. E., Jr., and Hsieh, T., "The Influence of Trajectories of Gas Nuclei on Cavitation Inception," Sixth Symposium on Naval Hydrodynamics, Washington, D. C., 1966, pp. 163–182.

7 Kline, J., and McClintock, F. A., "Describing Uncertainties in Single-Sample Experiments," Mechanical Engineering, Jan. 1953, pp. 3–8.

8 Arakeri, V. H., and Acosta, A. J., "Viscous Effects in the Inception of Cavitation on Axisymmetric Bodies," ASME JOURNAL OF FLUIDS ENGINEERING, Vol. 95, Dec. 1973, pp. 519–527.

9 Huang, T. T., et al., "Pressure Fluctuations in the Regions of Flow Transition," AD–A022935, Dec. 1975, David W. Taylor Naval Ship Research and Development Center, Bethesda, Md.

10 Gates, E. M., "The Influence of Freestream Turbulence, Freestream Nuclei Population and a Drag-Reducing Polymer on Cavitation Inception on Two Axisymmetric Bodies," Ph.D. thesis, 1977, California Institute of Technology.

11 Arndt, R. E. A., and Keller, A. P., "Free Gas Content Effects on Cavitation Inception and Noise in a Free Shear Flow," Proceedings of IAHR – Symposium, Grenoble, France, 1976, pp. 3–16.

12 Keller, A. P., and Weitendorf, E. A., "Influence of Undissolved Air Content on Cavitation Phenomena at the Propeller Blades and on Induced Hull Pressure Amplitudes," Proceedings of IAHR – Symposium, Grenoble, France, 1976, pp. 65–76.

13 Feldberg, L. A., and Shlemenson, K. T., "The Holographic Study of Cavitation Nuclei," Discussions to Proceedings IUTAM Symposium on Non-Steady Flow of Water at High Speeds, Leningrad, USSR (English version; Moscow, 1973), pp. 106–111.

14 Peterson, F. B., Daniel, F., Keller, A., and Lecoffre, Y., "Determination of Bubble and Particulate Spectra and Number Density in a Water Tunnel with Three Optical Techniques," 14th ITTC, 1975, pp. 27–52.

15 Gavrilov, L. R., "Free Gas Content of a Liquid and Acoustical Techniques for Its Measurement," Soviet Physics – Acoustics, Vol. 15, No. 3, 1970, pp. 285–295.

C. Samuel Martin
Professor,
School of Civil Engineering,
Georgia Institute of Technology,
Atlanta, Ga.

H. Medlarz
Graduate Research Assistant,
Institute for Hydromechanics,
University of Karlsruhe,
Karlsruhe, West Germany

D. C. Wiggert
Associate Professor,
Department of Civil Engineering,
Michigan State University,
East Lansing, Mich.

C. Brennen
Associate Professor,
Department of Mechanical Engineering,
California Institute of Technology,
Pasadena, Calif.

Cavitation Inception in Spool Valves

Cavitation has been investigated in directional control valves in order to identify damage mechanisms characteristic of components of aircraft hydraulic systems. Tests have been conducted in a representative metal spool valve and in a model three times larger. Data taken under noncavitating conditions with both valves showed that the position of the high-velocity annular jet shifts orientation, depending upon valve opening and Reynolds number. By means of high-frequency response pressure transducers strategically placed in the valve chamber cavitation could be sensed by the correlation of noise with a cavitation index. The onset of cavitation can be detected by comparing energy spectra for a fixed valve opening and a constant discharge. Another sensitive indicator of cavitation inception is the ratio of cavitating to noncavitating spectral densities. The incipient cavitation number as defined in this investigation is correlated with the Reynolds number for both valves.

Introduction

Cavitation is not nearly as well documented in oil hydraulic systems as it is in such water hydraulic systems as pumps, propellers, hydraulic turbines, and hydrofoils. In aircraft hydraulic systems, cavitation most frequently occurs in system valves, pumps, and actuators. Large differences in pressure is a frequent cause of small-scale cavitation in chambers of four-way spool valves, while high frequency motion of a valve-controlled actuator can lead to large-scale cavitation in the cylinder. Another source of cavitation in aircraft hydraulic systems is the improper filling of the pistons on an axial-piston pump. Either during transient loading or under steady-state operation, cavitation can occur in the return chamber of directional control valves because of the large pressure drop across the orifice. It is of interest to know the potential cavitation damage, as well as any effect of cavitation on system performance under both steady and unsteady flow conditions. Criteria should be established for the onset of cavitation, and damage mechanisms need be identified once cavitation is extensive.

The amount of literature on cavitation in oil hydraulic components is rather sparse. The major publications in the English language are referred to in the book by McCloy and Martin [1]. There is also important literature in German, principally from the fluid power group at the Technical University of Aachen. Cavitation was investigated to a limited extent by MacLellan, et al. [2], in their laboratory study in an enlarged two-dimensional model of a piston type control

valve. Later, but more complete, work on cavitation in spool valves was reported by McCloy and Beck [3], who established criteria for cavitation inception in two valves, both two dimensional, one with water and the other with oil as the test liquid. Backé and Benning [4], Backé and Riedel [5], and Riedel [6] all report on cavitation in short orifices using hydraulic oil. Recent work by Kleinbreuer [7, 8] has enhanced the understanding of the effect of dissolved gas, viscosity, and jet proximity on erosion of various metals by high velocity discharge of hydraulic oil from an orifice. Eich [9, 10] applied the diagnostic tool of noise detection in his investigation of cavitation in oil hydraulic components. The effect of gas content and orifice length on desinent and incipient cavitation is reported by Lichtarowicz and Pearce [11]. Flow pattern changes under both noncavitating and cavitating flow conditions were documented by McCloy and Beck [12]. A review of the literature on cavitation in oil hydraulic systems is reported by Wiggert, et al. [13].

An experimental investigation was undertaken to study cavitation damage mechanisms in aircraft hydraulic systems. The purpose of the investigation was to identify mechanisms which lead to damage. A test facility was designed which allowed for the measurement of hydraulic parameters under both noncavitating and cavitating conditions. Diagnostic techniques were developed to detect the onset and the extent of cavitation. Cavitation inception, its definition, and the formulation of criteria are the subject of this paper.

Test Facility

Cavitation has been investigated in directional control valves in order to identify damage mechanisms characteristic of components of aircraft hydraulic systems. Tests have been
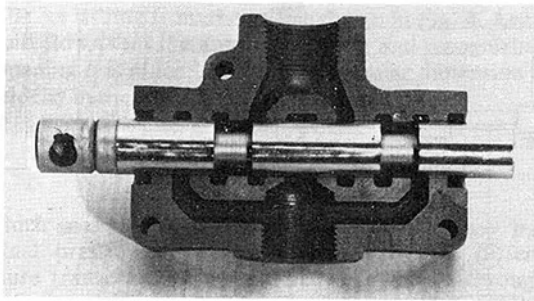
Fig. 1 Cutaway and spool of prototype valve

Fig. 2 Longitudinal section of model valve

conducted in both a metal prototype valve and a plexiglass model three times its size. A common test facility was designed that allowed for control of flow, upstream pressure, downstream pressure, dissolved gas content, and spool position. In order to facilitate the continuous positioning of the spool, as well as the mounting of instrumentation on the spool itself, a simple industrial four-way lever-operated spool valve was chosen as the prototype. A cutaway of this valve, which has a spool diameter of 19.05 mm (0.75 in.), is shown in Fig. 1. In order to maximize the pressure differential across the valve, only one-half of the valve was used, resulting in effect a two-way valve.

The model valve was made of plexiglass with a spool diameter of 57.2 mm (2.25 in.). The size of the valve chamber, lands, and ports of the model valve were scaled up from the metal prototype valve. Figure 2 is a longitudinal view of the body of the model valve. The opening of the annular space could be controlled by the mechanism attached to the end of the spool. A similar mechanism was installed on the end of the prototype valve. The supply and return ports in the vicinity of the model spool were made to scale with the prototype valve.

The common hydraulic test loop consisted of an axial piston pump with a pressure regulator, a high pressure supply line, a flow meter, a bypass system, the particular test valve and its instrumentation, downstream valves for back pressure control, and a low pressure return line to the pump. A high pressure filter with an absolute rating of $3\mu m$ was in continuous use for control of contaminants. An auxiliary system consisting of a vacuum tank, tubing and valves, and a rubber bag storage reservoir was used to degas the oil. Oil was pumped from the closed bag through a nozzle on top of the vacuum tank and allowed to flow down the sides of the tank as a film. The total air content was monitored by use of an Aerometer, a commercial device similar to a Van Slyke ap-
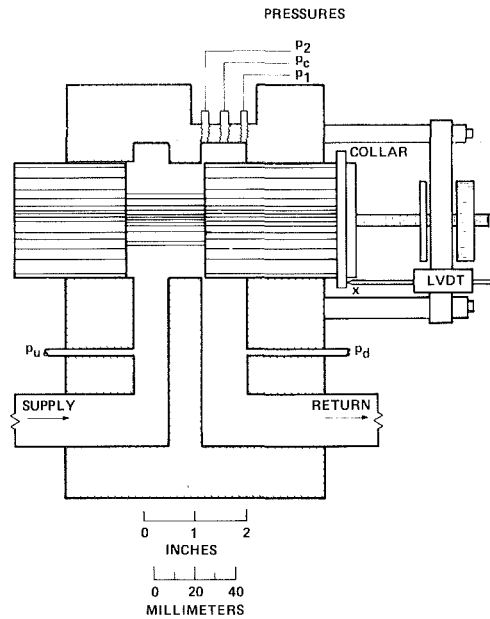
paratus, which uses a filming technique to remove the gas. At room temperature and atmospheric pressure, the dissolved gas content of the oil employed in this investigation varied between 9.5 and 10 percent by volume. The minimum value achieved after several hours of degassing was 4 percent.

For the entire investigation, a petroleum-based hydraulic oil (MIL-H-5606C) was employed as the test liquid. A brief listing of some of the pertinent characteristics of this particular oil are:

Temperature (°C)	Specific gravity	Viscosity (cS)	Vapor pressure (mm Hg abs)
20	0.872	29.5	11.6
40	0.857	16.8	25.0
60	0.843	10.4	53.0

Instrumentation and Data Acquisition

For the steady-flow results reported here, mean flow rates and pressures were measured to characterize the test conditions, while dynamic pressures and acceleration were monitored to assess the onset and extent of cavitation.

———— Nomenclature ————

A = area of annular orifice
A_c = area of vena contracta
a = acoustic velocity
B_1, B_2, B_3 = coefficients
C_c = coefficient of contraction
C_d = coefficient of discharge
c = radial distance between spool and wall
D = spool diameter
d = radial distance between spool neck and valve body
e = radial eccentricity between spool and valve body
f = frequency
K = coefficient
l = axial distance along jet
p = pressure
p' = fluctuating pressure
p_1 = pressure at transducer P_1
p_2 = pressure at transducer P_2

p_c = mean pressure in chamber
p_L = load (upstream) pressure
p_R = return (downstream) pressure
p_v = vapor pressure
$R = Q/\pi D\nu$ = Reynolds number
t = time
u_0' = fluctuating velocity on jet centerline
V_c = velocity in vena contracta
V_j = jet velocity
V_0 = approach velocity
x = axial position of valve spool
$\ddot{x}$ = acceleration of spool
Δf = width of frequency channel
$\Delta p = p_L - p_R$ = pressure differential across valve
μ = dynamic viscosity of liquid
ν = kinematic viscosity of liquid
ρ = mass density of liquid
$\sigma = p_c - p_v/\Delta p$ = cavitation index

Mean Quantities. For both test valves, a drag-type flow meter was used to measure the flow rate. This device consists of a circular target mounted on the end of a strain-gage instrumented cantilever beam. A resistance detector was used to monitor the oil temperature immediately upstream of the test valve in question. An accurate determination of the position of the specific valve was essential because of the relative small openings in practice. For each valve, a linear variable displacement transducer (LVDT) was used to measure the relative position x of the spool.

Pressure transducers were used to measure mean upstream (load $-p_L$), differential (Δp), chamber (p_c), and downstream (return $-p_R$) pressures. Figure 2 shows the location of the pressure taps for the model valve. In this case, the differential pressure is defined by $p_L - p_R$. For the model, the load pressure p_L was not measured directly. The load, return, and differential pressure were measured by either strain-gage or variable reluctance diaphragm pressure transducers. The mean chamber pressure p_c for each valve was sensed by semiconductor pressure transducers. As shown in Fig. 2, transducer P_c is located exactly in the middle of the model chamber. For the prototype valve, the chamber transducer is located somewhat downstream of the center of the port.

Dynamic Quantities. Fluctuating pressures in the chamber of each valve were measured for the detection of cavitation by high-frequency response piezoelectric pressure transducers. These transducers were flush mounted in the chamber of each valve, as shown in Fig. 2 for the model valve. The diameter of the sensing surface is 2.51 mm (0.099 in.). The transducers had a resonant frequency in air of 250 kHz. The larger size model allowed for the installation of two piezoelectric transducers, referred to as P_1 and P_2 on Fig. 2. The single piezoelectric transducer in the prototype valve chamber is called P_1. This transducer is located somewhat downstream of the middle of the chamber.

For the expected detection of mechanical effects in the spool related to cavitation, a high-frequency response quartz accelerometer was mounted on the end of the spool of the prototype valve. The miniature accelerometer had an undamped natural frequency in air of 120 kHz.

Data Acquisition System. The data acquisition system used to sample the mean and dynamic signals will be described with reference to Fig. 3. The test valve shown in the illustration could either be the model or the prototype valve. For the model valve, there was no measurement of load pressure p_L, nor any accelerometer signal $\ddot{x}$. On the other hand, for the prototype valve, usually only one piezoelectric pressure transducer (P_1) was used.

The central device regarding the collection of mean quantities to characterize the flow conditions is a desktop computer. This computer controlled a multiplexer and a 6½-digit voltmeter. The analog signal from any of the six input channels shown in Fig. 3 could be transferred through the multiplexer by the controller to the voltmeter, which digitized the signal and transferred the data to the computer. For a given channel, 20 samples were averaged to obtain a mean value. At the completion of the entire test series, the data were then stored on a cassette tape of the desktop computer for future retrieval and analysis.

As illustrated on Fig. 3, the dynamic quantities monitored in this investigation are the fluctuating pressures p_1 and p_2 and the fluctuating spool acceleration $\ddot{x}$. Any two of these signals could be simultaneously input into the signal analyzer, which is an all-digital instrument capable of providing both time and frequency domain analysis of complex analog signals in the range of d-c to 25.6 kHz. Although it is recognized that cavitation noise usually exists at frequencies greater than 25.6 kHz, no data were collected beyond this limit because of equipment limitations.
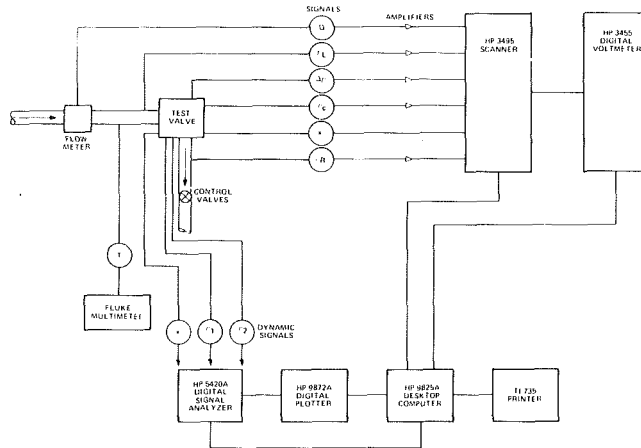

Fig. 3 Data acquisition system

Table 1 Estimates of experimental uncertainty

Quantity and units	Mean value	Fluctuating value
Flow rate (m^3/s)	$\pm\ 1 \times 10^{-5}$	--
Valve position (m)	$\pm\ 5 \times 10^{-6}$	--
Temperature (°C)	$\pm\ 0.5$	--
Pressure (Pa)	$\pm\ 2 \times 10^4$	± 2
Acceleration (g)	--	$\pm 5 \times 10^{-5}$

Test Procedure. Although occasionally the cross spectrum and coherence between P_1 and P_2 for the model or P_1 and $\ddot{x}$ for the prototype valve were measured, the most frequent and useful measurements were the auto power spectra for the two channels. The frequency resolution or Δf for the analysis was 1/256 of the bandwidth, or 100 Hz. The signals were analyzed using a modified Hanning-type window. The power spectral density function for the auto spectra will be in units of $\sqrt{\overline{p'^2}}/\Delta f$ for the pressure transducers and $[\overline{(d^2x'/dt^2)^2}]^{1/2}/\Delta f$ for the accelerometer. The total energy over any frequency range could be quickly extracted from the analyzer, facilitating the real-time analysis and the establishment of criteria for cavitation inception.

Experimental Uncertainty. The flow meter, LVDT, and the seven pressure transducers used to measure mean pressures in the two valves were all calibrated *in situ* using the same signal conditioning and data acquisition system as employed in the dynamic studies. For each of these instruments, from 8-20 calibration points were analyzed using a least-square regression technique. The manufacturer's calibration constants were used for the temperature detector, the accelerometer, and the three piezoelectric pressure transducers. For all instruments, the least-square analyses yielded a value of the coefficient of determination $r^2 \geq 0.99$.

Considering all factors, the experimental uncertainties are as listed in Table 1.

Valve Characteristics

The mean-flow characteristics of each valve were determined by direct measurement before embarking upon the main cavitation study. It was essential to know accurately the value of the discharge coefficient of the valve in question because of the difficulty in measuring the valve opening with the desired precision. Once the value of the discharge coefficient was known for the particular test conditions, the valve opening could then be calculated from the known flow rate and pressure difference across the valve, both of which could be measured quite accurately.

As demonstrated by McCloy and Beck [3], for certain Reynolds numbers free streamline theory can be applied to the

annular jet issuing from the orifice shown in Fig. 4. Assuming inviscid flow from the approach region and recognizing that the opening b is much less than the annular dimension d, the jet velocity in the vena contracta is defined by

$$V_c = \sqrt{\frac{2\Delta p}{\rho}} \qquad (1)$$

in which ρ is the fluid density, and $\Delta p = p_L - p_R$, the nominal pressure difference measured by the differential pressure transducer. The volumetric flow rate through the valve is given by

$$Q = A_c V_c = C_c \pi D b V_c \qquad (2)$$

in which A_c is the area of the contracted jet, which is usually defined in terms of the area of the annular orifice, C_c is the contraction coefficient, and D is the diameter of the spool. The resulting relationship for the flow rate is

$$Q = C_d \pi D b \sqrt{\frac{2\Delta p}{\rho}} \qquad (3)$$

in which C_d is the discharge coefficient and, in the case for which $b < < d$, is equal to C_c. The preceding equation suggests a linear relationship between Q and b.

Because of the relatively small values of b employed in this study, tests were instead conducted by varying b while holding Δp constant. In this instance, a slightly modified coefficient of discharge could be computed from

$$C_d = \frac{dQ/dx}{\pi D \sqrt{\frac{2\Delta p}{\rho}}} \qquad (4)$$

in which x is the axial position of the spool as measured by the LVDT. Tests conducted at a constant Δp and varying x yielded a linear relationship between Q and x, allowing for the determination of C_d from the slope of the curve.

In general, it would be expected that C_d would be a function of the Reynolds number and a cavitation index. For simplicity, the Reynolds number is defined on the basis of the average velocity at the annular opening instead of in terms of V_c at the vena contracta. The length dimension chosen in the definition is b, yielding

$$R = \frac{\rho(Q/A)b}{\mu} = \frac{Q}{\pi D \nu} \qquad (5)$$

in which μ and ν are the dynamic and kinematic viscosities of the liquid, respectively. For a given temperature, equation (5) suggests that the Reynolds number is independent of the valve opening b at a constant discharge.

The cavitation index is normally defined as the ratio of a reference pressure minus the vapor pressure of the liquid to a dynamic pressure, the latter of which is referenced to the approach velocity V_0. A more appropriate dynamic pressure for the spool valve would be that based on the jet velocity V_j which is not measured directly, but instead directly related to Δp. The cavitation number is defined as

$$\sigma = \frac{p_c - p_v}{\Delta p} \qquad (6)$$

In general, it would be expected that the discharge coefficient would depend upon both R and σ, or

$$C_d = C_d(R, \sigma) \qquad (7)$$

Extensive testing over a range of R from 150 to 1500 under noncavitating conditions showed that C_d was virtually independent of viscous effects, yielding an average value of C_d equal to 0.68 for the prototype valve and 0.66 for the model
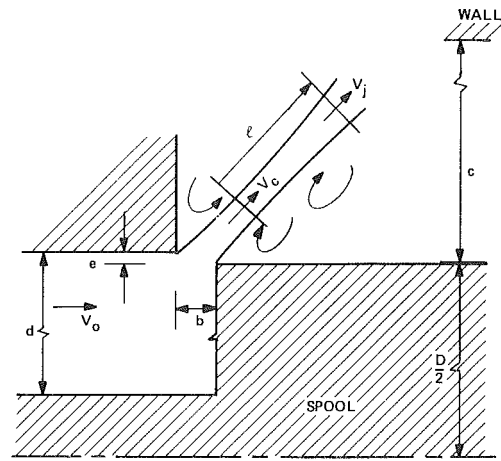

Fig. 4 Definition of valve and jet characteristics

valve. These values, which are reported in Martin, et al. [14], correspond closely to the theoretical value of 0.677 calculated by von Mises using two-dimensional inviscid theory. A summary of the theory is reported by Robertson [15]. Experimental results published by McCloy and Beck [3] show a similar trend. Apparently the Reynolds number defined by equation (5) must be less than approximately 100 before viscous effects commence to influence the mean flow characteristics of the valve.

As shown by a number of researchers in the study of cavitation in pipe orifices, cavitation has to become quite extensive before there is any effect on C_d. For the non-cavitating and moderate cavitation reported in this paper, it will suffice to use the constant values of 0.68 (prototype valve) and 0.66 (model valve) in any calculations of b from equation (3). Further details on the effect of R and σ on C_d may be found in the report by Martin, et al. [14].

Noncavitating Spectra

Prior to the establishment of criteria for the inception of cavitation, the level of fluctuations of pressure and acceleration had to be understood for noncavitating flow in each valve. Extensive testing was conducted to correlate energy levels of pressure fluctuations with flow rate and valve opening. Care was taken to insure that the chamber pressure p_c was large enough to inhibit any cavitation. This was accomplished by monitoring the total mean-square energy over the entire spectra for various values of σ. It was found that, for a constant discharge Q and valve opening b, the total energy did not vary if σ was above a certain threshold value, to be discussed later. The tests under noncavitating conditions were also of value in observing changes in the jet flow pattern for different conditions.

The pressure transducers P_1 and P_2 in the model and P_1 in the prototype chamber experience the acoustical noise from the confined jet issuing from the annular orifice. The fact that the discharge coefficient is constant over the range of Reynolds numbers tested would suggest a turbulent jet. As shown by McCloy and Beck [12] in their study of jet hysteresis, the jet can either reattach on the surface of the spool or on the wall of the port, or issue freely. A shifting jet pattern was clearly indicated in the model chamber by observing the energy levels on the two transducers, which were located at the extremities of the cavity.

The dynamics of an unconfined plane jet issuing from a nozzle are fairly well documented, albeit at higher Reynolds numbers than experienced with the two valves. As experimentally shown by Albertson, et al. [16], and later by Gutmark and Wygnanski [17], the mean centerline velocity of a plane jet decreases as the square root of the ratio of the

initial jet diameter to the axial distance. In terms of the definition sketch on Fig. 4

$$\frac{V_j}{V_c} = K\sqrt{\frac{b}{l}} \qquad (8)$$

in which K is a constant for plane jets at large Reynolds number and l is the axial distance from the nozzle, or from the vena contracta in the case of an orifice. For a plane turbulent jet, Gutmark and Wygnanski [17] found that the rms value of the fluctuating velocity u_0' on the centerline of the jet was a constant when normalized with V_j, or

$$\sqrt{\frac{\overline{u_0'^2}}{V_j}} = \text{constant} \qquad (9)$$

Reethof [18] states that a fluctuating mass flow rate with in-phase pressure fluctuations would correspond to a monopole source, for which the rms energy of fluctuating pressure in this case are assumed to be correlated by

$$\sqrt{\overline{p'^2}} = B_1 \rho V_j^2 \qquad (10)$$

in which B_1 is a dimensionless coefficient which would depend upon transducer location, Reynolds number, etc. If, instead the fluctuations emanate from dipole sources – which may be related directly to fluctuating pressures

$$\sqrt{\overline{p'^2}} = B_2 \rho V_j^2 \left(\frac{V_j}{a}\right) \qquad (11)$$

in which a is the acoustic velocity.

For a monopole source, equation (10) along with the jet relationships (2) and (8) yield the mean-square energy

$$\overline{p'^2} = B_1^2 \left[\frac{K}{\pi C_c}\right]^4 \frac{\rho^2}{D^4 b^2 l^2} Q^4 \qquad (12)$$

In the case of dipole sources

$$\overline{p'^2} = B_2^2 \left[\frac{K}{\pi C_c}\right]^1 \frac{\rho^2 Q^6}{D^6 b^3 l^3 a^2} \qquad (13)$$

In the following discussion of the slope of the energy spectra and the correlation of mean-square energy with the flow rate, a direct comparison of the results for the two valves is somewhat subjective because of the size of the pressure transducer relative to the respective valve chamber dimensions, which was three times greater in the prototype valve than in the model valve. For certain jet flow patterns there are, however, striking similarities between the noncavitating spectra for the two valves.

All noncavitating spectra measured by transducer P_1 in the chamber of the prototype valve indicate that the mean-square energy can be correlated in terms of a dipole, or fluctuating pressure, source. The mean-square energies measured with this transducer correlate well with Q^6, as shown by the two data sets in Fig. 5. The data shown in Fig. 5 were taken at virtually the same opening b, but quite different Reynolds numbers. If l is assumed to be fixed and to correspond to the distance from the orifice opening to transducer P_1, then equation (13) can be reduced to

$$\overline{p'^2} = B_3 \rho^2 Q^6 \qquad (14)$$

as a, D, and b are virtually constant. Although there is a Reynolds number variation for each data set, the coefficient B_3 appears to be a constant for each. Energy spectra for two of the data points plotted on Fig. 5 are presented in Fig. 6. The slope of each curve can be approximated by -1 for the
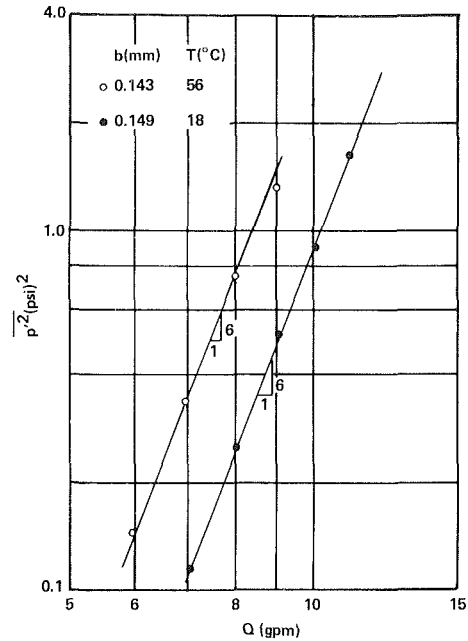

Fig. 5 Noncavitating mean-square energy versus discharge for prototype valve at a fixed opening (1 psi = 6895 Pa; 1 gpm = 6.31 × 10^{-5} m³/s)

a.) b = 0.143 mm and T = 56°C b.) b = 0.149 mm and T = 18°C
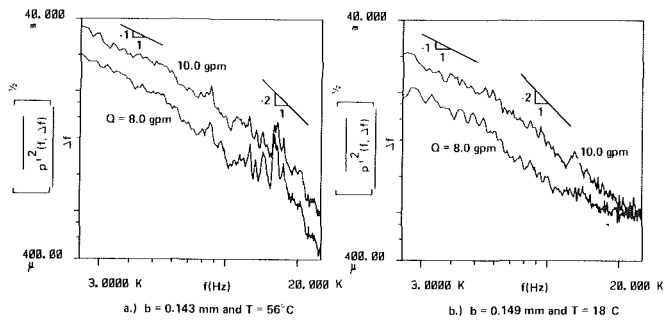
Fig. 6 Noncavitating energy spectra for prototype valve at a fixed opening (1 psi = 6895 Pa; 1 gpm = 6.31 × 10^{-5} m³/s)

lower frequency range and -2 for the higher frequencies. As demonstrated by Lush [19], a dipole source will produce energy spectra with a -1 slope. As most of the energy is in the first half of the frequency range shown in Fig. 6, the dipole source dominates, resulting in a relationship represented by equation (13). An examination of many noncavitating spectra shows that, as the flow rate and hence jet velocity V_j is increased for a fixed opening b, the extent of the spectrum corresponding to a -1 slope increases. Indeed, for high frequencies, the values of the noncavitating spectra approach the background noise level, which was 6.9 Pa (0.001 psi) for the pressure transducer in the prototype valve.

The two pressure transducers in the model were located such that any significant changes in the jet orientation could be noticed. The noncavitating results presented here suggest that the jet did flip back and forth, confirming the conclusions of McCloy and Beck [12] that the jet may reattach to either the spool surface or the port wall, or issue freely at an angle depending upon the opening b and any clearance between the spool and the land of the valve body.

The variation of mean-square energy with flow rate is shown in Fig. 7 for various openings of the model valve. The pressure difference Δp was maintained constant under noncavitating conditions. For a free jet for which Δp is a constant, the velocity at the vena contracta V_c as given by equation (1) should have been a constant for all of the data shown in Fig. 7. According to equation (8), the jet velocity at
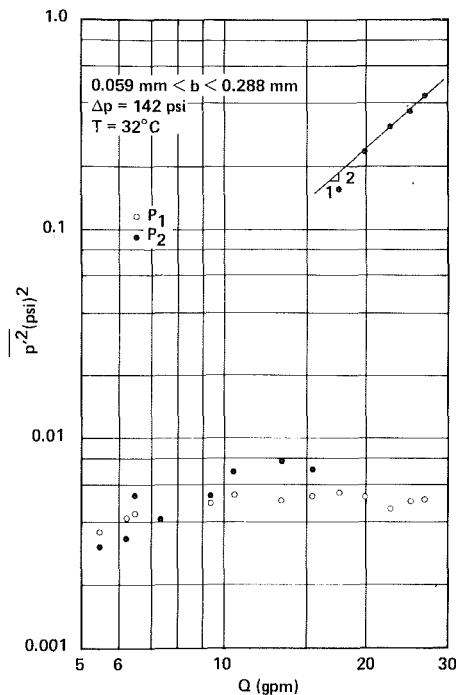
Fig. 7 Noncavitating mean-square energy versus discharge for model valve at a variable opening and constant pressure difference (1 psi = 6895 Pa; 1 gpm = 6.31 × 10^{-5} m^3/s)
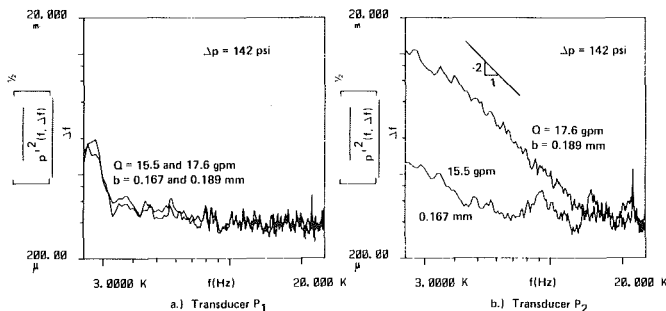

Fig. 8 Noncavitating energy spectra for model valve at two values of opening b and constant pressure difference (1 psi = 6895 Pa; 1 gpm = 6.31 × 10^{-5} m^3/s)

Fig. 9 Noncavitating mean-square energy versus discharge for model valve at a fixed opening (1 psi = 6895 Pa; 1 gpm = 6.31 × 10^{-5} m^3/s)

Fig. 10 Noncavitating energy spectra for model valve at a fixed opening (1 psi = 6895 Pa; 1 gpm = 6.31 × 10^{-5} m^3/s)

some position l from the vena contracta would increase directly with the square root of the opening b. The nearly constant output from transducer P_1 over the range of openings would indicate that the jet was not directed toward P_1. For flows less than $9.78 × 10^{-4}$ m^3/s (15.5 gpm), the jet is probably between P_1 and P_2 because of the relatively low energy levels, which are only slightly greater than the background noise level. As shown by Fig. 7 and the corresponding spectra in Fig. 8 for transducer P_2, there is an apparent shift in the flow pattern as the flow increased slightly from $9.78 × 10^{-4}$ to $11.2 × 10^{-4}$ m^3/s (15.5 to 17.6 gpm). As the valve was opened further, the energy level sensed by P_2 increased as the square of the flow, suggesting a monopole source in accordance with equations (3) and (12) for a variable opening b. It is suspected that the increase in energy is either due to direct impingement of a reattached jet or the nearly direct effect of a free jet. The slope of the energy spectra at location P_2 can be approximated by -2 over a range of frequencies.

Noncavitating data were collected with the model valve fixed at openings of $b = 0.108$ and 0.237 mm. For the smaller opening, the plot of mean-square energy versus flow rate shown in Fig. 9 and energy spectra for two of the higher flow rates plotted in Fig. 10 indicate that the jet may have been free, and furthermore directed toward transducer P_1. At the
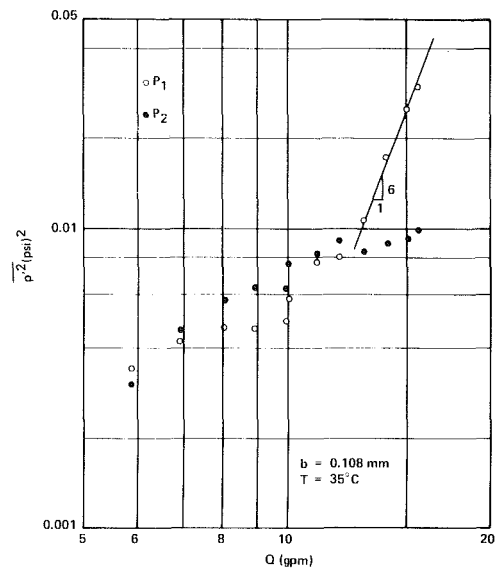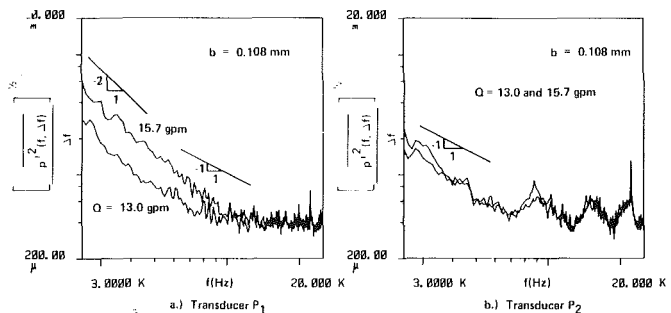
greater opening, however, the transducer P_1 hardly experienced any change in energy fluctuations as the flow increased, as shown in Figs. 11 and 12(a). There is some indication that the slope of the mean-square energy versus flow rate correlation changes from a dipole source (6 to 1) to a monopole source (4 to 1) at the higher flow rates. Portions of the jet-induced spectra plotted in Fig. 12(b) can be approximated by slopes of -1, and others by -2.

The direct effect of pressure fluctuations from a jet are clearly shown in Figs. 8(b), 10(a), and 12(b) for the model, in contrast to Figs. 8(a) and 12(a), for which there is little to no jet effect, but instead only background noise. As recently reviewed by Arndt [20], the effect of a turbulent shear flow on noncavitating pressure spectra has recently received attention by George [21], Fuchs and Michalke [22], and George and Beuther [23]. References on noise in an underwater environment are cited by Ross [24]. The effect of any shifting of the jet is more evident in the larger model than in the prototype valve because of the size of the piezoelectric transducers relative to the length of the valve chamber.

Cavitating Spectra

In order to define and determine the condition of cavitation inception, tests were conducted over a range of values of the cavitation number σ. Because of the sensitivity of pressure fluctuations to changes in jet velocity, care was taken to maintain the volumetric flow Q constant and to hold the respective spool at a fixed position. As shown by the noncavitating energy spectra, slight differences in valve opening b can lead to significant changes in energy levels if there is a
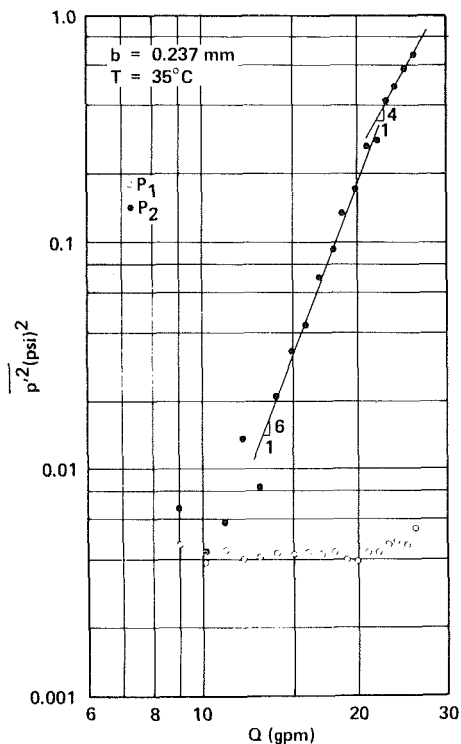
Fig. 11 Noncavitating mean-square energy versus discharge for model valve at a fixed opening (1 psi = 6895 Pa; 1 gpm = 6.31 × 10⁻⁵ m³/s)
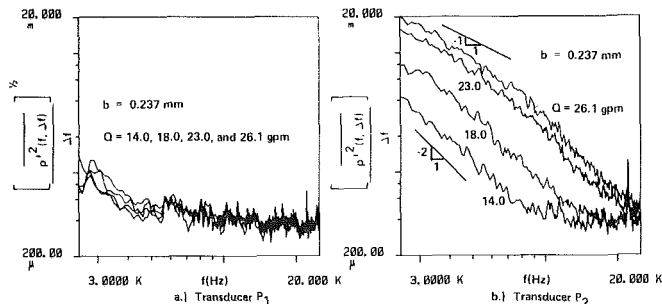

Fig. 12 Noncavitating energy spectra for model valve at a fixed opening (1 psi = 6895 Pa; 1 gpm = 6.31 × 10⁻⁵ m³/s)

direct effect of the jet. On the other hand, however, cavitation noise in the model valve can be several orders of magnitude greater than that due to a noncavitating jet.

Acoustical noise, pressure fluctuations, and accelerometer readings have been employed by numerous investigators over a span of years to detect cavitation inception and to correlate developed cavitation with the cavitation number. The effect of cavitation on the energy spectra measured by various instruments are reported by Jorgensen [25] for a cavitating submerged water jet, by Deeprose, et al. [26], for a cavitating pump, by Ōba and Ito [27] for a cavitating venturi, and by Blake, et al. [28], for cavitation on a hydrofoil. For cavitation in orifices and water valves,Tullis and Govindarajan [29], and Ball and Tullis [30] used the rms accelerometer output as a criterion of defining cavitation inception, choking, etc. Tullis [31] later relates acceleration spectra with cavitation. In this investigation, it is shown that the use of rms energies must be applied with care in the definition of cavitation inception. It will be demonstrated that a more foolproof technique will be the careful study of energy spectra under similar geometric and flow conditions.

Prototype Valve. The results of varying σ as b and Q are maintained nearly constant are presented in Fig. 13 for several
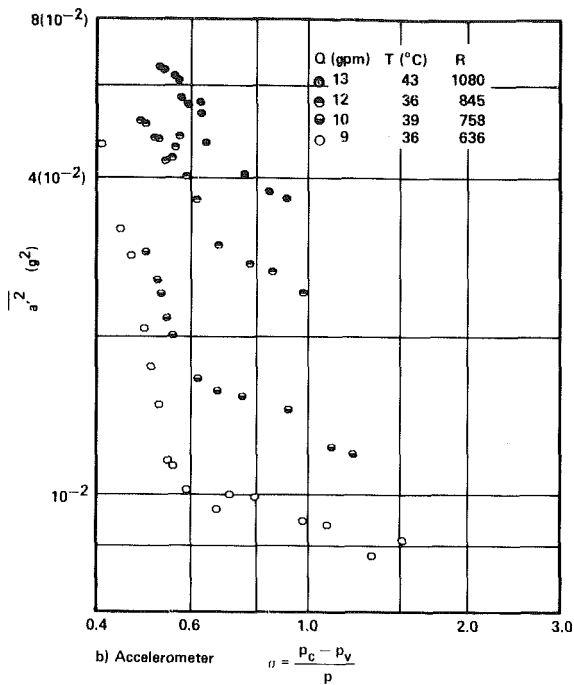
b) Accelerometer $\sigma = \dfrac{p_c - p_v}{p}$
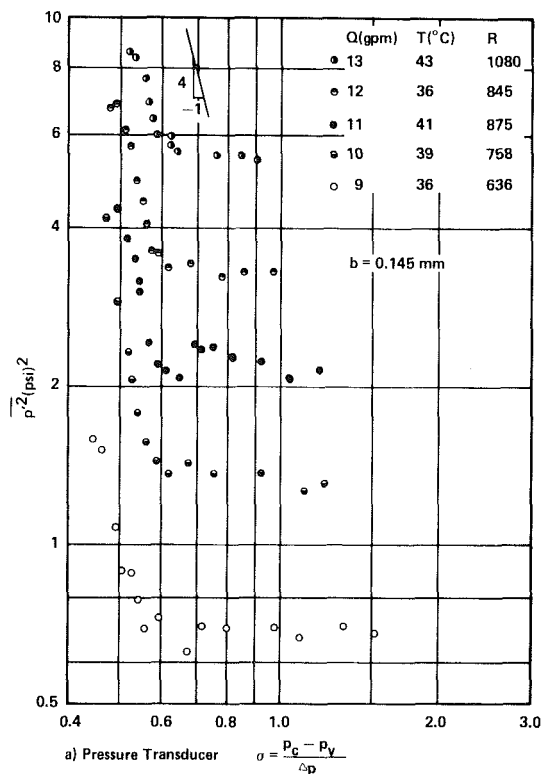
a) Pressure Transducer $\sigma = \dfrac{p_c - p_v}{\Delta p}$

Fig. 13 Mean-square energy versus cavitation index for prototype valve at a fixed opening and constant discharges (1 psi = 6895 Pa; 1 gpm = 6.31 × 10⁻⁵ m³/s)

flow rates. Although for each flow rate there is eventually a continual increase in the fluctuating energy measured by the pressure transducer P_1 and the accelerometer A_1 as the chamber pressure p_c is lowered, it is not clear where cavitation inception occurs. The definition of incipient cavitation is especially difficult with the prototype valve because of the relatively large jet energy under noncavitating conditions. In order to illustrate this difficulty, the data points for $Q = 6.94$ × 10⁻⁴ m³/s (11 gpm) are plotted on Figs. 14(a) and (b) at a
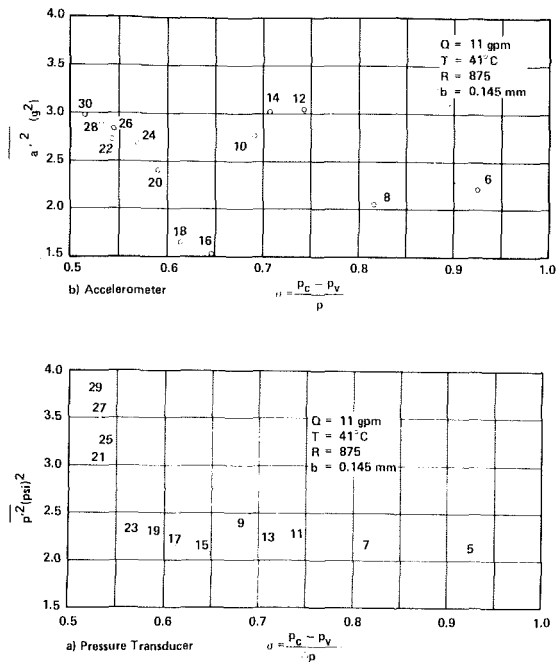
Fig. 14 Mean-square energy versus cavitation index for prototype valve at a fixed opening and $Q = 11$ gpm (1 psi = 6895 Pa; 1 gpm = 6.31×10^{-5} m^3/s)

Fig. 15 Noncavitating and cavitating energy spectra for prototype valve at a fixed opening and $Q = 11$ gpm (1 psi = 6895 Pa; 1 gpm = 6.31×10^{-5} m^3/s)

Fig. 16 Ratio of cavitating to noncavitating ($\sigma_0 = 0.647$) spectral density for prototype valve at a fixed opening (1 gpm = 6.31×10^{-5} m^3/s)

different scale. For reference, each data point is given a number which actually corresponds to a data file on a storage tape. The definition of cavitation inception would be very difficult if not impossible on the basis of mean-square energy, because of the sudden decrease in energy level from point 9 to point 15 for P_1 and corresponding points 10 to 16 for the accelerometer. It was discovered that the respective energy spectra for each test proved more revealing that the total energy in the entire spectrum. In Figs. 15(a) (P_1) and 15b (A_1), individual spectra for the seven points for which $\sigma >$ 0.6 are superimposed on the left while the spectra for two or three values of σ are plotted on the right. The coincidence of the data on the left plot of pressure spectra suggests only noncavitating jet noise. Apparently few if no cavitation events occurred for $\sigma = 0.614$ (17 and 18) but many were present once the cavitation number was slightly reduced to 0.591 (19 and 20). Due to the relatively high energy levels at the low frequency end of the spectrum resulting from jet noise, small increases in the spectral density at the higher frequencies as a result of limited cavitation do not contribute much to the total energy over the entire pressure spectrum. The parameter total energy becomes more indicative of cavitation levels once cavitation becomes more extensive. Although the acceleration spectra under noncavitating conditions are not as similar as the pressure spectra, it is fairly evident at high frequencies that cavitation has occurred between $\sigma = 0.614$ and 0.591.

The spectra in Fig. 15 indicate that cavitation noise is restricted to the higher frequencies, but extends over a wider band as the cavitation number decreases. Another measure of cavitation noise is the ratio of the power spectral density of each frequency channel Δf under cavitating conditions to that under noncavitating conditions. Choosing points 15 and 16 ($\sigma_0 = 0.647$) as the noncavitating reference values, the ratio of power spectral densities are plotted in Fig. 16 for points 17 and 18 ($\sigma = 0.614$) and points 19 and 20 ($\sigma = 0.591$). Additional ratios of the power spectral density are presented in Fig. 16 for lower values of the cavitation index, showing a progressive expansion of the cavitation noise to lower frequencies as σ is decreased. A sensitive measure of the extent of cavitation noise is the area under the curve of the ratio of power spectral density versus frequency, as shown on Fig. 17
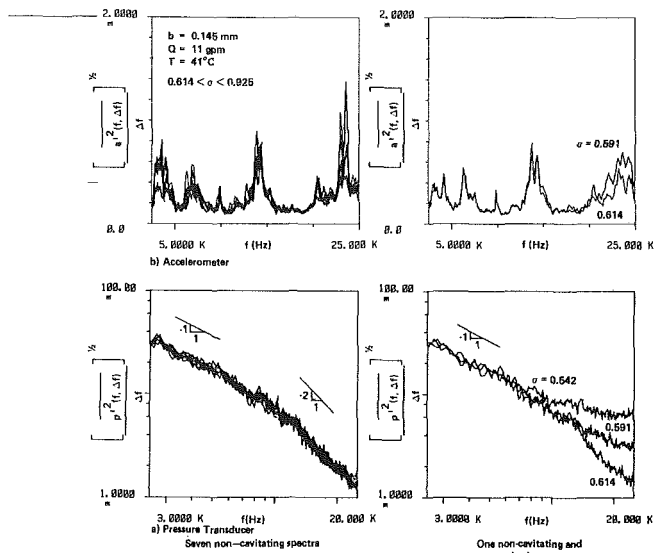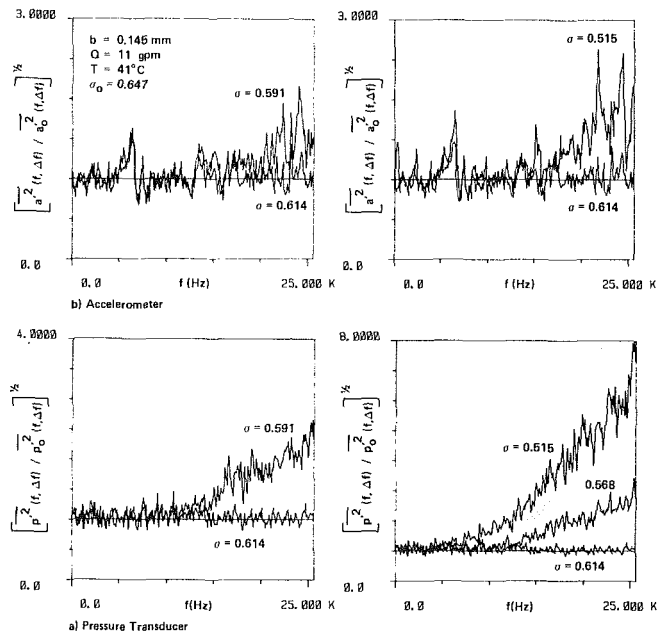
for transducer P_1 for a flow of $Q = 7.57 \times 10^{-4}$ m^3/s (12 gpm). Similar correlations occurred for other flow rates. In comparing the sensitivity of the piezoelectric pressure transducer with the accelerometer, it is clear that both sense the onset of cavitation, but the pressure transducer is probably a better detector for inception because (1) it is located close to the source and (2) the accelerometer is more sensitive to valve noise from the downstream throttling valves, especially for large values of p_R and hence σ.

Model Valve. Noncavitating and cavitating spectra for the model valve are shown in Fig. 18 for pressure transducers P_1 and P_2. The six spectra shown on the left plots suggest no cavitation for $\sigma \geq 0.385$. As shown by the plots on the right figure, a slight lowering of σ to 0.373 resulted in an increase in the power spectrum at the higher frequencies. The ratio of the power spectral density for the same data shown in Fig. 19 is
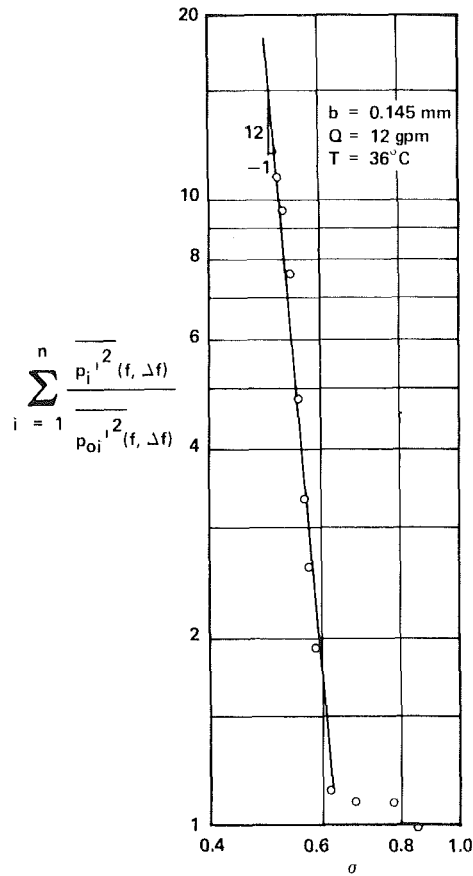
Fig. 17 Area under ratio of cavitating to noncavitating mean-square spectral density curve for fluctuating pressure versus cavitation index for prototype valve at a fixed opening and $Q = 12$ gpm (1 gpm = 6.31 × 10^{-5} m^3/s)
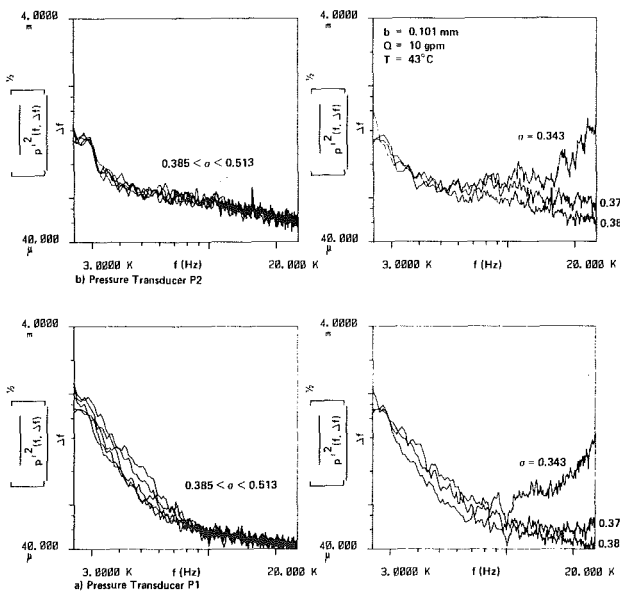

Fig. 18 Noncavitating and cavitating energy spectra for model valve at a fixed opening (1 psi = 6895 Pa; 1 gpm = 6.31 × 10^{-5} m^3/s)

Fig. 19 Ratio of cavitating to noncavitating ($\sigma_0 = 0.421$) spectral density for model valve at a fixed opening (1 gpm = 6.31 × 10^{-5} m^3/s)

Fig. 20 Area under ratio of cavitating to noncavitating mean-square spectral density curve versus cavitation index for model valve at a fixed opening (1 gpm = 6.31 × 10^{-5} m^3/s)

also quite revealing regarding both the coincidence of non-cavitating results, as well as the onset of cavitation. In fact, as illustrated by Fig. 20 for these data set and by Fig. 21 for another data set taken at a higher flow, the area under the curve of the ratio of power spectral density at any condition to a reference noncavitating condition is quite sensitive to cavitation events. Over a range of σ of 0.15 in Fig. 20, the area function varied by nearly four orders of magnitude. For the
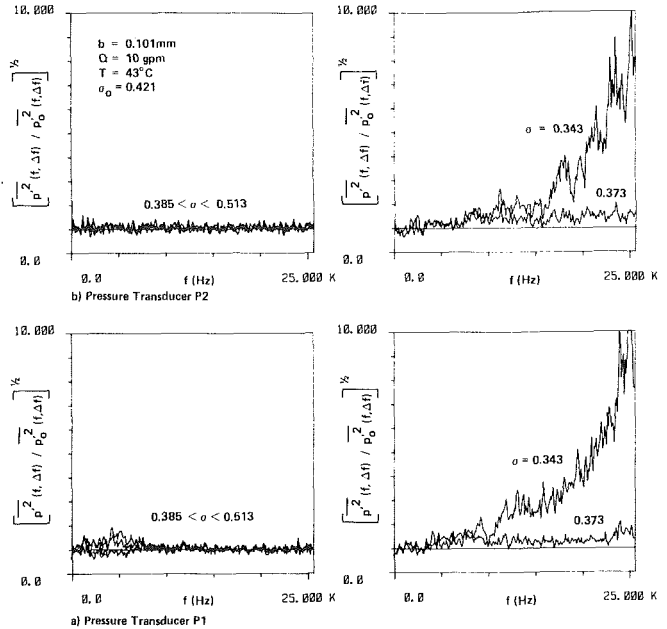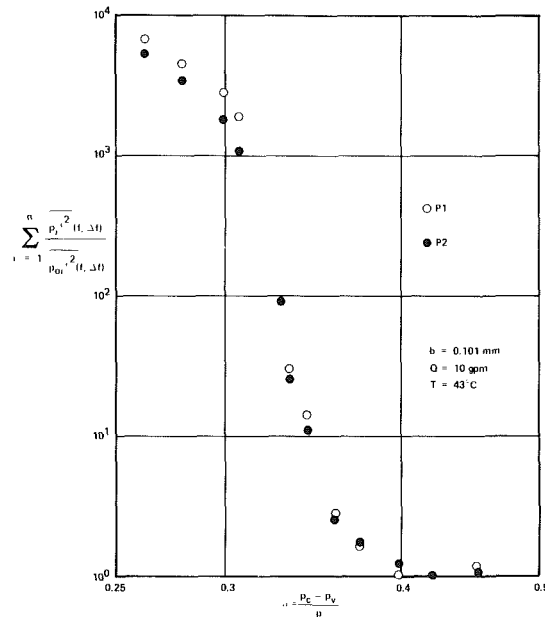
larger opening and corresponding greater flow rate for the data of Fig. 21, the area function for P_1 also varied by nearly four orders of magnitude from $\sigma = 0.6$ to $\sigma = 0.4$, while for P_2 the increase was not as great because of the hydrodynamic jet noise caused by the jet being directed toward that transducer. Nevertheless, the area functions of Figs. 20 and 21 are very sensitive indicators of cavitation events.

For both valves, it was found that, under identical conditions of valve opening b, flow rate Q, and temperature, the plots of energy with flow rate were repeatable. Comparisons of repeatability from test to test may be found in Martin, et al. [14]. Similarities in noncavitating spectra for the two valves are apparent in comparing the prototype valve results, Fig. 6, with those of transducer P_2 in the model, Fig. 12(b). As shown by Figs. 15(a) and 18(b), and more extensively in [14], spectra near cavitation inception are also qualitatively similar.

Cavitation Inception

Attempts were made to formulate a criterion for the definition of incipient cavitation. Although the model was made of transparent walls for the purpose of visualization of the formation and collapse of bubbles, and the bubbles could be clearly seen as the valve was made to cavitate somewhat extensively, the onset of cavitation was extremely difficult to define visually because of the small openings, high jet velocities, and relatively small bubbles. After a number of somewhat unsuccessful attempts to establish incipient and desinent cavitation visually, reliance was placed upon the pressure transducers and the accelerometer, as well as aural sensing using a stethoscope. The identification of inception was much easier in the model using transducer P_1 because of the dramatic change once cavitation commences. Because of the difficulty of separating jet noise from cavitation noise, the criterion for inception used for the prototype valve differed slightly from that applied to the model valve, the latter of which will be discussed first.

Model Valve. Because of the relatively low levels of energy in the model under noncavitating conditions, except when the jet was apparently directed onto transducer P_2, it was not difficult to sense the occurrence of a few cavitation events by comparing cavitating with noncavitating spectra. The data were taken by maintaining a constant flow with the spool locked in a fixed position. The cavitation number was reduced as the pressure difference Δp, and consequently the discharge Q, was maintained constant as nearly as possible. For each value of σ, the dynamic signal for transducer P_1 was processed and the total fluctuating energy noted. It was observed that this value hardly changed under noncavitating conditions. Cavitation inception was defined at the condition for which this nominal value increased by approximately 50 to 100 percent, which corresponded to only the slightest change in the cavitation index. Usually aural sensing by means of a stethoscope yielded the same value of the critical cavitation number. The cavitation number at the 50 to 100 percent energy increase is defined as the incipient cavitation index σ_i, and is plotted as a function of the Reynolds number in Fig. 22. The two sets of data correspond to a range of flow rates for each value of the fixed opening b.

Prototype Valve. As mentioned earlier, a comparison of fluctuating energies measured by the pressure transducer in the chamber of the prototype valve did not clearly indicate the difference between cavitation inception or limited cavitation and no cavitation because of the high level of jet noise. The points shown on Fig. 14 for $\sigma > 0.6$ illustrate the difficulty inherent with comparing solely mean-square energy, while the spectra on Fig. 15 suggest there is no cavitation. Only by comparing spectra or by normalizing the spectral density with the corresponding noncavitating spectra, Fig. 16, could the presence of cavitation be determined. The criterion for incipient cavitation for the prototype valve was defined as the departure of the area under the normalized pressure spectral density curves versus cavitation number from the noncavitating value, which usually varied from approximately 0.9 to 1.1, depending upon which noncavitating test was chosen as the reference value. The value of σ_i was obtained from expanded versions of Fig. 17 by interpolating between the intersection of the extrapolated curve on the cavitating leg of the plot and the noncavitating horizontal line. Various criteria yielded differences in the incipient cavitation number of only 0.005 to 0.01. The results of two series of tests at virtually the identical valve opening and nearly the same range of flow rates 4.42×10^{-4} to 8.20×10^{-4} m^3/s (7 to 13 gpm) are shown in Fig. 22. The only difference in the two series was the oil temperature, which resulted in a significant difference in the range of Reynolds numbers.

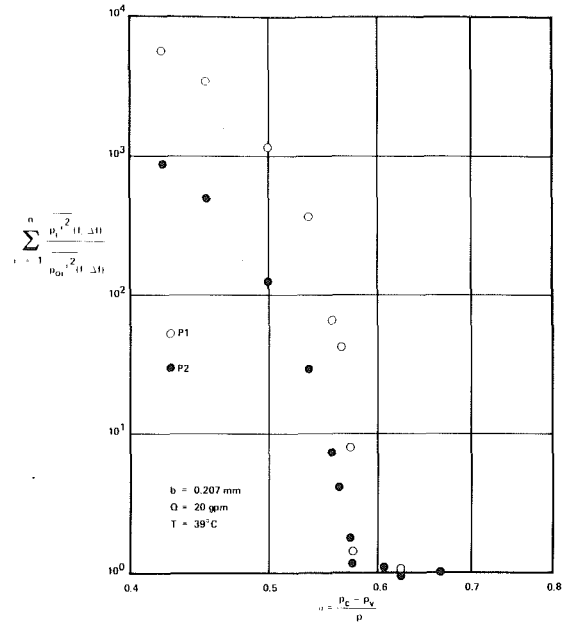Although the use of the area function was not employed for

Fig. 21 Area under ratio of cavitating to noncavitating mean-square spectral density curve versus cavitation index for model valve at a fixed opening (1 gpm = 6.31 × 10^{-5} m^3/s)
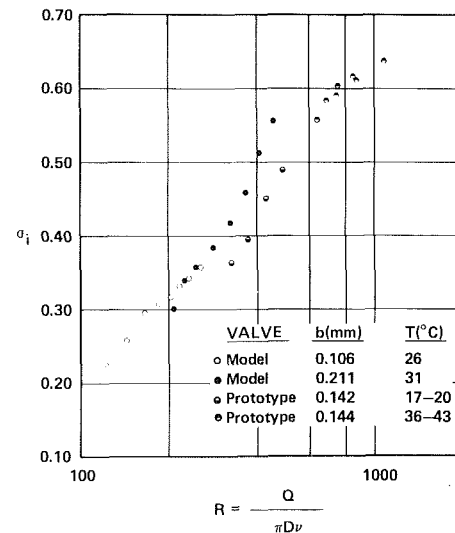
Fig. 22 Incipient cavitation index versus Reynolds number for model and prototype valves

the model valve, inspection of Figs. 20 and 21 illustrates that such a criterion could be as valid, or even more so, as it was for the prototype valve. The expanded σ scale on Fig. 20 suggests that the effect of an increasing number of cavitation events as σ is lowered below σ_i, which is somewhat of an arbitrary criterion, is to produce an exponential effect on the area function. The use of an energy spectrum with 50 ensemble averages does yield a reasonable statistical summary of cavitation events, however.

Discussion of Results

The criteria of cavitation inception employed in this investigation corresponds to a few, but unknown number, of cavitation events during the 50 ensemble averages taken over the sampling period. Single bubble formation in the transparent model could not be observed under these conditions. In fact, the cavitation index corresponding to the formation of a series of bubbles around the annulus was approximately 0.18

less than the values shown on Fig. 22. Even a desinent cavitation number defined at the condition of the elimination of all visible bubbles was 0.10 smaller than the corresponding values of σ_i depicted on Fig. 22. Because of the smallness of the bubbles, the high jet velocity, and apparently few cavitation events, bubbles at the condition σ_i are difficult to observe.

No attempt was made to measure the size of free nuclei in the oil, although the high pressure filter limited the absolute size of any contaminant to 3 μm. Because of the continual filtering of the test liquid, the nuclei size and distribution probably did not vary much from test to test, as was evident from a comparison of energy spectra from test series to test series at the same conditions. As shown by the data on Fig. 6, for two different temperatures there is an apparent viscous effect on the noncavitating energy spectra. Since cavitation inception is affected by the level of turbulence, as shown by Arndt [32, 33], the variation of σ_i with Reynolds number shown in Fig. 22 can be directly correlated with the non-cavitating fluctuating energy shown in Fig. 6. The data of McCloy and Beck [3] indicate a similar trend of σ_i versus R for two two-dimensional models. Their incipient cavitation index was based on the aural detection of the initial presence of a sharp crackling sound. For the range of Reynolds numbers, the critical values of σ_i reported by McCloy and Beck [3] are 0.05 to 0.10 lower than the corresponding ones plotted on Fig. 22, however. Perhaps the criterion employed in this investigation corresponds to a smaller number of cavitation events at σ_i. The effect of viscosity on cavitation inception is also evident in the results of Backé and Riedel [5] and Riedel [6], who evidently defined inception at the condition of the change in the discharge coefficient of an orifice, or a situation correspondiong to wider spread cavitation. Noise data taken by Rouse [34] with a water jet issuing from a nozzle yielded $\sigma_i = 0.55$ from a plot of noise versus σ. Intermittent bursts of noise were observed for values of σ as high as 0.7, however, Obviously, the criterion employed for cavitation inception is somewhat subjective.

For the range of values of dissolved air content present in this study, there was no apparent effect of hysteresis on σ_i. The critical σ_i did not appear to depend upon whether the downstream pressure was being decreased or increased. As discussed later, for dissolved air content at the two extremes experienced in the investigation – 4.5 and 9.0 percent by volume – there was no apparent difference in σ_i nor cavitation noise over the entire range of the cavitation index. Evidently the low residence time of the bubbles in the jet and valve chamber precluded any significant effect of gaseous cavitation. Even for the lowest values of the cavitation number experienced by the model valve, the bubbles disappeared as the flow left the downstream port, suggesting presence of only vaporous cavitation. Baker, et al. [35], also found in their study of cavitation inception in confined jets that σ_i was independent of gas content if the liquid was undersaturated at test-section pressure.

Although the accelerometer mounted on the end of the spool of the prototype valve was not quite as sensitive to the onset of cavitation, it proved to be quite a good indicator of the level of cavitation once inception occurred. As the cavitation index was lowered toward σ_i, as represented by Fig. 13(b), there was a very gradual increase in the fluctuating acceleration levels, making the formulation of a criterion of cavitation inception on the basis of the accelerometer quite difficult. The low level response on the accelerometer for $\sigma > \sigma_i$ is attributed to mechanical effects caused by the method utilized to vary σ – the operation of downstream valves.

Conclusions

Changes in flow pattern and jet orientation in the chamber of spool valves can be sensed by high-frequency response pressure transducers strategically placed. Under noncavitating conditions, jet noise can frequently be directly correlated with the valve opening and flow rate. For the Reynolds numbers tested in this study, there is a definite effect of viscosity on pressure fluctuations emanating from a turbulent non-cavitating jet.

The effect of dissolved gas content on cavitation in spool valves is minimal if the gas content does not exceed that corresponding to atmospheric conditions.

High-frequency response pressure transducers are good diagnostic tools for detection of cavitation inception and cavitation intensity, while a high-frequency response accelerometer is a sensitive indicator of noise levels under cavitating conditions.

The ratio of cavitating noise to noncavitating noise is greater at higher frequencies than at lower frequencies, especially if there is the direct influence of jet noise.

Cavitation inception can be identified most easily by (a) comparison of auto power spectra and (b) ratio of cavitating spectra to noncavitating spectra for the same test conditions. In the case of a high-energy confined jet, root-mean-square values can be much less valid in indicating cavitation inception than individual spectra and, in fact, can be misleading.

For the range of data presented in this paper, the critical cavitation number is a function of the Reynolds number.

Acknowledgments

References

1 McCloy, D., and Martin, H. R., *The Control of Fluid Power*, Longman, London, 1973.

2 MacLellan, M. A., Mitchell, A. E., and Turnbull, D. E., "Flow Characteristics of Piston-Type Control Valves," *Proceedings of the Symposium on Recent Mechanical Engineering Developments in Automatic Control*, Institution Mechanical Engineers, London, Jan. 1960, pp. 13–30.

3 McCloy, D., and Beck, A., "Some Cavitation Effects in Spool Valve Orifices," *Proceedings Institution Mechanical Engineers*, Vol. 182, Part I, No. 8, 1967–1968, pp. 163–174.

4 Backé, W., and Benning, P., "Über Kavitationserscheinungen in Querschnittsverengungen von ölhydraulischen Systemen," *Industrie-Anzeiger*, Vol. 63, 1962, pp. 35–42.

5 Backé, W., and Riedel, H.-P., "Kavitation in ölhydraulischen Systemen," *Industrie-Anzeiger*, Vol. 94, 1972, pp. 153–158.

6 Riedel, H.-P., "Kavitationsverhalten von verschiedenen Druckflüssigkeiten," *Industrie-Anzeiger*, Vol. 94, 1972, pp. 1724–1727.

7 Kleinbreuer, W., "Kavitationserosion in hydraulischen Systemen," *Industrie-Anzeiger*, Vol. 99, 1977, pp. 609–613.

8 Kleinbreuer, W., "Untersuchung der Werkstoffzerstörung durch Kavitation in ölhydraulischen Systemen," Dr.-Ing. dissertation, Technical University of Aachen, 1979, 306 pp.

9 Eich, O., "Massnahmen zur Minderung von Kavitationsgeräuschen in Geräten in Ölhydraulik," *Industrie-Anzeiger*, Vol. 98, May 1976, pp. 739–743.

10 Eich, O., "Entwicklung geräuscharmer Ventile der Ölhydraulik," Dr.-Ing. dissertation, Technical University of Aachen, 1979, 157 pp.

11 Lichtarowicz, A., and Pearce, I.D., "Cavitation and Aeration Effects in Long Orifices," Cavitation Conference, Institution Mechanical Engineers, Edinburgh, Sept. 3-5, 1974, pp. 129–144.

12 McCloy, D., and Beck, A., "Flow Hysteresis in Spool Valves," *Proceedings of the First BHRA Fluid Power Symposium*, Cranfield, 1969, pp. 170–182.

13 Wiggert, D. C., Martin, C. S., and Medlarz, H., "Cavitation Damage Mechanisms: Review of Literature," Technical Report AFAPL-TR-79-2125, U.S. Air Force Aero Propulsion Laboratory, Feb. 1980, 53 pp.

14 Martin, C. S., Wiggert, D. C., and Medlarz, H., "Cavitation Damage Mechanisms: Experimental Study of Cavitation in a Spool Valve," Technical Report AFAPL-TR-79-2121, U.S. Air Force Aero Propulsion Laboratory, Feb. 1980, 131 pp.

15 Robertson, J. M., *Hydrodynamics in Theory and Application*, Prentice-Hall, New York, 1965.

16 Albertson, M. L., Dai, Y. B., Jensen, R. A., and Rouse, H., "Diffusion of Submerged Jets," *Transactions*, ASCE, Vol. 115, 1950, pp. 639-664.

17 Gutmark, E., and Wygnanski, I., "The Planar Turbulent Jet," *Journal of Fluid Mechanics*, Vol. 73, 1976, pp. 465-495.

18 Reethof, G., "Turbulence-Generated Noise in Pipe Flow," *Annual Review of Fluid Mechanics*, Vol. 10, 1978, pp. 333-367.

19 Lush, P. A., "Measurements of Subsonic Jet Noise and Comparison with Theory," *Journal of Fluid Mechanics*, Vol. 46, 1971, pp. 477-500.

20 Arndt, R. E. A., "Cavitation in Fluid Machinery and Hydraulic Structures," *Annual Review of Fluid Mechanics*, Vol. 13, 1981, pp. 273-328.

21 George, W. K., "The Equilibrium Range of Turbulent Pressure Spectra," *Bulletin, American Physical Society*, Vol. 19, 1974, p. 1158.

22 Fuchs, H. V., and Michalke, A., "On Turbulence and Noise of an Axisymmetric Shear Flow," *Journal of Fluid Mechanics*, Vol. 70, 1975, pp. 179-265.

23 George, W. K., and Beuther, P. D., "Pressure Spectra in a Turbulent Shear Flow," *Bulletin, American Physical Society*, Vol. 22, 1977, p. 1285.

24 Ross, D., *Mechanics of Underwater Noise*, Pergamon Press, New York, 1976.

25 Jorgensen, D. W., "Noise from Cavitating Submerged Water Jets," *Journal of the Acoustical Society of America*, Vol. 33, Oct. 1961, pp. 1334-1338.

26 Deeprose, W. M., King, N. W., McNulty, P. J., and Pearsall, I. S., "Cavitation Noise, Flow Noise and Erosion," Cavitation Conference, *Institution Mechanical Engineers*, Sept. 3-5, 1974, Edinburgh, pp. 373-381.

27 Ōba, R., and Itō, Y., "Cavitation Shock Pressures in a Venturi," ASME *Cavitation and Polyphase Flow Forum*, 1975, pp. 2-6.

28 Blake, W. K., Wolpert, M. J., and Geib, F. E., "Cavitation Noise and Inception as Influenced by Boundary-Layer Development on a Hydrofoil," *Journal of Fluid Mechanics*, Vol. 80, 1977, pp. 617-640.

29 Tullis, J. P., and Govindarajan, R., "Cavitation and Size Scale Effects for Orifices," *Journal of the Hydraulics Division*, ASCE, Vol. 99, Mar. 1973, pp. 417-430.

30 Ball, J. W., and Tullis, J. P., "Cavitation in Butterfly Valves," *Journal of the Hydraulics Division*, ASCE, Vol. 99, Sept. 1973, pp. 1303-1318.

31 Tullis, J. P., "Testing Valves for Cavitation," Cavitation Conference, *Institution Mechanical Engineers*, Sept. 3-5, 1974, Edinburgh, pp. 47-55.

32 Arndt, R. E. A., "Pressure Fields and Cavitation," *Proceedings of the 7th IAHR Symposium on Hydraulic Machinery*, Vienna, 1974, Paper IX.

33 Arndt, R. E. A., "Investigation of the Effects of Dissolved Gas and Free Nuclei on Cavitation and Noise in the Wake of a Sharp Edged Disk," *Proceedings of Joint ASME-IAHR-ASCE Symposium on Hydraulic Machinery*, Fort Collins, Colo., 1978, pp. 543-556.

34 Rouse, H., "Cavitation in the Mixing Zone of a Submerged Jet," *La Houille Blanche*, Vol. 8, No. 1, 1953, pp. 9-19.

35 Baker, C. B., Holl, J. W., and Arndt, R. E. A., "The Influence of Gas Content and Polyethylene Oxide Additive upon Confined Jet Cavitation in Water," ASME *Cavitation and Polyphase Flow Forum*, 1976, pp. 6-8.

15 Robertson, J. M., *Hydrodynamics in Theory and Application*, Prentice-Hall, New York, 1965.

16 Albertson, M. L., Dai, Y. B., Jensen, R. A., and Rouse, H., "Diffusion of Submerged Jets," *Transactions*, ASCE, Vol. 115, 1950, pp. 639-664.

17 Gutmark, E., and Wygnanski, I., "The Planar Turbulent Jet," *Journal of Fluid Mechanics*, Vol. 73, 1976, pp. 465-495.

18 Reethof, G., "Turbulence-Generated Noise in Pipe Flow," *Annual Review of Fluid Mechanics*, Vol. 10, 1978, pp. 333-367.

19 Lush, P. A., "Measurements of Subsonic Jet Noise and Comparison with Theory," *Journal of Fluid Mechanics*, Vol. 46, 1971, pp. 477-500.

20 Arndt, R. E. A., "Cavitation in Fluid Machinery and Hydraulic Structures," *Annual Review of Fluid Mechanics*, Vol. 13, 1981, pp. 273-328.

21 George, W. K., "The Equilibrium Range of Turbulent Pressure Spectra," *Bulletin, American Physical Society*, Vol. 19, 1974, p. 1158.

22 Fuchs, H. V., and Michalke, A., "On Turbulence and Noise of an Axisymmetric Shear Flow," *Journal of Fluid Mechanics*, Vol. 70, 1975, pp. 179-265.

23 George, W. K., and Beuther, P. D., "Pressure Spectra in a Turbulent Shear Flow," *Bulletin, American Physical Society*, Vol. 22, 1977, p. 1285.

24 Ross, D., *Mechanics of Underwater Noise*, Pergamon Press, New York, 1976.

25 Jorgensen, D. W., "Noise from Cavitating Submerged Water Jets," *Journal of the Acoustical Society of America*, Vol. 33, Oct. 1961, pp. 1334-1338.

26 Deeprose, W. M., King, N. W., McNulty, P. J., and Pearsall, I. S., "Cavitation Noise, Flow Noise and Erosion," Cavitation Conference, *Institution Mechanical Engineers*, Sept. 3-5, 1974, Edinburgh, pp. 373-381.

27 Ōba, R., and Itō, Y., "Cavitation Shock Pressures in a Venturi," ASME *Cavitation and Polyphase Flow Forum*, 1975, pp. 2-6.

28 Blake, W. K., Wolpert, M. J., and Geib, F. E., "Cavitation Noise and Inception as Influenced by Boundary-Layer Development on a Hydrofoil," *Journal of Fluid Mechanics*, Vol. 80, 1977, pp. 617-640.

29 Tullis, J. P., and Govindarajan, R., "Cavitation and Size Scale Effects for Orifices," *Journal of the Hydraulics Division*, ASCE, Vol. 99, Mar. 1973, pp. 417-430.

30 Ball, J. W., and Tullis, J. P., "Cavitation in Butterfly Valves," *Journal of the Hydraulics Division*, ASCE, Vol. 99, Sept. 1973, pp. 1303-1318.

31 Tullis, J. P., "Testing Valves for Cavitation," Cavitation Conference, *Institution Mechanical Engineers*, Sept. 3-5, 1974, Edinburgh, pp. 47-55.

32 Arndt, R. E. A., "Pressure Fields and Cavitation," *Proceedings of the 7th IAHR Symposium on Hydraulic Machinery*, Vienna, 1974, Paper IX.

33 Arndt, R. E. A., "Investigation of the Effects of Dissolved Gas and Free Nuclei on Cavitation and Noise in the Wake of a Sharp Edged Disk," *Proceedings of Joint ASME-IAHR-ASCE Symposium on Hydraulic Machinery*, Fort Collins, Colo., 1978, pp. 543-556.

34 Rouse, H., "Cavitation in the Mixing Zone of a Submerged Jet," *La Houille Blanche*, Vol. 8, No. 1, 1953, pp. 9-19.

35 Baker, C. B., Holl, J. W., and Arndt, R. E. A., "The Influence of Gas Content and Polyethylene Oxide Additive upon Confined Jet Cavitation in Water," ASME *Cavitation and Polyphase Flow Forum*, 1976, pp. 6-8.

DISCUSSION

R. G. Cunningham[1]

The authors correctly note that cavitation information for oil hydraulic systems is relatively scarce. Their well-instrumented study of two spool valves is a valuable contribution particularly in terms of detecting cavitation using mean-square energy measurements vis-a-vis energy spectra and more commonly used methods such as observation of bubbles and aural detection of the onset of cavitation.

Cavitation is a problem because of resulting noise, or damage, or both. From a design standpoint, cavitation is important if it is severe enough to cause a departure of performance from the theoretical model. Low-intensity cavitation, i.e., below these thresholds is of research interest but not from an engineering design point of view.

A prime objective is the establishment of a cavitation coefficient which predicts the onset of cavitation and which is relatively unaffected by the internal flow contours of the fluid machinery.

It would appear that the authors' equation defining the cavitation coefficient σ in equation 6 could be improved. The

denominator $\Delta p = (p_L - p_R)$ is a poor approximation to the dynamic or jet pressure $\rho V_c^2 / 2$; while the use of p_R is convenient from a pressure measurement standpoint, it is seriously flawed because the pressure rises from p_c to p_R, essentially by a "sudden expansion" deceleration and disorganized flow pattern which may include reentry flow. The use of $\Delta p = (p_L - p_c)$ seems more logical as an index to dynamic pressure and also less sensitive to hardware design effects.

Caution should be exercised regarding the apparent immunity of this cavitation to the dissolved air-content of the hydraulic oil. Cavitation in oil systems—while producing the same undesirable effects as water cavitation—differs in two significant respects, (1) the vapor pressure of an oil is relatively low and complicated by the fact that an oil is a mixture of components ranging from light to heavy ends. (2) The solubilities of gases are much larger in organic liquids such as oils, than in water. The solubility of air in water (room temperature and pressure) is about 2 percent by volume; it ranges from 8-10 percent for lubricating oils, 12 percent for diesel fuel and 18-25 percent for gasoline. As a result, "gas cavitation" occurs readily in oil systems if the oil is at or near saturation conditions [1].

The authors' test conditions produced oil with an extremely low air content. The solubility of air in oil follows Henry's law, i.e., the mass of gas dissolved is proportional to the partial pressure of the gas in the space above the liquid under equilibrium conditions. The extremes of dissolved air reported (4.5 percent up to 9 percent at 14.7 psia) translate to only 0.013 percent and 0.026 percent for this oil raised to the pressure of 5000 psia implied for some of the prototype tests. Air nuclei are important as the sites of cavitation events. At least in static bodies of liquid, extreme deaeration delays or prevents vapor cavitation upon pressure release. Flowing liquids at some extreme degree of deaeration may similarly become resistant to vapor cavitation—and perhaps also more sensitive to the vapor pressure of the oil.

Transient or hysteresis cavitation effects have been noted in other oil systems [2, 3] containing dissolved air. Air evolves quite rapidly on release of pressure—e.g., in a venturi throat—and then dissolves again relatively slowly, upon pressurization. As a result some oil systems with large pressure gradients effectively deaerate the fluid during warm-up. This subject of this work—high-speed actuators and spool valves—may well be affected by this phenomenon.

References

1 Schweitzer, P. H., and Szebehely, V. G., "Gas Evolution in Liquids and Cavitation," *J. of Applied Physics*, Vol. 21, December 1950, pp. 1218-1224.

2 Cunningham, R. G., and Brown, F. B., "Oil Jet Pump Cavitation," *ASME 1970 Cavitation Forum*, May 24-27, 1970, Detroit Michigan, pp. 13-16.

3 Cunningham, R. G., "The Jet Pump as a Lubrication Oil Scavenge Pump for Aircraft Engines," The Pennsylvania State University, WADC Tech. Rept., July 1954, pp. 55-143.

A. Lichtarowicz[2]

The authors should be congratulated on their interesting paper describing methods of detecting cavitation inception in spool valves. As pointed out in the paper, it is very dificult to establish the exact point of cavitation inception in an actual piece of engineering hardware.

The comparison of the ratio of cavitating to noncavitating energy spectra, as used by the authors, seems to be a very useful method of detecting cavitation inception, though perhaps it is a little cumbersome.

The writer, from his experiences, fully endorses the

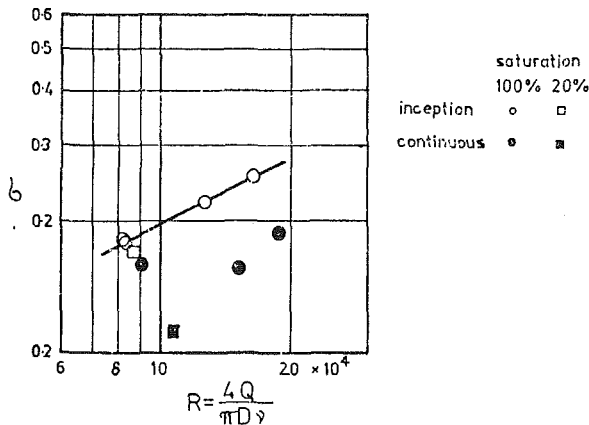[1] The Pennsylvania State University, University Park, Pa. 16802.

Fig. 1 Cavitation index-Reynolds number variation for shape edge orifice plate

statement made that in laboratory models the use stethoscope gives a very reliable indication of the inception point which agrees with the data obtained with much more sophisticated electronic equipment.

Another useful method used by the writer [reference A] is to place a small "hydrophone" made from a piezo-electric crystal in the vicinity of the emerging jet, but not in its path. The change in the output as observed on an oscilloscope screen proved to be very reliable method of detecting the cavitation inception, especially as cavitation initially occurred in bursts.

Figure 1 shows results extracted from Pearce [B]. They relate to the cavitation inception for a sharp edge orifice plate (similar to that used for flow measurement). The orifice diameter was 2.5 mm and the test fluid was aviation kerosene. Each point was obtained by holding the downstream pressure constant and increasing the upstream pressure till the cavitation was well established. The results are similar to the author's Fig. 22. Two additional points were obtained with reduced air content in the test liquid. These points seem to confirm the author's statement that the air content changes do not affect the cavitation inception, at least for the range of air contents tested.

Finally the writer would like to sound a word of warning. Both the authors' Fig. 22 and Fig. 1 in the discussion relate

the cavitation number with Reynolds number. In both cases the variation Reynolds number was obtained mainly by flow variation and by size variation, but fluid properties varied only by a factor of about 2. To ensure that these graphs can be generalized, further testing with different liquids is required.

Additional References

A. Lichtarowicz, A., and Pearce, I. D., "Cavitation and aeration effects in long orifices," Conf. on Cavitation, Institution of Mechanical Engineers, London. 3-5 Sept 1974.

B. Pearce, I. D., "Cavitation in Orifices," Ph.D. thesis, University of Nottingham. July 1969.

Author's Closure

The comments of Dr. Cunningham are most welcome as they address issues that were not discussed in detail in the paper. Except for the consideration of noise he is correct in stating that the low-intensity cavitation very close to inception is of only limited consequence in oil hydraulic systems.

The definition of the pressure difference across the value $\Delta p = p_L - P_R$ was chosen rather than $p_L - p_c$ because of the influence of partial or complete jet stagnation of p_c. For all of the data, the difference in Δp for the two definitions was less than 4 percent. For the prototype valve the chamber pressure was larger than p_R, while for the model valve the opposite was observed. In either case the cavitation index would not have differed by more than 4 percent.

The authors recognize that air is much more soluble in hydraulic oil than in water and the attendant likelihood of enhanced gaseous cavitation. Although the local instantaneous pressures in the turbulent jet surely dropped to the saturation pressure, which was atmospheric or lower, the mean pressure in each valve chamber was always well above atmospheric pressure at cavitation inception. It should also be noted that the residence time for the fluid in each valve was small, inhibiting any significant growth of air bubbles by gaseous diffusion.

The maximum upstream pressure p_L was 2700 psi and 400 psi for the prototype and model valve, respectively. The 500 psi pressure quoted in the paper only related to the maximum level attainable by the hydraulic pump. Most hydraulic systems are not saturated with air at the high pressures mentioned by Dr. Cunningham.

A Possible Criterion for Cavitation Inception on Hemispherical Headforms

B. R. Parkin

The Pennsylvania State University,
Garfield Thomas Water Tunnel,
Applied Research Laboratory,
State College, Pa.   16801,
Mem. ASME

The present paper reviews several pertinent papers about the onset of bubble-ring cavitation on hemispherical headforms in which a laminar bubble is present. From this review, a likely sequence of events for cavitation inception, or desinence, can be discerned. When this sequence is postulated, the observational basis for each event is discussed. Once the physical aspects of the inception process have been noted, a mathematical formulation of key relationships required to establish an inception criterion can be undertaken. From these results, a quantitative criterion for the inception of bubble ring cavitation is stated and we give a discussion which interprets this possible inception criterion for future use. The use of this criterion in a theory of inception and a comparison of analytical and experimental results is left to a future publication.

Introduction

A traditional difficulty apears to bedevil those who would determine the flow parameters characterizing cavitation inception by means of calculations based upon the first principles of physics. One problem is that often the properties of the noncavitating flow governing the basic nature of the environment which can lead to cavitation are not well enough understood. Moreover, the interactions between the onset process and the noncavitating flow may not be fully revealed by the available experimental data. As a result of these deficiencies, calculations based on bubble dynamics have generally been disappointing, and it seems safe to say that this situation will continue to exist until a criterion for cavitation inception for each flow under investigation can be established.

While we cannot yet claim that all aspects of the flow around hemispherical headforms are fully understood, this particular flow has received much study in the past. Therefore, there is probably more information available about this flow than any other, and it seems useful to examine this body of significant past work to see if one can use it in order to postulate a tentative criterion for cavitation inception. Therefore, in the following, we shall attempt to formulate a criterion for the onset of cavitation for a rather special flow on an axially symmetric body which consists of a hemispherical nose attached to an afterbody which is a right circular cylinder of diameter equal to that of the hemisphere. The freestream flow velocity (V_0) is aligned with the body axis. The static pressure at upstream infinity is P_0, and the liquid density is ρ. This flow configuration, which often has a laminar separation bubble in laboratory experiments, is illustrated schematically in Fig. 1.

Indeed, it has been estimated [1, 2] that the flow about hemispherical bodies will generally have a laminar separation bubble on the body downstream of the minimum pressure
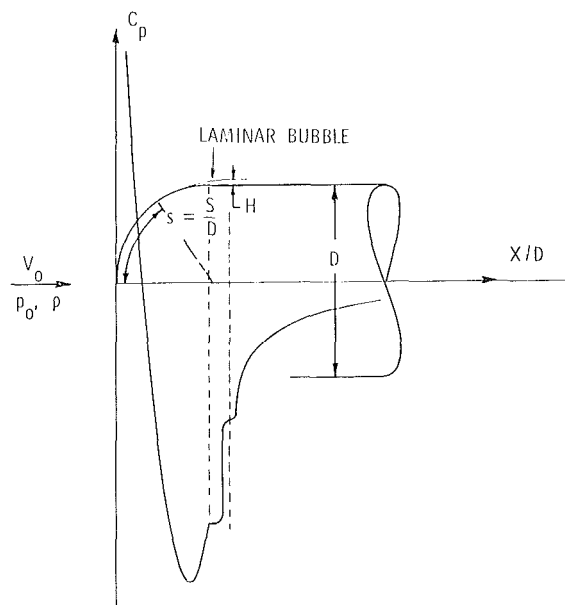
Fig. 1 Schematic diagram of flow about a hemispherical headform when laminar separation is present

point up to Reynolds numbers, based on body diameter, D, of about five and one half million [1, 3]. This Reynolds number limit is greater than the Reynolds numbers of the majority of data reported from cavitation-tunnel experiments with such bodies. Therefore, there are considerable experimental data on cavitation inception or desinence in the presence of laminar separation which can be used to test the validity of theoretical findings. Our goal is to formulate a criterion for cavitation onset which accounts for the main physical processes which appear to take place in this rather special flow. In a subsequent paper, we hope to compare the

theoretical findings which follow from this criterion with experiment.

The analysis planned is certainly not the first such study to appear in the literature. A concise review of a number of previous investigations has been given by Holl [4]. As we have noted already, those features of the noncavitating flow, which may have a decisive influence on inception, were not as well-known when those earlier theoretical studies were carried out as they are today. Therefore, previous theories for cavitation inception on bodies which are now known to exhibit laminar separation show, at best, only qualitative agreement with the experiment.

The Sequence of Events

Perhaps the most direct way to describe the several physical aspects of a theory for cavitation inception when the flow contains a laminar separation bubble is to list in sequence the key events or phases of cavitation bubble growth as they might apply to a typical nucleus. Once we have given this sequence, the observational basis for each hypothesis will be discussed.

(a) It assumed that cavitation bubbles originate from small nuclei which contain air or water vapor or both. Generally such nuclei are not visible to the unaided eye. In this study, we will suppose that these nuclei are distributed throughout the liquid.

(b) A typical nucleus of radius R_0, once it is in the boundary layer on the body, will encounter a low-pressure region which is favorable to vaporous bubble growth. That is, the local static pressure on the body is less than p_v, the vapor pressure of the water. As it moves through this region of low pressure, the bubble will experience vaporous growth from the initial radius R_0 to some maximum radius R_m.

(c) The very small radius R_m is achieved at a point on the body where the local static pressure has risen to a value which is greater than the vapor pressure. Therefore if left to itself, the bubble would collapse.

(d) The microbubble of radius R_m comes to rest at a point on the body within the laminar bubble. After it has become fixed inside the laminar bubble, its subsequent growth is caused by air diffusion from the liquid into the bubble.

(e) This gaseous growth continues until the bubble has become large enough to interact with the free shear layer between the outer flow and the inner region of the laminar bubble.

(f) The process of interaction with the shear layer, which causes further gaseous growth to cease, will lift the bubble from the surface of the body by a slight amount and permit it to move downstream with the flow. This motion will take place very close to the body and it will cover a very short distance because the bubble will soon find itself at the downstream end of the laminar bubble where the boundary layer becomes turbulent.

(g) When the bubble is exposed to the turbulent boundary layer flow, low pressures in the turbulent eddies can cause a second short period of vaporous growth. However, this final growth phase cannot proceed unchecked. As the bubble grows, it will become large enough to experience the turbulent shearing motions in the boundary layer. These motions so distort the bubble that it is torn apart and it will appear to the observer as a part of the frothy narrow band of cavitation which appears at the downstream end of the laminar bubble. Indeed, it is the first appearance of this white band or cloud of extremely small bubbles which we identify as desinent or incipient cavitation. Some authors call this state desinence or incipience "bubble-ring cavitation" because of its very limited streamwise extent and because of the fact that very short exposure photographs show that this cavitation cloud actually consists of a ring of very small bubbles in the boundary layer as illustrated in Fig. 2.

The foregoing description of events outlines the occurrences which are of immediate concern in this study. However, it is worth noting that the events previously noted have centered upon the history of a typical nucleus, which is only one of many nuclei, sharing the fate of the typical bubble. The number of nuclei which are similarly affected increases as the degree of cavitation is intensified and the extent of the cloud increases visibly. However, this intensification is limited by the extent of the laminar bubble because it will soon be filled by the cloud. When this filling reaches its limit, the cloud is transformed into a circumferential band of small clear cavities with their leading edges attached to the body just behind the point of laminar separation. Thus an entirely

Nomenclature

C_p = pressure coefficient = $(p - p_0)/\frac{1}{2}\rho V_0^2$

C_{p_s} = static pressure coefficient in laminar separation bubble = $(p_s - p_0)/\frac{1}{2}\rho V_0^2$

C_σ = ratio of characteristic surface tension pressure to dynamic pressure = $4\sigma/(R_0\rho V_0^2)$

D = diameter of the water tunnel model

H = maximum height of the laminar separation bubble

K = cavitation number = $(p_0 - p_v)/\frac{1}{2}\rho V_0^2$

n = surface tension parameter which governs the slope of the linearly increasing part

of the surface tension law $S(r,\sigma)$

p = static pressure at any point in the flow

p_a = partial pressure of air in the freestream nucleus at the measured dissolved air concentration

p_0 = static pressure at upstream infinity

p_v = pressure of the vapor inside the cavitation bubble

p_s = static pressure of the liquid at laminar separation

r = dimensionless radius = R/R_0

r_c = critical dimensionless bubble radius

r_m = maximum dimensionless bubble radius

r_{max} = maximum dimensionless radius $= r_m$

R = bubble radius

Re = Reynolds number based on body diameter

R_m = maximum bubble radius

R_0 = "radius" of typical nucleus

$S(r,\sigma)$ = surface tension law

t_m = time available for vaporous growth

V_0 = freestream velocity

β = dimensionless parameter characterizing static pressure in laminar separation zone, $\beta = (K + C_{p_s})/C_\sigma$

γ = dissolved air content parameter, $\gamma = p_a R_0/2\sigma$

θ = ratio of maximum vapor bubble diameter to the maximum laminar separation bubble height

ρ = liquid density

σ = coefficient of surface tension

different cavitation flow regime, called band cavitation, is established. A region in which pressures are less than the vapor pressure of water may no longer exist upstream in the vicinity of the minimum pressure point of noncavitating flow, although this remains to be investigated in complete detail. The small cavities now on the body are actually cavity flows which are sustained by evaporation from the cavity wall and by air diffusion from the liquid into the cavity. Presumably the methods of free streamline theory could be adapted to the analysis of this flow. However, such considerations are outside the scope of this study.

Free stream and Surface Nuclei. Let us consider next the observational basis for the preceding outline of the life of a typical cavitation bubble. It seems logical to start with a brief discussion of nuclei. This topic has received considerable study, and there is rather extensive literature about the origin and the nature of cavitation nuclei. Instead of presenting a review of this material here, we shall refer the reader to a few sources for further information. For relatively concise or somewhat longer discussions of the topic, one can consult Holl [4], Plesset [5], Beyer [6], Ross [7], or Knapp, Daily, and Hammit [8]. A fairly complete list of original sources is given in the last of these citations.

For our purposes, it seems sufficient to note that it is thought that ordinary water contains impurities, usually with some air stabilized upon them, which can act as "weak spots" in the liquid and form seats for cavitation bubble growth. When one performs cavitation experiments in a closed-circuit water tunnel, the events which take place in the test section can also produce small air-bubble nuclei unless the tunnel is equipped with a resorber which drives these bubbles into solution or it has some other device which removes such gas bubbles from the flow before they re-enter the test section.

It is known that a spherical air bubble in still water will dissolve because of surface tension if its radius is less than a critical value. On the other hand, if the radius is greater than this critical value, a bubble can grow by air diffusion from the water into the bubble. Such a bubble will rise to the surface and will also be lost as a cavitation nucleus. Thus, much of the literature in the foregoing references deals with reasons for the observed fact that cavitation nuclei are found in ordinary water even though it may have been quiescent for a very long time. On the other hand, we have noted that cavitation testing in a water tunnel, by its very nature, can generate very small bubbles which serve as cavitation nuclei. Although such nuclei may have short lives, their presence can affect water-tunnel observations.

In order to account for the persistence of certain classes of nuclei, we shall employ a model in which the net surface energy is initially zero [9]. Such a nucleus could be composed of a microscopic solid particle which has absorbed air, which has a small crack, or which is porous so that air is stabilized on it. We will also want to account for some nuclei which are actually spherical air bubbles. We will use a simple analytical model which can accommodate both of these possibilities.

Those conditions which can cause stable nuclei in the flow can also pertain to the surface of the body. This fact has led to the concept of surface nuclei which consist of small crevices or pores which can act as seats for the generation of air-bubble nuclei on the body surface. Such surface imperfections become sources of air bubbles by a process of convective air diffusion [10]. In some ways, such nuclei resemble free stream nuclei because they produce bubbles which enter the boundary-layer flow. However, if surface nuclei are the predominant source of nuclei in a flow and the water is supersaturated in the vicinity of such nuclei, inception is observed as patch cavitation even in regions where the local static pressure exceeds the vapor pressure.

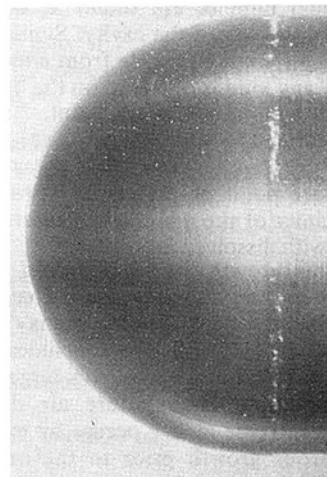Gupta [11] was among the first to perform systematic tests

Fig. 2 Bubble-ring cavitation on a hemispherical nose ($K = 0.626$, $V_0 = 18.3$ mps, dissolved air 9.5 ppm) from reference [3]

designed to compare the effects of cavitation inception from surface nuclei and free stream nuclei. In experiments using Teflon and Polyethylene models, he found that surface nuclei on such porous bodies exhibit gaseous cavitation inception, which is quite different from the kind of cavitation inception under consideration here. The cavitation process we plan to consider was observed on stainless-steel hemispherical bodies. Stainless-steel bodies were also tested by Gupta, and his observations of inception and desinence were considered to be consequences of free stream nuclei. Subsequently, Van der Meulen [12] carried out boundary-layer studies on hemispherical models made of stainless steel and Teflon which showed that the noncavitating flows about bodies of these materials were the same. He also found that the Teflon body exhibited gaseous cavitation and that the stainless-steel model exhibited desinence and inception typical of free stream nuclei. In this respect, the findings of Gupta and Van der Meulen are in agreement. However, Van der Meulen found a strong cavitation hysteresis for the Teflon body and practially no hysteresis on the stainless-steel model. Gupta's experiments showed the opposite. Reasons for these contradictory findings are as yet unknown.

Evidently, bodies which provide active sites of surface nuclei will exhibit cavitation inception characteristics differing from bubble-ring cavitation and which cannot be described by the sequence of events stated. Therefore, we shall restrict our considerations to cavitation which originates from free stream nuclei as stated in aforesaid item (a).

Initial Vaporous Growth. Interestingly enough, in spite of the many experimental investigations of cavitation-bubble growth, no direct observations of vaporous growth of microbubbles in the boundary layer have been made. The difficulty of such experiments is manifest. Although larger traveling bubbles have been photographed and gaseous growth in the laminar bubble has been recorded, we only have indirect evidence that the microbubbles undergo a short period of vaporous growth prior to the time that a bubble becomes stabilized in the laminar bubble. Nevertheless, the evidence now available does argue for the existence of an initial phase of vaporous growth [10]. Four observations may be made in support of this argument.

1 There are tensions in the liquid at the minimum-pressure point on the body during inception. By tensions, we mean static pressures less than vapor pressure.

2 When the cavitation is observed to change from the incipient or desinent forms to sheet cavitation, the tension at the minimum pressure point is lost (or at least greatly reduced)

and no individual bubbles are found at any point in the boundary layer upstream of the cavity. Similarly, as the free stream pressure is lowered, starting from noncavitating flow, no cavitation of any kind is observed on the body unless there is a tension at the minimum-pressure point.

3 In the experiments cited in reference [10], the local pressures were such, just before a tension was produced at the minimum-pressure point or just after it was lost, that the water in the vicinity of the minimum-pressure point was still supersaturated with dissolved air.

4 Thus, bubble growth by air diffusion would be only slightly affected by the above pressure changes if it could occur at all. Evidently the stream nuclei may be too small to permit such growth [13] and one concludes, tentatively at least, that the bubble must grow to a larger size than the original size of the nucleus before air diffusion starts. Presumably this increase in size occurs by means of a short period of vaporous growth prior to the onset of gaseous growth in the laminar-separation zone.

Bubble Size After Initial Growth. Having indicated the reasons for vaporous growth, one must now consider the smallest possible size that the bubble must attain and its location on the body after this growth has occurred. As we have noted, the smallest size must correspond to that radius which will just permit gaseous growth. One can determine this radius, R_m, by using the theory of Epstein and Plesset [14]. This theory supposes that the bubble is at rest in an air-water solution which can be undersaturated or oversaturated. The rate at which a bubble dissolves or grows is calculated from the theory of diffusion. In reference [10], it is noted that when the liquid flows past a fixed bubble, the rate of air diffusion into or out of the bubble increases greatly compared to the quiescent-fluid case of reference [14]. However, in the present study, our interest centers on threshold conditions under which gaseous bubble growth is possible. The subsequent growth rate is another matter and the Epstein-Plesset formulation is the correct one for the problem at hand. The location on the body where bubbles of at least the critical radius R_m are to be found is in the laminar bubble. It is in this location that subsequent gaseous growth has been observed [1, 10].

On the other hand, suppose that upon conclusion of vaporous growth the bubble is large enough to interact immediately with the free shear layer. Then it will be transported downstream into the region of the turbulent eddies, as noted in the aforesaid event (f). No gaseous growth will occur and visible inception will be observed. Thus, depending upon the height of the laminar bubble, there can be a second criterion for R_m. We will need to consider both of these possibilities later.

Finally, it must be confessed that events (e), (f), and (g) have been enumerated for the sake of providing a reasonably complete picture of the inception process when laminar separation is present. If the cavitation bubble becomes stabilized in the laminar bubble at the radius R_m, as indicated in step (d), the subsequent events will occur automatically. Therefore, our theory of inception need not take the analysis beyond step (d).

Having drawn the picture of the basic physical factors to be considered in the theory, we now turn to a mathematical formulation for a criterion of inception for bubble ring cavitation.

A Stable Nucleus

Previously, we have noted that it may be desirable to allow for nuclei which can exist indefinitely in the flow, as well as those which are small spherical air bubbles. In the latter form, the nucleus will have a short life and there are situations of

practical interest in which one would not expect such unstable nuclei to be present.

In most cases, the water will contain dissolved air and the nuclei will contain both air and water vapor. As one can see from the literature cited previously by [4–8, 11] a number of physical alternatives have been proposed to explain the existence of persistent nuclei. For our purpose, we will suppose that air or vapor bubbles are attached to small solid particles in the liquid. In this case, we may take the effective surface energy to be zero initially so that the nuclei can exist indefinitely [14], and by Henry's law [15], the partial pressure of air in the gas pocket will be proportional to the concentration of air dissolved in the water. We will characterize the size of the initial gas pocket by an initial effective radius, R_0. At this radius, the "effective surface tension" will be zero.

As the bubble grows from its initial size, it will eventually assume a spherical shape and the effect of surface tension on the gases inside it will be given by $2\sigma/R$, where σ is the coefficient of surface tension. The required behavior of the surface tension may be approximated by $p_\sigma = 2S(R, \sigma)/R$ where the "surface-tension law" $S(R, \sigma)$ is characterized by $S(R_0, \sigma) = 0$ and $S(R_1, \sigma) = \sigma$, in which we let R_1 be that bubble radius at which the surface-tension law first achieves its full value, σ, and further, we let $R_1 = n R_0$ with $n \geq 1$. The simplest assumption which will approximate the complex variation of effective surface tension $S(R, \sigma)$ with bubble growth is that $S(R, \sigma)$ is a linear function of R. Then $S = (R - R_0)\sigma/R_0(n-1)$ for $R_0 \leq R < n R_0$ and $S = \sigma$ when $R \geq n R_0$. If one puts $r \equiv R/R_0$, then the surface-tension law can be written as

$$S = \begin{cases} \dfrac{r-1}{n-1}\sigma & , \quad 1 \leq r < n \quad , \\[2mm] \sigma & , \quad n \leq r \quad . \end{cases} \tag{1}$$

Note that the interval of linearly increasing variation of S with r does not include the dimensionless radius $r = n$. This value of r is included with those values which can also be greater than n because we can then put $n = 1$ and get $S = \sigma$, corresponding to a spherical bubble for all physically attainable values of r.

The surface-tension law of equation (1) is an attempt to account for an average behavior of a large number of nuclei of many possible initial sizes [16]. Compared to the molecular scale, bubble nuclei are macroscopic and ordinary concepts of surface tension for macroscopic systems apply. In order to obtain a stable nucleus, we have introduced another parameter, n, which governs the slope of the linearly increasing part of $S(r, \sigma)$. We are encouraged to ascribe an average behavior to such a large number of nuclei of many possible initial sizes because experiments involving bubble-ring cavitation show that the zone of cavitation numbers at which cavitation starts is quite narrow. Thus, we can approximate the observations by assigning a definite value of the cavitation number for inception (or desinence) for a given flow state.

Critical Bubble Radius After The Initial Vaporous Growth

As we have indicated in previous discussions of steps (c) and (d), we shall take the radius R_m to be the maximum radius attained in the course of vaporous growth. At the same time, it will be required that this radius be such that subsequent growth by air diffusion only is possible. We shall determine this critical condition for further gaseous growth under the assumption that R_m will be so small that the diameter, $2R_m$ is still small enough to avoid immediate interaction between the

cavitation bubble and the free shear layer at the edge of the laminar bubble. The height of the laminar bubble is shown schematically in Fig. 1 with the maximum height, H, being near the downstream end of the laminar separation zone. Measured values of H have been reported by Van der Meulen [12, 17], and by Arakeri [18]. Their data are presented in reference [13] which shows H/D plotted against Re, the Reynolds number based on body diameter, D. Also given in reference [13] is an analytical approximation for these data, namely:

$$\frac{H}{D} = \frac{111}{\text{Re}^{0.79}} \qquad . \qquad (2)$$

The laminar bubble forms a kind of parabolic wedge-shaped region in the flow. Therefore, it may not be appropriate for us to equate the critical bubble diameter directly to the maximum bubble height although this is one alternative to consider. Another is to use one-half of this value and put

$$4 R_m = 111 D/\text{Re}^{0.79} \qquad .$$

for the time being at least. In terms of the dimensionless bubble radius, $r_m \equiv R_m/R_0$, we have

$$r_m = \frac{55.5\theta D}{\text{Re}^{0.79} R_0} \qquad . \qquad (3)$$

where $0.5 \leq \theta \leq 1.0$, is the range of the ratio of bubble diameter to laminar bubble height which is to be considered here. The consequences of using one or the other of these estimates for r_m will be considered elsewhere.

Turning now to the matter of gaseous growth in the laminar separation zone, we will also neglect all convective effects of bubble-wall velocity upon the process of air diffusion into or out of the cavitation bubble. Moreover, we will neglect the effect on diffusion rates of dissolved air convection caused by the main stream over the body. Our interest is restricted to ascertaining whether or not diffusion is possible in the first place, using only the simplest considerations. We shall not be concerned with the rates of air diffusion into or out of the bubble because once gaseous growth starts, the fact that the bubble is sitting in the laminar-separation zone makes the time required for gaseous growth of no importance.

A previous publication [13] presents an analysis of the conditions which are favorable for gaseous microbubble growth in laminar-separation bubbles under the assumptions noted earlier. The major findings resulting from that study can be summarized as follows.

It appears that when there is a laminar-separation bubble on a hemispherical headform, the separation zone can provide a favorable environment for gaseous growth when bubble-ring cavitation or even when band cavitation is observed. We have also found that the gaseous growth must be preceded by a period of vaporous growth which starts in the low-pressure region upstream of the laminar-separation zone. For example, isothermal flaccid microbubbles either will dissolve if they could reach the laminar bubble or they will experience vaporous growth before reaching the laminar separation zone. Moreover, it is found that the most favorable condition for gaseous growth occurs at the time when a bubble, undergoing vaporous growth, just reaches its maximum radius. Therefore, the probability of bubble stabilization at a fixed point in the laminar-separation zone would be highest at this instant. The conditions for subsequent gaseous growth, once the vapor bubble has become fixed on the body, are somewhat more demanding. Nevertheless, it is found that the liquid in the water surrounding the bubble in the separation zone is definitely supersaturated for most flows of experimental or practical interest. Therefore, gaseous growth is almost certain to occur once the vapor bubble is in the separation zone.

In terms of the present considerations, the chief analytical finding for the threshold of subsequent gaseous growth is that

$$r_m = (\gamma - \beta)^{-1} \qquad , \qquad (3a)$$

which is valid only if $r_m \geq n$. In equation (3a), γ is the dimensionless dissolved-air-content parameter,

$$\gamma \equiv p_a R_0/2\sigma \qquad ,$$

and β is another dimensionless parameter characterizing the static pressure in the laminar-separation zone:

$$\beta \equiv (K + C_{p_s})/C_\sigma \qquad ,$$

where the cavitation number K is defined as usual by

$$K \equiv (p_0 - p_v)/\frac{1}{2} \rho V_0^2 \qquad .$$

C_{p_s} is the pressure coefficient at laminar separation,

$$C_{p_s} \equiv (p_s - p_0)/\frac{1}{2} \rho V_0^2$$

and C_σ is related to the Weber number based on initial nucleus size R_0,

$$C_\sigma \equiv 4\sigma/(R_0 \rho V_0^2) \qquad .$$

The value of r_m at the conclusion of vaporous growth must be greater than or equal to the value given by equation (3a) or less than or equal to the value given by equation (3).

We may now turn to the statement for the criterion of cavitation inception.

The Inception Criterion

In view of the foregoing discussion, we can express the basic criterion for a theory of inception as the inequality,

$$n \leq (\gamma - \beta)^{-1} < r_m \leq 55\theta D/\text{Re}^{0.79} R_0 \qquad , \qquad (4)$$

where θ is the ratio of maximum vapor bubble diameter to the maximum laminar bubble height, $\theta \equiv 2R_m/H$.

Although condition (4) is the basic criterion as stated, there is still some need for further interpretation in order to guide its use. For example, condition (4) simply states two facts. The first is that the vaporous growth phase of a typical nucleus will end when the cavitation bubble reaches a *maximum* radius. The second is that this maximum radius is definitely limited. It must be large enough to insure gaseous growth once the microbubble comes to rest in the laminar-separation zone. However, it cannot be very much larger than the laminar-bubble height. If these restrictions are satisfied, bubble-ring cavitation will definitely occur.

Returning to event (b), we must also recognize that the time available for the nucleus to undergo vaporous growth from $r = 1$ to $r = r_m$ is limited by the extent of the region of favorable pressure on the body as well as the magnitude of β. This maximum time for vaporous growth, t_m, is measured from the instant that

$$K + C_p = 0 \qquad ,$$

where $C_p \equiv (p - p_0)1/2 \rho V_0^2$. At this instant, it is convenient to assume that

$$r(0) = 1$$

and

$$\dot{r}(0) = 0 \qquad ,$$

although other more accurate initial conditions can be selected. We have already noted that the cavitation bubble will be carried into the laminar separation bubble and its arrival there establishes the duration, t_m, of vaporous growth of the microbubble. At this time, the radius will also be at its maximum

Conclusion

The establishment of the inception criterion given by the inequality (4) and its subsequent interpretation complete the objective set of this paper. At this point, it can be regarded only as a possible criterion for bubble-ring cavitation inception which must be tested by theoretical findings which follow from it and which can be compared with appropriate experimental results. It is planned to present this final phase of the work in a subsequent paper in which only vaporous growth in the range,

$$1 \leq r \leq r_m \qquad ,$$

need be considered.

Acknowledgment

References

1 Arakeri, V. H., and Acosta, A. J., "Viscous Effects in the Inception of Cavitation on Axisymmetric Bodies," ASME JOURNAL OF FLUIDS ENGINEERING, Vol. 95, No. 4, Dec. 1973, pp. 519–527.

2 Arakeri, V. H., "A Note on the Transition Observation on an Axisymmetric Body and Some Related Fluctuating Wall Pressure Measurements," ASME JOURNAL OF FLUIDS ENGINEERING, Vol. 97, No. 1, Mar., 1975, pp. 82–86.

3 Holl, J. W., and Carroll, J. A., "Observations of the Various Types of Limited Cavitation on Axisymmetric Bodies," International Symposium on Cavitation Inception, The American Society of Mechanical Engineers, New York, Dec., 1979, p. 87.

4 Holl, J. W., "Limited Cavitation," in Cavitation State of Knowledge, ASME United Engineering Center, 345 East 47th Street, New York, 1969, pp. 46–58.

5 Plesset, M. S., "The Tensile Strength of Liquids," in Cavitation State of Knowledge, ASME United Engineering Center, 345 East 47th Street, New York, 1969, pp. 15–25.

6 Beyer, R. T., Nonlinear Acoustics, Naval Sea Systems Command, Department of the Navy, Washington, D.C., 1974, pp. 288–292.

7 Ross, D., Mechanics of Underwater Noise, Pergamon Press, New York, 1976, pp. 202–205.

8 Knapp, R. T., Daily, J. W., and Hammitt, F. H., Cavitation, McGraw-Hill, New York, N.Y. pp. 51–93.

9 Parkin, B. R., "Scale Effects in Cavitating Flow," Report No. 21–8, Hydrodynamics Laboratory, California Institute of Technology, Pasadena, Calif., July 31, 1952.

10 Numachi, F., ed., Cavitation and Hydraulic Machinery, Proceedings of IAHR Symposium Published by the Local Organizing Committe, Sendai, Japan, 1963. See Parkin, B. R., and Kermeen, R. W., "The Roles of Convective Air Diffusion and Liquid Tensile Stresses During Cavitation Inception," pp. 17–36.

11 Gupta, S. K., "The Influence of Porosity and Contact Angle on Incipient and Desinent Cavitation," M.S. thesis, Department of Aerospace Engineering, The Pennsylvania State University, University Park, Pa, 1969.

12 Van der Meulen, J. H. J., "A Holographic Study of the Influence of Boundary Layer and Surface Characteristics on Incipient and Developed Cavitation on Axisymmetric Bodies," Proceedings 12th Symposium on Naval Hydrodynamics, Office of Publications, National Academy of Sciences, 2101 Constitution Ave. NW, Washington, D.C., 1979, pp. 433–451.

13 Parkin, B. R., "Conditions Favorable for Gaseous Microbubble Growth in Laminar Separation Bubbles," Cavitation and Polyphase Flow Forum 1980, The American Society of Mechanical Engineers, United Engineering Center, 345 East 47th Street, New York, pp. 1–6. See also "The Initiation of Gaseous Microbubble Growth in Laminar Separation Bubbles," ASME, JOURNAL OF FLUIDS ENGINEERING, in press.

14 Epstein, P. S., and Plesset, M. S., "On The Stability of Gas Bubbles in Liquid-Gas Solutions," Journal of Chemical Physics, Vol. 18, 1959, pp. 1505–1509.

15 Epstein, P. S., Textbook of Thermodynamics, Wiley, (1937), Chapter IX, p. 159.

16 Gates, E. M., and Bacon, J., "A Note on the Determination of Cavitation Nuclei Distributions by Holography," Journal of Ship Research, Vol. 22, No. 1, Mar., 1978, pp. 29–31.

17 Van der Meulen, J. H. J., "A Holographic Study of Cavitation on Axisymmetric Bodies and the Influence of Polymer Additives," Ph.D. thesis, Enschede, 1976.

18 Arakeri, V. H., "Viscous Effects in Inception and Development of Cavitation on Axi-Symmetric Bodies," Ph.D. thesis, California Institute of Technology, 1973. (Also released as Report No. 3183.1, Division of Engineering and Applied Science, California Institute of Technology, 1973.)

D. A. Drew

R. T. Lahey, Jr.
Mem. ASME

Rensselaer Polytechnic Institute,
Troy, N.Y.   12181

Phase Distribution Mechanisms in Turbulent Two-Phase Flow in Channels of Arbitrary Cross Section

An analytical model for the phase distribution mechanisms in fully developed turbulent two-phase flow in channels of arbitrary cross sections has been derived. The model has been applied to the special case of cylindrical pipe flow, and compared with existing data. It has been found that, for bubbly flow, it is the distribution of the liquid phase turbulence which determines the void distribution. Furthermore, the void distribution depends on the anisotropic nature of the turbulent two-phase flow.

Introduction

The subject of two-phase flow has important practical application in such diverse areas as the petroleum, chemical, and power industries. Recently, the study of the safety of nuclear power reactors has led to an increased demand for understanding two-phase flow systems under a variety of conditions.

Most experimental investigations of two-phase flow have consisted only of the measurement of global parameters, such as static pressure drop and quality. As a consequence, empirical and semiempirical correlations, which are restricted to specific geometries and flow conditions, have attained unusual prominence.

One of the least understood, but most important aspects of two-phase flow, is the multidimensional effects which occur. The constitutive equations needed to complete the set of conservation equations are not yet known, and thus we are currently unable to adequately explain many phenomena of interest, such as flow regime effects and measured rod bundle subchannel void distributions [1].

Two-phase vertical cocurrent bubbly flow in a circular pipe exhibits bubble layers near the wall [2]. This feature of the flow is not due to the method of injection of the vapor phase [3], but is an intrinsic property of the two-phase flow. Beattie [4] has derived void profiles based on a simple momentum balance (i.e., constancy of the Reynolds stress) and an empirical relation between the local void fraction and local liquid phase axial velocity.

The purpose of this paper is to provide a framework for the detailed understanding of two-phase flow multidimensional void distribution mechanisms from the point of view of momentum conservation, and thus to provide a basis with which experimental data can be compared and interpreted.

Discussion

To analyze the mechanisms of phase distribution, it is necessary to derive a model which represents the physical phenomena. We shall derive the analytical model for adiabatic, fully developed turbulent two-component two-phase flow in a channel using the time-averaged conservation equations for mass and momentum.

Ishii [5] has formulated the two-fluid model by considering each phase separately. Following Ishii, we define the time-average of function $\phi(\underline{r},t)$ by,

$$\bar{\phi}(\underline{r},t) = \frac{1}{T}\int_{t-T}^{t}\phi(\underline{r},t')\,dt'$$

The volume fraction of phase-k, α_k, is defined by,

$$\alpha_k = \bar{X}_k$$

where X_k is the phase indicator, or characteristic function, $\underline{r}$, given by:

$$X_k = \begin{cases} 1, & \text{if } \underline{r} \text{ is in phase-}k \\ 0, & \text{otherwise.} \end{cases}$$

The average densities and pressures are defined in terms of the X-weighted average, defined by,

$$\bar{\phi}_k^X = \overline{X_k\phi_k}/\bar{X}_k$$

The average velocities are defined in terms of the $X\rho$-weighted average, defined by,

$$\bar{\phi}_k^{X\rho} = \overline{X_k\rho_k\phi_k}/\overline{X_k\rho_k}$$

The time-averaged equations of conservation of mass and momentum are (dropping the symbols for the averages):

$$\frac{\partial}{\partial t}(\alpha_k\rho_k) + \frac{\partial}{\partial x}(\alpha_k\rho_k u_{x_k}) + \frac{\partial}{\partial y}(\alpha_k\rho_k u_{y_k})$$

$$+ \frac{\partial}{\partial z}(\alpha_k\rho_k u_{z_k}) = \Gamma_k \tag{1}$$

The phasic momentum equation for the x-direction is,

$$\alpha_k \rho_k \left[\frac{\partial u_{x_k}}{\partial t} + u_{x_k} \frac{\partial u_{x_k}}{\partial x} + u_{y_k} \frac{\partial u_{x_k}}{\partial y} + u_{z_k} \frac{\partial u_{x_k}}{\partial z} \right]$$

$$= -\alpha_k \frac{\partial p_k}{\partial x} + \alpha_k \rho_k g_{x_k} + \frac{\partial}{\partial x}[\alpha_k(\tau_{xx_k} + \tau_{xx}^T{}_k)]$$

$$+ \frac{\partial}{\partial y}[\alpha_k(\tau_{xy_k} + \tau_{xy}^T{}_k)] + \frac{\partial}{\partial z}[\alpha_k(\tau_{xz_k} + \tau_{xz}^T{}_k)]$$

$$+ (p_{ki} - p_k) \frac{\partial \alpha_k}{\partial x} + (u_{x_{ki}} - u_{x_k})\Gamma_k + M_{x\,k}^d \qquad (2)$$

for the y-direction,

$$\alpha_k \rho_k \left[\frac{\partial u_{y_k}}{\partial t} + u_{x_k} \frac{\partial u_{y_k}}{\partial x} + u_{y_k} \frac{\partial u_{y_k}}{\partial y} + u_{z_k} \frac{\partial u_{y_k}}{\partial z} \right]$$

$$= -\alpha_k \frac{\partial p_k}{\partial y} + \alpha_k \rho_k g_{y_k} + \frac{\partial}{\partial x}[\alpha_k(\tau_{xy_k} + \tau_{xy}^T{}_k)]$$

$$+ \frac{\partial}{\partial y}[\alpha_k(\tau_{yy_k} + \tau_{yy}^T{}_k)] + \frac{\partial}{\partial z}[\alpha_k(\tau_{yz_k} + \tau_{yz}^T{}_k)]$$

$$+ (p_{k_i} - p_k) \frac{\partial \alpha_k}{\partial y} + (u_{y_{ki}} - u_{y_k})\Gamma_k + M_{y\,k}^d \qquad (3)$$

and for the z-direction,

$$\alpha_k \rho_k \left[\frac{\partial u_{z_k}}{\partial t} + u_{x_k} \frac{\partial u_{z_k}}{\partial x} + u_{y_k} \frac{\partial u_{z_k}}{\partial y} + u_{z_k} \frac{\partial u_{z_k}}{\partial z} \right]$$

$$= -\alpha_k \frac{\partial p_k}{\partial z} + \alpha_k \rho_k g_{z_k} + \frac{\partial}{\partial x}[\alpha_k(\tau_{xz_k} + \tau_{xz}^T{}_k)]$$

$$+ \frac{\partial}{\partial y}[\alpha_k(\tau_{yz_k} + \tau_{yz}^T{}_k)] + \frac{\partial}{\partial z}[\alpha_k(\tau_{zz_k} + \tau_{zz}^T{}_k)]$$

$$+ (p_{k_i} - p_k) \frac{\partial \alpha_k}{\partial z} + (u_{z_{k_i}} - u_{z_k})\Gamma_k + M_{z\,k}^d \qquad (4)$$

Here,

$$\tau^T \overset{\Delta}{=} -\overline{(\underline{u}_k - \tilde{\underline{u}}_k^{X\rho}(\underline{u}_k - \tilde{\underline{u}}_k^{X\rho})}^{x\rho}$$

and,

$$\underline{M}_k = \underline{M}_k{}^p + \underline{M}_k{}^d + \underline{M}^\Gamma$$

where,

$$\Gamma_k \overset{\Delta}{=} -\sum_{\text{disc}} \underline{n}_k \cdot \rho_k (\underline{u}_k - \underline{u}_i)/u_{n_i} T$$

$$\underline{M}_k{}^p = -\sum_{\text{disc}} \underline{n}_k p_k / u_{n_i} T \simeq -p_{k_i} \nabla \alpha_k$$

$$\underline{M}_k{}^d \overset{\Delta}{=} \sum_{\text{disc}} \underline{n}_k \cdot \underline{\underline{\tau}}_k / u_{n_i} T$$

$$\underline{M}_k{}^\Gamma \overset{\Delta}{=} \sum_{\text{disc}} \underline{n}_k \cdot \rho_k (\underline{u}_k - \underline{u}_i) \underline{u}_k / u_{n_i} T \simeq \underline{u}_{k_i} \Gamma_k$$

with Σ_{disc} representing the sum over the totality of interface crossings at point $\underline{r}$, during time interval $t - T \le t' \le t$, and $\underline{n}_k$ is the unit normal exterior to phase-k.

We shall assume vertical flow, thus $g_{z_k} = -g$, $g_{x_k} = g_{y_k} = 0$. We shall also assume that $p_{k_i} = p_k = p$. We shall further assume that $\underline{M}_v^d = b^M (u_{z_l} - u_{z_v}) = -\underline{M}_l^d$. Also, ρ_v and ρ_l will be taken to be constant.

For steady, fully developed, adiabatic, two-component two-phase (i.e., air/water) flows, in which there is no secondary flow structure, the transverse velocities are zero (i.e., $u_{x_k} = u_{y_k} = 0$). In this case, the phasic continuity equations are identically satisfied, and, neglecting viscous effects, the phasic momentum equations can be written [Ishii, 1975], in the x-direction:

$$-\alpha \frac{\partial p}{\partial x} + \frac{\partial}{\partial x}[\alpha \tau_{xx\,v}^T] + \frac{\partial}{\partial y}[\alpha \tau_{xy\,v}^T] = 0 \qquad (5)$$

$$-(1-\alpha) \frac{\partial p}{\partial x} + \frac{\partial}{\partial x}[(1-\alpha)\tau_{xx\,l}^T] + \frac{\partial}{\partial y}[(1-\alpha)\tau_{xy\,l}^T] = 0 \qquad (6)$$

in the y-direction:

$$-\alpha \frac{\partial p}{\partial y} + \frac{\partial}{\partial x}[\alpha \tau_{xy\,v}^T] + \frac{\partial}{\partial y}[\alpha \tau_{yy\,v}^T] = 0 \qquad (7)$$

$$-(1-\alpha) \frac{\partial p}{\partial y} + \frac{\partial}{\partial x}[(1-\alpha)\tau_{xy\,l}^T] + \frac{\partial}{\partial y}[(1-\alpha)\tau_{yy\,l}^T] = 0 \qquad (8)$$

--------- Nomenclature ---------

b^M = interfacial drag coefficient

C_1 = constant of proportionality between liquid and vapor phase Reynolds stresses

C_2 = constant of integration for isotropic pipe flow

$\hat{C}_2$ = constant of integration for nonisotropic pipe flow

$\hat{C}_3$ = constant of integration for flow conduits of arbitrary cross section

$F(\alpha) = \overset{\Delta}{=} \ln [\alpha^q / (1 - \alpha)]$

$F_{ij}(x,y) = \overset{\Delta}{=} \overline{(u_{i_l}{}' u_{j_l}{}')} / [\overline{(u_{xl}')^2} + \overline{(u_{y_l}')^2} + \overline{(u_{z_l}')^2}]$

g_{ik} = gravitational acceleration component of phase-k in i-direction

g = gravitational acceleration

$G(\alpha, K_l) = \overset{\Delta}{=} \ln \{\alpha^q / [(1-\alpha)K_l^{1-q}]\}$

i, j = coordinates $(x,y,z$ or $r,\theta,z)$

$I(x,y)$ = anisotropy function

k = phase indicator $(l = $ liquid, $v = $ vapor)

K_k = turbulent kinetic energy of phase-k

j_l = liquid phase superficial velocity

M_{ik}^d = interfacial drag on phase-k in ith direction

p_k = pressure of phase-k

p_{ki} = interfacial pressure of phase-k

$q = \overset{\Delta}{=} C_1 \dfrac{\rho_V}{\rho_l}$

r = radial position

R = radius of pipe

t = time

u_{jk} = velocity of phase-k in j-direction

u_{jk_i} = interfacial velocity of phase-k in j-direction

$u'_{j\,k}$ = velocity fluctuation of phase-k in j-direction

x,y,z = Cartesian coordinates (z is in axial direction)

X = flow quality

X_k = phase indicator function

α = vapor volume fraction (i.e., void fraction)

α_k = volume fraction of phase-k

Γ_k = interfacial mass transfer rate of phase-k (per unit volume)

Θ = aximuthal angle

ρ_k = density of phase-k

τ_{ij_k} = viscous stress of phase-k

$\tau_{ij\,k}^T$ = turbulent Reynolds stress of phase-k

Subscripts

1ϕ = single-phase

2ϕ = two-phase

in the z direction:

$$-\alpha \frac{\partial p}{\partial z} - \alpha \rho_v g + \frac{\partial}{\partial x}[\alpha \tau_{xz\,v}^T] + \frac{\partial}{\partial y}[\alpha \tau_{yz\,v}^T]$$
$$+ b^M (u_{z_l} - u_{z_v}) = 0 \qquad (9)$$

$$-(1-\alpha)\frac{\partial p}{\partial z} - (1-\alpha)\rho_l g + \frac{\partial}{\partial x}[(1-\alpha)\tau_{xz\,l}^T]$$

$$+ \frac{\partial}{\partial y}[(1-\alpha)\tau_{yz\,l}^T] + b^M (u_{z_v} - u_{z_l}) = 0 \qquad (10)$$

It should be noted that equations (5)–(8) involve α, p, and the x and y-components of the Reynolds stresses.

We can eliminate the pressure gradient from equations (5)–(8) by multiplying equations (6) and (8) by $\alpha/(1-\alpha)$ and subtracting the result from equations (5) and (7), respectively. The resulting equations are,

$$\frac{\partial}{\partial x}[\alpha \tau_{xx\,v}^T] + \frac{\partial}{\partial y}[\alpha \tau_{xy\,v}^T] - \frac{\alpha}{(1-\alpha)}\frac{\partial}{\partial x}[(1-\alpha)\tau_{xx\,l}^T]$$

$$- \frac{\alpha}{(1-\alpha)}\frac{\partial}{\partial y}[(1-\alpha)\tau_{xy\,l}^T] = 0 \qquad (11)$$

$$\frac{\partial}{\partial x}[\alpha \tau_{xy\,v}^T] + \frac{\partial}{\partial y}[\alpha \tau_{yy\,v}^T] - \frac{\alpha}{(1-\alpha)}\frac{\partial}{\partial x}[(1-\alpha)\tau_{xy\,l}^T]$$

$$- \frac{\alpha}{(1-\alpha)}\frac{\partial}{\partial y}[(1-\alpha)\tau_{yy\,l}^T] = 0 \qquad (12)$$

These equations relate the turbulence structure to the void profile. If we expand out equations (11) and (12), we obtain,

$$\left(\tau_{xx\,v}^T + \frac{\alpha}{(1-\alpha)}\tau_{xx\,l}^T\right)\frac{\partial \alpha}{\partial x} + \left(\tau_{xy\,v}^T + \frac{\alpha}{(1-\alpha)}\tau_{xy\,l}^T\right)\frac{\partial \alpha}{\partial y}$$

$$+ \alpha\left\{\frac{\partial \tau_{xx\,v}^T}{\partial x} - \frac{\partial \tau_{xx\,l}^T}{\partial x} + \frac{\partial \tau_{xy\,v}^T}{\partial y} - \frac{\partial \tau_{xy\,l}^T}{\partial y}\right\} = 0 \qquad (13a)$$

and,

$$\left(\tau_{xy\,v}^T + \frac{\alpha}{(1-\alpha)}\tau_{xy\,l}^T\right)\frac{\partial \alpha}{\partial x} + \left(\tau_{yy\,v}^T + \frac{\alpha}{(1-\alpha)}\tau_{yy\,l}^T\right)\frac{\partial \alpha}{\partial y}$$

$$+ \alpha\left\{\frac{\partial \tau_{xy\,v}^T}{\partial x} - \frac{\partial \tau_{xy\,l}^T}{\partial x} + \frac{\partial \tau_{yy\,v}^T}{\partial y} - \frac{\partial \tau_{yy\,l}^T}{\partial y}\right\} = 0 \qquad (13b)$$

Let us assume that the turbulent structure of the vapor phase is proportional to that of the liquid phase. That is, let us assume,

$$\overline{u_{iv}' u_{jv}'}^{X_\rho} = C_1 \overline{u_{il}' u_{jl}'}^{X_\rho} \qquad (14)$$

which can be more conveniently written as,

$$\tau_{ij\,v}^T = \frac{\rho_v}{\rho_l} C_1 \tau_{ij\,l}^T \triangleq q\tau_{ij\,l}^T \qquad (15)$$

where C_1 is not a function of the local dependent variables, but is likely a function of the cross sectionally averaged void fraction, $<\alpha>$, and perhaps the flow rate.

Assumption (14) is a reflection of the strong coupling expected between the motions of the separate phases. For low-quality bubbly flows, most of the gas phase velocity fluctuations are due to the tendency for the bubbles to follow the liquid phase velocity fluctuations. In this low-quality range, we expect $C_1 \simeq 1$. Serizawa's data [2] on the gas phase velocity fluctuations confirms this, and further indicate that C_1 increases with increasing quality. For higher quality flows, however, there are other considerations. First, Serizawa's gas velocity fluctuation data must be treated with caution, since his experimental technique was based on the measurement of interface crossings, and thus cannot capture all the gas phase velocity fluctuations. Second, the assumption that equation

(14) is valid assumes that the bubbles are smaller than the integral scale of the turbulence, since it has been assumed that the liquid phase turbulence drives the bubble fluctuations.

The implication of equation (14) is that the vapor turbulent stresses are negligible compared with those of the liquid. Indeed, perturbing q produced no appreciable effect on the solutions of the equations, as long as C_1 was of order one.

Combining equation (15) with equations (13a) and (13b), and dividing through by α, we obtain,

$$\tau_{xx\,l}^T\left\{q/\alpha + \frac{1}{(1-\alpha)}\right\}\frac{\partial \alpha}{\partial x} + \tau_{xy\,l}^T\left\{q/\alpha + \frac{1}{(1-\alpha)}\right\}\frac{\partial \alpha}{\partial y}$$

$$+ (q-1)\left\{\frac{\partial \tau_{xx\,l}^T}{\partial x} + \frac{\partial \tau_{xy\,l}^T}{\partial y}\right\} = 0 \qquad (16a)$$

$$\tau_{xy\,l}^T\left\{q/\alpha + \frac{1}{(1-\alpha)}\right\}\frac{\partial \alpha}{\partial x} + \tau_{yy\,l}^T\left\{q/\alpha + \frac{1}{(1-\alpha)}\right\}\frac{\partial \alpha}{\partial y}$$

$$+ (q-1)\left\{\frac{\partial \tau_{xy\,l}^T}{\partial x} + \frac{\partial \tau_{yy\,l}^T}{\partial y}\right\} = 0 \qquad (16b)$$

Equations (16a) and (16b) can be conveniently rewritten in terms of the variable $F(\alpha)$, where,

$$F(\alpha) \triangleq \ln\left[\frac{\alpha^q}{(1-\alpha)}\right] \qquad (17)$$

combining equations (16) and (17) we obtain,

$$\tau_{xx\,l}^T \frac{\partial F(\alpha)}{\partial x} + \tau_{xy\,l}^T \frac{\partial F(\alpha)}{\partial y} = (1-q)\left\{\frac{\partial \tau_{xx\,l}^T}{\partial x} + \frac{\partial \tau_{xy\,l}^T}{\partial y}\right\} \qquad (18a)$$

$$\tau_{xy\,l}^T \frac{\partial F(\alpha)}{\partial x} + \tau_{yy\,l}^T \frac{\partial F(\alpha)}{\partial y} = (1-q)\left\{\frac{\partial \tau_{xy\,l}^T}{\partial x} + \frac{\partial \tau_{yy\,l}^T}{\partial y}\right\} \qquad (18b)$$

If we multiply equation (18a) by τ_{yy}^T and equation (18b) by τ_{xy}^T and subtract, the resulting equation is,

$$\frac{\partial F(\alpha)}{\partial x} = \frac{(1-q)}{[\tau_{xx\,l}^T \tau_{yy\,l}^T - (\tau_{xy\,l}^T)^2]}\left\{\tau_{yy\,l}^T \frac{\partial \tau_{xx\,l}^T}{\partial x}\right.$$

$$\left. + \tau_{yy\,l}^T \frac{\partial \tau_{xy\,l}^T}{\partial y} - \tau_{xy\,l}^T \frac{\partial \tau_{xy\,l}^T}{\partial x} - \tau_{xy\,l}^T \frac{\partial \tau_{yy\,l}^T}{\partial y}\right\} \qquad (19a)$$

Similarly, if we multiply equation (18a) by $\tau_{xy\,l}^T$, and subtract it from equation (18b), times $\tau_{xx\,l}^T$, we obtain,

$$\frac{\partial F(\alpha)}{\partial y} = \frac{(1-q)}{[\tau_{xx\,l}^T \tau_{yy\,l}^T - (\tau_{xy\,l}^T)^2]}\left\{\tau_{xx\,l}^T \frac{\partial \tau_{yy\,l}^T}{\partial y}\right.$$

$$\left. + \tau_{xx\,l}^T \frac{\partial \tau_{yx\,l}^T}{\partial y} - \tau_{xy\,l}^T \frac{\partial \tau_{xy\,l}^T}{\partial y} - \tau_{xy\,l}^T \frac{\partial \tau_{xx\,l}^T}{\partial x}\right\} \qquad (19b)$$

At this point, it is convenient to introduce some additional notation for the turbulence terms. The total turbulent kinetic energy of the liquid phase is given by,

$$K_l \triangleq \frac{1}{2}\rho_l[\overline{(u_x'{}_l)^2} + \overline{(u_y'{}_l)^2} + \overline{(u_z'{}_l)^2}] \qquad (20)$$

while the ratio of the turbulent kinetic energy in a given direction, to the total turbulent kinetic energy, is defined as,

$$F_{xx}(x,y) \triangleq \overline{(u_x'{}_l)^2}/[\overline{(u_x'{}_l)^2} + \overline{(u_y'{}_l)^2} + \overline{(u_z'{}_l)^2}] \qquad (21a)$$

$$F_{xy}(x,y) \triangleq \overline{u_x'{}_l u_y'{}_l}/[\overline{(u_x'{}_l)^2} + \overline{(u_y'{}_l)^2} + \overline{(u_z'{}_l)^2}] \qquad (21b)$$

$$F_{yy}(x,y) \triangleq \overline{(u_y'{}_l)^2}/[\overline{(u_x'{}_l)^2} + \overline{(u_y'{}_l)^2} + \overline{(u_z'{}_l)^2}] \qquad (21c)$$

Using equations (11), (20), and (21) we can write,

$$\tau_{xx\,l}^T = -2K_l F_{xx} \qquad (22a)$$

$$\tau_{xy\,l}^T = -2K_l F_{xy} \qquad (22b)$$

$$\tau^T_{yy\,l} = -2K_l F_{yy} \tag{22c}$$

Combining equations (22) with equation (19a), we obtain (after some algebra),

$$\frac{\partial F}{\partial x} = \frac{(1-q)}{K_l}\frac{\partial K_l}{\partial x} + \frac{(1-q)}{[F_{xx}F_{yy}-F_{xy}^2]}\left\{ F_{yy}\frac{\partial F_{xx}}{\partial x} \right.$$
$$\left. + F_{yy}\frac{\partial F_{xy}}{\partial y} - F_{xy}\frac{\partial F_{xy}}{\partial x} - F_{xy}\frac{\partial F_{yy}}{\partial y} \right\} \tag{23a}$$

Similarly, equation (19b) becomes,

$$\frac{\partial F}{\partial y} = \frac{(1-q)}{K_l}\frac{\partial K_l}{\partial y} + \frac{(1-q)}{[F_{xx}F_{yy}-F_{xy}^2]}\left\{ F_{xx}\frac{\partial F_{yy}}{\partial y} \right.$$
$$\left. + F_{xx}\frac{\partial F_{xy}}{\partial x} - F_{xy}\frac{\partial F_{xy}}{\partial y} - F_{xy}\frac{\partial F_{xx}}{\partial x} \right\} \tag{23b}$$

Equations (23) can be written more compactly if we define a new parameter, G, which is given by,

$$G \triangleq F(\alpha) - \ln K_l^{1-q} = \ln\left\{ \frac{\alpha^q}{(1-\alpha)K_l^{1-q}} \right\} \tag{24}$$

Combining equations (23) and (24), and noting that,

$$\frac{\partial G}{\partial x_i} = \frac{\partial F}{\partial x_i} - \frac{(1-q)}{K_l}\frac{\partial K_l}{\partial x_i}$$

we obtain,

$$\frac{\partial G}{\partial x} = \frac{(1-q)}{[F_{xx}F_{yy}-F^2_{xy}]}\left\{ F_{yy}\frac{\partial F_{xx}}{\partial x} + F_{yy}\frac{\partial F_{xy}}{\partial y} - F_{xy}\frac{\partial F_{xy}}{\partial x} \right.$$
$$\left. - F_{xy}\frac{\partial F_{yy}}{\partial y} \right\} \tag{25a}$$

and,

$$\frac{\partial G}{\partial y} = \frac{(1-q)}{[F_{xx}F_{yy}-F_{xy}^2]}\left\{ F_{xx}\frac{\partial F_{yy}}{\partial y} + F_{xx}\frac{\partial F_{xy}}{\partial x} - F_{xy}\frac{\partial F_{xy}}{\partial y} \right.$$
$$\left. - F_{xy}\frac{\partial F_{xx}}{\partial x} \right\} \tag{25b}$$

Let us recall from the definition of a line integral,

$$G(x,y) = G(x_0,y_0) + \int_{x_0,y_0}^{x,y}\left\{ \frac{\partial G}{\partial x}dx + \frac{\partial G}{\partial y}dy \right\} \tag{26}$$

thus, combining equations (25) and (26),

$$G(x,y) = G(x_0,y_0) - (1-q)I(x,y) \tag{27}$$

where,

$$I(x,y) = -\int_{x_0,y_0}^{x,y}\frac{1}{[F_{xx}F_{yy}-F_{xy}^2]}\left\{ F_{yy}\frac{\partial F_{xx}}{\partial x} \right.$$
$$\left. + F_{yy}\frac{\partial F_{xy}}{\partial y} - F_{xy}\frac{\partial F_{xy}}{\partial x} - F_{xy}\frac{\partial F_{yy}}{\partial y} \right\}dx$$
$$+ \left\{ F_{xx}\frac{\partial F_{yy}}{\partial y} + F_{xx}\frac{\partial F_{xy}}{\partial x} - F_{xy}\frac{\partial F_{xy}}{\partial y} - F_{xy}\frac{\partial F_{xx}}{\partial x} \right\}dy \tag{28}$$

Combining equations (24) and (27), and taking the exponential of the resultant equation,

$$\frac{\alpha^q}{(1-\alpha)} = \hat{C}_3 K_l^{1-q} e^{-(1-q)I(x,y)} \tag{29}$$

where,

$$C_3 = e^{G(x_0,y_0)} \tag{30}$$

Since $q \ll 1$, the relation between α and K_l given by equation (29) is quite insensitive to the value of q. Thus, mines the lateral void distribution.

It is also interesting to note that $I(x,y)$ is a line integral

which quantifies the amount of anisotropy in the turbulent structure. For the special case of isotropic flow,

$$F_{xx} = F_{yy} = 1/3 \tag{31a}$$

and,

$$F_{xy} = 0 \tag{31b}$$

Thus, for isotropic turbulence, equation (28) implies,

$$I(x,y) = 0 \tag{32}$$

and equation (29) reduces to,

$$\frac{\alpha^q}{(1-\alpha)} = \hat{C}_3 K_l^{1-q} \tag{33}$$

In order to evaluate $I(x,y)$ for the more general case of nonisotropic turbulence, we must have information on, $\overline{(u'_{x_l})^2}$, $\overline{(u'_{y_l})^2}$, $\overline{(u'_{z_l})^2}$ and, $\overline{u'_{x_l}u'_{y_l}}$.

Application to Pipe Flow

Serizawa, et al. [2], have made detailed measurements in axisymmetric turbulent two-phase air/water flow in a circular pipe. To be able to use their data, it is convenient to express equation (29) in terms of the polar coordinates r and θ, where,

$$x = r\cos\theta \tag{34a}$$
$$y = r\sin\theta \tag{34b}$$

This can be done by converting $I(x,y)$ to polar coordinates. This conversion is straightforward, but rather lengthy and tedious. It is much easier to proceed directly from the radial momentum equations to the corresponding result. We shall do this here. First, the radial momentum equation for the gas phase, corresponding to equations (5) and (7), is,

$$-\alpha\frac{\partial p}{\partial r} + \frac{d}{dr}[\alpha\tau^T_{rr_v}] + \frac{1}{r}\alpha[\tau^T_{rr_v} - \tau^T_{\theta\theta_v}] = 0 \tag{35}$$

and for the liquid phase,

$$-(1-\alpha)\frac{\partial p}{\partial r} + \frac{d}{dr}[(1-\alpha)\tau^T_{rr_l}] + \frac{1}{r}(1-\alpha)[\tau^T_{rr_l}$$
$$- \tau^T_{\tau\tau_l}] = 0 \tag{36}$$

The pressure gradient, $\partial p/\partial r$, can be eliminated as before by subtracting $\alpha/(1-\alpha)$ times equation (36) from equation (35). Also, if we assume the equality in equation (14), and define,

$$K_l \triangleq \frac{1}{2}\rho_l[\overline{(u_{r_l'})^2} + \overline{(u_{\theta_l'})^2} + \overline{(u_{z_l'})^2}] \tag{37}$$

$$F_{rr} \triangleq \overline{(u_{r_l'})^2}/[\overline{(u_{r_l'})^2} + \overline{(u_{\theta_l'})^2} + \overline{(u_{z_l'})^2}] \tag{38a}$$

$$F_{\theta\theta} \triangleq \overline{(u_{\theta_l'})^2}/[\overline{(u_{r_l'})^2} + \overline{(u_{\theta_l'})^2} + \overline{(u_{z_l'})^2}] \tag{38b}$$

We obtain,

$$\frac{dG}{dr} \triangleq \frac{d}{dr}\left[\ln\left(\frac{\alpha^q}{(1-\alpha)K_l^{1-q}}\right)\right] = (1-q)\left\{ \frac{F_{\theta\theta}-F_{rr}}{rF_{rr}} \right.$$
$$\left. + \frac{dF_{rr}/dr}{F_{rr}} \right\} \tag{39}$$

which is analogous to equations (25).

Integrating equation (39) with respect to r gives,

$$\frac{\alpha^q}{(1-\alpha)K_l^{1-q}} = \hat{C}_2 F_{rr}^{1-q}\exp\left[-(1-q)\int_R^r \right.$$
$$\left. \frac{F_{\theta\theta}(r')-F_{rr}(r')}{r'F_{rr}(r')}dr' \right] \tag{40}$$

where $\hat{C}_2$ is the constant of integration. We see that equations (40) and (29) have the same functional form.

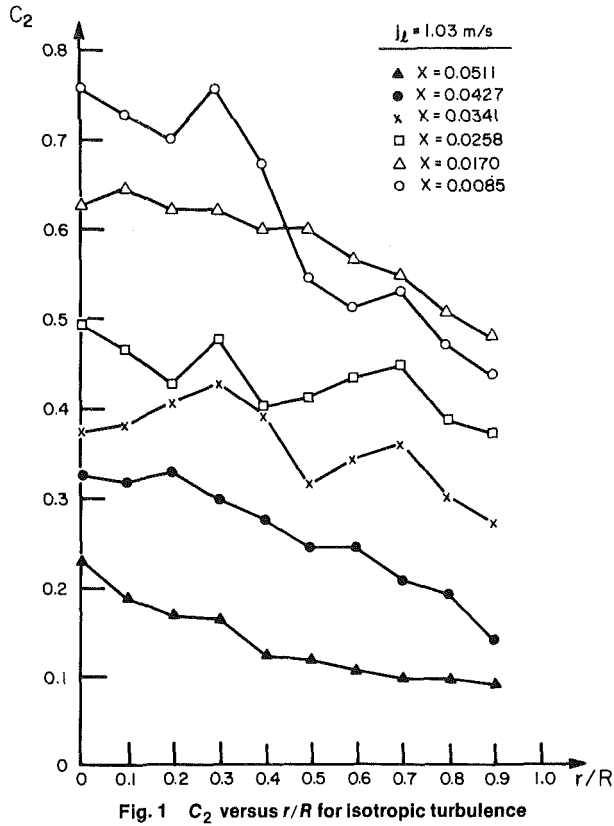Unfortunately, there exist very little data on the turbulence

Fig. 1 C_2 versus r/R for isotropic turbulence

Fig. 2   Laufer's data (1954) in terms of $F_i(r)$

Fig. 3 $\hat{C}_2$ evaluated using the data of Laufer (1954)

structure of two-phase flows. However, let us now compare equation (40) with those data which do exist. The most comprehensive set of data in the literature is that of Serizawa, et al. [4]. In Serizawa's experiment, a bubbly air/water, two-phase mixture at atmospheric pressure flowed upward in a vertical pipe of 60 mm dia. Local turbulence and void fraction data were taken at different axial positions in the pipe with various probes.

While not enough measurements were made to completely define the anisotropic structure of the liquid phase turbulence, they did measure the radial void fraction and phasic velocity fluctuations in the axial direction. Since Serizawa, et al., did not measure the phasic velocity fluctuations in the other directions, it was not possible to directly calculate the functions $F_{rr}(r)$ and $F_{\theta\theta}(r)$ needed to completely verify equation (40). We have therefore investigated the implications of various assumptions about the turbulence structure. This was accomplished using reasonable assumptions about the functions F_{rr} and $F_{\theta\theta}$, and employing Serizawa's data for $\alpha(r)$ and $K_{z_l}(r)$. The parameter q was taken to be 0.001. The constant of integration, $\hat{C}_2$, was calculated from Serizawa's data on α and the assumptions about the F's, and was plotted as a function of r/R. If the parameter $\hat{C}_2$ was independent of radial position (as it must be), then it was assumed that the F_{rr} and $F_{\theta\theta}$ chosen were correct.

The most obvious assumption to try first is isotropy. For this case,

$$F_{rr} = F_{\theta\theta} = \frac{1}{3} \qquad (41)$$

and,

$$C_2 \triangleq \hat{C}_2 3^{-(1-q)} \qquad (42)$$

Figure 1 shows the result if the turbulent structure is assumed to be isotropic. It is obvious that the constant of integration $(\hat{C}_2)$ is not radially constant, and thus the isotropic assumption is not valid. Moreover, void profiles
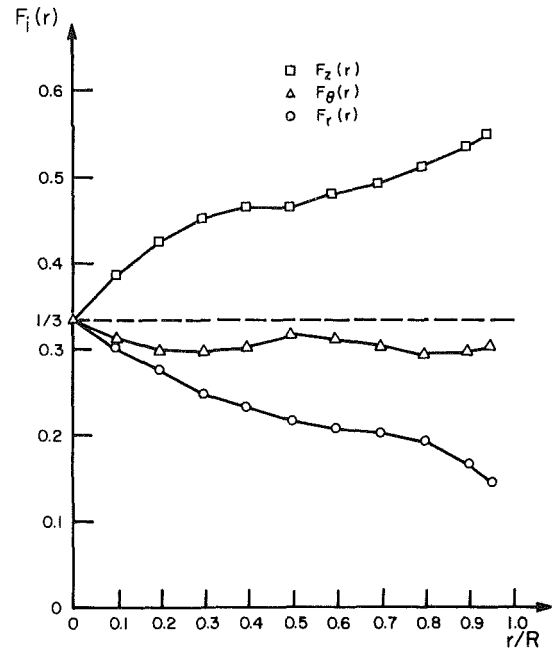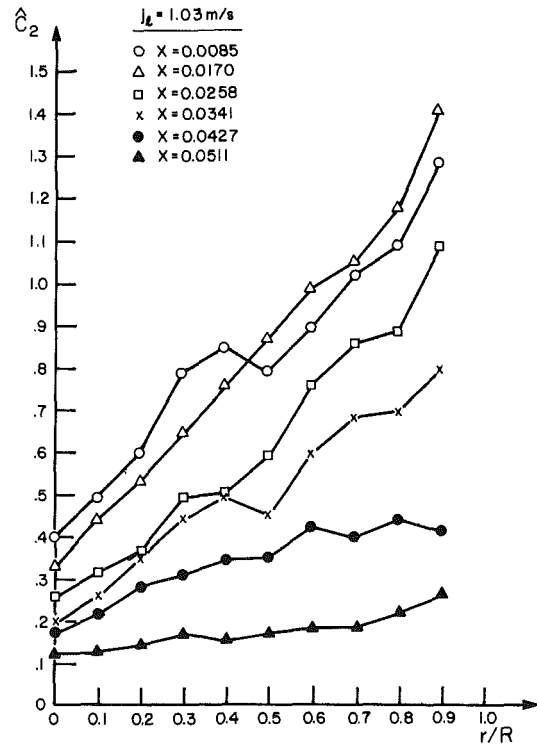
predicted from the isotropic assumption were not physically reasonable.

A less obvious assumption about the turbulence structure is that it has the same F-values as in single-phase pipe flow. While this has no more basis than assuming isotropy, the two drastically different cases seem to bracket the data, and suggest that the actual degree of anisotropy lies between. Thus, let us assume that the $F_{rr}(r)$ and $F_{\theta\theta}(r)$ can be determined by using Laufer's single-phase turbulence data [6]. These data imply F_{rr} and $F_{\theta\theta}$ which are shown in Fig. 2. The resultant constants of integration $(\hat{C}_2)$ are shown in Fig. 3.
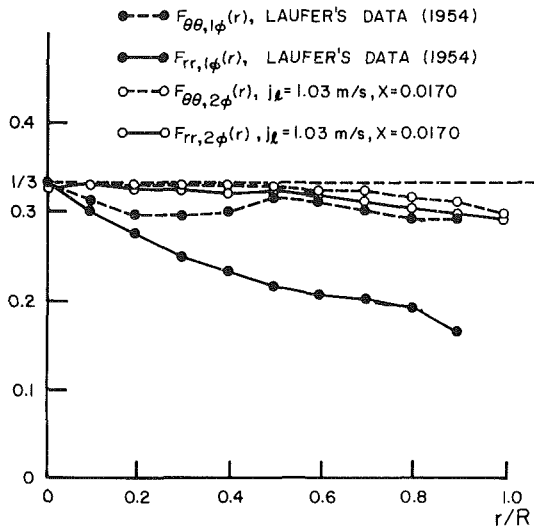
Fig. 4 Comparison of $F_{i,1\phi}(r)$ and $F_{i,2\phi}(r,X,jl)$

Fig. 5 $\hat{C}_2$ versus r/R for $j_l = 1.03$ m/s

Comparison of Figs. 1 and 3 indicates that the correct assumption about the two-phase turbulent structure lies somewhere between isotropic and single-phase anisotropic turbulence. That is, in Fig. 3, $\hat{C}_2$ increases, rather than decreases, with radial position as in Fig. 1. Thus the appropriate two-phase turbulence is obviously more isotropic than the corresponding single-phase turbulence, but is clearly not isotropic. It appears that the presence of the bubbles breaks up the large eddy structure characterizing single-phase turbulence, resulting in less anisotropy.

In order to better appreciate the effect of the anisotropy, an optimization analysis was performed using interactive graphics [7]. Using this technique, we were able to make $\hat{C}_2$ radially constant by optimizing $F_{rr}(r)$ and $F_{\theta\theta}(r)$ for each cross-sectionally averaged flow quality X. A typical determination of the functions $F_{rr}(r)$ and $F_{\theta\theta}(r)$ is shown in Fig. 4. The corresponding results for $\hat{C}_2$ are shown in Fig. 5, and are seen to be radially independent. We note that $\hat{C}_2 = \hat{C}_2(<\alpha>,j_l)$, where j_l is the superficial velocity of the liquid phase.

Figure 6 shows the comparison of $\alpha(r)$ for various X, as predicted by equation (40), using the functions $F_{rr}(r)$ and $F_{\theta\theta}(r)$ deduced using interactive graphics. It is obvious that equation (40) captures the observed data trends when a reasonable turbulent structure is assumed.

Summary and Conclusions

The mechanisms involved in lateral void distribution in two-phase flows are complex on the microscopic scale, and involve interactions of the phasic flow fields, the pressure distribution, and the wall. Nonetheless, an exact analytical expression relating the time-averaged radial void distribution to the turbulence structure of the continuous phase has been derived for fully-developed, adiabatic two-phase flows, in conduits of arbitrary cross section. Thus, in spite of the complex microscopic processes, the radial void distribution can be predicted from an adequate model of the turbulence structure.

It appears that the void distribution in channels with arbitrary cross section is governed by the anisotropic nature of the turbulent two-phase flow. From examining axisymmetric pipe flow, we conclude an adequate model for the anisotropy is important for predicting the void distribution. However, for two-component bubbly flows, the void distribution is well described by the model proposed herein.

For the special case of axisymmetric flow in a cylindrical pipe, the corresponding expression relating the void profile to
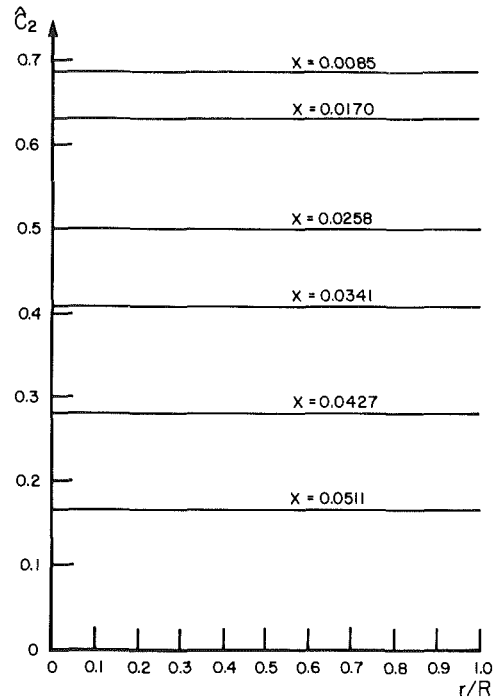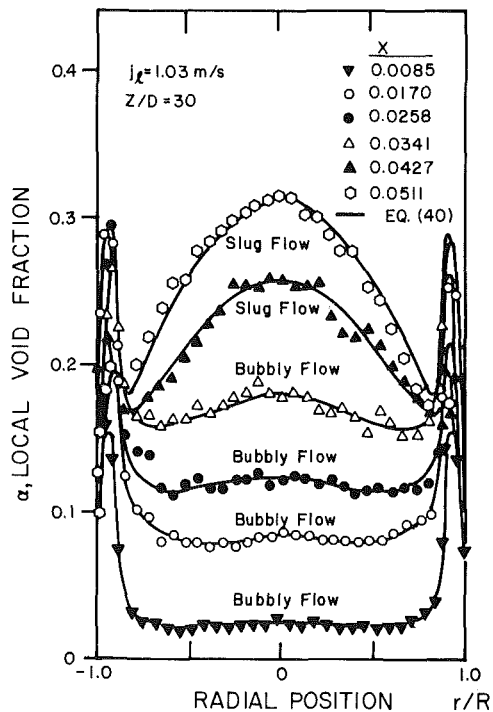

Fig. 6 Predicted void fraction, $\alpha(r)$, profiles for $j_l = 1.03$ m/s (data of Serizawa, et al., 1976)

the turbulence structure is given, and shown to be consistent when compared with existing data. However, more complex information about the turbulence structure is required to predict the void profile both in the axisymmetric pipe and in arbitrary cross sections. This suggests that more work on two-phase turbulence structure is needed to have a fully predictive void profile equation. It is hoped that future experimental work will provide the necessary data for complete verification of the model.

Acknowledgment

References

1 Lahey, R. T., Jr., Shiralkar, B. S., and Radcliffe, D. W., 1971, "Mass Flux and Enthalpy Distribution in a Rod Bundle for Single and Two-Phase Flow Conditions," ASME *Journal of Heat Transfer*.

2 Serizawa, A., Kataoka, I., and Michiyoshi, I., 1976, "Turbulent Structure of Air/Water Bubbly Flow," *International Journal of Multiphase Flow*, Vol. 2.

3 Herringe, R. A., and Davis, M. R., 1976, "Structural Development of Gas-Liquid Mixture Flows," *Journal of Fluid Mechanics*, Vol. 73.

4 Beattie, D. R. H., 1972, "Two-Phase Flow Structure and Mixing Length Theory," *Nuclear Engineering and Design*, Vol. 21.

5 Ishii, M., 1975, *Thermo-Fluid Dynamic Theory of Two-Phase Flow*, Eyrolles.

6 Laufer, J., 1954, NACA Technical Report 1174.

7 Drew, D. A., Lahey, R. T., Jr., and Sim, S., 1978, "Radial Phase Distribution Mechanisms in Two-Phase Flow," *Proc. OECD* (NEA) CSNI Report No. 31.

A Four Hole Pressure Probe for Fluid Flow Measurements in Three Dimensions

I. C. Shepherd

Experimental Officer,
Division of Mechanical Engineering,
Commonwealth Scientific and Industrial
Research Organization,
Highett, Victoria, Australia

A pressure probe which facilitates measurement of mean flow quantities in three dimensions simultaneously is described. Its main feature is a tip shaped like the frustrum of a pyramid, with three-side holes equispaced around a central hole. Flow quantities are related to the hole pressures by calibration, so that the tedious procedure of nulling or pressure balancing can be avoided. The advantages of this configuration over five-hole probes are that a simpler probe with a smaller head results, fewer pressures need to be recorded and because no redundant information is collected, determination of the dependent flow quantities is simpler and unambiguous.

Introduction

Multihole pressure probes have been used in various forms over many years for measurements of mean fluid velocity and direction [1]. Probes with four equispaced side holes around a central hole (five-hole probes) are commonly used where measurements are to be made in three dimensions [1-4].

Originally, a technique of rotating the probe until the pressures on opposite side holes are balanced was employed with five-hole probes [1]. Thus, four symmetrically disposed side holes were preferred. Pressure probes have also been operated at fixed orientation; the flow angles, velocity, and total pressure being calculated from the hole pressures using relationships which are predetermined by calibration [2-5]. This technique involves a large amount of work in calibration but since tedious rotations to balance pressures are not required, a calibrated probe is very quick and convenient to use, particularly when an automated data collection system is available. Furthermore, inaccuracies in probe construction, which would produce errors with a nulling technique, are accounted for by calibration. Some methods [6] use a combination of nulling and calibration.

The practice of using five pressure holes for three dimensional probes involves redundant information. Since there are only four independent quantities to be measured, say, two direction angles, speed, and total pressure, it is possible to determine them with only four measurements of pressure provided that the pressures measured are independent values, that is, none can be determined from the other three.

The advantages of a four-hole probe over a five-hole probe are that less measurements need to be made during operation and calibration of the probe, a simpler probe with a smaller head can be produced, less pressure measurements are required, and since no redundant information is collected, determination of the dependent flow values is simpler and unambiguous.

This paper describes the design, calibration, and use of a four-hole pressure probe for measurement of flow direction, speed, and total pressure in three dimensions.

Probe Design

Details of the probe construction are shown in Fig. 1. A "cobra" configuration was chosen to allow rotation about the shaft axis without altering the measuring position. This feature is of considerable advantage during calibration and it allows selection of the most suitable region of the calibration function during measurement.

A central hole gives accurate measurements of total pressure. At low incidence angles, the pressure recorded at the central hole is close to the total pressure and therefore error in the calibrated difference is less critical. Equal spacing of the remaining three holes around the central hole gives the most nearly uniform angular sensitivity.

Although its sensitivity is reportedly less, a pyramidal shaped head was chosen instead of a spherical or conical head for several reasons. It is relatively easy to manufacture, accurate location of the side holes is less critical because of the absence of steep pressure gradients over most of the flat area in which the hole is located [1], and the positive location of flow separation at the junctions of the flat surfaces insures minimal sensitivity to Reynolds number [1].

The side hole surfaces were ground flat to 45 deg to give maximum angular sensitivity at low incidence angles.

Calibration Functions

Pitch and yaw α and θ, shown in Fig. 2, were chosen as measures of relative flow direction. This allowed θ to be varied (without altering α) by rotating the probe about its axis, a feature which is convenient.
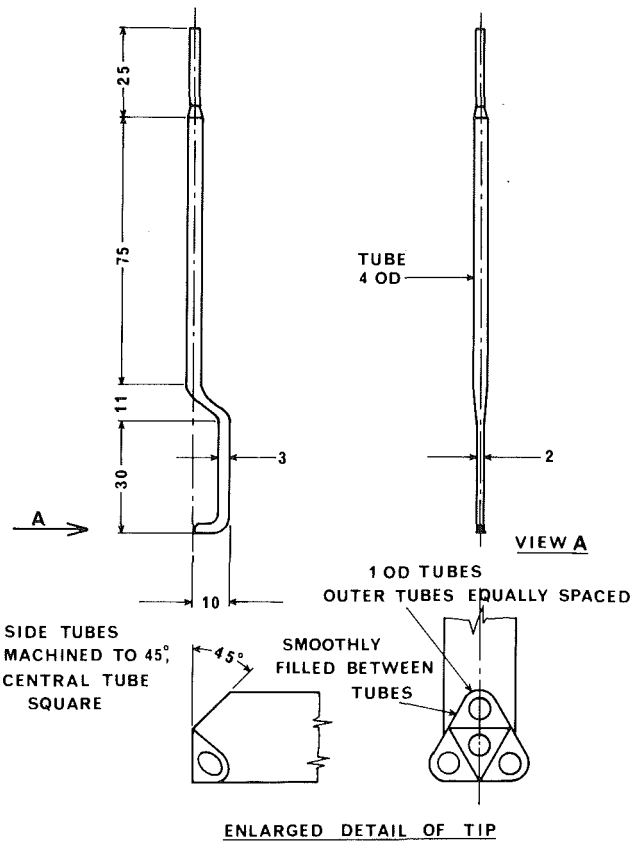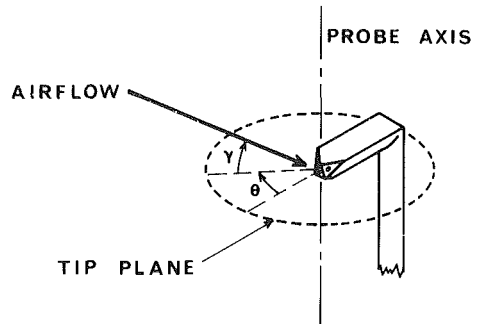
Fig. 1 Details of probe construction

Fig. 2 Convention for flow angles

p_1, p_2, and p_3 in order of decreasing magnitudes, the dimensionless ratios

$$X_1 = \frac{p_2 - p_3}{p_0 - p_3} \qquad (2)$$

$$X_2 = \frac{p_1 - p_2}{p_0 - p_3} \qquad (3)$$

$$X_D = \frac{\frac{1}{2}\rho u^2}{p_0 - p_3} \qquad (4)$$

and

$$X_T = \frac{p_T - p_0}{p_0 - p_3} \qquad (5)$$

will be independent positive finite values. Note that because of the zoning convention, the common denominator $p_0 - p_3$ can never be zero or negative. Because of the choice of numerators in X_1 and X_2, each zone corresponds to a quadrant in the X_1, X_2 plane.

The influence of Reynolds number on the foregoing ratios is expected to be small for values of Reynolds number greater than 1500 (based on the outside dimension of the tip) [1]. Thus for moderate speed variations about the region of calibration, each ratio can be considered a function of the angles α and θ only, i.e.,

$$X_1 = X_1 \, (\alpha, \theta)$$

$$\qquad (6a)$$

$$X_2 = X_2 \, (\alpha, \theta)$$

$$X_D = X_D \, (\alpha, \theta)$$

$$\qquad (6b)$$

$$X_T = X_T \, (\alpha, \theta)$$

Since X_1 and X_2 are independent functions of α and θ, the relationships (6a) allow determination of the inverse relationships

$$\alpha = \alpha \, (X_1, \, X_2)$$

$$\qquad (7)$$

$$\theta = \theta \, (X_1, \, X_2)$$

To utilize the symmetries of the probe tip, the space immediately upstream was divided into six similar zones, as shown in Fig. 3, by the following convention regarding side hole pressures p_A, p_B, and p_C:

$p_A > p_B > p_C$, zone 1

$p_B > p_A > p_C$, zone 2

$p_B > p_C > p_A$, zone 3

$p_C > p_B > p_A$, zone 4

$p_C > p_A > p_B$, zone 5

$p_A > p_C > p_B$, zone 6 $\qquad (1)$

Consider the probe at orientation (α, θ) in a fluid stream of speed u.

If the three-side hole pressures p_A, p_B, and p_C, are labeled

and by substitution into (6b)

$$X_D = X_D (X_1, X_2)$$

$$X_T = X_T (X_1, X_2) \tag{8}$$

Equations (7) and (8) are the relationships to be determined in each zone by calibration.

The flow quantities can be estimated by calculating X_1 and X_2 from measurements with a calibrated probe, determining α, θ, X_D and X_T using relationships (7) and (8), and then calculating u and p_T thus

$$u = [2X_D (p_0 - p_3)/\rho]^{\frac{1}{2}} \tag{9}$$

$$p_T = p_0 + X_T (p_0 - p_3) \tag{10}$$

It should be noted that the form of functions $\alpha (X_1, X_2)$ and $\theta (X_1, X_2)$ will vary between zones because the probe tip is not symmetrical about the pitch axis. However, the functions $X_D (X_1, X_2)$ and $X_T (X_1, X_2)$ will theoretically be similar throughout the zones. Had flow direction been expressed in terms of a cone angle and a dihedral angle between the flow and meridian plane, each of the flow functions would have theoretically been identical in all zones. The present convention was chosen because α and θ relate directly to the mechanism for manipulating the probe.

Calibration Procedure

The probe was calibrated in a small windtunnel comprising a bellmouth entry, a 4.25 to 1 contraction and a 0.203 x 0.305 m working section. In the free stream of the working section, the spatial variation of velocity was ±0.5 percent and the turbulence level 0.5 percent. A velocity of 38 m s^{-1} was used for the calibration (Reynolds number based on tip width Re $\cong$ 8 × 10^3).

The probe was held in a tooth-tracked guide rod throughout the calibration and remained fixed in that rod during use. The rod was held in a traversing mechanism which allowed translation of the probe along, and rotation about, its axis. A protractor permanently attached to the traverse mechanism was used to determine rotation (yaw angle).

The mechanism was mounted on an arm which could be rotated about an axis normal to the probe axis and the tunnel axis. The arm rotated about the probe tip. Thus the pitch angle α could be altered without moving the probe tip.

Point calibrations were carried out at all combinations of pitch and yaw angles from -50 to $+50$ deg in 5 deg increments. At each orientation, the four head pressures, the air velocity, and total pressure was recorded. The four ratios X_1, X_2, X_D, and X_T were calculated and the relationships

$$\alpha = \alpha (X_1, X_2),$$

$$\theta = \theta (X_1, X_2),$$

$$X_D = X_D (X_1, X_2),$$

and

$$X_T = X_T (X_1, X_2)$$

were then determined at regular intervals in X_1 and X_2.

Results

Figures 4, 5, and 6 show the relationships between α, θ, X_D, X_T and (X_1, X_2) for zone 1. In the region of zero pitch and yaw angles, X_1 and X_2 have sensitivities of about 0.06 per deg, which is higher than the reported sensitivity of a five-hole spherical tipped probe [1].

Figure 5 shows X_D as a function of X_1 and X_2. Over the calibration range, X_D varies between 0.65 at $(X_1, X_2) = (0.96, 0.00)$ to 2.2 at $(X_1, X_2) = (0.8, 1.6)$. At yaw angles less than 20 deg, X_D is less sensitive to probe orientation and
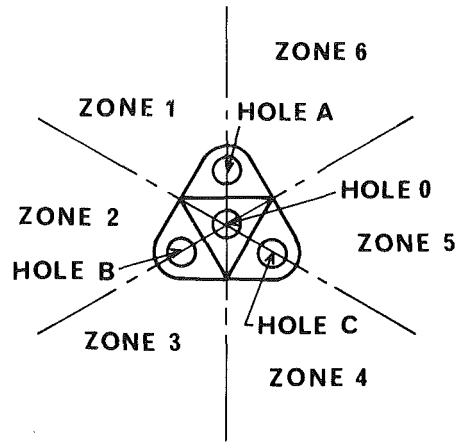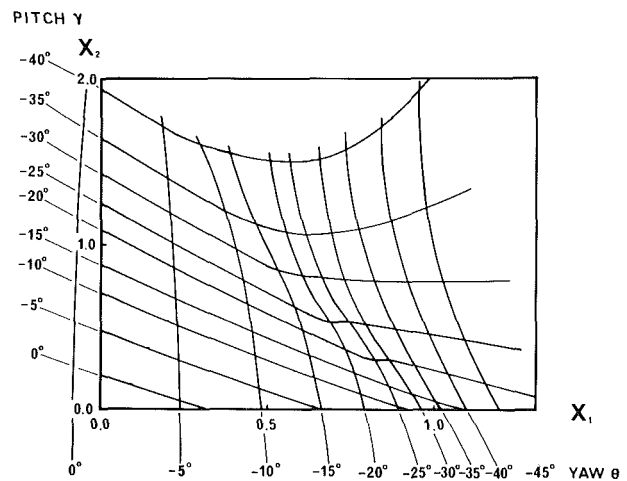

Fig. 3 Zone numbering convention

Fig. 4 Pitch angle γ and yaw angle θ versus (X_1, X_2); zone 1

therefore very accurate measures of u can be expected in this region.

The relationship between X_T and (X_1, X_2) is shown in Fig. 6. At pitch angles less than 20 deg, X_T is relatively insensitive and approaches zero in the form of a parabaloid as (α, θ) approaches (0,0). Therefore, very accurate estimates of p_T are obtainable in this region.

Use of the Probe

After calibration, the probe remained in the toothed guide rod and traversing mechanism, in which it was calibrated. The complete mechanism, including protractor and rotatable mount, was transferred from the dowelled calibration mounting bracket to an identical bracket at the desired measuring location. Thus, the datums for pitch and yaw angles were defined relative to features of the mounting bracket.

Having measured the four pressures p_0, p_A, p_B, and p_C, the side hole pressures are ranked in decreasing order and labeled p_1, p_2, and p_3 respectively. This operation also determines the approach zone. The pressure ratios X_1 and X_2 can be calculated and the calibration data for the appropriate zone utilized to estimate α, θ, X_D, and X_T. This last operation requires two dimensional interpolation in the X_1, X_2 plane between the actual calibration points. Although this can be done by hand, a computer program was found to be more accurate and convenient.

A third order polynomial surface was fitted to the 20 calibration points nearest the point of interest in the X_1, X_2 plane using the least squares criterion. The polynomial function so determined was used for interpolation. Finally, the velocity u and total pressure p_T are determined using equations (9) and (10).

Accuracy

Errors in the estimates of mean values could arise from errors in pressure measurement, errors in the calibration function used, a sheared velocity distribution in the region of

Fig. 5 X_D versus (X_1, X_2); zone 1

Fig. 6 X_T versus (X_1, X_2); zone 1

the probe tip, and high turbulence levels in the airflow. The last two factors were not investigated in this work, but are discussed in references [1], [7], and [8].

The uncertainty due to errors in the calibration function can be estimated by processing the calibration data as though it were experimental data and comparing the estimates with the known values. The differences will show errors due to lack of fit of the calibration function and random scatter due to errors in estimating the mean pressures from fluctuating signals during calibration. The latter variance can be estimated from the raw data and thus the remaining variance due to lack of fit can be estimated by subtraction. The 95 percent confidence intervals due to lack of fit in the calibration function, as calculated from 238 calibration points, are given in Table 1. The confidence intervals due to uncertainty in pressure measurement, as calculated by standard statistical methods [9], are shown in Table 1 for an accuracy in pressure measurement of ± 1.0 percent (95 percent confidence interval).

An error may occur in the calibration functions due to Reynolds number influence when the probe is used in airspeeds greatly different from the calibration airspeed. It is suggested [1] (Pg. 36) that for Reynolds numbers above 1500 (based on the outside dimension of the tip), the Reynolds number influence would be small. A Reynolds number of 1500 corresponds to an airspeed of about 7.5 m s^{-1} on the four-hole probe. If high accuracy is required over a wide speed range, particularly at speeds below 10 m s^{-1}, the probe should be calibrated at two or more speeds so that, if necessary, the calibration parameters can be estimated by interpolation.

After calibration and several months' use, the probe was remounted in the calibration tunnel to test its accuracy. The estimated and true values of α, θ, u, and p_T are compared in Table 2. The accuracy was approximately as predicted by statistical methods, although some evidence of a small change is apparent since most of the errors in yaw angle are negative. Apparently the head had twisted slightly during the period of use.
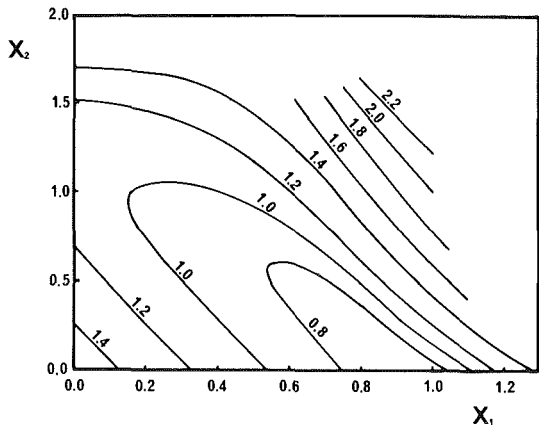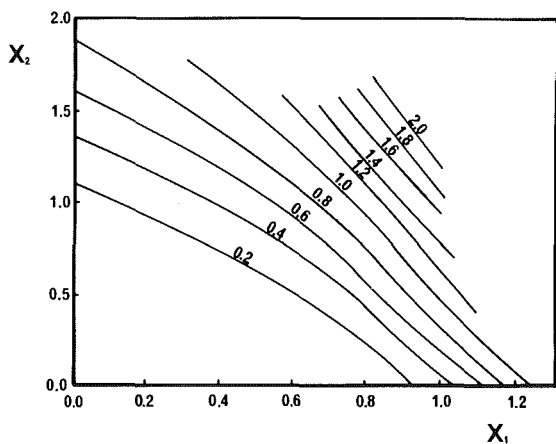
Table 1   95 percent confidence intervals

	Pitch ϵ_α (deg)	Yaw ϵ_θ (deg)	Velocity $\epsilon_{u/u}$ (%)	Pressure $\epsilon_{pT/\frac{1}{2}\rho u^2}$ (%)
Calibration fit	± 0.24	± 0.30	± 1.2	± 0.6
Pressure Measurement	± 0.50	± 0.70	± 1.5	0 to ± 5
Total	± 0.55	± 0.76	± 1.9	± 0.6 to ± 5

Table 2   Probe measurement errors

Pitch angle α (deg) Actual	Measured	Error	Yaw angle θ (deg) Actual	Measured	Error	Velocity u (m/s) Actual	Measured	Error	Total pressure (Pa) Actual	Measured	Error $(\frac{1}{2}\rho u^2)$
− 20	− 19.8	0.2	− 20	21.7	1.7	38.7	39.8	1.1	− 26	1	0.027
− 20	− 19.8	0.2	0	− 0.5	− 0.5	38.6	39.0	0.4	− 26	− 25	0.002
− 20	− 19.9	0.1	20	20.5	0.5	38.7	40.3	1.6	− 26	2	0.030
0	0.0	0.0	20	19.4	− 0.6	38.7	38.5	− 0.2	− 26	− 30	− 0.004
0	− 0.1	− 0.1	0	− 0.9	− 0.9	38.7	38.7	0.0	− 26	− 26	0.000
0	0.0	0.0	− 20	− 20.7	− 0.7	38.7	38.4	− 0.3	− 26	− 31	− 0.005
20	19.7	− 0.3	− 20	− 20.4	− 0.9	38.7	38.7	0.0	− 26	− 21	0.006
20	19.9	− 0.1	0	− 0.4	− 0.4	38.7	38.6	− 0.1	− 26	− 21	0.006
20	19.3	− 0.7	20	19.5	− 0.5	38.6	38.9	0.3	− 26	− 25	0.001
− 30	− 29.4	0.6	20	19.6	− 0.4	38.6	39.1	0.5	− 26	− 26	0.000
− 30	− 29.6	0.4	0	− 0.2	− 0.2	38.5	39.2	0.7	− 26	− 28	− 0.002
− 30	− 29.5	0.5	− 20	− 21.1	− 1.1	38.5	38.8	0.3	− 26	− 22	0.005
30	29.5	− 0.5	− 20	− 20.0	0.0	38.5	38.6	0.1	− 26	− 31	− 0.005

Conclusions

A four-hole pressure probe can be used successfully to measure mean flow quantities simultaneously in three dimensions.

A cobra type probe with a pyramid shaped head and three equispaced holes around a central hole provides a small but robust instrument. When in use, the probe is fixed and the four head pressures, together with predetermined calibration functions, allow determination of the flow quantities.

Sensitivity and accuracy are approximately equal to that obtainable with a five-hole probe. The four-hole probe is smaller, requires less measurements to be made, and because no redundant information is collected, determination of the flow quantities is simpler and unambiguous.

In the absence of high turbulence and high velocity gradient, the probe can be used successfully between ± 45 deg in pitch and yaw angles. Uncertainties of ± 0.6 and ± 0.8 deg for pitch and yaw angles, respectively, ± 2.0 percent for velocity and 0 to ± 5 percent for total pressure ratio $(p_T - p_0)/\frac{1}{2}\rho u^2$ are claimed.

References

1 Bryer, D. W., and Pankhurst, R. C., "Pressure Probe Methods for Determining Wind Speed and Flow Direction," H.M.S.O. 1971.

2 Lee, J. C., and Ash, J. E., "A Three Dimensional Spherical Pitot Probe," Trans. ASME Apr. 1956.

3 Wright, M. A., "The Evaluation of a Simplified Form of Presentation for Five-Hole Spherical and Hemispherical Pitometer Calibration Data," J. Phys., E., Sci. Inst., Vol. 3, 1970.

4 Judd, A. M., "Calibration of a Five Tube Probe for Measuring Wind Speed and Direction," J. Phys. E., Sci. Inst., Vol. 8, 1975.

H. R. Asare
Former Research Assistant.

R. K. Takahashi
Research Assistant.

M. A. Hoffman
Professor of Mechanical Engineering.

Department of Mechanical Engineering,
University of California,
Davis, Calif.   95616

Liquid Sheet Jet Experiments: Comparison With Linear Theory

It has been proposed to protect the structural walls of a future laser fusion reactor with a curtain or fluid-wall of liquid lithium jets. As part of the investigation of this concept, experiments have been performed on planar sheet water jets issuing vertically downward from slit nozzles. The nozzles were subjected to transverse forced harmonic excitation to simulate the vibrational environment of the laser fusion reactor, and experiments were run at both 1 atm and at lower ambient pressures. Linear stability theory is shown to predict the onset of the unstable regime and the initial spatial growth rates quite well for cases where the amplitudes of the nozzle vibration are not too large and the waveform is nearly sinusoidal. In addition, both the linear theory and a simplified trajectory theory are shown to predict the initial wave envelope amplitudes very well. For larger amplitude nozzle excitation, the waveform becomes highly nonlinear and nonsinusoidal and can resemble a sawtooth waveform in some cases; these latter experimental results can only be partially explained by existing theories at the present time.

1 Introduction

The study of planar or sheet jets of liquid is of interest in atomization studies for droplet production, in fuel injection and combustion studies, in coating and spraying processes and more recently in connection with a new laser fusion reactor design concept [1, 2]. In this latter application, which motivated this present research, it has been proposed to use near-vertical liquid lithium jets inside the fusion reactor in front of the inner walls of the reactor vessel. The array of liquid lithium jets would be thick enough (on the order of half a meter to one meter total thickness) to absorb the X-ray and ion energy, as well as a good part of the energy of the neutrons released in the pulsed fusion reactions. In this way, the solid structure would be protected from erosion, embrittlement, and severe neutron damage, and its useful life increased significantly. The lithium jets act as a "self-healing" liquid first wall of the reactor vessel.

One of the most important potential problem areas in this application of liquid jets arises because the reactor vessel and jet nozzles will probably be subject to significant vibrations due to the "ringing" of the entire structure caused by the pulsed nature of the laser-fusion microexplosions. Our initial studies of annular liquid jets [3] and thin liquid films on the walls [4] indicated that additional experimentation with sheet jets (and round jets) would provide a valuable data base for the design of a liquid lithium curtain for a future fusion reactor. The objective of this study was to determine whether transverse forced vibration of the nozzle would cause jet instability and breakup. Breakup might allow neutrons, ions, and X-rays to stream directly through to the solid walls and seriously shorten the useful life of the structure.

Extensive studies of the breakup of fan-shaped sheet jets and sprays have been performed by Dombrowski and his colleagues in connection with spraying and atomization studies (e.g., see reference [5]). However, for our particular geometry of a nearly-constant-width sheet jet, only two stability analyses have been uncovered in our literature search which are directly applicable. In 1953, Squire [6] published a theoretical study of the linear temporal stability of a horizontal sheet jet. Two years later, Hagerty and Shea [7] independently published a very similar theoretical analysis along with some experimental data directly relevant to our study. Their experiments employed a very thin, horizontal sheet of water with a thickness of only about 1.6 mm and with jet velocities of about 3 to 5 m/s (equivalent to non-dimensional thickness parameters, $(kh)_0$ from about 0.25 to 0.44 where k_0 is the initial jet wave number and h_0 is the initial jet half-thickness). The jet nozzle was vibrated transverse to the flow direction at frequencies up to about 200 Hz. Unfortunately, the vibration amplitudes were not given. Measurements of the exponential growth rates were made from flash photographs of the edge view of the sheet jets and their growth rate data agreed very well with the predictions of the linear theory.

In the present experimental study, we have extended the work of Hagerty and Shea in several directions in order to better simulate the laser fusion reactor environment. We have employed:

(a) Thicker sheet water jets such that nondimensional thickness parameters, $(kh)_0$, up to 0.84 (using Nozzle B) were investigated.

(b) Forced excitation up to several hundred Hz over a wide range of forcing amplitudes to jet half-thickness, A_0/h_0, from about 0.10 to 0.40. The resultant wave envelope amplitude ratio, A_e/A_0, often reached values as high as 80.

(c) Vertical (downward) jet orientation in order to include the effect of gravity acceleration.

(d) Experiments at low ambient pressures in a vacuum vessel as well as at 1 atm.

In Section 2, we briefly review the key results of the linear stability theories of references [6] and [7]. Then in Section 3 we compare the linear theory to a simplified "trajectory theory." The experimental apparatus is described in Section 4, and the results are compared to the various theories in Section 5.

2 Review of Linear Stability Theory

The theories developed in references [6] and [7] are essentially equivalent and both are basically extensions of the theories of Rayleigh [8] and Lamb [9] for the *temporal* growth of waves on a single free surface to the present case of two free surfaces. In developing the linear theory, it is assumed that the effect of gravity is negligible so that the mean sheet thickness, $b = 2h$, and velocity, U, stay constant at the initial values b_0 and U_0 respectively. The width of the sheet, w, is assumed to be much greater than h. In addition, it is assumed that both the liquid and the surrounding gas are incompressible and inviscid and that the surface tension between the two fluids is constant. We will assume also that the surrounding fluid, air, is at rest.

The wave amplitude, η, is assumed to be much less than $h_0 = b_0/2$, so that the interface boundary conditions can be applied at $\pm h_0$ as part of the linearization of the problem. The geometry of the sheet jet with two types of waves on it is shown in Fig. 1. For case (a), the waves on the two surfaces are in phase, and this is referred to as the sinuous or "snake" mode. For case (b), the waves are 180 deg out of phase, and this is referred to as the dilational or "sausage" mode. Reference [7] proves that only these two cases are permitted by the linear theory, and that the sinuous waves of case (a) always have a higher growth rate in the unstable regime and hence will tend to be the dominant waves observed. The linear theory assumes a wave amplitude of the form

$$\eta(x,t) = \text{Real}\left[a_1 e^{i(kx-\omega t)} + a_2 e^{-i(kx-\omega t)}\right] \qquad (1)$$

where the wave number, k, is real and ω is complex ($\omega = \omega_r + i\omega_i$) in the case of temporal instabilities. This implies waves which move along the sheet with a wave speed $C_r = \omega_r/k$ and grow in time everywhere along the sheet with a growth rate ω_i.

The solution for the wave amplitude and growth rates is obtained by solving Laplace's equation for the velocity potential in each region subject to a linearized kinematic
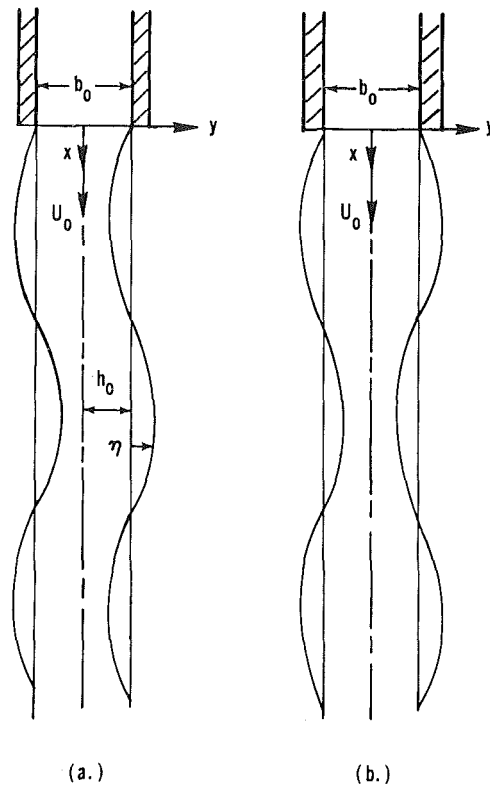

(a.)   (b.)

Fig. 1 Edge view of the two modes of instability predicted by linear temporal stability theory for a planar sheet jet subject to small perturbations, where (a) is the sinuous or "snake" mode and (b) is the dilational or "sausage" mode

constraint at the interface and a linearized pressure boundary condition.

Solution of the linearized equations and boundary conditions leads to the following characteristic equation [6, 7]:

$$\rho\left(\frac{\omega}{k} - U_0\right)^2 \tanh(kh)_0 + \rho_a\left(\frac{\omega}{k}\right)^2 - \sigma k = 0 \qquad (2)$$

For the case of temporal instabilities where ω is complex and k is real, this is a quadratic equation in $\omega(k)$ which is easily solved. However, we are actually interested in the case of spatial instabilities where k is complex and ω is real, since in our experiments the waves grow spatially as the liquid sheet jet flows from the vibrating nozzle.

The characteristic equation is nonlinear in k and must be solved numerically for the spatial growth rates, k_i. The

_____ Nomenclature _____

A_e	=	wave envelope amplitude	t	=	time	
A_0	=	amplitude of the nozzle excitation	U	=	vertical component of mean jet velocity	
b	=	sheet jet thickness ($2h$)	v	=	transverse component of mean jet velocity	
C_r	=	wave speed	$\hat{W}e$	=	Weber number, $\rho U_0^2 h_0/\sigma$	
f	=	forcing frequency	w	=	sheet jet width	
g	=	acceleration of gravity	x	=	vertical coordinate	
h	=	sheet jet half-thickness ($b/2$)	y	=	transverse coordinate	
k	=	wave number, $2\pi/\lambda$	β	=	coefficient in trajectory theory	
m	=	mass	δ	=	differential amount	
p	=	pressure	η	=	wave surface amplitude in linear theory	
r	=	radius	λ	=	wavelength	
r_d	=	ratio of ambient density to liquid density, ρ_a/ρ				

ρ	=	density
σ	=	surface tension coefficient
ω	=	complex frequency in linear temporal theory

Subscripts

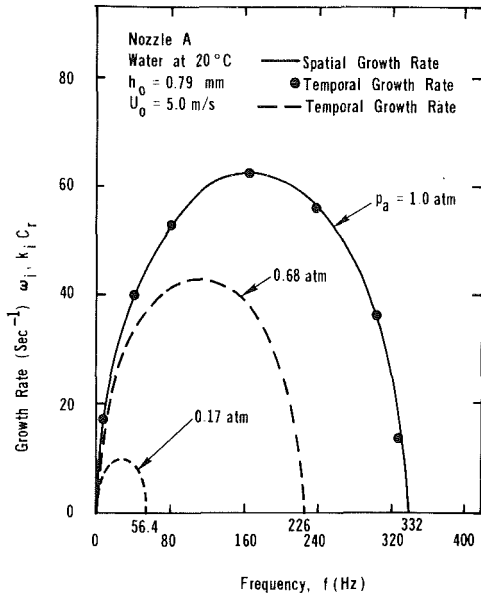|		
a	=	ambient (or aerodynamic)
c	=	critical
i	=	imaginary part
N	=	nozzle
0	=	at the nozzle exit (initial value)
r	=	real part
σ	=	surface tension

Fig. 2(a) Comparison of growth rates for the water jets from Nozzle A predicted by the linear temporal and linear spatial stability theories for three representative experimental conditions
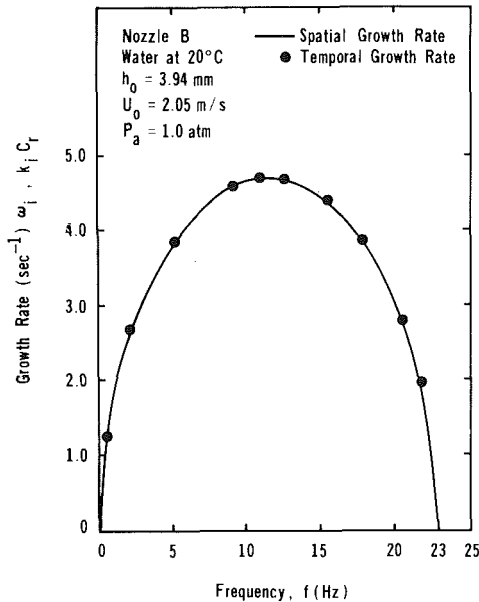

Fig. 2(b) Comparison of the growth rates from Nozzle B predicted by linear temporal and linear spatial stability theories for one representative set of experimental conditions

equation has been solved for k_i as a function of forcing frequency $f = \omega/2\pi$ for many sets of conditions and compared to the temporal growth rate, ω_i, based on the following transformation. It has been shown by Gaster [10] that the temporal growth rate should be related to the spatial growth rate by the group velocity, C_g. Then Asare [11] proved that for our case of a single wave train with a single imposed forcing frequency, the group velocity is equal to the wave velocity, C_r. Thus the transformation between the temporal and spatial growth rates should be given by:

$$\omega_i = k_i C_g = k_i C_r \qquad (3)$$

The solutions for $k_i C_r$ for two typical cases at 1 atm pressure are shown by the solid curves of Fig. 2(a) (for Nozzle A) and Fig. 2(b) (for Nozzle B). The spatial growth rates can be seen to be essentially identical to the temporal growth rates, ω_i, shown by the black dots. (It was also found that the

wave speed, C_r, was essentially equal to U_0 in all cases.) Consequently, in the following discussions we will simply refer to both the linear temporal and the linear spatial theories as the "linear theory."

It is useful to have an analytical expression for the growth rate, but this is only possible using the temporal theory solution since the spatial theory requires numerical solution. With this in mind, we present the following key analytical results from the temporal theory in order to be able to show the functional dependence of the growth rate on the various parameters of the problem. These results will be used to obtain the spatial waveform using the transformation of equation (3).

For the case where the air-to-liquid jet density ratio, $r_d \equiv \rho_a/\rho$, is much less than tanh $(kh)_0$, as is the case here, the solution indicates that the sheet is *unstable* for frequencies less than a critical frequency:

$$f_c \simeq \frac{\rho_a U_0^3}{2\pi\sigma}$$

We also find that the wave speed, $C_r \simeq U_0$; the corresponding temporal growth rate is then given by:

$$\frac{\omega_i}{2\pi f} \simeq \sqrt{\left[\frac{r_d U_0}{2\pi f h_0} - \frac{1}{\hat{We}}\right]\left[\frac{(kh)_0}{\tanh(kh)_0}\right]} \qquad (4)$$

where the jet Weber number is based on the sheet half thickness, h_0:

$$\hat{We} \equiv \frac{\rho U_0^2 h_0}{\sigma}$$

For the special case where $(kh)_0 < < 1$, the last factor under the radical, $(kh)_0/\tanh (kh)_0$, is essentially unity; this limiting case defines what we refer to as "thin" jets. The "thick" jets are assumed somewhat arbitrarily to be those for which $(kh)_0 > > 0.25$ (where $(kh)_0/\tanh (kh)_0 > > 1.02$).

The theoretical results shown in Figs. 2(a) are for the experimental conditions for the water jets from the thinnest nozzle (Nozzle A with $h_0 = 0.79$ mm) at $U_0 = 5.0$ m/s. We see that both the growth rate at a given frequency and the critical frequency decrease significantly as the ambient air pressure is reduced. In a vacuum, the sheet jet should be stable to all disturbance frequencies according to the linear theory. Shown in Fig. 2(b) are the predicted temporal growth rates for the thickest water jet from Nozzle B ($h_0 = 3.94$ mm) at a velocity of 2.05 m/s and 1 atm pressure. The values from these figures will be compared to the experimental results in Section 5.

The solution for the wave amplitude in the unstable regime ($f < f_c$) is:

$$\eta(x,t) = A_e(t)\cos(kx - \omega_r t) = (a_1 e^{\omega_i t} + a_2 e^{-\omega_i t})\cos(kx - \omega_r t) \quad (5)$$

where $A_e(t)$ is the mean envelope amplitude of the waves. We must next interpret this result for our spatially growing waves with a forced nozzle vibration assumed to be given by:

$$y_N(t) = A_0 \sin(2\pi f t) \qquad (6)$$

where $f = \omega_r/2\pi$.

The initial conditions become

$$\eta(x,0) = 0 \qquad (7a)$$

$$\dot{\eta}(x,0) = \dot{y}_N(0)\cos kx = (2\pi f A_0)\cos kx \qquad (7b)$$

These initial conditions require that:

$$a_1 = -a_2 = \frac{\pi f A_0}{\omega_i} \qquad (8)$$

Finally, the mean wave-envelope amplitude takes the following spatial form in the unstable regime:

$$A_e(x) = A_{0(\text{eff})} (e^{\omega_i x/U_0} - e^{-\omega_i x/U_0}) \qquad (9)$$
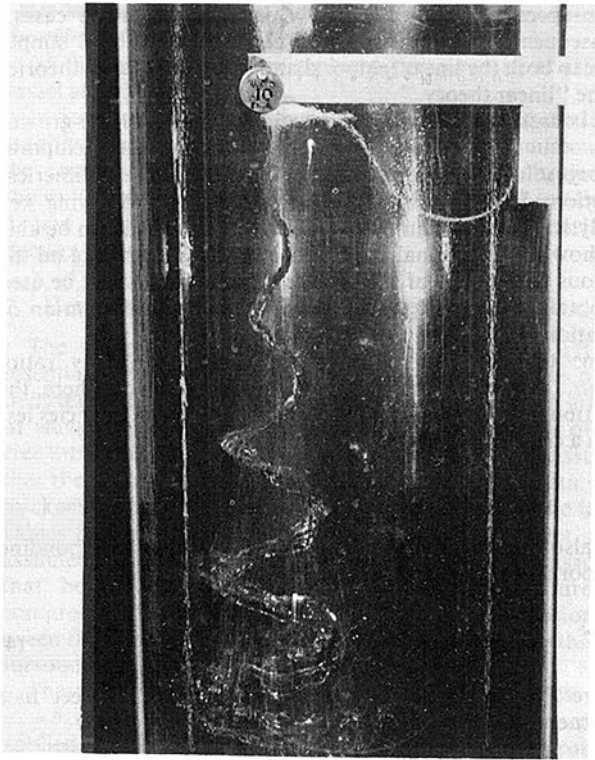
where

Journal of Fluids Engineering

Fig. 3 Edge view of a typical near-sinusoidal, exponentially-growing waveform of the sheet jet from Nozzle C with forced excitation of the nozzle at $f = 70$ ($h_0 = 1.25$ mm, $U_0 = 4.75$ m/s, $A_0 = 1.06$ mm, $p_a = 1.0$ atm)

$$A_{0(\text{eff})} \equiv \frac{\pi f A_0}{\omega_i} \qquad (10)$$

3 Simplified Spatial Trajectory Theory

In our experiments, we purposely imposed rather large amplitude forced excitation on the sheet jet nozzles to simulate the worst situation for the laser-fusion application. The resulting wavy motion of the sheet jets was of very large amplitude, with peak amplitudes often more than an order of magnitude larger than the jet thickness as illustrated in the typical photograph of the edge view of the sheet jet shown in Fig. 3. It occurred to us to try to better understand the behavior of such large-amplitude wavy jets accelerating vertically downward by hypothesizing a simple physical model which we called the "spatial trajectory theory."

3.1 General Case of Increasing $U(x)$. The basic idea of this simplified, physical approach to the problem is illustrated in Fig. 4. We consider the fluid particle, δm, which is at the crest of the wave shortly after the flow leaves the nozzle. It is then assumed that the wave speed, $C_r(x)$, is approximately equal to the vertical component of the local jet velocity, $U(x)$. This assumption implies that a fluid particle which starts in the wave crest stays in the wave crest, even with gravity acceleration, and that its trajectory traces out the envelope of the waves.

A simple experiment was performed to verify this approximation, since it is one of the key assumptions of the trajectory theory. A dimple was made in the wave crests on one side of the flow with a pointed object as the waves passed a point a few centimeters below the nozzle exit. By viewing this dimple with a strobe, it was ascertained that the dimple did stay in the wave crests on the side where the dimple was originally produced, even for very large amplitude waves. (Also, the initial wave lengths, λ_0, closely agreed with U_0/f, confirming that the wave speed, C_r, was close to U_0.)

A second basic assumption is that the particle which ends
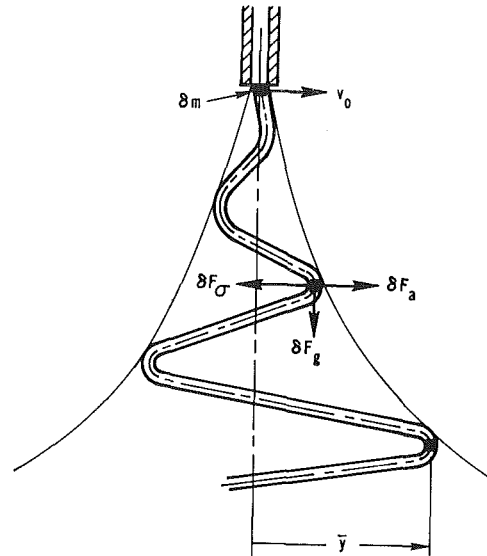

Fig. 4 Model used in the development of the simplified trajectory theory showing the motion of the fluid particle which is hypothesized to stay in the crest of the falling wave as it grows spatially to large amplitudes

up in the wave crest is the one which leaves the nozzle with the maximum initial transverse velocity, v_0 (as the vibrating nozzle passes through the vertical axis), where $v_0 = 2\pi f A_0$.

The basic equations for the trajectory of the fluid particle in the wave crest are:

$$\ddot{x}\delta m = g\delta m \qquad (11)$$
$$\ddot{\bar{y}}\delta m = \delta F_a - \delta F_\sigma \qquad (12)$$

where $\bar{y}$ is the mean wave crest amplitude measured to the mean jet thickness (as shown in Fig. 4). The aerodynamic force, δF_a, due to the air pressure difference across the wavy jet has been estimated using the solution for the linearized pressure distribution on a wavy wall of sinusoidal shape (e.g., reference [12]). Taking twice the pressure at the wavy wall peaks we obtain:

$$\delta F_a = \left[\frac{4\pi r_d f U}{b} \right] \bar{y}\delta m \qquad (13)$$

The surface tension force, F_σ, on the fluid particle in the wave crest has been evaluated approximately by using the mean radius of curvature at the crest of a sine wave [13]:

$$\delta F_\sigma \simeq \frac{2\sigma}{\bar{r}} \delta A_s \simeq \left(\frac{8\pi^2 f^2 \sigma}{\rho b U^2} \right) \bar{y}\delta m \qquad (14)$$

where $\delta A_s = w\delta x =$ surface area of one side of the fluid element.

These estimates for δF_a and δF_σ could possibly be improved for the larger amplitude, nonlinear waves by taking account of the nonsinusoidal shape of the wavy jet at the wave crests. However, for the present paper, we will use the simple linearized estimates of δF_a and δF_σ given by equations (13) and (14) (assuming a near-sinusoidal waveform). Substituting these results in equation (12) gives

$$\ddot{\bar{y}} - \beta^2 \bar{y} = 0 \qquad (15)$$

where

$$\beta(t)^2 \equiv \frac{4\pi r_d f U(t)}{b(t)} - \frac{8\pi^2 f^2 \sigma}{\rho b(t) U(t)^2} \qquad (16)$$

It should be noted that both the vertical jet velocity, U, and the jet thickness, b, are functions of the vertical coordinate x or equivalently functions of the fall time, t. $U(t)$ is evaluated
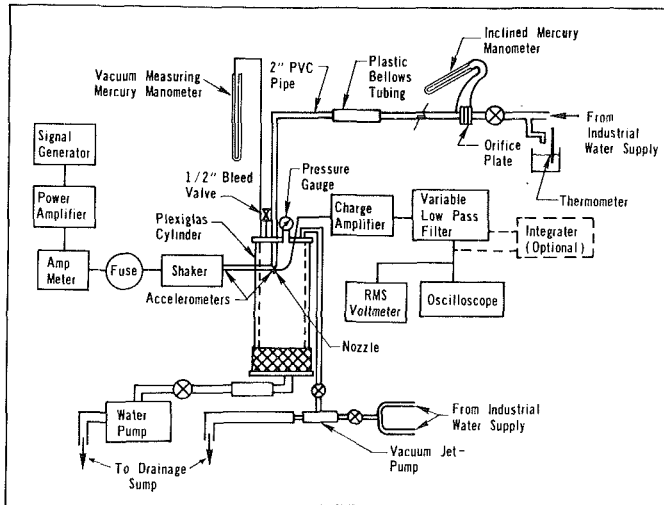
Fig. 5 Schematic diagram of the water flow system, vacuum tank apparatus and forced excitation instrumentation used in the sheet jet experiments

by integrating equation (11) and then $b(t)$ can be evaluated using the continuity equation (assuming a constant sheet jet width):

$$b(t) = \frac{b_0 U_0}{U(t)} \qquad (17)$$

3.2 Special Case of Constant U. For the special case of high initial jet velocities ($U_0 \geq 5$ m/s), the velocity and jet thickness changes in the fall times of the experiments were small. In the limiting case of constant $U = U_0$ and $b = b_0 = 2h_0$, β becomes a constant, designated β_0:

$$\beta_0 = 2\pi f \sqrt{\frac{r_d U_0}{2\pi f h_0} - \frac{1}{\hat{W}e}} \qquad (18)$$

Comparison of this result with equation (4) reveals that β_0 equals ω_i, the growth rate from the linear temporal stability theory when β_0 is real (i.e., when ω is complex) for the case where $r_d \ll 1$ and $(kh)_0 \ll 1$. Thus real values of β_0 correspond to the case of the unstable sheet jet where the aerodynamic destabilizing force exceeds the stabilizing surface tension force ($f < f_c$). The wave envelope equation will be identical to the linear theory equation (9) for this limiting case of constant velocity, and we can thus identify $\bar{y}$ with A_e of the linear theory solution (equation (9)).

4 Experimental Apparatus and Procedure

A schematic diagram of the experimental apparatus is shown in Fig. 5. The water source was a 7.62 cm (3 in.) dia industrial-grade water supply line with a flow rate capability of about 13 liters/s (200 gpm). A 5.08 cm (2 in.) dia pipe about 10 meters long connected the industrial water supply to the apparatus. A standard ASME-type orifice was installed in this pipe about 1 meter downstream of the main ball valve. The pipe contained a section of crush-proof, flexible hose for vibration isolation and several sections of clear cast-acrylic pipe to allow viewing of the flow (and, in particular, to view any bubbles present).

The flow pipe entered the vacuum vessel vertically and was attached to the various nozzles used in the experiments by means of a custom-made flexible silicone rubber coupling which provided a smooth transition on the inner surface. The nozzles were fabricated from 5.08 cm (2 in.) cast acrylic tubes heated and pressed at one end to form a constant-width slit exit [14].

The vacuum chamber was constructed from a 30 cm dia cast-acrylic cylinder about 120 cm high. The flat acrylic end plates had O-ring grooves machined in them, as well as holes for the many feedthroughs. Due to the large amount of water vapor produced by the sheet water jets during the subatmospheric experiments, a water-jet ejector pump was selected for the vacuum pumping. With the present jet-pump water supply of about 0.8 liters/s (12 gpm), we were able to pump down to about 0.2 atm.

The nozzles were vibrated approximately transversely by means of an electromechanical shaker. (The large radius to the effective hinge point of the nozzles was about 24 cm; this coupled with the relatively small maximum vibration amplitudes of about 1.6 mm resulted in negligibly small departures from a purely transverse motion.) The shaker was mounted outside the vacuum tank and was attached to the nozzle by means of a steel rod which passed through a specially designed bellows-type feedthrough into the vacuum chamber (see reference [14] for design details).

The water exited the nozzle and fell about 70 cm to a small pool at the bottom of the vacuum tank. For the atmospheric pressure runs, the water then simply flowed out a drain pipe in the bottom end plate to a drainage sump (see Fig. 5). For the subatmospheric tests, a helical-rotor water pump was used to pump out the water to the drainage sump and maintain a constant head of about 30 cm of water in the bottom of the vacuum tank. Although the water pump usually cavitated and vibrated severely, the use of a crush-proof, flexible hose between the vacuum tank and the pump isolated the experimental apparatus from these vibrations quite well. This open-loop arrangement was found to be much superior to a closed-loop arrangement originally tried. The main disadvantage of the open-loop arrangement was that we had to use the industrial water supply which had substantial amounts of dissolved gases in it. This tended to create problems with bubble formation in the subatmospheric runs (see reference [14] for more details).

The mass flow rate was measured by the orifice plate in conjunction with an inclined manometer. All the flow rate calibration data in the range of the experiments fell on a straight line with a standard deviation of about ± 1.5 percent, at atmospheric pressure. However, for the subatmospheric runs, air bubbles produced both a small amount of air leaking in through some of the subatmospheric pipe joints and by the dissolved gas coming out of solution caused somewhat larger uncertainties in the velocity measurement; we estimate that the jet exit velocities have an overall uncertainty of about ± 3 percent for the 1 atm runs and about ± 5 percent for the subatmospheric runs. (All uncertainties are limtied sample values with approximately 20:1 odds.)

The vacuum tank pressure was measured roughly by a pressure gauge installed in the top end plate. It was also measured more precisely by a mercury manometer with an estimated uncertainty in the reading of ± 10 percent, due primarily to the fact that the vacuum chamber pressure fluctuated. The water temperature (typically 20°C) was measured to better than ± 1°C by a mercury/glass thermometer. This was considered to be adequate accuracy for estimating the water density and surface tension coefficient.

The electromechanical shaker amplitude was measured by two independent accelerometers, one placed on the shaker face and the other mounted on the nozzle itself. The accelerometers were calibrated over the range of frequencies from 10 to 1000 Hz on a large electromechanical shaker with a built-in, calibrated accelerometer [14]. Based on these calibrations, the estimated uncertainty in the nozzle amplitude is ± 4 percent, due primarily to the limited number of digits on the digital voltmeter available at the time.

The basic wave amplitude data were obtained from photographs of the edge view of the wavy sheet jet such as
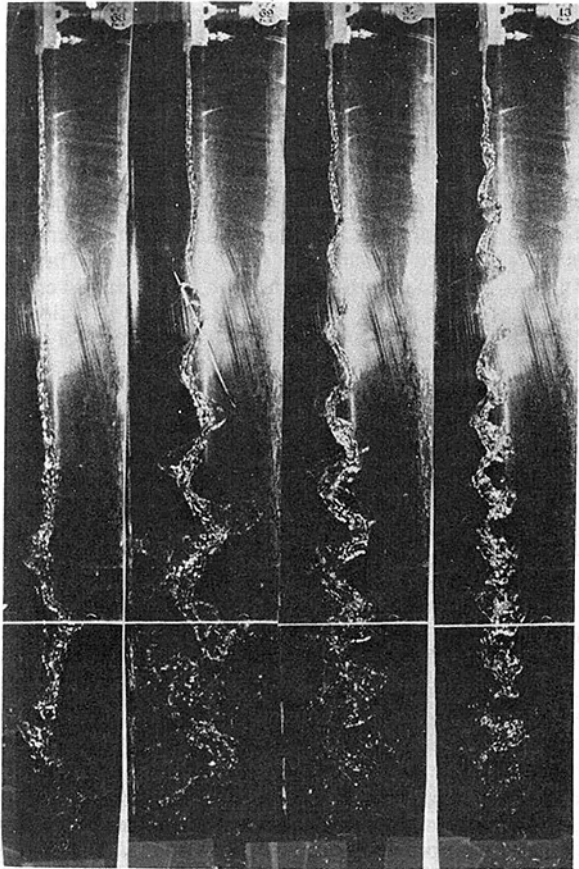
Fig. 6 Edge view of the sheet jets from Nozzle A ($h_0 = 0.79$ mm, $U_0 = 5.0$ m/s, $A_0 = 0.2$ mm, $p_a = 1.0$ atm) for four nozzle forcing frequencies: 30, 50, 70, and 100 Hz (going from left to right)

Fig. 7 Comparison of the linear theory (solid curves) to the experimental results for Nozzle A of Fig. 6. Dashed lines are best fits to the linear portion of the data.

shown in Figs. 3 and 6. These photographs were often the superposition of a relatively long exposure photo used to define the wave envelope and a short flash exposure to show up the wave form.

For the larger vibrational amplitudes, where A_0 could also be read from the photos, the values of A_0 measured agreed with those calculated from the accelerometer readings to within about $\pm$ 5 percent. For smaller vibrational amplitudes, only the accelerometer values were used.

In reading the amplitude of the mean wave envelope, A_e, at various vertical positions, it was necessary to subtract out the thickness of any fluid accumulations in the sheet edges, as well as any fluid lumps or "blobs" near the edge regions of the wave crests, which were often present at large wave amplitudes and low jet velocities. Reasonably accurate corrections were possible after careful visual study of the jet wave shapes using a stroboscope. The estimated uncertainty of these mean wave envelope amplitude data is $\pm$ 0.75 mm for Nozzle A and $\pm$ 1.0 mm for Nozzle B. However, this is more like a bias error, since the eye can integrate and smooth the data read off the photos quite well. (The small scatter of the readings shown in figures such as Figs. 7 and 8 illustrates this point).

5 Discussion of Results

Extensive experimental results using three different nozzles were obtained in the course of this research [11, 14]. Due to space limitations only a small, but representative, sample for two nozzles can be given here.

5.1 Results for Nozzle A. Figure 6 shows typical photographs of the wave growth using Nozzle A ($b_0 = 2h_0 = 1.59$ mm, $w_0 = 78$ mm) for four forcing frequencies [11]. For
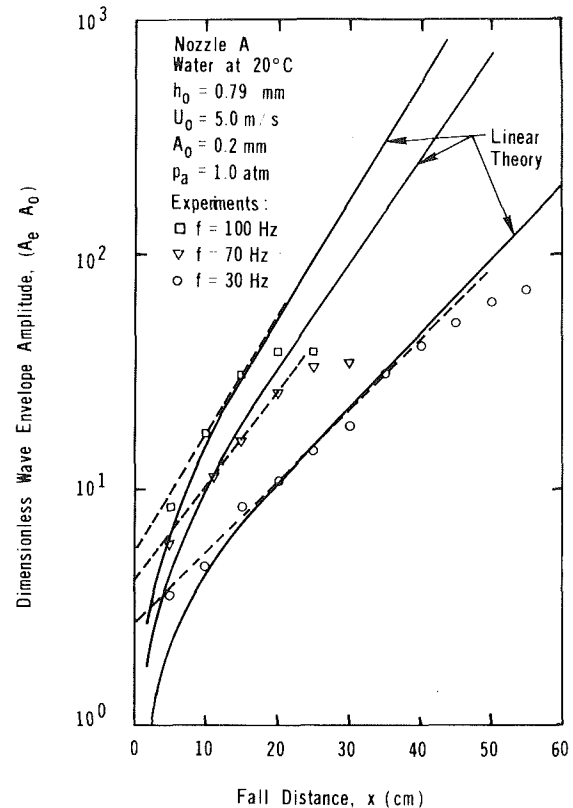
$U_0 = 5$ m/s, the dimensionless parameter $(kh)_0$ ranged from about 0.03 for 30 Hz to about 0.1 for 100 Hz. Since $(kh)_0 << 1$ for these runs, approximations based on assuming tanh $(kh)_0 \simeq (kh)_0$ will be valid. Consequently, these Nozzle A runs are considered to be representative of "thin-jet" cases. The initial Weber number was about 274.

The wave envelope data read from the photographs of Fig. 6 are plotted in Fig. 7 for three forcing frequencies along with the predictions of the linear theory (equation (9)). The experimental growth rates (based on the slopes of the dashed lines through the data points in Fig. 7) are within about 3.2 percent of the theoretical values for forcing frequencies of 30 and 100 Hz and within about 10 percent for 70 Hz. The intercepts of the dashed lines with the $x=0$ axis agree with the predictions for $A_{0(eff)}$ of equation (10) within about $\pm$ 4 percent.

As can be seen from Fig. 7, the experimental results appear to deviate from the linear theory at very small fall distances, near $x=0$. This is partly because it is virtually impossible to read the wave amplitudes accurately very close to the nozzle. The experimental results also deviate from the linear theory at large x when nonlinear effects begin to become important. It can be seen that the nonlinear effects do not come in until a fall distance of about 35 cm for 30 Hz, but become important at only about $x = 15$ cm for 100 Hz; this may be due to the increase of $A_{0(eff)}$ with forcing frequency (equation (10)).

Shown in Fig. 8 is the effect of forcing amplitude, A_0, on the wave envelope shape for a fixed forcing frequency of 70 Hz. As A_0 (and hence $A_{0(eff)}$) increases, the nonlinear effects can be seen to appear sooner. The linear theory of equation (9) (solid line) can be seen to explain the data reasonably well in the initial development region when the amplitudes are not too large and when a near-sinusoidal wave profile is evident on the photographs.
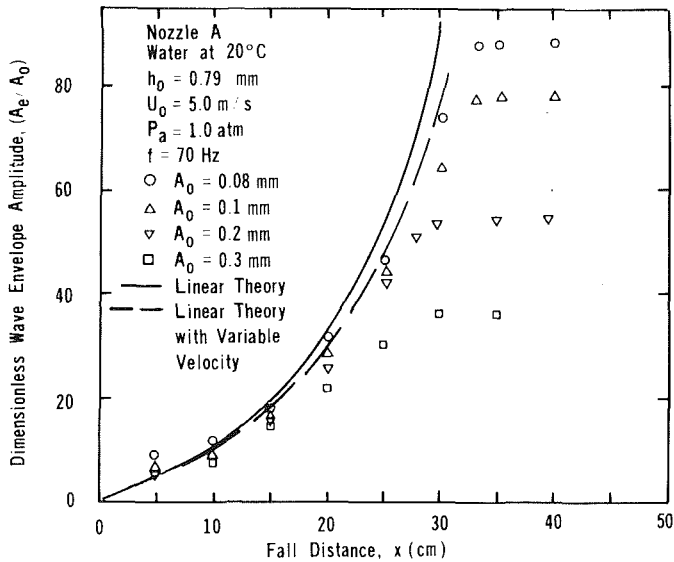
Fig. 8 Comparison of the linear theory to experimental data for Nozzle A for four nozzle forcing amplitudes
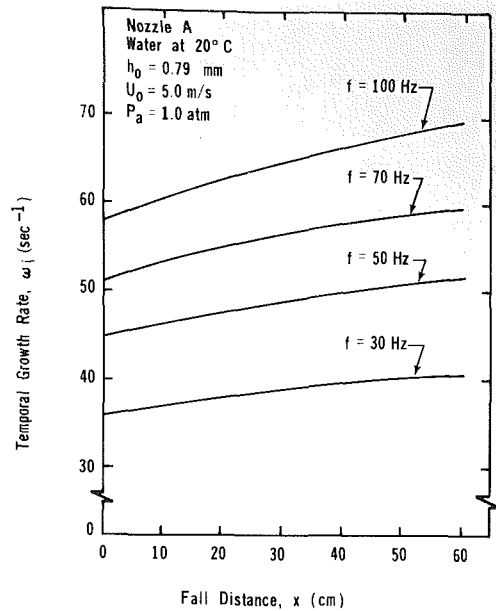

Fig. 9 Local growth rate predictions of the linear theory for Nozzle A taking account of the variable sheet jet velocity and thickness with fall distance due to the acceleration of gravity
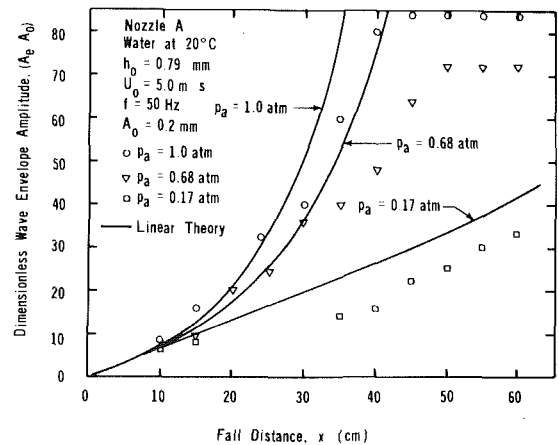

Fig. 10 Comparison of the linear theory to the experimental data for Nozzle A for three ambient pressures

Due to the acceleration of gravity, the sheet jet velocity increases somewhat with fall distance x and the sheet thickness, b, decreases. This causes the local growth rate predicted by the linear theory (equations (3) and (4)) to increase somewhat with fall distance, as shown in Fig. 9. Using the variable velocity form of the trajectory theory (equations (15) and (16)), we can estimate the effect of these changes on the predictions of the linear theory. For the relatively small changes in the growth rates for Nozzle A flows, we have found these results to be essentially the same as an approximate, variable-velocity linear theory where the local values of $U(x)$, $b(x)$, and $\omega_i(x)$ are used at each step of the numerical solution of equation (9). The dashed curve in Fig. 8 shows that these variable velocity effects are not large for these run conditions, and they do not explain the experimental results at large fall distances. (As can be seen from the photographs of Fig. 6, the wave envelope amplitude appears to saturate at large fall distances. Close examination of the photographs on a light table revealed that the sheet jets actually are beginning to break up where the wave sheet envelope appears to saturate.)

Data from runs made at two subatmospheric pressures as well as at 1 atm are shown in Fig. 10. The predictions of linear theory can be seen to be in reasonably good agreement with the data for the initial development region. This verifies that the growth rate does indeed decrease as the ambient pressure decreases, as predicted by the linear theory (Fig. 2(a)).

In summary, the linear theory appears to predict the initial behavior of the sheet jets from Nozzle A quite well up to ratios of A_e/A_0 of between 15 and 30 (depending on A_0, f and p_a) for forcing amplitudes, A_0 up to almost 0.4 h_0 (i.e., $A_0 \simeq 0.3$ mm).

5.2 Results for Nozzle B. For the runs with the largest initial sheet jet thickness ($b_0 = 2h_0 \simeq 7.9$ mm, $w_0 = 75$ mm), the maximum initial jet velocity we could conveniently achieve was about 2.05 m/s; this low initial velocity resulted in substantial change in velocity due to the gravity acceleration. For forcing frequencies from 20 to 70 Hz, $(kh)_0$ ranged from 0.24 to 0.84. Since $(kh)_0 > 0.25$ for most of these runs, we can consider the Nozzle B results as representative of fairly "thick jet" cases. The initial Weber number was about 230.

For the 1 atm pressure runs at $U_0 = 2.05$ m/s, the initial critical frequency was $f_{(crit)0} = 23.0$ Hz (see Fig. 2(b)). Typical

photographs for runs made for forcing frequencies both below and above $f_{(crit)0}$ are shown in Fig. 11 [11]. The dramatic change in the waveform from near-sinusoidal to a sawtooth or zigzag shape with fall distance can be seen clearly on these photographs for the higher forcing frequencies. For $f = 50$ Hz, an additional phenomenon is visible. Using a stroboscope, fluid was observed to accumulate near the wave crests at the *front* and *back* edges of the sheet. (The locations of the fluid accumulations are not obvious from the edge-view photographs.) The fluid accumulations show up on photographs such as Fig. 11 as "blobs" or "globules" of fluid at the wave crests which appear to be trying to break free of the main wavy sheet. In reading the *mean* wave envelope data from such figures, we always excluded the fluid blobs and read the amplitude of the zigzag waveform of the main sheet jet, as mentioned previously.

Typical data for Nozzle B are plotted in Fig. 12 along with the predictions of the linear theory. At the lower frequency of 20 Hz, the linear theory predicts that the sheet jet will always be unstable. For the 20 Hz run at $A_0 = 1$mm, the constant-velocity linear theory agrees very well the data even though the velocity doubles in a fall distance of 60 cm and the temporal growth rate increases by about a factor of 5. (The
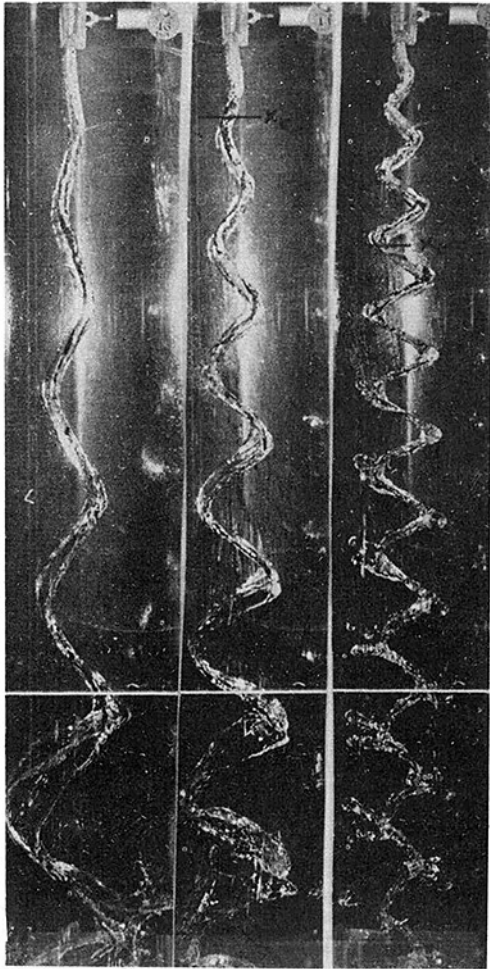
Fig. 11 Edge views of the sheet jets from Nozzle B ($h_0 = 3.94$ mm, $U_0 = 2.05$ m/s, $A_0 = 1.0$ mm, $p_a = 1.0$ atm) for three nozzle forcing frequencies: 20, 30, and 50 Hz (going from left to right)

Fig. 12 Comparison of the linear theory to experimental data for Nozzle B at two typical frequencies

resulting spatial growth rate increases by about a factor of 2.5.) The dashed curve shows the effect of variable velocity (using the approximate linear theory where the local values of $U(x)$, $b(x)$, and $\omega_i(x)$ were used at each computation step, as mentioned previously). For the 20 Hz runs, it appears that the variable velocity effects account for at least a part of the difference between the experimental data and the constant-velocity linear theory. However, it appears from Fig. 12 that nonlinear effects become important at very short fall distances for a forcing amplitude of 1.6 mm at 20 Hz forcing frequency.

For the higher forcing frequencies above the critical frequency of 23 Hz (Fig. 2(b)), the sheet jet is initially stable, but as it accelerates downward, the critical frequency increases until the jet becomes unstable at a transition point indicated by x_t (where $f_{\text{crit}}(x) = f$) in Fig. 11. Even though the sheet jet becomes unstable at $x_t \simeq 24$ cm for the 70 Hz run shown in Fig. 12, the data points show that the wave envelope amplitude continues to decrease. This behavior might be incorrectly identified with the behavior of sheet jets in the stable regime ($f > f_{\text{crit}}$) as shown by the half-sinusoidal linear theory curve for constant U_0, b_0, and ω_i in Fig. 12. In the stable regime, linear theory predicts that the wave envelope amplitude will increase initially due to the initial transverse momentum given the fluid particles as they leave the vibrating nozzle (not due to any instability). This can also be seen from equation (15) of the trajectory theory, since β^2 is negative in the stable regime (i.e., $\delta F_\sigma > \delta F_a$ in equation (16)).

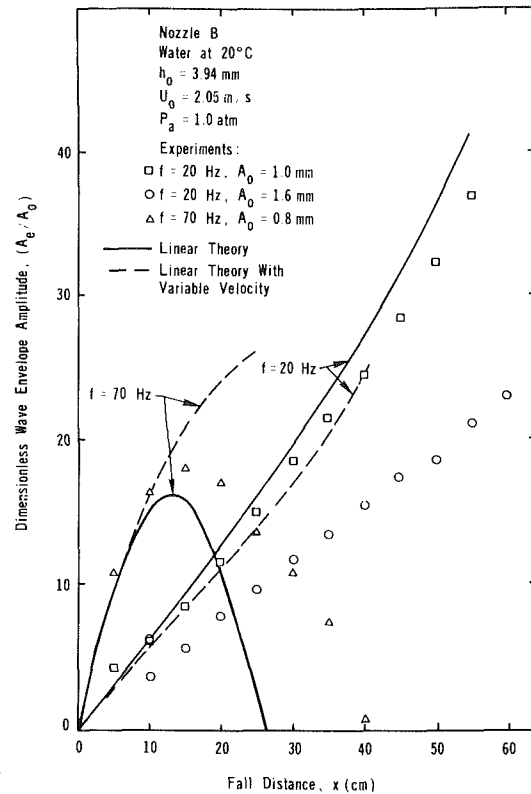After reaching a maximum, the wave envelope in the stable regime begins to decrease toward zero as the dominant surface tension forces overcome the initial transverse momentum and the weaker aerodynamic forces. For our inviscid theory, the wave envelope amplitude is predicted to continue to oscillate indefinitely due to the absence of any damping forces.

Including the effects of variable $U(x)$, $b(x)$, and $\omega_i(x)$ in the linear theory actually results in poorer agreement with the data for 70 Hz as can be seen from dashed curve in Fig. 12. We can tentatively conclude from this that the nonlinear effects are more important than the variable velocity effects for this initially-stable case. We can also surmise that the nonlinear effects must be stabilizing for this case in order to counteract the tendency of the variable velocity effects to cause the wave envelope to continue to grow with fall distance, contrary to the experimental results.

In summary, it appears that the linear theory does explain the behavior of the thicker jets from Nozzle B almost as well as for the thinner jets from Nozzle A in the initial region where the waveform is nearly sinusoidal; i.e., up to ratios of A_e/A_0 of about 15 to 20 for values of the forcing amplitude A_0 up to about $0.25 h_0$ (i.e., $A_0 \simeq 1$ mm).

Work is in progress on a paper comparing a nonlinear theory developed in reference [11] to the data. This theory appears to explain the trends in the data beyond the initial linear region up to the point where the sheet jet amplitude appears to saturate (and the jets begin to break up) [15].

6 Conclusions

Sheet jet experiments have verified that the predictions of the linear theory explain the data well for both our thin (small $(kh)_0$) and thick (larger $(kh)_0$) sheet jets in the initial region where the waveform is nearly-sinusoidal and the wave amplitude is not too large. The transformed linear temporal stability theory is compared to the linear spatial theory and is shown to yield the correct growth rates and wave amplitudes provided that the correct initial conditions are used. A simple

spatial trajectory theory proposed agrees very well with the approximate linear theory for thin jets and provides additional physical insight into the forces which control the spatial development of the sheet jets in both the unstable and stable regimes.

Acknowledgments

References

1 Maniscalco, J. A., Meier, W. R., and Monsler, M. J., "Conceptual Design of a Laser Fusion Powerplant," UCRL-79652, Lawrence Livermore Laboratory, July 14, 1977.

2 Monsler, M. J., Maniscalco, J. A., Blink, J., Hovingh, J., Meier, W. R., and Walker, P., "Electric Power from Laser Fusion: The HYLIFE Concept," UCRL-81259, Rev. 1, Lawrence Livermore Laboratory, June 1978.

3 Hoffman, M. A., Takahashi, R. K., and R. Monson, "Annular Liquid Jet Experiments," ASME JOURNAL OF FLUIDS ENGINEERING, Vol. 102, Sept. 1980, pp. 344–349.

4 Hoffman, M. A., and Potts, W. W., "Experimental Behavior of Falling Liquid Films at High Surface Tension Numbers," *Indus. & Eng. Chem. Fundamentals*, Vol. 18, No. 1, 1979, pp. 27–33.

5 Dombrowski, N., and Munday, G., "Spray Drying," Chapter 16 in *Biochemical and Biological Engineering Science*, Vol. 2, ed., N. Blakebrough, Academic Press, London, 1968.

6 Squire, H. B., "Investigation of the Instability of a Moving Liquid Film," *British J. of Applied Physics*, Vol. 4, June 1953, pp. 167–9.

7 Hagerty, W. W., and Shea, J. F., "A Study of the Stability of Plane Fluid Sheets," ASME *Journal of Applied Mechanics*, Vol. 77, Dec. 1955, pp. 509–514.

8 Rayleigh, Lord, *Theory of Sound*, 1894, Reprinted Dover Publications, N.Y., Vol. 2, 1954, pp. 376–381.

9 Lamb, H., *Hydrodynamics*, 5th Ed., Chapter 9, Cambridge Univ. Press, 1932.

10 Gaster, M., "A Note on the Relation between Temporally-Increasing and Spatially-Increasing Disturbances in Hydrodynamic Stability," *Journal of Fluid Mechanics*, Vol. 14, 1962, pp. 222–224.

11 Asare, H. R., "Theoretical and Experimental Investigation of Water Sheet Jets Under Forced Vibration," Ph.D. thesis, Department of Mechanical Engineering, University of California, Davis Campus, Nov. 1980.

12 Shapiro, A. H., *The Dynamics and Thermodynamics of Compressible Fluid Flow*, Vol. I, Chapter 10, Ronald Press, N.Y. 1953.

13 Hoffman, M. A. et al. "Research on the HYLIFE Liquid-First-Wall Concept for Future Laser-Fusion Reactors," Final Report No. 4, Department of Mechanical Engineering, University of California, Davis Campus, Mar. 1979.

14 Takahashi, R. K., "Experimental Investigation of the Stability of Liquid Sheet Jets," M.S. thesis, Department of Mechanical Engineering, University of California, Davis Campus, Dec. 1978.

15 Asare, H. R., and Hoffman, M. A., "Liquid Sheet Jet Experiments: Comparison with a Nonlinear Theory" (in preparation).

spatial trajectory theory proposed agrees very well with the approximate linear theory for thin jets and provides additional physical insight into the forces which control the spatial development of the sheet jets in both the unstable and stable regimes.

Acknowledgments

References

1 Maniscalco, J. A., Meier, W. R., and Monsler, M. J., "Conceptual Design of a Laser Fusion Powerplant," UCRL-79652, Lawrence Livermore Laboratory, July 14, 1977.

2 Monsler, M. J., Maniscalco, J. A., Blink, J., Hovingh, J., Meier, W. R., and Walker, P., "Electric Power from Laser Fusion: The HYLIFE Concept," UCRL-81259, Rev. 1, Lawrence Livermore Laboratory, June 1978.

3 Hoffman, M. A., Takahashi, R. K., and R. Monson, "Annular Liquid Jet Experiments," ASME JOURNAL OF FLUIDS ENGINEERING, Vol. 102, Sept. 1980, pp. 344–349.

4 Hoffman, M. A., and Potts, W. W., "Experimental Behavior of Falling Liquid Films at High Surface Tension Numbers," *Indus. & Eng. Chem. Fundamentals*, Vol. 18, No. 1, 1979, pp. 27–33.

5 Dombrowski, N., and Munday, G., "Spray Drying," Chapter 16 in *Biochemical and Biological Engineering Science*, Vol. 2, ed., N. Blakebrough, Academic Press, London, 1968.

6 Squire, H. B., "Investigation of the Instability of a Moving Liquid Film," *British J. of Applied Physics*, Vol. 4, June 1953, pp. 167–9.

7 Hagerty, W. W., and Shea, J. F., "A Study of the Stability of Plane Fluid Sheets," ASME *Journal of Applied Mechanics*, Vol. 77, Dec. 1955, pp. 509–514.

8 Rayleigh, Lord, *Theory of Sound*, 1894, Reprinted Dover Publications, N.Y., Vol. 2, 1954, pp. 376–381.

9 Lamb, H., *Hydrodynamics*, 5th Ed., Chapter 9, Cambridge Univ. Press, 1932.

10 Gaster, M., "A Note on the Relation between Temporally-Increasing and Spatially-Increasing Disturbances in Hydrodynamic Stability," *Journal of Fluid Mechanics*, Vol. 14, 1962, pp. 222–224.

11 Asare, H. R., "Theoretical and Experimental Investigation of Water Sheet Jets Under Forced Vibration," Ph.D. thesis, Department of Mechanical Engineering, University of California, Davis Campus, Nov. 1980.

12 Shapiro, A. H., *The Dynamics and Thermodynamics of Compressible Fluid Flow*, Vol. I, Chapter 10, Ronald Press, N.Y. 1953.

13 Hoffman, M. A. et al. "Research on the HYLIFE Liquid-First-Wall Concept for Future Laser-Fusion Reactors," Final Report No. 4, Department of Mechanical Engineering, University of California, Davis Campus, Mar. 1979.

14 Takahashi, R. K., "Experimental Investigation of the Stability of Liquid Sheet Jets," M.S. thesis, Department of Mechanical Engineering, University of California, Davis Campus, Dec. 1978.

15 Asare, H. R., and Hoffman, M. A., "Liquid Sheet Jet Experiments: Comparison with a Nonlinear Theory" (in preparation).

DISCUSSION

S. G. Lekoudis[1]

The authors state that they proved that for a single wavetrain with a single imposed frequency, the group velocity is equal to the phase velocity. The concept of the group velocity is related to the dispersion relationship of the medium and, by definition, involves frequencies and wave numbers as *functions* of each other. Thus, although a single component does have a group velocity, the group velocity cannot be estimated unless more components are assumed to exist. What is probably happening is that the medium is not very dispersive and the group velocity and the phase velocity are close to each other. Moreover, the spatial amplification rates are not that large, and they do not upset the transformation, between temporal and spatial stability.

P. J. Morris[2]

The authors have provided a useful and practical application of linear stability theory. The agreement between their carefully conducted experiments and the analysis in the initial regions of the jets is impressive. However the reason for the close agreement between the growth rates as predicted from either temporal or spatial analyses using Gaster's [10] transformation is not as stated in the paper. To show this it is convenient to write the dispersion relationship, equation (3), in nondimensional form. Using h_o, U_o and ρ, the sheet jet density as the reference length, velocity and density scales, equation (3) may be written,

$$\left(\frac{\omega^*}{k^*} - 1\right)^2 \tanh(k^*) + r_d\left(\frac{\omega^*}{k^*}\right)^2 - \frac{k^*}{\text{We}} = 0,$$

where an asterisk denotes a dimensionless quantity and the authors' notation has been used for the density ratio and Weber number. If the group velocity is determined from temporal stability theory as $\partial(\omega^*_r)/\partial k^*$ then it is readily shown to be given by

$$\frac{\partial(\omega^*_r)}{\partial k^*} = \frac{1}{[1 + r_d/\tanh(k^*)]}$$
$$+ \frac{r_d}{\tanh(k^*)}\left\{\frac{k^* \text{sech}^2(k^*)/\tanh(k^*)}{[1 + r_d/\tanh(k^*)]^2}\right\}$$

In the limit of $r_d \ll \tanh(k^*)$ and $k^*/\tanh(k^*)$ of order unity which corresponds, except for $k^* \ll 1$, to the authors' conditions, the group velocity is equal to unity and is also equal to the phase velocity, ω^*_r/k^*. However for larger values
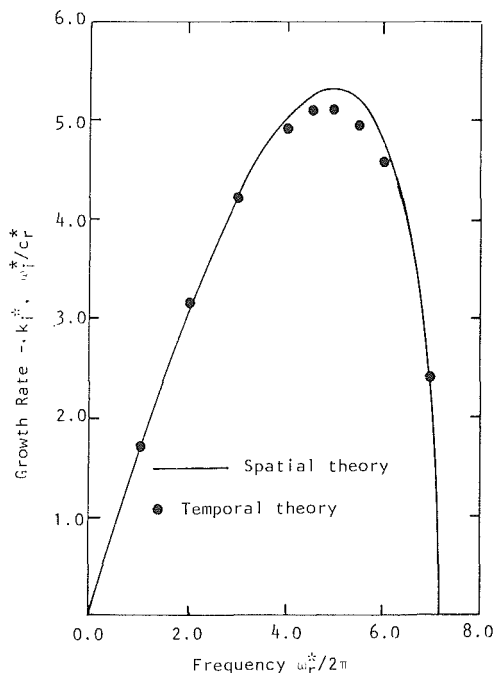

Fig. 13 Comparison of spatial and temporal growth rates. We = 713.5, $r_d = 0.0737$.

of density ratio this approximation is not valid. Another requirement for Gaster's transformation, which appears to have been developed for use in boundary layers, is that the amplification rates be small. For the present problem the nondimensional form of the temporal growth rate is

$$\frac{\omega_i^*}{2\pi f^*} = \sqrt{\left\{\frac{r_d}{2\pi f^*} - \frac{1}{\hat{We}}\right\}\frac{k^*}{\tanh(k^*)}},$$

where $f^* = \omega_r^*/2\pi \simeq k^*/2\pi$.

It is clear that the surface tension is always a stabilizing influence acting to reduce the growth rate. The growth rate is set by the magnitude of the density ratio. For the case of a water jet issuing into air at atmospheric pressure r_d is of order 10^{-3} and the associated growth rates are very small. However for lower density ratios the nondimensional growth rates are higher and the approximations in Gaster's analysis are more questionable. To demonstrate this effect a different fluid problem may be considered. If a jet of mercury is issuing into fresh water at 20°C with exit velocity of 5 m/s and $h_o = 0.79$ mm the density ratio $r_d = 0.0737$ and the Weber number We = 713.5. Calculations of the nondimensional, spatial growth rate are shown in the figure. The growth rates are calculated from solution of the dispersion relationship and from

transformation of the temporal growth rates using the phase velocity and group velocity. Since k^* is large for all but the lowest frequencies the phase velocity and group velocity are both equal to $1/(1 + r_d)$ for f^* greater than about 0.6 where tanh (k^*) is close to unity. It can be seen that the greatest differences occur for the largest rates.

These comments do not invalidate the numerical results of the paper which are correct. However it is clear that the relationship between temporal and spatial growth rates proposed by the authors is only valid in the limit of small density ratio. It should be emphasized that this condition is met for the applications considered in the paper however it is not generally true for all jet and ambient fluids.

Authors' Closure

The authors are indebted to Professors Morris and Lekoudis for their cogent observations. In particular, we agree with Professor Morris that it is a necessary condition that the density ratio, r_d, be very small compared to tanh k^* for the spatial growth rate to be given accurately by Gaster's transformation of the temporal growth rate for this particular problem of a liquid sheet jet injected into a fluid of lower density.

K. Bremhorst

Reader, Department of
Mechanical Engineering,
University of Queensland,
St. Lucia, Queensland, Australia,   4067

R. D. Watson

Engineer, Telecom Australia,
Formerly Postgraduate Student,
University of Queensland

Velocity Field and Entrainment of a Pulsed Core Jet

A pulsed core jet is one consisting of a steady annular flow with a core, the mass flow of which is unsteady. The combined jet exhausts into a still environment. The velocity field and entrainment characteristics for such a jet have been measured for various mass flow ratios of pulsed-to-steady flow and several frequencies of pulsation. Results show the radial distribution of mean velocity to be similar to those of steady jets except very close to the nozzle, the decay of the centerline mean velocity to be less than that of steady jets, and the entrainment to be larger than that of steady jets but less than fully pulsed ones. No significant sensitivity to frequency of pulsation was observed, but the velocity field is strongly dependent on the ratio of core flow to annular flow.

1 Introduction

Unsteady jet flows are slowly becoming of more interest as their potential of increased entrainment and spreading rate relative to steady jets is being recognized for possible application in thrust augmentation ejectors, combusting flows, and mixing processes. Such jets are also of interest in acoustics, as exhausts from many pneumatic and combustion machines are unsteady. A previous study [1] has summarized some of the unsteady jet results so far available.

In view of the many types of designs possible for pulsed jets, it is difficult to draw significant conclusions from existing data other than that the type of pulsing, the strength of the pulsation, and the frequency of pulsation can significantly alter the velocity field. The purpose of the present note is to explore the characteristics of the pulsed core jet which was designed to combine the convenience and quietness of the steady jet with the high entrainment and mixing rate of the fully pulsed jet. Although the fundamentals of fully pulsed jets are not well understood, it was speculated that the "explosive" nature of the individual bursts produced in the pulsed core should modify the nature of the essentially steady annular jet surrounding it, thus altering its characteristics. For practical purposes, a pulsed core jet with a small diameter core is of interest as this would minimize additional power required to permit pulsing to take place.

2 Experimental Apparatus

The device used to generate the pulsed core jet is shown in Fig. 1. Flow rates to the two jets were measured with orifice flow meters. The flow meter for the pulsed flow was located upstream of a large plenum chamber where the flow was essentially free of pulsation. Velocities were measured with a single linearized hot-wire anemometer placed normal to the flow using the method of linearization already described in [2].
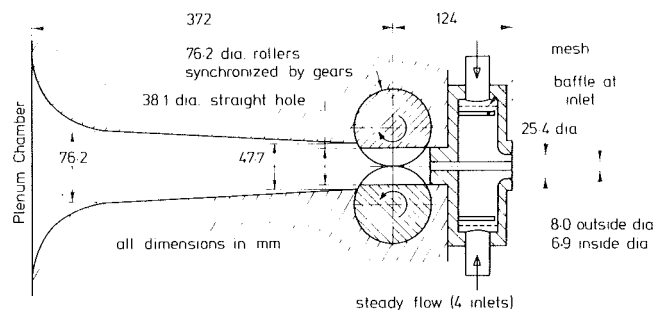
Fig. 1 Schematic of pulsed core jet

Preliminary traverses showed that the jets were close to axisymmetric thus requiring traverses to be conducted only along one diameter. The rollers in the pulsator were driven at a fixed speed and resulted in an on-to-off time ratio of 1:2. The maximum frequency of pulsation was limited to approximately 30 Hz by the mechanical design. U_c/U_a ratios were obtained by holding U_E approximately constant and varying the value of U_c.

3 Results

Measurements were obtained for pulsation frequencies of 10 and 25 Hz corresponding to Strouhal numbers based on the core diameter at exit (6.9 mm) of 0.0013 and 0.0033, respectively, for $U_c/U_a = 2.9$. Data were found to be almost invariant with frequency of pulsation so that only the results for 10 Hz pulsation are presented [3].

Typical radial velocity distributions are shown in Fig. 2 together with analytical expressions fitted to the test data. The two expressions used for this comparison are

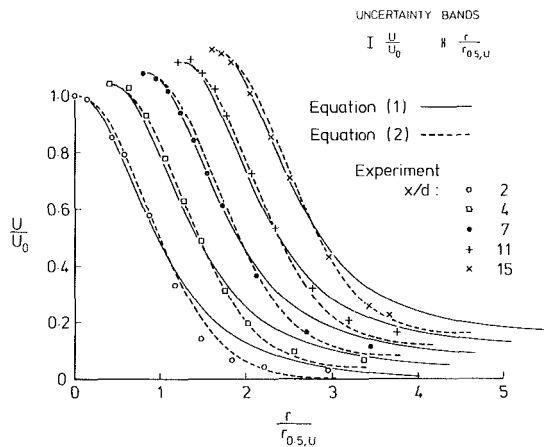$$\frac{U}{U_0} = \left[1 + \alpha (r/r_{0.5,U})^2\right]^{-2} \qquad (1)$$

and

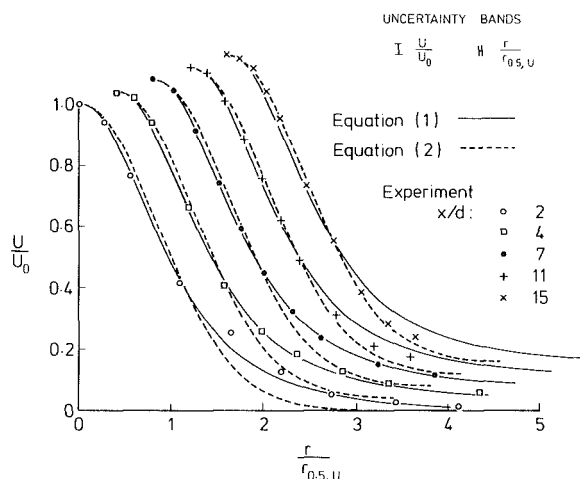Fig. 2(a) Mean velocity profiles, $U_c/U_a = 0.45$

Fig. 2(b) Mean velocity profiles, $U_c/U_a = 2.9$

$$\frac{U}{U_0} = \exp\left[-\beta(r/r_{0.5,U})^2\right] \qquad (2)$$

which have been used successfully for steady jets. In the case of fully pulsed jets, $\alpha = 0.44$ was found to give a good fit to experimental data [2] even though this value obviously does not satisfy equation (1) at $r = r_{0.5,U}$. The same constant was retained in the present work, whereas for equation (2) the traditional value of 0.693 was used for β thus satisfying equation (2) at $r = r_{0.5,U}$.

Axial decay of the centerline mean velocity, half-value radius for mean velocity, and jet volume flow are shown in Figs. 3, 4, and 5. The volume flow is defined as is in [2] and

[4], namely, as the area under a plot of rU versus r where the tail of this distribution is drawn in by eye such as to exclude the potential portion of the flow represented by the section of the curve where rU remains almost constant for increasing r. This method is simple and gives consistent results as the break-point between the turbulent region and the potential outer flow is generally clearly visible.

Axial changes of velocity and half-value radii tended to follow the following expressions for $2 \leq x/d \leq 15$,

$$\frac{U_0}{U_E} = A \frac{d}{x+a} \qquad (3)$$

$$2r_{0.5,U} = A_1(x+a_1) \qquad (4)$$

The constants for the various cases are summarized in Table 1, but these data are not to be interpreted as proof of similarity in this flow region. Comparison of experimental points in Figs. 2(a) and (b) with the curves representing equation (2) illustrates the effect of U_c/U_a on the radial distributions of mean velocity. Near the jet exit, U_0 is significantly affected by the core mass flow, but this is quickly damped out by the outer flow with no effect of U_o/U_a remaining visible at $x/d = 15$. This is to be expected as all nonsteady jets must degenerate into a steady jet at sufficiently large values of x/d for which equation (2) is a fair approximation. Some sensitivity to U_c/U_a is noted in the axial decay of U_0, Fig. 3, but it is most pronounced for the half-value radius, Fig. 4. As U_c/U_a increases for constant U_E, U_0/U_E becomes increasingly larger relative to the value it would have if steady jet conditions prevailed. This leads to a reduction in the half-width of the whole jet through a shift of the virtual origin, but the jet spreading rate, A_1, is unaffected and is almost the same as for steady and fully pulsed jets [2]. Most important, however, is the volume flow result, Fig. 5, from which it is evident that the volume flow and hence entrainment characteristics of the jet are significantly dependent on U_c/U_a. Unexpected, however, is the result that as U_c/U_a increases to the higher values tested, volume flow decreases. Thus, instead of the stronger pulsing, represented by higher U_c/U_a values, leading to more engulfing of ambient fluid, the opposite occurs. All cases are seen to be well above those of the undisturbed steady jet of [4].

Although the mean velocity distributions, Figs. 2(a) and (b), showed self-similarity to be attained relatively quickly, this was not found to be the case for the streamwise turbulence energy. At the high values of U_c/U_a, Fig. 6(a), the convenient bell-shaped distribution which can be represented by equations (5) and (6) was obtained, again with $\alpha = 0.44$ and $\beta = 0.693$.

$$\frac{\overline{u^2}}{\overline{u_0^2}} = \left[1 + \alpha(r/r_{0.5,\overline{u^2}})^2\right]^{-2} \qquad (5)$$

_____ Nomenclature _____

a, a_1, a_2, a_3 = effective origins for $U_0, r_{0.5,U}, \sqrt{\overline{u_0^2}}, r_{0.5,\overline{u^2}}$

A, A_1, A_2, A_3 = slopes of laws for $U_0, r_{0.5,U}, \sqrt{\overline{u_0^2}}, r_{0.5,\overline{u^2}}$

d = overall jet diameter at exit

Q, Q_E = jet volume flow at a plane downstream and at the jet exit plane, respectively

r = radial coordinate

$r_{0.5,U}, r_{0.5,\overline{u^2}}$ = half-value radii of U and $\overline{u^2}$

Re_i = Reynolds number of core based on U_c and core diameter

Re_0 = Reynolds number of annular flow based on U_a and the overall jet diameter at exit

u = instantaneous velocity fluctuation about

the local mean velocity

u_0 = u at jet centerline

U = time mean velocity at a point

U_a = bulk mean velocity of annular flow at jet exit

U_c = bulk mean velocity of core flow at jet exit

U_0 = mean velocity at jet centerline

U_E = bulk mean velocity of whole jet at exit based on total mass flow, overall jet diameter, and ambient temperature and pressure

α, β = constants in radial velocity distributions

Table 1 Summary of Data

Quantity	Data				Accuracy Percent
U_o/U_a	0	0.45	0.86	2.9	4.8
Re_i	0	6.3×10^3	9.9×10^3	2.4×10^4	2.0
Re_0	4.8×10^4	5.0×10^4	4.2×10^4	3.2×10^4	2.5
$U: a/d$	3.5	3.8	2.9	1.0	(1)
A	6.92	6.6	6.94	6.2	(1)
$r_{0.5,U}:a_1/d$	4.5	4.5	3.7	0.42	(1)
A_1	0.22	0.22	0.22	0.22	(1)
$\dfrac{\left(\overline{u_0^2}\right)^{0.5}}{U_E}:a_2/d$	5.1	6.04	3.67	1.67	(1)
A_2	2.17	2.1	1.9	4.91	(1)
$r_{0.5,u\overline{2}}:a_3/d$	4.04	4.04	0.96	-1.75	(1)
A_3	0.31	0.31	0.32	0.19	(1)

Note: Accuracies designated by (1) are not stated, as traditionally accepted functional forms are presented in the figures using the values of parameters shown in order to display deviations from these general forms.
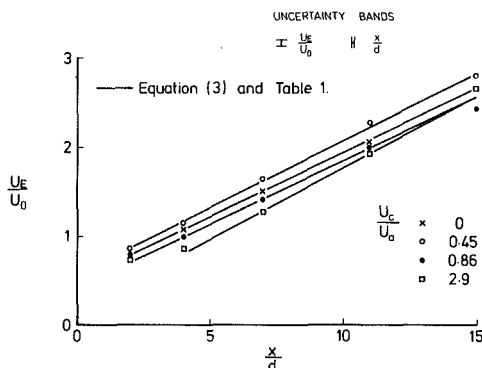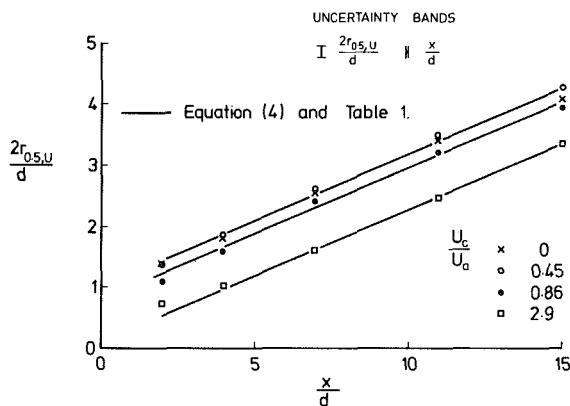

Fig. 3 Decay of mean axial velocity

Fig. 5 Axial dependence of volume flow for U_E constant

Fig. 4 Growth of mean velocity half-value radius

$$\frac{\overline{u^2}}{\overline{u_0^2}} = \exp\left[-\beta(r/r_{0.5,\overline{u}2}{}^2)\right]^{-2} \qquad (6)$$

At the lower values U_c/U_a, completely different profiles exist, Fig. 6(b). These are more typical of steady jet profiles where the peak energy occurs away from the jet centerline. This is to be expected, as for large U_c/U_a the turbulence in the center region consists mainly of a periodic velocity fluctuation superimposed on which are the small random fluctuations produced by the shear flow in the mixing region of the jet.

Axial decay of the centerline turbulence intensity is well represented by equations (7) for the majority of the flow, Fig. 7, whereas equation (8) represents the half-width of the turbulence energy distributions, Fig. 8. These two sets of data illustrate the role of the level of core pulsation. Again a lack
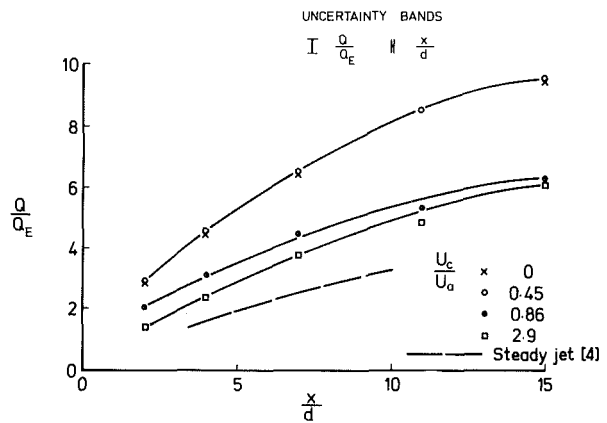
of self-similarity, as implied by departure from equation (7) and (8), is noted. The constants for the various cases are summarized in Table 1.

$$\frac{\left(\overline{u_0^2}\right)^{0.5}}{U_E} = A_2 \frac{d}{x+a_2} \qquad (7)$$

$$2r_{0.5,\overline{u}2} = A_3(x+a_3) \qquad (8)$$

4 Concluding Remarks

Limited comparison of the present data with those for other unsteady jets [1] is possible. Decay of mean velocity is somewhat less than for steady and most other types of partially pulsed jets, but is significantly higher than for a fully pulsed jet [2]. The rate of decay is not a strong function of U_c/U_a. However, as found for other unsteady jets, the virtual origin, a/d, is crucially dependent on the level of pulsation, in this case represented by U_c/U_a. Change of half-width with x/d is similar to other pulsed jets with little dependence on U_c/U_a, but the effective origin, a_1/d, varies with U_c/U_a. Volume flow relative to that at the jet exit, which is of interest whenever entrainment is considered, is larger than for steady jets with no interference in the center region (in contrast to the present case when $U_c/U_a = 0$), but is significantly below that for fully pulsed jets [2]. As U_c/U_a increases, the volume flow decreases which could be used as a means of controlling the entrainment of such a jet. No sensitivity to frequency of pulsation was observed at the low Strouhal numbers tested. The present data further illustrate the complexity of unsteady jets flows for which few theoretical predictions have been attempted and only limited data are available in the literature.
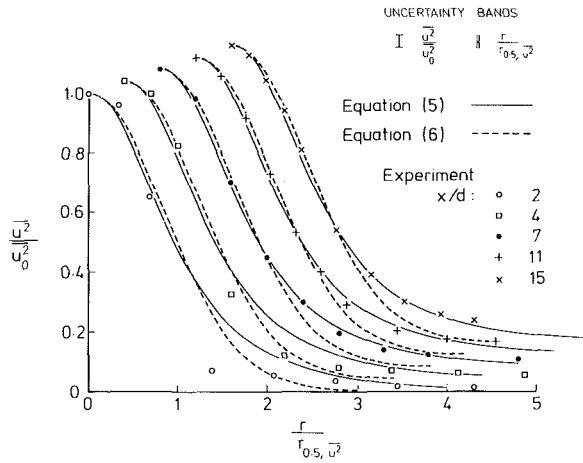
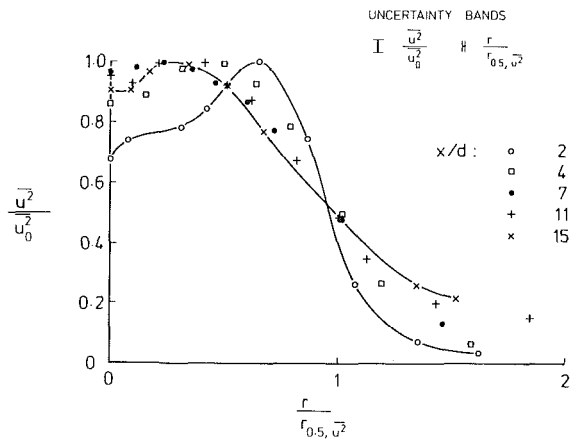Fig. 6(a)   Turbulence energy profiles, $U_c/U_a = 2.9$

Fig. 7   Decay of maximum turbulence intensity

Fig. 6(b)   Turbulence energy profiles, $U_c/U_a = 0.45$
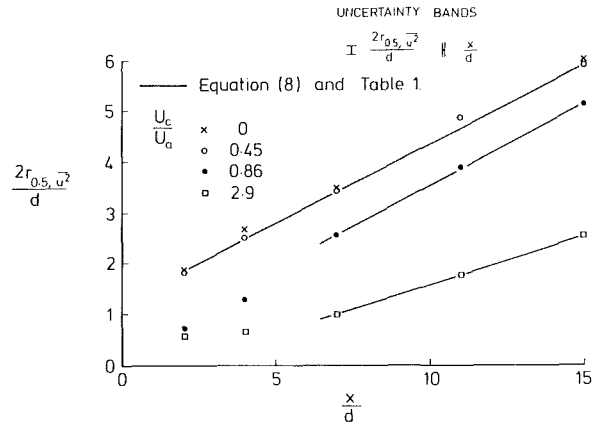
Fig. 8   Growth of turbulence energy half-value radius

5   Acknowledgments

References

1 Bremhorst, K., "Unsteady Subsonic Turbulent Jets," *Recent Develop-ments in Theoretical and Experimental Fluid Mechanics*, ed., U. Mueller, K. G. Roessner, and B. Schmidt, Springer, 1979.

2 Bremhorst, K., and Harch, W. H., "Mean Field Velocity Measurements in a Fully Pulsed Subsonic Air Jet," *Turbulent Shear Flows I*, ed., F. Durst, B. E. Launder, F. W. Schmidt, and J. H. Whitelaw, Springer, 1979.

3 Watson, R. D., "An Experimental Investigation into the Velocity Field of a Pulsed Core Jet," M. Eng. Sci. thesis, Department of Mechanical Engineering, University of Queensland, Brisbane, Australia, 1978.

4 Crow, S. C., and Champagne, F. H., "Orderly Structure in Jet Tur-bulence," *Journal of Fluid Mechanics*, Vol. 48, Part 3, 1971, pp. 547-591.

M. Favre-Marinet

G. Binder

Te. V. Hac

Institut de Mécanique,
Laboratoire associé au C.N.R.S.,
Université Scientifique et
Médicale de Grenoble,
38041, Grenoble-Cedex, France.

Generation of Oscillating Jets

It is shown that periodic angular oscillations can be forced on a jet issuing from a nozzle based on the Coanda effect by alternate blowing from the two sides. The influence of the various geometric and dynamic parameters such as the jet width, the blowing direction, the blowing generating pressure, the jet velocity, and frequency has been investigated. The angular deflection can conveniently be controlled by the blowing pressure.

1 Introduction

The most important property of jets for practical applications is their ability to mix with the ambient fluid, in particular in combustion chambers and ejectors. In recent years, various attempts have been made to improve the mixing rate of jets by swirl, by modifying the nozzle geometry, or by imposing periodic perturbations on the jet.

Swirl is at the present time commonly used to stabilize the flame and reduce its length, owing to faster mixing [1].

The effects of geometry have been studied by Quinn [2] with the two-dimensional hypermixing nozzle, which imposes alternatively positive and negative deflections in the spanwise direction. It was shown that ejector performances were effectively improved with such a nozzle. In the case of circular jets, Bradbury [3] has shown that the jet would spread faster if small obstacles destroying the axisymmetry were introduced in the nozzle.

The influence of forced modulation of the flow rate on the jet spread has been studied by various authors [4, 5]. The whistler nozzle [6] which also produces spontaneous pulsations falls into the same category.

In a preliminary investigation [7], it was shown that angular oscillations forced on a jet greatly enhanced its rate of spread. This result was confirmed by Viets [8]. This author has investigated the influence of various nozzle geometries on the thrust efficiency and on the fluidic oscillator: The frequency was controlled by the length of the feedback loop. The results given depend upon the particular shape of the nozzle.

For a more general purpose, it would be interesting to relate the properties of the jet to the initial conditions, in particular to the initial periodic deflection angle. Such an investigation is being undertaken in our laboratory. A first step of this investigation was to develop a nozzle able to produce periodic deflections which are regular, reproducible, and of controlled amplitude.

The nozzle used is based on the Coanda effect.

It is well known that a stream can be deflected by the presence of a wall. Since the wall is impermeable, the en-

trainment on the corresponding side is confined. This creates a negative pressure which can only be balanced by a curvature of the streamlines. The jet is therefore deflected toward the wall.

Thus in the presence of a curved wall and for appropriate values of the ratio d_0/R_s (d_0 being the jet width and R_s the radius of curvature of the wall), the jet may stay attached to the wall over a long distance [9-12]. For instance, for $d_0/R_s < 0.05$, the jet is deflected 180 deg, whereas for $d_0/R_s = 0.3$, the deflection is reduced to 30 deg.

In the present setup, the jet issues between two cylinders (Fig. 1) which form the Coanda surfaces. The jet is therefore in a bistable position and may attach to either side.

By injecting fluid through slots into the attachment region, the jet separates and flips over to the other cylinder. By alternate blowing from one cylinder to the other, the jet is forced to oscillate.

In most previous investigations, only steady-state jet deflections were studied. Dynamic oscillations of jets have of course been produced and investigated in fluid amplifiers, [8] but the nozzle used in the present research differs from fluid amplifiers in many aspects: physical size, lack of confinement of the flow downstream of the nozzle, and independent frequency control. Moreover, in fluid amplifiers, the deflection is fixed by the geometry itself. From previous studies, it was not possible to infer the value of the periodic angular deflection from the knowledge of the geometry and the value of the dynamic variables (velocities, frequency). A special study was therefore required.

In this paper, the influence of various geometric and dynamic parameters on the initial periodic oscillations of the jet is investigated.

2 Apparatus and Measurement Technique

2.1 Apparatus. The apparatus is a classical jet facility, with a blower, control valve, a settling chamber, and the nozzle, which is the original part of the setup. It consists of two parallel cylinders (radius R_s) which form a slot of width d_0 (Figs. 1-2). The length of the cylinders is $h = 100$ mm. Most measurements have been performed with $d_0 = 1$ cm or less, so the aspect ratio of the nozzle was ten or more. A fine slot
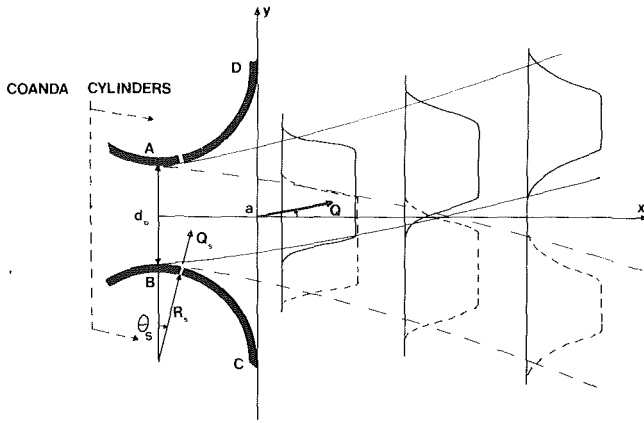
Fig. 1 Defining sketch

(width $d_s = 0.3$ mm) is cut along a generator of each cylinder for the injection of the secondary flow which blows the primary jet off one cylinder toward the other. Alternate blowing is obtained by a cylindrical valve with two mutually perpendicular passages, so that the secondary flow to one cylinder is blocked when it is maximum into the other one (Fig. 3). This is the only moving part of the system. Since the rotating part is cylindrical, it can be machined very easily and high rotational speeds can be reached without difficulty. This valve is driven by a variable speed motor which determines the frequency of oscillation of the jet: f, which is twice the motor speed, since after half a turn, the valve is again in the same position. The secondary flow was bled of the supply from the blower upstream of the main control valve. The main flow rate of the jet and the blowing rate may be controlled independently by separate valves. The generating pressures of the main jet p_0 and of the secondary flow p_s were measured, respectively, in the settling chamber and in the duct (dia: 50 mm) immediately upstream of the rotating valve. Different orientations of the blowing slots (θ_s) may be obtained by rotating the cylinders about their axes.

The velocity field of the jet is modified by the imposed oscillation. If we suppose that in the exit section ay, the jet velocity is uniform and nonturbulent, the velocity vector and therefore its angle θ with the mean direction are periodic functions of time

$$\begin{aligned} \theta &= \Theta g(t/T) \\ u &= Q\cos\theta \\ v &= Q\sin\theta \end{aligned} \tag{1}$$

where Q is the magnitude of the velocity, which is approximately time-independent, Θ is the amplitude of the angular oscillation which we shall call the flapping angle, and $g(t/T)$ is a periodic function of time.

Actually, because of wall friction on the nozzle, the jet at the exit is not perfectly uniform. Moreover, turbulence is generated in the region of interaction with the blowing jet and develops rapidly downstream. u, v, and θ depend, therefore, to some extent on the position and have random fluctuations. A more rigorous definition of the flapping angle would therefore be based on integral quantities, such as the ratio of the transverse to the longitudinal momentum flux. But this would demand the measurement of instantaneous u and v profiles. The purpose of the present study being the investigation of the influence of various geometric and dynamic parameters on the flapping angle, such a determination of θ would have required the collection of a considerable amount of data. We have therefore attempted to characterize the flapping angle by a local value. Since Θ varies little in the neighbourhood of the nozzle, as will be shown later, we have chosen to define the flapping angle by the value of Θ at the point $x=0$, $y=0$ (Fig. 1).
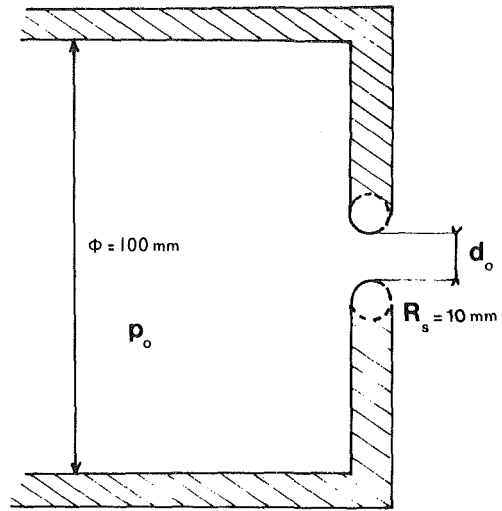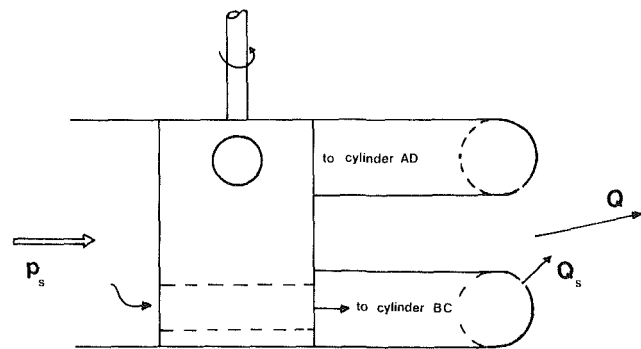

Fig. 2 Sketch of the nozzle

Fig. 3 Pulsator valve

Θ depends upon the following parameters:
* Geometric parameters: θ_s, d_s; d_0; R_s
* Dynamic parameters: Q or p_0, p_s, f

From these, five nondimensional numbers may be obtained: θ_s, d_0/R_s, d_s/R_s, $C_p = p_s/p_0$, and $S = fd_0/Q$, the Strouhal number.

The only parameter which cannot be varied is $d_s/R_s = 0.03$. Since the jet Reynolds number in the present study was always larger than 10^4, its influence on the flow was certainly small and was not investigated.

2.2 Measurement Technique. Turbulence develops in the flow downstream of the nozzle and a component of the velocity, u, say, has three parts:

$$u = \bar{u} + \tilde{u} + u' \tag{2}$$

$\bar{u} = $ mean velocity
$\tilde{u} = $ periodic fluctuation with zero mean, $(\bar{\tilde{u}} = 0)$
$u' = $ turbulent fluctuation

The ensemble average of u depends upon the phase angle $\varphi = 2\pi t/T$ of the basic cycle

$$<u>(\varphi) = \bar{u} + \tilde{u}(\varphi)$$

which is the same as the phase average defined by:

$$\lim_{N\to\infty} 1/N \sum_{i=0}^{N-1} u(\varphi + 2\pi i)$$

In order to eliminate the influence of the turbulence, the angle θ is defined with the phase averages of u and v

$$\theta(\varphi) = \arctan(<v>/<u>) \tag{3}$$

Since θ is not necessarily a simple harmonic function of time, we define the flapping angle as the amplitude Θ of the fundamental mode obtained by Fourier analysis of $\theta(\varphi)$.

The measurements were made with two constant tem-

perature anemometers. one hot wire was perpendicular to the mean direction and the other one was at an angle of 45 deg. The phase averages were determined by periodic sampling of the two hot wire signals $e_{1,2}$. A reference pulse phase-locked with the rotating valve was generated with a photoelectric device. This gave a reference phase angle φ_0. n samples of each signal were taken during one cycle: $e_{1,2}$ $[\varphi_0 + (j - 1)2\pi s/T]$, s being the sampling-time interval $(1 \leq j \leq n$, $ns = T)$. The beginning of each sampling cycle was triggered by the reference pulse. The averaging was performed over N cycles. The samples occurring at the same instant of the period (same j) were added to obtain the phase average:

$$<e_{1,2}[\varphi_0 + (j - 1)2\pi s/T]>$$
$$= 1/N \sum_{i=1}^{N} e_{1,2} [\varphi_0 + (j - 1)2\pi s/T + 2\pi(i - 1)]$$

Sampling and averaging were performed on a digital multichannel analyzer (Intertechnique, DIDAC 800) with the values: $n = 200$, $N = 4000$. The data of the analyzer were transfered to an IBM computer 1130 where the separation of the hot wire signals and the Fourier analysis were performed.

2.3 Measurement Accuracy. The error on the flapping angle may be estimated from the response of the two wires:

$$e_1 = K_1 u$$
$$e_2 = K_2(u\cos\gamma - v\sin\gamma)$$

where K_1 and K_2 are the sensitivity coefficients, γ is the angle between the normal to the inclined wire and the x-axis ($\gamma \simeq 45$ deg).

The instantaneous angle θ is defined by relation (3); for angles smaller than 15 deg, $\tan\theta \simeq \theta \simeq v/u$. The main source of error comes from the determination of v due to errors in the sensitivity coefficients and in γ. Straightforward calculation shows:

$$dv/u = - \left[\left(\frac{dK_1}{K_1} + \frac{dK_2}{K_2} \right) \text{ctn } \gamma + d\gamma \right]$$
$$+ \left(\frac{dK_2}{K_2} - d\gamma \text{ ctn } \gamma \right) \frac{v}{u} \qquad (4)$$

which is of the form:

$$dv/u = A + B\theta$$

The first term A corresponds to a constant shift of v and therefore introduces no error on the flapping angle. This includes, in particular, the effects of small temperature changes between calibration and measurement. The second term changes sign with v and introduces an error on the amplitude of v. According to (3) $d\theta \simeq dv/u$, so that the same errors occur in $d\theta$ as in dv.

On the other hand, the flapping angle is computed with the Fourier integral:

$$\Theta = \frac{1}{\pi} \int_0^\alpha \theta \cos \varphi \, d\varphi \qquad (\alpha \simeq 2\pi)$$

The uncertainty in Θ results from the error in θ calculated above and from the error in the integration interval α with respect to 2π.

$$d\Theta \simeq \frac{1}{\pi} \int_0^\alpha [A + B\theta]\cos\varphi d\varphi + \frac{1}{\pi} \theta(\alpha)\cos\alpha d\alpha$$

$$d\Theta \simeq B\Theta + \frac{d\alpha}{\alpha} . 2\theta(\alpha)\cos\alpha < \left(B + 2\frac{d\alpha}{\alpha} \right) \Theta$$

It follows that:

$$\Delta\Theta/\Theta \simeq [(\Delta K_2/K_2)^2 + (\Delta\gamma)^2 \text{ctn}^2\gamma + (2\Delta\alpha/\alpha)^2]^{1/2}$$
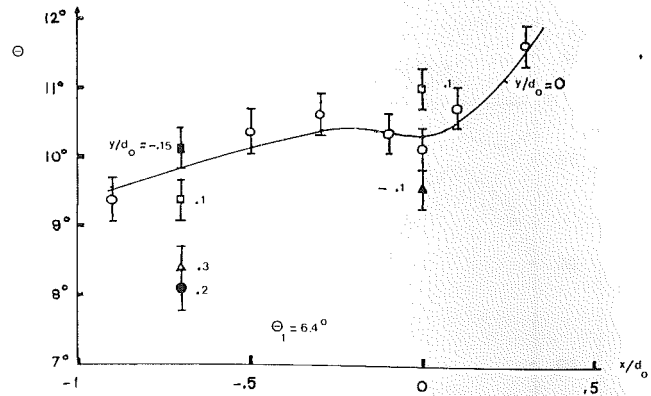

Fig. 4 Flapping angle versus position $\theta_s = 24$ deg $d_0/R_s = 1$ $C_p = 4.3$ $S = 2.3 \times 10^{-2}$ O , □ , ▲ , ■ , ● , △ , $y/d_0 = 0, .1, -.1, -.15, 0.2, 0.3$

For:
$$\Delta K/K \simeq \pm 1 \text{ percent } \Delta\alpha/\alpha \simeq \pm 1 \text{ percent } \Delta\gamma \simeq \pm 1 \text{ deg}$$
$$\Delta\Theta/\Theta \simeq \pm 3 \text{ percent}$$

one obtains:

$$\Delta\Theta \simeq \pm 0.3 \text{ deg for } \Theta = 10 \text{ deg}$$
$$\Delta\Theta \simeq \pm 0.4 \text{ deg for } \Theta = 15 \text{ deg}$$

3 Flapping Angle and Momentum Flux

The flapping angle of jet Θ depends upon two interdependent mechanisms – the periodic injection of transverse momentum and the attachment of the jet (Coanda effect). The latter one results from two effects – the separation from the cylinder due to the blowing through the slot on the same side and the length of attachment on the opposite cylinder. There may also be dynamic effects due to the oscillation of the main jet.

To evaluate the influence of the Coanda effect on the flapping angle is not an easy matter. But, on the contrary, the deviation of the jet due to the injection of lateral momentum through the slots may easily be evaluated in the absence of walls and is equal to the ratio of the momentum fluxes. Its maximum value Θ_1 is related to the maximum blowing velocity Q_{sm} by:

$$\tan \Theta_1 = J_y/J_x = (\rho Q_{sm}^2 d_s \cos\theta_s) / (\rho Q^2 d_0 + \rho Q_{sm}^2 d_s \sin\theta_s)$$

or

$$\tan\Theta_1 = (C_p \frac{d_s}{d_0} \cos\theta_s) / (1 + C_p \frac{d_s}{d_0} \sin\theta_s) \qquad (5)$$

where $Q_{sm}^2 = 2p_s/\rho$. This is justified because the unsteady term in the Bernoulli equation evaluated between the pressure tap and the slot exit in the most unfavorable conditions represent at most 10 percent of the $Q^2/2$ term. The difference between the angle Θ which is effectively measured and Θ_1 is essentially due to the Coanda effect.

4 Results

4.1 Variation of the Flapping Angle With the Position of the Measurement Point. Figure 4 shows the variation of the angle Θ with the position of the point of measurement $M(x,y)$.

If the point M is sufficiently close to the nozzle, the hot wires remain constantly in the core of the jet. The variations of $<u> (\varphi)$ are small with respect to the mean value $\bar{u}$, while the variations of $<v>$ and Θ are almost sinusoidal. This is especially the case at the point $M(x = 0, y = 0)$ (Fig. 5). It may be observed that the average value Θ is not exactly zero ($\Theta \simeq -3$ deg). This results from inaccuracies in the positioning and calibration of the probe, as well as from the difference between the mean direction of the jet and the x-axis
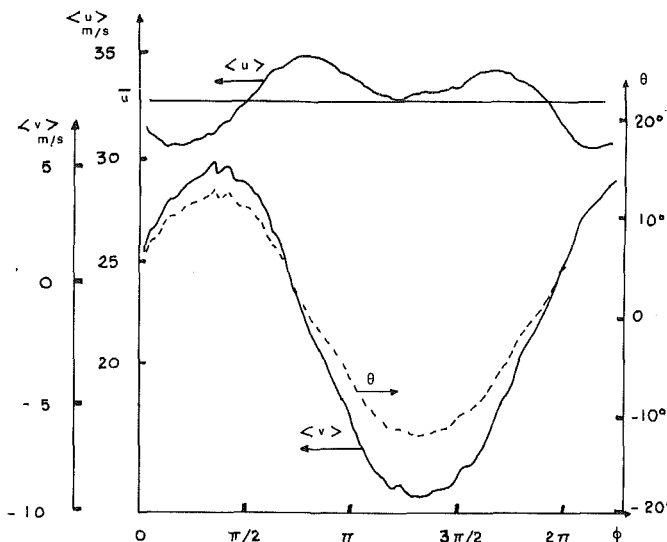
Fig. 5 Ensemble-averaged components of velocity and deflection versus phase angle. $\theta_s = 24$ deg, $d_0/R_s = 1$, $C_p = 8.7$, $S = 0.030$, $x/d_0 = 0$, $y/d_0 = 0$
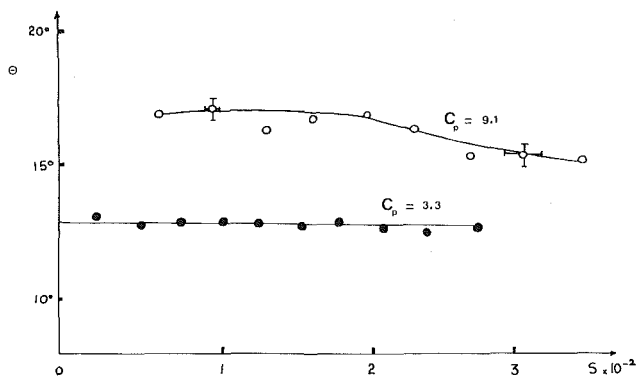

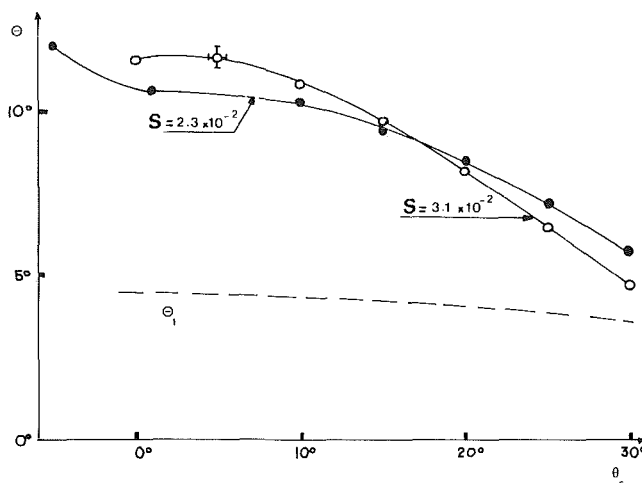Fig. 6 Flapping angle versus frequency $\theta_s = 24$ deg $d_0/R_s = 1.0$ $C_p = 3.1$ $Q = 28.1$ m/s ● $C_p = 3.3$ $Q = 35.8$ m/s

Fig. 7 Flapping angle versus direction of blowing $d_0/R_s = 1$ ● $C_p = 2.6$ $S = 2.3 \times 10^{-2}$; O $C_p = 2.3$, $S = 3.1 \times 10^{-2}$
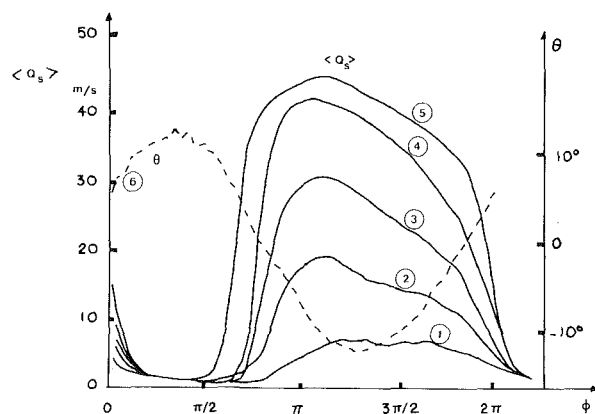

Fig. 8 Blowing velocity through cylinder AD versus phase angle for different blowing pressures (approximate velocity scale) $f = 100$ Hz 1:$p_s = 80$ mm H_2O; 2: 140 mm H_2O; 3: 200 mm H_2O; 4: 270 mm H_2O; 5: 300 mm H_2O; 6: 560 mm H_2O; $C_p = 8.7$; $\theta_s = 24$ deg

which is very sensitive to slightly non-symmetrical conditions in the geometry or in the blowing. The fact that Θ is not exactly zero has no bearing on the results on the flapping angle.

If the point M is moved sufficiently downstream or sidewards, the hot wires are on the edge of the jet, where the flow is turbulent, or even in entrained flow for the largest values of Θ (last point in Fig. 4). The measurement of the flapping angle is then meaningless and such a position must be avoided. Fig. 4 shows, moreover, that the flapping angle is well defined around the point $x = 0$, $y = 0$ and this point has therefore been chosen for subsequent measurements.

4.2 Influence of the Flapping Frequency. The angle Θ varies very little with the Strouhal number (Fig. 6) for the range of frequencies 0–100 Hz possible on the apparatus. These measurements have been made for fixed values of Q at ay and of the pressure p_s. Θ decreases slightly at higher frequencies for the higher value of C_p. This seems to show an influence of frequency on the Coanda effect and not of the unsteady losses in the pipe and the valve. These are higher at lower values of Q_{sm} and would therefore have been more important in the case $C_p = 3.3$.

4.3 Variations of Θ With the Blowing Angle. Figure 7 shows the variations of Θ versus the angle of the blowing slots Θ_s for different values of the main jet velocity but for roughly the same value of C_p. The difference in the two values of C_p gives only a difference of 0.7 deg in Θ at $\Theta_s = 0$ or 25 deg

according to Figs. 9 and 10. Figure 7 shows therefore that the Strouhal number independence remains true for different values of Θ_s. On the same figure, the calculated value of Θ_1 has also been drawn. It is clear that the values of Θ and Θ_1 are quite different when the injection is perpendicular to the main jet. But their difference becomes smaller when Θ_s is increased because the actual flapping angle decreases faster than cos Θ_s. It is seen that the Coanda effect is important for small values of Θ_s and decreases when the blowing is inclined. This shows that the attachment on one cylinder is mainly controlled by the blowing on the opposite side.

Actually the jet is attached to cylinder BC when blowing is through the slot of cylinder AD as is shown by Fig. 8. $<Q_s>$ was measured in the absence of main flow since $<Q_s>$ and Θ could not be measured simultaneously. A typical Θ versus φ curve at the same frequency and for $C_p = 8.7$ is drawn on Fig. 8. It is clear that when the blowing velocity $<Q_s>$ is maximum, the jet is deflected toward the opposite cylinder. The absolute values of $<Q_s>$ on the figure are only indicative because it was impossible to place the hot-wire into the potential core of the blowing jet, the slot width being only 0.3 mm. These curves are, however, a correct representation of the relative variations of the blowing flow.

Experiments [9, 10] on jet attachment in the steady case show that it is strongly dependent upon d_0/R_s and affected by the initial curvature of the streamline at the jet exit. In our case, the ratio d_0/R_s is large and the distance of attachment in the absence of blowing is therefore small. Blowing through cylinder AD affects simultaneously the instantaneous width
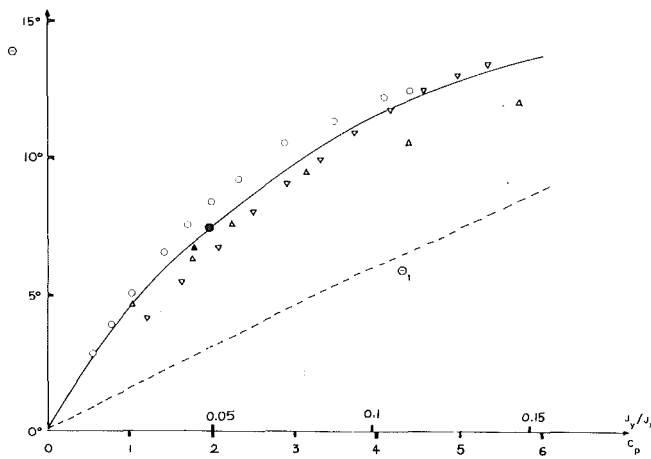
Fig. 9 Flapping angle versus blowing pressure and momentum ratio $\theta_s = 24$ deg, $d_0/R_s = 1$; 0:$p_0 = 13$ mm H_2O constant, $S = 2.1 \times 10^{-2}$, p_s variable; ∇ $p_0 = 4.5$ mm H_2O; $S = 3.6 \times 10^{-2}$; p_s variable; $\triangle$ $p_s = 8.6$ mm H_2O constant; P_0 variable; $\blacktriangle$ $P_0 = 5.3$ mm H_2O, $p_s = 12.1$ mm H_2O $\bullet$ $p_0 = 11.8$ mm H_2O; $p_s = 24.2$ mm H_2O

d_0 of the jet and the curvature of the streamlines because it leads to an earlier separation on cylinder AD. If the angle θ_s is increased, this point of separation moves downstream and the attachment length on cylinder BC is therefore shorter.

4.4 Variations of Θ With the Generating Blowing Pressure. The blowing pressure and the generating pressure of the main jet have been varied separately. The results collapse fairly well on a single curve showing that Θ depends upon the ratio $C_p = p_s/p_0$ and not separately upon p_s and p_0 (Fig. 9). The geometric parameters of the apparatus and the frequency were kept at fixed values. The Strouhal number also varies when Q changes, but we have seen that it has practically no influence on Θ.

As on Fig. 7, the values of Θ_1 are also drawn on Fig. 9. Here again we notice large differences between the two angles resulting from the Coanda effect. The difference between Θ and Θ_1 increases at first with C_p and beyond $C_p = 3$, this difference remains approximately constant, equal to 5 deg. For values of $C_p < 3$, the Coanda effect, measured by the difference $\Theta 1 - \Theta_1$ increases with C_p, a fact which confirms the influence of the blowing on the jet attachment. This limiting value of C_p depends upon the ratio d_0/R_s. It seems that for $C_p > 3$ the Coanda effect is maximum and that the increase of the flapping angle is solely due to the lateral momentum flux which becomes relatively important since for $C_p = 3$: $J_{y\text{max}}/J_x = 0.08$.

4.5 Variations of Θ With d_0/R_s. The jet attachment is strongly dependent upon the ratio d_0/R_s [10] and so is the flapping angle. Figure 10 shows the curves Θ versus C_p for three different values of d_0/R_s, in the case of perpendicular blowing. It is clearly seen that the Coanda effect decreases and that the maximum difference $\Theta - \Theta_1$ is reached for smaller values of C_p, when d_0/R_s is increased. For small values of d_0/R_s ($d_0/R_s = 0.7$), the jet attachment becomes much stronger and the oscillating motion of the jet becomes less regular. It is difficult to make the jet oscillate in regular fashion. The jet has a tendency to attach more strongly on one cylinder which gives rise to nonsymmetrical oscillations. This fact may explain the scatter of the data points.

5 Conclusion

The oscillation of a jet flowing between two cylinders and periodically subjected to lateral injections of momentum flux
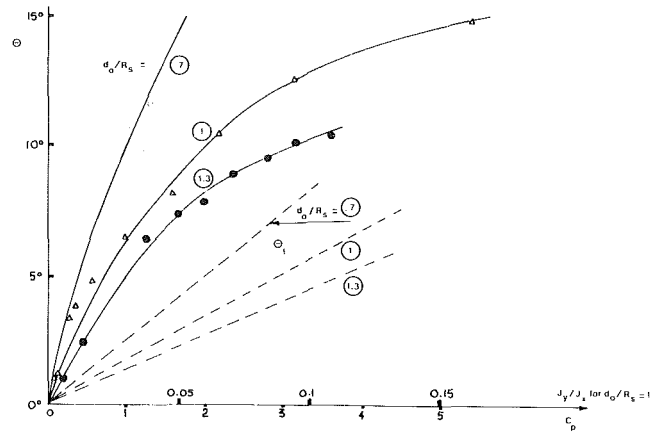

Fig. 10 Flapping angle versus blowing pressure for different values of $d_0/R_s - \theta_s = 0$ deg; R_s kept constant.

is dominated by the Coanda effect when the blowing flow rate is small. The jet attachment increases with the rate of injection due to the initial curvature of the streamlines and with the decrease in width of the main jet created by the blowing. When $J_y/J_x > 0.08$, the jet deflection due to the Coanda effect becomes constant and the subsequent increase on the flapping angle Θ is proportional to the lateral momentum flux. The orientation of the blowing direction has a limited influence on the angle Θ and the best flapping motion is obtained when the injection is perpendicular to the main jet. Moreover, the jet oscillation is practically independent of the frequency.

In practice, the flapping of the jet may easily be controlled by means of the blowing pressure, all other parameters being fixed, provided d_0/R_s has a value close to one. A whole family of flapping jets can therefore be generated with the same nozzle by varying only the blowing pressure.

Acknowledgment

References

1 Chigier, N. A., and Beer, J. M., "Combustion Aerodynamics," *Appl. Sci. Pub.*, 1972.

2 Quinn, B., "Compact Ejector Thrust Augmentation," *Journal of Aircraft*, Vol. 10, No. 8, Aug. 1973, pp. 481–486.

3 Bradbury, L. J. S., and Khadem, A. H., "The Distortion of a Jet by Tabs," *Journal of Fluid Mechanics*, Vol. 70, Part 4, 1975, pp. 801–813.

4 Crow, S. C., and Champagne, F. H., "Orderly Structure in Jet Turbulence," *Journal of Fluid Mechanics*, Vol. 48, Part 3, 1971, pp. 547–591.

5 Favre-Marinet, M., and Binder, G., "Structure des jets pulsants," *Journal de Mecanique*, Vol. 18, No. 2, 1979, pp. 355–394.

6 Hill, W. G., and Greene, P. R., "Increased Turbulent Jet Mixing Rates Obtained by Self-Excited Acoustic Oscillations," ASME JOURNAL OF FLUIDS ENGINEERING, Vol. 99, No. 3, 1977, pp. 520–525.

7 Binder, G., and Favre-Marinet, M., "Flapping Jets," IUTAM-IAHR, Symposium Karlsruhe, Aug. 14-16, 1972.

8 Viets, H., "Flip-Flop Jet Nozzle," *AIAA Journal*, Vol. 13, No. 10, Oct. 1975, pp. 1375–1379.

9 Kadosch, M., "The Curved Wall Effect," Second Cranfield Fluidics Conference, Cambridge, Jan. 3-5, 1967.

10 Fernholz, H., "Zur Umlenkung von Freistrahlen an konvex gekrummten Wanden," Deutsche Versuchsanstalt fur Luft and Raumfahrt, 1966, FB 66-21.

11 Felsing, G., and Moller, P., "Coanda Flow over a Circular Cylinder with Injection Normal to the Surface," *AIAA Journal*, Vol. 7, No. 5, May 1969, pp. 842–846.

12 Fekete, G. I., "Coanda Flow of a Two-Dimensional Wall Jet on the Outside of a Circular Cylinder," Mechanical Eng. Lab., McGill University, Report No. 63-11, 1963.

d_0 = jet width

R_s = radius of cylinders

h = length of cylinders

d_s = width of blowing slots

θ_s = orientation of blowing slots

f,T = frequency, period of oscillation

p_0 = generating pressure of the main jet

p_s = generating pressure of the secondary flow

C_p = p_s/p_0

Q = jet exit mean velocity

Q_s = blowing velocity

$S = fd_0/Q$ = Strouhal number

θ = angle between the main jet and the x-axis

Θ = flapping angle

Θ_1 = jet deflection due to lateral momentum injection.

x,y = coordinates (see Fig. 1)

u,v = axial, radial velocity component

J_x,J_y = axial, radial momentum flux per unit width of jet

$e_{1,2}$ = signals of hot wires

K_1,K_2 = sensitivity coefficients

γ = angle between the normal to the inclined wire and the x-axis

$< \ >$ = ensemble average

$(\ \tilde{}\ )$ = periodic part of the velocity

$(\ \bar{}\ )$ = mean of the velocity

$(\ )'$ = turbulent part of the velocity

O. C. Jones, Jr.

Professor of Nuclear Engineering,
Rensselaer Polytechnic Institute,
Troy, N.Y.   12181
Mem. ASME

J. C. M. Leung

Chemical Engineer,
Reactor Analysis and
Safety Division,
Argonne National Laboratory,
Argonne, Ill.   60439

An Improvement in the Calculation of Turbulent Friction in Smooth Concentric Annuli[1]

Data for smooth concentric annuli having an overall −25 to +35 percent scatter about the Colbrook prediction for smooth tubes, along with calculation techniques, are reviewed. It is shown that the accepted methods of Meter and Bird [22], and of Rothfus, Monrad, and Senecal [28] deviate substantially from the correct limit for small gaps. Further, neither correctly predicts the data trends with decreasing radius ratio. It is demonstrated that the theoretically determined laminar equivalent diameter which provides similarity in laminar flow for round tubes and concentric annuli also provides similarity in turbulent flow. The resultant equations behave correctly at both circular and flat plate limits. The combined results, when applied to objectively confirmed data, show a reduction in the observed data scatter to approximately ±5 percent.

Introduction

Numerous sets of single-phase frictional pressure drop data have been obtained in smooth concentric annuli. Existing turbulent data show a scatter of approximately −25 to +35 percent about the smooth circular tube correlation of Colebrook [4]. While it has been long realized that the hydraulic diameter is not sufficient for accurate description of the observed behavior, no existing correlation method has yet found general acceptance.

In a previous paper [11], it was demonstrated that the hydraulic diameter was insufficient to accurately correlate geometric effects for rectangular ducts in turbulent flow. Instead, a laminar equivalent diameter, d_L, was determined from theory and used in a modified Reynolds number, Re*, to yield good results for a broad range of geometries, (±5 percent maximum scatter and −0.23 percent mean deviation).

It is the purpose of this paper to describe the application of the method of reference [11] to turbulent flow in smooth concentric annuli.

Historical Review

Much frictional pressure loss data exists (Fig. 1) for fully developed steady state Newtonian flows in smooth concentric annuli: (references [1–3, 5, 6, 8, 9, 12, 14–16, 18–20, 23, 26, 27, 31, 34]). In turbulent flow, the scatter is approximately −25 to +35 percent, and many data disagree with the standard Colebrook [4] equation for smooth circular tubes even though in some cases extensive laminar data attest to the adequacy of the experimental techniques. This disagreement is well known and has been the subject of a number of studies as previously mentioned.

It is well known that the hydraulic diameter is insufficient to correlate frictional pressure drop for laminar flow in

annuli (cf: Knudsen and Katz [23], or Lamb [17], among others) and for turbulent flow. Instead, the need for a functional dependency on the radius ratio has generally been agreed upon, but its form in turbulent flow is a matter of continuing discussion. The pioneering works of Rothfus [27], Rothfus, Monrad, and Senecal [28], and of Rothfus and his students [29, 30], and Walker, Whan, and Rothfus [35], have indicated the need for the radius ratio as a correlating parameter and the use of "outer-zone" parameters has been adopted in this school of thought. On the other hand, Fredrickson and Bird [10] proposed the use of a laminar-based length dimension to predict the turbulent friction factors of power-law fluids in smooth concentric annuli. Extending this school of thought for Newtonian fluids, Meter and Bird [22] proposed two additional geometric functions in order to correlate turbulent friction. As shall be seen, however, neither this method nor that of Rothfus and his students adequately predicts magnitudes or trends of objectively confirmed existing data. Others, such as Quarmby [24], Deissler and Taylor [7], Teidt [33], Malak [21], and Rehme [25], have predicted similar (but not identical) effects, and geometrical parameters other than the hydraulic diameter have recently been shown to be required for correlation of turbulent friction in rod bundles (Rehme [25]), and in rectangular ducts (Jones [11]). The method of Malak [21] is quite unacceptable, requiring that the friction factor itself be redefined for each separate geometry rather than having the standard definition of $f = 8 \ \bar{\tau}_w/\rho v^2$. ($\tau_w$ is the perimeter-averaged wall shear stress, ρ is the fluid density, and v is the mass-averaged fluid velocity.) The method of Quarmby [24] is a graphical one yielding results quite similar to those of Jones [11][2] at Reynolds numbers less than 10^5 but rapidly approaching the smooth circular tube values at higher Reynolds numbers.[2] Similarly, the recent method of Rehme [25] is also a

---

[1] Work performed under the auspices of the U.S. Nuclear Regulatory Commission.

[2] Unfortunately, Figs. 5 and 8 in reference [11] were inadvertently interchanged, causing some degree of confusion for the reader.

| AUTHORS	YEAR	SYMBOL AND RADIUS RATIO
WALKER	1957	□ 0.0260 ó 0.499 ọ 0.0667
RHEME	1974	○ 0.020 ò 0.040 ọ 0.100
DALLE DONNE & MEERWALD	1973	● 0.503 ♦ 0.725
QUARMBY	1967	● 0.347 ●– 0.174 –● 0.107
WALKER	1957	■ 0.165 ♠ 0.125 ♥ 0.331
KOCH & FEIND	1958	▢ 0.840 ♂ 0.800 ọ 0.700
LAWN & ELLIOT	1972	○ 0.088 ò 0.176 ọ 0.396
KOCH & FEIND	1958	■ 0.600 ♠ 0.400 ♥ 0.200
BALL & AZER	1972	● 0.250
JONSSON	1965	♦ 0.750 ♥ 0.561 ● 0.281
BRAUN	1951	▢ 0.337
BRIGHTON & JONES	1964	○ 0.375 ó 0.562 ọ 0.118
ROTHFUS	1948	■ 0.650 ♠ 0.162
CROOKSTON	1966	♥ 0.0320 ●– 0.0627 –● 0.105
SARTORY	1962	● 0.0261 ♦ 0.0676
KNUDSEN	1960	▢ 0.278
BRIGHTON & JONES	1964	○ 0.0625 ó 0.125 ọ 0.200 ○ 0.400
KRATZ ET AL	1931	■ 0.514 ♠ 0.628 ♥ 0.806
DISKIND	1961	● 0.667 ♥ 0.687 ♥ 0.671 ●– 0.865
LEUNG	1975	▢ 0.787
WINKEL	1923	■ 0.833
LEE & BARROW	1963	♠ 0.258 ♥ 0.387 ●– 0.613
DODGE	1963	● 0.688 ♦ 0.750 ● 0.875
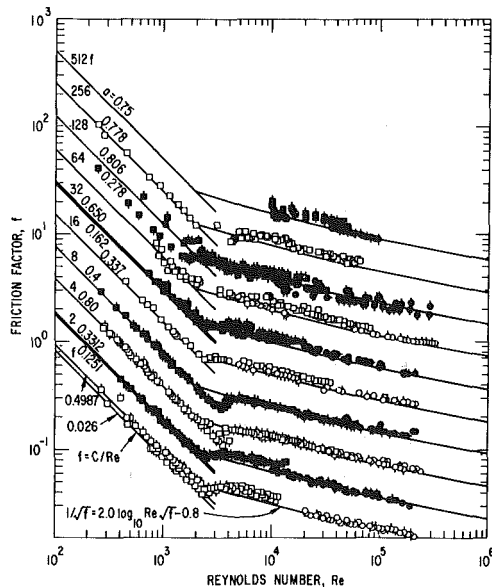
Fig. 1 Friction factor data for smooth concentric annuli existing in the literature. Reynolds number based on the hydraulic diameter.

graphical one based to some extent on the laminar coefficient, but insufficient to allow radius ratio near unity to be evaluated. Finally, the classical method of Deissler and Taylor [7], which was basically an iterative graphical technique, yields predicted friction factors for concentric annuli which are significantly above those for smooth circular tubes.

In what follows, it will be shown that concentric annuli and circular tubes are mathematically similar in laminar flow. The length dimension developed from laminar theory will be extended to turbulent flow, its use being confirmed by comparison with data existing in the literature.

Proposed Correlation Method

This development is concerned only with the case of vanishing roughness ratio. It is suggested that if a length dimension, L, is suitably selected, one should expect $f = f(\mathrm{Re}_L, \epsilon/L)$ to accurately predict both laminar and turbulent friction for concentric annuli using methods identical to those used for circular tubes. The only stipulation is that the peripheral wall shear stress variations remain similar and no gross distortions occur as in annuli with large eccentricities, narrow-apex triangles, or rod-rod or rod-wall proximity effects in rod bundles.

Lamiar Flow Recapitulation. The solution for laminar flow through concentric annuli is well known. The following development for incompressible flow may easily be extended to include variable density effects without affecting the resulting conclusions. For the case of steady state, fully developed, incompressible flows, the continuity equation specifies $dv/dz = 0$ so that the velocity is a function only of the radial coordinate. Radial and azimuthal momentum equations coupled with the continuity equation requires the pressure field to be independent of these coordinate directions. The axial momentum equation is

$$\frac{1}{r}\frac{d}{dr}\left(r\frac{dv}{dr}\right) = -\frac{1}{\mu}\frac{dp}{dz} \tag{1}$$

with boundary conditions at outer and inner walls given as follows: BC1—at $r = R_0$, $v = 0$; BC2—at $r = R_i$, $v = 0$. The pressure gradient is thus constant. The velocity and shear distributions are given as

$$v = -\frac{R_0^{\,2}}{4\mu}\left(\frac{dp}{dz}\right)\left[1 - \frac{r^2}{R_0^{\,2}} + \frac{1-a^2}{\ln\frac{1}{a}}\ln\frac{r}{R_0}\right] \tag{2}$$

and

$$\tau_{rz} = -\frac{R_0}{2}\left(\frac{dp}{dz}\right)\left[\frac{r}{R_0} - \frac{1-a^2}{2\ln\frac{1}{a}}\left(\frac{R_0}{r}\right)\right] \tag{3}$$

where $a = R_i/R_0$ is the radius ratio. The radius of maximum velocity and zero shear is given by the relation

---

Nomenclature

a = radius ratio (R_i/R_0)
A = cross-section area
C = laminar friction coefficient
d = diameter or hydraulic diameter if unsubscripted
f = friction factor $= 2d(-dp/dz)/\rho v^2$
G = coefficient in Meter and Bird correlation
H = coefficient in Meter and Bird correlation
L = general length dimension
p = pressure
P = cross-section perimeter
Q = volumetic flow rate

r = radial coordinate
R = radius
Re = Reynolds number
Re^* = modified Reynolds number (equation (8))
v = velocity
z = axial coordinate (streamline)
β = G/4, defined by equation (14)
η = coefficient defined by term in brackets of equation (15)
γ = coefficient defined by term in brackets of equation (13)
ϵ = roughness height
ϕ^* = geometry function (equation (7)) so $\mathrm{Re}^* = \mathrm{Re}\phi^*$ and $d_L = \phi^* d$

Φ = $1/\sqrt{f} - 2\beta\log_{10}\mathrm{Re}^*\sqrt{f}$
μ = dynamic viscosity
ρ = density

Subscripts
B = Blasius
i = inner
L = laminar equivalent
m = pertaining to maximum velocity
o = outer
r = radial direction
z = axial direction
2 = refers to region outside of maximum velocity

Table 1 Values of the shape function $\phi^*(a)$ according to radius ratio, a

a	0.0	10^{-8}	10^{-5}	10^{-3}	10^{-2}	0.05	0.1	0.3	1.0
ϕ^*	1.0	0.9457	0.9132	0.8569	0.7989	0.7419	0.7161	0.6820	0.6667

$$R_m = R_0 \sqrt{\frac{1-a^2}{2\ln\dfrac{1}{a}}} \ . \qquad (4)$$

The volumetric flow rate in terms of the pressure gradient is easily shown to be

$$Q = -\frac{\pi}{8\mu}\left(\frac{dp}{dz}\right)R_0{}^4(1-a^2)\left[1+a^2-\frac{1-a^2}{\ln\dfrac{1}{a}}\right] \ . \quad (5)$$

Now the D'Arcy friction factor written in terms of the mean wall shear stress is $f = 8\bar{\tau}_w/(\rho v^2)$ where the shear stress has been averaged over the wetted perimeter as $(P_i + P_0)\bar{\tau}_w = P_i\tau_{wi} + P_0\tau_{w0}$. From (3) and the equation for volumetric flow rate one obtains

$$f = \frac{64\mu}{\rho v d\phi^*} \qquad (6)$$

with

$$\phi^* = \frac{1}{(1-a)^2}\left[1+a^2-\frac{1-a^2}{\ln\dfrac{1}{a}}\right] \qquad (7)$$

where $d = 4A/P_w = 2R_0(1-a)$ is the usual hydraulic diameter. Typical values of ϕ^* are given in Table 1 and may be found plotted in many sources (cf [13]).

Limiting Case of Vanishing Inner Radius. For this case, several observations may be made:
 1. The limiting velocity distribution becomes
    $v \rightarrow (R_0{}^2/4\mu)(-dp/dz)(1-r^2/R_0{}^2)$.
 2. The limting shear distribution becomes
    $\tau_{rz} \rightarrow (R_0/2)(-dp/dz)(r/R_0)$.
 3. The point of maximum velocity, R_m moves to the axis,
    i.e., $R_m \rightarrow 0$.
 4. The limiting volumetric flow rate becomes
    $Q \rightarrow (\pi R_0{}^4/8\mu)(-dp/dz)$.
 5. With identical definitions for friction factor (equation (6)) and mean wall shear stress, the shape factor ϕ^* is continuous and uniformly valid over the entire range of a as a goes to unity so that the friction factor becomes identical to the round tube value, $f \rightarrow 64/\mathrm{Re}$.

These results express identically the well known solution for Poiseuille flow in a circular tube.

The purpose for including this exercise is to emphasize that the general case for laminar flow in a concentric annulus includes as a limiting subset laminar flow in a circular tube. That is, they are mathematically similar providing consistent definitions are utilized. The function $\phi^*(a)$ is uniformly valid for the entire geometric set.

Modified Reynolds Number and Laminar Equivalent Diameter. It has been shown through recapitulation of existing theory that both circular tubes and concentric annuli may be considered geometrically similar in laminar, steady state, fully developed, Newtonian flow. The equations which describe the hydraulic behavior include equations (1)–(7) for radius ratios in the closed domain [0, 1] when limiting conditons are considered.

Concentric Annuli—Laminar Flow. From the previous development, it is seen that the general coordinate pair for smooth ducts in laminar flow is described by equations (6) and (7) so that the friction coefficient f and *modified Reynolds number* Re^* are given by

$$f = \frac{64}{\mathrm{Re}^*} \quad \text{and} \quad \mathrm{Re}^* = \frac{\rho v d_L}{\mu} \quad \cdot \qquad (8)$$

The length dimension, d_L, is the *laminar equivalent diameter* expressed in terms of the hydraulic diameter, d, and the shape factor, ϕ^*, as

$$d_L = d\phi^*(a) \ \cdot \qquad (9)$$

For all smooth concentric annuli, the coordinate pair (f,Re^*) would be sufficient to describe the pressure loss in terms identical to those commonly used for circular tubes, i.e., the same graphical representation applies to both geometries in the set.

Limiting Circular Tube Case—Laminar Flow. Since $\phi^* \rightarrow 1.0$ as $a \rightarrow 0$, equations (8) and (9) show $d_L \rightarrow d$, $\mathrm{Re}^* \rightarrow \mathrm{Re}$, and $f \rightarrow 64/\mathrm{Re}$ in this limit. These equations will thus describe both concentric annuli and circular tubes. Furthermore, the graphical representation of f versus Re is identical to f versus Re^*, the former being the limiting case of the latter for $a \rightarrow 0$. A simple relabeling of the coordinates on existing "Moody" diagrams would thus suffice for the entire geometric set, at least in laminar flow.

General Set—All Flow Regimes. Although Rothfus, Monrad, and Senecal earlier proposed the need for redefining the Reynolds numbers between flow regimes, it is believed and herein proposed that this is not necessary. In many situations of which the authors are not aware, the Reynolds parameter requires no redefinition when the flows change from laminar to turbulent, including the case of flow in circular tubes; that is, for smooth tubes, the Reynolds number is the only parameter needed to determine the friction factor. It is thus proposed that the well known standard of comparison, the Colebrook equation [4], may be written in terms of the modified Reynolds number, Re^*, as

$$\frac{1}{\sqrt{f}} = 2.0 \log_{10} \mathrm{Re}^* \sqrt{f} - 0.8 \quad \cdot \qquad (10)$$

In view of the limiting behavior of d_L and Re^*, it is obvious that this equation degenerates to that generally accepted for smooth circular tubes as $a \rightarrow 0$ for vanishing radius ratio. In addition, the opposite limit of infinite parallel plates, $(a \rightarrow 1.0)$, has also been shown previously [11] to be expressed as the limit of the rectangular duct expressions, accurate to ± 5 percent.

To use this method, it is seen that the graphical equivalent of equation (10), the "Moody" diagram, need only have its ordinate redefined to the more general modified Reynolds number, Re^*, for it to be applicable to all three smooth geometries—circular tubes, concentric annuli, and rectangular ducts. Only the correct laminar equivalent diameter need then be specified through the appropriate shape factor for the given geometry. The balance of this paper will be devoted to providing a convincing demonstration of this proposal.

Previous Correlation Methods

The most widely accepted methods appear to be those of Rothfus, Monrad, and Senecal [18] and of Meter and Bird [22]. These will be described separately in what follows.

Correlation of Rothfus, Monrad, and Senecal [28]. These workers reasoned that if the flow in the annular gap were split into two zones on either side of the point of maximum velocity, either half, taken by itself, would look like the flow in a round tube and could be correlated identically. They used

Table 2 Comparison of formulations for Rothfus, Monrad, and Senecal [28] and of Meter and Bird [22] with that proposed herein for the D'Arcy friction factor as determined by the Colebrook-type equation

j	Method	U_j	V_j
1	Rothfus, Monrad, and Senecal [28]	2β	$0.8\beta\left[1 - 2.5\log_{10}\dfrac{\beta^3}{\phi^*}\right]$
2	Meter and Bird [22]	2β	$0.8\left[\dfrac{3}{4}\beta + \dfrac{5}{8}H\right]^{\dagger}$
3	Proposed method	2.0	0.8

[†]Values for H were obtained directly from reference [22] and may be extracted from the values of V given in Table 3.

the Colebrook equation in terms of the outer-zone, zone-2, parameters to give[3]

$$\frac{1}{\sqrt{f_2}} = 2.0\log_{10}\text{Re}_2\sqrt{f_2} - 0.8 \tag{11}$$

where the friction coefficient in terms of the average value, and Reynolds number for the outer zone were specified as

$$f_2 = \frac{R_0{}^2 - R_m{}^2}{R_0{}^2(1-a)}f \quad \text{and} \quad \text{Re}_2 = \frac{R_0{}^2 - R_m{}^2}{R_0{}^2(1-a)}\text{Re} \tag{12}$$

They thus based their hydraulic diameter on the outer-zone flow area and outer-tube perimeter only. Their data confirmed generally that the radius for zero shear in turbulent flow was the same as that for laminar flow given by equation (4). On the plane of f_2 versus Re_2, the correlation in turbulent flow is identical to the circular tube correlation. The average values differ markedly from the circular tube values at the same Re or Re_2, in some cases predicted to be more than 20 percent higher. For laminar flow, the applicable Reynolds number must be redefined to achieve circular tube equivalency, not a pleasing situation.

For comparison purposes, equation (11) may be rewritten in terms of the modified Reynolds parameter as defined using the laminar equivalent diameter. Combining (4), (7)–(9), (11), and (12) yields

$$\frac{1}{\sqrt{f}} = 2\beta(a)\log_{10}\text{Re}^*\sqrt{f}$$
$$-0.8\beta(a)\left[1 - 2.5\log_{10}\frac{\beta^3(a)}{\phi^*(a)}\right] \tag{13}$$

where $\beta(a)$ is a function of the radius ratio given by

$$\beta(a) = \sqrt{\frac{1-(1-a^2)/2\ln(1/a)}{(1-a)}} \quad . \tag{14}$$

The value of $\beta(\alpha)$ is in the range [0.9340,1.0]. The term in brackets in (13) is termed $\gamma(a)$ and varies monotonically from unity to 0.5600 as the radius ratio varies from zero to unity.

Correlation of Meter and Bird [22]. Meter and Bird developed a correlation for the Blasius friction factor in terms of the modified Reynolds number by assuming a Prandtl mixing length relation which they then integrated in terms of two arbitrary constants determined by analogy with circular tubes. Their result, rewritten in terms of the D'Arcy friction factor, is

$$\frac{1}{\sqrt{f}} = 2\beta(a)\log_{10}\text{Re}^*\sqrt{f} - 0.8\left[\frac{3}{4}\beta(a) + \frac{5}{8}H(a)\right] \quad . \tag{15}$$

---

[3]The expression actually used was in terms of the Blasius friction factor, one-fourth the D'Arcy value, given by $1/\sqrt{f_B} = 4\log_{10}\text{Re}_2\sqrt{f_B} - 0.4$. Rewriting in terms of the D'Arcy value results in a subtractive constant of 0.8021 rather than the 0.8 in (11). The relative difference in a calculated value of f would be $\delta f/f = -0.0021\,\delta f$, less than 4 parts in 10^4, and has been neglected herein.

The term in brackets is termed $\eta(a)$. In this term, the actual coefficient of 0.7526 was approximated by 0.75 in order to let $\eta(a) \to 1.0$ as $a \to 0.0$, thus compensating for the slight inconsistencies between rounded off versions of the Blasius and D'Arcy Colebrook equations. The radius parameter $H(a)$ was given in the original paper. It varied monotonically between 0.400 and 0.031 as the radius ratio was varied between zero and unity.

Comparisons with Previous Methods

Comparisons of the proposed method may be made with the two widely used formulations of references [22] and [28]. These comparisons will be made on both an algebraic-numerical basis and on the basis of existing data.

Algebraic and Numerical Comparisons. The correlations of references [22] and [28] are compared on the basis of their equivalent Colebrook-type formulations, $\psi_j(f_j,\text{Re}^*) = 1/\sqrt{f} - U_j\log_{10}\text{Re}^*\sqrt{f} + V_j$, in Table 2. In both references [22] and [28], correlations have identical coefficients U_j for the logarithmic terms which vary with radius ratio, $\beta(a)$ being unity at both extremes. In both cases, the coefficient V_j varies monotonically from a value of 0.800 at $a = 0$, to a lower value as the radius ratio approaches unity. The proposed method, however, has constant coefficients identical to the circular tube values, $U_j = 2.0$ and $V_j = 0.8$, so the similarity is accounted for entirely through the laminar equivalent diameter in Re^*.

Table 3 provides numerical comparisons of the three methods on the basis of specified values of $\text{Re}^* = \text{Re}\phi^*$. The circular tube values also given for comparison at the specified values of Re^* are seen to vary because Re varies when ϕ^* changes with radius ratio. The proposed method, of course, has friction factors identical to the circular tube values at the specified Re^* for $a = 0$, since in this case $\phi^* = 1.0$, $\text{Re}^* = \text{Re}$, and the coefficients U and V are identical to the circular tube values.

All three methods correctly approach the circular tube coefficients as the radius ratio vanishes. Both referenced methods are within 2 percent of each other for radius ratios of 0.3 and smaller but may differ by nearly 6 percent in the flat plate limit. The method of Rothfus, Monrad, and Senecal [28] predicts values which return to the circular tube values at the flat plate limit while the method of Meter and Bird [22] returns to a value higher than the circular tube value by about 5 percent $\text{Re}^* = 10^4$ but with decreasing deviation at increasing values of Re^*. Both are now known to be wrong in this limit [11]. The proposed method, however, correctly approaches the flat plate limit.

Data Comparisons. A rather sensitive test to compare the correlations with each other and with existing data arises from the grouping $\Phi(a; \text{Re}^*) = 1/\sqrt{f} - 2\beta(a)\log_{10}\text{Re}^*\sqrt{f}$. For the jth correlation where f_j may be specified according to the coefficients U_j and V_j identified in the previous section, the grouping may be written as $\Phi_j(\text{Re}^*;a) = [U_j - 2\beta(a)]\log_{10}\text{Re}^*\sqrt{f_j} - V_j$. In the specific case of any correlation where $U_j = 2\beta$, Φ_j becomes independent of the Reynolds parameter. For Meter and Bird's correlation, a plot of Φ_j versus a is identically a plot of $[-V_j - 0.8\eta(a)]$ versus a. For the Rothfus correlation, the result is a plot of $[-V_j - 0.8\beta(a)\gamma(a)]$ versus a. If U_j is not identically equal to $2\beta(a)$, the plot would be parametrically dependent on the Reynolds number, Re^*. For purposes of data comparisons, any data set $[f,\text{Re}^*]$ for a given geometry will yield a given value of Φ which can be plotted for the corresponding value of a. The data should follow the Φ_j behavior if the jth correlation is valid.

All data. The Fig. 1 data are replotted in Fig. 2 according to the Φ-parameter. (The Blasius friction factor was used here for convenience along the Meter and Bird's original G-

Table 3 Comparison of friction correlation coefficients and D'Arcy friction factors for references [22] and [28] with the circular tube values at given values of Re* and ϕ^*. For the present method $f=f(\text{Re}^*; 2.0,0.8)$.

a	0.0	0.05	0.10	0.15	0.20	0.30	0.50	0.70	1.00	Radius ratio
ϕ^*	1.0	0.7419	0.7161	0.7021	0.6930	0.6820	0.6719	0.6681	0.6667	Shape factor
U	2.000	1.874	1.868	1.869	1.873	1.886	1.917	1.950	2.000	Correlation of Rothfus,
V	0.800	0.6660	0.6425	0.6255	0.6110	0.5856	0.5421	0.5028	0.4479	Monrad, and Senecal [28]
f_{10^4}	0.03089	0.03367	0.03362	0.03341	0.3312	0.03242	0.03100	0.02965	0.02781	$f=f(\text{Re}^*;U,V)$
f_{10^5}	0.01799	0.01979	0.01980	0.01969	0.01954	0.01916	0.01837	0.01760	0.01655	
f_{10^6}	0.01165	0.01289	0.01291	0.01285	0.01276	0.01252	0.01202	0.01154	0.01088	
U	2.000	1.874	1.868	1.869	1.873	1.886	1.917	1.950	2.000	Correlation of Meter
V	0.800	0.7086	0.6799	0.6647	0.6549	0.6427	0.6305	0.6230	0.6155	and Bird [22]
f_{10^4}	0.03089	0.03413	0.03403	0.03383	0.03358	0.03301	0.03186	0.03075	0.02922	$f=f(\text{Re}^*;U,V)$
f_{10^5}	0.01799	0.02001	0.01999	0.01989	0.01976	0.01943	0.01877	0.01812	0.01722	
f_{10^6}	0.01165	0.01301	0.01301	0.01296	0.01288	0.01267	0.01224	0.01182	0.01123	
f_{10^4}	0.03089	0.02858	0.02832	0.02817	0.02808	0.02797	0.02787	0.02783	0.02781	Circular Tube Correlation
f_{10^5}	0.01799	0.01692	0.01680	0.01673	0.01668	0.01663	0.01658	0.01657	0.01656	$f=f(\text{Re}^*/\phi^*;2.0,0.8)$
f_{10^6}	0.01165	0.01107	0.01101	0.01097	0.01095	0.01092	0.01089	0.01088	0.01088	

NOTE: Since U_j and V_j are constants at 2.0 and 0.8 for the proposed method, and since the values of Re* are specified, the values for friction coefficient predicted at the specified Reynolds number (f_{Re^*}) by the proposed method are identical with those for the circular tube at $a=0.0$.

parameter which is just 4β.) Vertical bars at a radius ratio of 0.02 on the dotted lines indicate the sensitivity of the comparison method to approximately 1 percent changes in the friction factor.

The overall data scatter in Fig. 2 is quite large. In addition, the deviation between correlations at the flat plate limit is obvious, showing that neither correlation of references [22] or [28] can be correct in this limit.

The large scatter in the region near a radius ratio of 1.0 is indicative of the problems associated with building a closely held geometry with a narrow gap. For one thing, the friction factor calculated from a given set of experimental data is proportional to the cube of the gap so that small errors in small gaps can lead to large errors in the friction factor. Lack of concentricity can also be a problem especially with narrow gaps, while entrance length effects might persist in concentric annuli to hundreds of diameters (Rothfus, et al. [29]). Finally, the possibility of swirl or other unusual flow characteristics cannot be neglected as will be seen shortly.

Data Selection. From Fig. 2, while the weight of the data appear to follow the trends suggested herein, it is uncertain whether an unbiased observer would choose one method over another as best representative of all the data. Similar problems were faced by the principal author in the earlier work. In that case, a culling procedure was used wherein only data having verifiable laminar flow comparison with theory would be considered. Justification for this procedure was contained therein. Briefly, while it may be overly restrictive, it does not leave much room for questionable data to be included.

It should be mentioned that certain of the existing data have been corrected—specifically those 0.650 radius ratio data of Rothfus [27], the data of Braum [2], and the data of Knudsen [14]. In all cases, the laminar values of the product $f \cdot$ Re disagreed with theory and in these cases documentation was sufficiently good to allow the test section dimensions to be altered *within their stated tolerances* to provide closer agreement with theory in the laminar regime.

Comparisons Using Confirmed Data. The results of the confirming procedure are shown in Figs. 3 and 4. In Fig. 3, it is seen that obvious deviations exist between the confirmable data reported in the literature and the normally accepted smooth tube line. Figure 4 shows that the agreement with the current method is superior in both magnitude and trends to the other two methods when compared with all data. In fact, the presently proposed method predicts a monotonic increase in friction factor with increasing radius ratio with fixed velocity and state while the other two correlations predict maxima.

Discussion

Walker's Data [34]. Because the data of reference [34], although unconfirmed at Reynolds numbers over 1000, did agree with theory at lower values of Re, and since they figured prominently in earlier correlation development, they were examined quite carefully. Walker's were evidently a carefully contrived set of experiments where dimensions were well known, concentricity well maintained, and measurements accurately completed. In addition, Walker, being a student of Rothfus, took adequate precautions with respect to entrance length problems identified earlier.

The test apparatus, however, had no provisions to eliminate swirl. Walker stated (and their data clearly showed) that their results indicated ". . . a small upward deviation from the viscous relationship at Reynolds numbers below the lower critical point;" e.g., below the local minimum which occurred near a Reynolds number of 2000. These upward deviations for each of six annular geometries as well as 0.750-in. i.d. circular tubes were between approximately 6 and 20 percent in the

AUTHORS	YEAR	FLUID
REHME	1974	AIR
DALLE DOANE & MEERWALD	1973	AIR
BALL & AZER	1972	AIR
LAWN & ELLIOT	1972	AIR
QUARMBY	1967	AIR
BRIGHTON & JONES	1964	AIR
BRIGHTON & JONES	1964	WATER
SARTORY	1962	WATER
ROTHFUS	1948	AIR
KOCH & FEIND	1958	AIR
CROOKSTON	1966	AIR
JONSSON	1965	AIR
BRAUN	1951	WATER
KRATZ	1931	WATER
KRATZ	1931	BRINE (CCl_2)
KNUDSEN	1960	WATER
DISKIND	1961	WATER
DODGE	1963	AIR
WINKEL	1923	WATER
LEE & BARROW	1964	AIR
WALKER	1957	WATER
LEUNG	1975	WATER

——————— METER & BIRD (1961)
— — — — ROTHFUS, MONRAD & SENECAL (1957)
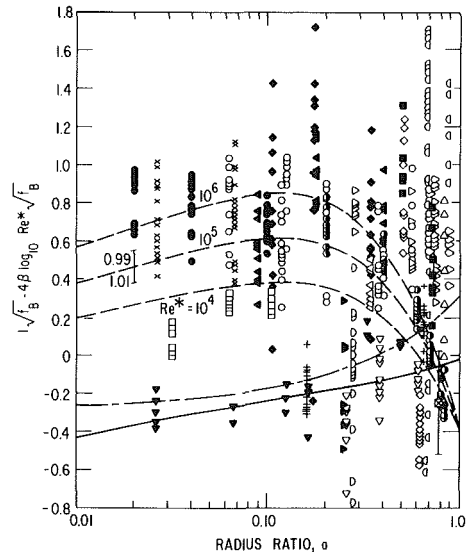– – – – – PROPOSED METHOD

Fig. 2 Comparison of the proposed method with the methods of Rothfus, Monrad, and Senecal [28], and of Meter and Bird [22] with all data shown in Fig. 1.

range of Reynolds numbers between 1000 and 2000. They further indicate that Rothfus and his co-workers had observed ". . . slight progressive departure from the friction factor equation for viscous flow . . . " in smooth tubes between Reynolds numbers of 1200 and 2030, and ". . . sinuous flow in the main stream . . ." over the same range.

In Walker's tests, the fluid, water, exited unrestricted through a tee at right angles to the axial flow direction, immediately downstream of the pressure tap. Since there were no provisions to eliminate swirl, it was felt the presence of this tee could have caused secondary flows which, in turn, would lead to the departure from laminar theory. A short experimental investigation simulating Walker's test was undertaken using nearly identical inlet and outlet, and with a radius ratio of 0.08. It was found that with flow progressing unrestricted to the exit tee, a strong secondary flow instability was reproducibly generated at modified Reynolds numbers as low as 700. This instability had the appearance of a double helical flow pattern, sometimes appearing to degenerate into a
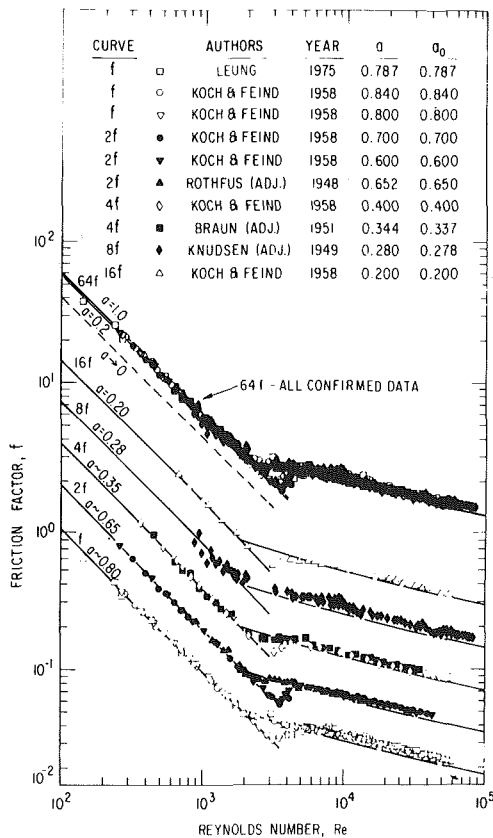
Fig. 3 Culled data accepted for comparison based on accurate laminar flow measurements taken from those shown in Fig. 1. Comparison is on the basis of the hydraulic diameter-based Reynolds number.
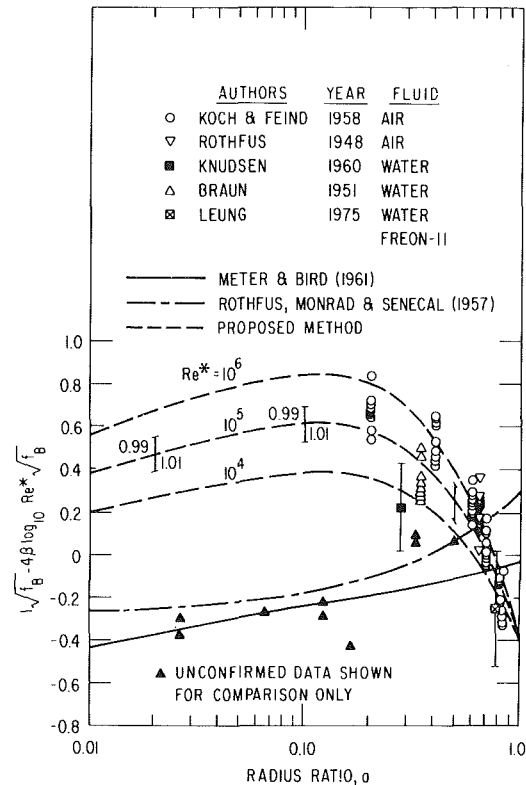

Fig. 4 Comparison of methods of Rothfus, Monrad, and Senecal [28], Meter and Bird [22], and the proposed method with all the confirmed data taken from Fig. 1

Fig. 5 Photograph of typical double helix dye pattern observed in the mockup of Walker's [34] geometry near a Reynolds number of 1560 (Re* = 1130)
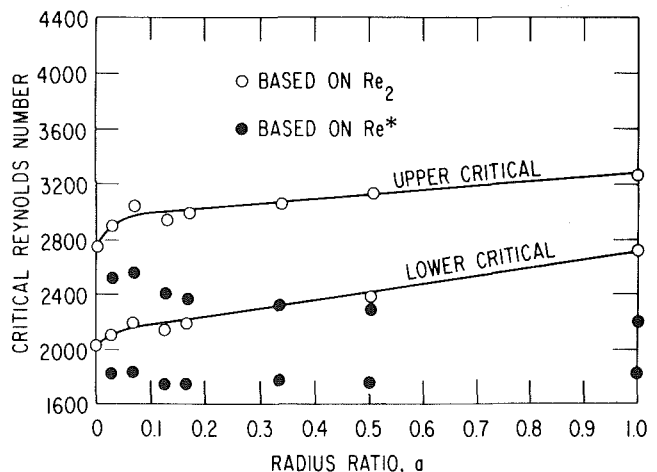

Fig. 6 Comparison of the use of the modified Reynolds number, Re*, with the outer-wall-based Reynolds number of Rothfus, Monrad, and Senecal [28], Re_2, for correlation of critical Reynolds number. Lines are taken from the original figure in reference [28].

definite swirl as shown in Fig. 5, and could easily have caused the higher friction observed in laminar flow, and probably also in turbulent flow.

Critical Reynolds Numbers for Transition. Walker [34] also examined his data in detail for lower and upper critical Reynolds numbers. A reproduction of his plot is shown in Fig. 6. These values, which represent the local maxima and minima of the data in the transition regime, were found to monotonically increase with increasing aspect ratio. Also shown in this figure are the equivalent modified Reynolds numbers for both lower and upper criticality. The standard deviation for the lower critical Re* is 2 percent and for the upper critical is 5 percent.

Comparisons Based on Modified Reynolds Number. Typical of the confirmed data of f versus Re* are those of Koch and Feind [15] for radius ratios of 0.2 and 0.4, and data of Leung [20] for a radius ratio of 0.787. These are shown in Figs. 7 and 8, respectively. In the latter case, radial vanes leading to and from large plenna at inlet and outlet eliminated the possibility of swirl. Laminar flow data in the latter case accurately spans two decades of modified Reynolds number. Mean deviations are less than 1 percent in both cases for modified Reynolds numbers over 7000, a difference of approximately 10 percent in the former case from the predictions of [22] or [28] for $a = 0.2$.

All confirmed data are shown in Fig. 9. The agreement is seen to be excellent in all cases with data scatter similar to that found to exist in the rectangular duct case [11]. If these confirmed data were to be compared on the basis of the hydraulic diameter-based Reynolds number, the scatter band would have been increased by approximately 12 percent above the tube correlation for a total deviation of approximately -5 to $+17$ percent. Rather, it is seen in this figure that when the

confirmed data are compared on the basis of the modified Reynolds number using the laminar equivalent diameter, the scatter is reduced to approximately ± 5 percent from the line represented by the Colebrook equation, equation (18), with a mean deviation of less than 1 percent for values of the modified Reynolds number, Re*, greater than 7000. This seems to be about the best one can expect when comparing
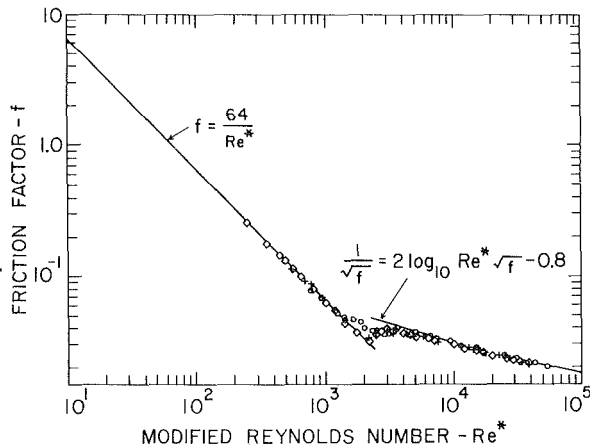
Fig. 7 Typical use of modified Reynolds number, Re*, in correlation of frictional pressure drop in concentric, smooth annuli. Data of Koch and Feind [15] for radius of: + 0.2, ◇ 0.4, ⊙ circular tube.

highly accurate data from various laboratories, and is compatible with the findings reported previously [11]. For design purposes, then, a 5 percent uncertainty should be placed on the predictions provided by using equation (18).

Finally, one should keep in mind the implications of the results presented with respect to heat and mass transfer, as well as regards the effects of roughness. These have been enumerated in the previous paper [11] and shall not be repeated herein.

Conclusions and Recommendations

Based on the work reported in this paper, the following conclusions appear to be valid:

1 The trends and limiting behavior of the methods of Rothfus, Monrad, and Senecal [28] and of Meter and Bird [22] for predicting turbulent frictional pressure loss in smooth concentric annuli appear to be incorrect.

2 Circular tubes and concentric annuli are mathematically shown to be geometrically similar in laminar flow, and by data comparison to be similar in turbulent flow.

3 The resultant equations which are thus proposed for use in predicting steady state, fully developed, flow friction factors in the entire smooth geometric set which comprises concentric annuli and circular tubes include:

(a) Laminar flow—$f = 64/\mathrm{Re}^*$

(b) Turbulent flow—$1/\sqrt{f} = 2 \log_{10} \mathrm{Re}^* \sqrt{f} - 0.8$

These equations behave correctly in both radius ratio limits. The uncertainty in these predictions is judged to be within 5 percent for turbulent flow above $\mathrm{Re}^* = 7000$, representing the resultant scatter in the objectively confirmed data base existing in the literature.

4 The correct definition for the modified Reynolds number, Re^*, which provides consistency for all geometries in the entire set uses the laminar equivalent diameter, d_L, given by the product of the hydraulic diameter and the shape function specified in equation (7), (i.e., see equation (9)), and applies uniformly for all radius ratios in the closed range of zero to unity.

5 The modified Reynolds number method proposed herein based on the laminar equivalent diameter provides complete geometric equivalency between the three geometries of smooth circular tubes, smooth rectangular channels, and smooth concentric annuli for both laminar and turbulent flows. The correlation procedure appears to be as accurate as the best available experimental data when differences between laboratories are taken into account.

6 No objectively confirmable data exist having radius ratios less than 0.2. Such data are needed to further test the
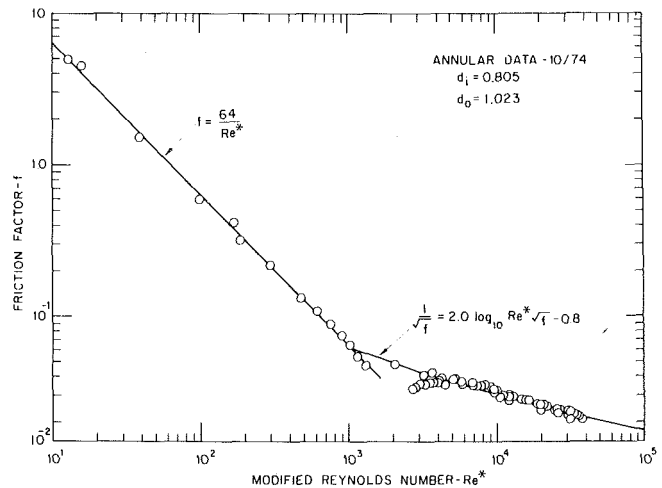

Fig. 8 Typical use of modified Reynolds number, Re*, in correlation of frictional pressure drop in concentric, smooth annuli. Data of Leung [20] for a radius ratio of 0.78.

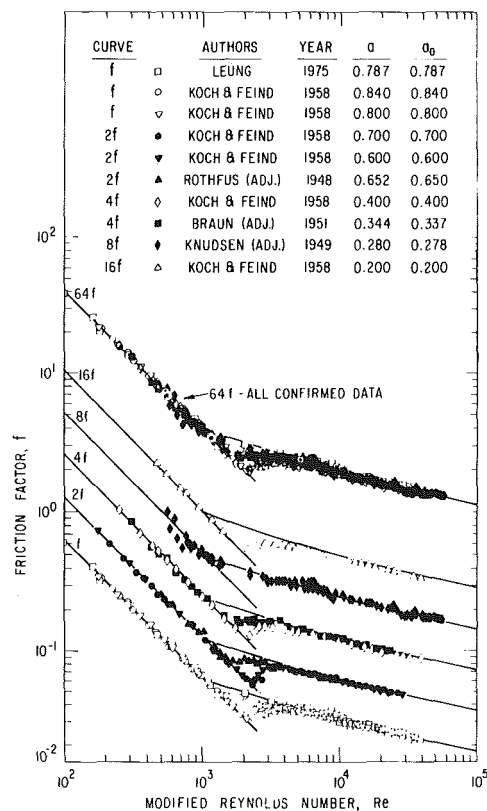| CURVE		AUTHORS	YEAR	a_i	a_0
f	□	LEUNG	1975	0.787	0.787
f	○	KOCH & FEIND	1958	0.840	0.840
f	▽	KOCH & FEIND	1958	0.800	0.800
2f	●	KOCH & FEIND	1958	0.700	0.700
2f	▼	KOCH & FEIND	1958	0.600	0.600
2f	▲	ROTHFUS (ADJ.)	1948	0.652	0.650
4f	◇	KOCH & FEIND	1958	0.400	0.400
4f	■	BRAUN (ADJ.)	1951	0.344	0.337
8f	◆	KNUDSEN (ADJ.)	1949	0.280	0.278
16f	△	KOCH & FEIND	1958	0.200	0.200

Fig. 9 All confirmed data accepted for comparison based on accurate laminar flow measurements on the basis of modified Reynolds number, Re*

trends predicted herein with vanishing radius ratios. Such data should be obtained with due consideration to the precautions described herein and enumerated as follows.

It is strongly recommended that any experimenter obtaining frictional pressure drop data on any noncircular geometry and especially on annuli obtain sufficient data in the laminar flow region to insure the adequacy of the experimental procedure. Any deviation from the theory at modified Reynolds numbers, Re^*, much less than 2000 is indicative of erroneous experimental technique and/or inaccurate knowledge of the actual geometry used. Specific difficulties and their symptoms include the following.

1 Lack of adequate knowledge of the true annular gap,

where the friction factor varies as the cube of the gap, will give difficulties. Data thus obtained will tend to be parallel to the theoretical line if no other difficulties exist.

2 Eccentricity can also be a difficulty, especially with small annular gaps and will have friction factors smaller than theoretical.

3 Swirl caused by distorted inlet conditions is expected to appear as higher than normal friction and can be eliminated by flow straighteners in the inlet and exit.

4 Secondary flows may be caused by any number of circumstances including the presence of an unrestricted bend at the exit as demonstrated herein. The symptom will be a deviation from the laminar theory above some Reynolds number which, in the present case, was found to be near $Re^* = 700$.

References

1 Ball, H. D., and Azer, N. Z., "Experimental Investigations of Eddy Diffusivities of Air in Turbulent Annular Flow," *Proc. 1972 Heat Transfer and Fluid Mechanics Institute,* Stanford University Press, 1972, pp. 19–38.

2 Braun, F. W., Jr., *Pressure Drop in Annuli Containing Plain and Transverse Fin Tubes,* M.S. thesis, Oregon State College, 1951.

3 Brighton, J. A., and Jones, J. B., "Fully Developed Turbulent Flow in Annuli," ASME *Journal of Basic Engineering,* Vol. 86, 1964, pp. 835–844.

4 Colebrook, C. R., "Turbulent Flow in Pipes with Particular Reference to the Transition Region Between the Smooth and Rough Pipe Laws," *J. Inst. Civ. Eng. (London),* Vol. 11, 1939, pp. 133–156.

5 Crookston, R. B., *Heat and Momentum Transfer for Turbulent Flow in Annuli with Small Cores,* Ph.D. thesis, Carnegie Inst. of Tech, 1966.

6 Dalle Donne, M., and Meerwald, E., "Heat Transfer and Friction Coefficients for Turbulent Flow of Air in Smooth Annuli at High Temperatures," *Int. J. Heat and Mass Trans.,* Vol. 16, 1973, pp. 787–809.

7 Deissler, R. G., and Taylor, M. F., "Analysis of Fully Developed Turbulent Heat Transfer and Flow in an Annulus with Various Eccentricities," NACA-TN-3451, 1955.

8 Diskind, T., "Heat Transfer and Pressure Drop in Eccentric Annuli," Eng. Res. Lab. Report NYO-9649, Columbia University, 1961.

9 Dodge, N. A., "Friction Losses in Annular Flow," ASME preprint 63-WA-11, 1963.

10 Fredrickson, A. G., and Bird, R. B., "Friction Factors for Axial Non-Newtonian Annular Flow," *Ind. and Eng. Chem.,* Vol. 50, 1958, pp. 1599–1600.

11 Jones, O. C., Jr., "An Improvement in the Calculation of Turbulent Friction in Rectangular Ducts," ASME *Journal of Fluids Engineering,* Vol. 98, 1976, pp. 173–181.

12 Jonsson, V., *Experimental Studies of Turbulent Flow Phenomena in Eccentric Annuli,* Ph.D. thesis, University of Minnesota, 1965.

13 Knudsen, J. G., and Katz, D. L., *Fluid Dynamics and Heat Transfer,* McGraw-Hill, New York, 1958.

14 Knudsen, J. G., *Heat Transfer, Friction, and Velocity Gradients in Annuli Containing Plain and Fin Tubes,* Ph.D. thesis, University of Michigan, 1949.

15 Koch, R., and Feind, K., "Drukverlust und Warmeubergang in Ringspalten," *Chem. Ing. Tech.,* Vol. 30, 1958, pp. 577–584.

16 Kratz, A. P., Macintire, H. J., and Gould, R. E., "Flow of Liquids in Pipes of Circular and Annular Cross Sections," University of Illinois Eng. Expt. Stat. Bul., No. 222, 1931.

17 Lamb, H., *Hydrodynamics,* Dover, 6th Edition, New York, 1932.

18 Lawn, C. J., and Elliot, C. J., "Fully Developed Turbulent Flow Through Concentric Annuli," *J. Mech. Eng. Sci.,* Vol. 14, 1972, pp. 195–204.

19 Lee, Y., and Barrow, H., "Turbulent Flow and Heat Transfer in Concentric and Eccentric Annuli," *Proc. Inst. Mech. Engrs.,* Vol. 178, Part 3I, 1964, pp. 1–16.

20 Leung, J. C. M., *Occurrence of Critical Heat Flux During Blowdown with Flow Reversal,* M.S. thesis, Northwestern University, 1975.

21 Malak, J., "Tlakove Ztraty a Prestup Tepla v Kanalech Nekruhovych Prurezu s Hydraulicky Hladkymi Stenami (Pressure Losses and Heat Transfer in Non-Circular Channels with Hydraulically Smooth Walls)," Czechoslovakian Nuclear Research Institute Report No. UJV 3891 R, 1972, (in Czechoslovakian).

22 Meter, D. M., and Bird, R. B., "Turbulent Newtonian Flow in Annuli," *AIChE Journal,* Vol. 7, 1961, pp. 41–45.

23 Quarmby, A., "An Experimental Study of Turbulent Flow Through Concentric Annuli," *Inst. J. Mech. Sci.,* Vol. 9, 1967, pp. 205–221.

24 Quarmby, A., "An Analysis of Turbulent Flow in Concentric Annuli," *Appl. Sci. Res.,* Vol. 19, 1968, pp. 250–273.

25 Rehme, K., "Simple Method of Predicting Friction Factors of Turbulent Flow in Non-Circular Channels," *Int. J. Heat Mass Trans.,* Vol. 16, 1973, pp. 933–950.

26 Rehme, K., "Turbulent Flow in Smooth Concentric Annuli with Small Ratios," *J. Fluid Mech.,* Vol. 64, 1974, pp. 263–287.

27 Rothfus, R. R., *Velocity Distribution and Fluid Friction in Concentric Annuli,* Sc.D. thesis, Carnegie Inst. Tech., 1948.

28 Rothfus, R. R., Monrad, C. C., and Senecal, V. E., "Velocity Distribution and Fluid Friction in Smooth Concentric Annuli," *Ind. Eng. Chem.,* Vol. 42, 1950, pp. 2511–2520.

29 Rothfus, R. R., Monrad, C. C., Sikchi, K. G., and Heideger, W. J., "Isothermal Skin Friction in Flow Through Annular Sections," *Ind. Eng. Chem.,* Vol. 47, 1955, pp. 913–918.

30 Rothfus, R. R., Sartory, W. K., and Kermode, R. I., "Flow in Concentric Annuli at High Reynolds Numbers," *AIChE Journal,* Vol. 12, 1966, pp. 1086–1091.

31 Sartory, W. K., *Turbulent Flow in Annular Ducts,* Ph.D. thesis, Carnegie Inst. of Tech., 1962.

32 Schlichting, H., *Boundary Layer Theory,* McGraw-Hill, New York, 1960.

33 Tiedt, W., "Berechnung des Laminaren und Turbulenten Reibungswiderstandes Konzentrischer und Exzentrischer Ringspatte, III," *Chemische Apparantur,* Vol. 91, No. 5, 1967, pp. 149–155.

34 Walker, J. E., *Characteristics of Isothermal Flow in Smooth Concentric Annuli,* Ph.D. thesis, Carnegie Inst. Tech., 1957.

35 Walker, J. E., Whan, G. A., and Rothfus, R. R., "Fluid Friction in Noncircular Ducts," *AIChE Journal,* Vol. 3, 1957, pp. 484–489.

36 Winkel, R., "Die Wasserbewegung in Leitungen mit Ringspalt-Durchflubquerschnitt," *Z. Angew. Math. Mech.,* Vol. 3, 1923, pp. 251–257.

Low-Reynolds-Number Turbulent Boundary Layers

B. R. White

University of California,
Department of Mechanical Engineering,
Davis, Calif.   95616

This paper presents experimental wind-tunnel data that show the universal logarithmic velocity profile for zero-pressure-gradient turbulent boundary layer flows is valid for values of momentum-deficit Reynolds numbers R_θ as low as 600. However, for values of R_θ between 425 and 600, the von Kármán and additive constants vary and are shown to be functions of R_θ and shape factor H. Furthermore, the viscous sublayer in the range $425 < R_\theta < 600$ can no longer maintain its characteristically small size. It is forced to grow, due to viscous effects, into a super sublayer (6-9 percent of the boundary layer height) that greatly exceeds conventional predictions of sublayer heights.

Introduction

A thorough analysis of the majority of creditable zero-pressure-gradient turbulent boundary layer data at low Reynolds number was done by Coles [1]. He found that the velocity profile of the inner layer ($y/\delta < 0.2$), excluding the viscous sublayer, obeys the high Reynolds number logarithmic velocity profile. Coles also shows that the outer layer similarity law at large Reynolds numbers is not valid for the low Reynolds number flows. He presents an analysis showing that the "wake" profile parameter π is a function of the momentum-deficit Reynolds number, R_θ.

Kline, et al. [2], present limited zero-pressure-gradient velocity profiles, some of which are at values of R_θ as low as 480. They found that the wall shear stress determined from a wall slope method did not agree with the predicted value from the universal logarithmic profile. Their wall-slope determination of the shear velocity U_τ is consistently found to be lower than the shear velocity determined from a Clauser fit of the logarithmic velocity profile.

Herring and Mellor [3] found better agreement with experiments by using a variable parameter α in the outer eddy-viscosity formula in their numerical calculations for the compressible turbulent boundary layer at low Reynolds numbers.

Simpson [4] presents an alternate approach to the low Reynolds number effect by varying the von Kármán constant K for $R_\theta < 6000$ and the additive constant C while holding α constant. This implies a breakdown of the logarithmic profile at low Reynolds numbers. K is shown to be a function of R_θ.

McDonald [5], following the theory of varying parameters in the outer layer, requires the eddy-viscosity formulation to be a function of Reynolds numbers to account for the effects of low Reynolds numbers.

Huffman and Bradshaw [6] attempt to resolve the controversy by analyzing the existing data in duct flow. They feel if K and C are found to be constant in the turbulent duct flow, it would demonstrate the constancy of K and C in the turbulent boundary layer flow since low Reynolds number turbulence is expected to be greater in duct flow than in

boundary flow. They show K and C to be constant throughout the range of Reynolds numbers.

Cebeci [7] examines the universality of K, C, and the parameter α in the Clauser-type outer layer eddy-viscosity formula. He found that K is constant; however, he also found α is not constant at low Reynolds numbers. He felt α should be expressed as a function of Reynolds number.

Granville [8] examines low Reynolds number data by means of an elaborate technique of curve-fitting and extrapolation. He estimates a minimum value of $R_\theta = 740$ for the existence of a turbulent boundary layer.

Later, Granville [9] derives a formula for predicting larger values of skin-friction coefficients, C_f, than conventional (high Reynolds number) theory. This is accomplished by "adding" viscosity to the outer layer in an intricate analysis of velocity similarity.

Recently, Purtell [10] performed low-velocity experiments which result in low Reynolds number boundary layer flows. He found that the logarithmic profile applies to all Reynolds number flows. Furthermore, if "proper" scaling, as defined by Purtell [10], of turbulence measurements is performed, it will produce similarity of the data at all Reynolds numbers in both the inner and outer layers.

It is observed from the foregoing studies that there is limited agreement about the nature of the turbulent boundary layer at low Reynolds numbers. In particular, the question about the universality of K and C is not settled. In the present paper, additional wind-tunnel data is presented to clarify the question about the constancy of K and C at low Reynolds numbers.

Experimental Facility and Wind Tunnel

The test facility is a low-pressure chamber located at NASA-Ames Research Center, Moffett Field, Calif. The chamber houses an atmospheric wind tunnel. The tunnel occupies the center floor area of the chamber. The present test section provides a zero-pressure-gradient test facility. Low-pressure experiments are currently being conducted with both air and carbon dioxide, CO_2, as working fluids. Vacuum to the tower is supplied from a five-stage steam ejector plant.

The low-pressure tunnel is a 1.2×0.9 m open-circuit wind tunnel with a total length of about 13 m. It consists of five

sections, each 2.4 m long, plus a 1 m entrance, see Fig. 1. The first section is wood enclosed and contains the entry cone and flow straighteners. The following two sections are constructed of 2.4 cm-thick Plexiglas on all sides. All measurements are taken in the third section at a distance of 6.36 m from the entrance. The fourth and fifth sections are diffusers.

A boundary layer trip of 1 cm dia pebbles is randomly placed over the first meter of the tunnel's floor adjacent to the entrance section. The test section is more than 25 boundary layers lengths from the pebble trip. A fairing of concave molding is installed in the four corners of the tunnel to reduce secondary flows. A flow straightener is used in the tunnel entry. It is constructed 25 cm wide by 0.1 cm thick with 10 × 10 cm openings. This results in a freestream turbulence level of 2 percent. A complete description of the test facility is given in reference [11].

The tunnel is driven by either high-pressure air or carbon dioxide ejected through a network of small orifice nozzles located at the end of tunnel section 4. There are 13 pipes, each with five or six orifices yielding a total of 72 equally spaced orifices. The maximum freestream wind speed through the tunnel is 15 m/s at atmospheric pressure and 170 m/s at 0.5 kPa pressure.

Instrumentation

Wind speed in the tunnel is monitored with two sets of Pitot-static tubes, four individual probes in all. The Pitot-static tube sets are each connected to a capacitive differential pressure transducer. One set of probes is used with a transverse mechanism to determine velocity profiles, while the other is fixed and measures the freestream speed.

Mean velocity profiles are measured by means of a flattened-tip Pitot tube (see insert on Fig. 7) designed by United Sensor. A 1/8 in. dia static pressure probe is mounted near the Pitot tube in the same downstream plane. The Pitot tube is mounted on a rack and pinion vertical transversing device. The pressure differential is measured by a Datametrics Barocel. For increased accuracy in determining the mean-velocity profiles, MacMillan's [12-13] low Reynolds number and shear displacement corrections are applied to the Pitot-
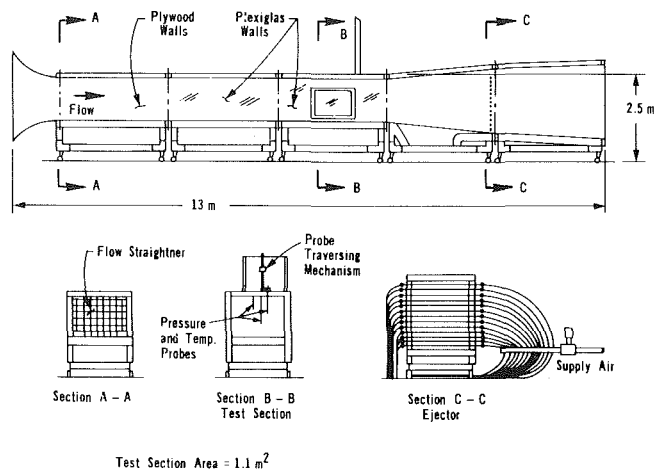

Fig. 1 Diagram of the wind tunnel showing entrance cone and flow straighteners (Section A-A), test section with various probes (Section B-B), and diffuser-drive system (Section C-C)

tube measurements. The maximum corrections applied to the Pitot-tube measurements are always less than 5 percent of the resultant velocity. Further, it is assumed that the Pitot tube responds only to the longitudinal component of turbulence.

Three gages, two mechanical and one electrical, are used to monitor the ambient pressure inside the chamber during an experiment. Chamber pressure is monitored by two-bourdon-tube gages and one strain-gage device. These vary in accuracy and sensitivity. A Wallace and Tiernan (Model FA 160) absolute pressure gage is used; its range is 0.1 to 20 mm Hg (±0.1 mm Hg). On the same line is another Wallace and Tiernan gage (Model FA 129) which reads from 0 to 800 torr (±5 torr). The third device is an electronic barometer. The signal is taken from a sensor mounted inside the chamber. Calibration is done with reference to a standard mercury barometer. Stagnation temperature is read from the output of a thermocouple probe located in the tunnel. The probe is a United Sensor silver-plated total temperature Chromel-Alumel thermocouple. Output from the thermocouple is fed

—————— Nomenclature ——————

C = additive constant in the inner layer logarithmic mean velocity profile; equal to 5.45

C_f = skin-friction coefficient, $2\tau_0/(\rho u_\infty^2)$

H = shape factor, δ^*/θ

P = static pressure inside and at the edge of the boundary layer

P_0 = stagnation pressure

Re_x = Reynolds number based upon downstream distance, $u_\infty x/\nu$

Re_y = Reynolds number based upon vertical height, $u_\infty y/\nu$

R_θ = Reynolds number based upon momentum-deficit thickness, $u_\infty \theta/\nu$

u = mean velocity component parallel to the wall

u^+ = nondimensional u velocity, u/u_τ

u_τ = friction speed, $(\tau_0/\rho)^{1/2}$

u_∞ = freestream value of velocity at edge of boundary layer

v = mean velocity component perpendicular to the wall

x = longitudinal coordinate parallel to the wall

y = perpendicular coordinate normal to the wall

y^+ = nondimensional wall distance, yu_τ/ν

α = coefficient in the outer eddy-viscosity formula

δ = thickness of the boundary layer

δ^* = displacement thickness, $\int_0^\delta \left(1 - \frac{u}{u_\infty}\right) dy$

δ_s = viscous sublayer thickness

θ = momentum thickness, $\int_0^\delta \frac{u}{u_\infty} \left(1 - \frac{u}{u_\infty}\right) dy$

k = von Kármán constant appearing in the "Law-of-the-Wall" equation

ν = kinematic viscosity

π = Coles's "wake" profile parameter

ρ = fluid density

τ = shear stress

τ_0 = wall shear stress

through Chromel-Alumel wires to an Omega Engineering MCJ Cold-Junction Compensator.

Analysis of Velocity Profiles

Mean-flow velocity profiles are determined from the differential pressure measurements of the Pitot-static probes. They are reduced from strip chart recordings of the pressure differential as a function of height. Time-averaged profiles are drawn by hand on the strip chart recording, thus ·establishing a mean profile. The profiles are required to have constant ambient chamber pressure (± 3 percent) and a constant freestream velocity (± 2 percent). Data are then recorded from the mean profile. Each profile data set contains at least 20 readings, the majority having many more than 20 data points.

As a result of drawing the mean profile through a continuous strip chart recorder pressure curve, it is feared this would introduce large errors into the velocity determination, since it is difficult to place the mean-pressure profile accurately. Hence, ten profiles were selected, with varying Reynolds numbers in both air and carbon dioxide, and for each profile an upper and lower estimate of the mean curve is drawn. In each profile, it is visibly noticeable that the upper profile overestimates the mean and the lower profile underestimates the mean. It is found that subsequent calculation of the shape factors never varied by more than 5 percent and were typically less than 3 percent, thus implying the shape factor to be accurate to within ± 2.5 percent (20:1 odds). Similarly, the calculation of R_θ displays a ± 10 percent variation (5:1 odds). The velocity profiles are found to be accurate with ± 5 percent of the true value by the same technique of error analysis. A thorough description is presented by Barr [14].

The data were reduced, taking into account Mach number and slip flow effects. For an isentropic compressible flow the local velocity u is given by

$$u^2 = 2C_p T_0 \left[1 - \left(\frac{P}{P_0} \right)^{\frac{\gamma-1}{\gamma}} \right]^{\frac{1}{2}} \quad (1)$$

where C_p is the specific heat, T_0 is the stagnation temperature, P is the static pressure, P_0 is the stagnation pressure, and γ is the ratio of specific heats (C_p/C_v). Equation (1) assumes no heat transfer. The variation of temperature is found from the velocity profile by using the expression

$$T = T_0 - u^2/2C_p \quad (2)$$

where T is the temperature. The local Mach number, density, and viscosity are calculated from the temperature distribution through the boundary layer. The Mach number is always less than 0.3. The slip flow effects are estimated by the slip to freestream speed ratio [15] and found to be negligible.

Each profile is numerically curve-fitted by means of a multipiece cubic spline technique. The displacement thickness δ^* and momentum-deficit thickness θ are determined by integrating the resultant curve fit using a numerical quadrature technique.

The low-density tunnel allows large changes in fluid properties. These changes yield a wide range of parameters. For example, the kinematic viscosity ν can be varied from 0.14 cm^2/s at atmospheric pressure to 40 cm^2/s at the lowest chamber pressures. The momentum-deficit thickness Reynolds number, R_θ, varies from 200 to 10,000.

Law of the Wall. The surface shear stress τ_0 can be determined by Coles's [1] method from the velocity profiles. This is accomplished by assuming the velocity profile obeys the logarithmic law

$$\frac{u}{u_\tau} = \frac{1}{K} \log \frac{u_\tau y}{\nu} + C \quad (3)$$
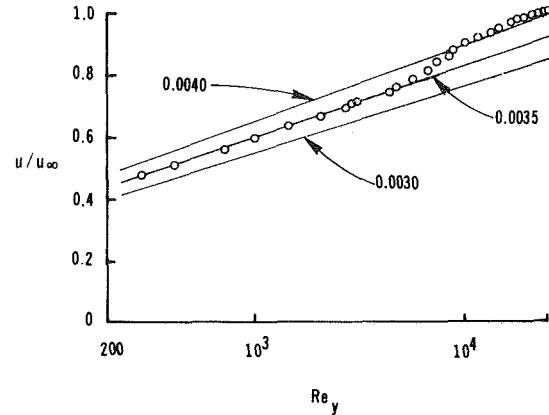

Fig. 2(a) u/u_∞ as a function of $u_\infty y/\nu$ and lines of constant C_f values as determined by equation (4). Test conditions: 9.21 percent atmospheric pressure; $u_\infty = 22.9$ m/s; $\nu = 1.60$ cm/s; $\delta = 16.0$ cm; and $R_\theta = 2060$. Test conducted in air. Uncertainty: velocity ratio ± 2 percent (odds 20:1); Reynolds number ± 2 percent (odds 10:1).
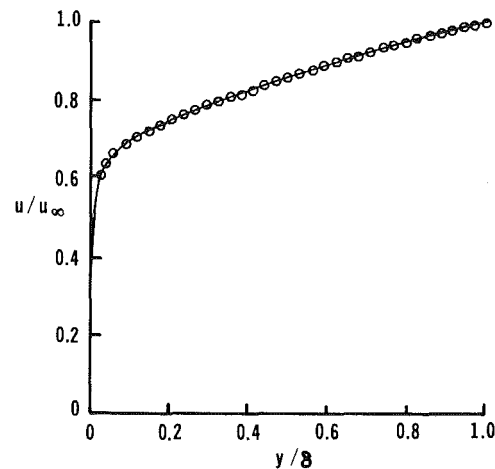

Fig. 2(b) u/u_∞ as a function of y/δ and cubic-spline curve fit (solid line). Test conditions same as those in Fig. 2 (a). Uncertainty: velocity ratio ± 2 percent (odds 20:1); height ratio ± 5 percent (odds 10:1).

for the wall region ($y/\delta < 0.2$) excluding the viscous sublayer. This technique is utilized in the present study to determine τ_0 using $K = 0.418$ and $C = 5.45$ as determined by Patel [16]. Hence,

$$u^+ = 5.5 \log_{10} y^+ + 5.45 \quad (4)$$

Coles also established that u^+ in the wake region ($y/\delta > 0.2$) is a function of Reynolds number for R_θ less than 5000, given by

$$u^+ = f_1(y/\delta) + (2/C_f)^{\frac{1}{2}} \quad (5)$$

where C_f is the skin-friction coefficient and f_1 is a universal function. The mean-velocity distribution outside the sublayer is described by the expression,

$$u^+ = \frac{1}{K} \log y^+ + C + \frac{\pi}{K} w(y/\delta) \quad (6)$$

where π is Coles's profile parameter given by:

$$\pi = 0.55[1 - \exp(-0.243 \xi^{\frac{1}{2}} - 0.298 \xi)] \quad (7)$$

where

$$\xi = R_\theta/425 - 1 \quad (8)$$

At a value of $R_\theta = 425$, the π function is zero and below this value of R_θ the boundary layer is not considered turbulent.

Boundary Layers With $R_\theta > 600$. Initially, a typical

Table 1 Experimental data[a] for air and carbon dioxide at low pressure for R_θ from 600 to 1200 and H from 1.36 to 1.49.

R_θ	Fluid	$u_\infty\left(\frac{m}{s}\right)$	$\nu\left(\frac{cm^2}{s}\right)$	P(kPa)	δ(cm)	δ*/δ	θ/δ	H	$c_f^b \times 10^3$	$c_f^c \times 10^3$
644	CO_2	32.7	11.5	0.693	19.5	0.169	0.116	1.46	4.51	4.72
655	CO_2	96.2	26.8	0.300	15.8	0.170	0.115	1.48	4.33	4.81
741	CO_2	28.3	7.74	1.03	19.5	0.150	0.104	1.45	4.35	4.81
750	AIR	98.7	21.4	0.720	16.4	0.137	0.0991	1.38	4.93	4.83
768	AIR	85.2	20.3	0.400	16.7	0.161	0.110	1.46	4.15	4.73
775	AIR	41.6	12.5	1.20	21.3	0.160	0.109	1.47	4.21	4.65
795	CO_2	91.8	21.5	0.387	17.0	0.153	0.109	1.40	4.64	4.60
937	CO_2	86.6	18.8	0.440	18.5	0.164	0.110	1.49	3.75	4.38
976	CO_2	97.5	20.8	0.400	18.5	0.154	0.112	1.38	4.49	4.50
982	CO_2	17.6	3.88	2.00	18.5	0.160	0.117	1.37	4.57	4.56
993	CO_2	77.9	15.9	0.507	19.0	0.152	0.107	1.42	4.11	4.40
1017	CO_2	61.0	11.7	0.653	18.0	0.160	0.109	1.47	3.78	4.43
1021	CO_2	70.2	13.3	0.600	17.5	0.160	0.111	1.44	3.92	4.41
1025	AIR	24.0	5.36	2.67	18.9	0.180	0.121	1.49	3.66	4.25
1033	CO_2	88.3	17.6	0.467	19.0	0.161	0.108	1.49	3.66	4.34
1058	AIR	20.7	3.88	4.00	17.2	0.168	0.115	1.46	3.85	4.35
1089	AIR	10.6	1.36	11.9	13.0	0.145	0.107	1.36	4.72	4.33
1094	AIR	20.7	3.88	4.00	18.1	0.161	0.113	1.42	3.99	4.27
1128	AIR	47.4	9.03	1.67	19.0	0.163	0.113	1.44	3.86	4.20
1142	AIR	10.8	1.88	8.26	18.0	0.157	0.111	1.41	4.04	4.30
1153	AIR	50.3	9.12	1.73	18.3	0.168	0.114	1.47	3.63	4.25
1155	CO_2	20.9	3.89	2.01	22.0	0.141	0.0975	1.45	3.81	4.15
1161	AIR	47.5	8.17	1.93	18.2	0.149	0.110	1.35	4.36	4.23
1164	AIR	10.6	1.85	8.40	17.5	0.166	0.117	1.42	3.92	4.15
1177	AIR	47.6	9.03	1.67	20.5	0.156	0.109	1.43	3.83	4.20
1202	CO_2	70.5	12.7	0.626	21.5	0.149	0.101	1.48	3.60	4.16

[a] Uncertainties are as follows: R_θ ± 5% (5:1 odds); u_∞ ± 2% (20:1 odds); P ± 3% (20:1 odds); δ ± 10% (10:1 odds); H ± 2.5% (20:1 odds); C_f (Clauser) ± 7% (10:1 odds).

[b] Skin-friction coefficient as calculated from Coles's relation, Equation (9).

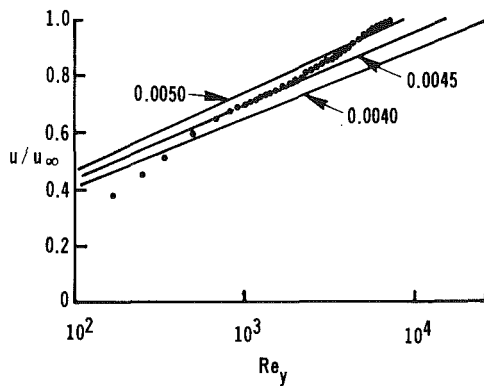[c] Skin-friction coefficient as determined from "Clauser velocity curves" (κ = 0.418 and C = 5.45).

Fig. 3 u/u_∞ as a function of $u_\infty y/\nu$ and lines of constant C_f (equation (4)). Test conditions: 1.1 percent atmospheric pressure; u_∞ = 41.6 m/s; ν = 12.5 cm²/s; δ = 21.3 cm; and R_θ = 775. Test conducted in air. Uncertainty: velocity ratio ±2 percent (odds 20:1); Reynolds number ±2 percent (odds 10:1).

boundary layer velocity profile is examined at a relatively large value of $R_\theta = 2060$ to examine the agreement with conventional results. The higher valued R_θ experiments are not of primary interest here but are conducted to establish the reliability of the test system. Next, flow with $600 < R_\theta < 1200$ is examined and are shown to exhibit conventional characteristics for high Reynolds number flows, e.g., K and C remain constant.

Figure 2(a) displays the dimensionless velocity u/u_∞ as a function of the Reynolds number, $Re_y = yu_\infty/\nu$. Figure 2(b) shows u/u_∞ as a function of y/δ. The C_f determined from the Clauser [17] technique is 0.00351. This compares well with a value of 0.00353 which was calculated from Coles's empirical expression [18].

$$C_f = \frac{0.3 \exp(-1.33H)}{(\log R_\theta)^{1.74 + 0.31H}} \qquad (9)$$

where H is the shape factor defined as δ*/θ. The measured value of π from the figure is 0.439 which agrees with Coles's expression (equation (7)) that yields a value of 0.441. This case is typical of the higher Reynolds number flows ($R_\theta > 1200$) in the sense it matches standard results for C_f, π, and it has characteristic values of δ* and θ.

Figure 3 displays a typical plot of u/u_∞ versus Re_y for

$R_\theta = 775$. The profile has a moderate wake and has an H of 1.46. The graphically determined value of C_f (Clauser) is 0.00465. The C_f as calculated from equation (9) is 0.00421, which is substantially lower. This is a common result of flows with $600 < R_\theta < 1200$. Equation (9) consistently underestimates the C_f value determined by the Clauser technique for $600 < R_\theta < 1200$.

Table 1 presents a partial summary (limited to data with a range of H from 1.36 to 1.49) of experimental data for $600 < R_\theta < 1200$. Also presented are calculated values of C_f as determined by equation (9). An empirical expression is developed to fit the experimentally determined C_f's (Clauser). The basic form of the equation is assumed to be [14].

$$C_f = 10^{-A_1} R_\theta^{-A_2} \qquad (10)$$

following the form of Schlichting [19]. Values of A_1 and A_2 are selected such that they minimized the normalizing error weighting each data point equally. This results in an expression of C_f of

$$C_f = 0.023 R_\theta^{-0.24} \qquad (11)$$

which is felt by the author to be more accurate in the range of $600 < R_\theta 1200$ than equation (9).

Figure 4 presents C_f as a function of R_θ. The solid line is given by equation (11). A comparison of the data to empirical expressions of Ludwig and Tillman [20], 1/7th power law (Schlichting [19]) and Coles's equation with different constants coefficients is performed. They are all found to be less accurate than equation (11) when compared to the C_f's (Clauser) in the range $600 < R_\theta < 1200$.

Figure 5 displays a typical plot of u^+ as a function of y^+ in the range $600 < R_\theta < 1200$; the normalizing shear velocity is determined by the Clauser technique. Figure 5 displays typical results for all flows with $600 < R_\theta < 1200$ that are examined. The logarithmic equation (4) is valid for all these velocity profiles in the near wall region. In summary, despite the low Reynolds numbers, K and C maintain constant.

Boundary Layer Flows With $R_\theta < 600$. The present experiments show variation in the values of K and C for flows with $R_\theta < 600$. This phenomenon is investigated by examining typical mean-velocity profiles.

A measure of the presence of turbulence is performed in the logarithmic portion of the boundary layer for the range $425 < R_\theta < 600$. The Pitot tube is held at a constant height in
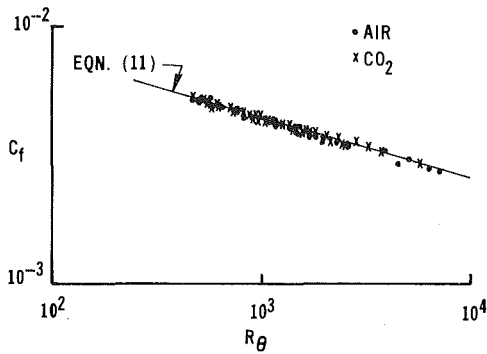
Fig. 4 C_f as a function of R_θ. The solid line is the predicted values of equation (11). Circular symbols represent data taken in air while the plus (+) symbols are data taken in carbon dioxide. Uncertainty: $C_f \pm 7$ percent (10:1 odds); $R_\theta \pm 5$ percent (10:1 odds).
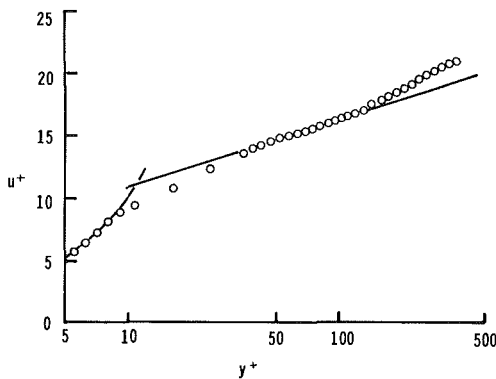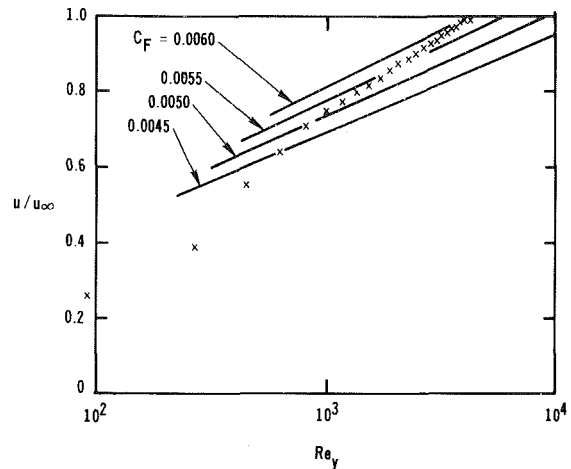

Fig. 5 u^+ as a function of y^+. Also shown is u^+ versus y^+ (curved solid line) and equation (4) (straight solid line). Test conditions same as those in Fig. 3. Uncertainty: u^+ ± 2 percent (20:1 odds); y^+ ± 2 percent (10:1 odds).

Fig. 6 u/u_∞ as a function of (yu_∞/ν) and lines of constant C_f (equation (4)). Test conditions: 0.67 percent atmospheric pressure; $u_\infty = 46.8$ m/s; $\nu = 19.4$ cm^2/s; $\delta = 21.2$ cm and $R_\theta = 492$. Test conducted in air. Uncertainty: velocity ratio ± 2 percent (20:1 odds); Reynolds number ± 2 percent (10:1 odds).
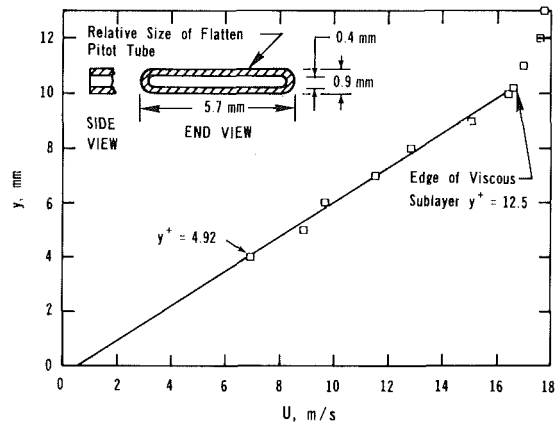

Fig. 7 Height y as a function of u. Determination of the wall shear stress by the wall-slope method is done from these curves in the range $425 < R_\theta < 600$. The shear velocity is calculated from the slope in forming the y^+'s. Test conditions: 1.45 percent atmospheric pressure; $u_\infty = 30.9$ m/s; $\delta = 16.0$ cm; and $R_\theta = 463$. Uncertainty: $y \pm 5$ percent (10:1 odds); $u \pm 5$ percent (10:1 odds).

the near-wall region and the pressure differential recorded as a function of time. The Barocel pressure transducer has a frequency response of 1kHz and the strip chart recorder 100-200 Hz. All differential pressure signals appear to be continuously turbulent. The total system response including the Pitot and static probes tubing is above 100-200 Hz, and it is only limited by the strip chart recorder.

Figure 6 presents u/u_∞ as a function of Re_y. This is typical of many profiles with $425 < R_\theta < 600$. As observed from the figure, it is impossible to select a value of C_f from the Clauser technique ($K = 0.418$ and $C = 5.45$). The logarithmic region of data is seen to cut across the predicted lines of constant C_f's, e.g., $C_f = 0.0045$, 0.0050, 0.0055, and 0.0060. This is a common result of nearly *all* profiles in the $425 < R_\theta < 600$ range. It is clear from this that the form of the logarithmic velocity equation (3) is correct, but K is not equal to 0.418 and C is not equal to 5.45.

K is observed to be a function of R_θ, but only in the range $425 < R_\theta < 600$. An approximate variation of K from the present data is given by

$$K = 0.0013 R_\theta - 0.362 \qquad (12)$$

for the range $425 < R_\theta < 600$. Above $R_\theta = 600$, $K = 0.418$. The additive constant C appears to be a function of both R_θ and H.

The thick boundary layers made it possible to obtain Pitot-tube data within the viscous sublayer. This, in turn, results in an estimate of the wall shear stress from the wall slope. A typical profile for the range $425 < R_\theta < 600$ is shown in Fig. 7. Since it is possible to obtain several points within the viscous sublayer, an estimate of the slope of the mean velocity profile could be made. This method will be referred to as the wall-

slope method for determining the shear velocity u_τ and C_f. Note that the result of variable K and C for $425 < R_\theta < 600$ does not depend on the determination of shear velocity. The edge of the sublayer, the point at which the velocity deviates from a linear relation with height, is found to be $y^+ = 12.5$. The height of the viscous sublayer is denoted by δ_s. The wall-slope method is used in determining u_τ for the y^+ calculation. This is the only way to determine u_τ in this range since the logarithmic equation (3) does not have constant K and C coefficients. The location of $y^+ = 12.5$ and relative size of the Pitot tube are shown on the figure. The solid line drawn through the data represents the least-squares linear-regression fit to the data. Here, $u_\tau = 128.5$ cm/s and hence $C_f = 0.00345$ for $R_\theta = 463$. This seems to underestimate the value of C_f since similar runs with slightly larger velocities, such as $R_\theta > 600$, yield values of C_f (Clauser) of 0.0045 or greater. Hence, it is unlikely that this run at a lower velocity and thus a lower R_θ, would have a value of C_f lower than 0.0045. Moreover, because of reduced value of R_θ, the viscous effect becomes greater and the value of C_f should be greater than 0.0045. Unfortunately, no direct means of measuring C_f is available. This same phenomenon was observed by Kline, et al. [2]. They examined zero-pressure-gradient data and found that the wall-slope method for determining u_τ underestimates the shear velocity as determined by the Clauser technique. A
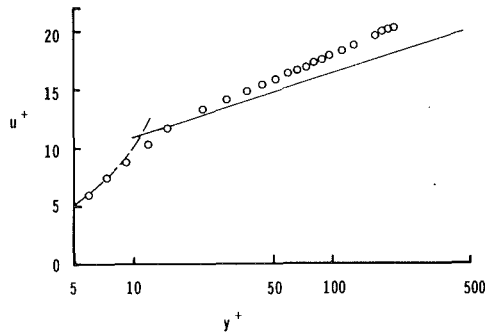
Fig. 8 u^+ as a function of logarithm y^+. Also shown is u^+ versus y^+ and equation (4). Test conditions same as in Fig. 7. Uncertainty: u^+ ±5 percent (10:1 odds); y^+ ±5 percent (10:1 odds).
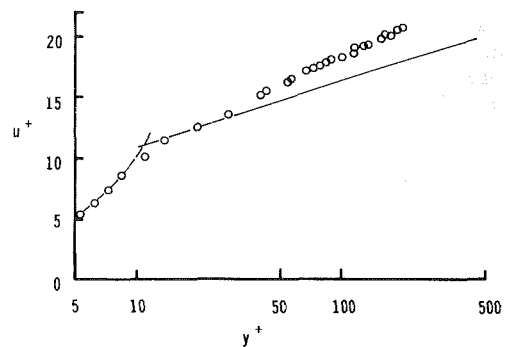

Fig. 9 Similar experimental results as those found in Fig. 8 with $R_\theta = 480$ and the shape factor H is 1.53. Test conditions: 1.05 percent atmospheric pressure; $u_\infty = 39.9$ m/s; $\nu = 13.3$ cm^2/s; $\delta = 15.0$ cm. Test conducted in air. Uncertainty: u^+ ±5 percent (10:1 odds); y^+ ±5 percent (10:1 odds).
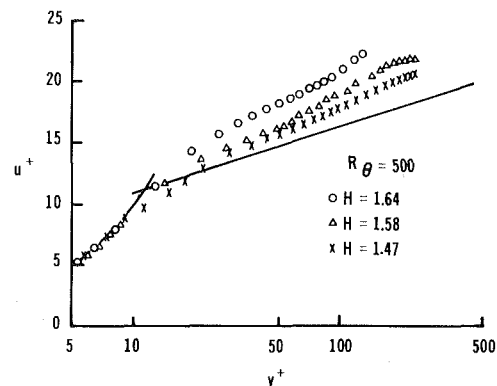

Fig. 10 u^+ as a function of y^+ for three experiments with R_θ approximately equal to 500. This shows variation of individual velocity distributions from equation (4) as a function of H. Uncertainty: u^+ ±5 percent (10:1 odds); y^+ ±5 percent (10:1 odds).

calculated value of C_f from equation (9) yields 0.00477 for the Fig. 7 velocity profile. Unfortunately, it is not possible to determine C_f (Clauser) due to the nature of the profile as discussed earlier.

By using $y^+ > 5$ data, reference [2] may have artificially lowered the value of u_τ (wall slope). The use of $y^+ > 5$ data to determine u_τ is known to underestimate the value of shear velocity. This would create the effect shown in Fig. 9(b) of reference [2]. That is, the data in the logarithmic region lie above that predicted by equation (4). Many profiles $(425 < R_\theta < 600)$ for the present data yield values of C_f (wall slope) approximately equal to 0.005. These profiles also have data that lie above that predicted by equation (4) in the logarithmic region. However, this seems to be a different phenomenon than that described in reference [2]. They found similar results for all values of R_θ. Here it happens only when $425 < R_\theta < 600$ when C_f (wall slope) is used in finding u_τ. It appears as the value of R_θ decreases a better estimate of C_f (wall slope) is obtained. For example, the C_f (wall slope) of Fig. 6 is 0.00527.

The nondimensional height, δ_s/δ, of the viscous sublayer increases in value with decreasing values of R_θ. In Fig. 7, the value of δ_s/δ is equal to 0.0629, which is common for velocity profiles in the range $425 < R_\theta < 600$. The height of the sublayer in the present experiments for this range varies from 6 percent to 9 percent of δ. The rule-of-thumb indicator of 10 $\nu/(U_\tau\delta)$ yields only maximum values of 4 percent or less. Hence the sublayer in this region $(425 < R_\theta < 600)$ is referred to as a viscous *super sublayer*.

It should be noted that the nondimensional sublayer thickness $\nu/[u_\tau\delta]$ gradually increases starting at a value of $R_\theta = 1200$ if u_τ (wall slope) is used. There is not a sudden growth of the physical sublayer height at $R_\theta = 600$, as may appear to be the case. This artificial effect stems from the replacing of u_τ (Clauser) with u_τ (wall slope) at $R_\theta = 600$, and there does not appear to be a physical change in the rate of growth of the sublayer height δ_s.

Figures 8 and 9 show u^+ as a function of y^+ with equation (4) presented. The shear velocities are determined by the wall-slope method. These figures indicate that the logarithmic region lies above the predicted values; note, however, that u_τ (wall slope) is used in normalizing y^+ and u^+. Of more than 20 experimentally-measured profiles in the range of $425 < R_\theta < 600$, all but a few exhibit the same basic trends. Both profiles are void of any substantial wake region and agree reasonably well with Coles's predicted π.

Figure 10 displays u^+ as a function of y^+ for three cases with nearly constant values of R_θ equal to 500. The variation of H, while maintaining a constant R_θ, is accomplished by varying the ambient chamber pressure and performing experiments at different freestream velocities. The u_τ is determined by the wall-slope method. Kline, et al. [2], found almost identical results by using the u_τ (wall-slope) method

instead of the shear velocity determined by the Clauser technique. Since it is not possible to determine the Clauser shear velocity in the present data, it is not possible to make the same comparison they made; however, it is clear that the form of the logarithmic profile equation (4) is appropriate for profiles $(425 < R_\theta < 600)$, but K and C are not constant.

A comparison between the present data and the data presented by Purtell [10] can be made. Such a comparison shows that for $R_\theta > 600$, the data are in complete agreement within experimental errors, namely, the u_τ's found in both cases, by different means, are approximately the same. Both sets of data are hence in agreement with the universal velocity profile and other high Reynolds number results.

All of Purtell's data are for $R_\theta > 600$ except for one velocity profile at $R_\theta = 500$, which seems to follow the universal profile. This result does not agree with the present data for R_θ between 425 and 600, in which the data do not follow the universal velocity profile. The strong majority of profiles measured in the present study are unable to fit the lines of constant C_f as shown in Fig. 6.

A warning is made that the flow in the R_θ range of 425 to 600 may not be in equilibrium or fully developed. Although the profiles appear to be developed as measured by the Coles's $\pi-$wake parameter and the signals appear to be continuously turbulent, it may be that the position of transition is fluctuating up and down the length of the tunnel. Furthermore, the boundary layer may not have recovered from the initial tripping of the flow. The roughness used to trip the boundary layer is 1 meter in length composed to randomly placed 1 cm pebbles placed at the entrance of the tunnel. This situation effectively creates a smooth-rough-smooth flow which slowly relaxes and may take downstream lengths greater than 50 boundary layer thicknesses to return to equilibrium. Also, the

present data are not infallible to other effects such as unusual flow history due to recirculating flow in the pressure chamber and the presence of large values of freestream turbulence.

Figure 11 shows u/u_∞ as a function of y/δ for various R_θ's. The well-known laminar solution is also shown. By examining individual runs made at different times under different conditions, a range of data is obtained. It seems reasonable to assume a gradual blending from the laminar profile to turbulent profile, as a function of R_θ and H, is a process the flow would experience as R_θ were gradually increased. It appears there are no rapid changes that occur at any one value of R_θ in the process. These flows are found to have intermittent laminar-turbulent flow within the logarithmic region as observed from the pressure transducer output while the Pitot tube is held at a constant height in the logarithmic region and the signal recorded.

Conclusions

Experiments measuring the mean-velocity profile for values of $R_\theta > 600$ suggest that the form of the logarithmic velocity profile is correct and K and C remain invariant. However, calculated values of C_f from Coles's relation (equation (9)) predict values of C_f's 7-15 percent lower than values obtained by the graphical Clauser technique. An empirical relation, equation (11), is presented that yields better agreement with Clauser C_f's than equation (9) for the limited low Reynolds number range $600 < R_\theta < 1200$.

In the range $425 < R_\theta < 600$, it is shown that the form of the logarithmic is valid, but the constants $K = 0.418$ and $C = 5.45$ do not fit to the experimental data. K and C are found to be functions of R_θ and H. When the data are plotted as u^+ versus y^+, each normalized by u_τ (wall slope), the logarithmic region is found to lie above that predicted by equation (4).

Lastly, these flows ($425 < R_\theta < 600$) develop an unusually large viscous sublayer, here described as a *super sublayer*. The measured heights of the *super sublayer* are 6-9 percent of the boundary layer heights, far exceeding conventional predictions.

Acknowledgment

References

1 Coles, D. E., "The Turbulent Boundary Layer in a Compressible Fluid," Rand Report 403-PR, 1962.

2 Kline, S. J., Reynolds, W. C., Schraub, F. A., and Runstadler, P. W., "The Structure of Turbulent Boundary Layers," *Journal of Fluid Mechanics*, Vol. 30, 1967, pp. 741-773.

3 Herring, H. J., and Mellor, G. L., "A Method of Calculating Compressible Turbulent Boundary Layers," NASA CR-1144, 1963.

4 Simpson, R. L., "Characteristics of Turbulent Boundary Layers at Low Reynolds Numbers With and Without Transpiration," *Journal of Fluid Mechanics*, Vol. 42, 1970, pp. 769-802.
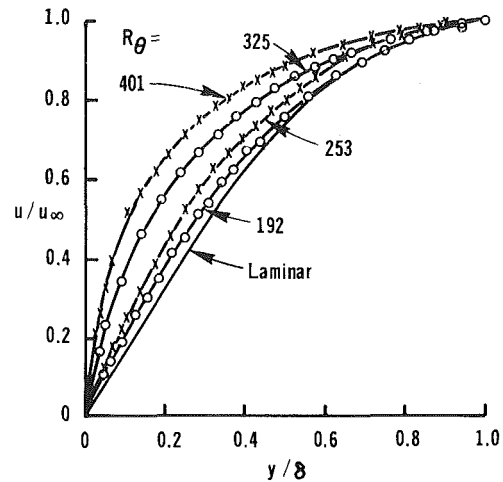
Fig. 11 u/u_∞ as a function of y/δ for value of $R_\theta = 192, 253, 401, 325$. Also shown is the laminar profile. Note the gradual transition with changing values of R_θ. Uncertainties: $u/u_\infty \pm 2$ percent (20:1 odds); $y/\delta \pm 5$ percent (10:1 odds).

5 McDonald, H., "Mixing Length and Kinematic Eddy Viscosity in a Low Reynolds Number Boundary Layer," United Aircraft Research Laboratories Report J214453-1, Sept. 1970.

6 Huffman, G. D., and Bradshaw, P., "A Note on von Karman's Constant in Low Reynolds Number Turbulent Flows," *Journal of Fluid Mechanics*, Vol. 53, 1972, pp. 45-69.

7 Cebeci, T., "Kinematic Eddy Viscosity at Low Reynolds Numbers," *AIAA Journal*, Vol. 11, 1973, pp. 102-104.

8 Granville, P. S., "A Modified Law of the Wake for Turbulent Shear Flows," ASME JOURNAL OF FLUIDS ENGINEERING, Vol. 98, 1976, pp. 578-580.

9 Granville, P. S., "Drag and Turbulent Boundary Layer of Flat Plates at Low Reynolds Numbers," *Journal of Ship Research*, Vol. 21, 1977, pp. 30-39.

10 Purtell, L. P., "The Turbulent Boundary Layer at Low Reynolds Number," Ph.D. dissertation, University of Maryland, 1978.

11 White, B. R., "Low-Reynolds-Number Turbulent Boundary Layers," from *Turbulent Boundary Layers: Forced, Incompressible, Non-Reacting*, ed., H. E. Weber, ASME, New York, 1979, pp. 209-220.

12 MacMillan, F. A., "Viscous Effects on Pitot Tubes at Low Speeds," *Journal of the Aeronautical Society*, Vol. 58, 1954, pp. 837-839.

13 MacMillan, F. A., "Experiments on Pitot Tubes in Shear Flows," Rep. Memor. Aero. Res. Coun. Lond., No. 3028, 1956.

14 Barr, P. K., "Calculation of Skin-Friction Coefficients for Low-Reynolds-Number Turbulent Boundary Layer Flow," M.S. thesis, University of California, Davis, 1979.

15 White, F. M., *Viscous Fluid Flow*, McGraw-Hill, New York, 1974, pp. 49-51.

16 Patel, V. C., "Calibration of the Preston Tube and Limitations on Its Use in Pressure Gradients," *Journal of Fluid Mechanics*, Vol. 23, 1965, pp. 185-208.

17 Clauser, F. H., "Turbulent Boundary Layers in Adverse Pressure Gradients," *Journal of Aeronautical Sciences*, Vol. 21, 1954, pp. 91-108.

18 Coles, D. E., and Hirst, E. A., (Editors) Proceedings, Computation of Turbulent Boundary Layers, 1968, AFOSR-IFP, Stanford Conference, Vol. 2, pp. 1-45 (Thermoscience Division, Stanford University, 1969).

19 Schlicting, H., *Boundary-Layer Theory*, 7th Edition, McGraw-Hill, New York, 1979, pp. 636-640.

20 Ludwieg, H., and Tillmann, W., "Untersuchungen über die Wandschubspannung in Turbulenten Reibungsschichten," *Ing-Arch.*, Vol. 17, 1949, pp. 288-299; translated as "Investigations of the Wall Shearing Stress in Turbulent Boundary Layers," National Advisory Committee Aeronautical, Washington, Technical Memorandum No. 1285, 1950.

Aerodynamic Effects of Shape, Camber, Pitch, and Ground Proximity on Idealized Ground-Vehicle Bodies

A. R. George

Professor and Director,
Sibley School of Mechanical and Aerospace
Engineering,
Cornell University,
Ithaca, N.Y.   14853

Results are presented from an experimental study of the lift, drag, pitching moment, and flow field of a series of rounded edge simple bluff bodies of various cambers and tapers. The bodies were proportioned to be similar to those of idealized ground vehicles such as automobiles, vans, and trucks. The models were tested with and without simulated wheels, underbody roughness, and proximity to a stationary and moving ground plane. The pitch angle was varied at zero yaw angle. The force and moment coefficients and flow visualization studies indicated the existence and importance of flow regimes characterized by a pair of trailing vortices on the leeward side of the body similar to those found over an inclined body of revolution and over slender delta wings. These flows can suppress bubble-type separation. The effects of a rough underbody are generally detrimental although less so if the rough surface is on the windward side. A moving ground plane was found to give significantly different lift and drag for small ground clearances characteristic of actual road vehicles.

Introduction

In the past several years, there has been a strong increase in interest in the field of aerodynamics of bluff bodies. Much of this interest originates in the desire to reduce drag and thus fuel consumption of road vehicles. Other interest is related to side forces, lift, and stability of road vehicles.

A very extensive base of aerodynamic knowledge exists in airplane aerodynamics, but it has not been as directly helpful to road vehicles as had been anticipated for two reasons. The first is that aircraft are, almost universally, intentionally designed to consist of an assemblage of components, each of which will support a nearly ideal simple unseparated flow. For example, some basic flows which are used are nearly two dimensional airfoils, slender bodies of revolution at zero angle of attack, delta wings, axisymmetric or 2-D inlets, etc. However, even in aircraft aerodynamics, most of the interesting problems occur when there is interference, three-dimensionality, or breakdown of these simple flows, for example, at wing-body junctions, tips, or in separated regions. On the other hand, bluff body flows, as characterized by automobiles and trucks for example, are designed primarily to meet other requirements such as payload shape and restricted overall dimensions. This usually results in shapes giving flows which are far from the ideal "clean" flows of aircraft.

The second reason why aerodynamic knowledge has not been widely and effectively applied in the automobile industry until recently is that aerodynamics usually had been con-

sidered as completely subsidiary to styling and was not given serious consideration except in that context. For example, as aircraft began to fly supersonically which required sharper edges, automobile stylists and designers also moved toward sharper edges even though they are inappropriate for the low speeds of automobiles. (A few manufacturers were exceptions; Citroen, Porsche, and Saab, for example, have historically given higher priority to aerodynamics and have produced relatively aerodynamically efficient vehicles over the years.)

An excellent compendium of papers on road vehicle aerodynamics can be found in the General Motors Research Laboratories symposium volume: *Aerodynamic Drag Mechanisms of Bluff Bodies and Road Vehicles* [1]. Road vehicles support flows which are quite different from those over typical aircraft components. The relations between lift and drag and body shape are quite complex, depending on ground proximity and on whether the body supports a classical attached flow followed by a simple separation bubble wake at the rear or whether longitudinal vortices form on the lee surface. Morel [2, 3] discussed this problem in detail and carried out a set of definitive experiments with inclined base bodies with sharp side edges.

The goals of the present work were to understand how taper, camber, pitch, ground proximity, and other shape changes affect road-vehicle lift, drag, and flow patterns. The results should be helpful to theoretical understanding as well as for vehicle design for low drag or controlled lift or downforce. The basic shapes tested were variations of road-vehicle-proportioned bluff with rounded edges. As low drag becomes more important to vehicle design, most will have
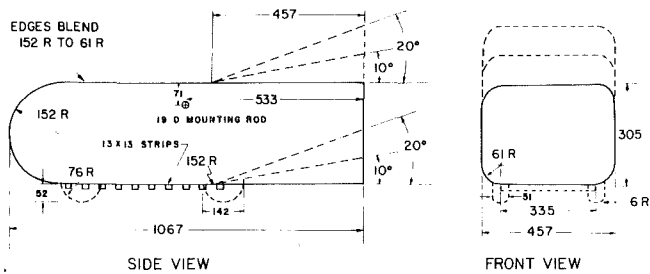
Fig. 1 Sketch of models used in study. All dimensions are in millimeters.

their front and side edges rounded enough to eliminate forebody separation and separation due to slight yaw. A series of force measurement and flow visualization tests were carried out on the bodies with varying camber, taper, and pitch as shown in Fig. 1. The configurations were all based on a rounded nose and a rectangular midsection with all longitudinal edges radiused at 20 percent of the body height. This large an edge radius has been shown to insure attached flow, independent of Reynolds number for small to moderate angles to the free stream [4-6]. One of the primary goals of the research was to delineate the types of flow found on this class of bluff body over wide range of pitch angles and to relate this flow to measured aerodynamic forces and moments.

Several investigators have considered the application of variations of slender body theory to the bluff bodies typical of road and rail vehicles [7, 8]. The present test results for a wide range of pitch angle, body camber, and body taper can serve as a data base to compare to such analytical approaches.

Another topic of great interest in road-vehicle aerodynamics is the mechanisms by which shape, underbody roughness, wheels, and proximity to a moving or fixed ground bring the drag coefficient of a vehicle up to of order 0.45 from the ideal streamlined body value of say 0.05. For some discussion of these effects, see reference [9] and the discussions in reference [1], pages 120–123 and 357–372. The tests reported here include tests with and without a rough underbody and/or additions representative of wheels. Also, the effects of varying proximity to fixed and moving ground plane surfaces were studied.

This study is primarily directed toward an understanding of flow patterns and their relation to lift and drag on idealized bodies rather than practical testing of present ground vehicle bodies.

Experimental Equipment and Procedures

The series of models tested are indicated in Fig. 1. They were constructed of wood with a variety of detachable rear end upper and lower pieces. (All joints were sealed with tape.) All tests reported were run using a 13 mm wide, boundary layer transition strip of 0.41 mm carborundum grit on double faced tape, located, as shown in Fig. 2, in a plane just before the shoulder of the nose. A series of tests on one configuration showed a maximum change of 2 percent in drag between any two tests with or without a range of transition strips and Reynolds numbers varying from 1.4 to 3.4 $\times$ 10^6 based on body length. Tests in free flow were carried out at Re = 2.5 $\times$ 10^6, those near the fixed ground at 2 $\times$ 10^6, and those with the moving or stationary ground belt at 1.5 $\times$ 10^6. The frontal area of the basic model without upswept rear deck, wheels, or roughness is 1.362 m^2. This value was used in the definition of all coefficients to keep comparisons on a common basis.

The wheel shapes used corresponded to 76 mm radius wheels. To simulate a rough underbody, ten 13 by 13 mm strips were added underneath the basic shape at 51 mm, but as previously mentioned, this was not included in the base area
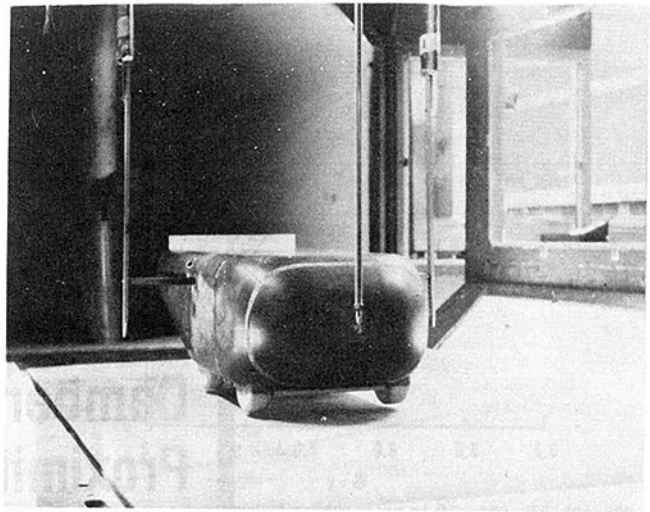

Fig. 2 Model mounted above moving ground belt

used to define force and moment coefficients. The clearances reported for the simulated ground tests were also always measured from the basic smooth underbody.

The models were tested at various pitch angles but zero yaw angle in the nominally rectangular 1.68 $\times$ 2.13 m (5.5 by 7 ft) cross section low speed wind tunnel of the Department of Aeronautics and Astronautics, the University of Southampton, Southampton, England. The test section is approximately 3.34 m^2, thus the blockage of the 0.14^2 base area model at zero angle of attach is only 4 percent. At this blockage, the correction recommended by Pope and Harper [10], conservatively based on a separated flow drag coefficient of 0.3, is less than 3 percent. Similar but smaller corrections may be derived from references [11] and [12]. Because of their small and uncertain size, no such corrections were applied to the data which are presented here. As the corrections are proportional to C_D, they might become significant at the highest angles of attack. Similarly, the floor and ceiling proximity to the ends of the models might have become significant at the more extreme angles of attack [12], but no corrections were applied for this effect either.

The University of Southampton wind tunnel is equipped with a three-component remotely-operated movable weight balance accurate and repeatable in the present experiments to ± 0.67N in lift, ± 1.33N in drag, and ± 0.41 N.m in pitching moment. The model was mounted on a rod halfway back on the model at a height as indicated in Fig. 1. Either a pitch rod or nose wire were also used depending on whether the ground belt was installed. The tare drags of the mounting rods, wires, and struts were estimated using two-dimensional C_D results for the component shapes as reported in reference [12]. The tare drag coefficients estimated were 0.113 for the free flow and ground plane tests using the pitch wire and 0.462 using the unfaired pitch rod. The estimated overall uncertainties, including both balance and tare uncertainties, are shown in the following table:

Estimated Overall Uncertainties

	Free flow	With fixed ground board	Near ground belt
C_L	± 0.005	± 0.01	± 0.015
C_D	± 0.01	± 0.03	± 0.04
C_M	± 0.005	± 0.01	± 0.015

The repeatability of tests is considerably better, being about ± 0.01 in C_D even near the ground belt. The angle of pitch of the model was accurate and repeatable to within about 0.1 deg. However, the moving ground belt angle could only be aligned with the flow to an accuracy of about 0.5 deg.
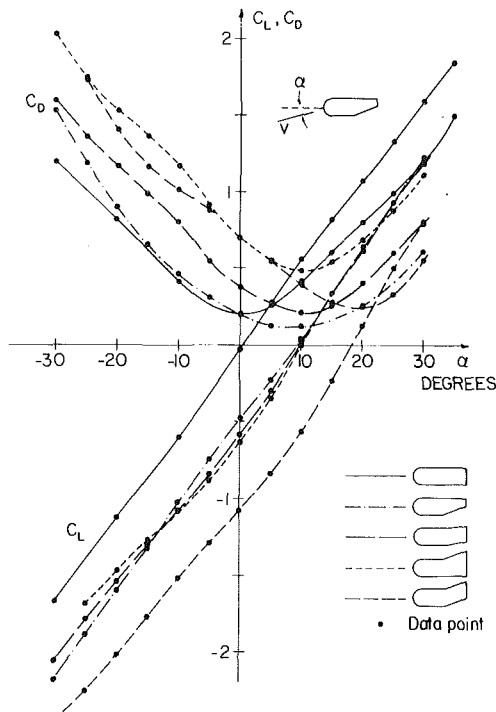
Fig. 3 Lift and drag of bodies with various mean cambers and tapers in free flow. Note lift and drag slope changes in different flow regimes.

Fig. 4 Pitching moments corresponding to Fig. 3

Fig. 5 Sketches of flow with lee side vortices

The thin fixed ground board was installed with the model remaining nominally centered in the tunnel test section. It extended about one-half body body length in front of the model and about one length behind. A 229 by 305 mm flat plate was installed normal to the flow, underneath the board to bring the dividing streamline in parallel to the ground board as observed with tufts and by the measured pressure difference between the top and bottom shoulders of the leading edge of the board.

The ground belt used consisted of a 3.2 mm thick fabric and rubber belt 1.12 m wide and 2.08 m long between roller centers. It was tensioned to prevent wave motion and rode over a perforated suction plate to keep the belt surface planar. The belt was driven by a hydraulic motor and its speed adjusted to match the free stream using a stroboscope to measure roller rotation rate. The belt was mounted in the tunnel floor and the tunnel floor boundary layer was bled away through a slot in front of the belt whenever it was installed in the tunnel. The modified test section with belt installed was recalibrated using a pitot static tube showing a 6.5 percent increase in test section dynamic pressure, which was accounted for in the flow velocity and force coefficient calculations. The velocity profile near the moving belt showed essentially no boundary layer remnant.

Results

Free Flow Forces and Moments. The first set of data were taken for five different models without rough underbodies or wheels tested in free flow nominally in the center of the wind tunnel test sections. The lift, drag, and pitching moment coefficients based on the nominal frontal area of the model front section and the overall model length are presented in Figs. 3 and 4. Data were taken every 5 deg of pitch angle. Several conclusions can be drawn from the curves.

Both the lift and drag coefficients show slight change in slope at various pitch angles as different flow patterns are established. For example, the results for the simple 0 deg top, 0 deg bottom model show a change in character at around plus or minus 10 to 15 deg with a small reduction in lift curve slope and a stabilizing of the rate of increase of C_D with α. As
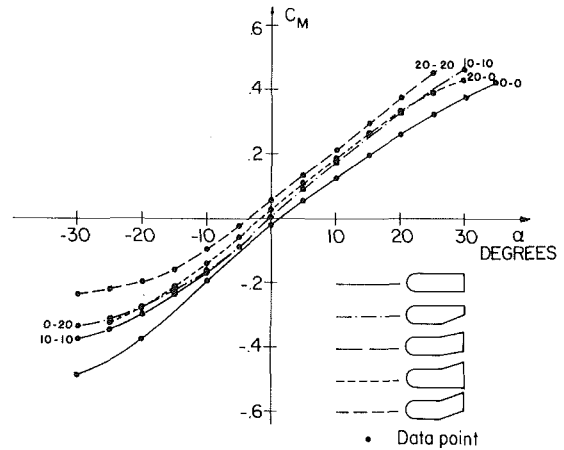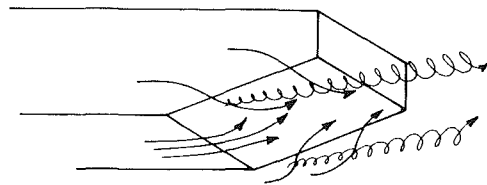
will be discussed subsequently, this change occurs when a pair of vortices is first observed to form on the lee surface of the model. With the 0–0 deg body, this occurs symmetrically. The other models are more complex with different surface angles on upper and lower sides and the flow changes are more complex. However, the bumps in C_D were still found to occur at angles where the pair of lee side vortices just become observable. These vortices, which are sketched in Fig. 5, produce lowered pressure and thus maintain lift.

These flows with pairs of lee side vortices fed by a separation shear layer are well known on delta wings and on inclined bodies of revolution (see, for example, the review by Peake in reference [14]). The flows are also similar to the slanted base flows studied by Morel [2, 3] and Hucho [6]. However, in the present cases, the vortices formed on top and bottom surfaces usually prevented any bubble-type separation on these surfaces. In the present case bubble-type separation only occurred at the base or locally near roughness or other shape changes. The flow transitions observed were associated with changes from fully attached flow to the lee vortex pair type. Such transitions to bubble separation were seen at about 30 deg (his 60 deg) on Morel's C_D and C_L results for his vehicle-like body (Figs. 17 and 18 of reference [2]). Because of the lower aspect ratio of the inclined surfaces and perhaps the more rounded side edges, the transition to vortex flow occurs gradually and the inflow produced by the closley spaced vortices prevents the quasi-axisymmetric (bubble) separation from occurring on the top or bottom surfaces.

Another conclusion which can be drawn from the curves is that lift depends almost entirely on angle of attack and on body mean camber (the shape of the line midway between upper and lower surfaces). The three bodies with a mean 10 deg upsweep have very similar lift curves while the body with the 20 deg upsweep has approximately twice as large a zero lift angle. It may be observed that the zero lift angle is essentially equal to the body mean line rear upsweep angle. This also nearly coincides with slender body theory and also with the rough approximation often used for 2-D airfoil sections whence the zero lift line is constructed between the mean line at midchord and at the trailing edge. It is not known if these results will hold for other camber line shapes.
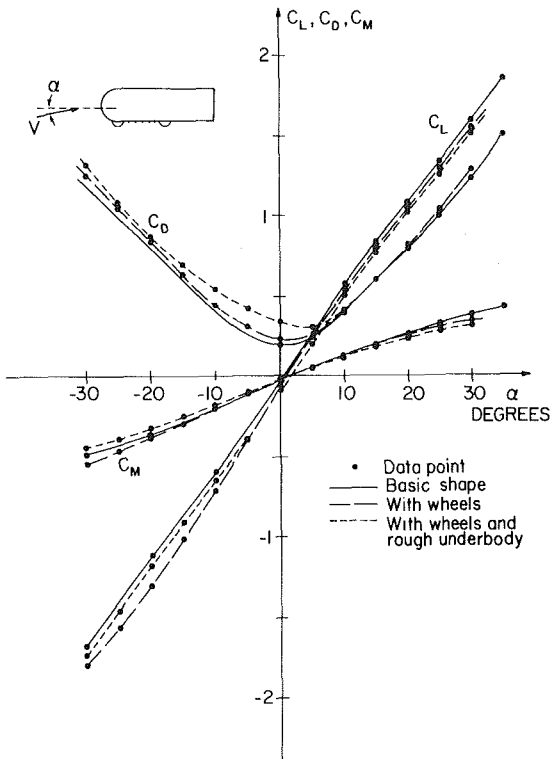
Fig. 6 Effects of "wheels" and rough underbody in free flow, untapered model

Fig. 7 Effects of "wheels" and rough underbody in free flow, tapered model.

From Fig. 3, the minimum drags of the bodies can be seen to be related primarily to the body taper or base area. Here the lowest drag coefficient of 0.12 is obtained, as would be expected [15] with the most tapered or boat-tailed body. The drag increases with base area but not in any simple way.

For this free flow case, it is clear that the minimum drag occurs at zero lift as would be expected from vortex or induced drag considerations without ground effect.

The effects of rough underbody and "wheels" can be seen in Figs. 6 and 7. The results show that these effects are most important at negative and near zero angle of attack. This is because they then affect the lee side vortex flow. On the other hand, at high positive angles of attack, the features are on the windward side and the effects on the lee side vortices are small. With wheels alone to leeward, the negative lift was stronger at angles past where vortex flow begins. The negative lift and drag correspond to that on the basic body at a slightly steeper angle of attack. Thus it appears from the force curves, and is confirmed by flow visualization, that the projecting wheels help trigger and stabilize the vortex formation in a similar manner to the strakes discussed by Peake [14]. However, if lateral forces are not desired, as they would not be on most road vehicles, it is clear that plain rounded edges should be used.

Flow Visualization. The flow patterns on and around the bodies were visualized by oil flow, smoke, and tufts. Figures 8 and 9 show surface flow lines obtained by using fluorescent green dye in light oil. Figure 8 shows the converging surface lines associated with the separating free shear layer which feeds the lee side vortices. This picture was taken of the bottom of a body which had top and bottom upswept at 10 deg and a pitch angle $\alpha = -10$ deg. For this angle, the vortex flow was well established. In Fig. 9, the windward side surface flow lines show the beneficial effects of the well rounded side edges.

Smoke was also injected into the flow for some flow conditions confirming the identification of lee side vortices by the oil and tuft studies. Short wool tufts were applied to the
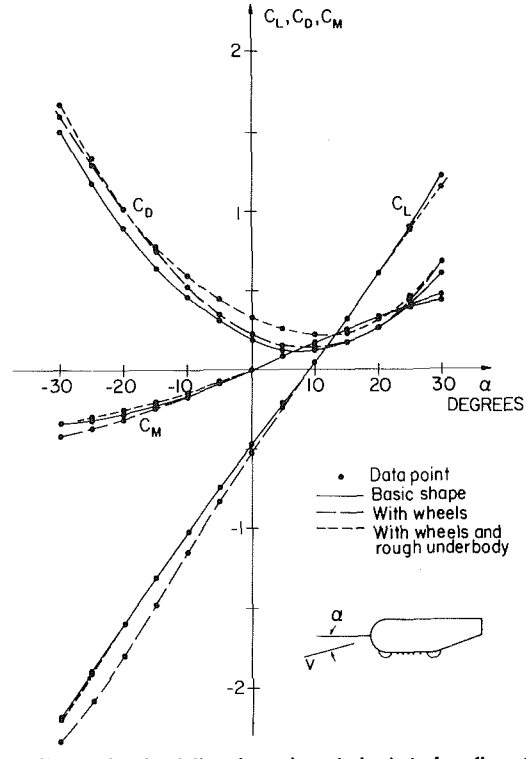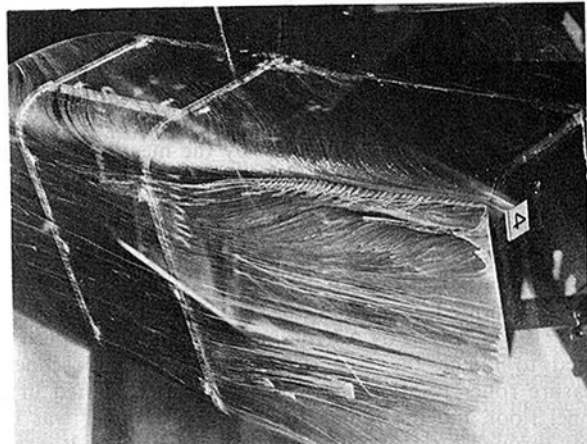

Fig. 8 Surface flow lines on bottom rear of body. Body with rear bottom and top upswept 10 deg and at $\alpha = -10$ deg. Thus surface is at -20 deg angle to free stream. Note separation line associated with leeward side vortex sheet origin (runs near line are due to gravity effect on accumulated dye-oil mixture).

model to visualize near surface flow and longer strands were used with conical paper ends to locate trailing vortices. The conical ends tend to keep the strands located in lower stagnation pressure regions and suppress whipping at the tuft ends.

Figures 10 through 12 show the progression of the vortex flow pattern with increasing inclination of the lee surfaces to the flow. The vortices first form at low angles of attack toward the rear of the body as shown in Fig. 10. As the angle of attack is increased, the vortices move forward and strengthen as seen in Fig. 11. They induce an inflow down to the body lee surface centerline which prevents the formation of the quasi-axisymmetric (or bubble) separation. It can be seen that even at extreme angles, as in Fig. 12 where a bubble type separation may form upstream on the body, the flow will be reattached further back by the strong vortices.

The next figure shows the effects of wheel-like projections and underbody roughness on the flow. Although, as men-
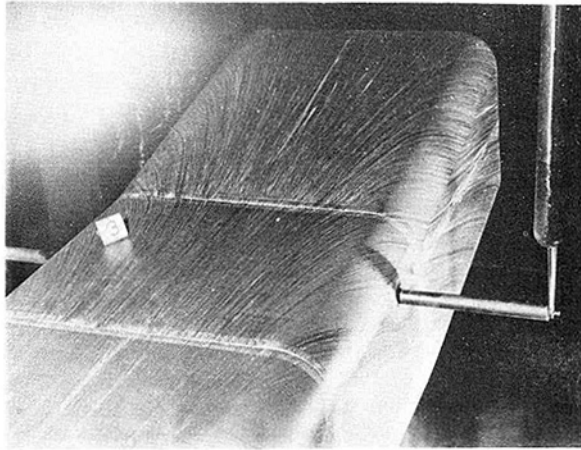
Fig. 9 Surface flow lines on top of body, conditions as Fig. 8, showing smooth flow around rounded edges on windward side
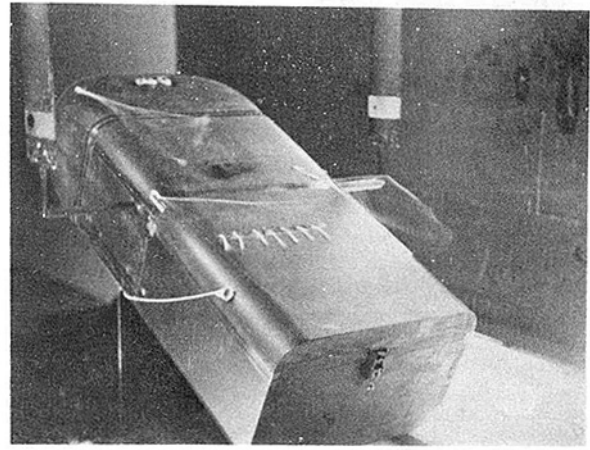

Fig. 11 Same as Fig. 10 except $\alpha = +25$ deg and vortices originate further forward
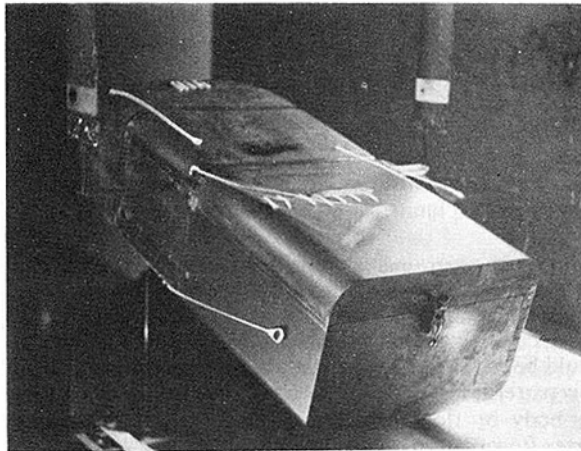

Fig. 10 Basic body at $\alpha = +15$ deg. Note that streamwise vortices have formed at rear but not near front.
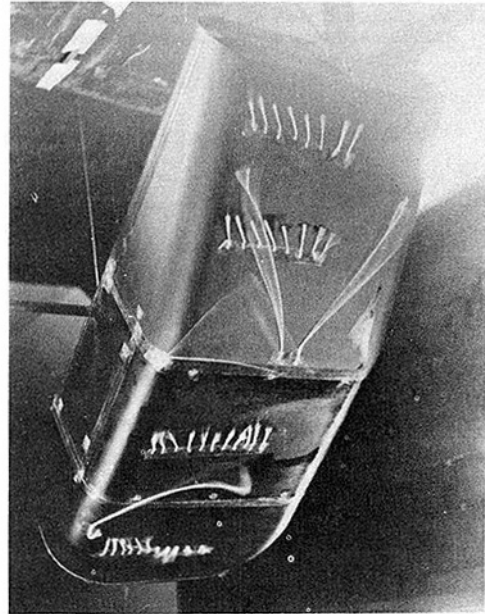

Fig. 12 Body with 20 deg upswept rear and α approximately 35 deg. Rear surface is approximately 55 deg to free stream but still unseparated. Bubble of separation near nose is reattached by vortex flow. Note outward flow on lee surface feeding vortex sheets.

tioned in the previous section, "wheels" trigger the vortices, the tuft studies showed that the flow structure remains basically unchanged [16]. In Fig. 13, roughness strips are added to the underbody and the flow still remains attached due to the vortices. In contrast, when the overall angle of attack was changed to +5 deg, the separation behind the roughness became somewhat *larger* due to the weaker lee side vortices [16].

The Effects of Proximity to Fixed and Moving Ground Planes. The problem of how vehicle flows are affected by ground proximity has been discussed for decades. Even the question of whether a moving ground plane is required seems to depend upon the particular tests as can be seen from the discussion on pages 120–123 of reference [1]. The present experiments include a number of tests adjacent to fixed and moving ground planes to investigate some of these effects.

In Fig. 14, the lift, drag, and pitching moment of a body with a 20 deg upswept rear underbody located near a fixed ground board are presented. At zero pitch angle, the clearance under the body was 71 mm which means that there was still a 29 mm clearance under the wheels when they were mounted. This clearance was used to allow variation in the pitch angle of the body with respect to the flow and ground plane. As can be seen from Fig. 14, the drag was quite large at α near zero degrees but decreased for higher angles of attack concurrent with the reduction in negative lift. Thus we see that near the ground, excess drag is still associated with nonzero lift as expected from trailing vortex energy concepts. This relation is also evident in the experiments of Morel [2, 3] where drag can also be correlated with lift. Of course, if a body is touching

the ground, lift need not be associated with trailing vortices and excess drag, but in practical situations it is found to be the case.

The flow visualizations for zero degrees angle of attack and a 20 deg upswept rear configuration showed that when wheels were added, any small separation was decreased slightly and the vortex flow was strengthened as was previously observed in the free flow cases [16]. This is reflected in the considerably greater negative lift of the body with wheels in Fig. 14. On the other hand, when underbody roughness was added, the rear underbody was nearly completely separated [16], and Fig. 14 shows a large reduction in negative lift and a large increase in drag. No definitive vortex structure was indicated by the streamers for this case, even in the wake [16].

This flow under the upswept rear underbody is somewhat analogous to a three-dimensional diffuser flow. The 20 deg angle was seen to be marginal for ordinary attached flow and the wheels help somewhat by triggering the vortex flow. On the other hand, the restriction and retardation of the flow by the rough bottom led to full stall.

As the angle of attack of the body was increased slightly, the diffuser angle was reduced and the flow began to reattach and drag was reduced [16]. In a situation where downforce
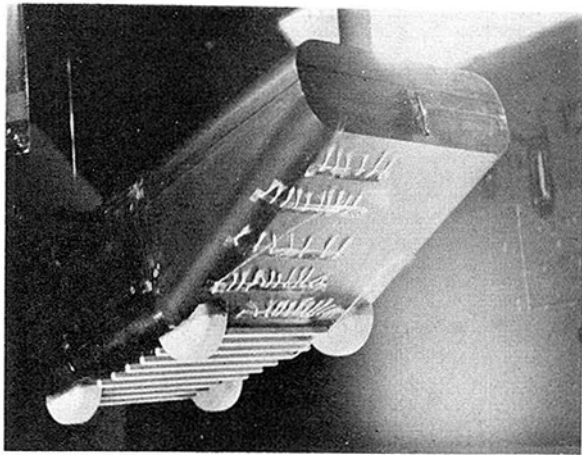
Fig. 13 Body with "wheels" and rough underbody and bottom upswept at 20 deg at $\alpha = -10$ deg. Photograph shows attached flow even close behind roughness due to flow towards surface from vortices.
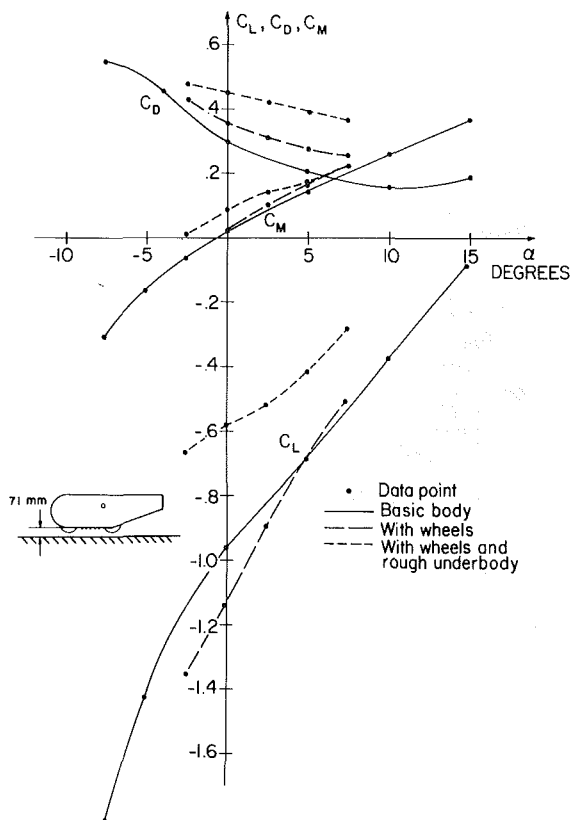

Fig. 14 Lift, drag, and pitching moment of various bodies near fixed ground board

Fig. 15 Lift, drag, and pitching moment of a body at various clearances from fixed and moving belt ground simulation

was desired, strakes might be used to trigger vortex flow as discussed by Peake in reference [14] for aircraft fuselages. (Vortex generators can also be used to maintain diffuser action as, for example, underneath the Lotus 79 Formula One racing car.)

The last full set of tests was performed with a model with wheels and rough underbody at several distances from both a running and stationary conveyer belt ground simulation. There are several reasons why flow around a body may be influenced by the speed of the ground. The first is that with a moving ground relatively more air will flow between the body and ground, changing both the body's circulation and the flow forces on the bottom surfaces of the model. The increased flow would be expected to increase drag and contribute toward negative lift. A second important effect can be the reduction or elimination of any separation which might
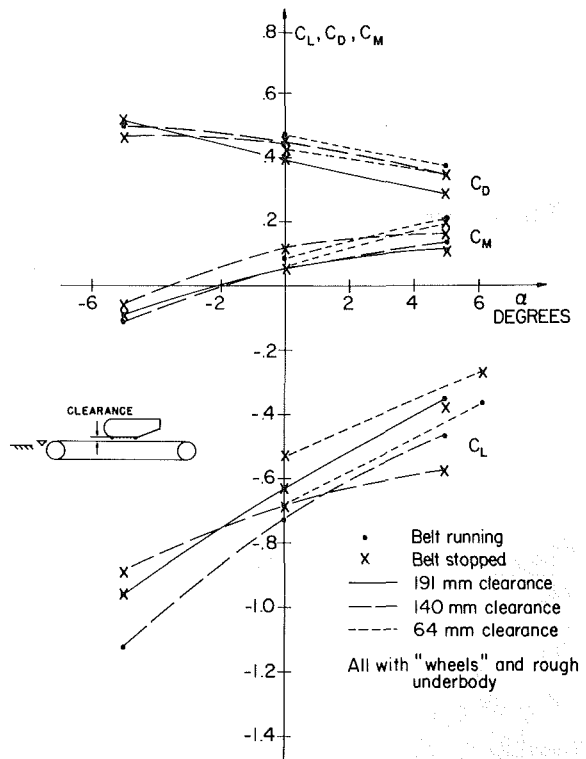
occur on a fixed ground plane. A third, secondary, effect would be felt if any of the primary effects changed the *type* of flow pattern. For example, a change in either flow underneath the body or floor separation could trigger or change the vortex flow pattern on leeward surfaces.

Figure 15 shows the results for the 20 deg upswept rear underbody model with wheels and rough bottom at various clearances from the ground belt. At 191 mm clearance (clearance to body length ratio $H/1 = 0.18$) no effect of belt motion is measured and the negative lift, drag, and pitching moment are all increased relative to the free flow results of Fig. 7. At 140 mm clearances ($h/1 = 0.13$), the effect of ground motion becomes significant, but its effect on lift reverses with change in angle of attack perhaps indicating a secondary effect of belt motion. At the smallest, most representative clearance of 64 mm ($h/1 = 0.05$), we see the expected result of increased negative lift and drag with a moving ground surface. At this clearance, little difference in the flow pattern between belt moving or stationary could be seen in the tuft studies [16].

Although a mechanical failure prevented further tests, one flow visualization photograph was obtained with the moving ground for the same model, but without the rough underbody. A small decrease in the area of separation was seen compared to similar conditions except with a fixed ground board [16]. The change in separation implies a significant change in forces and moments for this smooth underbody model as well.

Summary and Conclusions

1 A comprehensive series of lift, drag, and pitching moment measurements for a series of road-vehicle-related bluff bodies in free flow are presented. These should be of interest in testing analytical predictions for bluff body flows. Various changes in flow character were observed at different pitch angles. It would be desirable to obtain force data with a closer pitch angle resolution than the 5 deg used here to find out more about the details of the flow transitions.

2 From the flow visualizations it was seen that twin lee side vortices become important to the flow and forces at local angles of attack of the surface of about 15 deg, depending somewhat on taper. The transition to vortex flow appeared to be gradual with the rounded side edges used. The presence of wheel-like projections triggered the vortices at smaller angles. Further research on the effects of sharp edges and strakes on vortex flow on bodies is needed.

3 The vortex flow in these geometries reattaches or prevents bubble separation on the body except at the base. Thus this can be a desirable if one wishes to maintain a strong downforce.

4 A rough surface is detrimental to drag as is well known, but even separation behind a rough surface can be overcome by a strong vortex flow.

5 The effects of proximity to a moving and stationary ground are quite significant and similar to those of previous investigators' work with smooth underbodies [17]. However, the detrimental effects of a rough underbody are accentuated.

6 The need for a moving rather than a stationary ground becomes important for clearance to body lengths of less than about 0.1. The moving ground tends to increase drag and negative lift.

7 Away from the ground, minimum drag occurs at the pitch angle of zero lift as expected from trailing vortex energy concepts. Over the range of pitch angles studied in ground proximity, drag is also usually reduced when lift magnitude is reduced. This indicates that even with ground proximity lift is usually associated with vortex drag.

8 Future studies are needed to clarify the role of a moving ground for both rough and smooth bottomed vehicle shapes. Vehicles' bottoms with "skirts" as are used on many racing cars should also be investigated with stationary and moving ground. The use of rear body upsweep and strakes or "venturis" to give downforce or reduce net lift is also a promising area for further research.

Acknowledgment

References

1 Sovran, G., Morel, T., and Mason, W. T., Jr., ed., *Aerodynamic Drag Mechanisms of Bluff Bodies and Road Vehicles*, Plenum Press, New York, 1978.

2 Morel, T., "The Effect of Base Slant on the Flow Pattern and Drag of Three-Dimensional Bodies," in *Aerodynamic Drag Mechanisms*, Sovran, et al. (eds.), Plenum Press, New York, 1978, pp. 191-217.

3 Morel, T., "Aerodynamic Drag of Bluff Body Shapes Characteristic of Hatch-Back Cars," SAE Paper 780267, 1978.

4 Barth, R., "Effect of Unsymmetrical Wind Incidence on Aerodynamic Forces Acting on Vehicle Models and Similar Bodies," SAE Paper 650136 (948E), 1965 (also in *Automotive Aerodynamics*, SAE PT-78/16, 1978, pp. 11-35).

5 Carr, G. W., "The Aerodynamics of Basic Shapes for Road Vehicles, Part 1: Simple Rectangular Bodies," MIRA Report 1968/2, Motor Industry Research Association, England, 1967.

6 Hucho, W.-H., Janssen, L. J., and Emmelmann, H. J., "The Optimization of Body Details—A Method for Reducing the Aerodynamic Drag of Road Vehicles," SAE Paper 760185, 1976 (also in *Automotive Aerodynamics* SAE PT 78/16, 1978, pp. 191-208).

7 Woolard, H. W., "Slender-Body Aerodynamics for High-Speed Ground Vehicles," AIAA Paper 70-139, 1970.

8 Hucho, W.-H., and Emmelmann, H. J., "Theoretical Predictions of the Aerodynamic Derivatives of a Vehicle in Cross Wind Gusts," SAE Paper 730232, 1972 (also in *Automotive Aerodynamics* SAE PT-78/16, 1978, pp. 129-137).

9 Bearman, P. W., "Some Effects of Free-Stream Turbulence and the Presence of the Ground on the Flow Around Bluff Bodies," in *Aerodynamic Drag Mechanisms*, Sovran, et al. (eds.), Plenum Press, New York, 1978.

10 Pope, A., and Harper, J. J., *Low Speed Wind Tunnel Testing*, Wiley, New York, 1966, pp. 322-326.

11 Gross, D. S., and Sekscienski, W. S., "Some Problems Concerning Wind Tunnel Testing of Automotive Vehicles," SAE Paper 660385, 1966 (also in *Automotive Aerodynamics*, SAE PT 78/16, 1978, pp. 37-51.

12 Bettes, W. H., and Kelly, K. B., "The Influence of Wind Tunnel Solid Boundaries on Automotive Test Data," SAE Paper 741031, 1974 (also in *Automotive Aerodynamics*, SAE PT-78/16, 1978, pp. 167-180).

13 Hoerner, S. F., *Fluid-Dynamic Drag*, Hoerner Fluid Dynamics, Brick Town, N.J., 1965, Chapter III.

14 Peake, D. J., "Controlled and Uncontrolled Flow Separation in Three Dimensions," Report NRC No. 15471, ISSN 0077-5541 (Aeronautical Report LR-591), National Research Council Canada, Ottawa, 1976.

15 Mair, W. A., "Drag Reducing Techniques for Axi-Symmetric Bluff Bodies," in *Aerodynamic Drag Mechanisms*, Sovran, et al. (eds.), Plenum Press, New York, 1978, pp. 161-179.

16 George, A. R., "Aerodynamics of Simple Bluff Bodies Including Effects of Body Shape, Ground Proximity, and Pitch," in *Aerodynamics of Transportation*, T. Morel and C. Dalton (eds.), pp. 71-81, ASME, New York, 1979.

17 Stollery, J. L., and Burns, W. K., "Forces on Bodies in the Presence of the Ground," in *Proceedings of the First Symposium on Road Vehicle Aerodynamics*, The City University, London, 1970, pp. 1-1-1-26.

2 From the flow visualizations it was seen that twin lee side vortices become important to the flow and forces at local angles of attack of the surface of about 15 deg, depending somewhat on taper. The transition to vortex flow appeared to be gradual with the rounded side edges used. The presence of wheel-like projections triggered the vortices at smaller angles. Further research on the effects of sharp edges and strakes on vortex flow on bodies is needed.

3 The vortex flow in these geometries reattaches or prevents bubble separation on the body except at the base. Thus this can be a desirable if one wishes to maintain a strong downforce.

4 A rough surface is detrimental to drag as is well known, but even separation behind a rough surface can be overcome by a strong vortex flow.

5 The effects of proximity to a moving and stationary ground are quite significant and similar to those of previous investigators' work with smooth underbodies [17]. However, the detrimental effects of a rough underbody are accentuated.

6 The need for a moving rather than a stationary ground becomes important for clearance to body lengths of less than about 0.1. The moving ground tends to increase drag and negative lift.

7 Away from the ground, minimum drag occurs at the pitch angle of zero lift as expected from trailing vortex energy concepts. Over the range of pitch angles studied in ground proximity, drag is also usually reduced when lift magnitude is reduced. This indicates that even with ground proximity lift is usually associated with vortex drag.

8 Future studies are needed to clarify the role of a moving ground for both rough and smooth bottomed vehicle shapes. Vehicles' bottoms with "skirts" as are used on many racing cars should also be investigated with stationary and moving ground. The use of rear body upsweep and strakes or "venturis" to give downforce or reduce net lift is also a promising area for further research.

Acknowledgment

References

1 Sovran, G., Morel, T., and Mason, W. T., Jr., ed., *Aerodynamic Drag Mechanisms of Bluff Bodies and Road Vehicles*, Plenum Press, New York, 1978.

2 Morel, T., "The Effect of Base Slant on the Flow Pattern and Drag of Three-Dimensional Bodies," in *Aerodynamic Drag Mechanisms*, Sovran, et al. (eds.), Plenum Press, New York, 1978, pp. 191–217.

3 Morel, T., "Aerodynamic Drag of Bluff Body Shapes Characteristic of Hatch-Back Cars," SAE Paper 780267, 1978.

4 Barth, R., "Effect of Unsymmetrical Wind Incidence on Aerodynamic Forces Acting on Vehicle Models and Similar Bodies," SAE Paper 650136 (948E), 1965 (also in *Automotive Aerodynamics*, SAE PT-78/16, 1978, pp. 11–35).

5 Carr, G. W., "The Aerodynamics of Basic Shapes for Road Vehicles, Part 1: Simple Rectangular Bodies," MIRA Report 1968/2, Motor Industry Research Association, England, 1967.

6 Hucho, W.-H., Janssen, L. J., and Emmelmann, H. J., "The Optimization of Body Details—A Method for Reducing the Aerodynamic Drag of Road Vehicles," SAE Paper 760185, 1976 (also in *Automotive Aerodynamics* SAE PT 78/16, 1978, pp. 191–208).

7 Woolard, H. W., "Slender-Body Aerodynamics for High-Speed Ground Vehicles," AIAA Paper 70-139, 1970.

8 Hucho, W.-H., and Emmelmann, H. J., "Theoretical Predictions of the Aerodynamic Derivatives of a Vehicle in Cross Wind Gusts," SAE Paper

730232, 1972 (also in *Automotive Aerodynamics* SAE PT-78/16, 1978, pp. 129–137).

9 Bearman, P. W., "Some Effects of Free-Stream Turbulence and the Presence of the Ground on the Flow Around Bluff Bodies," in *Aerodynamic Drag Mechanisms*, Sovran, et al. (eds.), Plenum Press, New York, 1978.

10 Pope, A., and Harper, J. J., *Low Speed Wind Tunnel Testing*, Wiley, New York, 1966, pp. 322–326.

11 Gross, D. S., and Sekscienski, W. S., "Some Problems Concerning Wind Tunnel Testing of Automotive Vehicles," SAE Paper 660385, 1966 (also in *Automotive Aerodynamics*, SAE PT 78/16, 1978, pp. 37–51.

12 Bettes, W. H., and Kelly, K. B., "The Influence of Wind Tunnel Solid Boundaries on Automotive Test Data," SAE Paper 741031, 1974 (also in *Automotive Aerodynamics*, SAE PT-78/16, 1978, pp. 167–180).

13 Hoerner, S. F., *Fluid-Dynamic Drag*, Hoerner Fluid Dynamics, Brick Town, N.J., 1965, Chapter III.

14 Peake, D. J., "Controlled and Uncontrolled Flow Separation in Three Dimensions," Report NRC No. 15471, ISSN 0077–5541 (Aeronautical Report LR-591), National Research Council Canada, Ottawa, 1976.

15 Mair, W. A., "Drag Reducing Techniques for Axi-Symmetric Bluff Bodies," in *Aerodynamic Drag Mechanisms*, Sovran, et al. (eds.), Plenum Press, New York, 1978, pp. 161–179.

16 George, A. R., "Aerodynamics of Simple Bluff Bodies Including Effects of Body Shape, Ground Proximity, and Pitch," in *Aerodynamics of Transportation*, T. Morel and C. Dalton (eds.), pp. 71–81, ASME, New York, 1979.

17 Stollery, J. L., and Burns, W. K., "Forces on Bodies in the Presence of the Ground," in *Proceedings of the First Symposium on Road Vehicle Aerodynamics*, The City University, London, 1970, pp. 1-1–1-26.

DISCUSSION

K. Koenig[1]

Professor George presents a thorough set of measurements of the aerodynamic characteristics of some simple three-dimensional cambered bodies with proportions appropriate to ground vehicles. The shapes chosen have not previously been examined. The effects of several problem areas relevant to ground vehicles – attitude, underbody details, ground clearance and moving ground plane – are also explored. Although the automotive industry is the principal beneficiary of this work, the data should also be useful to the aerospace industry; many transport aircraft, for example, are characterized by fairly small fineness ratios and highly up-swept afterbodies much like the geometries in the present study.

Several aspects of the force measurements deserve comment. There are interesting similarities between the free field behavior (Fig. 3 and 4) and the characteristics of simple planform, thin wings. Of particular importance is the observation that minimum drag occurs very near the zero-lift angle of attack. A similar trend is indicated by Fig. 14 for bodies in ground proximity. Figure 3 also shows a definite correlation between lift and drag for a given body at varying angles of attack. However, and this point is sometimes not fully appreciated (see the discussion following reference [2] of this paper), there is *not* a correlation between lift and drag between different bodies; for example in Fig. 3 at +15° three bodies have identical lift coefficients but quite different drag coefficients. Another feature of these results which should be noted is the low drag, $C_D = 0.12$, observed for the boat-tailed body in a free field and the surprisingly small increase, $\Delta C_D = 0.04$, which occurs as the body approaches the ground. Although he has made no obvious attempt to optimize the body, Professor George has obtained a reasonably practical shape which approximates the minimum drag currently thought possible of ground vehicles. (To understand the significance of this, see the General Discussion of reference [1]). However, the drag is seriously degraded by the addition of underbody protrusions. With regard to items like underbody details, the data presented in this paper for wheels,

[1] Assistant Professor, Department of Aerospace Engineering, Mississippi State University, Mississippi State, Miss. 39762.

roughness, ground proximity and moving ground plane are somewhat limited as far as contributing to the overall data base for this class of bodies. Nevertheless, the results (Figs. 14 and 15) clearly show that these variables have strong influences on the aerodynamic characteristics and that designers and researchers should be cautioned to carefully account for them and make extrapolations only with the utmost care.

Professor George relates certain changes in the measured aerodynamic characteristics to changes in the observed flow fields. There are three types of flow associated with bodies having slanted afterbodies: fully attached, lee vortex pair and bubble flows. As the body attitude or afterbody slant angle changes transitions can occur between these types of flow, often accompanied by large changes in lift and drag. In this paper the transitions observed are primarily between the fully attached and vortex flows. Comparison is made to Morel's work (reference [2]) which, however, is chiefly concerned with transitions between vortex and bubble-type flows. In particular, reference is made to Fig. 17 of Morel's paper where a bubble to vortex transition occurs at 60° and a vortex to fully attached transition occurs in the vicinity of 82°. According to Dr. Morel (from a private communication), the small rise in drag coefficient at 30° on Fig. 17 in his paper does not correspond to any observed change in the flow field and is not yet fully explained.

B. H. Little, Jr.[2]

This reviewer is concerned that, while the intent of the research was to provide data useful in ground vehicle design, most of the data are for situations unlikely to be encountered by ground vehicles. Considerable emphasis is placed, for instance, on free air data; and all of the parametric variations of body taper, camber, and shape were performed in free air. It is not obvious that the effects of changing body camber, for

[2] Propulsion and Acoustics, Lockheed – Georgia, Co., Marietta, GA 30063

instance, in the proximity of the ground will be the same as in free air. The effects of ground proximity are reported for only one configuration.

This is generally the only criticism of this work – that it misses the intended target objective (as stated on page). From that general criticism, however, several smaller objections can be made. In the abstract it is stated that, "The effects of a rough underbody are generally detrimental although less so if the rough surface is on the windward side." The free air data do, in fact, show this to be the case, but the importance of this observation is obscure. Then, the free air data cover a range of incidence angles from −30 to +30 deg - a rather unlikely range for practical application. There is too much data for conditions whose relevance is questionable and too little which sheds new light on ground vehicle design problems.

Otherwise however, it is believed that the author has been accurate and scholarly in his observations and interpretations of the test results.

Author's Closure

I would like to thank Professor Koenig for his interesting discussion of my paper. As he points out drag changes are correlated with lift for a given body but drag level is also dependent on a particular body's shape (notably its base area and roughness). I agree with Mr. Little that the paper does not supply much data applicable to conditions close to those of present day ground vehicles. It is unfortunate that equipment breakdowns precluded wider parameter variations near the moving belt ground plane.

However the paper is primarily intended to contribute toward the understanding of bluff body flow regimes under a wide range of conditions. The data presented and the understanding of vortex flow and roughness and protusion effects should be useful in the development and testing of analytical and computational methods as well as helping toward better aerodynamic design of future vehicles.

W. L. Chow
Professor of Mechanical Engineering.
Mem. ASME

P. C. T. Chan
Graduate Research Assistant.

Department of Mechanical and
Industrial Engineering,
University of Illinois at Urbana-Champaign,
Urbana, Ill.   61801

The Effect of Gravity on Certain Curved Channel Potential Flows

It is shown that the method of hodograph transformation coupled with numerical calculations can be an effective method to account for the effect of gravity on certain two-dimensional potential flow problems. Specifically, the problem of a horizontal channel flow discharging an incompressible fluid through a circular-arc contraction has been worked out to illustrate the procedure. The upstream approaching flow conditions, the opening height, and also the downstream free surface flow must be compatible with each other. They must be determined through iterations. The method of iteration is also presented and discussed.

Introduction

The assessment of the effect of gravity on potential flow problems with free surfaces always offers considerable difficulties. Under these situations, the configuration of the free surface is not only unknown a priori, the free streamline is also no longer a surface of constant velocity as a result of its change in elevation. In the incompressible flow regime where the governing Laplace equation is linear, problems within this category have not been widely studied due to their extremely complicated nature. Early studies of flow with gravitation have been carried out by Marchi [1], Melkonan [2], and Gurevich [3] through approximations and conformal mapping, and by Keller and Weitz [4], Clarke [5], and Keller and Geer [6] through asymptotic expansions for problems of small gravity. More recent work by Larock on flows with planar sluice gates [7] and radial gates [8] relied upon the Riemann-Hilbert solution to a mixed boundary-value problem. As a result of the gravitational influence, an iterative procedure of calculation must be followed. Finite difference relaxational calculations on this type of problem were performed by Southwell and Vaisey [9]. However, direct calculation in the physical plane may require extensive use of nonuniform grid around regions with large curvatures. Instabilities also may occur and long computational times may be required [10]. Chan, Larock, and Herrmann [11, 12] and recently Varoglu and Finn [13] demonstrated that the finite element method could be more flexible than direct finite difference treatment in dealing with arbitrary solid boundaries. In the study of hodograph transformation, it was recently found [14–17] that numerical calculations in the hodograph plane could be an effective method in dealing with problems of channel flow dominated by gravity. However, these problems were restricted exclusively to solid walls of straight line configuration. The present investigation is an extension of these studies to channels of curved solid boundaries. It will become evident that problems with prescribed curved solid walls offer additional complications when treated through hodograph transformation.
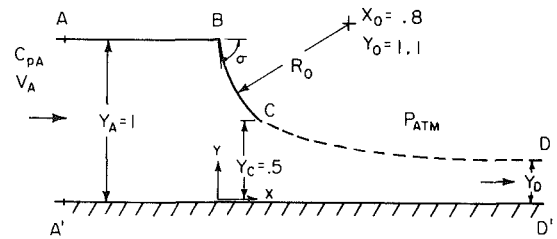
Fig. 1   Incompressible fluid discharge through a curved contraction

Theoretical Considerations

As shown in Fig. 1, an initial uniform horizontal flow of an incompressible fluid with a hydrostatic pressure distribution (denoted by state AA') approaches a curved contraction and discharges into the open atmosphere. The channel has a horizontal bed so that the flow eventually settles into a state of uniform flow with a hydrostatic pressure distribution at far downstream positions (denoted by DD'). For convenience, all flow quantities can be normalized by the corresponding upstream flow quantities V_A, y_A and the characteristic angle σ of the curved contraction as indicated at point B in Fig. 1. From Bernoulli's principle, the expression

$$C_p + V^2 + [2/(\mathrm{Fr}_A^2)]y = C_{pA} + 1 + [2/(\mathrm{Fr}_A^2)] \qquad (1)$$

holds throughout the regions where C_{pA} is the pressure coefficient defined by

$$C_{pA} = [p_A - p_{\mathrm{atm}}]/[(\rho V_A^2)/2] \qquad (2)$$

p_A being the absolute pressure at point A of the upstream approaching flow and Fr_A is defined by

$$\mathrm{Fr}_A = V_A/(g\ y_A)^{1/2} \qquad (3)$$

Specifically, for all points along the free surface boundary, the velocity is related to elevation through

$$V_f = [1 + C_{pA} + (2/\mathrm{Fr}_A^2)(1 - y_f)]^{1/2} \qquad (4a)$$

In particular, the velocity of point C with a lip opening y_c is given by

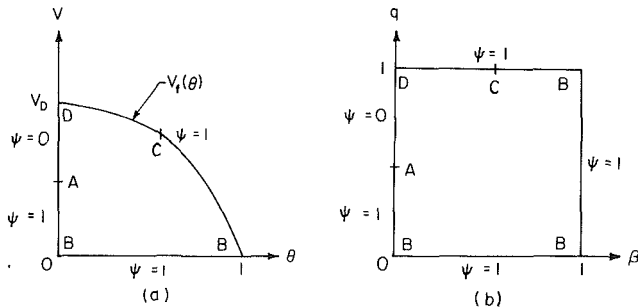$$V_c = [1 + C_{pA} + (2/\mathrm{Fr}_A^2)(1 - y_c)]^{1/2} \qquad (4b)$$

Fig. 2 The hodograph

For given Fr_A and C_{pA} values, the far downstream uniform velocity V_D satisfies the expression

$$V_D^3 - [1 + C_{pA} + (2/\mathrm{Fr}_A^2)]V_D + [2/\mathrm{Fr}_A^2] = 0 \qquad (5)$$

It is understood that values of C_{pA} should be restricted within the range where physically realistic solutions may be found from equation (5). Obviously, one would also have from the continuity principle,

$$y_D = 1/V_D \qquad (6)$$

It should be recognized that the flow conditions both at the upstream and downstream positions and the lip opening must be compatible to yield a sensible solution.

The governing equation of the stream function in the hodograph variables V, is given by [18]

$$V^2 \psi_{VV} + V \psi_V + \psi_{\theta\theta}/\sigma^2 = 0 \qquad (7)$$

(here subscripts indicate partial differentiation) where all quantities have been normalized. The dimensionless coordinates in the physical plane are also given by

$$dx = -[(\cos \sigma\theta/\sigma\, V^2)\psi_\theta + (\sin \sigma\theta/V)\psi_V] \cdot$$
$$dV - [(\sin \sigma\theta/V)\psi_\theta - \sigma(\cos \sigma\theta/V)\psi_V]d\theta \qquad (8a)$$
$$dy = -[(\sin \sigma\theta/\sigma V^2)\psi_\theta - (\cos \sigma\theta/V)\psi_V] \cdot$$
$$dV + [(\cos \sigma\theta/V)\psi_\theta + \sigma(\sin \sigma\theta)\psi_V]d\theta \qquad (8b)$$

The corresponding hodograph of the present problem is shown in Fig. 2(a). With the given geometrical configuration and selected upstream flow conditions, points C and D in Fig. 2(a) can be determined according to equations (4b) and (5) although the function $V_f(\theta)$ along the curved contraction BC and the free surface CD is yet unknown.

One now introduces a transformation according to

$$q = V/V_f(\theta), \quad \beta = \theta \qquad (9)$$

so that the hodograph assumes the shape of a square as shown in Fig. 2(b). Equations (7) and (8) become

$$q^2[1 + (V_f'/\sigma V_f)^2]\psi_{qq} + q[1 + (1/\sigma^2)[2(V_f'/V_f)^2$$
$$- (V_f''/V_f)]]\psi_q - 1/\sigma^2[2q(V_f'/V_f)\psi_{\beta q} - \psi_{\beta\beta}] = 0 \qquad (10)$$
$$dx = [1/q\, V_f][A\psi_q + B\psi_\beta]dq + [C\psi_q + D\psi_\beta]d\beta \qquad (11a)$$

$$dy = [1/q\, V_f][E\psi_q + F\psi_\beta]dq + [G\psi_q + L\psi_\beta]d\beta \qquad (11b)$$

with

$A = (V_f'/\sigma V_f)\cos(\sigma\beta) - \sin(\sigma\beta)$

$B = [\cos(\sigma\beta)]/\sigma q$

$C = [1/V_f][(1/\sigma)(V_f'/V_f)^2\cos(\sigma\beta) + \sigma\,\cos(\sigma\beta)]$

$D = [1/(q\, V_f)][(1/\sigma)(V_f'/V_f)\cos(\sigma\beta) + \sin(\sigma\beta)]$

$E = (V_f'/\sigma V_f)\sin(\sigma\beta) + \cos(\sigma\beta)$

$F = -[\sin(\sigma\beta)]/\sigma q$

$G = [1/V_f][(1/\sigma)(V_f'/V_f)^2\sin(\sigma\beta) + \sigma\,\sin(\sigma\beta)]$

$L = -[1/(q\, V_f)][(1/\sigma)(V_f'/V_f)\sin(\sigma\beta) - \cos(\sigma\beta)]$

where $V_f'(\theta)$ and $V_f''(\theta)$ are the first and second derivatives of the function $V_f(\theta)$.

It is now evident that the stream function is completely specified on the boundary of the transformed hodograph (Fig. 2(b)) and its value within the hodograph can be determined through relaxational calculations provided that the $V_f(\theta)$ and its derivatives are known along the curved contraction BC and the free surface CD. In addition, for the given geometry and the selected upstream Froude number Fr_A, there is only one pressure coefficient C_{pA} compatible with this set of conditions. These facts suggest that $V_f(\theta)$ and C_{pA} must be determined through iterations. A convergent iteration scheme must be developed if this method of treatment is to be successful. It is also worthwhile to remark that if the contraction BC assumes a straightline configuration, point C would be located vertically above point B in Fig. 2(a) and the velocity distribution between them is not a matter of concern. This information can easily be produced once the stream function is completely determined within the hodograph.

Method of Calculations and Results

For the circular arc-shaped contraction shown in Fig. 1, the surface slope is

$$dy/dx = \tan \sigma\beta = -[(x_w - x_0)/(y_w - y_0)] \qquad (12)$$

and the values of σ and θ_C can be determined for the completely specified geometry.[1] Upon selecting a Froude number Fr_A and a pressure coefficient C_{pA}, the velocities V_C and V_D may be determined from equations (4b) and (5). The $V_f(\theta)$ in the hodograph is initially approximated by two simple polynomials joining at the known point C. Their derivatives can be determined accordingly.

The stream function satisfying equation (10) may now be determined through a successive-over-relaxation (SOR) scheme in the $q - \beta$ plane. Once its value is stabilized within an arbitrarily selected small margin (e.g., 10^{-5}) at each grid point, the derivatives ψ_β, ψ_q may be computed for all points

---

[1] $x_B = 0$, $y_B = 1$, $\sigma = -1.446$, $x_C = 0.2614$, $y_C = 0.5$, $\beta_C = 0.5056$ for the present problem.

——— Nomenclature ———

A,B,C,D = points in hodograph and physical plane or the functions defined in text
C_p = pressure coefficient
E,F,G,L = functions defined in text
Fr = Froude number
g = gravitational acceleration
p = pressure
q = dimensionless velocity
V = velocity
$V_f(\theta)$ = velocity function along free streamline
x,y = coordinates

x_w, y_w, x_0, y_0 = coordinates of circular arc and its center
ρ = density
ψ = stream function
$\psi_V, \psi_\theta, \psi_q, \psi_\beta$ = $(\partial\psi/\partial V)$, $(\partial\psi/\partial\theta)$, $(\partial\psi/\partial q)$, $(\partial\psi/\partial\beta)$
σ = wall angle at point B
β = dimensionless angle
θ = streamline angle

Subscripts
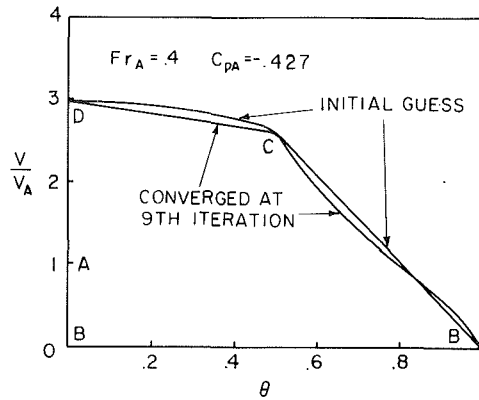
A,C,D = points A,C,D in hodograph or physical plane

Fig. 3 Initial and converged values of V_f (θ)

including those along the boundary where a one-sided finite difference form must be employed. Numerical integration of equation (8b) would lead to a revised function $V_f(\theta)$. Specifically, along the curved contraction BC in the hodograph, it is obvious that $dq = 0$ and $\psi_\beta = 0$, and equation (8b) yields

$$[d(\ln V_f)]/d\beta = - [(\sigma/\sin \sigma\beta)[(V_f/\psi_q)(dy/d\beta)$$
$$- \sigma \sin \sigma\beta]]^{1/2} \qquad (13)$$

Since β and $dy/d\beta$ are completely known for the curved contraction,[2] equation (13) may be numerically integrated from point B to point C by evaluating its right-hand side with the original $V_f(\theta)$. A new function $V_f(\theta)$ and its first derivatives $V_f'(\theta)$ are obtained. For the free surface CD, again $dq = 0$ and $\psi_\beta = 0$, numerical integration of equation (8) would yield its profile, x_f and y_f, in the physical plane and the revised $V_f(\theta)$ function may be directly computed from equation (4a). The first and second derivative of this part of the new $V_f(\theta)$ can only be obtained from numerical differentiation.

With revised values of V_f, V_f', and V_f'', the stream function must be calculated again from equation (10) through the SOR scheme. These iteration procedures must be repeated until the V_f function employed to determine the stream function agrees with V_f produced from the foregoing streamline tracing process within a small margin (e.g., 10^{-4}) at each grid point along the curved boundary and the free surface.

The example to show this convergence is given in Fig. 3. It is perhaps pertinent to remark that although fixed locations of points B, C, and D in the hodograph plane would only allow limited $V_f(\theta)$ variations, the development of a convergent scheme of iterations was the principle effort of attention. It has been learned from experience that the suggested scheme of iteration leads to rapidly convergent results while other different procedures may lead to divergence through iterations.

Thus far, the value of C_{pA} for the selected Fr_A is completely arbitrary and the tracing of free streamline CD in general would not produce y_D given by equation (6). Again, the correct value of C_{pA} would yield the set of values of V_D, y_D from equations (5) and (6) and also reproduce y_D from streamline tracing. A relationship to correct C_{pA} given by

$$C_{pA\,new} = [1 + C_{pA\,old} + (2/Fr_A^2)][y_{D\,old}/y_D] - [1 + (1/Fr_A^2)](14)$$

is found to be satisfactory where y_D is the value obtained from equation (6) while $y_{D\,old}$ is the asymptotic height obtained from streamline tracing. Although expressions different from equation (14) may also serve the purpose of obtaining the correct pressure coefficient C_{pA}, equation (14) is established from the fact that when y_D is correctly reproduced in the streamline tracing, the correction to C_{pA} should vanish,

---

[2]For the present circular contraction, $dy/d\beta = -\sigma\tan(\sigma\beta)(y - y_0)$.
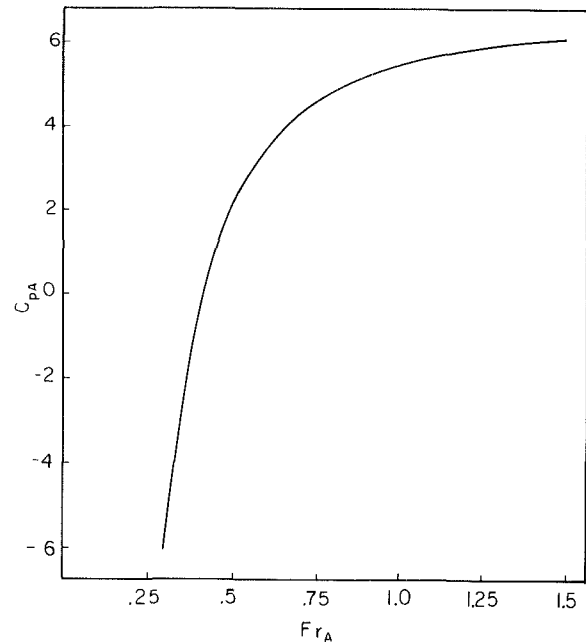

Fig. 4 Established upstream pressure coefficient with the Froude number Fr_A for the selected circular contraction
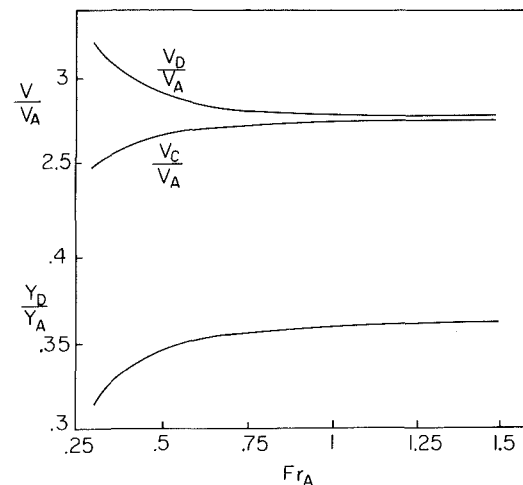

Fig. 5 Velocity and height ratios associated with the circular contraction

and the experience that a larger than correct y_D value obtained from streamline tracing needs a higher C_{pA} value to reduce this difference. Upon following such a correcting scheme, three to five corrections are usually needed to bring agreement in y_D within a margin of 10^{-4}. It is thus also a rapidly convergent process. It should be noted that calculation of the stream function ψ and V_f should also be repeated for every C_{pA} correction.

Figures 4 and 5 show the final established results of C_{pA}, V_C, and V_D for the present circular-arc contraction. It is interesting to observe that at large Fr_A values which reflect small gravitational influence, V_C and V_D approach each other as they should. Figure 6 shows the established free jet profile including the computed curved boundary for a specific case which agrees with the prescribed profile always within a margin of 2×10^{-2}. Figure 7 shows the profiles of the streamlines in both the hodograph and physical planes. Distribution of lines of constant pressure and velocity are also shown in Fig. 8. A momentum balance is employed to check the overall accuracy of calculations. The total horizontal force as a result of momentum balance on the curved con-
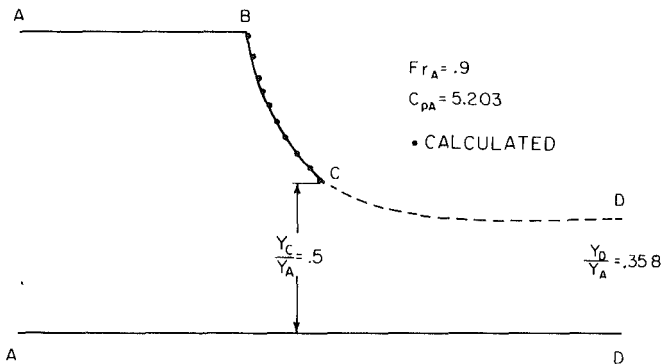
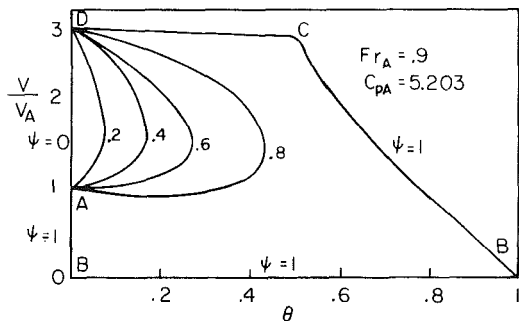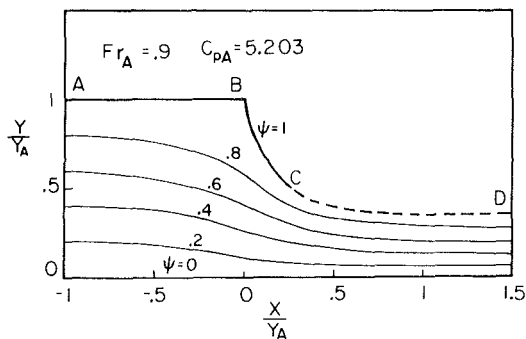**Fig. 6   The free streamline and the reproduced curved contraction**

Fig. 8(a)   Constant velocity lines

Fig. 8(b)   Constant pressure lines

Fig. 7   Streamlines in the physical and hodograph planes

Fig. 9   Check from momentum balance

traction is plotted in Fig. 9 and the integrated pressure force checks well with these results. Although the error may amount to 5 percent at $Fr_A \cong 0.5$ even when the absolute difference between them is not very large, a refined mesh for stream function calculations reduces the percentage error immediately to acceptable levels.

With a 21 × 21 grid and a relaxation factor of 1.8, a typical set of calculations takes 25 s on the CDC Cyber 175 computing system.

Discussion and Conclusions

The hodograph transformation is an interesting mathematical method in compressible fluid flow in that it changes the nonlinear problem in the physical plane into an equivalent problem in the hodograph plane. Although the linearity is a highly desirable feature, this method has not been fully exploited for engineering purposes since the physical configuration corresponding to an indirect solution in the hodograph plane usually has no practical interest. With the advent of high speed computers, the usefulness of hodograph transformation should be reexamined. The present application of this method to flow with gravitation adequately illustrates how this method can be applied to good advantage. It is true that this method invariably involves the
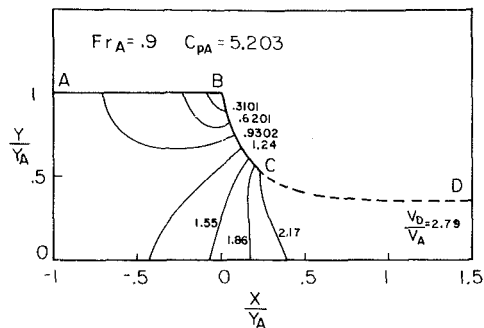
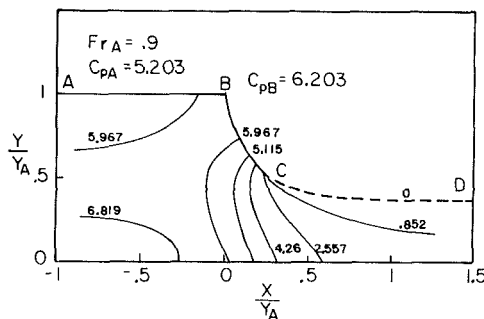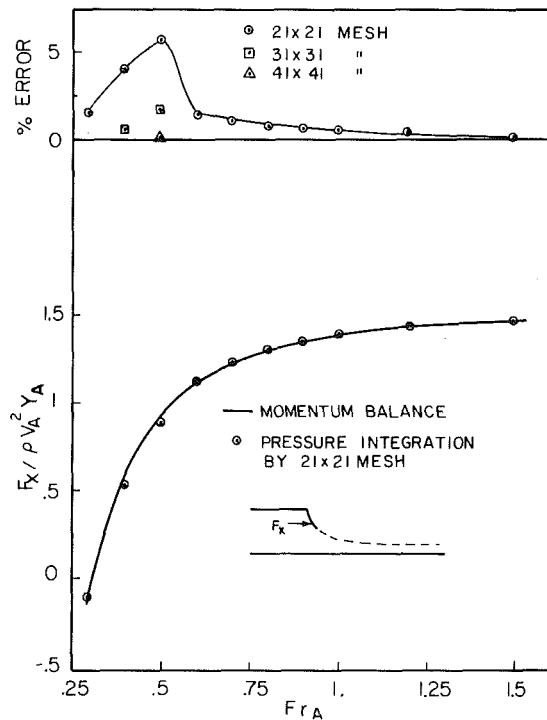determination of the boundary functions such as $V_f(\theta)$ of the hodograph. Along with the determination of the stream function of the problem, their strong mutual influence can only be handled through iterations. Fortunately, with reasonable initial estimation of these boundary functions, almost all these iteration processes [19] are rapidly convergent. It is also worthwhile to note that upon transforming the hodograph into rectangles to facilitate numerical calculations, derivatives up to second order of V_f appear in the governing equation and are directly involved in determination of the stream function. Invariably these derivatives are produced from numerical differentiations. Although the

exact solution of these boundary functions should yield agreement of derivatives up to any order during iterations, it is reasonable to define the convergence of iterations by imposing only the agreement of the boundary function itself since numerical differentiation is not an accurate process. For all problems studied so far [19], the unknown boundary functions vary monotonously in the hodograph plane and thus the secondary derivatives are always small. Even under this condition, imposing the agreement of the derivatives of these functions as a convergence criterion for iteration is not advised.

From the evidence produced so far, it may be concluded that the hodograph transformation coupled with numerical calculation is indeed an effective means to deal with certain inviscid flow problems strongly influenced by gravitation.

Acknowledgment

References

1 Marchi, E., "Sue fenomenidi efflusso piano da luci a bottente," *Ann. Mat. Pura ed Appl.*, Vol. 35, 1953, pp. 321–341.

2 Melkonan, G. I., "Reshenie Zadachi Struinogo Obtekaniia Ploskogo Zatvora S. Uchetom Sily Tiaszhesti po Metody Istochnikov I Stokov," *Izv. Akad. Nauk Armenian SSR, Ser. Phys.-Mat. Nauk*, Vol. 10, No. 3, 1957.

3 Gurevich, M. I., and Pykhteev, G. N., "Approximate Solution of the Problems of Flow of a Heavy Ideal Incompressible Fluid from under a Sluice Gate," *PMTF (Akad, Nauk)*, Vol. 2, 1960, pp. 3–14.

4 Keller, J. B., and Weitz, M. L., "A Theory of Thin Jets," *Proceedings, 9th International Congress Applied Mechanics*, Brussels, Vol. 1, 1957, pp. 316–323.

5 Clarke, N. S., "On Two-Dimensional Inviscid Flow in a Waterfall," *Journal of Fluid Mechanics*, Vol. 22, Part 2, 1965, pp. 359–369.

6 Keller, J. B., and Geer, J., "Flows of Thin Streams with Free Boundaries," *Journal of Fluid Mechanics*, Vol. 59, Part 3, 1973, pp. 417–432.

7 Larock, B. E., "Gravity Affected Flow from Planar Sluice Gates," *Journal of the Hydraulic Division*, ASCE, Vol. 95, No. HY4, 1969, pp. 1211–1226.

8 Larock, B. E., "A Theory for Free Outflow beneath Radial Gates," *Journal of Fluid Mechanics*, Vol. 41, Part 4, 1970, pp. 851–864.

9 Southwell, R. V., and Vaisey, G., "Relaxation Methods Applied to Engineering Problems: XII, Fluid Motion Characterized by Free Streamlines," *Philosophical Transactions of the Royal Society*, London, Series A, Vol. 240, 1946, pp. 117–161.

10 Mogel, T. R., and Street, R. L., "A Numerical Method for Steady State Cavity Flows," *Journal of Ship Research*, Vol. 18, No. 1, 1974, pp. 22–31.

11 Chan, S. T. K., Larock, B. E., and Herrmann, L. R., "Free Surface Ideal Fluid Flows by Finite Elements," *Journal of the Hydraulics Division*, ASCE, Vol. 99, No. HY6, 1973, pp. 959–974.

12 Chan, S. T. K., and Larock, B. E., "Fluid Flows from Axisymmetric Orifices and Valves," *Journal of the Hydraulics Division*, ASCE, Vol. 99, No. HY1, 1973, pp. 81–96.

13 Varoglu, E., and Finn, W. D. L., "Variable Domain Finite Element Analysis of Free Surface Gravity Flow," *Computer and Fluids*, Vol. 6, 1977, pp. 103–114.

14 Liu, S. K., and Chow, W. L., "Numerical Solution of the Compressible Hodograph Equation," *American Institute of Aeronautics and Astronautics Journal*, Vol. 16, No. 2, 1978, pp. 188–189.

15 Chow, W. L., Han, T., and Wu, C., "Hydrodynamics Solution for Incompressible Flow as Influenced by Gravitation," *American Institute of Aeronautics and Astronautics Journal*, Vol. 16, No. 10, 1978, pp. 1097–1098.

16 Chow, W. L., and Han, T., "Inviscid Solution for the Problem of Free Overfall," ASME *Journal of Applied Mechanics*, Vol. 46, No. 1, 1979, pp. 1–5.

17 Han, T., and Chow, W. L., "The Study of Sluice Gates and Sharp-Crested Weir through Hodograph Transformation," paper to be published in ASME *Journal of Applied Mechanics*; also, presented at 1981 Joint ASME/ASCE Mechanical Conference, June 22–24, 1981, Boulder, Colo.

18 Shapiro, A. H., *The Dynamics and Thermodynamics of Compressible Fluid Flow*, Vol. 1, Ronald Press, New York, 1953, pp. 338–341.

19 Han, T., "Applications of Hodograph Transformation to Hydrodynamic Problems Influenced by Gravitation," Ph.D. thesis, Dept. of Mech. and Ind. Engr., University of Illinois at Urbana-Champaign, 1979.

Turbomachines—A Guide to Design Selection and Theory, by O. E. Balje, Wiley-Interscience, New York, 1981, 528 pp. Price: $49.95.

REVIEWED BY DAVID JAPIKSE

A first perusal through this volume immediately reveals its greatest strength: a very wide diversity of machine types and performance information is reported. It may have been more appropriate to title the book "A Compendium of Fluid Machinery Performance."

It is impossible to give justice to every aspect of this volume; consequently attention was focused on the axial turbine, centrifugal compressor and diffuser sections for this review. Cited references are sufficient to support a very good text and are notable for their covering the international literature quite well. The author clearly works from his years of experience and success as a consultant. He has developed an approach which has been useful for him and for several design groups. The book follows this historical basis which stresses a foundation of similitude and the comprehensive mapping of basic performance characteristics according to the dimensionless parameters.

While it is fair to stress the comprehensive nature of the text, it should be pointed out that the material is not all inclusive. The author has not attempted to bring in other diverse viewpoints but has remained true to his basic work and theme. Beginners to this field should understand that this approach is used by a number of workers with satisfaction, whereas many other successful design groups avoid the approach and follow other design techniques which are not covered in this volume. Although the volume presents preliminary design techniques, little attention is given to actual blade layout and the consideration of the computational procedures necessary to establish detailed turbomachinery passage configurations.

Presentation of the physical foundation for the basic processes varies in quality from topic to topic. The presentation for diffusers is comparatively weak; by contrast, the explanation of the basic processes for the centrifugal compressor impeller is comparatively strong. To illustrate, the diffuser section was introduced by a single equation and then an attempt was made to show how the performance of the diffuser could be computed by using a boundary layer computation technique. After several pages of text, it was shown that the approach had its strengths and weaknesses. While the comparison was interesting to this reviewer, it must be noted that an essential design issue was neglected: excellent data has been prepared for broad classes of diffusers which should be the first source of information for designers. These data were not referenced and designers were not pointed in this important direction. Further, no mention is made of some of the very advanced diffuser computational work that is taking place today and is becoming part of our advanced computational tools within the next several years. As in-

dicated, the treatment of the centrifugal compressor was comparatively strong with the very acceptable discussion of the basic processes which occur within the centrifugal compressor impeller.

This material can be used as an important reference source in advanced turbomachinery courses; however, it should be used as a textbook unless the instructor is thoroughly skilled in turbomachinery design and prepared to offer differing viewpoints and to supplement the students' understanding of the fundamental flow processes when necessary. The depth of material presented in this book is a remarkable resource and should be exploited in our advanced educational process.

Is the title appropriate? Yes, Dr. Balje fully meets the subjects mentioned in the title with principal emphasis on machinery selection, preliminary design layout and background theory when viewed as a compendium of valuable information from a seasoned expert in the field. Many workers should find this to be a very useful resource volume. In the opinion of this reviewer, it would be unwise for any worker in the field to work with this volume alone; to ignore the wealth of experience contained in this volume would be equally inappropriate.

Fundamentals of Gas-Particle Flow by G. Rudinger, Vol. 2 – Handbook of Powder Technology, Elsevier Scientific Publishing Company, 1980, 142 pages. Price: $53.75.

REVIEWED BY CLAYTON T. CROWE

This book serves as both a good introduction to gas-particle flows and an excellent source of reference material.

The book is essentially divided into two parts: the first part dealing with fundamental definition and phenomena of gas-particle flows and the second part with applications and experimental techniques. The first chapter introduces the reader to examples and definitions of gas-particle flow and points out features which distinguish gas-particle flows from flows of a homogeneous gas. The second chapter gives an excellent review of particle drag and heat transfer coefficients and concludes by defining equilibrium flows. The third chapter covers the dynamics of single particles in a variety of gas flow fields. The fourth chapter deals with the thermodynamics of gas-particle mixtures. One very important point discussed in this chapter is the fact that the pressure due to random motion of the particles is negligible, a point often confused in the analysis of gas-particle flows.

The remaining chapters deal with gas-particle flows in specific applications. Chapter five is concerned with steady flow in ducts and nozzles. Shock waves in gas-particle mixtures and method of characteristic solutions are covered in chapter six. Other important applications, gas-particle flow in